ICSSM 2025

Proceedings

10th International Congres of the Serbian Society of Mechanics

June 18-20, 2025

Niš, Serbia

Кнеза Милоша 7
11000 Београд

Република Србија
МИНИСТАРСТВО НАУКЕ,
ТЕХНОЛОШКОГ РАЗВОЈА И ИНОВАЦИЈА

ICSSM 2025

Proceedings

10th International Congres of the Serbian Society of Mechanics

June 18-20, 2025
Niš, Serbia

DOI: 10.46793/ICSSM25

Кнеза Милоша 7
11000 Београд

Република Србија
МИНИСТАРСТВО НАУКЕ,
ТЕХНОЛОШКОГ РАЗВОЈА И ИНОВАЦИЈА

Impressum

10th International Congress of the Serbian Society of Mechanics
Niš, Serbia, June 18-20, 2025

Editors
Simić Srboljub, Professor, PhD, University of Novi Sad, Serbia
Čantrak Đorđe, Professor, PhD, University of Belgrade, Serbia
Stojanović Vladimir, Associate Professor, PhD, University of Niš, Serbia
Simonović Julijana, Associate Professor, PhD, University of Niš, Serbia

Technical Editor
Simonović Julijana, Associate Professor, PhD, University of Niš, Serbia

Technical Assistant
Marija Stamenković Atanasov, Teach. Assistant, PhD, University of Niš, Serbia
Nikola Despenić, Teach. Assistant, PhD, University of Niš, Serbia
Dunja Miljković, Teach. Assistant, University of Niš, Serbia
Petar Miljković, Teach. Assistant, University of Niš, Serbia

Publisher
Serbian Society of Mechanics,
9/1 Kneza Miloša, 11000 Belgrade, Serbia

Supported by:
Ministry of Education, Science and Technological Development, R. Serbia by Decision on the Allocation and Disbursement of Funds No. 451-03-386/2025-03, from 25.03.25.

Press
Online: https://sdm.org.rs/congress/2025/docs/proceedings.pdf
https://doi.ub.kg.ac.rs/icssm25/

DOI: 10.46793/ICSSM25

Year
2025

ISBN 978-86-905512-1-7

Organizers

- **Serbian Society of Mechanics (SSM)**
- **Faculty of Mechanical Engineering, University of Niš**
- **Faculty of Civil Engineering and Architecture University of Niš**
- **University of Niš**
- **Science and Technology Park, Niš**
- **Mathematical Institute of Serbian Academy of Sciences and Arts**
- **Faculty of Mechanical Engineering, University of Belgrade**
- **Union of Engineers and Technicians of Serbia**

with the support of

- **Ministry of Science, Technological Development and Innovation, R. Serbia**

Sponsors

- **Prager Elektronik, Wolkersdorf, Austria (https://www.prager-elektronik.at/en/)**
- **Dantec Dynamics, Skovlunde, Denmark (https://www.dantecdynamics.com/)**
- **Spajic DOO, Negotin, Serbia (https://spajic.com)**
- **Elixir Prahovo, Prahovo, Serbia (https://www.elixirgroup.rs)**

Table of Contents

Welcome Messages

Dear Colleagues,

The Serbian Society of Mechanics is pleased to announce its 10th International Congress, to be held in the city of Niš, from June 18 to 20, 2025.

This year's Congress is hosted by the Faculty of Mechanical Engineering and the Faculty of Civil Engineering and Architecture at the University of Niš, in collaboration with the Science and Technology Park Niš. Co-organizers include the Mathematical Institute of the Serbian Academy of Sciences and Arts (SASA) and the Faculty of Mechanical Engineering, University of Belgrade. The event is supported by the Ministry of Science, Technological Development and Education of the Republic of Serbia, with additional sponsorship from Prager Elektronik.

Held biennially, the Congress serves as a vital forum for academic scientists, researchers, and scholars to share their latest findings and experiences in various branches of Theoretical and Applied Mechanics. This year, 7 Plenary Lectures and 2 Invited Lectures will be given by leading scientists from Canada, the USA, Brazil, Russia, Germany, and China. A total of 88 Contributed Talks will be presented across four Sections (General Mechanics, Fluid Mechanics, Solid Mechanics, and Applied Mechanics), as well as within four Mini-Symposia (Mechanical Metamaterials, Turbulence, Biomechanics and Mathematical Biology, and Nonlinear Dynamics). These contributions involve a total of 258 authors. We sincerely thank all contributors and participants for their valuable efforts and engagement, which are essential to the success of this Congress.

We are honored to welcome all participants to Niš, a city rich in history and culture, and a vibrant academic hub with significant scientific and technological potential. We trust that the Congress will provide a stimulating environment for the exchange of ideas and the establishment of new scientific collaborations.

We extend our warmest welcome to **the 10th International Congress of the Serbian Society of Mechanics** and look forward to your participation.

Sincerely,

Srboljub Simić

President of the Serbian Society of Mechanics

Dear Colleagues,

With sincere pleasure and deep respect, we extend to you the warmest welcome to the **10th International Congress of the Serbian Society of Mechanics**, hosted in the city of **Niš**—one of the **oldest continuously inhabited urban settlements in Europe**, a city that has for centuries stood at the crossroads of cultures, ideas, and civilizations.

Marking its jubilee edition, the Congress returns to Niš after three decades, proudly organized by the **Faculty of Mechanical Engineering** and the **Faculty of Civil Engineering and Architecture** at the **University of Niš**. This special occasion not only celebrates a long-standing tradition of scientific dialogue but also affirms a continued dedication to excellence, innovation, and international cooperation in the field of mechanics.

Established in 1960, **the Faculty of Mechanical Engineering** and **the Faculty of Civil Engineering and Architecture** in Niš have grown into key institutions in the region, committed to academic progress and technological advancement. In the years to come, these Faculties aspire to shape their identity as modern European academic institutions, embracing international standards, advancing the quality of research and education, nurturing young scientific talent, and encouraging multidisciplinary collaboration. Their goal is clear: to become institutions whose degrees are increasingly recognized, respected, and valued across borders.

At the forefront of this development stands the **Department of Mechanics**, whose internationally recognized achievements have enabled collaboration with esteemed researchers from all over the world. The Department proudly plays a **central role** in organizing this Congress, continuing its mission of fostering high-level academic exchange and promoting the values of curiosity, rigor, and cooperation.

We extend our **cordial invitation** to all participants and guests from around the world, and we look forward to welcoming you to **Niš**, from **June 18 to 20, 2025**, where professional excellence will be met with **genuine hospitality and shared inspiration**.

With our kindest regards and collegial greetings,

Prof. Dr. Vladimir Stojanović
Chair of the Organizing Committee

Prof. Dr. Julijana Simonović
Co-Chair of the Organizing Committee

Organizing Committee

Co-chairs:

Faculty of Mechanical Engineering, University of Niš:

- Vladimir Stojanović, president
- Julijana Simonović, vice president

Local Members:

Faculty of Mechanical Engineering, University of Niš:

- Goran Janevski
- Ivan Pavlović
- Marija Stamenković-Atanasov
- Nikola Despenić
- Dunja Milić
- Živojin Stamenković
- Jasmina Bogdanović-Jovanović
- Miloš Kocić
- Jelena Petrović
- Veljko Begović
- Petar Miljković

Faculty of Civil Engineering and Architecture University of Niš:

- Marina Trajković Milenković
- Predrag Petronijević
- Andrija Zorić
- Žarko Petrović
- Dragana Turnić
- Biljana Mladenović
- Marija Spasojević Šurdilović
- Slobodan Ranković

Faculty of Natural Sciences and Mathematics University of Niš:

- Marko Petković

International Scientific Committee

Adhikari Sondipon, Professor, *PhD, University of Glasgow, Scotland, United Kingdom*
Atanacković Teodor, Academician, *PhD, Serbian Academy of Sciences and Arts, Belgrade, Serbia*
Atanasovska Ivana, Research Professor, *PhD, Mathematical Institute SANU, Serbia*
Baleanu Dumitru, Professor, *PhD, Institute of Space Sciences, Bucharest, Romania,*
Bauer Svetlana, Professor, *PhD, Saint-Petersburg State University, Russia*
Borovac Branislav, Professor, *PhD, University of Novi Sad, Serbia*
Brojan Miha, Associate Professor, *PhD, University of Ljubljana, Slovenia*
Bulatović Ranislav, Professor, *PhD, University of Montenegro, Podgorica, Montenegro*
Carpinteri Alberto, **Professor,** *PhD, Politecnico di Torino***,** *Italy*
Chernousko Felix, Academician, *PhD, Russian Academy of Sciences***,** *Russia*
Charalambakis Nicolas, Professor Emeritus, *PhD, Aristotle University of Thessaloniki, Greece*
Challamel Noël, Professor, *PhD, University of South Brittany, France*
Chen Wen, Professor, *PhD, Hohai University, China*
Cvetićanin Livija, Professor, *PhD, University of Novi Sad, Serbia*
Čantrak Đorđe, Professor, *PhD, University of Belgrade, Serbia*
Ćoćić Aleksandar, Professor, *PhD, University of Belgrade, Serbia*
Dosaev Marat, Professor, *PhD, Lomonosov Moscow State University*, *Russia*
Dragović Vladimir, Research Professor, *PhD, Mathematical Institute SANU, Serbia*
Dunić Vladimir, Associate Professor, *PhD, University of Kragujevac, Serbia*
Elek Predrag, Professor, *PhD, University of Belgrade, Serbia*
Federico Salvatore, Professor, ***PhD,*** *University of Calgary, Canada*
Filipović Nenad, Professor, ***PhD,*** *University of Kragujevac, Serbia*
Frischmuth Kurt, Professor, ***PhD,*** *Universität Rostock, Germany*
Gajić Borislav, Research Professor, *PhD, Mathematical Institute SANU, Serbia*
Glavardanov Valentin, Professor, *PhD, University of Novi Sad, Serbia*
Golubović-Bugarski Valentina, Professor, *PhD, University Banja Luka, R. Srpska, BiH*
Grillo Alfio, Professor, *PhD, Politecnico di Torino, Università degli Studi di Catania, Italy*
Hedrih-Stevanović Katica, Research Professor, *PhD, Mathematical Institute SANU, Serbia*
Ibrahimbegović Adnan, Professor, ***PhD,*** *Universite Technologie Compiegne (Alliance Sorbonne Universite), France*
Jarić Jovo, Professor, *PhD, University of Belgrade, Serbia*
Jovanović Božidar, Research Professor, *PhD, Mathematical Institute SANU, Serbia*
Jovanović Jovan, Professor, *PhD, Friedrich-Alexander-University Erlangen-Nürnberg*, *Germany*
Jovičić Gordana, Professor, *PhD, University of Kragujevac, Serbia*
Karličić Danilo, Research Associate Professor, *PhD, Mathematical Institute SANU, Serbia*
Katsikadelis John, Professor Emeritus, *PhD, National Technical University of Athens***,** *Greece*
Kenjereš Saša, Professor, *PhD, Delft University of Technology, Netherlands*
Kienzler Reinhold, Professor Emeritus, *PhD, University of Bremen, Germany*
Kojić Miloš, Academician, *PhD, Serbian Academy of Sciences and Arts, Belgrade, Serbia*
Kounadis Anthony, Academician, *PhD, Academy of Athens, Greece*
Kovačić Ivana, Professor, *PhD, University of Novi Sad, Serbia*
Kozak Dražan, Professor, ***PhD,*** *University of Slavonski Brod***,** *Croatia*
Krasilnikov Pavel, Professor, *PhD, Lomonosov Moscow State University, Russia*
Kuzmanović Dragoslav, Professor, *PhD, University of Belgrade, Serbia*
Lacarbonara Walter, Professor, *PhD, Sapienza University of Rome, Italy*
Lanusse Patrick, Professor, *PhD, Institut Polytechnique de Bordeaux***,** *France*
Lazarević Mihailo, Professor,*PhD, University of Belgrade, Serbia*
Lečić Milan, Professor, *PhD, University of Belgrade, Serbia*
Makris Nikos, Professor, *PhD, University of Patras, Greece*
Maksimović Stevan, Professor, *PhD, Military Technical Institute, Belgrade, Serbia*

Programme at a glance of the 10th ICSSM

Day 1, June 18, 2025

Time	Activity
08:00 - 09:30	Registration
09:30 - 10:10	Opening Ceremony
10:15 - 11:00	Plenary Lecture 1
11:00 - 11:15	Short Break
11:15 - 12:00	Plenary Lecture 2
12:00 - 13:10	Lunch Break
13:10 - 13:55	Plenary Lecture 3
14:00- 15:00	Plenary Session for Laureate for Rastko Stojanović Award (40 min + 20 min for comments) - 10ICSSM – Milic - C - 10ICSSM - Vrecica - B
15:00 - 15:30	Coffee Break (transfer from NTP to MFN building)
15:30 - 16:30	Parallel Sessions: - Session A: 3 papers (45 min + 15 min for comments) - Session M4: 3 papers (45 min + 15 min for comments) - Session D: 3 papers (45 min + 15 min for comments) -Session M3: 3 papers (45 min + 15 min for comments)
16:30 - 17:00	Coffee Break
17:00 - 18:20	Parallel Sessions: - Session M2: 3 papers (65 min + 15 min for comments) - Session B: 4 papers (60 min + 20 min for comments) - Session M3: 3 papers (45 min + 15 min for comments) - Session M4: 3 papers (45 min + 15 min for comments)

Day 2, June 19, 2025

Time	Activity
09:00 - 09:45	Plenary Lecture 4
09:45 - 10:00	Short Break
10:00 - 10:45	Plenary Lecture 5
10:45 - 11:15	Coffee Break
11:15 - 12:45	Parallel Sessions: - Session B: 4 papers (60 min + 20 min for comments) - Session C: 4 papers (60 min + 20 min for comments) - Session D: 4 papers (60 min + 20 min for comments) - Session M1: 4 papers (60 min + 20 min for comments)
12:45 - 14:00	Lunch Break
13:15-14:00	Sponsor Presentation
14:00 - 14:45	Plenary Lecture 6
14:50 - 16:10	Parallel Sessions: - Session B: 4 papers (60 min + 20 min for comments) - Session C: 4 papers (60 min + 20 min for comments) - Session D: 4 papers (60 min + 20 min for comments) - Session M2: 3 papers (65 min + 15 min for comments)
16:10 - 16:20	Short Break
16:20 - 17:20	Parallel Sessions: - Session A: 3 papers (45 min + 15 min for comments) - Session D: 3 papers (45 min + 15 min for comments) - Session M4: 3 papers (45 min + 15 min for comments) - Session M3: 3 papers (45 min + 15 min for comments)
17:20 - 17:50	Coffee Break
17:50 - 19:00	SSM Annual and Election Assembly
17:50 - 19:00	Sightseeing tour of Niš Fortress
19:30 - 22:00	Gala Dinner

Day 3, *June 20, 2025*

Time	Activity
09:30 - 10:15	Plenary Lecture 7
10:15 - 10:25	Short Break
10:25 - 11:45	Parallel Sessions: - Session C: 4 papers (60 min + 20 min for comments) - Session D: 4 papers (60 min + 20 min for comments) - Session M1: 4 papers (60 min + 20 min for comments) - Session M2: 4 papers (60 min + 20 min for comments)
11:45 - 12:15	Coffee Break
12:15 - 12:40	Closing Ceremony

Technical programme of the 10th ICSSM

Day 1, *June 18, 2025*

08:00 - 09:30	**Registration** At the registration desk in **the Scientific Technology Park (STP)**
09:30 - 10:10	**Opening Ceremony** • ***Prof. Srboljub Simić***, President of SSM • ***Prof. Vladimir Stojanović***, President of the Organizing Committee • ***Milan Ranđelović,*** *PhD,* director of the Science and Technology Park (STP) in Niš • ***Prof. Nenad Filipović,*** Director of the Science Fund of the Republic of Serbia • A representative of the Ministry of Science, Technological Development and Innovation of the Republic of Serbia • ***Vladimir Dragović***, Editor-in-Chief of journal Theoretical and Applied Mechanics
10:15 - 11:00	**Plenary Lecture** **A robust shell finite element and nonlocal approaches in mechanics -** Prof. J.N. Reddy, *Texas A&M University, College Station, Texas, USA (10ICSSM-Reddy)* ***Room:*** Ceremonial Hall STP, ***Chair***: Prof. Vladimir Stojanović
11:00 - 11:15	Short technical break
11:15 - 12:00	**Plenary Lecture** **Resolution of the twentieth century conundrum in elastic stability –** Prof. I. Elishakoff, *Florida Atlantic University, Boca Raton, Florida, USA, (10ICSSM-Elishakoff),* ***Room:*** Ceremonial Hall STP, ***Chair***: Prof. Julijana Simonović
12:00 - 13:10	**Buffet lunch** (At the foyer of the Scientific Technology Park)
13:10 - 13:55	**Plenary Lecture** **Modeling of contact fatigue fracture of deformable bodies in frictional interaction –** Prof. I. Goryacheva*, Ishlinsky Institute for Problems in Mechanics RAS, Moscow, Russia, (10ICSSM- Goryacheva)* ***Room:*** Ceremonial Hall STP, ***Chair***: Prof. Katica (Stevanivić) Hedrih
14:00 - 15:00	**Session for Candidates for "Rastko Stojanović Award"** ***Room:*** Ceremonial Hall STP, ***Chair***: Prof. Ivan Pavlović • C.5 **- Comparative vibration stability analysis of a complex moving object with two novel stabilizers –** *Milic D. (10ICSSM - Milic - C)* • B.13 **- Infragravity waves –** *Vrecica T. (10ICSSM - Vrecica - B)*
15:00 - 15:30	**Coffee Break** (transfer from the STP to the FME building)
15:30 - 16:30	**Parallel Sessions**
Day 1, June 18 **15:30 - 16:30**	**Session A,** Room: **FME 608 A** **Chairs:** ***Gajic B.***, *Mathematical Institute SANU, Belgrade, Serbia*

3 papers (15 min + 5 min for comments every):

- A.1 **- On a stability of the beams with and without elastic foundation**– *Berecki A., Mihok S., Rehlicki Lukesevic L. (10ICSSM - Berecki et al. - A)*

- A.2 - **On the properties of friction to maintain the state of rest of a tripod on a rough surface** – *Dosaev M.* *(10ICSSM - Dosaev-A)*
- A.3 - **Bridging mechanics with statistics and geometry** – *Dragovic V., Gajic B.* *(10ICSSM - Dragovic and Gajic - A)*

Day 1, June 18 **15:30 - 16:30**	**Session M4,** Room: **FME 608 B** **Chairs:** ***Nestorovic T.,*** *Mechanics of Adaptive Systems, Ruhr-Universität Bochum, Germany* and ***Simonovic J.***, *Faculty of Mechanical Engineering, University of Nis, Serbia*

3 papers (15 min + 5 min for comments every):

- M.4.1 - **Motion analysis of a single-mass vibro impact system** – *Garic Lj, Nesic N., Lekic J., Jovanovic S., Stosovic D.* *(10ICSSM - Garic et al. - M4)*
- M.4.2 - **Asymptotic methods of nonlinear mechanics through a series of scientific projects, magister's and doctoral dissertations: nonlinear phenomena, trigger of coupled singularies and frequencies as bifurcation parameters** – *Stevanovic Hedrih K.* *(10ICSSM - Hedrih (Stevanovic) - M4)*
- M.4.4 - **Elliptical, circular orbits and applications** – *Mateljevic M.* *(10ICSSM - Mateljevic - M4)*

Day 1, June 18 **15:30 - 16:30**	**Session D,** Room: **FME 607 A** **Chairs:** ***Slavkovic N.***, *Faculty of Mechanical Engineering, University of Belgrade, Serbia*

3 papers (15 min + 5 min for comments every):

- D.1 - **Critical temperature of FGM plates resting on elastic foundations using layerwise finite element** – *Cetkovic M.* *(10ICSSM - Cetkovic - D)*
- D.2 - **A system engineering approach for robot manipulator design using game engine simulation and computational modelling** – *Devic A., Vidakovic J., Slavkovic N., Lazarevic M., Zivkovic N.* *(10ICSSM - Devic et al. - D)*
- D.3 - **Ballistic impact of fragment-simulating projectiles on steel targets: a multi-approach study** – *Elek P., Markovic M., Jevtic D., Djurovic R.* *(10ICSSM - Elek et al - D)*

Day 1, June 18 **15:30 - 16:30**	**Session M3,** Room: **FME 607 B** **Chairs:** ***Dosaev M.***, *Institute of Mechanics of Lomonosov Moscow State University, Russia*

3 papers (15 min + 5 min for comments every):

- M.3.1 - **Deformation of human chest as an elastic truss**– *Alpatov I., Dosaev M., Samsonov V., Vorobyeva E., Dubrov V.* *(10ICSSM - Alpatov et al. - M3)*
- M.3.2 - **Numerical simulations of blood flow in vessels with different geometries** – *Antonova N., Xu D.* *(10ICSSM - Antonova and Xu - M3)*
- M.3.3 - **A contiunous–time SIS criss–cross model of co–infection in a in heterogeneous population** – *Choiński M.* *(10ICSSM - Choinski - M3)*

16:30 - 17:00	**Coffee Break** (At the lobby area of sixth floor FME)
17:00- 18:20	**Parallel Sessions**
Day 1, June 18 **17:00 - 18:25**	**Session M2,** Room: **FME 607 A** **Chairs:** ***Cantrak Dj.***, *Faculty of Mechanical Engineering, University of Belgrade, Belgrade, Serbia* and ***Pei J.***, *NationalResearch Center of Pumps,*

	Jiangsu University, Zhenjiang, Jiangsu Province, China
Day 1, June 18 **17:00 - 17:40**	**Invited lecture** M.2.9 **- Towards the characterisation of flow perturbation transmission in convergent nozzles affecting free water jet surfaces** – Bernhard Semlitsch, *TU Wien, Institute of Energy Systems and Thermodynamics, Austria* *(10ICSSM - Semlitsch - M2)*

2 papers (15 min + 5 min for comments every):

- M.2.10 **-Comparison of noise spectra of the flow past a cylinder computed by different turbulence models** – *Svorcan J., Vilotijevic V. (10ICSSM - Svorcan and Vilotijevic - M2)*
- M.2.2 **-Application of air torque position dampers for airflow measurement** – *Bikic S., Radojcin M., Pavkov I., Debski H., Al Afif R. (10ICSSM - Bikic et al. - M2)*

Day 1, June 18 **17:00 - 18:20**	**Session B,** Room: **FME 608 A** **Chairs: *Bogdanovic Jovanovic J.***, *Faculty of Mechanical Engineering, University of Nis, Serbia* and **Kocic M.,** *Faculty of Mechanical Engineering, University of Nis, Serbia*

4 papers (15 min + 5 min for comments every):

- B.1 - **Gas flow blockage in the near-wellbore region: Freshwater stimulation against the salting-out effect** – *Afanasyev A., Grechko S. (10ICSSM - Afanasyev et al. - B)*
- B.2 - **Influence of rotation on drag coefficient and unsteady flow around an NFL ball** – *Begovic V., Miljkovic P, Stamenkovic Z., Kocic M. (10ICSSM - Begovic et al. - B)*
- B.3. - **Iterative procesure for determinig meridional streamlines of averaged flow in a turbomachine impeller** – *Bogdanovic Jovanovic J., Stamenkovic Z., Kocic M., Petrovic J. (10ICSSM - Bogdanovic Jovanovic et al. - B)*
- B.9. - **Numerical investigation of fluid mixing in a micromixer using CFD simulations** – *Mirovic M., Begovic V., Miljkovic P., Sreckovic D. (10ICSSM - Mirovic et al. - B)*

Day 1, June 18 **17:00 - 18:00**	**Session M3,** Room: **FME 607 B** **Chairs: *Antonova N. M.***, *Institute of Mechanics Bulgarian Academy of Sciences, Sofia, Bulgaria*

3 papers (15 min + 5 min for comments every):

- M.3.4 - **The physics of intelligence: can the fermionic mind hypothesis provide a theoretical framework for understanding consciousness?** – *Déli E., Kiss Z. (10ICSSM - Deli and Kiss - M3)*
- M.3.6 - **FSI analysis of parametric stent geometry influence on WSS-induced in-stent restenosis** – *Khairulin A., Kuchumov A. (10ICSSM - Khairulin and Kuchumov - M3)*
- M.3.5 - **Modelling zona pellucida as a thermosensitive polymer under mechanical load** – *Hedrih A., Jovanovic Dj. (10ICSSM - Hedrih and Jovanovic - M3)*

Day 1, June 18 **17:00 - 18:00**	**Session M4,** Room: **FME 608 B** **Chairs: *Lazarevic M.***, *Faculty of Mechanical Engineering, University of Belgrade, Serbia and* ***Simonovic J.***, *Faculty of Mechanical Engineering, University of Nis, Serbia*

3 papers (15 min + 5 min for comments every):

- M.4.6 - **Model identification of a locally nonlinear structure** – *Nestorovic T., Ul-Hasnain A., Oveisi A. (10ICSSM - Nestorovic et al. - M4)*
- M.4.7 - **Nonlinear pushover analysis: Assessment of a moment-resisting steel frame** – *Slavkovic K., Zoric A., Trajkovic Milenkovic M., Petronijevic P. (10ICSSM - Slavkovic et al. - M4)*

- M.4.5 - **Nonlinear vibration of a platform system with non-ideal motor** – *Nesic N., Simonovic J., Lima J., Balthazar J.M., Tusset A.M.* *(10ICSSM - Nesic et al. - M4)*

Day 2, *June 19, 2025*

Day 2, June 19 **09:00 - 09:45**	**Plenary Lecture** **Dynamic Stability of Structures under Multi-Hazards** – Prof. J. Deng, *Lakehead University, Thunder Bay, Ontario, Canada* *(10ICSSM- Deng)* ***Room:*** 611 FME, ***Chair:*** Prof. Vladimir Dragović
09:45 - 10:00	Short technical break
Day 2, June 19 **10:00 - 10:45**	**Plenary Lecture** **Strain-gradient crystal plasticity models for predicting microstructure, length-scale, and strain path sensitive deformation behavior of polycrystalline metals** – M. Knezevic, *University of New Hampshire, USA,* *(10ICSSM- Knezevic)* ***Room:*** 611 FME, ***Chair:*** Prof. Marina Trajković Milanković
10:45 - 11:15	**Coffee Break**
11:15 - 12:45	**Parallel Sessions**
Day 2, June 19 **11:15 - 12:45**	**Session B,** Room: **FME 608 A** **Chairs: *Madjarevic D***, *Faculty of Technical Science, University of Novi Sad, Serbia*

4 papers (15 min + 3 min for comments every):

- B.4 - **Numerical solutions of compressible gas flow in microtube in the continuum regime** – *Guranov I, Milicev S., Stevanovic N.* *(10ICSSM - Guranov et al. - B)*
- B.5 - **Magnetohydrodynamic (MHD) flow and heat transfer of electrically conducting micropolar fluid in a parallel plate channel with induced magnetic field** – *Kocic M., Stamenkovic Z., Bogdanovic Jovanovic J., Petrovic J., Nikodijevic Djordjevic M.* *(10ICSSM - Kocić et al. - B)*
- B.6 - **A macroscopic multi-temperature model with transport properties in comparison with kinetic models in the context of binary mixtures** – *Madjarevic D.* *(10ICSSM - Madjarevic - B)*
- B.7 - **On the modelling of korteweg fluids** – *Matic Z., Simic S.* *(10ICSSM - Matic and Simic - B)*

Day 2, June 19 **11:15 - 12:45**	**Session C**, Room: **FME 608 B** **Chairs: *Dunic V,*** *Faculty of Engineering, University of Kragujevac, Serbia*

4 papers (15 min + 5 min for comments every):

- C.1 - **Phase-field modeling of concrete: numerical simulation and experimental verification** – *Dunic V., Zivkovic M., Rakic D., Milovanovic V.* *(10ICSSM - Dunic et al. - C)*
- C.2 - **Prediction of free-edge stresses in composite laminates using full-layerwise-theory-based finite elements** – *Jocic E., Zivkovic M., Marjanovic M.* *(10ICSSM - Jocic et al. - C)*
- C.3 - **An estimate of penetration depth of rigid rods through materials susceptible to microcracking: Part 1 – theory** – *Mastilovic S.* *(10ICSSM - Mastilovic - C-1)*

- C.4. - **An estimate of penetration depth of rigid rods through materials susceptible to microcracking: Part 2 – validation and parameter sensitivity** – *Mastilovic S.* (*10ICSSM - Mastilovic - C-2)*

Day 2, June 19 **11:15 - 12:45**	**Session D**, Room: **FME 607 A** **Chairs: *Lazarevic M,*** *Faculty of Mechanical Engineering, University of Belgrade, Serbia and* ***Pavlovic I,*** *Faculty of Mechanical Engineering, University of Niš, Serbia*

4 papers (15 min + 5 min for comments every):

- D.4. - **Trapezoidal control for prevention of unwanted vibrations of mechanical systems** – *Formalskii A., Selyutskiy Y. (10ICSSM - Formalskii and Selyutskiy - D)*
- D.5. - **Motion analysis of a vibratory conveyor's trough during its operation** – *Ilic U., Lazarevic M., Veg E., Despotovic Z. (10ICSSM - Ilic - D)*
- D.6. - **PSO-based resonant controller for trajectory tracking of robot manipulator** – *Mandic P., Lazarevic M., Sekara T. (10ICSSM - Mandic et al-D)*
- D.12 - **Motion control of a copter with a slung load partially filled with liquid** – *Selyutskiy Y., Lokshin B., Holub A. (10ICSSM - Selyutskiy et al. - D)*

Day 2, June 19 **11:15 - 13:05**	**Session M1**, Room: **FME 607 B** **Chairs: *Paunović S.*,** *MISASA, Belgrade, Serbia* and ***Liang Y.***, *College of Mechanics and Engineering Science, Hohai University, Nanjing, China*

5 papers (15 min + 5 min for comments every):

- M.1.1 - **An overview of coupled mechanical problems including contact phenomena solved by FEA** – *Atanasovska I. (10ICSSM - Atanasovska - M1)*
- M.1.3 - **Machine-learning-based optimization design of combined seismic metamaterials** – *Fu Z., Ding Y., Chen H. (10ICSSM - Fu et al.- M1)*
- M.1.8 - **Upscaling anomalous transport in fractured media using fractional advection-dispersion equation model** – *Sun H.G. (10ICSSM - Sun - M1)*
- M.1.5 - **Simulation of thermal field in mass concrete structures with cooling pipes by the localized meshless method** – *Lin J., Hong Y.X.* (*10ICSSM - Lin and Hong- M1)*
- M.1.9- **Data-driven diffusion law for multiscale dynamics in granular materials via an improved deep physical symbolic regression**– *Yan S., Liang Y. (10ICSSM - Yan and Liang - M1)*

Day 2, June 19 **12:45 - 14:00**	**Buffet lunch** (At the lobby area of sixth floor FME)
13:15-14:00	**Sponsor's Presentation** (At the lobby area of sixth floor FME) Prager Elektronik, Wolkersdorf, Austria *https://www.prager-elektronik.at/en/*
Day 2, June 19 **14:00 - 14:45**	**Plenary Lecture** **Global Nonlinear Dynamics in the Analysis and Safety of Multistable Dynamical Systems** – P. B. Gonçalves, *Pontifical Catholic University of Rio de Janeiro, Brasil (10ICSSM- Gonçalve)* ***Room:*** 611 FME, ***Chair:*** Dr Anđelka Hedrih
14:50 - 16:10	**Parallel Sessions**

Day 2, June 19 14:50 - 16:10	**Session B,** Room: **FME 608 A** **Chairs:** ***Petrovic J,*** *Faculty of Mechanical Engineering, University of Niš, Serbia and* ***Kocic M****, Faculty of Mechanical Engineering, University of Niš, Serbia*

4 papers (15 min + 5 min for comments every):

- B.10 - **Particle dynamics in inertial microfluidics: review of forces and channel design principles** – *Oluski N., Zivkov A., Kozomora V., Bukurov M., Tasin S. (10ICSSM - Oluski et al. - B)*
- B.11 - **EMHD convection of a trihybrid nanofluid through a porous medium in a vertical channel with thermal radiation** – *Petrovic J., Nikodijevic Djordjevic M., Kocic M., Bogdanovic Jovanovic J., Stamenkovic Z. (10ICSSM - Petrovic et al-B)*
- B.12 - **Stability analysis of the generalized washburn equation**– *Rapajic I., Simic S. (10ICSSM - Rapajic and Simic - B)*
- B.14 - **Numerical simulation of isothermal rarefied gas flow between two plates** – *Vulicevic P., Milicev S., Stevanovic N. (10ICSSM - Vulicevic et al. - B)*

Day 2, June 19 14:50 - 16:10	**Session C**, Room: **FME 608 B** **Chairs:** ***Tomovic A,*** *Faculty of Mechanical Engineering, University of Belgrade, Serbia and* ***Pavlovic I,*** *Faculty of Mechanical Engineering, University of Niš, Serbia*

4 papers (15 min + 5 min for comments every):

- C.6 - **Energy based fatigue damage model** – *Perovic Z., Coric S., Koprivica M. (10ICSSM - Perovic et al. - C)*
- C.7 -**Vibration characteristics of 3D printed stepped cantilever beam** – *Pjevic M., Tomovic A., Veg M., Zoric N., Popovic M. (10ICSSM - Pjevic et al. - C)*
- C.8 - **Vibration characteristics of an optimized cantilever beam** – *Tomovic A., Pjevic M., Veg M., Obradovic A., Mitrovic Z. (10ICSSM - Tomovic et al. - C)*
- C.9 - **Predictive reanalysis in structural dynamics** – *Trisovic N., Mankovits T., Petrovic A. (10ICSSM - Trisovic et al. - C)*

Day 2, June 19 14:50 - 16:10	**Session D**, Room: **FME 607 A** **Chairs:** ***Simic V****, Institute for Information Technologies, University of Kragujevac, Serbia*

4 papers (15 min + 5 min for comments every):

- D.11 - **Truss structure optimization using particle swarm optimization with direct FEM coupling** – *Ristic O., Trisovic N. (10ICSSM - Ristic and Trisovic - D)*
- D.8 - **Data-driven nonlinear modelling of recycled aggregate concrete-filled steel tube columns** – *Nikolic J., Tosic N., Kostic S. (10ICSSM - Nikolic et al. - D)*
- D.9 - **Design and experimental verification of the composite blade of the main rotor of an unmanned helicopter** – *Radulovic R., Milic M. (10ICSSM - Radulovic and Milic - D)*
- D.17 - **ILC-MPC controller for robotic manipulators based on the ultra-local model**– *Zivkovic N., Lazarevic M., Vidakovic J., Mandic P. (10ICSSM - Zivkovic et al. - D)*

Day 2, June 19 14:50 - 16:10	**Session M2**, Room: **FME 607 B** **Chairs:** ***Svorcan J.****, Faculty of Mechanical Engineering, University of Belgrade, Belgrade, Serbia and* ***Semlitsch B.****, Institute of Energy Systems and Thermodynamics, TU Wien, Vienna, Austria*
Day 2, June 19 14:50 - 15:30	**Invited lecture** M.2.4 - **Approaching a modified swarm intelligence in hydraulic optimization of an inline pump,** *Xingcheng Gan,*

	Coauthors: Prof. Ji Pei, Assoc. Prof. Wenji Wang, Prof. Jia Chen and Prof. Shouqi Yuan, National Research Center of Pumps, Jinagsu University, China (10ICSSM - Gan - M2)

2 papers (15 min + 5 min for comments every):

- M.2.6 - **LES for modelling wind flow in urban block: accuracy, challenges and applications** – *Kostadinovic Vranesevic K., Jockovic M., Glumac A. (10ICSSM - Kostadinovic Vranesevic et al. - M2)*
- M.2.11 - **Transient simulation on internal flow characteristics and pressure pulsation of variable speed Francis turbines during acceleration process**– *Wang W., Liu S., Pei J. (10ICSSM - Wang et al. - M2)*

16:10 - 16:20	Short technical break
16:20 - 17:20	**Parallel Sessions**
Day 2, June 19 **16:20- 17:20**	**Session A**, Room: **FME 608 A** **Chairs:** ***Spasic D***, *Faculty of Technical Science, University of Novi Sad, Serbia*

3 papers (15 min + 5 min for comments every):

- A.5 - **New rheological discrete dynamic systems of the fractional type rheological oscillator or creeper type: An overview of author's new research results** – *Stevanovic Hedrih K. (10ICSSM - Hedrih (Stevanovic) - A)*
- A.4 - **Magnetic flows on spheres** – *Dragovic V., Gajic B., Jovanovic B. (10ICSSM - Dragovic et al. - A)*
- A.6 - **A simple engineers-friendly method for non-holonomic systems** – *Spasic D. (10ICSSM - Spasic - A)*

Day 2, June 19 **16:20 - 17:20**	**Session D,** Room: **FME 607 A** **Chairs:** ***Trisovic N***, *Faculty of Mechanical Engineering, University of Belgrade, Serbia*

3 papers (15 min + 5 min for comments every):

- D.7. - **Computational modeling of drug transport from drug coated ballons (DCB)** – *Milosevic M., Milicevic B., Simic V., Nikolic A., Filipovic N., Kojic M. (10ICSSM - Milosevic et al. - D)*
- D.13 - **Computational modeling and parametric study of circulating tumor cells motion through capillaries and interaction with non/ thrombin activated platelets** – *Simic V., Milosevic M., Nikolic A., Ning S., Leonard F., Liu X., Kojic M. (10ICSSM - Simic et al. - D)*
- D.14 - **Kinematics modeling of compliant and extensible stewart-like platform** – *Tanaskovic N., Lazarevic M., Krkljes D. (10ICSSM - Tanaskovic et al. - D)*

Day 2, June 19 **16:20 - 17:20**	**Session M4,** Room: **FME 608 B** **Chairs:** ***Nesic N.***, *University of Pristina in Kosovska Mitrovica, Faculty of Technical Sciences, Serbia*

3 papers (15 min + 5 min for comments every):

- M.4.3 - **A novel finite time stability analysis of a class nonlinear fractional order multi-state time delay systems: a new gronwall - bellman inequality approach** – *Lazarevic M., Pisl S., Radojevic D. (10ICSSM – Lazarevic et al. - M4)*
- *M.4.8* - ***The influence of the radius of curvature on the forced oscillations of an elastically coupled system of two doubly curved shallow nano-shells*** – *Stamenkovic Atanasov M., Simonovic J., Pavlovic I. (10ICSSM - Stamenkovic Atanasov et al. - M4)*
- M.4.9 - **Convergence of analytical-numerical algorithm for inverse kinematics of Niryo One robot** – *Todorovic V., Nesic N., Jovic S. (10ICSSM - Todorovic et al. - M4)*

Day 2, June 19 16:20 - 17:20	**Session M3**, Room: **FME 607 B** **Chairs:** ***Dosaev M.***, *Institute of Mechanics of Lomonosov Moscow State University, Russia*

3 papers (15 min + 5 min for comments every):

- M.3.7 - **A tailed robot on three supports** – *Klimina L.* *(10ICSSM - Klimina - M3)*
- M.3.8 - **A numerical study of the Belousov-Zhabotinsky reaction network** – *Macesic S., Ivanovic Sasic A., Cupic Z.* *(10ICSSM - Macesic et al. - M3)*
- M.3.9 -**Biomechatronic system for monitoring eating behaviour**–*Magomedov M., Magomedov R.* *(10ICSSM - Magomedov and Magomedov - M3)*

17:20 - 17:50	**Coffee Break** (At the lobby area of sixth floor FME)
Day 2, June 19 **17:50 - 19:00**	**SSM Annual and Election Assembly** Room: 611 FME
Day 2, June 19 **17:50 - 19:00**	**Sightseeing tour** Walk and Guided Tourof Niš Fortress
Day 2, June 19 **19:30 - 22:00**	**Gala Dinner** (The banquet hall at New City Hotel & Restaurant in Niš)

Day 3, *June 20, 2025*

Day 3, June 20 **09:30 - 10:15**	**Plenary Lecture** **Dimension Reduction in Elasticity** - R. Kienzler, *University of Bremen, Germany ,* *(10ICSSM- Kienzler)* ***Room:*** 611 FME, ***Chair:*** Prof Srboljub Simić
10:15 - 10:25	Short technical break
10:25 - 11:45	**Parallel Sessions**
Day 3, June 20 **10:25 - 11:25**	**Session C**, Room: **FME 608 B** **Chairs:** ***Šalinic S.,*** *Faculty of Mechanical and Civil Engineering in Kraljevo, University of Kragujevac, Serbia*

3 papers (15 min + 5 min for comments every):

- C.10 - **Mode orthogonality conditions of spatial vibrations of an Euler-Bernoulli cantilever beam with an eccentric rigid tip load** – *Veg M., Tomovic A., Obradovic A., Salinic S., Selyutskiy Y.* *(10ICSSM - Veg et al. - C)*
- C.11 - **Friction Stir Welding – Thermo-mechanical quantities and energy dissipation for different joint shapes** – *Veljic D., Medjo B., Radovic N., Radosavljevic Z., Mihajlovic D., Sedmak A.* *(10ICSSM - Veljic et al. - C)*
- C.12 - **Generalized Einstein tensor for euclidean surfaces with mechanical point of view** – *Vesic N., Slavkovic K.* *(10ICSSM - Vesic et al. - C)*

Day 3, June 20 **10:25 - 11:25**	**Session D**, Room: **FME 607 A** **Chairs:** ***Petronijevic P.,*** *Faculty of Civil Engineering and Architecture, University of Niš, Serbia*

3 papers (15 min + 5 min for comments every):

- D.15 - **Inverse kinematics solutions of robotic manipulators using Paden-Kahan subproblems and screw theory**– *Todorovic V., Nesic N., Lazarevic M.* *(10ICSSM - Todorovic et al. - D)*
- D.16 - **Analysis of steel plate girders subjected of patch loading with geometrical and structural imperfections** – *Turnic D., Spasojevic Surdilovic M., Zivkovic S., Petrovic Z., Petronijevic P.* *(10ICSSM - Turnic et al. - D)*
- D.10 - **Different types of the deformed exponential functions in the statistical mechanics** – *Rajkovic P., Marinkovic S., Stankovic M.* *(10ICSSM - Rajkovic et al. - D)*

Day 3, June 20 **10:25 - 11:45**	**Session M1**, Room: **FME 607 B** **Chairs:** ***Atansovska I.,*** *MISASA, Belgrade, Serbia,* ***Fu Z.,*** *College of Mechanics and Engineering Science,Hohai University, China*

4 papers (15 min + 5 min for comments every):

- M.1.2 - **Shear striping phenomena in viscoelastic liquid crystal elastomers**– *Cajic M., Karlicic D., Paunovic S.* *(10ICSSM - Cajic et al. - M1)*
- M.1.4 - **A finite electro-viscoelastic model for nematic liquid crystal elastomers** – *Karlicic D., Cajic M., Paunovic S.* *(10ICSSM - Karlicic et al. - M1)*
- M.1.6 - **Application of soft MREs for magnetically induced actuation with implementation in FEniCSx**– *Paunovic S., Karlicic D., Cajic M.* *(10ICSSM - Paunovic et al. - M1)*

- M.1.7 - **Inertial amplification effects on wave dispersion in metastructures with elastic and rigid segments** – *Rosic N., Karlicic D., Lazarevic M.* *(10ICSSM - Rosic at al. - M1)*

Day 3, June 20 **10:25 - 11:45**	**Session M2**, Room: **FME 608 A** **Chairs: *Ilić D.***, *Faculty of Mechanical Engineering, University of Belgrade, Belgrade, Serbia and* ***Bikić S.***, *Faculty of Agriculture, University of Novi Sad, Novi Sad, Serbia*

4 papers (15 min + 5 min for comments every):

- M.2.5 - **A short discussion on the circulation in the turbulent swirling flow in the axial fan jet** – *Jankovic N., Cantrak Dj, Ilic D.* *(10ICSSM - Jankovic et al. - M2)*
- M.2.7 - **Numerical study of natural convection in a square enclosure with a circular cylinder at different vertical positions** – *Milosavljevic N., Radenkovic D.* (*10ICSSM - Milosavljevic and Radenkovic - M2)*
- M.2.3 - **Analysis of turbulent swirling flow in a pipe downstream of an axial fan impeller: experimental and numerical approach** – *Bulajic M., Jankovic N., Lecic L., Cantrak Dj.* *(10ICSSM - Bulajic et al. - M2)*
- M.2.1 - **PIV experiment in a scaled operating room with laminar airflow ventilation** – *Angiero T., Discetti S., Ianiro A. (online)* *(10ICSSM - Angiero et al. - M2)*

11:45 - 12:15	**Coffee Break** (At the lobby area of sixth floor FME)
Day 3, June 20 **12:15 - 12:40**	**Closing Ceremony** Room: 611 FME

Plenary Lectures

Dynamic Stability of Structures under Multi-Hazards

Thuesday, June 19, 2025

09:00 - 09:45

Dr. Jian Deng is a Professor at Lakehead University with 30 years of experience in Engineering Sciences. Specializing in dynamic stability and structural reliability, he advances theories and techniques for analyzing and designing underground excavations, structural elements, and engineering systems. He holds a Ph.D. from the University of Waterloo, Canada, and is passionate about research, teaching, and programming.

Natural hazards pose significant risks to people and infrastructure worldwide. Traditional stability assessment approaches often focus on individual hazards, overlooking the cumulative and cascading effects of multi-hazard scenarios. This can lead to inaccurate stability estimations, as the combined impact of multiple hazards—such as earthquakes, vibrations, landslides, and water waves—may differ significantly from the sum of their individual effects.

This talk explores the dynamic stability of structures under multi-hazard conditions, using pile foundations in Lake Superior as a case study. The equations of motion for pile foundations subjected to multiple excitations are derived using Hamilton's principle. Analytical and numerical methods are employed to identify dynamic instability regions, with a particular focus on parametric resonances. The numerically accurate diagrams are used to calibrate the approximate analytical instability boundaries of various orders of the method harminc balance. The numerical method can also overcome the limitations of small-parameter assumptions inherent in perturbative and averaging techniques. The findings provide new insights into structural behavior under complex hazard interactions, contributing to more robust and resilient infrastructure design.

Resolution of the Twentieth Century Conundrum in Elastic Stability

Wednesday, June 18, 2025

11:15 - 12:00

.

Isaac Elishakoff is a Distinguished Research Professor at Florida Atlantic University, USA, with 54 years of experience in theoretical and applied mechanics. His expertise spans probabilistic and deterministic mechanics, composite materials, nanotechnology, structural stability, vibrations, and functionally graded structures. He earned his Ph.D. from the Moscow Power Engineering Institute and State Research University. Professor Elishakoff is the author of over 620 scientific papers and has

This lecture deals with the buckling of some structural elements in mechanical, aerospace, ocean, and marine engineering. For beams and plates, the theoretical and experimental values of buckling loads are in close vicinity. However, for stability of thin shells, the experimental predictions do not conform with the theory, due to presence of small geometric imperfections that are deviations from the ideal shape. This fact of discrepancy has been characterized to in the literature as ‘embarrassing’, ‘paradoxical,’ and ‘perplexing.’

Indeed, the popular adage, “In theory there is no difference between theory and practice. In practice there is”, very much applies to thin shells whose experimental buckling loads may constitute a small fraction of the theoretical prediction based on classical linear theory. Therefore, in practice, engineers use knockdown factors that are not theoretically substantiated.

This lecture presents a probabilistic approach that tames this prima-donna-like and capricious behaviour of structures that has been dubbed as ‘imperfection sensitive’ — thus resolving the conundrum that has occupied the best minds of elastic stability throughout the twentieth century, including Theodore von Kármán of RWTH Aachen University and Caltech, Warner Koiter of TU Delft, Bernard Budiansky of Harvard, Vladimir Bolotin of Russian Academy of Sciences, and others.

Global Nonlinear Dynamics in the Analysis and Safety of Multistable Dynamical Systems

Thuesday, June 19, 2025

14:00 - 14:45

Paulo Batista Gonçalves is an Emeritus Professor at the Pontifical Catholic University of Rio de Janeiro, PUC-Rio with 45 years of experience in Structural Stability and Dynamics. Specializing in Nonlinear Dynamics, Paulo B. Gonçalves has successfully published More than 500 articles published in the areas of structural instability and nonlinear dynamics. Organizer and editor of several national and international conferences. Editorial board of Nonlinear Dynamics, Meccanica, Proceedings of the Institution of Mechanical Engineers, Part C and REM International Engineering Journal. Paulo B. Goncalves holds a D.Sc. from Federal University of Rio de Janeiro and post-doctorate from University College Londonand is passionate about the interplay between stability and global dynamics.

In recent years, an increasing number of investigations have been published on the advantageous use of buckling in science and diverse engineering fields. These applications include actuators, energy harvesters, micromechanical systems (MEMS), robotics, energy absorbers, and metamaterials, among others. Researchers have proposed various structural systems, materials, and fabrication procedures. Special attention has been given to bistable and multistable structures—those with two or more stable configurations at the same load level, particularly those exhibiting snap-through buckling. Many of these systems consist of chains of bistable elements, flexibly or rigidly connected, which respond to applied loads or displacements in a progressive manner. However, their nonlinear dynamic behavior and stability remain poorly understood. To analyze these systems and ensure their safety, global dynamic analysis tools are essential. These tools enable investigation of the interplay between coexisting solutions. This presentation focuses on the nonlinear global dynamics of such systems and the appropriate design tools.

Modeling of Contact Fatigue Fracture of Deformable Bodies in Frictional Interaction

Wednesday, June 18, 2025

13:10 - 13:55

Irina Goryacheva is a Professor and Head of the Tribology Laboratory of Ishlinsky Institute for Problems in Mechanics RAS with more than 50 years of experience in the Mechanical Engineering. Specializing in thecontact mechanics, Irina Goryacheva is the author of more than 200 papers and 8 books and has developed analytical methods of solutions of various contact mechanics problems taking into account friction and wear of contacting bodies. Irina Goryacheva holds a Ph.D. degree from Lomonosov Moscow State University and is passionate about microgeometry effects in contact interaction.

The accumulation of contact fatigue damage is one of the main causes of the fracture of the surface layers of the contacting bodies in cyclic loading. This process exists at different scales: at microscale, it leads to fatigue wear of friction pair materials, at macroscale - to the formation of contact fatigue cracksunder the contacting surfaces.

The approach to modeling the contactfatigue fracture of deformable bodies under cyclic loading is based on calculation of a damage function, which depends on the amplitude values of the internal stressesinside the contacting bodies. These stresses are determined by both the macro- and microgeometry of the contacting bodies.

The lecture provides the approach for studying the contact and internal stresses and modeling the accumulation of fatigue damage in sliding and rolling with slippage of elastic bodies of given shapes. The influence of the contact conditions on the subsurface damage accumulation process and fatigue crack formation is analyzed. The similar approach is also used to study the contact fatigue wear process for the given surface microgeometry and loading conditions.

Dimensional Reduction in Elasticity

Friday, June 20, 2025
09:30 - 10:15

R. Kienzler is a professor i.R. at the University of Bremen, Germany, with 50 years of experience in applied mechanics specializing in fracture, material and structural mechanics. R. Kienzler was Editor-in-Chief of the Archive of Applied Mechanics and Vice Secretary of the GAMM. He published ten books and about 250 papers in scientific journals. R. Kienzler is Honorary Member of the Polish and the Hellenic Societies of Theoretical and Applied Mechanics and holds a Dr. h.c. from the Ilia Vekua Institute of Applied Mathematics of the Ivane Javakhishvili Tbilisi State University, Georgia.

Consistent two- and one-dimensional theories are derived from the three-dimensional theory of linear elasticity by the combination of the uniform-approximation method with the pseudo-reduction technique. Well-known equations and extended theories for structural components both for two-dimensional members as plates and discs as well as one-dimensional members as bars, beams and shafts. Neither a-priori assumptions nor any correction factors are invoked.

Strain-gradient Crystal Plasticity Models for Predicting Microstructure, Length-Scale, and Strain Path Sensitive Deformation Behavior of Polycrystalline Metals

Thuesday, June 19, 2025

10:00 - 10:45

Marko Knezevic earned his BS degree in Mechanical Engineering from the University of Novi Sad (Serbia) in 2004 and his Ph.D. in Materials Science and Engineering from Drexel University in 2009. After graduate school, he joined Scientific Forming Technologies Corporation in Columbus, OH from 2009 to 2011 as a principal research scientist for development of the commercial finite-element software DEFORM used for analysis of manufacturing processes. After industrial experience, he was with the Materials Science and Technology Division at Los Alamos National Laboratory in Los Alamos, NM from 2011 to 2013 as the LANL Seaborg Institute Postdoctoral Fellow. He then joined the faculty of the Mechanical Engineering Department at the University of New Hampshire. Prof. Knezevic's research is focused on understanding of materials behaviour under complex loading using a combination of computational methods and experiments, development of constitutive material models, design and manufacturing at component levels, materials design at microstructural length scales, as well as the development of high-performance computational applications integrating multi-scale material models for predicting materials behaviour. His work has produced about 250 archival journal articles

The presentation will begin by summarizing a full-field strain-gradient (SG) crystal plasticity finite element (CPFE) model, which considers the roles of microstructural length-scales. The potential and utility of the model to simulate mechanical response, strain gradients, and associated slip-system level geometrically necessary dislocations (GNDs) will be demonstrated via a few simulation case studies involving a set of strain-path change deformation conditions of AA6016. A high-fidelity verification of the predicted GNDs will involve comparisons with those observed using 3D structures extracted, via serial sectioning, following application of the strain paths. A key limitation of such SG-CPFE modeling pertains to the scale and requirements for microstructural meshes of explicit grain structures. In light of this, the subsequent part of the presentation will describe a formulation of a homogenization-based SG formulation linking micro-scale single-crystal to meso-scale polycrystalline aggregate to macro-scale component level modeling of geometrical shape changes under complex deformation boundary conditions while predicting mechanical response and microstructural evolution.

A Robust Shell Finite Element and Nonlocal Approaches in Mechanics

Wednesday, June 18, 2025

10:15 - 11:00

Dr. Reddy is a Distinguished Professor, Regents' Professor, and the holder of the O'Donnell Foundation Chair IV in Mechanical Engineering at Texas A&M University, College Station, Texas. Dr. Reddy, an ISI highly cited researcher, is known for his significant contributions to the field of applied mechanics through the authorship of a large number of textbooks (25) and journal papers (>800). His pioneering works on the development of shear deformation theorieshave had a major impact and have led to new research developments and applications. In recent years, Reddy's research has focused on thedevelopment of locking-free shell finite elements and nonlocal and non-classical continuum mechanics problems dealing with architected materials and structures and damage and failures in brittle solids

The lecture consists of the speaker's recent research in: (1) the development of higher-order, locking-free shell finite element for large deformation of laminated and functionally graded plate and shell structures (G.S. Payette and J.N. Reddy, Computational Methods in Applied Mechanics and Engineering, 278, 664-704, 2014) and (2) nonlocal approaches for modeling architected materials and structures and fracture in brittle solids (Praneeth Nampally, Anssi Karttunen, and J.N. Reddy, European Journal of Mechanics, A/Solids, 74, 431-439, 2019; P. Thamburaja, K. Sarah, A. Srinivasa, J.N. Reddy, Proceedings of the Royal Society A, 477 (2021) 20210398). The seven-, eight-, and twelve-parameter shell elements developed are based on modified first-order and third-order thickness stretch kinematics, and they require the use of fully three-dimensional constitutive equations. Through the numerical simulation of carefully chosen benchmark problems, it is shown that the developed shell elements are insensitive to all forms of numerical locking and are the best alternative to 3-D finite elements in saving computational resources while predicting accurate stresses. A non-local continuum model that accounts for material and/or structural length scales in a phenomenological way through the micromorphic plate theory to model architected materials and structures (e.g., web-core sandwich panels) is also discussed and its accuracy compared to 3D finite elements is brought out through numerical examples. In addition, a thermodynamically consistent fracture model for brittle and quasi-brittle solids based on Graph-based Finite Element Analysis (GraFEA) with appliocations to concrete structures.

Contributed Talks and Papers

A: General Mechanics

10th International Congress of the Serbian Society of Mechanics
Niš, Serbia, June 18-20, 2025

A.1
Original Scientific Paper
DOI:10.46793/ICSSM25.032B

ON A STABILITY OF THE BEAMS WITH AND WITHOUT ELASTIC FOUNDATION

Armin D. Berecki[1][0000-0001-5694-3161]**, Sanja J. Mihok**[1][0000-0003-4297-4527]**,**
Lidija Z. Rehlicki Lukešević[1][0000-0002-1741-9014]

[1] Faculty of Technical Sciences,
The University of Novi Sad, Trg Dositeja Obradovića 6, 21000 Novi Sad
e-mail: armin@uns.ac.rs, sanjao@uns.ac.rs, lidijarl@uns.ac.rs

Abstract:

In this paper, we analyze the stability of the four beams with different types of boundary conditions on a Winkler-type elastic foundation. We examine both the nonlinear and linearized problems for all beams. We show influence of boundary conditions on the number of solutions for the unique values of the critical force and foundation stiffness. Finally, we compared results of this analysis with the results of classical Euler's axially loaded rods for several types of boundary conditions without elastic foundation.

Key words: stability, beams, boundary conditions, elastic foundation

1. Introduction

The stability analysis of elastic rods started with the famous work of Euler in 1744, when Euler used a static method to determine the stability boundary of axially loaded rods for several types of boundary conditions. Result of that analysis is presented in [1]. The basis of Euler's analysis lies in the fact that under the same boundary conditions and load, a beam can exist in equilibrium in several different positions. From this it follows that the question whether some equilibrium position is stable reduces to the question of whether the system basic equation of the plane deformation of the rod has one or more solutions. Analyzing the equations describing equilibrium often involves solving systems of nonlinear equations, therefore, in each specific case, the relationship between the linearized and nonlinear problems must be carefully examined. One of the methods for such analysis is the so-called alternative method, which is based on the Lyapunov-Schmidt reduction procedure (see [4], [5]).

Beams on elastic foundations are frequently used in structures and their stability analysis has been in the focus of attention of the researchers for many years. In this paper were chosen the beams with four different boundary conditions similar to classical Euler's beams but all on a Winkler-type elastic foundation. This Winkler model treats foundation as a system of mutually independent springs, assuming that pressure at the observed point of the base causes the deflection of that point only. Thus, the properties of the base are described only by one parameter μ which represents the stiffness coefficient of the soil. Although it is the simplest base model, it has a wide practical application. Many articles such as [2], [3], consider beams on Winkler foundation where authors analyzed stability of an elastic simply supported beam on the Winkler type elastic foundation.

In this paper, four elastic beams with different boundary conditions (simple supported beam, cantilever simple supported beam, rigidly fixed beam and cantilever beam) on an elastic Winkler-type foundation are analyzed. A fully nonlinear equilibrium equation and linearized problem are examined. The solutions for each beam are shown and a comparison of the results with beams of the corresponding boundary conditions only without elastic lining is given.

2. Formulation of the problem

Consider four elastic beams of length L positioned on a Winkler type elastic foundation. The four types of beams are shown in Figure 1: a) simply supported beam, b) cantilever simple supported beam, c) rigidly fixed beam and d) cantilever beam.

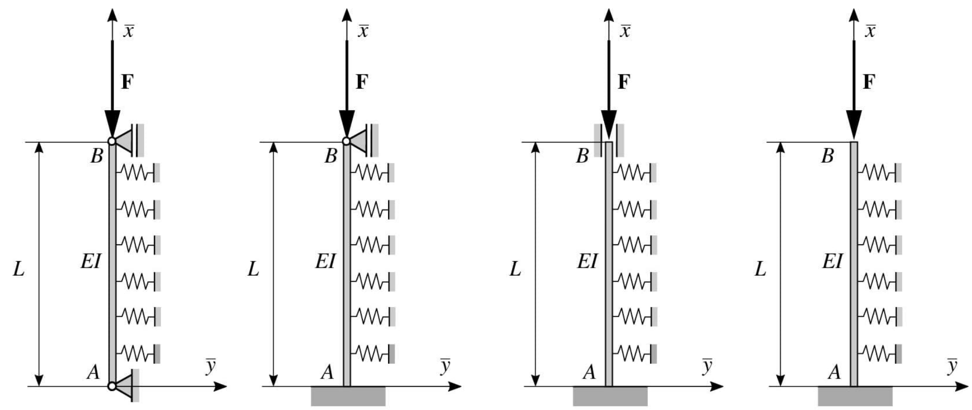

Fig. 1. Beams with four types of boundary conditions on a Winkler-type elastic foundation

All beams have constant cross-sectional area, they are inextensible and loaded at point B (see Figure 1) by axial compressive force F which is coincident with x axes. Equilibrium equations for the rod are:

$$H' = 0; \quad V' = \mu \bar{y}; \quad M' = -V\cos\theta + H\sin\theta \, ; \tag{1}$$

where μ is constant stiffness of the foundation. Note that $(\cdot)' = d(\cdot)/dS$ represent derivatives with respect to S which is the arc-length of the rod axis. H and V are components of the contact force in an arbitrary section of the rod along $\bar{x}$ and $\bar{y}$ axes, respectively, M is the bending moment, and θ is the angle between the tangent to the column axis and the $\bar{x}$ axis. Geometrical relations are:

$$\bar{x} = \cos\theta; \qquad \bar{y} = \sin\theta; \tag{2}$$

and the constitutive equation is:

$$M = EI\frac{d\theta}{dS}; \tag{3}$$

where E is the modulus of elasticity and I is the moment of inertia of the cross section. Relation (3) corresponds to the classical Bernoulli-Euler rod theory.

Boundary conditions for each rod in Figure 1 are given below, respectively:

a) $\bar{x}(0)=0; \quad \bar{y}(0)=\bar{y}(L)=0; \quad M(0)=M(L)=0; \quad H(L)=-F;$ (4)

b) $\bar{x}(0)=0; \quad \bar{y}(0)=\bar{y}(L)=0; \quad \theta(0)=M(L)=0; \quad H(L)=-F;$ (5)

c) $\bar{x}(0)=0; \quad \bar{y}(0)=\bar{y}(L)=0; \quad \theta(0)=\theta(L)=0; \quad H(L)=-F;$ (6)

d) $\bar{x}(0)=0; \quad \bar{y}(0)=V(L)=0; \quad \theta(0)=M(L)=0; \quad H(L)=-F;$ (7)

2.1 Nonlinear problem

Horizontal component of the contact force is obtained by solving $(1)^1$ and by using $(4)^4$:

$$H=-F. \tag{8}$$

Trivial solution of the system (1)-(3) is

$$\begin{aligned} &H^0=-F; \quad V^0=0; \quad M^0=0; \\ &x^0=S; \quad y^0=0; \quad \theta^0=0; \end{aligned} \tag{9}$$

where the axis of the rod remains straight. Let $H = H^0 + \Delta H$, $V = V^0 + \Delta V$, ... This results with:

$$\begin{aligned} &H=-F+\Delta H; \quad V=\Delta V; \quad M=\Delta M; \\ &x=S+\Delta x; \quad y=\Delta y; \quad \theta=\Delta\theta. \end{aligned} \tag{10}$$

Substituting (10) into the system of equation (1)-(3) the nonlinear system of equations is obtained as given:

$$\begin{aligned} &\Delta H'=0; \quad \Delta V'=\mu\Delta y; \quad \Delta M'=-\Delta V\cos\Delta\theta+(-F+\Delta H)\sin\Delta\theta; \\ &\Delta x'=\cos\Delta\theta-1; \quad \Delta y'=\sin\Delta\theta; \quad \Delta M'=EI\Delta\theta'. \end{aligned} \tag{11}$$

Integrating $(11)^1$ we obtain that $\Delta H = const$. Since $\Delta H(L) = 0$, it follows that $\Delta H = 0$. Following dimensionless quantities are introduced:

$$\begin{aligned} &\zeta=\frac{\Delta x}{L}; \quad \eta=\frac{\Delta y}{L}; \quad t=\frac{S}{L}; \quad \lambda_1=\frac{\mu L^4}{EI}; \\ &\lambda_2=\frac{FL^2}{EI}; \quad v=\frac{\Delta VL^2}{EI}; \quad m=\frac{\Delta ML}{EI}. \end{aligned} \tag{12}$$

Substituting (12) in (11) we obtain

$$\dot{v}=\lambda_1\eta; \quad \dot{m}=-v\cos\theta-\lambda_2\sin\theta; \quad \dot{\eta}=\sin\theta; \quad \dot{\zeta}=\cos\theta-1; \quad \dot{\theta}=m; \tag{13}$$

where $(\cdot)^{\cdot}=d(\cdot)/dt$.

2.2 Linearized problem

Let $\tilde{\mathbf{y}}=[v \quad m \quad \eta \quad \zeta \quad \theta]^T\in C^1([0,1])^5$ where C^1 is Banach space of continuous function with continues first derivative. Let M be the nonlinear operator $M:(C^1([0,1]))^5\times\mathbb{R}^2\to(C([0,1]))^5$. Now, the system (13) can be written as

$$M\left(\tilde{\mathbf{y}},\lambda_1,\lambda_2\right)=\frac{d}{dt}\begin{bmatrix} v \\ m \\ \eta \\ \zeta \\ \theta \end{bmatrix}-\begin{bmatrix} \lambda_1\eta \\ -v\cos\theta-\lambda_2\sin\theta \\ \sin\theta \\ \cos\theta-1 \\ m \end{bmatrix}=\mathbf{0};\tag{14}$$

where $(\lambda_1,\lambda_2)\in$. Problem (14) is linearized by introducing Frechet derivative of *M*, with respect to $\tilde{\mathbf{y}}$, at $\tilde{\mathbf{y}}=0$ as given:

$$D_{\tilde{\mathbf{y}}}M\left(\mathbf{0},\lambda_1,\lambda_2\right)=\tilde{B}\left(\lambda_1,\lambda_2\right)\tilde{\mathbf{y}}=\mathbf{0};\tag{15}$$

where $\tilde{B}(\lambda_1,\lambda_2)$ is a linear operator acting on $\tilde{\mathbf{y}}$. The following is obtained:

$$\dot{v}=\lambda_1\eta;\qquad \dot{m}=-v\theta-\lambda_2\theta;\qquad \dot{\eta}=\theta;\qquad \dot{\zeta}=0;\qquad \dot{\theta}=m.\tag{16}$$

Using $\zeta(0)=0$ from $(16)^4$ we get that $\zeta=0$. Linear problem can be simplified as $\tilde{B}(\lambda_1,\lambda_2)\tilde{\mathbf{y}}=\mathbf{0}$, using (16), by omitting ζ from $\tilde{\mathbf{y}}$:

$$\tilde{B}\left(\lambda_1,\lambda_2\right)\mathbf{y}=\mathbf{0},\ y=\begin{bmatrix} v & m & \eta & \theta\end{bmatrix}^T\in\left(C^1\left([0,1]\right)\right)^4;\tag{17}$$

the action of linear operator is given by:

$$\dot{v}=\lambda_1\eta;\qquad \dot{m}=-v\theta-\lambda_2\theta;\qquad \dot{\eta}=\theta;\qquad \dot{\theta}=m.\tag{18}$$

In following analysis we will consider reduced nonlinear system

$$M\left(\mathbf{y},\lambda_1,\lambda_2\right)=\mathbf{0}.\tag{19}$$

From (18) we get the equivalent problem as follows

$$\ddot{\ddot{\eta}}+\lambda_2\ddot{\eta}+\lambda_1\eta=0.\tag{20}$$

Let $\lambda_2^2-4\lambda_1>0$. Solution of equation (20) is:

$$\eta=C_1\cos\delta_1 t+C_2\sin\delta_1 t+C_3\cos\delta_2 t+C_4\sin\delta_2 t;\tag{21}$$

where

$$\delta_1=\sqrt{\frac{\lambda_2-\sqrt{\lambda_2^2-4\lambda_1}}{2}};\qquad \delta_2=\sqrt{\frac{\lambda_2+\sqrt{\lambda_2^2-4\lambda_1}}{2}}.\tag{22}$$

If $\lambda_2^2-4\lambda_1<0$ the buckling is not possible. This implies that there is a maximal value for stiffness of the foundation where buckling is possible. Setting $\lambda_1=0$ the result is in agreement with [1].

3. Influence of boundary conditions on the number of solutions

In this section we compare the solutions of the system determinant and analyze their influences on the critical force, assuming that auxiliary parameter λ_2 is fixed.

3.1 Simple supported beam (see Figure 1a)

$$\begin{aligned}
&\eta(0)=0 \to C_1 + C_3 = 0;\\
&\eta(1)=0 \to C_1\cos\delta_1 + C_2\sin\delta_1 + C_3\cos\delta_2 + C_4\sin\delta_2 = 0;\\
&\ddot{\eta}(0)=0 \to C_1\delta_1^2 + C_3\delta_2^2 = 0;\\
&\ddot{\eta}(1)=0 \to C_1\delta_1^2\cos\delta_1 + C_2\delta_1^2\sin\delta_1 + C_3\delta_2^2\cos\delta_2 + C_4\delta_2^2\sin\delta_2.
\end{aligned} \tag{23}$$

By solving the determinant we get

$$-\left(\delta_1^2-\delta_2^2\right)^2\sin\delta_1\sin\delta_2 = 0. \tag{24}$$

Notice that:

$$\left(\delta_1^2-\delta_2^2\right)^2 = \lambda_2^2 - 4\lambda_1. \tag{25}$$

Equation (24) takes form:

$$-\left(\lambda_2^2-4\lambda_1\right)\sin\delta_1\sin\delta_2 = 0. \tag{26}$$

Assuming that relation $\lambda_2^2 - 4\lambda_1 \neq 0$ is satisfied the equation (26) has same solutions λ_2 for the fixed λ_1 in the first two buckling modes. This implies that for one eigenvalue (i.e. critical point) we have two mutually orthogonal eigenvectors $\eta(t)$ (see [2]).

3.2 Cantilever simple supported beam (see Figure 1b)

$$\begin{aligned}
&\eta(0)=0 \to C_1 + C_3 = 0;\\
&\eta(1)=0 \to C_1\cos\delta_1 + C_2\sin\delta_1 + C_3\cos\delta_2 + C_4\sin\delta_2 = 0;\\
&\dot{\eta}(0)=0 \to C_2\delta_1 + C_4\delta_2 = 0;\\
&\ddot{\eta}(1)=0 \to C_1\delta_1^2\cos\delta_1 + C_2\delta_1^2\sin\delta_1 + C_3\delta_2^2\cos\delta_2 + C_4\delta_2^2\sin\delta_2.
\end{aligned} \tag{27}$$

By solving the determinant we get

$$\left(\delta_1^2-\delta_2^2\right)^2\left(-\delta_2\sin\delta_1\cos\delta_2 + \delta_1\cos\delta_1\sin\delta_2\right) = 0. \tag{28}$$

Since (25) holds and $\lambda_2^2 - 4\lambda_1 \neq 0$ is satisfied, equation (28) can be written in the form:

$$\delta_2\sin\delta_1\cos\delta = \delta_1\cos\delta_1\sin\delta_2. \tag{29}$$

In this case there is unique pair (λ_1, λ_2) for each buckling mode. In other words, for fixed buckling mode, and for all values $0 < \lambda_1 < \frac{\lambda_2^2}{4}$ there is a unique solution $\lambda_2 \in \mathbb{R}$ that satisfies (29). This implies that for one eigenvalue (i.e. critical point) we have unique eigenvector $\eta(t)$. Similar work can be found in [6].

3.3 Rigidly fixed beam (see Figure 1c)

$$\eta(0)=0 \to C_1+C_3=0;$$
$$\eta(1)=0 \to C_1\cos\delta_1+C_2\sin\delta_1+C_3\cos\delta_2+C_4\sin\delta_2=0;$$
$$\dot{\eta}(0)=0 \to C_2\delta_1+C_4\delta_2=0;$$
$$\dot{\eta}(1)=0 \to -C_1\delta_1\sin\delta_1+C_2\delta_1\cos\delta_1-C_3\delta_2\sin\delta_2+C_4\delta_2\cos\delta_2=0. \tag{30}$$

By solving the determinant we get

$$2\delta_1\delta_2-2\delta_1\delta_2\cos\delta_1\cos\delta_2-\left(\delta_1^{\,2}+\delta_2^{\,2}\right)\sin\delta_1\sin\delta_2=0. \tag{31}$$

Notice that:

$$\delta_1^{\,2}+\delta_2^{\,2}=\lambda_2; \tag{32}$$

$$\delta_1\delta_2=\sqrt{\lambda_1}. \tag{33}$$

Equation (31) takes form:

$$2\sqrt{\lambda_1}\left(1-\cos\delta_1\cos\delta_2\right)-\lambda_2\sin\delta_1\sin\delta_2=0. \tag{34}$$

Equation (34) has different kinds of solutions depends on the parameters (λ_1,λ_2). The first kind is when $\left(1-\cos\delta_1\cos\delta_2\right)\neq 0$. In this case there is a unique solution $\lambda_2\in\mathbb{R}$ for a fixed buckling mode and for all values $0<\lambda_1<\frac{\lambda_2^{\,2}}{4}$ which is similar to the last case (Cantilever simple supported beam). However, if the $\left(1-\cos\delta_1\cos\delta_2\right)=0$ then the solution behaves as in Simple supported beam, i.e. the equation (34) has the same solutions λ_2 for fixed λ_1 in the first two buckling modes.

3.4 Cantilever beam (see Figure 1d)

$$\eta(0)=0 \to C_1+C_3=0;$$
$$\ddot{\eta}(1)=0 \to C_1\delta_1^{\,2}\cos\delta_1+C_2\delta_1^{\,2}\sin\delta_1+C_3\delta_2^{\,2}\cos\delta_2+C_4\delta_2^{\,2}\sin\delta_2=0;$$
$$\dot{\eta}(0)=0 \to C_2\delta_1+C_4\delta_2=0;$$
$$-\dddot{\eta}(1)-\lambda_2\dot{\eta}(1)=0. \tag{35}$$

By solving the determinant we get

$$\delta_1\delta_2[-\delta_1^{\,4}-\delta_2^{\,4}-\delta_1^{\,2}\lambda_2-\delta_2^{\,2}\lambda_2+\left(\delta_2^{\,2}\lambda_2+\delta_1^{\,2}\left(2\delta_2^{\,2}+\lambda_2\right)\right)\cos\delta_1\cos\delta_2$$
$$+\delta_1\delta_2\left(\delta_1^{\,2}+\delta_2^{\,2}+2\lambda_2\right)\sin\delta_1\sin\delta_2]=0. \tag{36}$$

In addition to (25) and (32, 33), notice that:

$$-\delta_1^{\,4}-\delta_2^{\,4}-\delta_1^{\,2}\lambda_2-\delta_2^{\,2}\lambda_2=-\lambda_2; \tag{37}$$

$$\delta_2^{\,2}\lambda_2+\delta_1^{\,2}\left(2\delta_2^{\,2}+\lambda_2\right)=\lambda_2^{\,2}+2\lambda_1; \tag{38}$$

$$\delta_1\delta_2\left(\delta_1^2+\delta_2^2+2\lambda_2\right)=3\sqrt{\lambda_1}\lambda_2 . \tag{39}$$

Equation (36) takes form:

$$\left(\lambda_2^2+2\lambda_1\right)\cos\delta_1\cos\delta_2+3\sqrt{\lambda_1}\lambda_2\sin\delta_1\sin\delta_2=\lambda_2 . \tag{40}$$

In this case there are no solution for λ_2. This case can not be solved using this method of analyzing the critical force [1].

The table below compares the solutions for the four types of beams, both with and without an elastic foundation.

Case			Equation	Nature of solution for fixed λ_1
(a)		$\lambda_1=0$ $\lambda_2=\lambda$	$\sin\sqrt{\lambda}=0$	Unique solution $\lambda_2\in\mathbb{R}$ for each buckling mode
	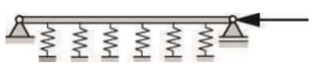	$\lambda_1\in\mathbb{R}^+$	$\sin\delta_1\sin\delta_2=0$	Same solution $\lambda_2\in\mathbb{R}$ for *i* and *i+1* buckling mode
(b)	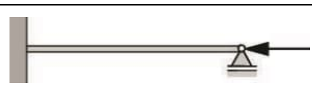	$\lambda_1=0$ $\lambda_2=\lambda$	$\tan\sqrt{\lambda}=\sqrt{\lambda}$	Unique solution $\lambda_2\in\mathbb{R}$ for each buckling mode
	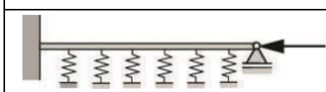	$\lambda_1\in\mathbb{R}^+$	$\delta_2\sin\delta_1\cos\delta=\delta_1\cos\delta_1\sin\delta_2$	Unique solution $\lambda_2\in\mathbb{R}$ for each buckling mode
(c)	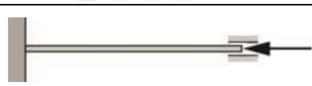	$\lambda_1=0$ $\lambda_2=\lambda$	$\tan\frac{\sqrt{\lambda}}{2}=\frac{\sqrt{\lambda}}{2}$	Unique solution $\lambda_2\in\mathbb{R}$ for each buckling mode
	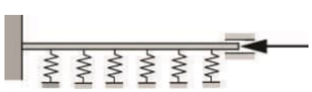	$\lambda_1\in\mathbb{R}^+$	$2\sqrt{\lambda_1}\left(1-\cos\delta_1\cos\delta_2\right)$ $=\lambda_2\sin\delta_1\sin\delta_2$	If λ_1 is such that $1-\cos\delta_1\cos\delta_2=0$ then: Same solution $\lambda_2\in\mathbb{R}$ for *i* and *i+1* buckling mode
				If λ_1 is such that $1-\cos\delta_1\cos\delta_2\neq0$ then: Unique solution $\lambda_2\in\mathbb{R}$ for each buckling mode
(d)	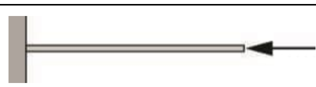	$\lambda_1=0$ $\lambda_2=\lambda$	$\sqrt{\lambda}\cos\sqrt{\lambda}=0$	Unique solution $\lambda_2\in\mathbb{R}$ for each buckling mode
	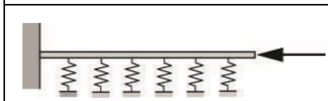	$\lambda_1\in\mathbb{R}^+$	$\left(\lambda_2^2+2\lambda_1\right)\cos\delta_1\cos\delta_2$ $+3\sqrt{\lambda_1}\lambda_2\sin\delta_1\sin\delta_2=\lambda_2$	

Table 1. The different cases of boundary conditions and their influence on the nature of the solution for critical force

It can be easily shown that if $\lambda_1=0$ and $\lambda_2=\lambda$ are applied into the solution for beams with an elastic foundation, the resulting equations are identical to the solutions for beams without an elastic foundation.

3. Conclusions

This paper provides clear example of how changes in boundary conditions can significantly influence the results regarding the critical force acting on a rod. It can be seen that beams without elastic foundation have unique solution for each buckling mode, while beams on elastic foundation have different situation depending on boundary conditions. The Cantilever simply supported beam has unique solution, while simply supported beam exhibits identical solutions λ_2 for fixed λ_1 for first two buckling modes. It is also shown that rigidly fixed beam has both solutions (unique and bimodal) depending on some input parameters. Cantilever beam can not be solved using this method; therefore, future research should consider alternative approaches and compare with these results.

References

[1] Atanacković, T.,M., *Stability Theory of Elastic Rods*, World Scientific, 1997.

[2] Rehlicki, L.,Z., Janev, M.,B., Novakovic, B.,N., and Atanacković, T.,M., *On post-critical behavior of a beam on an elastic foundation*, International Journal of Structural Stability and Dynamics, 18(06):1850082, 2018.

[3] V. Glavardanov, N. Grahovac, A. Berecki, and M. Zigic. *The inuence of foundation nonlinearity on the post-buckling behavior of a shearable rod near double eigenvalues*, International Journal of Solids and Structures, 203:236-248, 2020.

[4] Golubitsky, M. and Schaeffer, D.,G., *Singularities and groups in bifurcation theory: Volume I*, Applied Mathematical Sciences, Springer, New York, 1985.

[5] Chow, S.,N., Hale, J.,K., *Methods of Bifurcation Theory*, Grundlehren der mathematischen Wissenschaften, Springer, New York, 2012.

[6] Atanacković, T.,M., *Stability of rotating compressed rod with imperfections*, Mathematical Proceedings of the Cambridge Philosophical Society, 101(3):593–607, 1987.

10th International Congress of the Serbian Society of Mechanics
Niš, Serbia, June 18-20, 2025
A.2

Extended abstract

ON THE PROPERTIES OF FRICTION TO MAINTAIN THE STATE OF REST OF A TRIPOD ON A ROUGH SURFACE

Marat Z. Dosaev[1][0000-0002-3859-4065]

[1] Institute of Mechanics, Michurinskiy pr-t, 1, Moscow, Russia
e-mail: dosayev@imec.msu.ru

Abstract

The results of a constructive study of the ability of dry friction to hold a tripod in a state of rest under the influence of external forces are presented. In addition to the reaction forces of the supports, the tripod is subject to the force of gravity, a horizontal force, and a pair of forces with a vertical moment. A constructive discussion of the distribution of limit friction in the tripod supports is proposed. In particular, it is shown that the sum of the moduli of the limiting friction forces is strictly less than the product of the friction coefficient and the weight of the body.

The identified features will ensure a rest phase for the body of a vibration robot resting on a rough plane with three points.

Key words: tripod, dry friction, limit friction force

1. Introduction

A vibration robot has a phase of motion during which its body is motionless and rests on a rough surface. At this time, the internal elements perform intensive movements, creating significant relative forces and moments. These forces generated by the rotating internal elements affect the reactions of the robot body supports, that is, the position, in a sense, of the local center of pressure and the instantaneous force of pressure. After these effects are reduced to the center of mass, a pair of forces is released, with a vertical moment, and one horizontal force. Therefore, a serious problem arises associated with the need to keep the robot body at rest, which is fundamental for the implementation of the robot control algorithm. It is necessary to determine the conditions under which these external effects are unable to move the robot body from its rest. A similar problem of finding the ultimate forces in supports was considered in [1].

2. Method

The problem of maintaining the rest of a rigid body supported by three points on a rough plane under the action of external forces is considered. For simplicity, it is assumed that the support points form a regular triangle *ABC* (Fig. 1). In addition to gravity, the body is affected by a horizontal force whose line of action passes through the center of mass of the robot body, and a force couple with a vertical moment. For some individual cases, the distribution of reaction forces between the supports is considered, and conclusions are made about the magnitude of the limit force (moment), that is, such a force whose effect does not disturb the rest of the body, while any force with a magnitude greater than the limit one leads to the onset of body motion. Let us consider the model of classical dry friction. We assume that each support point cannot begin to slide until the values of its horizontal and vertical reactions are related by the following relationship: $R_i \leq \mu Z_i, i = A, B, C$, where Z_A, Z_B, Z_C are magnitudes of the normal support reactions, R_A, R_B, R_C are modules of the horizontal support reactions (dry friction forces between supports and the supporting plane).

An algorithm is proposed for determining the minimum coefficient of friction at which a body on three supports maintains a state of rest under a given load. The conditions for maintaining the rest of the body are determined by solving the problem on the extremum of the sum of the squares of the moduli of horizontal reactions. In most typical cases of the location of the center of mass, the problem is solved analytically; for an arbitrary location of the center of mass inside the support triangle, a numerical approach is used.

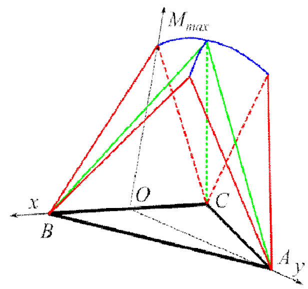

Fig. 1. Dependence of the magnitude of the maximum moment that will not disturb the rest of the body on the position of the projection (*x*,*y*) of the center of mass onto the support triangle

3. Conclusions

Friction provides maximum resistance to the external moment when the center of mass is projected onto the center of the triangle (Fig. 1). The ability of friction to resist an external moment decreases faster if the projection of the center of mass is shifted from the center of the triangle along the median toward the triangle vertex than toward the nearest side.

It was shown that the sum of the modules of the ultimate friction forces is, as a rule, strictly less than the product of the friction coefficient and the body weight. Equality is achieved only in special individual cases.

Since the time of N.E. Zhukovsky ([2]), it has been known that an external moment reduces the ability of friction to maintain the rest of the body. It has been shown that even if the force is applied to the center of mass (the moment is zero), the ultimate friction force in many cases is less than the product of the friction coefficient and the body weight.

The revealed features will allow ensuring the rest phase of the body of a vibration robot resting on a rough plane with three points.

References

[1] Sumbatov A.S., *On equilibrium of the stand of a physical pendulum on a horizontal plane with dry friction*, International Journal of Non-Linear Mechanics, Vol. 126, 1-5, 2020.

[2] Zhukovsky N.E., *Equilibrium condition of a rigid body supported by a certain platform on a fixed plane and capable of moving along this plane with friction,* Volchaninov Publ., Moscow. 1897.

A.3
Extended abstract

BRIDGING MECHANICS WITH STATISTICS AND GEOMETRY

Vladimir Dragović[1,2][0000-0002-0295-4743], **Borislav Gajić**[2][0000-0002-1463-0113]

[1]The University of Texas at Dallas, Richardson, Texas, USA
e-mail: dragovic@first.com, vladad@mi.sanu.ac.rs
[2]Mathematical Institute SANU, Knez Mihailova 36, 11000 Beograd, Serbia
e-mail: gajab@mi.sanu.ac.rs

Abstract:

We emphasize the importance of bridges between statistics, mechanics, and geometry. We develop and employ links between pencils of quadrics, moments of inertia, and linear and orthogonal regressions. For a given system of points in $\mathbf{R}^k$ representing a sample of a full rank, we construct a pencil of confocal quadrics which appears to be a useful geometric tool to study the data: (i) All the hyperplanes for which the hyperplanar moments of inertia for the given system of points are equal, are tangent to the same quadrics from the pencil of quadrics. We develop regularization procedures for the orthogonal least square method, analogues of lasso and ridge methods from linear regression. (ii) For any given point P among all the hyperplanes that contain it, the best fit is the tangent hyper plane to the quadric from the confocal pencil corresponding to the maximal Jacobi coordinate of the point P; the worst fit among the hyperplanes containing P is the tangent hyperplane to the ellipsoid from the confocal pencil that contains P. The confocal pencil of quadrics provides a universal tool to solve the restricted principal component analysis restricted at any given point. Some of the obtained results can be seen as generalizations of classical results of Pearson on orthogonal regression. Applications include statistics of errors-in-variables models and restricted regressions, both ordinary and orthogonal ones. For the orthogonal regression, a new formula for test statistic is derived, using the Jacobi elliptic coordinates associated to the pencil of confocal quadrics. The developed methods and results are illustrated in natural statistics examples.

Key words: data ellipsoid, confocal pencil of quadrics, planar moments of inertia, restricted regression

References

[1] V. Dragović and B. Gajić, *Points with rotational ellipsoids of inertia, envelopes of hyperplanes which equally fit the system of points in* R^k, *and ellipsoidal billiards*, Physica D: Nonlinear Phenomena, 15 p. Volume 451, 133776, 2023.

[2] V. Dragović and B. Gajić, *Orthogonal and Linear Regressions and Pencils of Confocal Quadrics,* Statistical Science, Vol. 40, No. 2, 2025.

10th International Congress of the Serbian Society of Mechanics
Niš, Serbia, June 18-20, 2025
A.4
Extended abstract

MAGNETIC FLOWS ON SPHERES

Vladimir Dragović [1] [0000-0002-0295-4743], **Borislav Gajić**[2] [0000-0002-1463-0113], and **Božidar Jovanović**[3] [0000-0002-3393-4323]

[1]Department of Mathematical Sciences, The University of Texas at Dallas, USA, Mathematical Institute SANU, Belgrade, Serbia, email: Vladimir.Dragovic@utdallas.edu

[2]Mathematical Institute SANU, Belgrade, Serbia, e-mail: gajab@mi.sanu.ac.rs

[3]Mathematical Institute SANU, Belgrade, Serbia, e-mail: bozaj@mi.sanu.ac.rs

Abstract. We consider a motion of a material point of mass m placed in a constant homogeneous magnetic field in $\mathbb{R}^n$ given by the 2-form

$$\mathbf{F} = s\sum_{i<j} \kappa_{ij} d\gamma_i \wedge d\gamma_j. \tag{1}$$

and restricted to the sphere $S^{n-1} = \{\gamma \in \mathbb{R}^n \,|\, \langle\gamma,\gamma\rangle = 1\}$. Here $\kappa \in \mathrm{so}(n)$ is a fixed skew-symmetric matrix and s is a real parameter.

We work in redundant coordinates and consider the phase space T^*S^{n-1} as a submanifold of $\mathbb{R}^{2n}(\gamma, p)$ given by equations

$$\phi_1 = \langle\gamma,\gamma\rangle = 1, \qquad \phi_2 = \langle p,\gamma\rangle = 0,$$

and endowed with the twisted symplectic form $\omega + \mathbf{f}$, $\omega = \sum_{i=1}^n dp_i \wedge d\gamma_i|_{T^*S^{n-1}}$, $\mathbf{f} = \mathbf{F}|_{T^*S^{n-1}}$.

The Hamiltonian of the system is

$$H(\gamma, p) = \frac{1}{2m}\langle p, p\rangle$$

and the corresponding Hamiltonian equations on the magnetic cotangent bundle $(T^*S^{n-1}, \omega + \mathbf{f})$ are given by

$$\dot\gamma = \frac{1}{m}p, \qquad \dot p = \frac{s}{m}\kappa p + \mu\gamma, \qquad \mu = \frac{1}{m}\big(s\langle p, \kappa\gamma\rangle - \langle p, p\rangle\big). \tag{2}$$

The function μ is the Lagrange multiplier and $\mu\gamma$ is the reaction force of the holonomic constraint $\phi_1 = 1$.

For $n = 3$, by using the standard identification $\mathbb{R}^3 \cong \mathrm{so}(3)$,

$$\vec\kappa = (k_1, k_2, k_3) \longleftrightarrow \kappa = \begin{pmatrix} 0 & -k_3 & k_2 \\ k_3 & 0 & -k_1 \\ -k_2 & k_1 & 0 \end{pmatrix}, \tag{3}$$

we get that the term $\frac{s}{m}\kappa p$ represents the usual Lorentz force

$$\frac{s}{m}\kappa p = \frac{s}{m}\vec\kappa \times p.$$

In [1], we derived equations (2) as the reduced equations of a gyroscopic nonholonomic Chaplygin system representing a ball rolling over a sphere. The system of a ball rolling over a sphere is

a generalization of the Demchenko integrable system [2]. In [1], we also performed explicit integration of the equations of motion (2) of the systems on S^2 and S^3 in elliptic functions. To aline the notation from this talk with the notation from [1], one should set

$$m = \tau/\varepsilon^2, \qquad s = 1/\varepsilon^2 \qquad (s/m = 1/\tau).$$

Other examples of integrable natural Hamiltonian systems on magnetic cotangent bundles of homogeneous spaces can be found in [3, 4].

We choose an orthonormal basis $[\mathbf{e}_1, \dots, \mathbf{e}_n]$ of $\mathbb{R}^n$ in which the magnetic 2-form (1) becomes

$$\mathbf{F} = s(\kappa_{12} d\gamma_1 \wedge d\gamma_2 + \kappa_{34} d\gamma_3 \wedge d\gamma_4 + \cdots + \kappa_{2[n/2]-1,2[n/2]} d\gamma_{2[n/2]-1} \wedge d\gamma_{2[n/2]}),$$

such that $\kappa_{12} \geq 0$, $\kappa_{34} \geq 0, \dots, \kappa_{2[n/2]-1,2[n/2]} \geq 0$.

Thus, the system (2) becomes

$$\dot{\gamma}_{2i-1} = \frac{1}{m} p_{2i-1}, \qquad \dot{p}_{2i-1} = \frac{s}{m} \kappa_{2i-1,2i} p_{2i} + \mu \gamma_{2i-1}, \tag{4}$$

$$\dot{\gamma}_{2i} = \frac{1}{m} p_{2i}, \qquad \dot{p}_{2i} = -\frac{s}{m} \kappa_{2i-1,2i} p_{2i-1} + \mu \gamma_{2i}, \qquad i = 1, \dots, [n/2], \tag{5}$$

and, if n is odd:

$$\dot{\gamma}_n = \frac{1}{m} p_n, \qquad \dot{p}_n = \mu \gamma_n. \tag{6}$$

In this talk we will present a proof of complete integrability of the system for $n \leq 6$:

Theorem. *For $n = 2,4,6$ the magnetic systems* (4), (5) *and for $n = 3,5$ the magnetic systems* (4), (5), (6) *are Liouville integrable for any κ. Moreover:*

(i) If $n = 5$ and $\kappa_{12} = \kappa_{34}$, then the magnetic system (4), (5), (6) *is integrable in the non-commutative sense: generic motions are quasi-periodic over* 3*-dimensional invariant isotropic sub-manifolds.*

(ii) If $n = 6$ and $\kappa_{12} = \kappa_{34} \neq \kappa_{56}$, then the magnetic system (4), (5) *is integrable in the non-commutative sense: generic motions are quasi-periodic over* 4*-dimensional invariant isotropic sub-manifolds.*

(iii) If $n = 6$ and $\kappa_{12} = \kappa_{34} = \kappa_{56}$, then the magnetic system (4), (5) *is integrable in the non-commutative sense: generic motions are quasi-periodic over* 3*-dimensional invariant isotropic sub-manifolds.*

Keywords: Magnetic geodesics, Liouville integrability, Non-commutative integrability

References

[1] Dragović, V., Gajić, B., Jovanović, B., *Gyroscopic Chaplygin systems and integrable magnetic flows on spheres*, J. Nonlinear Sci. Vol. **33**, paper no. 43, 2023, arXiv:2110.09938 [math-ph].

[2] Dragović, V., Gajić, B., Jovanović, B., *Demchenko's nonholonomic case of a gyroscopic ball rolling without sliding over a sphere after his 1923 Belgrade doctoral thesis*, Theor. Appl. Mech. Vol. **47**, 257–287, 2020, arXiv:2011.03866.

[3] Bolsinov, A., V., Jovanović, B., *Magnetic Geodesic Flows on Coadjoint Orbits*, J. Phys. A: Math. Gen. Vol. **39**, L247–L252, 2006, arXiv: math-ph/0602016.

[4] Bolsinov, A., V., Jovanović, B., *Magnetic Flows on Homogeneous Spaces*, Comm. Math. Helv, Vol. **83**, 679–700, 2008.

A.5

Extended abstract

NEW RHEOLOGICAL DISCRETE DYNAMIC SYSTEMS OF THE FRACTIONAL TYPE RHEOLOGICAL OSCILLATOR OR CREEPER TYPE: AN OVERVIEW OF AUTHOR'S NEW RESEARCH RESULTS

Katica R. (Stevanović) Hedrih[1,2][0000-0002-2930-5946]

[1] Mathematical Institute of Serbian Academy of Sciences and Arts, Belgrade, Serbia
e-mail: katicah@mi.sanu.ac.rs,khedrih@sbb.rs

[2] Faculty of Mechanical Engineering, The University of Niš, Niš, Serbia
e-mail: katicahedrih@gmail.com

Abstract:

New rheological discrete dynamic systems of the fractional type rheological oscillator or creeper type are presented through an overview of Author's new research results. Laplace transformations of solutions for independent generalized coordinates, external and internal degrees of freedom of system dynamics were determined.

Key words: Standard light rheological complex models of the fractional type, Newton's ideally viscous fluid flow of the fractional type, new rheological discrete dynamic systems of the fractional type, internal degrees of freedom of movement, rheological oscillators, rheological creeper, Laplace transformations, surfaces of elongations of Laplace transformations

1. Introduction

Using the newly introduced, by author, basic complex, as well as hybrid complex rheological models, of the fractional type, the dynamics of a series of mechanical rheological discrete dynamic systems of rheologic oscillators or creepers of the fractional type, with corresponding independent generalized coordinates, external and internal degrees of freedom of movement were studied. Laplace transformations of solutions for independent generalized coordinates, external and internal degrees of freedom of system dynamics were determined. On those specimens, it was shown that rheological complex models, of the fractional type, introduce internal degrees of freedom into the dynamics of the rheological discrete dynamic system.

2. Main results

A series of characteristic surfaces of elongations of Laplace transformations of independent generalized coordinates of the dynamics of rheological discrete dynamic systems of the rheologic oscillator type, i.e. rheologic creeper type, as a function of fractional order differentiation exponent and Laplace transformation parameter are shown. The manuscript presents the scientific results of theoretical research on dynamics of rheologic discrete dynamic systems of the fractional type through new models and rigorous mathematical analytical analysis with differential equations fractional order and Laplace transforms.

Table 1. Tabular comparative overview of new class of complex rheological discrete dynamic systems of fractional type with one or finite number of degrees of freedom

	Rheological oscillator fractional type	Rheological creeperfractional type
A rheological Kelvin-Voigt discrete dynamic system of fractional-type rheological oscillator (left) and a rheological Maxwell discrete dynamic system, a fractional-type-rheological creeper(right)	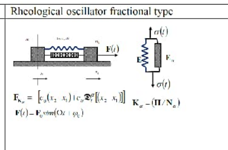	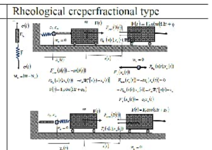
A rheological Kelvin-Voigt-Faraday discrete dynamic system of fractional-type with piezoelectric property-rheological oscillator (left) and a rheological Lethersich discrete dynamic system, a fractional-type-rheological creeper (right)	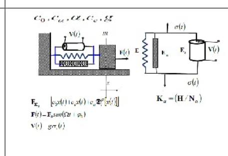	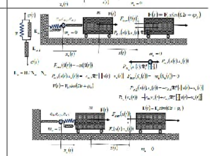
A rheological Jeffrys-II discrete dynamic system of fractional-type rheological oscillator (left) and a rheological Jeffrys discrete dynamic system, a fractional-type-rheological creeper (right)	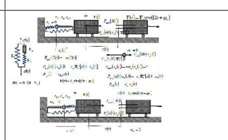	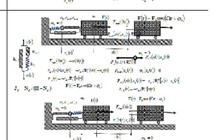
A rheological Burgers-Faraday discrete dynamic system of fractional-type with piezoelectric property-rheological oscillator (left) and a rheological Burgers discrete dynamic system, a fractional-type-rheological creeper (right)	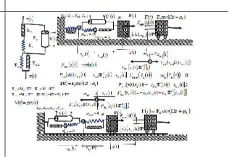	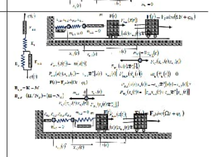
A rheological Kelvin-Voigt-Faraday discrete dynamic system of fractional-type with piezoelectric property-rheological chain oscillator (left) and a rheological Maxwell-Faraday discrete dynamic system, a fractional-type-rheological chain creeper (right)	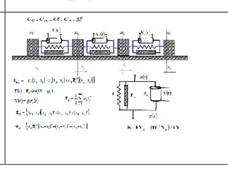	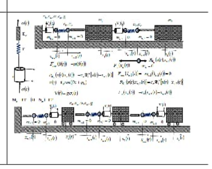

3. Conclusions

The manuscript presents the scientific results of theoretical research on dynamics of rheologic discrete dynamic systems of the fractional type through new models and rigorous mathematical analytical analysis with differential equations fractional order and Laplace transforms. The results of the research on internal degrees of freedom and new ideal rheological elements offer valuable insights into the behavior of materials. These results can serve for new experimental research.

References

[1] Hedrih (Stevanović), K. R, Machado, J. T. (2015), Discrete fractional order system vibrations, *International Journal Non-Linear Mechanics*, 73, 2–11 .

[2] Hedrih (Stevanović), K. R, Milovanovic G.V.,, Elements of mathematical phenomenology and analogies of electrical and mechanical oscillators of the fractional type with finite number of degrees of freedom of oscillations: linear and nonlinear modes, Commun. Anal. Mech. **16**(4) (2024), 738 – 785; DOI: 10.3934/cam.2024033.

[3] Hedrih (Stevanović), K.R.; Hedrih, A.N. *Rheological Burgers–Faraday Models and Rheological Dynamical Systems with Fractional Derivatives and Their Application in Biomechanics*. Fractal Fract. 2024, 8, x. https://doi.org/10.3390/xxxxx,

[4] Hedrih (Stevanović), K. R, , (2025), An Overview: New Class of Complex Models of Materials Piezoelectric Properties with Differential Constitutive Relation of Fractional Order, Editors: A.Lopes, S. A/ David and A.a M.S.F. Galhano. Fractal and Fractional, 2025, 9, x, https://doi.org/10.3390/xxxxx

10th International Congress of the Serbian Society of Mechanics
Niš, Serbia, June 18-20, 2025
A.6
Extended abstract

A SIMPLE ENGINEERS-FRIENDLY METHOD FOR NON-HOLONOMIC SYSTEMS

Dragan T. Spasic[0000-0003-1848-5379]

University of Novi Sad, Faculty of Technical Sciences, Serbia, e-mail: spasic@uns.ac.rs

Abstract:

This paper deals with the following question: which concepts should complement axioms of motion to generate tools for non-holonomic problems. It turns out that only three notions, recognizable but insufficiently emphasized in the literature on non-holonomic mechanics can supply the answer. For a particle, a mathematically correct concept of possible accelerations, the Polyakhov nabla operator applied to the non-holonomic constraint equation, and the complementary, constitutive axiom describing reaction forces in terms of the Polyakhov operator were enough. For plane rigid body motions appropriate adaptations of these three were proposed. The simplicity of this new pattern was confirmed on several examples.

Key words: Polyakhov's nabla, Possible accelerations, Motion axioms, Sledge, Lineikin's model.

1. Introduction

The usual patterns for mechanical systems with non-holonomic constraints bear on variational methods. These methods are very important for engineers but require significant both time and efforts for acquisition of skills and learning. This work deals with alternatives. For the particle, starting with the Newton axiom as well as the non-linear non-holonomic constraint equation, the arguments presented in [1] yield the corresponding reactionless equation of motion. Namely, the reaction force was determined in advance and belongs to the framework of the Newtonian mechanics. This pattern comprises mathematically correct concept of possible accelerations [2], the Polyakhov nabla operator applied to the non-holonomic constraint equation [3], and the complementary, constitutive axiom describing reaction forces in terms of Polyakhov's nabla, [4]. Introduced by analogy, appropriate adaptations of these three will decouple reaction forces and motion attributes stated within the Newton-Euler axioms for plane rigid body motions.

2. Methodology

Consider a plane rigid body motion in the presence of linear non-holonomic constraint equations containing time, position and velocity of mass center, angle of rotation and its angular velocity. Introducing two Polyakhov's nabla (for translation and for rotation) both applied to the non-holonomic constraints, the possible center of mass accelerations as well as the possible angular accelerations can be found. Similarly to arguments of [3], the complementary constitutive axioms expressing reaction forces and torques in terms of the introduced Polyakhov operators complete the set of equations yielding reactionless equations of plane motion. Namely, using the fact that the actual center of mass acceleration as well as the actual angular accelerations are chosen among all possible ones one can determine the reaction forces and torques in advance.

3. Results

The simplicity of the suggested alternative for either the Udwadia-Kalaba equations [5] or the Routh-Voss equations [6] was shown by reexamination of the particle problem first proposed by Appell in 1911. In doing so neither Lagrange's multiplier nor the Appell-Chetaev condition among variations of generalized coordinates were used. More particle problems were presented in [7]. For plane rigid body motions, the reactionless differential equations of motion for the Caratheodory-Chaplygin sledge and the turning movement of a car according to the Lineikin model were derived. It was shown that this new pattern can serve as an alternative for the Lagrange equations of the second kind with unknown multipliers [8] and the Maggi equations [9].

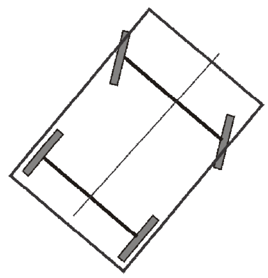

Figure 1: The scheme of the car

3. Closure

The proposed method, say the vectorial approach to non-holonomic problems, seems to be more engineers-friendly and less time and efforts demanding then the standard methods for non-holonomic systems. It can be used to enlarge the set of problems dealt within the classical courses since just three new concepts are to be added to the fundamental ones.

References

[1] Soltakhanov Sh.,Kh., Yushkov M.,P.,,Zegzhda S.,A., *Mechanics of non-holonomic systems, a new class of control systems*, Springer, 2009.

[2] Markeev A.,P., *Theoretical mechanics*, Regular and chaotic dynamics, 1999.

[3] Polyakhov N.,N., *Equations of motion of mechanical systems under nonlinear, nonholonomic constraints in the general case*, Vestn. Leningr. Univ. No. 1. pp. 124-132, 1972.

[4] Polyakhov N.,N., Zegzhda S.,A., Yushkov M.,P., *Theoretical and applied mechanics*, Vol. I: General issues of theoretical mechanics, St. Petersburg State University, 2021.

[5] Udwadia F.,E., Wanichanon Th., *Hamel's paradox and the foundations of analytical dynamics, Applied Mathematics and Computation*, 217, 1253-1265, 2010.

[6] Papastavridis J.,G., *Analytical mechanics, A Comprehensive Treatise on the Dynamics of Constrained Systems*, World Scientific, 2014.

[7] Spasic D.,T., On nonlinear nonholonomic constraints, possible acceleration concept and the Polyakhov operator, The 8th International Conference on Contemporary Problems of Mathematics, Mechanics and Informatics, Novi Pazar, Serbia, 2024.

[8] Dobronravov V.,V., *Basic mechanics of nonholonomic systems*, Higher School, 1970.

[9] Byachkov A.,B., Cattani C., Nosova E.,M., Yushkov M.,P., *The Simplest Model of the Turning Movement of a Car with its Possible Sideslip*, Technische Mechanik, Band 29, Heft 1, 1-12, 2009.

B: Fluid Mechanics

B.1

Extended abstract

GAS FLOW BLOCKAGE IN THE NEAR-WELLBORE REGION: FRESH WATER STIMULATION AGAINST THE SALTING-OUT EFFECT

Andrey Afanasyev[1[0000-0002-2284-7144]], **Sergey Grechko**[1[0000-0002-9551-341X]]

[1] Institute of Mechanics

Lomonosov Moscow State University, Michurinkiy av. 1, 119192 Moscow, Russia

e-mail: afanasyev@imec.msu.ru

Abstract:

We consider the injection of CO_2 into a saline aquifer through a vertical well. We assume that the well is stimulated by the fresh water treatment to reduce the salting-out effect. By using a radial reservoir model, we simulate the increase in the skin factor caused by the salt precipitation and deposition in the near-wellbore region. We demonstrate that the capillary-driven backflow can magnify the skin factor by orders of magnitude as compared to the case with zero capillary pressure. It can eventually lead to a complete clogging of the porous medium. We introduce the capillary number, which characterizes the influence of the capillary pressure and the intensity of halite deposition. We demonstrate that there exists the critical capillary number separating two qualitatively different scenarios of CO_2 injection. At the supercritical numbers, the injection cannot be blocked by the salt deposition, although the skin factor monotonically increases with the volume of injected CO_2. The flow blockage cannot occur in such cases. At the subcritical numbers, the conditions of the complete clogging and zero well injectivity are always reached at a finite time. The fresh water stimulation can only postpone the flow blockage in time, but it cannot exclude such a negative manifestation. The derived estimates for the critical capillary number can be useful for predicting the evolution of the CO_2 well injectivity and mitigating the development of the situations with the complete flow blockage.

Key words: porous media, geological storage, CO_2, phase transitions, shock, Riemann wave

The increasing degree of climate change debate is stimulating the development of low-greenhouse gas development strategies. A promising way to reduce human impact on nature is the geological storage of greenhouse gases, in particular CO_2, in saline aquifers. It involves injecting millions of tons of CO_2 into geological formations for a long-term storage and disposal. The presentation considers the injection of carbon dioxide into a geological reservoir saturated with brine [1]. It is assumed that the injection is carried out through a vertical well, that can initially be stimulated by pumping a finite volume of fresh water. We investigate the development of the salting-out effect in the bottom-hole zone of the well. The concomitant decrease in permeability leads to a decrease in the well injectivity, that is, to a decrease in the rate of CO_2 injection.

To quantify the effect of salt deposition on well injectivity, the self–similar Riemann problem describing the axisymmetric flow of gas from the well into a saline aquifer was solved (Figure 1). The study was conducted within the framework of modeling a three-component three-phase flows of a CO_2-H_2O-NaCl mixture. It is shown that such a system in the limiting case of zero capillary pressure has two types of characteristics responsible for the transport of volatile components and salt. A graphical method is proposed for constructing an exact solution to the Riemann problem. It is shown that the solution contains two shocks and a Riemann wave in between. The slower shock limits the area where salt is deposited due to water evaporation. This is a skin zone, i.e. a zone of reduced reservoir permeability. From the condition that the slower shock moves at a characteristic velocity, we obtain a relation for the skin factor, a dimensionless similarity criterion that characterizes hydraulic losses in the skin zone

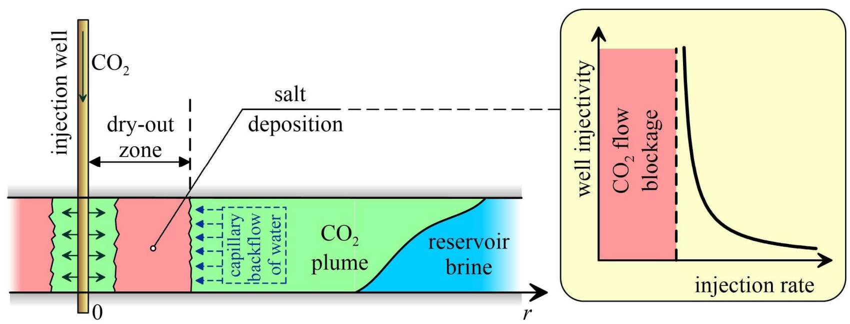

Fig. 1. Sketch of the axisymmetric study of CO_2 injection into a saline aquifer. The injection results in a complete evaporation of water in the dry-out zone and associated halite deposition. The latter can cause permeability reduction and CO_2 flow blockage.

Then, in the case of a finite capillary pressure, we show that a capillary counterflow of water to the well can significantly intensify salt deposition as compared to the limiting case of a small capillary pressure (Figure 1). In some cases, a capillary counterflow of water can lead to a complete blockage of the pore space and a decrease in the permeability and well injectivity down to zero. A capillary number is introduced, which characterizes the intensity of the processes of counterflow of water and salt deposition. It is shown that there is a critical value of the capillary number separating two fundamentally different regimes of CO_2 injection into the reservoir. At supercritical capillary numbers, the gas flow from the well cannot be blocked by salt deposition. In such conditions, the well can be operated indefinitely. At subcritical capillary numbers, the condition of complete blockage of the gas flow and the concomitant reduction of the injectivity to zero is achieved over a finite time interval. The possibility of stimulating the well by pumping fresh water to reduce the impact of the salting-out effect is being investigated. It is shown that such stimulation can only postpone in time the complete blockage of the pore space, but it does not allow us avoiding such a negative manifestation. The estimates obtained for the critical capillary number can be useful for predicting the intake values of wells used for CO_2 injection and preventing the development of situations with a complete blockage of the gas flow.

Thus, we can conclude that CO_2 injection into saline aquifers should be operated at supercritical capillary numbers, i.e. at large injection rates. Then, the gas flow cannot be blocked by the salt deposition in the near-wellbore region. If the well is allowed to go subcritical, then the gas flow can be rapidly blocked by halite. The fresh water stimulation can only postpone the blockage but cannot prevent it.

References

[1] Afanasyev A., Grechko S. Analytical expression for the skin factor of the salt deposition zone around a CO_2 injection well: Extension to the case of ternary miscible displacement // 2023 Geoenergy Sci. Eng. 228, 212036.

B.2
Extended abstract

INFLUENCE OF ROTATION ON DRAG COEFFICIENT AND UNSTEADY FLOW AROUND AN NFL BALL

Veljko Begović[1][0000-0001-8578-8287], Petar Miljković[1][0000-0003-0450-3599], Živojin Stamenković[1][0000-0001-8722-3191], Miloš Kocić[1][0000-0002-6216-5113]

[1]Faculty of Mechanical Engineering,
The University of Niš, Aleksandra Medvedeva 14, 18000 Niš, Serbia
e-mail: veljko.begovic@masfak.ni.ac.rs, petar.miljkovic@masfak.ni.ac.rs, zivojin.stamenkovic@masfak.ni.ac.rs, milos.kocic@masfak.ni.ac.rs

Abstract:

In this paper, the unsteady hydrodynamic characteristics of flow around a scaled model of a National Football League (NFL) ball in water are investigated. The objective of this research is a detailed numerical analysis of the unsteady flow around an NFL ball submerged in water using CFD, with a particular focus on determining and analyzing the drag coefficient (*Cd*). Water is employed as the working fluid, a less common approach compared to aerodynamic studies, yet relevant considering the body's geometry. The investigation encompasses two configurations: flow around a non-rotating ball and flow around a ball rotating about its longitudinal axis. Numerical simulations were performed using the Ansys Fluent software package, employing the k-ω SST turbulence model on an unstructured mesh generated around the same geometry used in previous studies, covering a Reynolds number range up to 200,000. The results provide insights into the temporal evolution of the drag force, identify dominant frequencies in the flow field (e.g., due to vortex shedding), and quantify the influence of rotation on the mean drag coefficient, its fluctuations, and the wake structure. This research contributes to a better understanding of the complex fluid dynamics surrounding rotating and non-rotating non-spherical bodies in water. **Key words**: CFD, Unsteady Flow, Ansys Fluent, NFL Ball, Drag Coefficient, Rotation, Hydrodynamics, Water, k-ω SST.

10th International Congress of the Serbian Society of Mechanics
Niš, Serbia, June 18-20, 2025

B.3
Original scientific paper

DOI:10.46793/ICSSM25.054BJ

ITERATIVE PROCESURE FOR DETERMINIG MERIDIONAL STREAMLINES OF AVERAGED FLOW IN A TURBOMACHINE IMPELLER

Jasmina Bogdanović Jovanović[1[0000-0002-8331-2880]], Živojin Stamenković[1[0000-0001-8722-3191]], Miloš Kocić[1[0000-0002-6216-5113]], Jelena Petrović[1[0000-0001-6768-9779]]

[1] Department of Theoretical and Applied Fluid Mechanics, Faculty of Mechanical Engineering, University of Niš, A. Medvedeva 14, 18000 Niš, Serbia;
e-mail: jasmina.bogdanovic.jovanovic@masfak.ni.ac.rs, živojin.stamenkovic@masfak.ni.ac.rs, milos.kocic@masfak.ni.ac.rs, jelena.nikodijevic.petrovic@masfak.ni.ac.rs ;

Abstract:

Designing a turbomachine impeller is a very demanding procedure, which is largely based on empirical experience. Each turbopump has its own specifics, but for all of them the assumption of axisymmetric fluid flow in their impellers is used. The flow space is divided into a certain number of axisymmetric sections in which the flow calculation is performed. To determine the kinematic characteristics of the fluid flow in the impeller of a turbomachine, the flow can be averaged over a circular coordinate, which results in averaged axisymmetric flow surfaces. According to the averaged fluid flow velocities obtained from numerical simulations of flow in turbomachine impeller, it is possible, using the integral continuity equation, to determine the meridional streamlines of the averaged fluid flow. This paper presents an iterative procedure for determining averaged axisymmetric flow surfaces in the impeller, using the integral continuity equation and the basic differential equation of averaged flow. Solving this task has a theoretical significance, because it does not aim at correcting the average velocities obtained from the results of numerical simulation of flow in the turbomachine impeller. However, determining these surfaces, using some numerical methods, can provide a better insight into how close the assumption of axisymmetric flow in the impeller is to the reality in a specific impeller design.

Key words: turbomachine, impeller, averaged axisymmetric flow surface, meridian streamline.

1. Introduction

Designing the turbomachine, particularly its rotating part(s) is a demanding task due to many reasons, primarily due to the complexity of the impeller geometry and the complexity of the fluid flow equations. In addition, fluid properties, such as compressibility and viscosity, should also be taken into account. The complexity of the calculation of such a system of partial differential equations requires certain simplifications and relies on some empirical equations. Such simplifications, on the other hand, lead to certain inaccuracies, which ultimately leads to deviations from the desired operating parameters.

The basic assumptions of fluid flow in the impeller of a turbomachine are stationarity and axisymmetricity. Also, flow theory refers to an impeller with an infinite number of infinitely thin blades [1-3], in order to simplify the complex flow inside the rotating impeller. Continual fluid flow increases flow energy in the non-turbine impellers, while the flow energy decreases in turbine type impellers [1-4].

Different procedures and methodologies for turbomachinery optimizations have been proposed [5]. One of the proposed methods is flow averaging according to the circular coordinate, in order to obtain the flow equal to the case of flow in a fictitious impeller with an infinite number of extremely thin blades which achieve the same flow deflection [6-8]. Such a procedure, combined with the results of numerical simulation of flow, enables comparing the meridian streamlines with assumed ones.

This paper will present the iterative procedure for determining the meridian streamlines of the averaged flow in a turbomachine impeller.

2. Determination of average axisymmetric flow surfaces in the blade area of the impeller

To determine the kinematic characteristics of the fluid flow in the impeller, the flow can be averaged over the circular coordinate, which results in averaged axisymmetric flow surfaces. This can be done by using the averaged continuity equation and the averaged flow equation of the inviscid fluid. When integrating the differential flow equation, flow energy losses due to viscous friction can also be empirically taken into account.

Fig. 1 shows characteristic cross-section of a centrifugal pump impeller, where *l* denotes the suction side and *g* denote the pressure side of the blade.

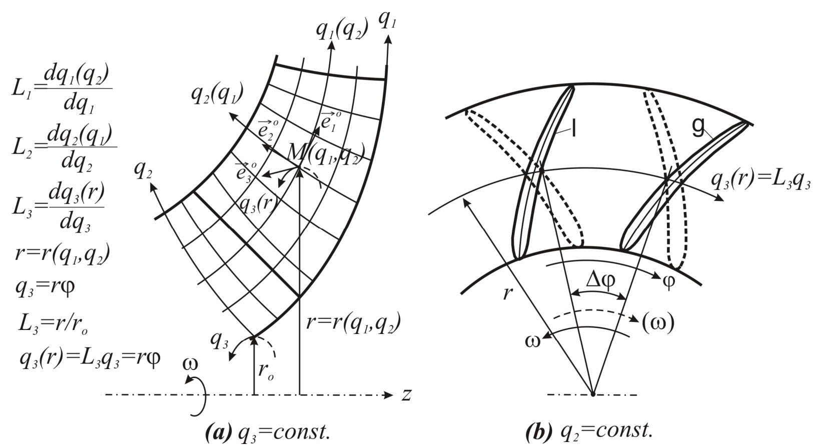

Fig. 1. Characteristic cross-sections of centrifugal impeller: a) meridian q_3=const. and b) q_2=const.

2.1 Using integral continuity equation and differential equation of averaged fluid flow

Averaged flow equation (over the circular coordinate) for inviscid flow is:

$$div\left(\Delta q_3 \cdot \tilde{\tilde{w}}\right)+\frac{1}{L_3}\Delta\left(\frac{\vec{n}}{n_3},\vec{w}\right)=0, \tag{1}$$

Using inviscid flow model, it becomes:

$$div\left(\Delta q_3 \cdot \tilde{\vec{w}}\right)=0, \text{ i.e. } \frac{\partial}{\partial q_1}\left(L_2L_3\Delta q_3\tilde{w}_1\right)+\frac{\partial}{\partial q_2}\left(L_3L_1\Delta q_3\tilde{w}_2\right)=0, \tag{2}$$

where Lame coefficients are: $L_1=L_1(q_1,q_2)$, $L_2=L_2(q_1,q_2)$ and $L_3=r(q_1,q_2)/r_o$.

Equation (2) can be transformed:

$$\frac{\partial}{\partial q_1}\left(2\pi r_o kL_2L_3\tilde{w}_1\right)=-\frac{\partial}{\partial q_2}\left(2\pi r_o kL_3L_1\tilde{w}_2\right), \tag{3}$$

Which represents a necessary and sufficient condition for the existence of the flow function $\tilde{\psi}_m = \tilde{\psi}_m(q_1, q_2)$ for average meridional velocities $\tilde{\vec{w}}_m = \tilde{w}_1\vec{e}_1^{\,o} + \tilde{w}_2\vec{e}_2^{\,o}$. The meridian streamlines over the circular coordinate represent traces of the intersection of the axisymmetric flow surface of the averaged flow and meridian plane. Therefore,

$$\text{i.e. } \frac{\partial}{\partial q_1}\left(2\pi r_o k L_2 L_3 \tilde{w}_1\right) = -\frac{\partial}{\partial q_2}\left(2\pi r_o k L_3 L_1 \tilde{w}_2\right). \tag{4}$$

Furthermore, volume flow rate through the axisymmetric flow surface, for the meridian trace dL, can be calculated:

$$dQ = 2\pi k r_o \left(L_2 L_3 \tilde{w}_1 dq_2 - L_3 L_1 \tilde{w}_2 dq_1\right). \tag{5}$$

Where $k = \Delta\varphi / \tau = \Delta q_3 / \tau r_o = k(q_1, q_2)$. i.e. $\Delta q_3 = k\tau r_o = 2\pi k r_o$.

Fig. 2 shows meridian streamlines, which are defined in polar cylindrical coordinate system a) and b) (q_1=z, q_2=r, q_3=$r_o\varphi$, $\tilde{w}_1 = \tilde{w}_z$, $\tilde{w}_2 = \tilde{w}_r$ ($L_1 = 1$, $L_2 = 1$, $L_3 = r/r_o$). Only if define the averaged meridian streamlines over a circular coordinate, it is possible to introduce a natural curvilinear orthogonal coordinate system (Fig.2.c), where q_2=const. is axisymmetric flow surface of the averaged flow and coordinates $q_1(q_2)$ represents meridian streamlines.

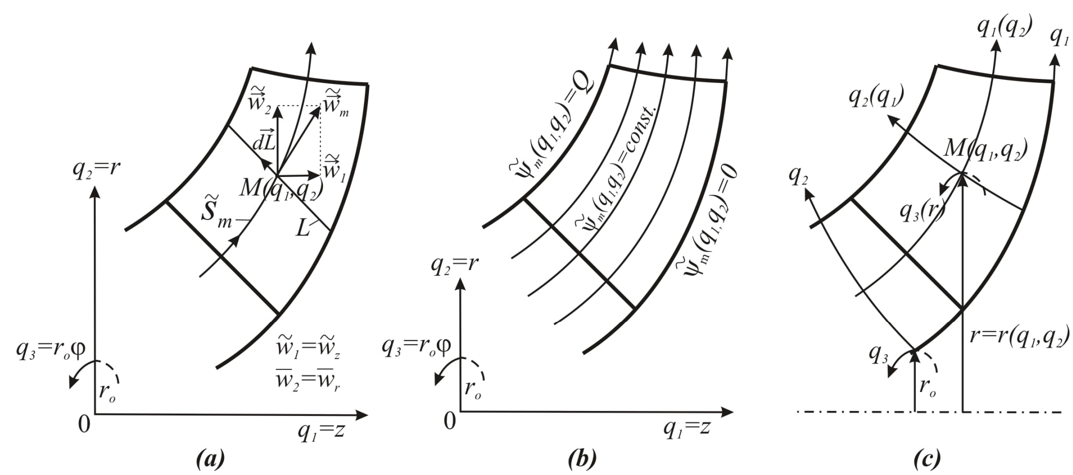

Fig. 2. Meridian streamlines

The differential equation for the relative steady state flow of an in viscous compressible fluid, ignoring the influence of the earth's gravity, can be written:

$$\left[\vec{w}, rot\vec{c}\right] = grad\left(e_R\right), \tag{6}$$

Where, c is the absolute flow velocity and Bernuli's integral for relative flow is:

$$e_R = \frac{p}{\rho} + \frac{w^2}{2} - \frac{\omega^2 r^2}{2}. \tag{7}$$

Averaging equation (6) becomes:

$$\left[\tilde{\vec{w}}, rot\tilde{\vec{c}}\right] + \vec{F}^{(1)} + \vec{F}^{(2)} + \vec{F}^{(3)} = grad\left(\tilde{e}_R\right), \tag{8}$$

Where:

$$\vec{F}^{(1)} = \left[\vec{w}, \frac{1}{L_3 \Delta q_3} \Delta \left[\frac{\vec{n}}{n_3}, \vec{w}^* \right] \right],\ \vec{F}^{(2)} = -\frac{1}{L_3 \Delta q_3} \Delta \left(e_R^*, \frac{\vec{n}}{n_3} \right),$$
$$\vec{F}^{(3)} = \left[\vec{w}^*, rot\vec{w}^* \right] \ and \ \tilde{e}_R = \frac{\tilde{p}}{\rho} + \frac{\tilde{w}^2}{2} - \frac{\omega^2 r^2}{2}. \tag{9}$$

The force $\vec{F}^{(3)}$ is much smaller than other two and can be neglected, and for axsisymetric flow surfaces $F^{(2)} = 0$, therefore $\vec{F} = \vec{F}^{(1)}$. Then equation (8) becomes:

$$\left[\tilde{\vec{w}}, rot\tilde{\vec{c}} \right] + \vec{F}^{(1)} = grad\left(\tilde{e}_R \right). \tag{10}$$

Vector multiplication of previous equation (10) with vector $\vec{n}_{sr}^{(1)}$, which is a vector perpendicular to the force vector F ($[\vec{n}_{sr}^{(1)}, \vec{F}^{(1)}] = 0$ and $(\vec{n}_{sr}^{(1)}, \tilde{\vec{w}}) = 0$, yields:

$$\tilde{\vec{w}}\left(\vec{n}_{sr}^{(1)}, rot\tilde{\vec{c}} \right) = \left[\vec{n}_{sr}^{(1)}, grad\left(\tilde{e}_R \right) \right]. \tag{11}$$

Further mathematical transformations bring equation (11) to the form:

$$\left(\tilde{w}_1 \vec{e}_1^o + \tilde{w}_2 \vec{e}_2^o + \tilde{w}_3 \vec{e}_3^o \right) \left(\frac{n_{1_{sr}}^{(1)}}{rL_2} \frac{\partial(r\tilde{c}_3)}{\partial q_2} - \frac{n_{2_{sr}}^{(1)}}{rL_1} \frac{\partial(r\tilde{c}_3)}{\partial q_1} + \frac{n_{3_{sr}}^{(1)}}{L_1 L_2} \left(\frac{\partial(L_2 \tilde{c}_2)}{\partial q_1} - \frac{\partial(L_1 \tilde{c}_1)}{\partial q_2} \right) \right) +$$
$$+ n_{3_{sr}}^{(1)} \frac{1}{L_2} \frac{\partial \tilde{e}_R}{\partial q_2} \vec{e}_1^o - n_{3_{sr}}^{(1)} \frac{1}{L_1} \frac{\partial \tilde{e}_R}{\partial q_1} \vec{e}_2^o - \left(n_{1_{sr}}^{(1)} \frac{1}{L_2} \frac{\partial \tilde{e}_R}{\partial q_2} - n_{2_{sr}}^{(1)} \frac{1}{L_1} \frac{\partial \tilde{e}_R}{\partial q_1} \right) \vec{e}_3^o = 0. \tag{12}$$

The first of three scalar equations resulting from equation (12) is:

$$\left(\frac{n_1}{n_3} \right)_{sr}^{(1)} \frac{1}{rL_2} \frac{\partial(r\tilde{c}_3)}{\partial q_2} - \left(\frac{n_2}{n_3} \right)_{sr}^{(1)} \frac{1}{rL_1} \frac{\partial(r\tilde{c}_3)}{\partial q_1} + \frac{1}{L_1 L_2} \left(\frac{\partial(L_2 \tilde{c}_2)}{\partial q_1} - \frac{\partial(L_1 \tilde{c}_1)}{\partial q_2} \right) + \frac{1}{\tilde{w}_1} \frac{1}{L_2} \frac{\partial \tilde{e}_R}{\partial q_2} = 0. \tag{13}$$

where:

$$\tilde{e}_R(\tilde{\psi}_m) = \tilde{e}_0(\tilde{\psi}_m) - \omega(rc_u)_0(\tilde{\psi}_m) - \Delta\tilde{e}_g(\tilde{\psi}_m). \tag{14}$$

Since $\tilde{c}_1 = \tilde{w}_1$, $\tilde{c}_2 = \tilde{w}_2$, $\tilde{c}_3 = \tilde{w}_3 - \omega \cdot r$, for $\vec{e}_3^o = -\vec{u}^o$ and $\tilde{c}_3 = \tilde{w}_3 + \omega \cdot r$,

for $\vec{e}_3^o = \vec{u}^o$, equation (13) becomes:

$$\frac{\mp ctg\beta_{sr}^{(1)}}{rL_2} \frac{\partial(r\tilde{c}_3)}{\partial q_2} \pm \frac{ctg\alpha_{sr}^{(1)}}{rL_1} \frac{\partial(r\tilde{c}_3)}{\partial q_1} + \frac{1}{L_1 L_2} \left(\frac{\partial(L_2 \tilde{c}_2)}{\partial q_1} - \frac{\partial(L_1 \tilde{c}_1)}{\partial q_2} \right) + \frac{1}{\tilde{c}_1} \frac{1}{L_2} \frac{\partial \tilde{e}_R}{\partial q_2} = 0. \tag{15}$$

While equation (14) becomes:

$$\tilde{e}_R(\tilde{\psi}_m) = \tilde{e}_0(\tilde{\psi}_m) \pm \omega(r\tilde{c}_3)_0(\tilde{\psi}_m) - \Delta\tilde{e}_g(\tilde{\psi}_m). \tag{16}$$

Finally, the differential equation of axisymmetric flow in blade passages are:

$$\mp \frac{ctg\beta_{sr}^{(1)}}{rL_2} \frac{\partial(r\tilde{c}_3)}{\partial q_2} \pm \frac{ctg\alpha_{sr}^{(1)}}{rL_1} \frac{\partial(r\tilde{c}_3)}{\partial q_1} + \frac{1}{L_1 L_2} \left(\frac{\partial(L_2 \tilde{c}_2)}{\partial q_1} - \frac{\partial(L_1 \tilde{c}_1)}{\partial q_2} \right) +$$
$$+ \frac{1}{\tilde{c}_1 L_2} \frac{\partial \tilde{e}_0(\tilde{\psi}_m)}{\partial q_2} \pm \frac{\omega}{\tilde{c}_1 L_2} \frac{\partial(r\tilde{c}_3)_0(\tilde{\psi}_m)}{\partial q_2} - \frac{1}{\tilde{c}_1 L_2} \frac{\partial\left(\Delta\tilde{e}_g(\tilde{\psi}_m) \right)}{\partial q_2} = 0. \tag{17}$$

3. Differential equation for determining the distribution of average flow velocities along selected meridian flow line in the turbomachine impeller

Using orthogonal curvilinear coordinate system in which the coordinate surfaces $q_2=const.$ are axisymmetric flow surfaces of averaged flow and the coordinate lines $q_1(q_2)$ are the meridian streamlines of the mean flow, differential equation (2), for $L_3 = r / r_o$ and $\tilde{w}_1 = \tilde{c}_1$ becomes:

$$\frac{\partial}{\partial q_1}\left(krL_2\tilde{c}_1\right)=0, \quad i.e. \quad \frac{\partial \tilde{c}_1}{\partial q_1} = -\tilde{c}_1\left(\frac{1}{L_2}\frac{\partial L_2}{\partial q_1}+\frac{1}{r}\frac{\partial r}{\partial q_1}+\frac{1}{k}\frac{\partial k}{\partial q_1}\right). \tag{18}$$

Differential equation of averaged axisymmetric fluid flow in the blade area (eq. (17) for $\tilde{c}_2 = 0$) is:

$$\begin{aligned}&\mp\frac{ctg\beta_{sr}}{rL_2}\frac{\partial(r\tilde{c}_3)}{\partial q_2}\pm\frac{ctg\alpha_{sr}}{rL_1}\frac{\partial(r\tilde{c}_3)}{\partial q_1}-\frac{1}{L_1L_2}\frac{\partial(L_1\tilde{c}_1)}{\partial q_2}+\frac{1}{\tilde{c}_1L_2}\frac{\partial\tilde{e}_0(\bar{\psi}_m)}{\partial q_2}\pm\\&\pm\frac{\omega}{\tilde{c}_1L_2}\frac{\partial(r\tilde{c}_3)_0(\bar{\psi}_m)}{\partial q_2}-\frac{1}{\tilde{c}_1L_2}\frac{\partial\left(\Delta\tilde{e}_g(\tilde{\psi}_m)\right)}{\partial q_2}=0\end{aligned} \tag{19}$$

Where upper sign is for $\vec{e}_3^{\,o} = -\vec{u}^{\,o}$ and lower sign for $\vec{e}_3^{\,o} = \vec{u}^{\,o}$.

In the orthogonal curvilinear coordinate system averaged meridian flow velocity $\tilde{c}_1 = \tilde{c}_m$, and previous differential equations for determining this velocity component can be written:

$$\frac{d\tilde{c}_m}{dl}+M(l)\cdot\tilde{c}_m = N(l), \tag{20}$$

where,

$$\begin{aligned}M(l)=&\frac{1}{r}\cos\gamma\cos\delta\cos^2\beta_{sr}-K_1\cos\delta\sin^2\beta_{sr}+\\&+\sin\delta\left(K_2+\frac{\sin\gamma}{r}+\frac{1}{k}\frac{\partial k}{\partial s_1}\right)+\cos\delta\, ctg\alpha_{sr}ctg\beta_{sr}\sin^2\beta_{sr}\left(K_2+\frac{1}{k}\frac{\partial k}{\partial s_1}\right)+\\&+\left(\sin\delta\, ctg\beta_{sr}+\cos\delta\, ctg\alpha_{sr}\right)\frac{\partial\beta_{sr}}{\partial s_1}-ctg\beta_{sr}\frac{\partial\beta_{sr}}{\partial l},\\N(l)=&\frac{\sin^2\beta_{sr}}{\tilde{c}_1}\left[\frac{d\tilde{e}_0(\bar{\psi}_m)}{dl}-\omega\frac{d(r\tilde{c}_u)_0(\tilde{\psi}_m)}{dl}-\frac{d\left(\Delta\tilde{e}_g(\tilde{\psi}_m)\right)}{dl}+\sin\delta\frac{\partial\left(\Delta\tilde{e}_g(\tilde{\psi}_m)\right)}{\partial s_1}\right]+\\&+2\omega\cos\delta\sin^2\beta_{sr}\left(ctg\beta_{sr}\cos\gamma-ctg\alpha_{sr}\sin\gamma\right).\end{aligned} \tag{20'}$$

Angle γ is the angle between the line parallel to the axis z of the impeller and the tangent to the line $q_1(q_2)$ in some point in the flow space, where:

$$\frac{\partial r}{\partial s_1}=\sin\gamma \quad and \quad \frac{\partial r}{\partial s_2}=\cos\gamma, \tag{21}$$

and $r = r(q_1,q_2)$ is the radius of the particular point.

Equation (20) is quasilinear differential equation of averaged meridional velocity and can be solved iteratively:

$$\tilde{c}_m = P(l)+L(l)\cdot\tilde{c}_{m.0}, \tag{22}$$

where,

$$P(l)=exp\left(-\int_{l_0\neq\phi}^{l} M(l)\cdot dl\right)\left[\int_{l_0\neq\phi}^{l} N(l)\cdot exp\left(\int_{l_0\neq\phi}^{l} M(l)\cdot dl\right)dl\right]$$
$$L(l)=exp\left(-\int_{l_0\neq\phi}^{l} M(l)\cdot dl\right) \tag{22'}$$

Using the volume flow rate, averaged meridian flow velocity $\tilde{c}_{m.0}=\tilde{c}_m(l_0)$ can be calculated:

$$\tilde{c}_{m.0}=\frac{Q-2\pi\int_{l_0\neq\phi}^{l_n} P(l)\cdot k\cdot r\cdot cos\,\delta\cdot dl}{2\pi\int_{l_0\neq\phi}^{l_n} L(l)\cdot k\cdot r\cdot cos\,\delta\cdot dl}, \tag{23}$$

where, $k=k(l)$, $r=r(l)$, $\tilde{c}_m=\tilde{c}_m(l)$ and $\delta=\delta(l)$.

Given the previous formula (23), the distribution function of averaged meridian can be transformed into the form:

$$\tilde{c}_m=A(l)+B(l)\cdot Q, \tag{24}$$

where,

$$A(l)=P(l)-L(l)\frac{\int_{l_0\neq\phi}^{l_n} P(l)\cdot k\cdot r\cdot cos\,\delta\cdot dl}{\int_{l_0\neq\phi}^{l_n} L(l)\cdot k\cdot r\cdot cos\,\delta\cdot dl}\quad and\quad B(l)=\frac{L(l)}{2\pi\int_{l_0\neq\phi}^{l_n} L(l)\cdot k\cdot r\cdot cos\,\delta\cdot dl} \tag{24'}$$

After determining the velocity distribution $\tilde{c}_m(l)$ on the observed meridian flow line *l*, the distribution of $\tilde{\psi}_m(l)=Q_{0.l}=Q(l)$ can also be determined:

$$\tilde{\psi}_m(l)(=Q(l))=2\pi\int_{l_0\neq\phi}^{l_n} k\cdot r\cdot\tilde{c}_{m.0}\,cos\,\delta\cdot dl, \tag{25}$$

Where $\tilde{\psi}_m(l)=0$ for $l=l_0$ and $\tilde{\psi}_m(l)=Q$ for $l=l_n$.

4. Differential equation for determining the distribution of average flow velocities along selected meridian flow line in the turbomachine impeller

In order to determine the meridian streamlines of the averaged flow in the impeller, it is necessary to select a series of meridian flow lines. This task can be solved iteratively, when in the initial (first) approximation, the meridian streamlines of the average flow are determined by using the integral continuity equation. According to the geometric parameters of the blades and the results of the numerical simulation of the flow in the impeller, on the selected meridian flow lines in the impeller, it is possible to determine:

$$k(l),\ \beta_{sr}(l),\ \alpha_{sr}(l)\ and\ r\tilde{c}_u(l). \tag{26}$$

Functional graph (25) can be interpolated according to the values determinate into the calculation points on the chosen meridian flow lines *l*.

Values (25) don't depend on the shape of the averaged meridian streamlines, but following values do:

$$\left.\begin{aligned}&K_1(l),\ K_2(l),\ \gamma(l),\ \delta(l),\ \partial\beta_{sr}/\partial s_1 = f_1(l),\ \partial k/\partial s_1 = f_2(l),\ \tilde{e}_0(\tilde{\psi}_m) = f_3(l),\\&(r\tilde{c}_u)_0(\tilde{\psi}_m) = f_4(l),\ \Delta\tilde{e}_g(\tilde{\psi}_m) = f_5(l),\ \partial(\Delta\tilde{e}_g(\tilde{\psi}_m))/\partial s_1 = f_6(l).\end{aligned}\right\} \tag{27}$$

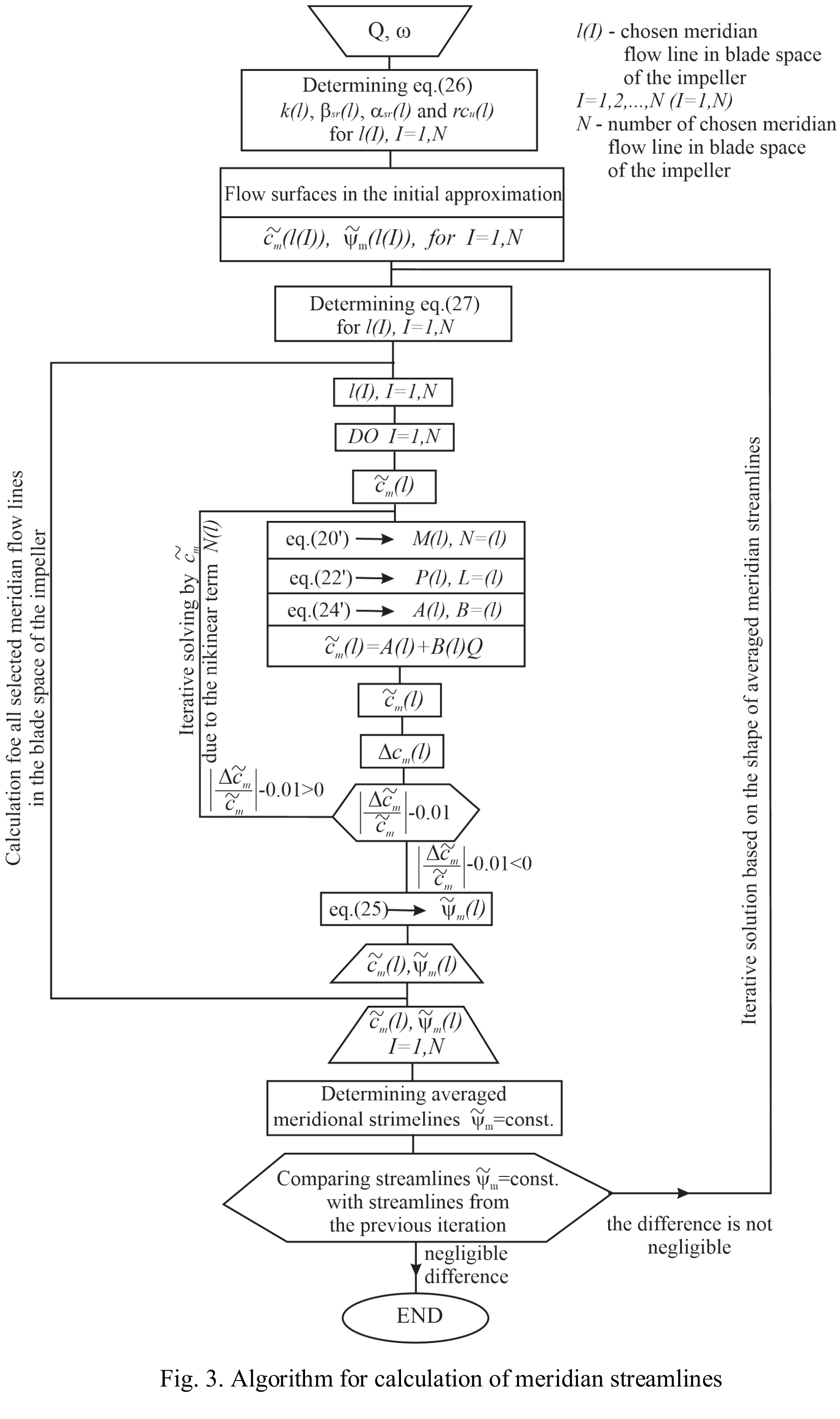

Fig. 3. Algorithm for calculation of meridian streamlines

Figure 3 shows the global algorithm for determining averaged meridian streamlines ($\tilde{\psi}_m = const.$) in the blade area of the turbomachine impeller.

Due to the nonlinear term $N(l)$, in equations (20) in which the required velocity $\tilde{c}_m(l)$ also appears, the procedure for solving the problem is doubly iterative. In each iterative step of solving the problem according to the shape of the averaged meridian streamlines, the velocity $\tilde{c}_m(l)$ distributions are determined by an iterative procedure.

When solving this iterative task, at least five averaged meridian streamlines are used, including border meridian streamlines.

Considering that an equal flow rate passes between adjacent averaged meridian streamlines ($\Delta Q = Q/(n_s - 1)$, when n_s is a number of streamlines), the averaged meridian streamlines are defined by the flow functions:

$$\tilde{\psi}_m = j\frac{Q}{n_s - 1}, \quad j = 0,1,2,...,(n_s - 1). \tag{28}$$

5. Conclusions

The procedure for determining the average axisymmetric flow surfaces in the blade area of the turbomachine impeller is iterative and complex, and it is impossible to carry it out without using numerical methods and computer applications. For this purpose, the paper presents an algorithm for calculating the averaged meridian streamlines in the blade area of the impeller.

Comparing velocity values in the turbomachine impeller gives us an insight into how the flow behaves in the flow domain, in relation to the assumptions that was made in the designing process. Any deviation from axisymmetric fluid flow can lead to the consequences that the designed turbomachine does not achieve the its operating parameters.

Acknowledgments:

This research was financially supported by the Ministry of Science, Technological Development and Innovation of the Republic of Serbia (Contr. No. 451-03-136/2025-03/200109).

References

[1] Krsmanović, Lj., Gajić, A., Turbomachinery - theoretical basics, University of Belgrade, Faculty of Mechanical Engineering Belgrade, Belgrade, Serbia (in Serbian), 2005.
[2] Obradović, N., Basics of Turbomachinery, Gradjevinska knjiga, Belgrade, Serbia (in Serbian), 1973.
[3] Ristić, B., Pumps and Fans, Naučna knjiga, Belgrade, Serbia (in Serbian), 1987.
[4] Babić, M., Stojković, S., Basics of Turbomachinery: operating principles and mathematical modeling, Naučna knjiga, Belgrade, Serbia (in Serbian), 1990.
[5] An, Z., Zhounian, L., Peng, W., Linlin, C., Dazhuan, W., Multi-objective optimization of a low specific speed centrifugal pump using an evolutionary algorithm, Engineering Optimization, Vol. 48(7), 1251-1274, 2015.
[6] Bogdanović-Jovanović, J., Bogdanović, B., Milenković, D., Determination of Averaged axisymmetric flow surfaces according to results obtained by numerical simulation of flow in turbomachinery, Thermal Science, Vol.16 (2), 647-662, 2012.
[7] Bogdanović-Jovanović, J., Determination of Averaged Axisymmetric flow in hydraulic turbomachinery runner, PhD Thesis, University of Niš, Faculty of Mechanical Engineering, Serbia, 2014.
[8] Bogdanović-Jovanović, J., Milenković, D., Stamenković, Ž., Spasić, Ž., Determination of averaged axisymmetric flow surfaces and meridian streamlines in centrifugal pump using numerical simulation results, Facta Universitatis, series: Mechanical Engineering, Vol. 15(3), 479-493, 2017.

B.4

Extended abstract

NUMERICAL SOLUTIONS OF COMPRESSIBLE GAS FLOW IN MICROTUBE IN THE CONTINUUM REGIME

Iva I. Guranov[1][0000-0002-2411-389X], Snezana S. Milicev[1][0000-0003-3055-5544], Nevena D. Stevanovic[1][0000-0003-4385-3882]

[1] Faculty of Mechanical Engineering,
The University of Belgrade, Kraljice Marije 16, 11120 Belgrade 35
e-mail: iguranov@mas.bg.ac.rs , smilicev@mas.bg.ac.rs , nstevanovic@mas.bg.ac.rs

This paper presents a comparison between numerical and analytical [1] solutions for steady, compressible, isothermal gas flow through a long circular microtube of constant cross-section. Gas flows in micro-scale geometries have gained increasing attention due to their relevance in micro-electromechanical systems (MEMS), vacuum technologies, and aerospace applications. Regions characterized by sufficiently small Knudsen numbers can still be accurately described using classical continuum-based approaches.

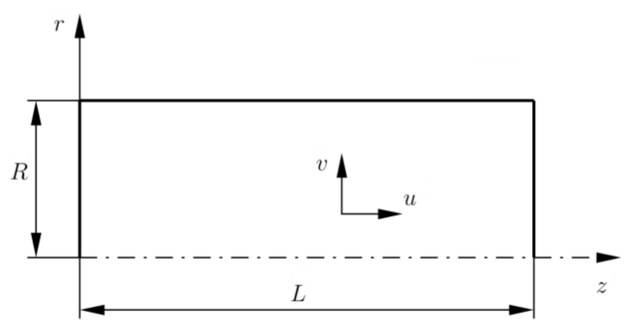

Fig. 1. Microtube geometry.

The aim of this study is to evaluate the accuracy of numerical results in comparison with analytical solutions for compressible, isothermal flow through a cylindrical microtube. Argon is considered as a monoatomic ideal gas, flowing under steady-state conditions. The numerical simulations are performed using Ansys Fluent CFD software, by solving the Navier–Stokes equations using the finite volume method. A structured computational mesh is employed, and a second-order spatial discretization scheme is used to ensure accurate resolution of the flow field. Boundary conditions include standard no-slip at the walls, with specified pressure values at the inlet and outlet. A two-dimensional, axisymmetric model was used, representing half of the geometry due to the axisymmetry of the problem, which reduced computational cost. A mesh independence study was performed to ensure that the solution was not sensitive to the grid size. Once the numerical setup was validated, the simulation results were compared with analytical solutions to assess their accuracy. The pressure and velocity distributions obtained from CFD are compared with those predicted by analytical solutions [1]. The results are shown in Fig. 2, where subfigures (a) and (b) correspond to a pressure ratio between the inlet and outlet cross-section 2, and subfigures (c) and (d) to a pressure ratio of 3. The pressure field results show a more noticeable deviation at higher inlet-to-outlet pressure ratios.

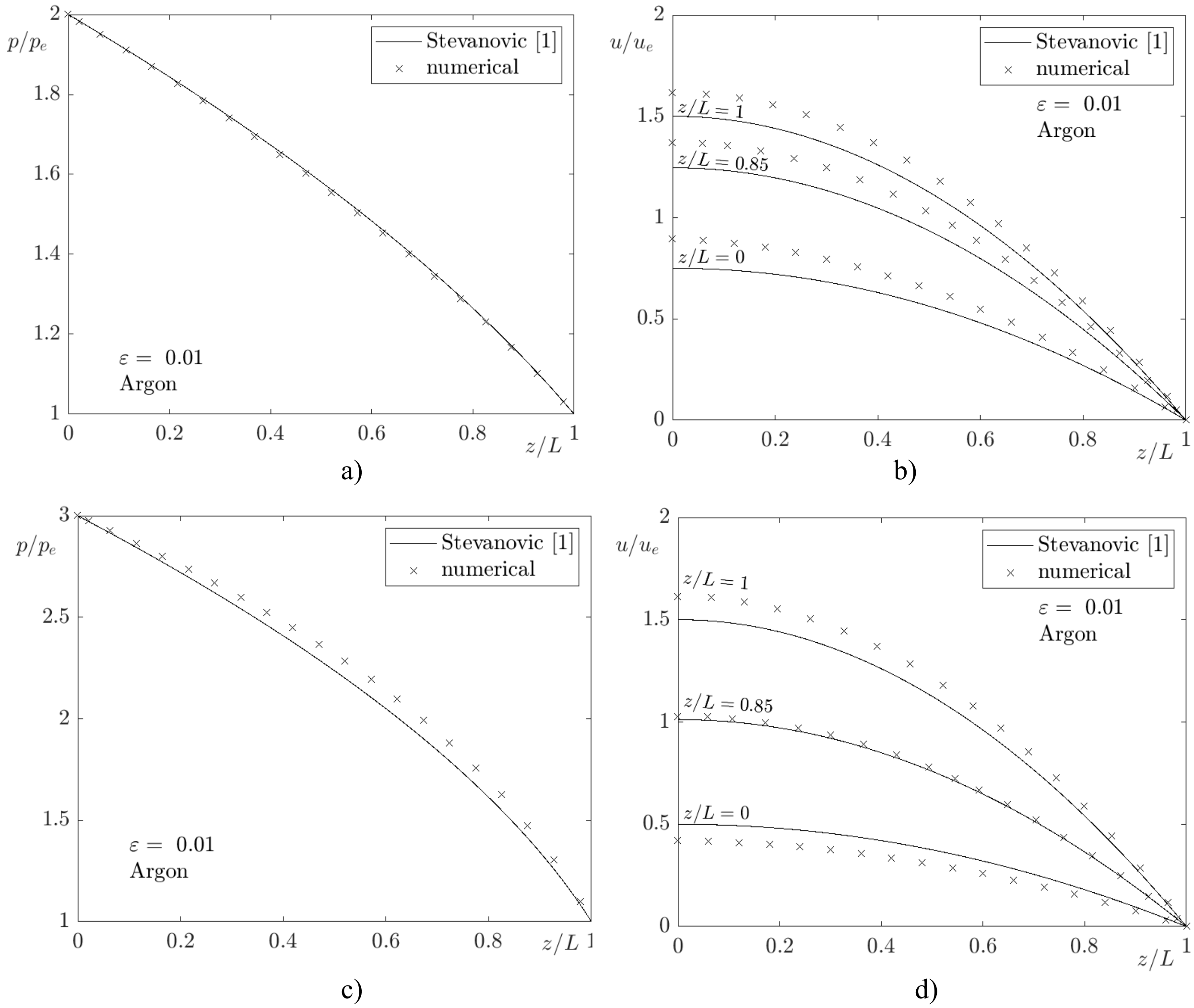

Fig. 2. Pressure distribution (a and c) and velocity profiles (b and d) along the microtube obtained from CFD simulations and analytical solutions.

Regarding the velocity field, it was observed that the velocities at the outlet cross-section remain consistent across cases. This outlet section was taken as a reference, meaning that all flow quantities in the domain are compared relative to the values at the outlet. The velocity profiles also align well across different cross-sections, confirming the accuracy of both approaches. The overall agreement between CFD and analytical results is very good, supporting the reliability of CFD in describing compressible isothermal flow. These findings highlight the strengths and complementary roles of analytical and numerical methods in modeling microtube flows. The results confirm that both CFD and analytical approaches yield reliable predictions for compressible isothermal flow in microtubes. Analytical models are useful for obtaining solutions in simple cases, while numerical solutions remain a powerful tool for handling more complex scenarios. Future work will aim to incorporate more advanced boundary conditions, slip boundary conditions, to extend the analysis to a broader range of micro-scale flow regimes.

Key words: numerical, analytical, microtube, compressible, isothermal

References

[1] Stevanovic N., *Fundamentals of Microfluidics and Nanofluidics,* University of Belgrade –Faculty of Mechanical Engineering, 2014.

[2] *Ansys Fluent Theory Guide*, Ansys, Inc., Canonsburg, January 2025.

10th International Congress of the Serbian Society of Mechanics
Niš, Serbia, June 18-20, 2025

B.5
Original scientific paper

DOI:10.46793/ICSSM25.064K

MAGNETOHYDRODYNAMIC (MHD) FLOW AND HEAT TRANSFER OF ELECTRICALLY CONDUCTING MICROPOLAR FLUID IN A PARALLEL PLATE CHANNEL WITH INDUCED MAGNETIC FIELD

M. Kocić[1][0000-0002-6216-5113], Ž. Stamenković[1][0000-0001-8722-3191], J. Bogdanović-Jovanović[1][0000-0002-8331-2880], J. Petrović[1][0000-0001-6768-9779], M. Nikodijević Đorđević[2][0000-0002-6031-1666]

[1] Faculty of Mechanical Engineering, University of Niš, Aleksandra Medvedeva 14, Niš, Serbia
e-mail: milos.kocic@masfak.ni.ac.rs. , zivojin.stamenkovic@masfak.ni.ac.rs. , jasmina.bogdanovic.jovanovic@masfak.ni.ac.rs. , jelena.petrović@masfak.ni.ac.rs.
[2] Faculty of Occupational Safety, Univerity of Niš, Čarnojevića 10a, Niš, Serbia
e-mail: milica.nikodijevic@znrfak.ni.ac.rs

Abstract:

The flow of micropolar fluids has very wide practical applications. Starting from biomedical engineering (drug delivery and tissue engineering), through industrial processes (lubrication) to environmental engineering (wastewater treatment and enhanced oil recovery). Due to that, laminar and fully developed MHD flow of a micropolar fluid is considered, between plates that extend in the direction x and z, and are at a distance h from each other. An external magnetic field of intensity B acts perpendicular to the flow direction. Due to the electrically conducting micropolar fluid fluid flow and the effect of the external magnetic field, the internal magnetic field of intensity B_x is induced in the direction of the fluid flow. During the flow of micropolar fluid between the parallel plates, they will be maintained at constant and different temperatures. The considered physical model of micropolar fluid flow, defined by partial differential equations, was analytically transformed to ordinary differential equations and solved in closed form under physically appropriate boundary conditions. The obtained solutions were used for further flow analysis. The results of the analysis are presented in the form of graphs, on which the influence of the characteristic dimensionless parameters on the basic physical parameters of the micropolar fluid is given. Based on the analysis given in the paper, unambiguous conclusions can be drawn regarding the very nature of the flow of micropolar fluids, with special reference to the influence of the induced magnetic field.

Key words: micropolar fluid, MHD, induced magnetic field, heat transfer

1. Introduction

MHD flow, or magnetohydrodynamic flow, refers to the behavior of electrically conductive fluids (like plasmas or liquid metals) in the presence of a magnetic field. It combines principles from both fluid dynamics and electromagnetism. In MHD, the motion of the fluid is influenced by magnetic forces, which can affect its velocity, pressure, and other flow characteristics. Key aspects of MHD flow include: *magnetic field interaction*—the magnetic field can exert forces on the charged particles in the fluid, affecting the flow pattern; and *electromagnetic induction*—moving conductive fluids can generate electric currents, which, in turn, produce magnetic fields that influence the fluid's motion. Accordingly, MHD concepts are important in various fields, including astrophysics (like solar flares and stellar dynamics), engineering (like cooling systems in nuclear reactors), and plasma physics.

The significance of magnetohydrodynamics is vast. First, there is the possibility of generating force between two different environments without making contact. Also, there is the potential to design and create machines that have no moving parts and are used for starting fluid without changing its properties during use (e.g., EMHD pumps [1], MHD flow meters, MHD generators, etc.). One of the most significant advantages is the ability to transport liquid metals, aggressive liquids, and plasma across a wide range of operating temperatures. This can be used in nuclear reactors [2] when controlling the flow of cooling liquids or even for medical purposes when precisely dosing and guiding medicine to a diseased organ. Today, technological possibilities are growing, enabling the application of theoretical research. MHD can also be used in metallurgy [3], where MHD techniques can improve processes like metal casting and alloy production by controlling the flow of molten metals, or in advanced propulsion systems such as magnetohydrodynamic drives, which can propel ships without traditional propellers.

Micropolar fluids are fluids that consist of rigid, randomly oriented particles, which have the ability to rotate around their axes, suspended in a viscous liquid, where the deformation of these particles is neglected. The consequence of their presence is a change in the hydrodynamic behavior of the fluid, which can be distinctly non-Newtonian. These fluids belong to the class of fluids with an asymmetric stress tensor, known as polar fluids, which are a more general class of fluids than those studied by the classical theory of hydrodynamics. The first model describing the flow of micropolar fluids was defined by Eringen through two papers published in 1964 and 1966 [4, 5]. The Navier-Stokes model of classical hydrodynamics has a major limitation—it cannot describe fluids containing microstructures. To accurately describe the behavior of these fluids, a theory is needed that takes into account the internal motion of individual material particles. In the micropolar theory, each particle has a finite size and represents a microstructure that can rotate. This type of continuum contains a continuous collection of such particles of finite dimensions. Three additional rotational degrees of freedom are defined by the microrotation vector.

Micropolar fluids can be classified based on various characteristics, including the nature of the microconstituents, their interactions with the base fluid, and their specific applications. Some common types of micropolar fluids are: suspensions, colloids, polymer solutions, and even some kinds of granular materials. The flow of micropolar fluids has a wide range of practical applications, from biomedical engineering (e.g., drug delivery and tissue engineering) to industrial processes (e.g., lubrication) and environmental engineering (e.g., wastewater treatment and enhanced oil recovery).

Starting with the first works of Eringen [4, 5], which were extended to the theory of thermomicrofluids in 1972 [6], through the works of Willson [7], Peddieson, and McNitt [8] in 1970, which dealt with the theory of the boundary layer in micropolar fluids, and up to the recent works of Kumar [9], Baranovskii [10], and also the author of this work, Kocic [11], the theory of micropolar fluids has occupied the attention of scientific researchers for more than five decades.

The continued interest of the scientific community in the topic of micropolar fluid flow indicates the importance of this research. Also, considering the wide field of application of the theory of micropolar fluids, we consider the theoretically addressed flow problem in this paper to be a very good basis for understanding the practical use of micropolar fluids.

2. Physical and mathematical model of the considered problem

The aim of this study is to explore the magnetohydrodynamic (MHD) flow and heat transfer behavior of incompressible micropolar fluid within a parallel plate channel, considering the effects of an induced magnetic field. The analysis will be presented through graphs, illustrating the impact of various characteristic parameters on the velocity vector, microrotation vector, temperature distribution, and induced magnetic field.

2.1 Physical model

The problem of laminar magnetohydrodynamic (MHD) flow and heat transfer of an incompressible, electrically conductive micropolar fluid between two parallel plates is addressed. Typically, MHD flow analysis assumes constant electrical conductivity of the fluid and simplifies the problem to a one-dimensional scenario. The physical setup, as depicted in Figure 1, consists of two infinite parallel plates extending along the *x* and *z* axes. Fully developed flow occurs between these plates, which are separated by a distance *h*, as shown in the figure. The electrically conductive fluid flows through the channel driven by a constant pressure gradient. A uniform magnetic field of strength *B* is applied in the *y*-direction, while the flow direction, with velocity *u*, is along the *x*-axis. Due to the fluid motion, an induced magnetic field of strength B_x is generated along the *x*-axis (with the Reynolds magnetic number around one). The upper and lower plates are maintained at two constant temperatures, T_{w1} and T_{w2}, respectively, where it should be taken into account that $T_{w1} > T_{w2}$.

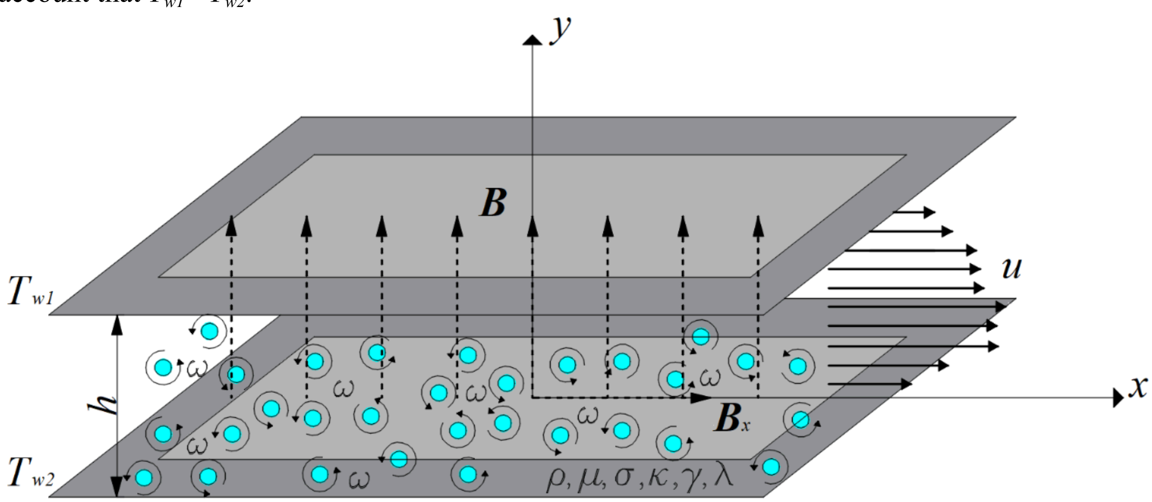

Fig. 1. Physical model and coordinate system

2.2 Mathematical model

Due to the flow of an electroconductive fluid in the presence of an external magnetic field, there is an induction of an electric field of intensity **v**×**B** that causes the generation of a current density vector **j**. If a uniform magnetic field of intensity *B* acts in the direction of the *y* axis, the fluid motion in the direction of flow generates an induced magnetic field of intensity $B_x(y)$. The magnetic field vector is written in the following form:

$$\mathbf{B} = B_x\left(y\right)\vec{i} + B\vec{j} . \tag{1}$$

The complete system of differential equations [12], which describe the considered problem, consists of the momentum equation (2), the angular momentum conservation equation (3), the energy conservation equation (4) and the magnetic induction equation (5):

$$\left(\mu+\lambda\right)\frac{d^2u}{dy^2}+\lambda\frac{d\omega}{dy}+\frac{B}{\mu_0}\frac{dB_x}{dy}-\frac{dp}{dx}=0\quad, \tag{2}$$

$$\gamma\frac{d^2\omega}{dy^2}-\lambda\frac{du}{dy}-2\lambda\omega=0\quad, \tag{3}$$

$$k\frac{d^2T}{dy^2}+\left(\mu+\lambda\right)\left(\frac{du}{dy}\right)^2+\frac{1}{\sigma\mu_0^2}\left(\frac{dB_x}{dy}\right)=0\quad, \tag{4}$$

$$\frac{1}{\sigma\mu_0}\frac{d^2B_x}{dy^2}+B\frac{du}{dy}=0\quad. \tag{5}$$

To solve the given system of equations, it is essential to establish the boundary conditions for the problem at hand. Since the plates are stationary, we assume that both the velocity and microrotation at the plates are zero. For the temperature and induced magnetic field, it is assumed that the walls are isothermal and non-conductive. Based on these assumptions, the boundary conditions are defined as follows:

$$\begin{aligned}&u=0,\ \omega=0,\ T=T_{w2},\ B_x=0\quad for\quad y=0,\\&u=0,\ \omega=0,\ T=T_{w1},\ B_x=0\quad for\quad y=h.\end{aligned}\quad. \tag{6}$$

The next step is to reduce the previous system of equations (2) - (5), as well as the boundary conditions (6), to a dimensionless form, and therefore we first introduce the following transformations, which are usual and generally known in the theory of MHD flow of micropolar fluids:

$$u^*=\frac{u}{U},y^*=\frac{y}{h},\omega^*=\frac{\omega}{\omega_0},b=\frac{B_x}{B},\ U=\frac{h^2P}{\mu},P=-\frac{dp}{dx}=const,\omega_0=\frac{U}{h},\theta=\frac{T-T_{w2}}{T_{w1}-T_{w2}}. \tag{7}$$

Further, Hartmann's, Prandtl's, Eckert's number and Reynolds' magnetic number are defined in order, as well as the characteristic parameters for microplanar fluid flow, the coupling parameter K and the spin-gradient viscosity parameter Γ:

$$Ha=Bh\sqrt{\frac{\sigma}{\mu}},\ \Pr=\frac{\mu c_p}{k},\ Ec=\frac{U^2}{c_p\left(T_1-T_2\right)},\ Rm=\sigma\mu_0Uh,\ K=\frac{\lambda}{\mu},\ \Gamma=\frac{\gamma}{\mu h^2}\quad. \tag{8}$$

Now the system of equations (2) - (5) in dimensionless form is given by the following equations:

$$\left(1+K\right)\frac{d^2u^*}{dy^{*2}}+K\frac{d\omega^*}{dy^*}+\frac{Ha^2}{Rm}\frac{db}{dy^*}+1=0\quad, \tag{9}$$

$$\Gamma\frac{d^2\omega^*}{dy^{*2}}-K\frac{du^*}{dy^*}-2K\omega^*=0\quad, \tag{10}$$

$$\frac{d^2\theta}{dy^{*2}}+\left(1+K\right)\Pr Ec\left(\frac{du^*}{dy^*}\right)^2+\Pr Ec\frac{Ha^2}{Rm^2}\left(\frac{db}{dy^*}\right)^2=0\quad, \tag{11}$$

$$\frac{1}{Rm}\frac{d^2b}{dy^{*2}}+\frac{du^*}{dy^*}=0 \quad . \tag{12}$$

The corresponding boundary conditions given by expressions (6) were transformed into a dimensionless form, as well:

$$\begin{aligned} &u^*=0,\ \omega^*=0,\ \theta=0,\ b=0 \quad \text{za} \quad y^*=0,\\ &u^*=0,\ \omega^*=0,\ \theta=1,\ b=0 \quad \text{za} \quad y^*=1. \end{aligned} \tag{13}$$

When solving the system of equations (9) - (12), it becomes clear that equations (9) and (10) are coupled. To begin solving this system, the first derivative of the quantity *b* is extracted from equation (9), and the resulting equation is differentiated with respect to *y* to obtain the second derivative of *b*. This second derivative is then substituted into equation (12), yielding a new equation that involves only the first and third derivatives of the velocity and the second derivative of the microrotation. The resulting equation, along with equation (10), forms a system of coupled equations. Through further manipulation, a fourth-order equation is derived in the following form:

$$\frac{d^4\omega^*}{dy^{*4}}-a\frac{d^2\omega^*}{dy^{*2}}+b\omega^*=0 \quad , \tag{14}$$

in which the constants are defined by the following expressions:

$$a=RmB^*-(A\text{-}2)D^*,\ b=2RmB^*D^*,\ A=\frac{K}{1+K},\ B^*=\frac{1}{1+K}\frac{Ha^2}{Rm},\ C=\frac{1}{1+K},\ D^*=\frac{K}{\Gamma}. \tag{15}$$

When solving the fourth-order equation (14), there are three possible solutions for vector microrotation depending on the root of the characteristic equation. Those solutions are given by the following expressions:

$$\omega^*=C_1\exp\left(\delta_1y^*\right)+C_2\exp\left(\delta_2y^*\right)+C_3\exp\left(\delta_3y^*\right)+C_4\exp\left(\delta_4y^*\right) \quad , \tag{16}$$

$$\omega^*=\left(C_5+C_6y^*\right)\exp\left(\xi_1y^*\right)+\left(C_7+C_8y^*\right)\exp\left(\xi_2y^*\right) \quad , \tag{17}$$

$$\begin{aligned} \omega^*=&\left[C_9\cos\left(\beta_1y^*\right)+C_{10}\sin\left(\beta_1y^*\right)\right]\exp\left(\alpha_1y^*\right)+\\ &+\left[C_{11}\cos\left(\beta_1y^*\right)+C_{12}\sin\left(\beta_1y^*\right)\right]\exp\left(-\alpha_1y^*\right). \end{aligned} \tag{18}$$

Respectively, the corresponding velocity solutions are given by the following expressions:

$$u^*=C_1\mathsf{D}_1\exp\left(\delta_1y^*\right)+C_2\mathsf{D}_2\exp\left(\delta_2y^*\right)+C_3\mathsf{D}_3\exp\left(\delta_3y^*\right)+C_4\mathsf{D}_4\exp\left(\delta_4y^*\right)+D_1 \quad , \tag{19}$$

$$\begin{aligned} u^*=&[\frac{1}{D^*}\left(C_6+\xi_1C_5\right)-2\frac{C_5}{\xi_1}+2\frac{C_6}{\xi_1^2}]\exp\left(\xi_1y^*\right)+\\ &+[\frac{1}{D^*}\left(C_8+\xi_2C_7\right)-2\frac{C_7}{\xi_2}+2\frac{C_8}{\xi_2^2}]\exp\left(\xi_2y^*\right)+\\ &+\left(\frac{1}{D^*}\xi_1C_6-2\frac{C_6}{\xi_1}\right)y\exp\left(\xi_1y^*\right)+\left(\frac{1}{D^*}\xi_2C_8-2\frac{C_8}{\xi_2}\right)y\exp\left(\xi_2y^*\right)+D_2, \end{aligned} \tag{20}$$

$$u^* = \left[\left(-\Im_1 C_9 + \Im_2 C_{10}\right)\sin\left(\beta_1 y^*\right) + \left(\Im_1 C_{10} + \Im_2 C_9\right)\cos\left(\beta_1 y^*\right)\right]\exp\left(\alpha_1 y^*\right) + \\ +\left[-\left(\Im_1 C_{11} + \Im_2 C_{12}\right)\sin\left(\beta_1 y^*\right) + \left(\Im_1 C_{12} - \Im_2 C_{11}\right)\cos\left(\beta_1 y^*\right)\right]\exp\left(-\alpha_1 y^*\right) + D_3, \tag{21}$$

for dimensionless temperature:

$$\theta = -\left(1+K\right)\Pr Ec[\mathrm{T}_1 \exp\left(2\delta_1 y^*\right) + \mathrm{T}_2 \exp\left(2\delta_2 y^*\right) + \mathrm{T}_3 \exp\left(2\delta_3 y^*\right) + \\ +\mathrm{T}_4 \exp\left(2\delta_4 y^*\right) + \mathrm{T}_6 \exp\left(\left(\delta_1+\delta_3\right) y^*\right) + \mathrm{T}_7 \exp\left(\left(\delta_1+\delta_4\right) y^*\right) + \\ +\mathrm{T}_8 \exp\left(\left(\delta_2+\delta_3\right) y^*\right) + \mathrm{T}_9 \exp\left(\left(\delta_2+\delta_4\right) y^*\right) + \mathrm{T}_{11} \exp\left(\delta_1 y^*\right) + \mathrm{T}_{12} \exp\left(\delta_2 y^*\right) + \\ +\mathrm{T}_{13} \exp\left(\delta_3 y^*\right) + \mathrm{T}_{14} \exp\left(\delta_4 y^*\right) + (\mathrm{T}_5 + \mathrm{T}_{10} + \mathrm{T}_{15}) y^{*2} + D_7 y^* + D_8], \tag{22}$$

$$\theta = -\left(1+K\right)\Pr Ec\{\mathrm{T}_{31} \exp\left(2\xi_1 y^*\right) + \mathrm{T}_{32} \exp\left(2\xi_2 y^*\right) + \\ +\mathrm{T}_{34} \exp\left(\xi_1 y^*\right) + \mathrm{T}_{35} \exp\left(\xi_2 y^*\right) + \mathrm{T}_{36} y^{*2} \exp\left(2\xi_1 y^*\right) + \mathrm{T}_{37} y^{*2} \exp\left(2\xi_2 y^*\right) + \\ +\mathrm{T}_{39} y^* \exp\left(2\xi_1 y^*\right) + \mathrm{T}_{40} y^* \exp\left(2\xi_2 y^*\right) + \mathrm{T}_{42} y^* \exp\left(\xi_1 y^*\right) + \mathrm{T}_{43} y^* \exp\left(\xi_2 y^*\right) + \\ +\frac{1}{2}\mathrm{T}_{30}^* y^{*2} + \frac{1}{6}\mathrm{T}_{27} y^{*3} + \frac{1}{12}\mathrm{T}_{24} y^{*4} + D_9 y^* + D_{10}\}, \tag{23}$$

$$\theta = -\left(1+K\right)\Pr Ec\left\{\left[R_{28}\cos\left(2\beta_1 y^*\right) + R_{29}\sin\left(2\beta_1 y^*\right) + R_{36}\right]\exp\left(2\alpha_1 y^*\right) + \right. \\ +\left[R_{30}\cos\left(2\beta_1 y^*\right) - R_{31}\sin\left(2\beta_1 y^*\right) + R_{37}\right]\exp\left(-2\alpha_1 y^*\right) + \\ +\left[R_{32}\sin\left(\beta_1 y^*\right) + R_{33}\cos\left(\beta_1 y^*\right)\right]\exp\left(\alpha_1 y^*\right) + \\ +\left[R_{34}\cos\left(\beta_1 y^*\right) - R_{35}\sin\left(\beta_1 y^*\right)\right]\exp\left(-\alpha_1 y^*\right) - \\ \left. -R_{38}\cos\left(2\beta_1 y^*\right) - R_{39}\sin\left(2\beta_1 y^*\right) + \frac{1}{2}R_{19} y^{*2} + D_{11} y^* + D_{12}\right\}, \tag{24}$$

and for the induced magnetic field:

$$b = -\frac{1}{B^*}\left[C y^* + C_1 \mathrm{A}_1 \exp\left(\delta_1 y^*\right) + C_2 \mathrm{A}_2 \exp\left(\delta_2 y^*\right) + \right. \\ \left. +C_3 \mathrm{A}_3 \exp\left(\delta_3 y^*\right) + C_4 \mathrm{A}_4 \exp\left(\delta_4 y^*\right) + D_4\right], \tag{25}$$

$$b = -\frac{1}{B^*}[C y^* + \left(A C_5 + \Im_3 C_5 + \Im_5 C_6\right)\exp\left(\xi_1 y^*\right) + \\ +\left(A C_7 + \Im_4 C_7 + \Im_6 C_8\right)\exp\left(\xi_2 y^*\right) + \\ +C_6\left(A + \Im_3\right) y^* \exp\left(\xi_1 y^*\right) + C_8\left(A + \Im_4\right) y^* \exp\left(\xi_2 y^*\right) + D_5], \tag{26}$$

$$b = -\frac{1}{B^*}\{C y^* + \left[\mathrm{N}_9 \cos\left(\beta_1 y^*\right) + \mathrm{N}_{10}\sin\left(\beta_1 y^*\right)\right]\exp\left(\alpha_1 y^*\right) + \\ +\left[\mathrm{N}_{11}\cos\left(\beta_1 y^*\right) + \mathrm{N}_{12}\sin\left(\beta_1 y^*\right)\right]\exp\left(-\alpha_1 y^*\right) + D_6\}. \tag{27}$$

The constants introduced during the process of solving for microrotation, velocity, temperature, and the induced magnetic field are not included here, as their numerous and complex nature would overly complicate the presentation of the paper.

3. Analysis and discussion

In the continuation of this paper, an analysis of the results obtained through the mathematical model of the considered MHD flow of a micropolar fluid is given, in this case not neglecting the induced magnetic field. Analysis of the influence of the induced field is of great importance, as shown by numerous works in this field [13, 14]. On the given graphs, the influence of the magnetic field through the Hartmann number (*Ha*), as well as the additional viscosities of the mircopolar fluid λ and γ, through the parameters of the coupling parameter (*K*) and the spin-gradient viscosity parameter (*Γ*), on the field of velocity, microrotation, temperature and the induced magnetic field will be considered.

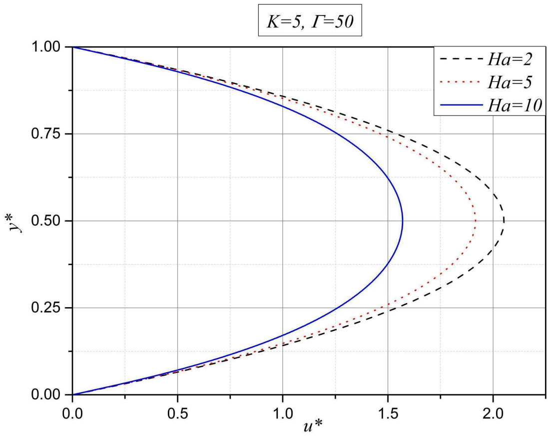

Fig. 2. The influence of the Hartmann number *Ha* on the velocity profile

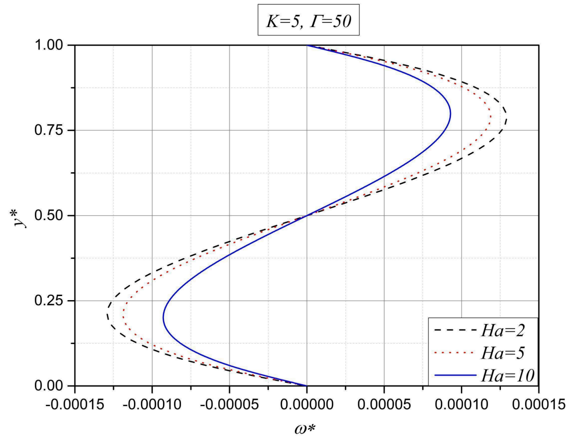

Fig. 3. The influence of the Hartmann number *Ha* on microrotation

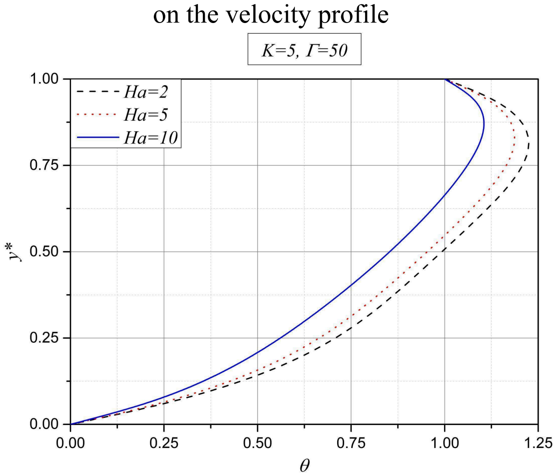

Fig. 4. The influence of the Hartmann number *Ha* on the dimensionless temperature profile

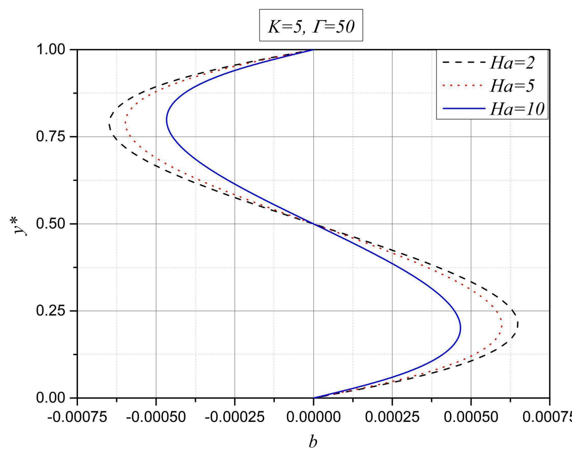

Fig. 5. The influence of the Hartmann number *Ha* on the induced magnetic field

The influence of the Hartmann number on the characteristics of the considered flow problem is given in the first four graphs (Fig. 2-5). The influence of the Hartmann number on the velocity and microrotation profiles of micropolar fluids has been extensively analyzed in previous studies [11]. The conclusions drawn from these analyses are applicable to the current model as well. As shown in Fig. 2., an increase in the Hartmann number results in a reduction of the velocity field across the entire channel width. This behavior is expected, as it reflects the effect of the vertical magnetic field—specifically, the Lorentz force—on the flow direction of the electrically conductive fluid. The Lorentz force opposes the fluid's motion, leading to a decrease in velocity and a "flattening" of the velocity profile. Likewise, Fig. 3 demonstrates that higher Hartmann numbers correspond to a decrease in microrotation in absolute terms. This suggests that stronger magnetic fields diminish the impact of the micropolar fluid's characteristics.

Figure 4. illustrates that at lower Hartmann numbers, viscous heating occurs near the plates in the fluid stream. As the Hartmann number increases, the temperature field within the channel becomes more uniform. Lastly, Fig. 5. depicts the effect of the Hartmann number on the induced magnetic field. As the Hartmann number rises, the intensity of the induced field diminishes because the influence of the externally applied field becomes more dominant than the induced field. This weakening of the induced field relative to the external field leads to a decrease in the flow rate of the micropolar fluid as the Hartmann number increases, which is directly correlated with the results shown in Fig. 2.

The following four graphs will present the influence of the coupling parameter K on the characteristic physical quantities of the flow of the considered problem.

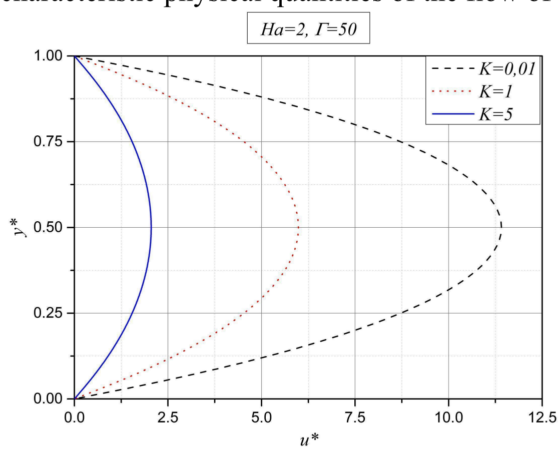

Fig. 6. Velocity profiles for different values of the coupling parameter K

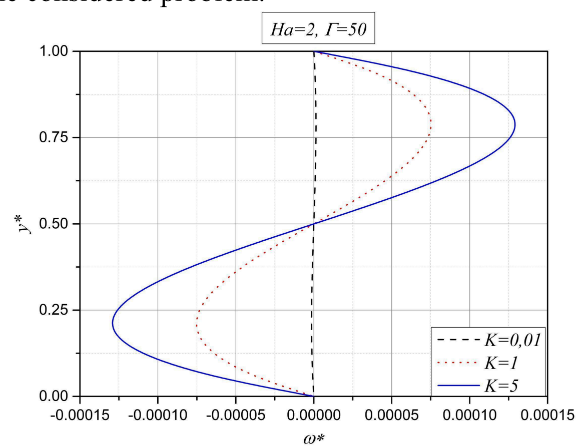

Fig. 7. Micro-rotation for different values of the coupling parameter K

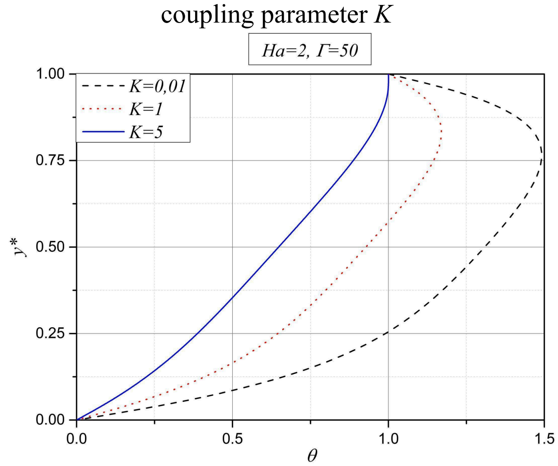

Fig. 8. Dimensionless temperature in function of the coupling parameter K

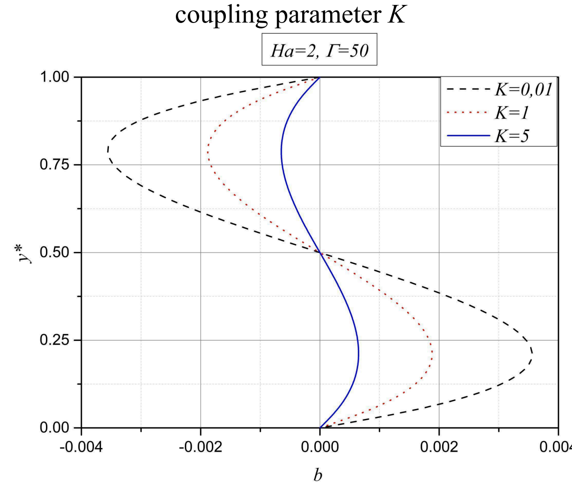

Fig. 9. Induced magnetic field in function of the coupling parameter K

From the given Fig. 6. and 7., it can be clearly seen that an increase in the coupling parameter K leads to a decrease in velocity, and on the other hand, to an increase in the absolute value of the microrotation by the height of the current space between the plates. From this, the conclusion is drawn that increasing the coupling parameter K creates resistance to the flow of the fluid, while on the other hand it intensifies the characteristics of the micropolar fluid through the additional viscosity λ, which is reflected in a more intense microrotation.

Figure 8., which illustrates the effect of the coupling parameter K on the dimensionless temperature, shows that an increase in K results in a decrease in the dimensionless temperature across the entire height between the plates. Figure 9. displays the influence of the coupling parameter K on the induced magnetic field. From this graph, it is evident that as K increases, the induced magnetic field b decreases throughout the height of the channel. This behavior aligns with the findings in Fig. 6., where we observed that the supplementary viscosity λ increases flow resistance. Since the induced field arises from the motion of the electrically conductive fluid, the effect of the coupling parameter K on the induced magnetic field is therefore expected.

The last four graphs will show the influence of the spin-gradient viscosity parameter Γ on the field of velocity, microrotation, temperature and induced magnetic field.

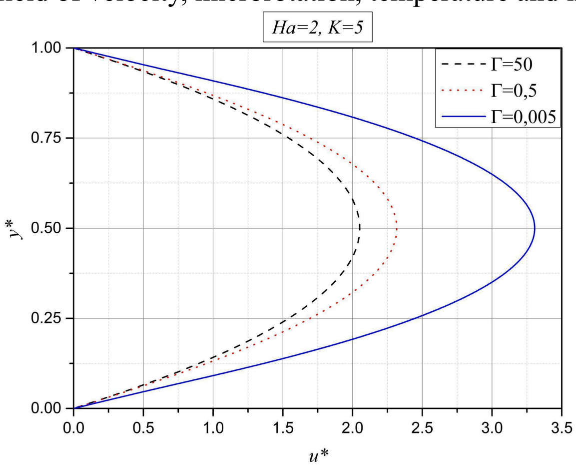

Fig. 10. Influence of the spin-gradient viscosity parameter Γ on the velocity profile

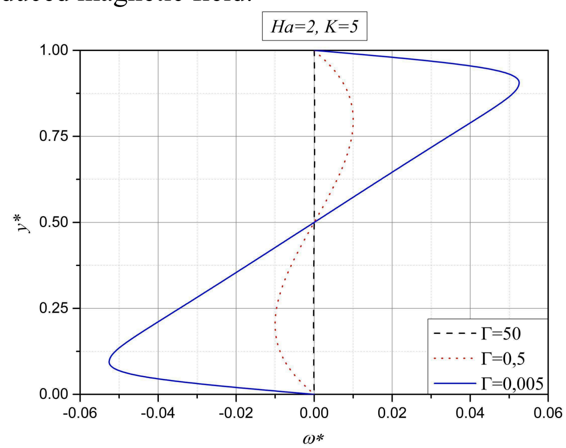

Fig. 11. Influence of the spin-gradient viscosity parameter Γ on microrotation

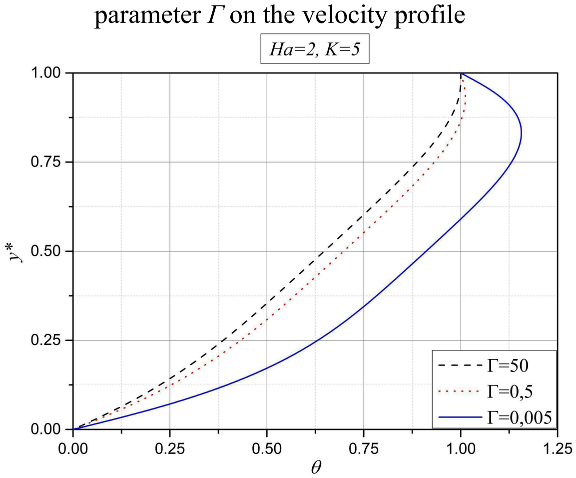

Fig. 12. Dimensionless temperature in function of the spin-gradient viscosity parameter Γ

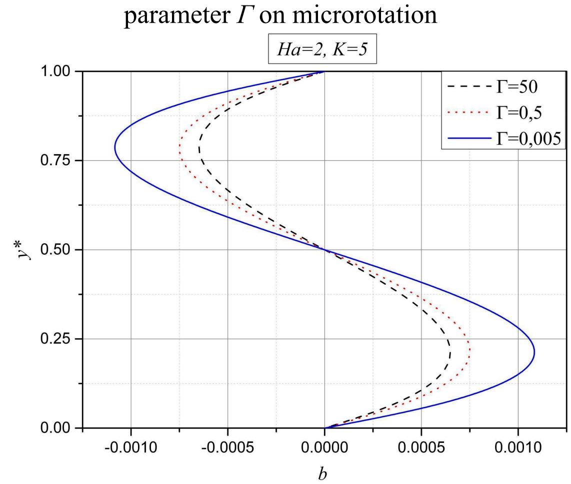

Fig. 13. Induced magnetic field in function of the spin-gradient viscosity parameter Γ

Figures 10. and 11. demonstrate that increasing the spin-gradient viscosity parameter Γ reduces both the velocity and microrotation intensity across the entire height between the plates, compared to a viscous fluid. Figure 12. shows that higher Γ values lead to a decrease in the dimensionless temperature, indicating less energy transformation within the fluid. Finally, Fig. 13. illustrates that an increase in Γ results in a decrease in the induced magnetic field throughout the channel height. Since the induced field is linked to the flow velocity, and Fig. 10. shows that increasing Γ reduces velocity, this trend in the induced magnetic field is expected.

4. Conclusions

In conclusion, the analysis of the MHD flow of a micropolar fluid, including the induced magnetic field, reveals several key findings. Increasing the Hartmann number reduces both the velocity and microrotation, with the Lorentz force opposing fluid motion and "flattening" the velocity profile. Additionally, higher Hartmann numbers decrease the induced magnetic field due to the dominance of the externally applied field. The coupling parameter K increases flow resistance and intensifies microrotation, while also decreasing temperature and the induced magnetic field. Lastly, the spin-gradient viscosity parameter Γ reduces both velocity and microrotation, decreases the dimensionless temperature, and weakens the induced magnetic field. These trends highlight the complex interactions between the magnetic field, fluid characteristics, and flow dynamics.

Acknowledgments

This research was financially supported by the Ministry of Science, Technological Development and Innovation of the Republic of Serbia (Contract No. 451-03-137/2025-03/200109).

References

[1] Al-Habahbeh O.M., Al-Saqqa M., Safi M., Abo Khater T., *Review of magnetohydrodynamic pump applications*, Alexandria Engineering Journal, Volume 55(2), 1347-1358, 2016.

[2] Morley, N. B., Malang, S. and Kirillov, I. *Thermo-fluid magnetohydrodynamic issues for liquid breeders*, Fusion Science and Technology, Vol. 47, 488-501, 2005.

[3] Sivak B. A., Grachev V. G., Parshin V. M., Chertov A. D., Zarubin S. V., Fisenko V. G., Solovev A. A., *MHD processes in the electromagnetic stirring of liquid metal in continuous section and bloom casters*, Metallurgist, Volume 53(7), 469-481, 2009.

[4] Eringen A. C., *Simple micro fluids*; International Journal of Engineering Science, Vol. 2, 205 - 217, 1964.

[5] Eringen A. C., *Theory of micropolar fluids*, Journal of Mathematics and Mechanics. Vol. 16, 1 - 16, 1966.

[6] Eringen A. C., *Theory of thermomicrofluids*, Journal of Mathematical Analysis and Applications, Vol. 38, pp. 480-496, 1972.

[7] Willson A. J., *Boundary Layers in Micropolar liquids*, Mathematical Proceedings of the Cambridge Philosophical Society, Vol. 67. pp. 469-476, 1970.

[8] Peddieson J. and McNitt R. P., *Boundary layer theory for a micropolar fluid*, Recent Advances in Engineering Science, Vol. 5, pp. 405 – 426, 1970.

[9] Vinoth Kumar B., Sreenivasulu P., Bilal S., Poornima T., *Thermal performance of a micropolar fluid flowing around a vertical cone with consideration of spatially varying heat source*, Case Studies in Thermal Engineering, Vol. 65, 1-25, 2025.

[10] Baranovskii E.S., Prosviryakov E.Yu., Ershkov S.V., *Mathematical analysis of steady non-isothermal flows of a micropolar fluid*, Nonlinear Analysis: Real World Applications, Vol. 84, 2025.

[11] Kocić M., Stamenković Ž., Petrović J., Bogdanović-Jovanović J.. *MHD micropolar fluid flow in porous media*, Advances in Mechanical Engineering. Vol. 15(6), 2023.

[12] Kocić M., *Research of magentohydrodynamic flow and heat transfer of micropolar fluids*, doctoral dissertation, 2019.

[13] Mekheimer Kh. S., *Peristaltic Flow of a Magneto-Micropolar Fluid: Effect of Induced Magnetic Field*, Journal of Applied Mathematics, Vol. 2008, 23 pages, 2008.

[14] Sajid M., Ali N., Abbas Z. and Javed T., *On modelling of two-dimensional MHD flow with induced magnetic field: solution of peristaltic flow of a couple stress fluid in a channel*, Iranian Journal of Science & Technology, Vol. 39, 35-43, 2015.

10th International Congress of the Serbian Society of Mechanics
Niš, Serbia, June 18-20, 2025
B.6

Extended abstract

A macroscopic multi-temperature model with transport properties in comparison with kinetic models in the context of binary mixtures

Damir Madjarević[1] [0000-0003-0487-1842]

[1]University of Novi Sad, Faculty of Technical Sciences, Serbia, email: damirm@uns.ac.rs

Abstract. Our objective is to conduct a comparative analysis of two highly interrelated theoretical frameworks within the contemporary mixture theory field - extended thermodynamics and kinetic theory of gases [1, 2]. The current research examines the shock wave profiles that emerge as a test problem within the context of the macroscopic multi-temperature (MT) model for binary gaseous mixtures. In order to achieve our research objectives, we have adopted the hyperbolic model that was developed within the framework of extended thermodynamics, wherein we have incorporated both viscosity and thermal conductivity to eliminate restrictions on the parameters of the model [3]. This inclusion facilitates a comparative analysis of our results against more sophisticated kinetic solutions that have been computed for hypothetical mixtures of gases [4]. Furthermore, it is noteworthy that the numerical implementation of the multi-temperature model is significantly less complex in comparison to the computational processes required for the Boltzmann equations pertinent to gaseous mixtures or the Direct Simulation Monte Carlo Method (DSMC), which is known for its computational intensity and complexity.

Keywords: Shock waves, Mixtures, Extended thermodynamics, Kinetic theory.

1. Introduction

With diffusion as only dissipative mechanism, the structure of the source terms is determined using the general principles of extended thermodynamics - invariance of equations with respect to the Galilean transformation and the entropy principle [3]. In this simplest case, where diffusivity and relaxation times are taken from kinetic theory for mixture of monatomic gases, excellent agreement was obtained but with restriction on the shock strength, i.e. Mach number. Adding extra dissipation terms into the initial hyperbolic model we are able to extend analysis to a larger set of parameters.

The following shock structure equations, which describe the thermodynamic processes are the following:

$$
\begin{aligned}
&\frac{d}{d\xi}(\rho u)=0, \quad \frac{d}{d\xi}\left(\rho u^2+p-(\sigma_1+\sigma_2)+\frac{J^2}{\rho c(1-c)}\right)=0,\\
&\frac{d}{d\xi}\left\{\left(\frac{1}{2}\rho u^2+\rho\varepsilon+p\right)u-(\sigma_1+\sigma_2)u+q_1+q_2-\left(\frac{\sigma_1}{\rho c}-\frac{\sigma_2}{\rho(1-c)}\right)\right.\\
&\left.+J\left(\frac{uJ}{\rho c(1-c)}+\frac{1}{\beta}\right)J\right\}=0, \quad \frac{d}{d\xi}(\rho cu+J)=0, \quad \frac{d}{d\xi}\left\{\rho cu^2+\frac{J^2}{\rho c}+2uJ+p_1-\sigma_1\right\}=\hat{m}_1,\\
&\frac{d}{d\xi}\left\{\left(\frac{1}{2}\rho c\left(u+\frac{J}{\rho c}\right)^2+\rho c\varepsilon_1+p_1\right)\left(u+\frac{J}{\rho c}\right)-\sigma_1\left(u+\frac{J}{\rho c}\right)+q_1\right\}=\hat{m}_1u+\hat{e}_1,
\end{aligned}
\tag{1}
$$

where $J = \rho c(v_1 - u) = \rho(1-c)(v_2 - u)$ is the diffusion flux and c the concentration of the first constituent. The model takes into account dissipation through the relaxation and diffusion type source terms. Phenomenological relations of diffusion type are used for describing behavior of the stress tensor and heat flux vector:

$$\sigma_\alpha = \frac{4}{3}\mu_\alpha \frac{dv_\alpha}{d\xi}, \quad q_\alpha = -\kappa_\alpha \frac{dT_\alpha}{d\xi}, \quad v_1 = u + \frac{J}{\rho c}, \quad v_2 = u - \frac{J}{\rho(1-c)} \quad (\alpha = 1,2), \tag{2}$$

where v_α and T_α stands for velocity and temperatures of the constituents. Viscosity μ_α and thermal conductivity κ_α of the constituents are determined using the results of kinetic theory of gases for hard spheres model of interaction in equilibrium in the case of monatomic gases [5]:

$$\mu_\alpha = \frac{5}{16 d_\alpha^2}\left(\frac{k m_\alpha T_\alpha}{\pi}\right)^{1/2}, \qquad \lambda_\alpha = \frac{5}{2}\mu_\alpha c_{V\alpha} \quad (\alpha = 1,2). \tag{3}$$

where k is the Boltzmann constant, $c_{V\alpha} = 3k/2m_\alpha$ stands for the specific heats at constant volume and m_α denotes atomic masses of the mixture constituents.

Relaxation type terms for the diffusion $\hat{m}_1$ and $\hat{e}_1$ were previously explained in [3]. This gives us ten ordinary differential equations of the first order for the unknown state variables $\mathbf{U} = (\rho, u, T, c, J, \Theta, \sigma_1, \sigma_2, q_1, q_2)$, where $\Theta = T_2 - T_1$. Equations for the shock wave structure in dimensionless form were given in [3]. It is important to mention that atomic diameters of the mixture constituents d_α, which are not present in inviscid model, now come out as a parameter $\mathrm{DR} = d_1/d_2$.

Acknowledgement. This work was supported within project of the Department of Technical Mechanics, Faculty of Technical Sciences, titled ”Modeling and Analysis of Mechanical Systems”.

References

[1] Bae G.C., Ha S.Y., Hwang G., Ruggeri T., *On the comparison between phenomenological and kinetic theories of gas mixtures with applications to flocking*, Physica D: Nonlinear Phenomena, 469, p.134321., 2024.

[2] Čolić M., *Explicit model for a mixture of Eulerian fluids based on kinetic theory*, Physics of Fluids, 36(6), 2024.

[3] Madjarević, D., *Shock structure and temperature overshoot in macroscopic multi-temperature model of binary mixtures*. In From Particle Systems to Partial Differential Equations II: Particle Systems and PDEs II, Braga, Portugal, Springer International Publishing, 129, 253-272, 2015.

[4] Kosuge, S., Aoki, K., Takata, S., *Shock-wave structure for a binary gas mixture: finite-difference analysis of the Boltzmann equation for hard-sphere molecules*, European Journal of Mechanics-B/Fluids, 20(1), 87-126, 2001.

[5] Chapman, S., Cowling, T. G., *The mathematical theory of non-uniform gases: an account of the kinetic theory of viscosity, thermal conduction and diffusion in gases*. Cambridge university press, 1990.

10th International Congress of the Serbian Society of Mechanics
Niš, Serbia, June 18-20, 2025

B.7
Extended abstract

ON THE MODELLING OF KORTEWEG FLUIDS

Zagorka Matić[1] and **Srboljub Simić**[2] [0000-0003-3726-2007]

[1]University of Novi Sad, Faculty of Technical Scienes, email: zagorka.mat@uns.ac.rs [2]University of Novi Sad, Faculty of Scienes, e-mail: ssimic@uns.ac.rs

Abstract. Korteweg fluid is a continuum model that appropriately describes capillary effects through diffuse interfaces. In this study, nonequilibrium modelling of Korteweg fluids is discussed using the Liu method of multipliers. Korteweg stresses are recovered in a generalized form, and the structure of specific internal energy is analyzed.

Keywords: Capillarity; Diffuse interface; Korteweg fluids; Nonequilibrium; Liu's method

1. Nonequilibrium modelling of Korteweg fluids

Thermodynamically consistent continuum models are assumed to be compatible with entropy balance law (entropy inequality). In such a way, admissible constitutive relations are determined that are valid for any thermomechanical process. Korteweg fluids represent the continuum model that inherits capillary effects by means of diffuse interfaces. Classical approach to the problem relies on the Coleman-Noll procedure [1]. On the other hand, Liu's method of multipliers [2] provides strict mathematical procedure that needs certain generalizations in the case of Korteweg fluids [3, 4]. In this study, the latter approach is used to discuss nonequilibrium modelling of Korteweg fluids.

To describe capillary effects by means of diffuse interfaces, the model of Korteweg fluids inherits the mass density gradient as a field variable. Consequently, the governing equations consist of mass, momentum and energy conservation laws, and the balance law that governs evolution od the mass density gradient. This equation is obtained as a gradient of the mass conservation law:

$$\begin{gathered}
\mathscr{E}^{\rho} \equiv \frac{\partial \rho}{\partial t} + \frac{\partial}{\partial x_j}(\rho v_j) = 0, \quad \mathscr{E}^{v_i} \equiv \frac{\partial}{\partial t}(\rho v_i) + \frac{\partial}{\partial x_j}(\rho v_i v_j - t_{ij}) = 0, \\
\mathscr{E}^{e} \equiv \frac{\partial}{\partial t}\left(\frac{1}{2}\rho|\mathbf{v}|^2 + \rho e\right) + \frac{\partial}{\partial x_j}\left(\left(\frac{1}{2}\rho|\mathbf{v}|^2 + \rho e\right) v_j - t_{ij} v_i + q_j\right) = 0, \\
\mathscr{E}_i^{\nabla\rho} \equiv \frac{\partial}{\partial t}\frac{\partial \rho}{\partial x_i} + \frac{\partial}{\partial x_j}\left(\frac{\partial \rho}{\partial x_i} v_j + \rho \frac{\partial v_j}{\partial x_i}\right) = 0.
\end{gathered} \tag{1}$$

Balance laws (1) have to be compatible with the entropy balance law:

$$\frac{\partial}{\partial t}(\rho s) + \frac{\partial}{\partial x_j}(\rho s v_j + \varphi_j) = \Sigma, \quad \Sigma \geq 0. \tag{2}$$

This compatibility is achieved through the use of multipliers:

$$\frac{\partial}{\partial t}(\rho s) + \frac{\partial}{\partial x_j}(\rho s v_j + \varphi_j) - \Lambda^{\rho}\mathscr{E}^{\rho} - \Lambda^{v_i}\mathscr{E}^{v_i} - \Lambda^{e}\mathscr{E}^{e} - \Lambda_i^{\nabla\rho}\mathscr{E}_i^{\nabla\rho} = \Sigma \geq 0. \tag{3}$$

Analysis of the extended entropy balance law (3) yields the following multipliers:

$$\Lambda^{e} = \frac{1}{\theta}, \quad \Lambda_i^{\nabla\rho} = \frac{1}{\theta}\alpha(\rho,\theta)\frac{\partial \rho}{\partial x_i}, \quad \Lambda^{v_i} = -\frac{v_i}{\theta}, \quad \Lambda^{\rho} = \frac{1}{\theta}\left(e - \theta s + \frac{p}{\rho} - \frac{1}{2}|\mathbf{v}|^2\right). \tag{4}$$

2. Constitutive relations

Constitutive relations are obtained through analysis of the residual inequality, which expresses non-negativity of the entropy production Σ. First, the entropy flux which inherits the capillary effects is obtained:

$$\varphi_j = \frac{1}{\theta}\left(q_j + \rho\alpha(\rho,\theta)\frac{\partial\rho}{\partial x_j}\frac{\partial v_k}{\partial x_k}\right). \tag{5}$$

Minimization of the entropy production Σ in equilibrium determines the equilibrium stress tensor (and the heat flux), which recover the Korteweg stresses in a bit generalized form:

$$t_{ij}^{eq} = -\left[p + \rho\frac{\partial\alpha(\rho,\theta)}{\partial\rho}\frac{\partial\rho}{\partial x_k}\frac{\partial\rho}{\partial x_k} + \rho\alpha(\rho,\theta)\frac{\partial^2\rho}{\partial x_k\partial x_k}\right]\delta_{ij} + \alpha(\rho,\theta)\frac{\partial\rho}{\partial x_i}\frac{\partial\rho}{\partial x_j}, \quad q_k^{eq} = 0_k. \tag{6}$$

Important feature of the method of multipliers is that the Gibbs relation is not an assumption, but it is obtained as a consequence of the analysis. In the case of Korteweg fluids, Gibbs relation is extended and inherits the mass density gradient:

$$\theta \mathrm{d}s = \mathrm{d}e - \frac{p}{\rho^2}\mathrm{d}\rho + \frac{\alpha(\rho,\theta)}{\rho}\frac{\partial\rho}{\partial x_i}\mathrm{d}\left(\frac{\partial\rho}{\partial x_i}\right). \tag{7}$$

This is in accordance with the nature of capillarity as an equilibrium effect.

3. Conclusions

In this study, constitutive relations for Korteweg fluids were derived using Liu's method of multipliers. Although the method is technically demanding, it is mathematically consistent and it is not burdened with restrictive physical assumptions. It facilitated consistent derivation of entropy flux, Korteweg stresses and Gibbs relation. As such, the method has great potential for analysis of the mixtures of Korteweg fluids [5, 6], which is supposed to be the next step in its applications.

References

[1] Heida, M., Málek, J., *On compressible Korteweg fluid-like materials*, International Journal of Engineering Science, 48, 1313–1324, 2010.

[2] Liu, I-S., *Method of Lagrange Multipliers for Exploitation of the Entropy principle*, Arch. Rational Mech. Anal., 46, 131–148, 1972.

[3] Cimmelli, V.A., Oliveri, F., Pace, A.R., *On the Thermodynamics of Korteweg Fluids with Heat Conduction and Viscosity*, J. Elast, 104, 115–131, 2011.

[4] Ván, P., *Holographic fluids: A thermodynamic road to quantum physics*, Phys. Fluids, 35, 057105, 2023.

[5] Cimmelli, V.A., Gorgone, M., Oliveri, F., Pace, A.R., *Weakly nonlocal thermodynamics of binary mixtures of Korteweg fluids with two velocities and two temperatures*, European Journal of Mechanics/B Fluids, 83, 58–65, 2020.

[6] Gorgone, M., Oliveri, F., Rogolino, P., *Thermodynamical analysis and constitutive equations for a mixture of viscous Korteweg fluids*, Phys. Fluids, 33, 093102, 2021.

10th International Congress of the Serbian Society of Mechanics
Niš, Serbia, June 18-20, 2025

B.9
Original scientific paper

DOI:10.46793/ICSSM25.079M

NUMERICAL INVESTIGATION OF FLUID MIXING IN A MICROMIXER USING CFD SIMULATIONS

Mina Mirović[1] [0009-0002-2097-6863], Veljko Begović[2] [0000-0001-8578-8287], Petar Miljković[3] [0000-0003-0450-3599], Danijela Srećković[4] [0009-0006-2858-9269]

[1] Altera ECD
Vojvođanska 12, 11073 Belgrade, Serbia
e-mail: mmirovic@altera-ecd.rs

[2] Faculty of Mechanical Engineering
The University of Niš, Aleksandra Medvedeva 14, 18000 Niš, Serbia
e-mail: veljko.begovic@masfak.ni.ac.rs

[3] Faculty of Mechanical Engineering
The University of Niš, Aleksandra Medvedeva 14, 18000 Niš, Serbia
e-mail: petar.miljkovic@masfak.ni.ac.rs

[4] eCon Engineering Kft.
Kondorosi út 3, 1116 Budapest, Hungary
e-mail: danijela.sreckovic@econengineering.com

Abstract:

This study investigates the mixing behavior of water and colored water in a complex micromixer geometry, using CFD simulations with Ansys Fluent® and ParticleWorks® to analyze performance. The two solvers employ distinct numerical methods: the Finite Volume Method (FVM) in Ansys Fluent®, which uses a computational mesh, and the meshless Moving Particle Simulation (MPS) method in ParticleWorks®. The simulations assess concentration profiles, pressure drop, and the mixing index across different Reynolds numbers and flow rates. Additionally, the impact of temperature differences between the inlet fluids on mixing quality was examined. The results of this study were validated against previously conducted experimental data and the CFX® numerical results confirm their accuracy and reliability.

The micromixer features a Y-mixer and an S-type microchannel, designed for improved fluid blending.

Key words: Computational Fluid Dynamics (CFD), Micromixer, Mixing Index, Finite Volume Method (FVM), Moving Particle Simulation (MPS)

1. Introduction

Mixing, defined as the dispersion of one phase into another, is essential in chemical, pharmaceutical, and biochemical processing to eliminate compositional inhomogeneities and ensure uniform product quality. Since direct measurement of full compositional fields is difficult, homogeneity is typically assessed via statistical analysis of sampled data.

Micromixers are key in microfluidic systems, enabling efficient mixing under laminar flow through diffusion and geometry-driven advection. Designs like curved channels, split-and-recombine structures, and obstacles enhance mass and heat transfer. T-shaped micromixers, in particular, are widely used to study mixing across flow regimes, employing mechanisms such as chaotic advection.

Pioneering work by Bökenkamp et al. [1] demonstrated effective mixing in T-mixers. Subsequent studies by Engler et al. [2], Hoffmann et al. [3], and Dreher [4] explored flow regimes and transient effects during symmetric 1:1 mixing.

This study analyzes water flow in a T-micromixer using two CFD tools, Ansys Fluent® (FVM-based) and ParticleWorks® (MPS-based). Fluent is mesh-based and suited for laminar/turbulent, multiphase, and thermal flows, while the mesh-free ParticleWorks® excels in handling complex geometries and free-surface flows with minimal preprocessing.

By comparing both approaches to reference data from [5], including experiments and Ansys CFX® simulations, the study assesses accuracy in predicting microscale flow behavior. In addition to mixing index and pressure drop, temperature distribution and its effect on mixing are also analyzed, contributing to improved design of efficient microfluidic systems in process engineering.

2. Simulation Software Methodology

Ansys Fluent® provides a comprehensive suite of modeling capabilities for analyzing both incompressible and compressible fluid flows across laminar and turbulent regimes. For all flow types, it solves the fundamental conservation equations for mass and momentum. In cases involving heat transfer or compressibility, an additional energy conservation equation is also solved. The governing equations are discretized using the Finite Volume Method (FVM), ensuring that the continuity, momentum, and energy equations are accurately satisfied within each control volume (cell).

2.1. Mass Conservation Equation

The fundamental mass conservation principle is expressed by the continuity equation:

$$\frac{\partial \varrho}{\partial t} + \nabla \cdot (\varrho \vec{v}) = S_m \tag{1}$$

Equation (1) is the general form of the mass conservation equation and is valid for incompressible as well as compressible flows. The source term S_m represents the mass added to the continuous phase from the dispersed secondary phase, ϱ denotes the fluid density and $\vec{v}$ is the velocity vector [6].

2.2. Momentum Conservation Equations

For an inertial (non-accelerating) reference frame, the conservation of momentum is described by [6]:

$$\frac{\partial}{\partial \mathrm{t}}(\rho \vec{v}) + \nabla \cdot (\rho \vec{v} \vec{v}) = -\nabla p + \nabla \cdot (\bar{\tau}) + \rho \vec{g} + \vec{F} \tag{2}$$

Here, p denotes static pressure, $\bar{\tau}$ is the stress tensor, $\varrho \vec{g}$ and F represent gravitational and external body forces, respectively [6]. The stress tensor $\underline{\tau}$ is given by

$$\bar{\tau} = \mu\left[\left(\nabla \vec{v} + \nabla \vec{v}^{T}\right) - \frac{2}{3} \nabla \cdot \vec{v} I\right] \tag{3}$$

where μ is the dynamic viscosity, I is the unit tensor, and the second term on the right hand side is the effect of volume dilation [6].

2.3. Energy Conservation Equation

Conservation of energy is described by:

$$\frac{\partial}{\partial t}(\rho E) + \nabla \cdot (\vec{v}(\rho E + p)) = -\nabla \cdot \left(\sum_j h_j J_j\right) + S_h \tag{4}$$

where E represents the total specific energy, and on the right side h_j denotes specific enthalpy of species j, J is the diffusive flux of species j and S_h is the volumetric energy source term [6].

2.4. ParticleWorks®

ParticleWorks® is a mesh-free CFD software package that implements the Moving Particle Semi-implicit (MPS) method. In mesh-free particle methods like MPS, the fluid domain is discretized into moving particles which carry fluid properties. The MPS method, originally introduced by Koshizuka and Oka [7], is designed for stable simulation of incompressible fluids, particularly free-surface flows. Unlike traditional mesh-based CFD, MPS eliminates the need for mesh generation and can directly use complex CAD geometries

The Moving Particle Semi-implicit (MPS) method was developed for simulating incompressible viscous flows with free surfaces [7]. A semi-implicit algorithm is used to enforce incompressibility. Free surface boundaries are evaluated based on a decrease in particle number density. Spatial discretization relies on the differences among neighboring particles. As this method does not use a mesh for discretization, it can handle topological changes and large deformations of free surfaces without issues such as mesh tangling.

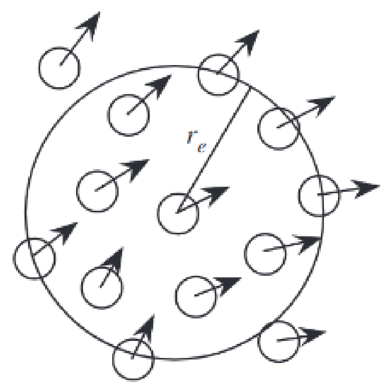

Fig. 1. Concept of particle methods [8]

Particle methods can generally be classified into two types [7]:

a) those based on probabilistic models;
b) those based on deterministic models.

The first group represents macroscopic properties as statistical behavior of microscopic particles. Therefore, a large number of particles must be tracked over extended periods to obtain accurate average values. The second group requires less computational time and memory.

2.5. Particle Interaction Models

A particle interacts with neighboring particles within a region defined by a kernel function $w(r)$,where r is the distance between two particles [7].

$$w(r) = \begin{cases} \frac{r_e}{r} = 1 & (0 \le r < r_e) \\ 0 & (r_e \le r) \end{cases} . \tag{5}$$

Since the kernel has a finite support radius, each particle only interacts with a finite number of neighbors. The radius of the interaction domain is defined by the parameter r_e. Compared to infinite-support kernels, such as the Gaussian function, the current kernel requires less memory and computational cost. The kernel function is infinite at which enhances numerical stability in incompressibility models [7].

2.6. Particle Number Density

Particle number density at coordinate r_i where particle *i* is located and defined by:

$$\langle n \rangle_i = \sum_{j \neq i} w\left(\left|r_j - r_i\right|\right). \tag{6}$$

The contribution from particle *i* itself is not included. When the number of particles in a unit volume is denoted by $\langle N \rangle_i$, the relation between $\langle n \rangle_i$ and $\langle N \rangle_i$ is written as:

$$\langle N \rangle_i = \frac{\langle n \rangle_i}{\int_V w(r)dv} \tag{7}$$

The denominator of equation (7) is the integral of the kernel in the whole region, excluding a central part occupied by particle i. Assuming that all particles have identical mass m, the fluid density is proportional to the particle number density:

$$\langle \varrho \rangle_i = m\langle N \rangle_i = \frac{m\langle n \rangle_i}{\int_V w(r)dv} \tag{8}$$

Hence, the continuity equation is satisfied if the particle number density remains constant. This constant value is denoted by n^0 [7].

2.7. Modeling of Gradient

A gradient vector between two particles *i* and *j* possessing scalar quantities ϕ_i and ϕ_j at coordinates r_i and r_j is simply defined by $\left(\phi_i - \phi_j\right)\left(r_i - r_j\right) / \left|r_j - r_i\right|^2$. The gradient vector can be evaluated with any combination of two particles [7]. The gradient vectors between particle *i* and its neighboring particles *j* are weighted with the kernel function and averaged to obtain a gradient vector at particle *i*:

$$\langle \nabla \phi \rangle_i = \frac{d}{n^0} \sum_{j \neq i} \left[\frac{\phi_j - \phi_i}{\left|r_j - r_i\right|^2} \left(r_j - r_i\right) w\left(\left|r_j - r_i\right|\right) \right] \tag{9}$$

where *d* is the number of space dimensions. This model is applied to the pressure gradient term in MPS. The equation (9) gives a larger force to a shorter distance between two particles. This is a good property to avoid the clustering of particles [7].

3. Geometrical Modeling and Mesh Generation

The micromixer geometry used in this study replicates the design presented in [5], featuring a complex channel structure characterized by integrated chicanes or an S-shaped configuration.

The investigated micromixer contains a Y-mixer and S-type microchannel (or “chicane” type), the latter includes specially designed meander elements (here and further, the term “meander” is associated with the repeated part of the “chicanes” channel). The micromixer is shown in Fig. 2.

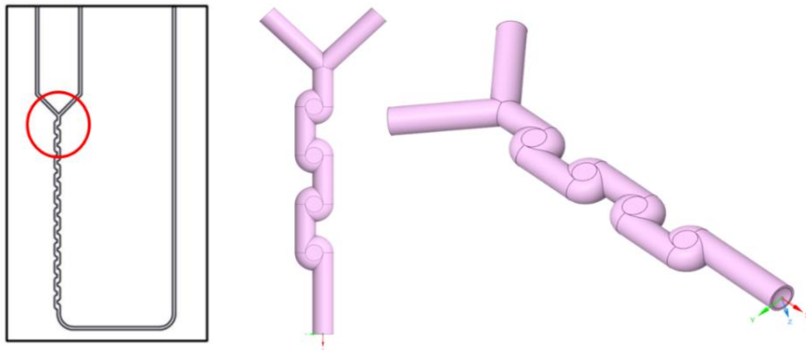

Fig. 2. Geometrical model of micromixer

The total length of the micromixer is 21 mm, with an inlet radius of 1mm. Meshing was performed in Ansys Fluent® (version 2023 R1), resulting in a total of 968 688 computational cells. The mesh includes 10 boundary layers to adequately resolve near-wall flow behavior. The mesh is shown on Fig. 3.

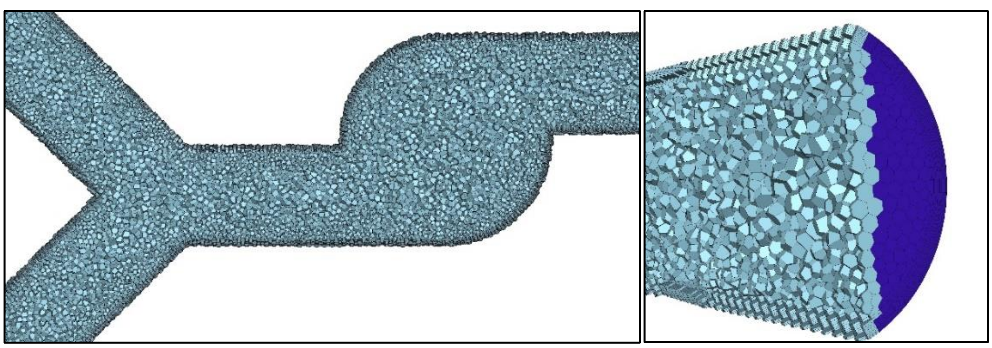

Fig. 3. Mesh representation for micromixer

4. Numerical Setup and Boundary Conditions

The numerical simulations were conducted using two distinct computational fluid dynamics platforms, Ansys Fluent® and ParticleWorks®. In both software environments, identical boundary conditions and fluid properties were prescribed in order to ensure a consistent basis for comparison. The physical model assumed isothermal, incompressible flow under steady-state conditions, unless otherwise stated.

Due to the use of highly diluted solutions, as described in [5], the working fluid properties were approximated using those of pure water at a reference temperature of T = 20 °C. The density, dynamic viscosity, and mass diffusion coefficient were respectively set to: $\varrho = 998\ \mathrm{kg/m^3}$, $\mu = 1.0\times 10^{-3}\ \mathrm{Pa\cdot s}$, $\mathrm{D} = 2.0\times 10\ \mathrm{m^2/s}$, respectively.

The inlet boundary conditions were defined using the Reynolds number (Re), which characterizes the flow regime and governs the mixing behavior. Simulations at Re = 2.6, 13, 26, 78, 156, and 260 were used to analyze the resulting flow variations.

4.1. Temperature Field Analysis

To evaluate the influence of thermal gradients on the mixing dynamics, a supplementary series of simulations was conducted in Ansys Fluent® with the energy equation enabled. This allowed for the resolution of temperature fields and thermally driven flow structures within the domain. The investigation focused on scenarios in which the two inlet streams entered the domain at different temperatures. The primary goal was to determine whether a temperature difference between the fluid streams enhances the mixing rate, potentially due to induced buoyancy or altered viscosity profiles. Two temperature configurations were analyzed:

– 22 °C / 42 °C (moderate temperature difference)
– 22 °C / 82 °C (high temperature difference)

In each case, one fluid stream was maintained at a reference temperature of 22 °C, while the second was heated to the respective elevated temperature. The resulting temperature distribution is shown in this paper. The analysis aimed to identify correlations between thermal gradients and mixing efficiency, particularly under low Reynolds number conditions where thermal effects could be more pronounced due to limited inertial mixing.

5. Results and Comparative Analysis

In following part results obtained from two CFD software tools covering the analysis of flow behavior, mixing homogeneity, pressure drop comparison, and temperature profiles in the micromixer are visually presented and validated against the results published in [5].

5.1. Flow Behavior in the Micromixer

The flow behavior in the micromixer was analyzed using streamlines, with red and blue colors indicating flows from different inlets (Fig. 4). A comparison between Ansys CFX® (left) and Ansys Fluent® (right) reveals distinct variations in predicted flow behavior across cases (a–d). At low flow rates (case a), both solvers exhibit similar, well-separated streamlines. As the Reynolds number increases (cases b–d), Fluent predicts earlier and stronger vortex formation, promoting better mixing. In contrast, CFX maintains clearer stratification and a sharper interface, indicating lower mixing efficiency, especially noticeable in cases (c) and (d), where Fluent shows more intense interpenetration of streams.

In summary, while CFX produces sharper flow features and more distinct separation of layers, Fluent demonstrates more effective fluid mixing at higher Reynolds numbers due to the presence of more developed secondary flows and smoother transitions between streams.

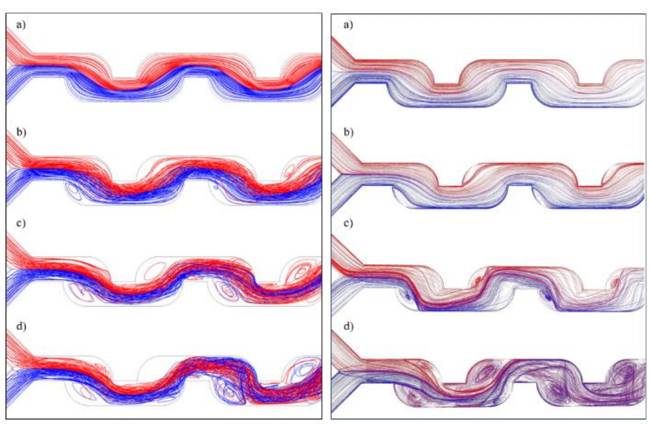

Fig. 4. Comparison of simulated streamlines at different Reynolds numbers from CFX (left) [5] and Fluent (right): (a) *Re* = 2.6; (b) *Re* = 26; (c) *Re* = 156; (d) *Re* = 260.

Figure 4 presents the concentration field evolution within the micromixer, where red and blue indicate unmixed components and green represents ideal mixing. A comparison between Ansys CFX® (left) and Ansys Fluent® (right) across four flow regimes (a–d) reveals notable differences in mixing predictions. At lower Reynolds numbers (a, b), both solvers capture alternating concentration patterns; however, CFX shows sharper interfaces and clearer periodic structures, suggesting lower numerical diffusion. Fluent, by contrast, produces smoother gradients, indicating stronger diffusive effects or differing numerical treatment. As Re increases (c, d), these differences become more pronounced. In case (d), CFX maintains a structured pattern, while Fluent shows greater homogenization and diminished periodicity.

5.2. ParticleWorks®

The simulation in ParticleWorks® was conducted using identical boundary conditions and fluid properties as defined in Ansys Fluent® to ensure consistency and comparability. Figure 5 presents a comparison between experimental results and numerical predictions obtained from three simulation platforms: Ansys CFX®, AnsysFluent®, and ParticleWorks®.

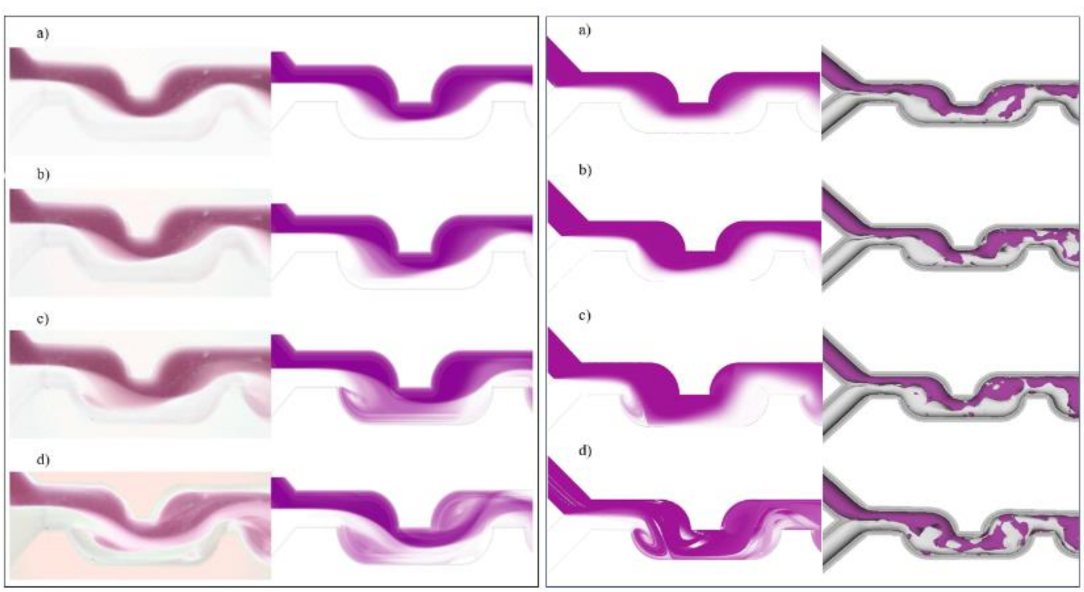

Fig. 5. Comparison of experimental and CFX simulation results (left) with Fluent and ParticleWorks® simulation results (right) at different Reynolds numbers: (a) Re = 13; (b) Re = 26; (c) Re = 78; (d) Re = 260.

Figure 5 presents a comparison of experimental and CFX simulation results (left) with Fluent and ParticleWorks® simulations (right) at different Reynolds numbers (a) Re = 13, (b) Re = 26, (c) Re = 78, and (d) Re = 260, demonstrating generally good consistency across all software tools. In Figure 6, only the ParticleWorks® results are shown, visualized through particles that effectively capture the detailed fluid breakup and complex flow structures characteristic of the physical phenomena.

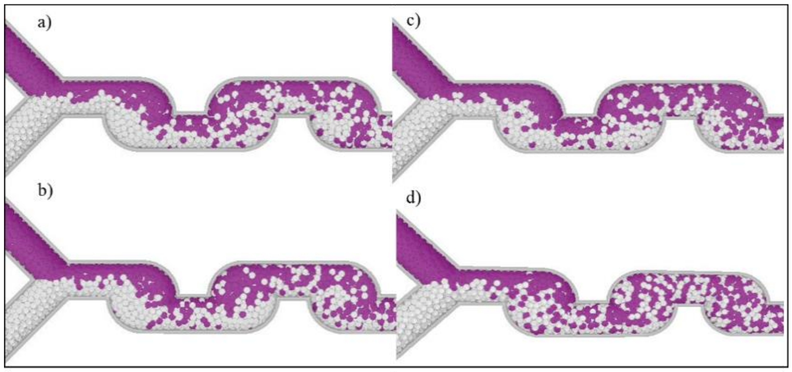

Fig. 6. ParticleWorks® simulation results at different Reynolds numbers: (a) *Re* = 13; (b) *Re* = 26; (c) *Re* = 78; (d) *Re* = 260.

5.3. Mixing Index

The mixing index I_M quantifies the degree of homogeneity of species distribution within the system, ranging from 0 – indicating complete segregation of species, to 1– corresponding to perfect mixing. In this study was evaluated using the formulation proposed by Danckwerts [9].

$$I_M = 1 - \left(I_S\right)^{1/2} = 1 - \left(\sigma^2 / \sigma^2{}_{max}\right)^{1/2} \tag{10}$$

where σ is the variance of concentration, σ_{max} denotes the maximum variance of concentration and I_S represents the degree of segregation.

Based on the Figure 7, it can be observed that the difference in Mixing Index values [10] between Fluent® and CFX® results [5] is more pronounced at a higher Reynolds number (*Re* = 260) than at a lower one (*Re* = 2.6). For *Re* = 2.6, both simulations yield similar Mixing Index values along the micromixer, with minimal deviations, indicating limited mixing under laminar flow conditions. In contrast, at *Re* = 260, Fluent results show a significantly higher Mixing Index along the entire micromixer compared to CFX, with a particularly noticeable difference from the third to the sixth section. This suggests that Fluent more effectively predicts mixing at higher flow velocities and more complex fluid motion patterns, likely due to better modeling of secondary flows and vortex structures that contribute to mixing.

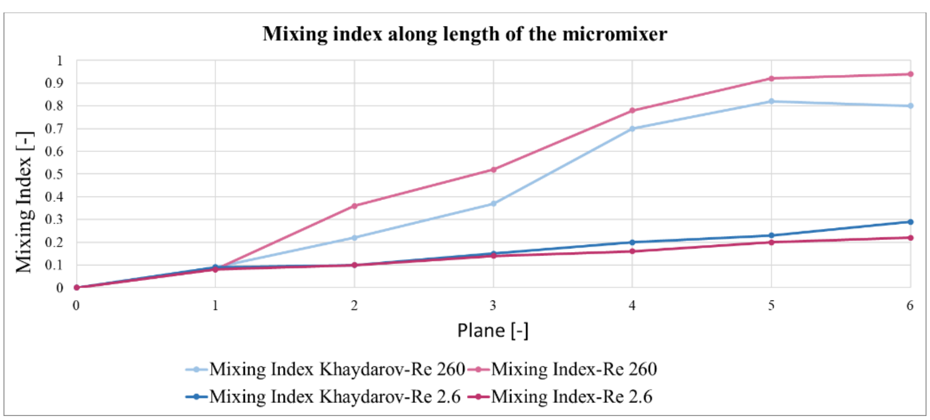

Fig. 7. Comparison of the Mixing Index along the length of the micromixer at *Re* = 2.6 and *Re* = 260

5.4. Pressure drop

Figure 8 presents the relationship between pressure drop and Reynolds number. As expected, the pressure drop increases with the Reynolds number, in accordance with theoretical fluid flow behavior. While the differences between the two are minimal at lower Reynolds numbers, the discrepancies become more noticeable at higher values of *Re*. These variations may be due to differences in the modeling approach or the specific settings applied in each simulation software.

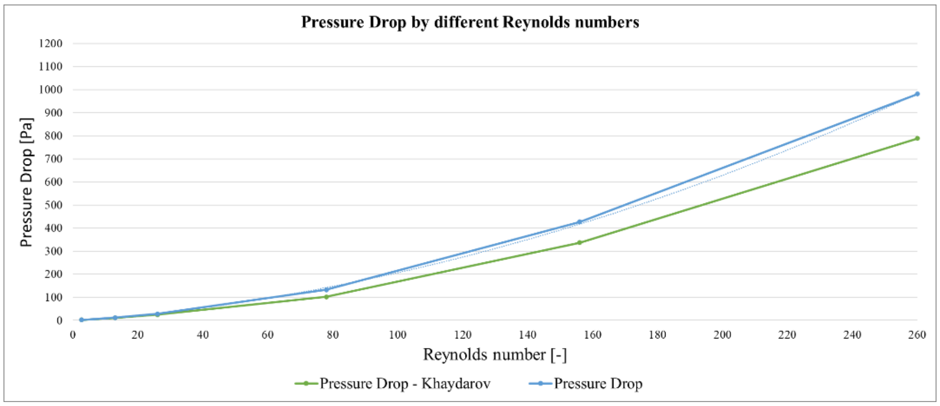

Fig. 8. Pressure drop by different Reynolds numbers

5.5. Temperature field

Figure 9 presents the temperature field distributions in the micromixer for two imposed temperature differences, ΔT = 20 °C (left) and ΔT = 60 °C (right), at two Reynolds numbers: (a) *Re* = 13 and (b) *Re* = 260. Regardless of the flow regime and thermal conditions, rapid temperature homogenization occurs along the channel in all cases. The small dimensions of micromixers enable efficient heat transfer even at low Reynolds numbers, which quickly reduces temperature gradients. It has been shown that the temperature difference of the fluid does not significantly affect the mixing quality, as confirmed by the results of numerous studies [11].

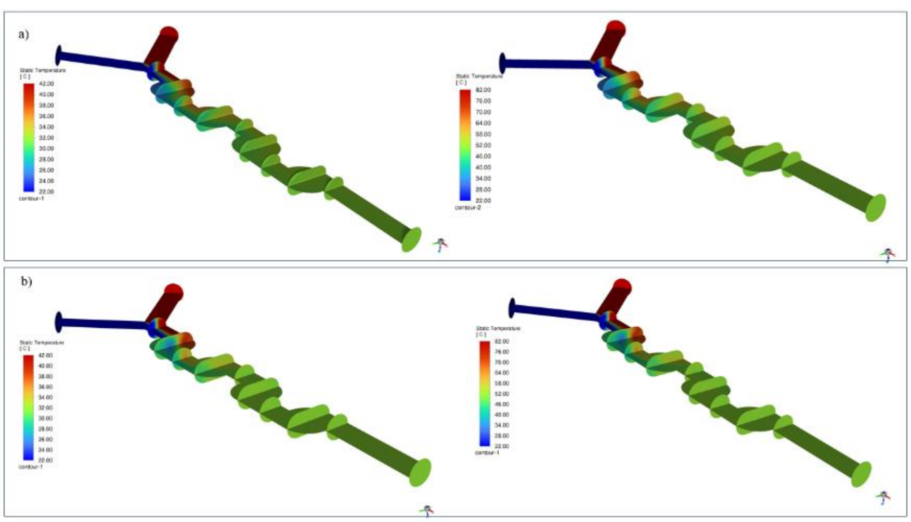

Fig. 9. Temperature field for a temperature difference of ΔT = 20 °C (left) and ΔT = 60 °C (right) at different Reynolds numbers: (a) *Re* = 13; (b) *Re* = 260.

6. Conclusions

This study examined the performance of a micromixer with meandering channels using computational fluid dynamics (CFD) simulations. The results were compared with previously obtained experimental data and numerical outputs from Ansys CFX® [5]. In addition to CFX, two other CFD tools were applied, Ansys Fluent® and ParticleWorks®. Ansys Fluent employs the finite volume method (FVM), whereas ParticleWorks® is based on a meshless, particle-driven approach. The comparison showed that Ansys Fluent produced results consistent with both the experimental findings and the CFX simulations. It achieved a slightly higher mixing index, though this improvement came with an increase in pressure drop. This indicates a trade-off between mixing efficiency and flow resistance.

For ParticleWorks®, only visual results were available. Based on qualitative evaluation, the simulated mixing patterns exhibited good alignment with experimental observations. This outcome suggests that meshless particle-based simulations can offer reliable qualitative insights into micromixing behavior.

Temperature effects were investigated in Ansys Fluent for two cases with fluid temperature differences of 20 °C and 60 °C. The simulations indicated that the temperature field stabilized quickly and had no significant influence on the mixing index. Under the examined conditions, thermal gradients did not meaningfully affect the mixing process. These findings demonstrate that different CFD platforms, despite varying in numerical methodology, can provide mutually reinforcing insights and contribute to a comprehensive understanding of micromixing performance.

References

[1] Bökenkamp, D., Desai, A., Yang, X., Tai, Y.C., Marzluff, E.M., Mayo, S.L., *Microfabricated Silicon Mixers for Submillisecond Quench-Flow Analysis*, Anal. Chem., Vol. 70, No. 2, 1998, pp. 232–236.

[2] Engler, M., Kockmann, N., Kiefer, T., Woias, P., *Numerical and Experimental Investigations on Liquid Mixing in Static Micromixers*, Chemical Engineering Journal, Vol. 101, No. 1–3, 2004, pp. 315–322.

[3] Hoffmann, M., Räbiger, N., Schlüter, M., Blazy, S., Bothe, D., Stemich, C., Warnecke, H.-J., *Experimental and Numerical Investigations of T-Shaped Micromixers,* Proceedings of the 11th European Conference on Mixing, Bamberg, Germany, 2003, pp. 269–276.

[4] Dreher, S., Kockmann, N., Woias, P., *Characterization of Laminar Transient Flow Regimes and Mixing in T-Shaped Micromixers*, Taylor & Francis, 2011.

[5] Khaydarov, V., Borovinskaya, E.S., Reschetilowski, W., Numerical and Experimental *Investigations of a Micromixer with Chicane Mixing Geometry*, Technische Universität Dresden and Saint-Petersburg State Institute of Technology, 2018.

[6] Ansys, Inc., *Ansys Fluent Theory Guide*, Release 2021 R2, ANSYS, Inc., July 2021.

[7] Koshizuka, S., Oka, Y., *Moving-Particle Semi-Implicit Method for Fragmentation of Incompressible Fluid, Nuclear Science and Engineering*, Vol. 123, No. 3, July 1996, pp. 421–434.

[8] Koshizuka, S., *Current Achievements and Future Perspectives on Particle Simulation Technologies for Fluid Dynamics and Heat Transfer*, 2010, pp. 155–168.

[9] Danckwerts, P.V., *The Definition and Measurement of Some Characteristics of Mixtures*, Applied Scientific Research Section A, Vol. 3, 1952, pp. 279–296.

[10] Cullen, P.J., Romañach, R.J., Abatzoglou, N., Rielly, C.D. (Eds.), *Pharmaceutical Blending and Mixing*, John Wiley & Sons Ltd, Chichester, UK, 2015.

[11] Lobasov, A.S., Shebeleva, A.A., *Initial Temperatures Effect on the Mixing Efficiency and Flow Modes in T-shaped Micromixer*, J. Phys.: Conf. Ser., Vol. 899, 2017, 022010.

10th International Congress of the Serbian Society of Mechanics
Niš, Serbia, June 18-20, 2025

B.10
Original scientific paper

DOI: 10.46793/ICSSM25.089O

PARTICLE DYNAMICS IN INERTIAL MICROFLUIDICS: REVIEW OF FORCES AND CHANNEL DESIGN PRINCIPLES

Nikola Oluški[1][0000-0003-1766-4797], Andreja Živkov[1][0009-0000-0267-7013], Vladimir Kozomora[1][0009-0008-9431-2932], Maša Bukurov[1][0000-0002-6171-2226] , Slobodan Tašin[1][0000-0002-9410-9255]

[1] Faculty of Technical Sciences
University of Novi Sad, Trg Dositeja Obradovića 6, 21000 Novi Sad, Serbia
e-mail: oluski.n@uns.ac.rs

Abstract:

This paper aims to introduce readers and future researchers to the field of inertial microfluidics, presenting key principles, forces, and practical applications. By analyzing over 40 studies, the work systematizes the basic hydrodynamic mechanisms influencing particle motion in microchannels: inertial lift force, Dean drag force, and centrifugal force. The theoretical framework explains the role of dimensionless parameters, Reynolds number and clogging ratio λ, in determining stable particle positions and separation efficiency. A tabular overview summarizes the performance of each geometry, straight, curved and serpentine, and highlights their strengths and limitations. Major challenges include minimizing clogging in narrow channels, scaling throughput for industrial volumes, and adapting systems for complex biological samples like blood or environmental mixtures for microplastic removal. Future research directions should focus on hybrid geometries combining straight and curved segments to balance resolution and throughput, numerical optimization using machine learning algorithms to predict particle trajectories, and applications in emerging fields such as single-cell analysis or nanomaterial synthesis. By linking theoretical models, experimental validations, and industrial requirements, this paper serves as a practical guide for researchers designing inertial microfluidic systems tailored to specific separation tasks.

Key words: *particle dynamics, inertial microfluidics, separation*

1. Introduction

Microfluidics, as an interdisciplinary science based on the principles of fluid mechanics, offers a wide range of possibilities for precise separation and filtration, where understanding the forces acting on particles in microchannels plays a key role. As early as the 19th century, Poiseuille, while studying blood flow through capillaries, observed that blood cells were not uniformly distributed across the cross-section but formed regions of reduced concentration near the walls. A whole century later, Simha [1] analytically demonstrated, using the linearized Navier-Stokes equation, that under low Reynolds number (*Re*) conditions and in the absence of walls, particles do not experience radial forces. Subsequently, Vejlnes [2] experimentally determined that spherical particles in square cross-section channels move away from the walls, with the effect becoming more pronounced for larger particles. Johnson and Taylor [3] built upon

Poiseuille's observation, noting an additional region of reduced concentration in the center of the tube, where the velocity is at its maximum. These studies led to the discovery of the "tubular pinch" effect, documented by Segré and Silberberg in 1962 [4], where particles in laminar flow through circular tubes migrate radially toward a stable equilibrium position at ~0.6*R* (*R* – tube radius) (Fig. 1). Theoretical advancements enabled a deeper understanding. Saffman [5] was the first to derive the lift force on a small sphere, while Ho and Leal [6] analyzed lateral migration in two-dimensional Poiseuille flow. Schonberg and Hinch [7] investigated the shift of equilibrium positions with increasing *Re*, proving that the equilibrium position moves toward the wall as *Re* increases. In 1999, Asmolov [8] developed a model for inertial lift force at higher *Re*, laying the foundations for modern microfluidics.

At the beginning of the 21st century, advancements in micro- and nanotechnology enabled the expansion of passive microfluidic separation systems utilizing hydrodynamic forces. Numerous studies have focused on optimizing microchannel geometry and the influence of dimensionless parameters. In 2007, Di Carlo et al. [9] laid the foundation for continuous inertial focusing and defined lift forces in microchannels. They demonstrated that particles occupy stable positions at specific locations within square cross-section channels, allowing for precise separation. Two years later, they confirmed these findings through numerical simulations [10]. During the same period, Yoon et al. [11] experimentally validated size-selective separation using secondary flows in curved microchannels. Martel and Toner [12] provided a comprehensive review of inertial focusing principles, followed by Liu et al. [13], who conducted an in-depth analysis of spherical particle focusing in rectangular channels across a wide range of *Re* values. More recent research has shifted toward optimizing microchannel geometry. Raoufi et al. [14] and Ince et al. [15] emphasized the importance of channel curvature in determining equilibrium particle positions and improving separation efficiency, while Amani et al. [16] and Ebrahimi et al. [17] contributed to the enhancement of serpentine channel designs for faster and more precise separation. Wiede et al. [18] demonstrated the effective application of Dean vortices for mixing and focusing, while the latest studies by Valani et al. [19, 20] model dynamic bifurcations in spiral channels, opening new possibilities for particle separation.

The aim of this review, presented in this papaer, is to systematize the key forces in inertial microfluidics, along with their theoretical models and experimental validations, providing a comprehensive overview of the achieved results. Additionally, it highlights some of the key factors influencing the lateral migration of particles. A tabular summary of various studies enables a clearer comparative analysis, which can contribute to the further development of inertial separation techniques in microfluidics.

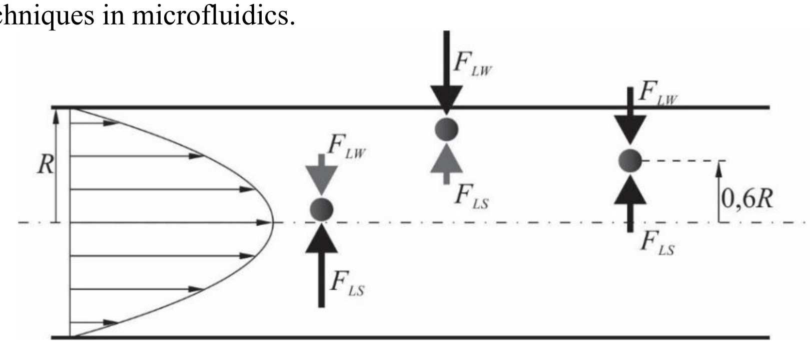

Fig. 1 Inertial lift force – Equilibrium position

2. Particle Dynamics in Microfluidic Environments

2.1 Governing Equations of Fluid Dynamics and Nondimensional Numbers

The governing equations of fluid flow are the Navier-Stokes (1) and continuity equations (2), which are fundamental to microfluidics

$$\frac{\partial \vec{v}}{\partial t} + (\nabla \cdot \vec{v})\vec{v} = \vec{f} - \frac{1}{\rho}\nabla p + \upsilon \nabla^2 \vec{v} \quad \text{and} \tag{1}$$

$$\nabla \cdot \vec{v} = 0 \tag{2}$$

where v, ρ, p, f and υ are the fluid velocity, fluid density, pressure, external forces acting on the fluid and kinematic viscosity, respectively. The left side of equation (1) describes inertial effects, while the right side includes terms for body, pressure and viscous forces.

The dynamics of particle motion in microfluidics is characterized by several key dimensionless numbers. The Reynolds number (*Re*), representing the ratio of inertial to viscous forces, is crucial for determining the flow regime. In microchannels with rectangular cross-sections, the hydraulic diameter (D_h), defined as the ratio of the cross-sectional area to the wetted perimeter, is commonly used instead of the pipe diameter [8, 9, 13, 21]. Index '*c*' indicates that it refers to the channel

$$Re_c = \frac{v_\mathrm{m} D_h}{\upsilon} = \frac{\rho v_\mathrm{m} D_h}{\mu} \tag{3}$$

where v_m is maximum velocity and μ is dynamic viscosity. Some authors use the maximum flow velocity to determine the flow regime, with relation v_m=1,5·v_{sr} for square channels. Since particle behavior depends on the flow regime, the particle Reynolds number (Re_p) is often defined and used in theoretical studies to analyze forces [8, 9, 22]

$$Re_p = Re_c \frac{a^2}{D_h^2} = \frac{\rho v_m a^2}{\mu D_h} \tag{4}$$

The ratio of particle diameter to channel height can play a crucial role in focusing and is referred to as the particle blocking ratio. In the literature, it is denoted by various symbols, such as κ [22] or $\lambda = a/h$ [23]. Studies [10, 12, 24, 25] have established that this ratio should satisfy $\lambda >$ 0.07 to achieve high efficiency. In addition to the particle-to-channel ratio, experimental studies often consider the aspect ratio (*AR*), defined as the ratio of channel height (*h*) to width (*w*), denoted as *AR*=*h*/*w*.

The Dean number (*De*) is a dimensionless quantity that describes the intensity of secondary flows in curved channels, as given by equation (5). It was first described by William Dean in 1928 [26], who demonstrated that the velocity difference between the center and the walls of the channel generates additional forces that push the fluid toward the outer wall of the curve.

$$De = Re_c\sqrt{\delta} = Re_c\sqrt{\frac{D_h}{2r}}\,, \tag{5}$$

where δ is the curvature ratio of the channel, and *r* represents the radius of curvature. The additional momentum arises from the pressure difference between the inner and outer walls. Vortices form in the upper and lower halves of the channel, as shown in Fig. 2, and act as a drag force on the particle, influencing its motion. The literature suggests that the conditions De<50 [9] and $\lambda \cdot r$>0.04 [18] must be satisfied for inertial separation to be feasible and effective. If *De* exceeds the proposed limit, particle mixing will occur due to increased vorticity.

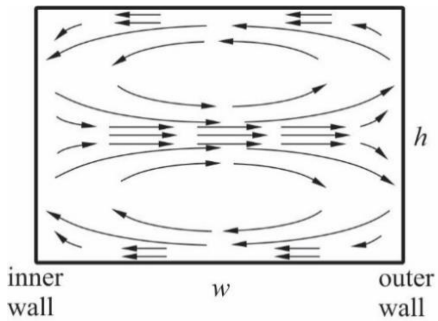

Fig. 2 Dean flow in a channel cross-section

2.2 Forces acting on microparticles

The motion of a body through a viscous fluid is accompanied by various forces exerted by the fluid flow on the body itself. A general expression can be derived from Newton's second law,

$$m_p \frac{\partial \vec{v}}{\partial t} = \Sigma \vec{F} = \vec{F}_D + \vec{F}_L + \vec{F}_C + \vec{F}_B + \vec{F} \,, \tag{6}$$

where is F_D drag force, F_L lift force, F_C centrifugal force, F_B buoyant force, and F represents any additional force (e.g., the Magnus force). The buoyant force can be neglected due to the dominance of viscous forces and when the particle density is approximately equal to the fluid density; therefore, it will not be considered in this study.

2.2.1 Drag force (Stokes force)

Particles suspended in a liquid experience a drag force caused by the fluid's viscosity. Under conditions of very low Reynolds number (Re<1), simplifying equation (1) leads to the expression for the drag force, commonly known as Stokes drag. By neglecting the fluid's inertial effects and replacing the drag coefficient C_D with the Stokes relation 24/Re , the following expression is obtained:

$$F_D = \frac{\rho_f v^2}{2} C_D A = 3\pi\mu a(v_f - v_p) \,, \tag{7}$$

where v_f is the fluid velocity, v_p is the particle velocity and μ is the dynamic viscosity [27]. In curved channels, secondary flows generate an additional drag force that acts on particles by keeping them in an equilibrium position, known as the Dean drag force (8).

$$F_{De} = 3\pi\mu a v_D, \ \text{ where } \ v_D = 1.8 \cdot 10^{-4} \pi\mu De^{1.63} \,, \tag{8}$$

where v_D is the Dean flow velocity [16]. The vortices assist in particle separation based on size, where smaller particles accumulate near the inner wall, while larger particles are displaced to the opposite side [28].

2.2.2. Inertial Lift Force

For many years it was assumed that in laminar flow (Re<1) inertial effects had no influence on the motion of bodies in fluid, and that their trajectory would coincide with the streamline passing through their center of mass. However, the flow regime in the range 1<Re<100 is particularly interesting because while the flow remains laminar, inertial forces become significant, generating lift forces [29]. The lift force, well known in the fields of gas dynamics and aerodynamics, has long been studied as a key factor in the movement of airfoils. However, in the case of fluid flow at low velocities (low Re), the effects of this force were often neglected. During the 1960s, experimental results revealed the formation of specific equilibrium positions depending on channel geometry. It became clear that there must exist a force causing lateral displacement. Saffman [5] proposed a mathematical model to describe this phenomenon.

$$F_L = 81.2 \cdot v a^2 \sqrt{\gamma/\upsilon}\,, \tag{9}$$

where γ is the velocity gradient magnitude. Subsequently, Ho and Leal [6] proposed a new expression for two-dimensional Poiseuille flow, where the particle diameter has the dominant influence, later adopted by numerous researchers in their calculations [13, 16, 22, 23, 30].

$$F_{LW} = c_L \rho v_{\max}^2\, a^4 / D_h^2\,, \tag{10}$$

where c_L is the lift coefficient, most commonly determined experimentally and ranging between 0.02 and 0.05 [15, 30]. They also proposed a criterion for achieving inertial effects, requiring AR to be between 0.5 and 2 and $Re_p>1$. Hood et al. [31] suggested that scaling the force with a^3 yields better numerical results. In rectangular channels where $w>h$, the relation holds $c_L \propto D_h^2 / a^2 \sqrt{Re}$ [32, 33]. This force is often called the wall-induced lift force.

Generally, research has established that the lift force, or the force causing lateral displacement, can be decomposed into two components: wall-induced and shear gradient-induced. Due to viscosity, the fluid velocity at walls equals zero (no-slip condition) while particles move with finite velocity. This velocity difference generates a force acting on particles from walls toward the channel center. Conversely, the laminar velocity profile and non-uniform flow velocity create shear rate gradients above and below the sphere, resulting in a force directed from the channel center toward the walls. The literature [31] provides the formula:

$$F_{LS} = c_L \rho v_{\max}^2\, a^3 / D_h\,. \tag{11}$$

When the particle is located in the central region of the channel, the shear gradient force dominates, while near the walls the opposite effect prevails. It is precisely for this reason that Di Carlo et al. [9, 24] formulated a general expression for the lift force that causes lateral particle displacement:

$$F_L = c_L(Re, x) \rho v_{\max}^2\, a^4 / D_h^2\,, \tag{12}$$

where the lift coefficient depends on both the particle position and Reynolds number, and in some cases may become negative [32].

2.2.3 Centrifugal Force

In curved or spiral-shaped channels, a centrifugal force arises, acting radially outward from the center of rotation. This force results from the inertia of the particle, which tends to maintain straight-line motion. Depending on the mass and diameter of the particle, a slight drift occurs during turns, causing the particle to shift to a specific streamline. If this process repeats multiple times, the outcome at the channel exit will be particle separation based on size or density [16, 17, 23, 27].

$$F_C = \frac{\left(\rho_p - \rho_f\right)\pi a^3 v_t^2}{6R}\,, \tag{13}$$

where is v_t tangential particle velocity. An example of how the centrifugal force acts is shown in Fig. 3. From equation (13), it can be concluded that increasing the velocity while decreasing the radius of curvature leads to an enhancement of the centrifugal force. Heavier particles move toward the outer wall of the channel, while smaller and lighter particles remain closer to the inner wall. If the centrifugal forces are significantly greater than the others, focus destabilization and poor separation may occur.

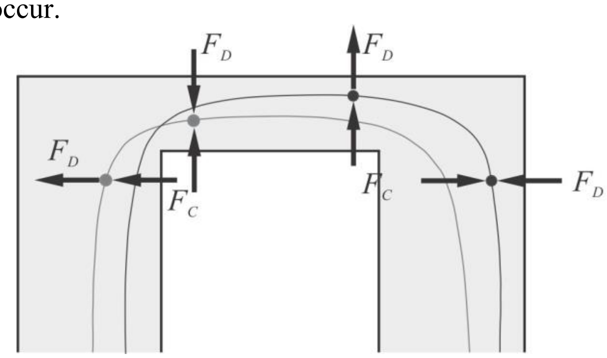

Fig. 3 Centrifugal force in elbow [17]

2.3 Effects of channel geometry

Both experimental and numerical studies demonstrate that particles in square cross-section channels focus at specific locations after a certain distance from the inlet, depending on the aspect ratio. When the previously mentioned criteria for λ, Re_p, and AR are satisfied, the required channel length for achieving focusing can be determined analytically using equation (14a) [9, 29, 34], while Bhagat et al. [35] propose equation (14b).

$$\text{a) } L_f = \frac{\pi\mu D_h^2}{c_L v_{\max}^2 a^2}, \, , \qquad \text{b) } L = \frac{3\pi\mu D_h^3}{\rho v_{\max} a^3} \, . \tag{14}$$

In square cross section channels, four stable focusing positions exist, whereas in rectangular channels the number of stable positions reduces to two, always located along the longer sides, as shown in Fig. 4. It has also been observed that with increasing Re, particles migrate closer to the walls [29].

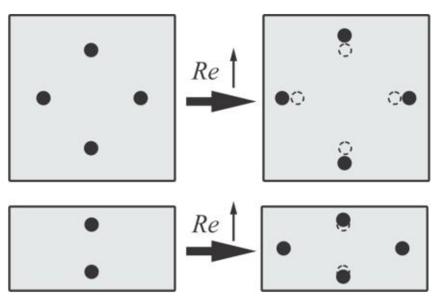

Fig. 4 Equilibrium positions in a rectangular cross section

The focusing length in straight channels can reach several dozen millimeters, which may take considerable time given the typically low flow rates. To reduce both the required length and separation time, researchers have recently begun combining straight and curved channels, as well as channels with variable cross sections [36]. Moloudi et al. [33] investigated inertial focusing in trapezoidal cross section channels and achieved better separation efficiency compared to conventional rectangular channels (Fig. 5). They introduced an additional force termed the cross-section lateral force F_{CL}, which is fundamentally equivalent to the wall-induced lift force but generated by vertical walls in horizontal direction. Mashhadian et al. [37] developed a method for rapid prediction of particle positions in channels with different cross-sections using numerical simulations.

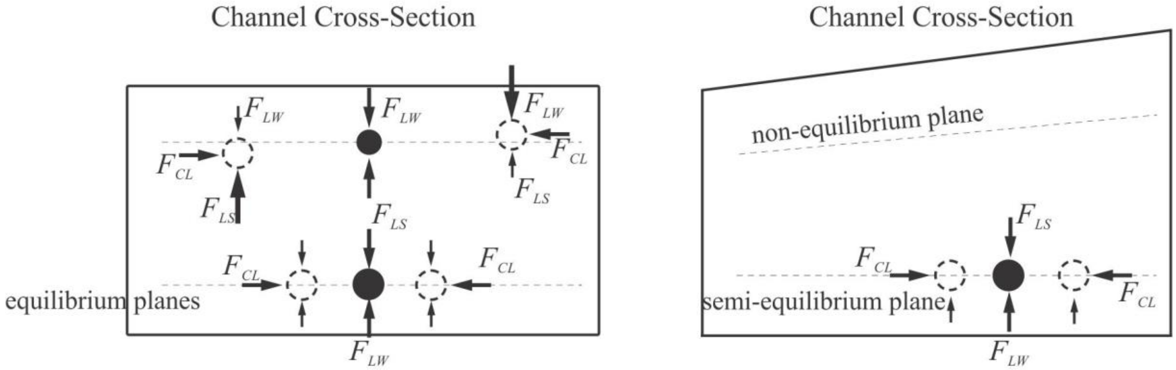

Fig. 5 Equilibrium positions of particles in microchannels with different cross-sectional geometries

3. Tabular overview of inertial microfluidics papers and discussion

Geometry	*a*<10	10<*a*<20	*a*>20	*Re*<10	10<*Re*<100	*Re*>100	λ<0.2	λ>0.2
Straight	[9, 13, 25, 30, 32-38, 41]	[9, 13, 30, 34, 37]	[32, 33, 34]	[9, 31, 35, 37, 41]	[13, 25, 30-35, 37, 38, 41]	[9, 13, 32-34, 37, 38]	[9, 13, 25, 30, 32, 34-38, 41]	[13, 30, 32-34]
Curved	[11, 14, 18, 22, 23, 28, 36, 39]	[14, 18, 22, 39]	[11, 39]	[11, 18, 28]	[18, 23, 28]	[22, 23]	[14, 22, 23, 28, 36, 39]	[11, 22, 39]
Serpentine	[9, 15-17, 22, 24, 27, 40]	[9, 16, 17, 22, 24, 27, 40]	[16, 17, 24, 40]	[9, 16]	[15, 27, 40]	[9, 15, 22, 24, 27, 40]	[9, 15, 22, 24, 40]	[16, 17, 22, 24, 27]

Table 1. Overview of key models and parameters

Table 1. presents a review of experimental and simulation studies on particle separation using inertial microfluidics. The studies are divided into three main groups based on channel geometry: straight, curved, and serpentine channels. The analysis highlights three critical parameters in inertial microfluidics: particle diameter a [μm], Reynolds number *Re* [-], and clogging ratio λ [-]. These parameters enable researchers to determine operational ranges for channel design, including channel width, height, and flow rates, that ensure efficient particle manipulation.

It can be observed that all three geometries predominantly focus on smaller particles (a<10 μm), which makes sense since the most common application is in medicine for the separation of various cells and bacteria [18, 34]. Most investigations are conducted in moderate flow regimes (10<*Re*<100), particularly in straight channels. As previously noted, this is the ideal range where inertial lift forces manifest. Curved channels stand out with medium-sized particles, especially in biomedical applications for CTCs (cancer tumor cells) isolation with 90% efficiency [17, 39]. Similarly, in serpentine channels, a slightly higher clogging ratio (λ>0.2) is tolerated due to Dean vortices. They are more efficient at higher *Re* (*Re*>100), enabling greater flow rates and faster processing of larger sample volumes [16, 17, 24].

4. Conclusions

Inertial microfluidics has proven to be a transformative approach for high-precision particle manipulation, driven by the interplay of hydrodynamic forces and optimized channel geometries.

Straight channels dominate in processing small particles (<10 μm) under moderate *Re* (10–100), while curved geometries leverage Dean vortices to achieve >90% efficiency in biomedical applications like CTCs isolation. Serpentine designs excel at high *Re* (>100), tolerating higher clogging ratios (λ>0.2) for rapid, large-volume processing. The systematic analysis of dimensionless parameters (a, *Re*, λ) across studies, Table 1, reveals a clear geometry-dependent optimization strategy: straight channels give good results for moderate *Re*, curved designs improve separation by secondary flow, and serpentine configurations balance flow and resolution. However, challenges remain in translating the efficiency of laboratory studies to industrial scale. While this review provides a strong theoretical foundation by analyzing hydrodynamic forces and particle behavior, further experimental and numerical studies are essential to validate these findings and bridge the gap between theoretical predictions and practical applications. Future work should prioritize hybrid geometries that combine these advantages, machine learning-based design optimization, and clogging mitigation strategies for complex biological samples, ensuring that inertial microfluidics meets the growing demands in diagnostics, environmental monitoring, and nanomaterial synthesis.

Acknowledgments

This research has been supported by the Ministry of Science, Technological Development and Innovation (Contract No. 451-03-137/2025-03/200156) and the Faculty of Technical Sciences, University of Novi Sad through project “Scientific and Artistic Research Work of Researchers in Teaching and Associate Positions at the Faculty of Technical Sciences, University of Novi Sad 2025” (No. 01-50/295).

References

[1] Simha, “Untersuchungen über die Viskosität von Suspensionen und Lösungen,” 1936.
[2] Vejlens, “The distribution of leucocytes in the vascular system,” 1939.
[3] C. G. Johnson and L. R. Taylor, “The development of large suction traps for airborne insects,” *Annals of Applied Biology*, vol. 43, no. 1, pp. 51–62, Mar. 1955, doi: 10.1111/j.1744-7348.1955.tb02452.x.
[4] G. Segré and A. Silberberg, “Behaviour of macroscopic rigid spheres in Poiseuille flow Part 2. Experimental results and interpretation,” *J. Fluid Mech.*, vol. 14, no. 1, pp. 136–157, Sep. 1962, doi: 10.1017/S0022112062001111.
[5] P. G. Saffman, “The lift on a small sphere in a slow shear flow,” *J. Fluid Mech.*, vol. 22, no. 2, pp. 385–400, Jun. 1965, doi: 10.1017/S0022112065000824.
[6] B. P. Ho and L. G. Leal, “Inertial migration of rigid spheres in two-dimensional unidirectional flows,” *J. Fluid Mech.*, vol. 65, no. 2, pp. 365–400, Aug. 1974, doi: 10.1017/S0022112074001431.
[7] J. A. Schonberg and E. J. Hinch, “Inertial migration of a sphere in Poiseuille flow,” *J. Fluid Mech.*, vol. 203, pp. 517–524, Jun. 1989, doi: 10.1017/S0022112089001564.
[8] E. S. Asmolov, “The inertial lift on a spherical particle in a plane Poiseuille flow at large channel Reynolds number,” *J. Fluid Mech.*, vol. 381, pp. 63–87, Feb. 1999, doi: 10.1017/S0022112098003474.
[9] D. Di Carlo, D. Irimia, R. G. Tompkins, and M. Toner, “Continuous inertial focusing, ordering, and separation of particles in microchannels,” *Proc. Natl. Acad. Sci. U.S.A.*, vol. 104, no. 48, pp. 18892–18897, Nov. 2007, doi: 10.1073/pnas.0704958104.
[10] D. Di Carlo, “Inertial microfluidics,” *Lab Chip*, vol. 9, no. 21, p. 3038, 2009, doi: 10.1039/b912547g.

[11] D. H. Yoon, J. B. Ha, Y. K. Bahk, T. Arakawa, S. Shoji, and J. S. Go, “Size-selective separation of micro beads by utilizing secondary flow in a curved rectangular microchannel,” *Lab Chip*, vol. 9, no. 1, pp. 87–90, 2009, doi: 10.1039/B809123D.

[12] J. M. Martel and M. Toner, “Inertial Focusing in Microfluidics,” *Annu. Rev. Biomed. Eng.*, vol. 16, no. 1, pp. 371–396, Jul. 2014, doi: 10.1146/annurev-bioeng-121813-120704.

[13] C. Liu, G. Hu, X. Jiang, and J. Sun, “Inertial focusing of spherical particles in rectangular microchannels over a wide range of Reynolds numbers,” *Lab Chip*, vol. 15, no. 4, pp. 1168–1177, 2015, doi: 10.1039/C4LC01216J.

[14] M. A. Raoufi, H. A. N. Joushani, S. Razavi Bazaz, L. Ding, M. Asadnia, and M. Ebrahimi Warkiani, “Effects of sample rheology on the equilibrium position of particles and cells within a spiral microfluidic channel,” *Microfluid Nanofluid*, vol. 25, no. 9, p. 75, Sep. 2021, doi: 10.1007/s10404-021-02475-2.

[15] D. Ince, H. Turhan, S. Cadirci, and L. Trabzon, “Experimental and numerical study of the effect of the channel curvature angle on inertial focusing in curvilinear microchannels,” *Journal of Applied Physics*, vol. 132, no. 22, p. 224703, Dec. 2022, doi: 10.1063/5.0117224.

[16] A. Amani, A. Shamloo, P. Vatani, and S. Ebrahimi, “Particles Focusing and Separation by a Novel Inertial Microfluidic Device: Divergent Serpentine Microchannel,” *Ind. Eng. Chem. Res.*, vol. 61, no. 38, pp. 14324–14333, Sep. 2022, doi: 10.1021/acs.iecr.2c02451.

[17] S. Ebrahimi *et al.*, “Optimizing the design of a serpentine microchannel based on particles focusing and separation: A numerical study with experimental validation,” *Sensors and Actuators A: Physical*, vol. 358, p. 114432, Aug. 2023, doi: 10.1016/j.sna.2023.114432.

[18] A. Wiede, O. Stranik, A. Tannert, and U. Neugebauer, “Microfluidic System for Cell Mixing and Particle Focusing Using Dean Flow Fractionation,” *Micro*, vol. 3, no. 3, pp. 671–685, Jul. 2023, doi: 10.3390/micro3030047.

[19] R. Valani, B. Harding, and Y. Stokes, “Utilizing bifurcations to separate particles in spiral inertial microfluidics,” *Physics of Fluids*, vol. 35, no. 1, p. 011703, Jan. 2023, doi: 10.1063/5.0132151.

[20] R. N. Valani, B. Harding, and Y. M. Stokes, “Inertial particle focusing in fluid flow through spiral ducts: dynamics, tipping phenomena and particle separation,” *J. Fluid Mech.*, vol. 990, p. A13, Jul. 2024, doi: 10.1017/jfm.2024.487.

[21] R. Nasiri, “Microfluidic-Based Approaches in Targeted Cell/Particle Separation Based on Physical Properties: Fundamentals and Applications,” 2020.

[22] C. Liu, C. Xue, J. Sun, and G. Hu, “A generalized formula for inertial lift on a sphere in microchannels,” *Lab Chip*, vol. 16, no. 5, pp. 884–892, 2016, doi: 10.1039/C5LC01522G.

[23] A. T. Aldemir, S. Cadirci, and L. Trabzon, “Investigation of inertial focusing of micro- and nanoparticles in spiral microchannels using computational fluid dynamics,” *Physics of Fluids*, vol. 35, no. 11, p. 112012, Nov. 2023, doi: 10.1063/5.0173356.

[24] D. Di Carlo, J. F. Edd, D. Irimia, R. G. Tompkins, and M. Toner, “Equilibrium Separation and Filtration of Particles Using Differential Inertial Focusing,” *Anal. Chem.*, vol. 80, no. 6, pp. 2204–2211, Mar. 2008, doi: 10.1021/ac702283m.

[25] J.-S. Park, S.-H. Song, and H.-I. Jung, “Continuous focusing of microparticles using inertial lift force and vorticity via multi-orifice microfluidic channels,” *Lab Chip*, vol. 9, no. 7, pp. 939–948, 2009, doi: 10.1039/B813952K.

[26] Dean, “Fluid motion in a curved channel,” *Proc. R. Soc. Lond. A*, vol. 121, no. 787, pp. 402–420, Nov. 1928, doi: 10.1098/rspa.1928.0205.

[27] J. Zhang, W. Li, M. Li, G. Alici, and N.-T. Nguyen, “Particle inertial focusing and its mechanism in a serpentine microchannel,” *Microfluid Nanofluid*, vol. 17, no. 2, pp. 305–316, Aug. 2014, doi: 10.1007/s10404-013-1306-6.

[28] S. Narayana Iyengar, T. Kumar, G. Mårtensson, and A. Russom, “High resolution and rapid separation of bacteria from blood using elasto-inertial microfluidics,” *Electrophoresis*, vol. 42, no. 23, pp. 2538–2551, Dec. 2021, doi: 10.1002/elps.202100140.

[29] H. Amini, W. Lee, and D. Di Carlo, “Inertial microfluidic physics,” *Lab Chip*, vol. 14, no. 15, p. 2739, 2014, doi: 10.1039/c4lc00128a.

[30] D. Di Carlo, J. F. Edd, K. J. Humphry, H. A. Stone, and M. Toner, “Particle Segregation and Dynamics in Confined Flows,” *Phys. Rev. Lett.*, vol. 102, no. 9, p. 094503, Mar. 2009, doi: 10.1103/PhysRevLett.102.094503.

[31] K. Hood, S. Lee, and M. Roper, “Inertial migration of a rigid sphere in three-dimensional Poiseuille flow,” *J. Fluid Mech.*, vol. 765, pp. 452–479, Feb. 2015, doi: 10.1017/jfm.2014.739.

[32] J. Zhou and I. Papautsky, “Fundamentals of inertial focusing in microchannels,” *Lab Chip*, vol. 13, no. 6, p. 1121, 2013, doi: 10.1039/c2lc41248a.

[33] R. Moloudi, S. Oh, C. Yang, M. Ebrahimi Warkiani, and M. W. Naing, “Inertial particle focusing dynamics in a trapezoidal straight microchannel: application to particle filtration,” *Microfluid Nanofluid*, vol. 22, no. 3, p. 33, Mar. 2018, doi: 10.1007/s10404-018-2045-5.

[34] S. C. Hur, N. K. Henderson-MacLennan, E. R. B. McCabe, and D. Di Carlo, “Deformability-based cell classification and enrichment using inertial microfluidics,” *Lab Chip*, vol. 11, no. 5, p. 912, 2011, doi: 10.1039/c0lc00595a.

[35] A. A. S. Bhagat, S. S. Kuntaegowdanahalli, and I. Papautsky, “Inertial microfluidics for continuous particle filtration and extraction,” *Microfluid Nanofluid*, vol. 7, no. 2, pp. 217–226, Aug. 2009, doi: 10.1007/s10404-008-0377-2.

[36] A. Shamloo, S. Abdorahimzadeh, and R. Nasiri, “Exploring contraction–expansion inertial microfluidic-based particle separation devices integrated with curved channels,” *AIChE Journal*, vol. 65, no. 11, p. e16741, Nov. 2019, doi: 10.1002/aic.16741.

[37] A. Mashhadian and A. Shamloo, “Inertial microfluidics: A method for fast prediction of focusing pattern of particles in the cross section of the channel,” *Analytica Chimica Acta*, vol. 1083, pp. 137–149, Nov. 2019, doi: 10.1016/j.aca.2019.06.057.

[38] K. Hood, S. Kahkeshani, D. Di Carlo, and M. Roper, “Direct measurement of particle inertial migration in rectangular microchannels,” *Lab Chip*, vol. 16, no. 15, pp. 2840–2850, 2016, doi: 10.1039/C6LC00314A.

[39] K. Akbarnataj, S. Maleki, M. Rezaeian, M. Haki, and A. Shamloo, “Novel size-based design of spiral microfluidic devices with elliptic configurations and trapezoidal cross-section for ultra-fast isolation of circulating tumor cells,” *Talanta*, vol. 254, p. 124125, Mar. 2023, doi: 10.1016/j.talanta.2022.124125.

[40] A. Özbey, M. Karimzadehkhouei, S. Akgönül, D. Gozuacik, and A. Koşar, “Inertial Focusing of Microparticles in Curvilinear Microchannels,” *Sci Rep*, vol. 6, no. 1, p. 38809, Dec. 2016, doi: 10.1038/srep38809.

[41] A. A. S. Bhagat, S. S. Kuntaegowdanahalli, and I. Papautsky, “Enhanced particle filtration in straight microchannels using shear-modulated inertial migration,” *Physics of Fluids*, vol. 20, no. 10, p. 101702, Oct. 2008, doi: 10.1063/1.2998844.

10th International Congress of the Serbian Society of Mechanics
Niš, Serbia, June 18-20, 2025
B.11
Original scientific paper

DOI:10.46793/ICSSM25.99P

EMHD CONVECTION OF A TRIHYBRID NANOFLUID THROUGH A POROUS MEDIUM IN A VERTICAL CHANNEL WITH THERMAL RADIATION

Jelena D. Petrović[1][0000-0001-6768-9779], Milica Nikodijević Đorđević[2][0000-0002-6031-1666], Miloš Kocić[1][0000-0002-6216-5113], Jasmina Bogdanović Jovanović[1][0000-0002-8331-2880], Živojin Stamenković[1][0000-0001-8722-3191]

[1] Faculty of Mechanical Engineering, Aleksandra Medvedeva 14, Niš, Serbia
[2] Faculty of Occupational Safety, Čarnojevića 10a, Niš , Serbia
e-mail: jelena.nikodijevic.petrovic@masfak.ni.ac.rs, milica.nikodijevic@znrfak.ni.ac.rs, milos.kocic@masfak.ni.ac.rs, jasmina.bogdanovic.jovanovic@masfak.ni.ac.rs, zivojin.stamenkovic@masfak.ni.ac.rs.

Abstract

Electromagnetic hydrodynamic (EMHD) convection of trihybrid nanofluid (THNF) is investigated in this paper, i.e. fluid in which three types of nanoparticles were inserted. This THNF flows through a porous medium located in a vertical channel, the walls of which are at constant but different temperatures. The channel is under the influence of external electric and magnetic fields. Viscous dissipation, Joule radiation, Darcy dissipation and thermal radiation are included in the energy equation. Analytical solutions were obtained for the THNF velocity and temperature distributions, as well as Nusselt numbers and shear stresses on the channel walls. Part of the obtained results is presented in the form of graphs and tables, and the effects of various introduced physical parameters on velocity, temperature, Nusselt numbers and shear stresses are analyzed.

Key words: EMHD, THNF, porous media, thermal radiation, nanoparticle convection, volume fraction

1. Introduction

Heat transfer is not only a technical issue in many industrial fields, but also a very big challenge for engineers, businessmen and researchers. They strive to improve heat transfer using different ways to achieve this. The first attempts were to increase the heat exchange surfaces, which led to bulky and uneconomical systems. It was noticed a long time ago that the fluids that are traditionally used for heat transfer have poor thermal conductivity, and research was started in order to improve it. One of, for now, the easiest ways to realize this is the use of nanofluids (NF), i.e. of traditional fluids in which metal particles of size (1-100) nm have been inserted, i.e. nanoparticles (NPs). The realization of this idea dates back to 1995, when the research by Choi and Eastman [1] was published. Research has continued and today, fluids with one, two and three types of NC are used, i.e. NF, hybrid nanofluids (HNF) and THNF, respectively.

These researches are still very current today and there are a large number of available results, a small number of which will be mentioned in this paper. The instability of Rayleigh-Benard convection was investigated by direct numerical simulation by Jovanović et al. [2]. The flow of two immiscible Newtonian fluids in a multi-effect inclined channel was investigated by Lima et al. [3], and Raju and Satish [4] investigated the MHD flow and heat transfer of two immiscible ionized gases in a horizontal channel. Kalyyan and Soliman [5] investigated the flow and heat transfer of immiscible micropolar and Newtonian fluids in a vertical channel, and Yadav et al. [6] entropy generation in a horizontal channel of a porous medium (PM) with an inclined magnetic field and radiant heat.

The effect of nanoparticles size on velocity and temperature in MHD mixed convection in a vertical channel with heat generation and thermal radiation was investigated by Gul et al. [7]. Mixed convection of three fluid layers where the end is NF and the middle clear fluid in the vertical channel is PM was investigated by Umavathi and Sheremet [8]. Petrović et al. [9,10] investigated the MHD mixed convection of immiscible NF and clear fluid through PM in a horizontal and vertical channel, respectively. MHD convection of immiscible NF and clear fluid in a horizontal suction/injection channel was investigated by Manjeet and Sharma [11]. A detailed review of the flow and heat transfer research of NF in PM in the period from 2018 to 2020 was given by Nabwey et al. [12]. The influence of different NCs on the mixed convection of two immiscible NFs through PM in an inclined channel of permeable walls with thermal radiation was investigated by Devi et al. [13].

Xu and Sun [14] investigated the mixed convective flow of HNF through PM in a vertical microchannel. MHD mixed convective flow of HNF in PS with radiation was investigated by Alzahrani et al. [15], Rao and Deka [16] and Khalil et al. [17] on a buckling plate, on a stretchable plate with slip conditions, and on an elastic plate with slip conditions, varying viscosity and thermal conductivity, respectively. Convective flow of THNF and PS on a horizontally stretching sheet was investigated by Algehyne et al. [18] and on a stretching sheet with radiation and the influence of a magnetic field, Nasir et al. [19]. EMHD flow and heat transfer in a PM between two clear fluids in an inclined channel was investigated by Subray et al. [20].

Heat transfer in MHD flow of THNF over a stretching/shrinking sheet with heat generation/absorption and slip conditions was investigated by Mahmood et al. [21]. MHD mixed convective flow of THNF through a porous medium in a vertical channel with slip boundary conditions was investigated by Hema et al. [22].

The authors of this paper conducted a review and analysis of numerous existing studies on NF, HNF, and THNF. After that review, they got the impression that there is very little research on the simultaneous influence of the magnetic field, electric field, PM factor and thermal radiation on the mixed convective flow of THNF. Bearing this in mind, and the possibility of applying such flow and heat transfer, this paper investigates MHD mixed convective flow THNF through PM in a vertical channel with thermal radiation, viscous dissipation, Darcy dissipation and Joule heating.

2. Mathematical formulation

Here, the flow and heat transfer of THNF through a porous medium of permeability K_0 in a vertical channel between flat walls located at a distance h is studied. The channel walls are impermeable, and their temperatures Tw_1 and Tw_2 are constant ($Tw_2 < Tw_1$). The applied external magnetic field is homogeneous, perpendicular to the walls, and its magnetic induction is B. The external electric field of strength E is homogeneous and perpendicular to the directions of the basic current and the magnetic field. It is assumed that the pressure gradient in the flow direction is constant and that the flow is fully developed. The XYZ coordinate system is adopted so that the X-axis is in the plane of the left wall and has the direction of the primary flow, and the Y-axis is perpendicular to the channel walls as shown in Figure 1.

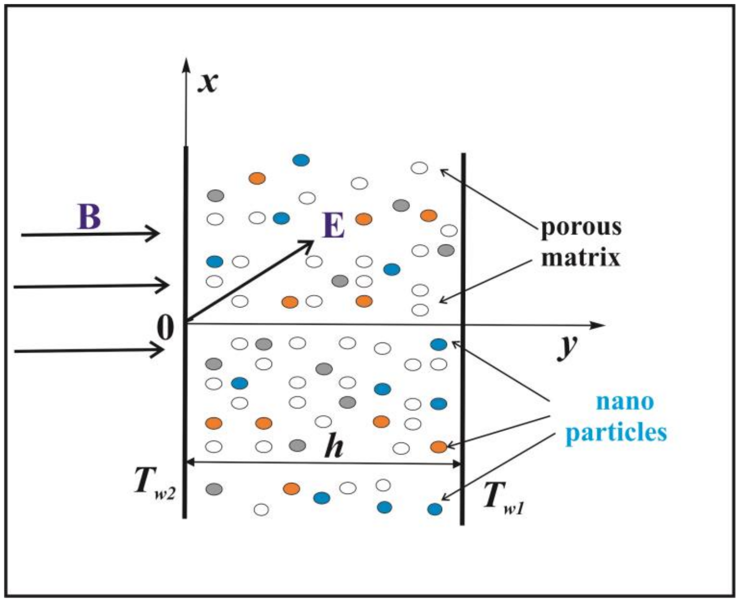

Fig. 1. Physical configuration

Bearing in mind that this fluid flow is affected by pressure, viscous friction, buoyancy, Darcy resistance and Lorentz forces, the momentum equation of the described problem can be written in the form:

$$-\frac{dp}{dX}+\mu\frac{d^2U}{dZ^2}-\frac{\mu}{K_0}U-B\sigma\left(E+BU\right)+g\left(\rho\beta\right)\left(T-T_{w2}\right)=0., \tag{1}$$

The energy equation of the described problem, taking into account viscous dissipation, Darcy dissipation, Joule heating and thermal dissipation, Joule heating and radiant heat, can be written in the form:

$$k\frac{d^2T}{dY^2}+\mu\left(\frac{dU}{dY}\right)^2-\frac{dq_r}{dY}+\frac{\mu}{K_0}U^2+\sigma(E+BU)^2=0., \tag{2}$$

The corresponding boundary conditions can be written as follows:

$$\left(\mathrm{U},T\right)(0)=\left(0,T_{w2}\right);\left(U,T\right)(h)=\left(0,T_{w1}\right)., \tag{3}$$

In the previous equations and boundary conditions, the symbols used are: U- flow velocity, T- temperature, ρ – density, σ – electrical conductivity, μ – dynamic viscosity coefficient, k – thermal conductivity, β – thermal expansion coefficient, q_r – thermal radiation flux THNF and g – gravitational acceleration.

For the physical properties of THNF, classical relations [21] are used in the following form:

$$\mu=\frac{\mu_f}{m},k=\varphi_2k_f,\sigma=\varphi_4\sigma_f,\left(\rho\beta\right)=\varphi_6\left(\rho\beta\right)_f,, \tag{4}$$

in which, for the sake of brevity, the labels are used:

$$m=(1-\phi_1)^{2.5}(1-\phi_2)^{2.5}(1-\phi_3)^{2.5},$$
$$H\left(\phi,S,R,M\right)=\frac{\left(1+2\phi\right)S+2\left(1-\phi\right)RM}{\left(1-\phi\right)S+\left(2+\phi\right)RM}\mathrm{M},$$
$$\Omega\left(\phi,M,i\right)=\left(1-\phi\right)M+\phi\frac{\left(\rho\beta\right)_i}{\left(\rho\beta\right)_f}, \qquad , \tag{5}$$
$$\varphi_0=H\left(\phi_1,k_1,k_f,1\right),\varphi_1=H\left(\phi_2,k_2,k_f,\varphi_0\right),\ \varphi_2=H\left(\phi_3,\mathrm{k}_3,\mathrm{k}_f,\varphi_1\right),$$
$$\eta_0==H\left(\phi_1,\sigma_1,\sigma_f,1\right),\varphi_3=H\left(\phi_2,\sigma_2,\sigma_f,\eta_0\right),\varphi_4=H\left(\phi_3,\sigma_3,\sigma_f,\varphi_3\right),$$
$$\eta_1=\Omega\left(\phi_1,1,1\right),\varphi_5=\Omega\left(\phi_2,\eta_1,2\right),\varphi_6=\Omega\left(\phi_3,\varphi_5,3\right),$$

where the subscript f refers to the base fluid, and $\phi_i[i=1,2,3]-$ the volume fraction of nanoparticles.

The Rasseland approximation [6] is used for the heat radiation flux:

$$q_r=-\frac{4\sigma^*}{3k^*}\frac{dT^4}{dY}, \tag{6}$$

in which are $\sigma^*-$the Stefan-Boltzmann constant and $k^*-$the mean value of the absorption coefficient THNF.

An approximation is obtained by developing in order:

$$T^4\approx T_{w2}^3\left(4T-3T_{w2}\right), \tag{7}$$

and then it's:

$$\frac{dq_r}{dY}=-\frac{16\sigma^*T_{w2}^3}{3k^*}\frac{d^2T}{dY^2}.\,, \tag{8}$$

For further investigation of this problem, equations (1) and (2) and boundary conditions (3) are transformed into dimensionless forms by introducing the following dimensionless quantities:

$$y=\frac{Y}{h},\ u=\frac{U}{U_0},\ \theta=\frac{T-Tw_2}{Tw_1-Tw_2},\ , \tag{9}$$

in which U_0 is characteristic velocity that will be determined in the future. After replacing relations (4), (6) and dimensionless quantities (9) in equations (1), (2) and boundary conditions (3), the corresponding equations and boundary conditions are obtained in dimensionless form:

$$y=\frac{Y}{h},\ u=\frac{U}{U_0},\ \theta=\frac{T-Tw_2}{Tw_1-Tw_2},\ , \tag{10}$$

$$\frac{d^2\theta}{dy^2}=-\frac{Br}{mb}\left[\left(\frac{du}{dy}\right)^2+\omega^2u^2+2Ru+R_2\right],\ , \tag{11}$$

$$\left(u,\theta\right)\left(0\right)=\left(0,0\right),\ \left(u,\theta\right)\left(1\right)=\left(0,1\right).\,, \tag{12}$$

The following notations were used in the last equations and boundary conditions:

$$\begin{aligned}
&\Lambda=\frac{h^2}{K_0}, Ha=Bh\sqrt{\frac{\sigma_f}{\mu_f}}, K=\frac{E}{BU_0}, P=-\frac{\partial p}{\partial X}\frac{h^2}{U_0\mu_f},\ a=m\varphi_6,\\
&\omega^2=\Lambda+m\varphi_4 Ha^2, R=m\varphi_4 KHa^2, R_1=R-mP,\\
&Br=\frac{\mu_f U_0^2}{k_f\left(Tw_1-Tw_2\right)}, \mathrm{R}^*=\frac{16\sigma^* T_{w2}^3}{3k_f k^*}, b=R^*+\varphi_2, R_2=KR,\\
&M=g\frac{\left(\rho\beta\right)_f h^2\left(Tw_1-Tw_2\right)}{\mu_f U_0},
\end{aligned} \tag{13}$$

where: Λ – porosity factor, K – external electric load factor, R^* – radiation parameter, and Ha and Br - Hartmann's and Brickmann's numbers, respectively.

3. Solution method

Equations (10) and (11) are coupled with nonlinear ordinary differential equations and for them, at least for now, it is not possible to find an exact analytical solution. However, for small values of the Br number, which is often the case in practice, an analytical approximate solution can be found using the regular perturbation method. Using this method, solutions for velocity and temperature schedules are assumed in the forms:

$$\left(u,\theta\right)\left(y\right)=\sum_{i=0}^{n} Br^i\left(u_i,\theta_i\right)\left(y\right)., \tag{14}$$

Substituting relations (14) in equations (10) and (11), it is obtained that the zero-order equations are:

$$\frac{d^2u_0}{dy^2}-\omega^2u_0+aM\theta_0=R_1,, \tag{15}$$

$$\frac{d^2\theta_0}{dy^2}=0,, \tag{16}$$

First order

$$\frac{d^2u_1}{dy^2}-\omega^2u_1+aM\theta_1=0,, \tag{17}$$

$$\frac{d^2\boldsymbol{\theta}_1}{dy^2}+\frac{1}{mb}\left[\left(\frac{du_0}{dy}\right)^2+\boldsymbol{\omega}{u_0}^2+2Ru_0+R_2\right]=0,, \tag{18}$$

Second order

$$\frac{d^2u_2}{dy^2}-\omega^2u_2+aM\theta_2=0,, \tag{19}$$

$$\frac{d^2\theta_2}{dy^2}+\frac{1}{mb}\left[2\frac{du_0}{dy}\frac{du_1}{dy}+2\omega^2u_0u_1+2Ru_1\right]=0., \tag{20}$$

The corresponding boundary conditions can be written in the form:

$$\left(u_0,u_1,u_2,\theta_0,\theta_1,\theta_2\right)\left(0,1\right)=\left(0,0,0,1,00;0,0,0,0,0,0\right).\,, \tag{21}$$

The solution of equations (15) and (16) with the corresponding boundary conditions (21) is:

$$\begin{aligned} &u_0\left(y\right)=D_1\exp\left(\omega y\right)+D_2\exp\left(-\omega y\right)+\frac{aM}{\omega^2}y-\frac{R_1}{\omega^2},\\ &\theta_0\left(y\right)=y, \end{aligned} \tag{22}$$

and the integration constants are:

$$D_1=\frac{R_1\left[1-\exp(-\omega)\right]-aM}{\omega^2\left[\exp(\omega)-\exp(-\omega)\right]},\ D_2=\frac{R_1}{\omega^2}-D_1.\,, \tag{23}$$

The solution of equations (17) and (18) with appropriate boundary conditions is:

$$\begin{aligned} &\theta_1(y)=-\frac{1}{mb}[\frac{1}{2}D_1^2\exp(2\omega y)+\frac{1}{2}D_2^2\exp(-2\omega y)+(R_3+R_4y)\exp(\omega y)+\\ &(R_5+R_6y)\exp(-\omega y)+R_7y^4+R_8y^3+R_9y^2+C_3y+C_4],\\ &u_1(y)=D_3\exp(\omega y)+D_4\exp(-\omega y)+R_{10}\exp(2\omega y)+R_{11}\exp(-2\omega y)+\\ &y\left(R_{12}+R_{13}y\right)\exp\left(\omega y\right)+y\left(R_{14}+R_{15}y\right)\exp\left(-\omega y\right)+\\ &R_{16}y^4+R_{17}y^3+R_{18}y^2+R_{19}y+R_{20} \end{aligned} \tag{24}$$

where the tags were used:

$$\begin{aligned} &R_3=\frac{2D_1}{\omega^2}(R-R_1-\frac{aM}{\omega}),R_4=\frac{2MaD_1}{\omega^2},\ R_5=\frac{2D_2}{\omega^2}(R-R_1+\frac{aM}{\omega}),\\ &R_6=\frac{2MaD_2}{\omega^2},R_7=\frac{a^2M^2}{12\omega^2},\ R_8=\frac{aM}{3\omega^2}(R-R_1),\\ &R_9=\frac{1}{2}(\frac{a^2M^2}{\omega^4}+\frac{R_1^2}{\omega^2}-\frac{2RR_1}{\omega^2}+R_2),C_4=-\frac{1}{2}(D_1^2+D_2^2)-R_3-R_5,\\ &C_3=-C_4-\frac{1}{2}\left[D_1^2\exp\left(2\omega\right)+D_2^2\exp\left(-2\omega\right)\right]-\\ &-\left(R_3+R_4\right)\exp\left(\omega\right)-\left(R_5+R_6\right)\exp\left(-\omega\right)-R_7-R_8-R_9,\\ &S=\frac{aM}{mb},R_{10}=\frac{SD_1^2}{6\omega^2},\ R_{11}=\frac{SD_2^2}{6\omega^2},\ R_{12}=S\frac{2\omega R_3-R_4}{4\omega^2},\\ &R_{13}=\frac{SR_4}{4\omega},\ R_{14}=-S\frac{2\omega R_5+R_6}{4\omega^2},\ R_{15}=-S\frac{R_6}{4\omega},\\ &R_{16}=-S\frac{R_7}{\omega^2},\ R_{17}=-S\frac{R_8}{\omega^2},\ R_{18}=-S\frac{12R_7+\omega^2R_9}{\omega^4},\\ &R_{19}=-S\frac{6R_8+\omega^2C_3}{\omega^4},\ R_{20}=-S\frac{24R_7+2\omega^2R_9+\omega^4C_4}{\omega^6},\\ &R_{21}=-R_{10}-R_{11}-R_{20},\ R_{22}=-R_{10}\exp\left(2\omega\right)-\\ &R_{11}\exp\left(-2\omega\right)-\left(R_{12}+R_{13}\right)\exp\left(\omega\right)-\left(R_{14}+R_{15}\right)\exp\left(-\omega\right)\\ &-R_{16}-R_{17}-R_{18}-R_{19}-R_{20},\\ &D_3=\frac{R_{22}-R_{21}\exp(-\omega)}{\exp(\omega)-\exp(-\omega)},\ D_4=R_{21}-D_3. \end{aligned} \tag{25}$$

The solution of the second-order equations is not given here, due to the long notes.

Thus, the analytical speed and temperature distributions of THNF of the observed problem were determined. Now the reactions for the dimensionless shear stress and the Nusselt number can also be determined. The dimensionless shear stresses on the left and right channel walls have the following notations:

$$\tau_1 = \frac{\mu}{\mu_f}\left(\frac{du}{dy}\right)_{y=0}, \quad \tau_2 = \frac{\mu}{\mu_f}\left(\frac{du}{dy}\right)_{y=1}, , \tag{26}$$

respectively, and the Nusselt numbers on these walls are:

$$Nu_1 = \frac{k}{k_f}\left(\frac{d\theta}{dy}\right)_{y=0}, Nu_2 = \frac{k}{k_f}\left(\frac{d\theta}{dy}\right)_{y=1}., \tag{27}$$

respectively.

4. Results and analysis

Analytical relations obtained in the previous chapter for distributions of velocity, temperature, shear stress and Nusselt numbers depend on the introduced physical parameters that are significant for the observed problem. Among the influential parameters is the parameter M, which depends on the choice of the characteristic velocity U_0. This velocity can be chosen in different ways and here it is chosen so that the parameter M is the Grashof number. Equating the expression for the quantity M with the expression for the Grashof number, the equation is obtained:

$$g\frac{\rho_f \beta_f h^2 \left(T_{w1} - T_{w2}\right)}{U_0 \mu_f} = g\frac{\rho_f^2 \beta_f h^3 \left(T_{w1} - T_{w2}\right)}{\mu_f^2}, \tag{28}$$

from which it follows that:

$$U_0 = \frac{\mu_f}{\rho_f h} = \frac{\nu_f}{h}, \tag{29}$$

where ν_f – is the coefficient of kinematic viscosity of the base fluid.

This chapter presents part of the obtained results for the case when THNF consists of water as the base fluid and nanoparticles of magnesium oxide (MgO), titanium dioxide (TiO_2) and aluminum oxide (Al_2O_3). The physical characteristics of water and nanoparticle materials used here are given in Table 1.

Substance properties	H_2O	Al_2O_3	T_iO_2	MgO
$\rho\left(kg/m^3\right)$	997.1	3970	4250	3560
$c_p\left(J/(kgK)\right)$	4179	765	686.2	955
$K\left(W/(Km)\right)$	0.613	40	8.9538	45
$\sigma\left(S/m\right)$	$5.5\cdot10^{-6}$	$35\cdot10^{6}$	$2.6\cdot10^{6}$	$5.392\cdot10^{-7}$
$\mu\left(Pas\right)$	0.001	-	-	-
β[K-1]	$0.18\cdot10^{-5}$	$0.85\cdot10^{-5}$	$0.90\cdot10^{-5}$	$1.13\cdot10^{-5}$

Table 1. Physical characteristics

Results are given for parameter values $\phi_1 = \phi_2 = \phi_3 = 0.01$, $Br = 0.3$, $K = -1$, $\Lambda = 5$, $Gr = 5$, $R^* = 0.5$, $Ha = 5$, except when they are individually changed. Figures 2 and 3 present graphs of the distribution of velocity and temperature for several values of the Ha number, respectively. As shown in Figure 2, an increase in the Ha number leads to a higher flow rate of THNF in the channel. This can be physically explained by the fact that the Lorentz force, which acts as the driving force, increases with the Ha number. It can be seen from Fig. 3 that the temperature of the fluid in the channel is higher for higher values of the Hartmann number and this can be attributed to the increase in Joule heat.

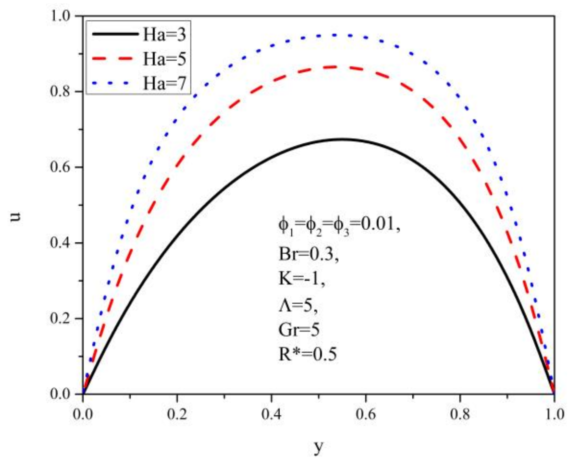

Fig. 2. Velocity distributions for different values of Ha

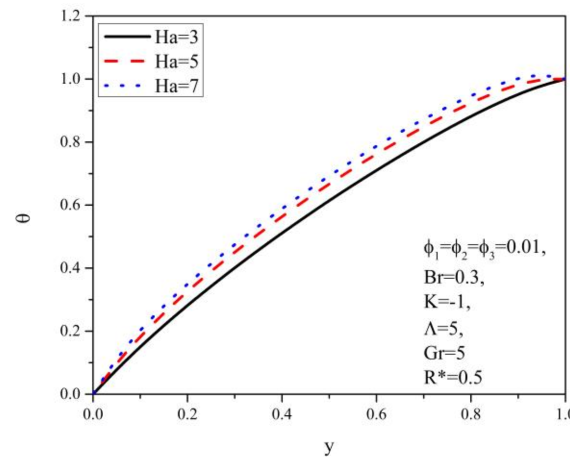

Fig. 3. Temperature distributions for different values of Ha

The velocity and temperature profiles for various Λ values are shown in Figures 4 and 5, respectively. From Figure 4, it is evident that higher Λ values lead to reduced fluid velocities, which can be attributed to the increased resistance force of the porous medium against the fluid flow. Conversely, Figure 5 shows that as Λ increases, the fluid temperature within the channel rises. This can be physically explained by the conversion of energy used to overcome the porous medium's resistance into thermal energy.

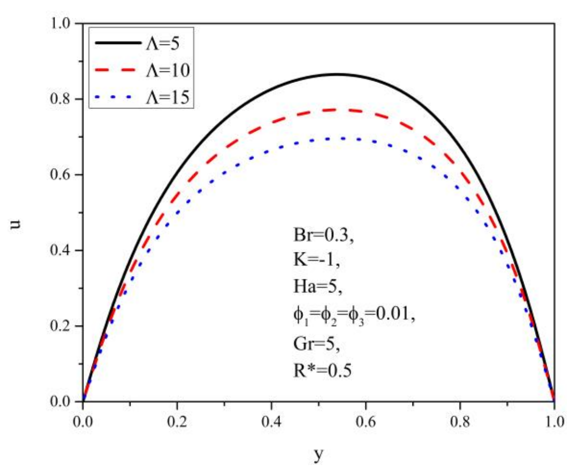

Fig.4. Velocity distributions for different values of Λ

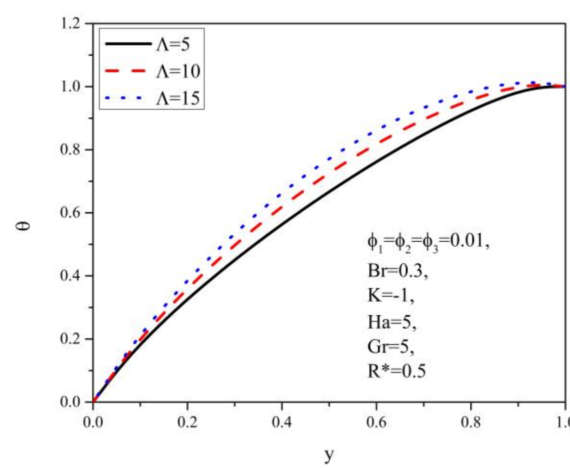

Fig. 5. Temperature distributions for different values of Λ

Figures 6 and 7 present graphical distributions of velocity and temperature for different values of K, respectively. It can be seen from Figure 6 that higher values of $|K|$ correspond to higher velocity intensities and that the change in the sign of the quantity K ie. a change in the direction of the external electric field leads to a change in the direction of the fluid flow in the channel. For the value K=0, the fluid velocity is very low. With Figure 7, it is noted that higher values $|K|$ correspond to lower fluid temperatures in the channel.

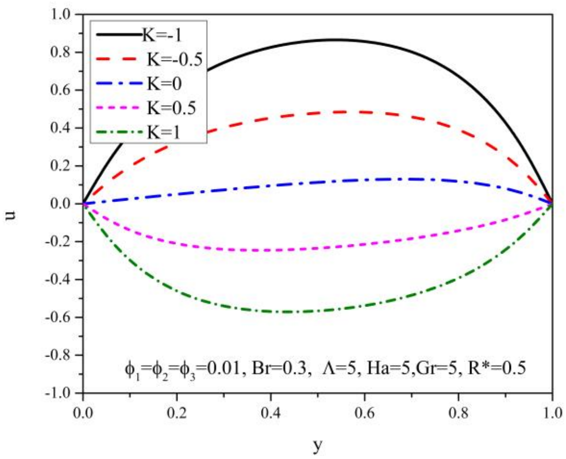

Fig.6 Velocity distributions for different values of K

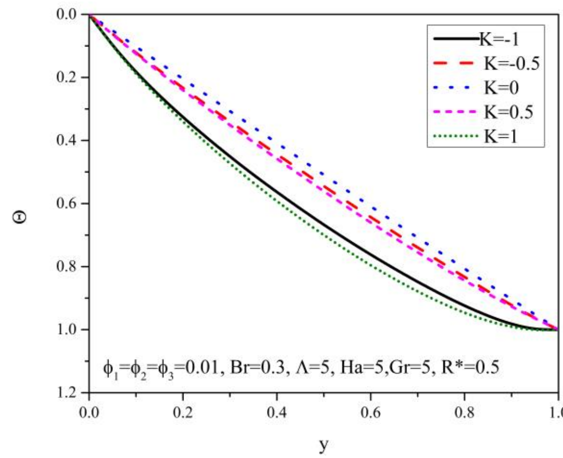

Fig.7 Temperature distributions for different values of K

The velocity and temperature distributions for different values of Gr are shown in Figures 8 and 9, respectively. With Fig. 8, it is noted that higher values of Gr correspond to higher velocities of fluid flow, which is physically explained by an increase in the intensity of the buoyancy force. The temperature of the fluid in the channel increases for higher values of Gr, which can be seen from Fig. 9.

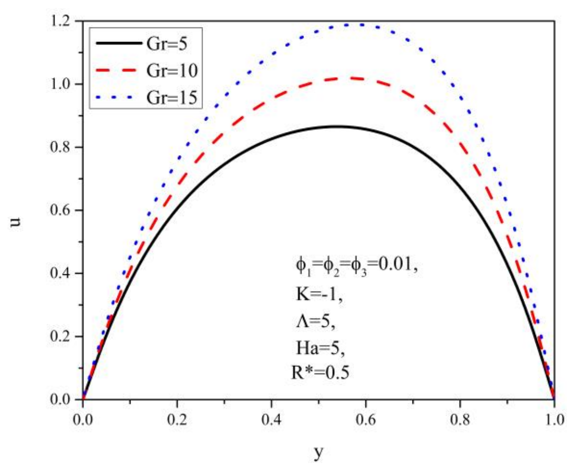

Fig. 8. Velocity distributions for different values of Gr

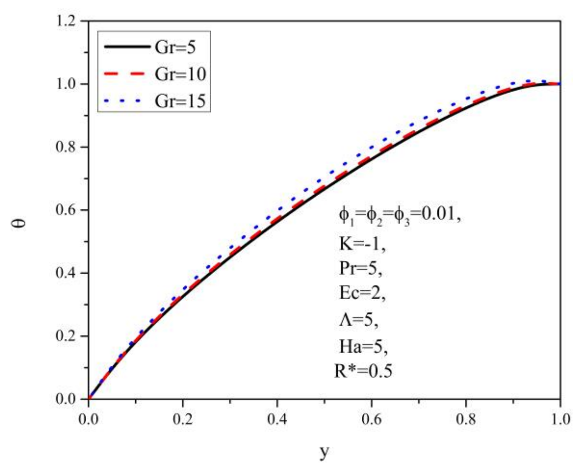

Fig. 9. Temperature distributions for different values of Gr

Plots of velocity and temperature distribution, for different values of R*, are presented in Figures 10 and 11, respectively. With Figure 10, it can be seen that higher values of R* correspond to lower velocities and from figure 11 to correspond to lower temperatures.

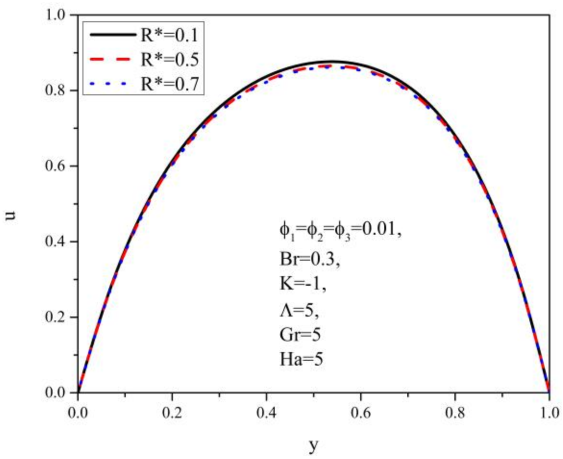

Fig. 10. Velocity distributions for different values of R*

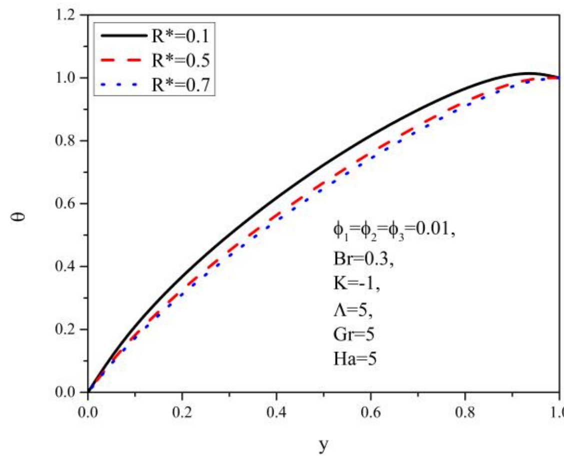

Fig. 11. Temperature distributions for different values of R*

Table 2 gives values of shear stress on channel walls and values of local Nusselt numbers on these walls for several values of introduced physical parameters. The results in this table are given for the same parameter values as for the graphics. Table 2 shows that higher values of the Ha number correspond to higher values of the shear stress on the channel walls, and higher values of the local Nu numbers. An increase in the value of the porosity factor leads to a decrease in the shear stress on the channel walls and to an increase in the Nu number on these walls.

Table 2. Shear stresses and Nusselt numbers for several parameter values

	τ_1	τ_2	Nu_1	Nu_2
$Ha=3$	3.058397	–4.15434	2.107867	–0.80533
$Ha=5$	5.204721	–6.14346	2.964628	–1.60951
$Ha=7$	7.33365	–8.12833	3.738687	–2.23564
$\Lambda=5$	5.204721	–6.14346	2.964628	–1.60951
$\Lambda=10$	4.837761	–5.7392	3.190565	–1.67173
$\Lambda=15$	4.533338	–5.40163	3.370728	–1.7369
$K=-1$	5.204721	–6.14346	2.964628	–1.60951
$K=-0.5$	2.708536	–3.64846	1.578781	0.164514
$K=0$	0.282222	–1.22333	1.123938	1.00753
$K=0.5$	–2.07422	1.131931	1.600101	0.919542
$K=1$	–4.3608	3.417324	3.007269	–0.09945
$Gr=5$	5.204721	–6.14346	2.964628	–1.60951
$Gr=10$	5.61465	–7.4971	3.056461	–2.57611
$Gr=15$	6.069284	–8.91003	3.222432	–3.68609
$R^*=0.1$	5.250883	–6.18938	2.964628	–1.60951
$R^*=0.5$	5.204721	–6.14346	2.964628	–1.60951
$R^*=0.7$	5.189398	–6.12822	2.964628	–1.60951

Higher absolute values of the external electric load factor correspond to higher shear stresses on the channel walls and higher Nusselt numbers. An increase in the value of R* reduces shear stresses and the values of Nusselt numbers are not affected for the analyzed values of R*. Higher values of Gr number correspond to higher values of Nusselt numbers and shear stress.

3. Conclusions

In this paper, electromagnetic hydrodynamic flow and heat transfer of three hybrid nanofluids in a porous medium in a vertical channel were investigated. The impact of viscous and Darcy dissipation, Joule heating and thermal radiation is considered. Analytical approximate solutions for velocity and temperature were determined using the regular perturbation method. The corresponding conclusions were drawn from the analysis of the obtained solutions. It was concluded that an increase in Hartmann's number and Grashof's number leads to an increase in velocity and temperature in the channel and to an increase in shear stress and Nusselt numbers on the channel walls. Higher values of the porosity factor correspond to smaller values and shear stresses and higher temperatures and higher Nusselt numbers. Higher radiation factor values correspond to lower velocities, shear stresses and lower temperatures. By changing the sign of the external load factor the direction of fluid flow in the channel can be changed.

References

[1] Choi and Eastman, Enhanicing thermal conductivity of fluids with nanoparticles, Presented at ASME international Mechanical Enginering Congress and Expositio, November 12-17, 1995, San Francisco, CA.

[2] Miloš M.Jovanović, Jelena D.Nikodijević, Milica D.Nikodijević, (2015), „Rayleigh-Bénard convection instability in the presence of spatial temperature modulation on both plates“, International Journal of Non-Linear Mechanics, Volume 73, Pages 69-74, doi: 10.1016/j.ijnonlinmec.2014.11.017

[3] J.A. Lima, G.E. Assad, H.S. Raiva, 2016, A simple approach to analyze the fully developed two-phase magnetoconvection type flows in inclined parallel-plate channels, Latin American Applied Research, 46(3). pp. 93-98, doi: 10.52292/jaar.2016.333

[4] T. Linga Raju and P. Satish (2023), Slip regime MHD 2-liquid plasma heat transfer flow with Hall curcents between parallel plates, Int. J. Of Applied Mehhanics and Engineering, Vol.28, No.3, pp. 65-85, doi:10.59441/ijame/172898

[5] Shreedevi Kalyan, Hussein Abd Allah Soliman, (2024), Analysis of Micropolar Immiscible Fluid Flow on Electrically Conducting Free Convective Flow in a Vertical Channel in the Presence of Chemical Reaction, International Journal of Advanced Engineering and Business Sciences, Volume 5, Issue 1, pp. 63-90, doi:10.21608/IJAEBS.2024.273140.1093

[6] Pramod Kumar Yadav, Ankit Kumar, Shreen El-Sapa, Ali J. Chamkha, 2022, Impact of thermal radiation and oriented magnetic field on the flow of two immiscible waves in random and complex media, doi: 10.1080/17455030.2022.218897.

[7] Aaiza Gul, Ilyas Khan and Sharidan Shafie (2018), Radiation and heat generation effects in magnetohydrodynamic mixed convection flow of nanofluids, Thermal Science, Vol. 22, No. 1A, pp. 51-62, doi:10.2298/TSCI150730049G

[8] Umavathi J.C., Sheremet M.A. (2020) Heat transfer of viscous fluid in a vertical channel sandwiched between nanofluid porous zones, Journal of Thermal Analysis and Calorimetry 144(4), doi:10.1007/S10973-020-09664-1

[9] Jelena Petrović, Živojin Stamenković, Jasmina Bogdanović-Jovanović, Milica Nikodijević, Miloš Kocić, Dragiša Nikodijević, 2022, Electro-Magnetoconvection of Conductive Immiscible Pure Fluid and Nanofluid, Transactions of FAMENA, Vol. 46 No. 3, pp. 13-28, doi: 10.21278/TOF.463036021.

[10] Jelena D. Petrović, Živojin Stamenković, Miloš Kocić, Milica Nikodijević, Jasmina Bogdanović Jovanović, Dragiša D. Nikodijević (2022), Magnetohydrodynamic flow and

mixed convection of a viscous fluid and a nanofluid a porous medium in a vertical channel, Thermal Science Volume 27, Issue 2 Part B, pp. 1453-1463, doi:10.2298/TSCI220903188P

[11] Manjet and Mukesh Kumar Sharma, 2020, MHD flow and heat convection in a channel filled with two immiscible Newtonian and nanofluid fluids, JP Journal of Heat and Mass Transfer, Vol. 21, No. 1, pp. 1-21;

[12] Nabwey, H.A.; Armaghani, T.; Azizimehr, B.; Rashad, A.M.; Chamkha, A.J. (2023), A Compehensive Review of Nanofluid Heat Transfer in Porous Media. Nanomaterials 2023, 13, 937. doi.org/10.3390/nano13050937

[13] M.Padma Devi, Komal Goyal, S. Srinivas, B. Satyanarayana (2024), Effects of different nanoparticles on the two immiscible liquids flow in an inclined channel with Joule heating and viscous dissipation, Gulf Journal of Mathematics Vol. 16, Issue 2, 278-290, https://doi.org/10.56947/gjom.v16i2.1815

[14] Hang Xu and Qiang Sun, (2019), Generalized Hybrid Nanofluid with the Application of Fully Developed Mixed Convection Flow in a Vertical Microchannel, Communications in theoretical Physics, Vol. 71, No. 8, 903-911, doi:10.1088/0253-6102/71/8/903

[15] Abdullah K. Alzahrani, Malik Zaka Ullah, Ali Sahes Alshomrani, Taza Gul, Hyrid nanofluid flo in a Darcy-Forchkeimer permeable medium over a plate due to solar radiatiion. Case Studies in Thermal Engineering 26(2021) 1009555, doi: 10.1016/j.csite.2021.10095

[16] Rao, S., Deka, P.N., (2024), Numerical Analysis of MHD Hybrid Nanofluid Flow a Porous Stretching Sheet with Thermal Radiation. Int. J. Appl. Comput. Math 10, 95 (2024). doi:10.1007/540819-024-01734-4.

[17] Salma Khalil, Humaira Yasmin, Tasawar Abbas, Taseer Muhammad, Analysis of thermal conductivity variation in magneto-hybrid nanofluids flow through porous medium with variable viscosity and slip boundary, Case Studies in Thermal Engineering 57(2024)104314, doi:10.1016/j.csite.2024.104314

[18] Ebrahem A. Algehyne, Haiffa F. Alrihieli, Muhammad Bilal, Anwar Saeed and Wajaree Weera (2022), Numerical Approach toward Ternary Hybrid Nanofluid Flow Using Variable Diffusion and Non-Fouriers Concept, ACS Omega 7 (33), 29380-29390, doi:10.1021/acsomega.2c03634

[19] Saleem Nasir, Sekson Sirisubtawee, Pongpol Juntharre, Adallah S Berrouk, Safyan Mukhtar, Taza Gul (2022), Heat transport study of ternary hyrid nanofluid flow under magnetic dipole together with nonlinear thermal radiation, Applied Nanoscience 12(2), doi:10.1007/s13204-022-02583-7

[20] P.V. Ananth Subray, B.N. Hannmagowda, C.S.K. Raju, S.V.K. Varma, Prakash Jagdish, Se-Jin Yook, Nehad Ali Shah, (2023), Analytical analysis of inclined three-layered composite channel with cobalt ferrite nanoparticles and Hall current in Darcy medium, Propulsion and Power Research 2023, 12 (4), 523-538, doi:10.1016/j.jpp.2023.11.001

[21] Zafar Mahmood, Sayed M. Eldin, Khadija Rafiqua, Umar Khan, Numerical analysis of MHD tri-hybrid nanofluid over a nonlinear stretching/shrinking sheet with heat generation/absorption and slip conditions, Alexandria Engineering Journal (2023), 76, 799-819, doi: 10.1016/j.aej.2023.06.081

[22] Hema, S., Venkatesh, P., Gireesha, B. J., Pavithra C. G., Flow and heat transffer analysis of MHD ternary hybrid nanofluid flow trough a vertical porous microchannel with slip bundary conditions, Multiscale and Multidiscp. Model. Exp. And Des. 8, 183(2025). https://doi.org/10.1007/s41939-025-00764-9

10th International Congress of the Serbian Society of Mechanics
Niš, Serbia, June 18-20, 2025

B.12
Extended abstract

STABILITY ANALYSIS OF THE GENERALIZED WASHBURN EQUATION

Isidora Rapajić[1] and Srboljub Simić[2] [0000-0003-3726-2007]

[1]Mathematical Institute of SASA, Belgrade Serbia, email: isidora.rapajic@turing.mi.sanu.ac.rs

[2]University of Novi Sad, Faculty of Scienes, e-mail: ssimic@uns.ac.rs

Abstract. Washburn's equation describes the flow of a viscous incompressible fluid through a narrow vertical cylindrical pipe. It is a simplified version of the Navier-Stokes equations. If the vertical pipe has circular cross section of constant radius, equilibrium height of the fluid is asymptotically stable. In this study, it is shown that in the case of slowly varying cross section equilibrium height remains asymptotically stable, but critical value of the parameter depends on the shape of the pipe. The model and its stability analysis generalize existing results, based upon lubrication theory approach, by inclusion of inertial term.

Keywords: Washburn's equation; Stability analysis

1. Washburn's equation

Motion of a Newtonian fluid is described by the Navier-Stokes equations. When the flow occurs in the narrow vertical pipe of constant circular cross section of radius R, simplifying assumptions lead to the Washburn equation [1]:

$$\rho \frac{\mathrm{d}}{\mathrm{d}t}\left[h(t)\frac{\mathrm{d}h(t)}{\mathrm{d}t}\right] + \rho g h(t) + \frac{8\mu}{R^2} h(t)\frac{\mathrm{d}h(t)}{\mathrm{d}t} = \frac{2\gamma\cos\theta}{R}. \tag{1}$$

There is a unique stationary solution of (1), $h(t) = h_e = \text{const.}$, which determines the equilibrium (Jurin's) height of the fluid column:

$$h_e = \frac{2\gamma\cos\theta}{\rho g R}. \tag{2}$$

Washburn's equation (1) may be put into dimensionless form:

$$\omega \frac{\mathrm{d}}{\mathrm{d}T}\left[H(T)\frac{\mathrm{d}H(T)}{\mathrm{d}T}\right] + H(T)\frac{\mathrm{d}H(T)}{\mathrm{d}T} + H(T) = 1, \tag{3}$$

where dimensionless parameter ω is defined by $\omega := \frac{\rho^2 R^4 g}{64\mu^2 h_e}$. Equilibrium height (stationary solution) is then $H(T) = H_e = 1$.

Linear stability analysis of the stationary solution of Washburn's equation (3) leads to the following results. There exists a critical value $\omega_* = 1/4$ of the dimensionless parameter which separates two types of stationary points (corresponding to stationary solutions):

(a) for $\omega < \omega_*$ the stationary point is a stable node;

(b) for $\omega > \omega_*$ the stationary point is a stable focus.

It can be concluded that equilibrium state of the fluid column is asymptotically stable, but local behavior in its neighborhood depends on the value of dimensionless parameter ω.

2. Generalized Washburn's equation and stability analysis

Generalized Washburn's equation describes motion of the fluid through the vertical pipe with variable circular cross section, $R = R(z)$. Using the lubrication theory, it was derived in [2, 3], but in that form inertial term was neglected. It can be derived from the local and global form of mass and momentum balance laws, under the assumption $|R'(z)| \ll 1$ and without neglecting inertial term. Using the same dimensionless variables as in standard Washburn's equation, generalized Washburn's equation can be cast into:

$$\omega \frac{\mathrm{d}}{\mathrm{d}T}\left[H(T)\frac{\mathrm{d}H(T)}{\mathrm{d}T}\Phi(H(T))\right] + H(T)\frac{\mathrm{d}H(T)}{\mathrm{d}T} + H(T)\Phi(H(T)) = \hat{R}(H(T)), \tag{4}$$

where $\Phi(\zeta) := (1/\zeta)\int_0^{\zeta}\hat{R}(Z)^2\mathrm{d}Z$, and $\hat{R}(Z)$ is dimensionless radius of circular cross section. In this case, equilibrium height is determined as solution of the nonlinear equation:

$$H_e\Phi(H_e) = \hat{R}(H_e). \tag{5}$$

Linear stability analysis is of the equilibrium solution $H(T) = H_e$ leads to the eigenvalue problem, with the eigenvalues:

$$\lambda_{1/2} = -\frac{1}{2}\varphi(\omega, H_e)\left[1 \mp \sqrt{1 - \frac{4\gamma(H_e)}{\varphi(\omega, H_e)^2}}\right], \tag{6}$$

$$\varphi(\omega, H_e) = \frac{1}{\omega\Phi(H_e)}, \quad \gamma(\omega, H_e) = \frac{1}{\omega H_e}\left\{1 - \frac{\hat{R}(H_e)}{\Phi(H_e)}\left[\frac{\hat{R}'(H_e)}{\hat{R}(H_e)} - \frac{\Phi'(H_e)}{\Phi(H_e)}\right]\right\}. \tag{7}$$

For $H_e > 0$, $\varphi(\omega, H_e) > 0$ by definition, whereas $\gamma(H_e) > 0$ due to assumption $|R'(z)| \ll 1$. If we define:

$$\omega_*(H_e) = \left[\frac{4\Phi(H_e)}{H_e}\left\{1 - \frac{\hat{R}(H_e)}{\Phi(H_e)}\left[\frac{\hat{R}'(H_e)}{\hat{R}(H_e)} - \frac{\Phi'(H_e)}{\Phi(H_e)}\right]\right\}\right]^{-1}, \tag{8}$$

the following stability result is obtained:

(a) for $\omega < \omega_*(H_e)$ the stationary point is a stable node;

(b) for $\omega > \omega_*(H_e)$ the stationary point is a stable focus.

This leads to a conclusion that stability of the equilibrium state of the fluid column in the pipe with slowly varying cross section shares the same features as in the case of constant cross section. However, critical value $\omega_*(H_e)$ of the parameter ω is determined by the shape of the pipe $\hat{R}(Z)$.

References

[1] Płociniczak Ł., Świtała M., Monotonicity, oscillations and stability of a solution to a nonlinear equation modelling the capillary rise, Physica D: Nonlinear Phenomena, 362, 1–8, 2018.

[2] Figliuzzi B. and Buie C.R., Rise in optimized capillary channels, Journal of Fluid Mechanics, 731, 142–161, 2013.

[3] Gorce J.-B., Hewitt I.J. and Vella, D., Capillary imbibition into converging tubes: beating Washburn's law and the optimal imbibition of liquids, Langmuir, 32 (6), 1560–1567, 2016.

10th International Congress of the Serbian Society of Mechanics
Niš, Serbia, June 18-20, 2025
B.13
Extended abstract

INFRAGRAVITY WAVES

Teodor Vrećica[1][0000-0001-6321-4338]

[1] Mathematical Institute of SANU
Kneza Mihaila 35, 11000 Belgrade, Serbia
e-mail: teodorv@mi.sanu.ac.rs

Abstract:

InfraGravity (IG) waves are surface water waves with frequencies in the range of 0.003 to 0.03 Hz corresponding to periods of around 30 to 300 seconds (see figure 1). Unlike the majority of waves in seas and oceans, which are generated through direct wind forcing, IG waves are generated through nonlinear interactions of the wave fields with themselves and spatiotemporal inhomogeneities of the environment.

While their amplitudes are much smaller than those of wind waves (on the order of centimeters in open seas), they possess a number of unique properties that make them relevant for various engineering applications and physical processes. This includes their speed of propagation and depth of velocity profile, which can far exceed those of wind waves in deep waters (hundreds of meters per second and reaching bottom of the ocean).

From a coastal and marine engineering point of view, IG waves can resonate with harbors (posing danger to ships and structures), and can contribute to flooding events (through wave runnup). They are also one of the main factors in shaping of the beach morphology, and during extreme events IG waves can dominate sediment transport.

From an oceanographic and physical point of view, IG waves can potentially lead to breaking and calving of ice shelves, generate atmospheric gravity waves that mix the atmosphere, distort satellite altimetry measurements, and are driver of deep ocean bottom vibrations known as the Earth's hum. However, despite all of these important processes, there is a significant lack of knowledge on IG wave magnitudes and properties on a global level, especially in the deep water.

Here, a summary of the state of the art approaches in modeling and measurements is given, together with that of the current state of theoretical knowledge. The main goal of this work is to drive forward improvements to large scale stochastic modeling and measurement practices, in order to establish global IG wave forecasting capabilities. Gaps that need to be filled are identified, and possible directions of research are outlined.

Key words: water waves, oceanography, nonlinear processes

1. Review of IG wave properties, measurements, and modelling

Due to all of the above mentioned reasons, IG waves have been extensively studied (Bertin et al., 2018). Yet, the focus of most of the previous studies was limited to small-scale nearshore areas. While models for nearshore generation of waves have long existed, and considered various generation mechanisms including radiation stress, variable breakpoint, and nonlinear wave-wave interactions (e.g. Longuet-Higgins et al. 1962), large-scale (global) models that cover the deep water areas are still relatively new. The model of Ardhuin et al. 2014, currently the only global IG wave model, and considers reflection of IG waves from coastlines, which then propagate into deep water. However, it is a purely empirical model, which does not take into account many of the generation mechanisms (including in deep water, see Vrećica et al., 2019).

One of the reasons for the lack of global models is that there is not enough measurement data, especially in deep waters, to serve as a guide in derivation of theory and as boundary/initial condition for models. The other reason is that IG waves can exhibit far more complex behavior than regular water waves. Besides having a significant amount of energy following free wave dispersion relation, they can also poses significant energy in bound (forced by other waves) and edge wave (where bathymetry enters the dispersion relation) modes.

To address the outstanding issues, an international initiative was formed, with researchers from many different countries, and with a wide range of expertise. There are two main goals of this initiative. The first one is to write an extensive review paper, which while covering many different aspects of IG waves, will focus on IG wave measurements. The second goal is to submit an application to the Global Ocean Observing System (GOOS) to recognize IG wave as an essential ocean variable, which will lead to establishment of the best measurement and modeling practices for IG waves and to IG waves being taken into account by policy makers.

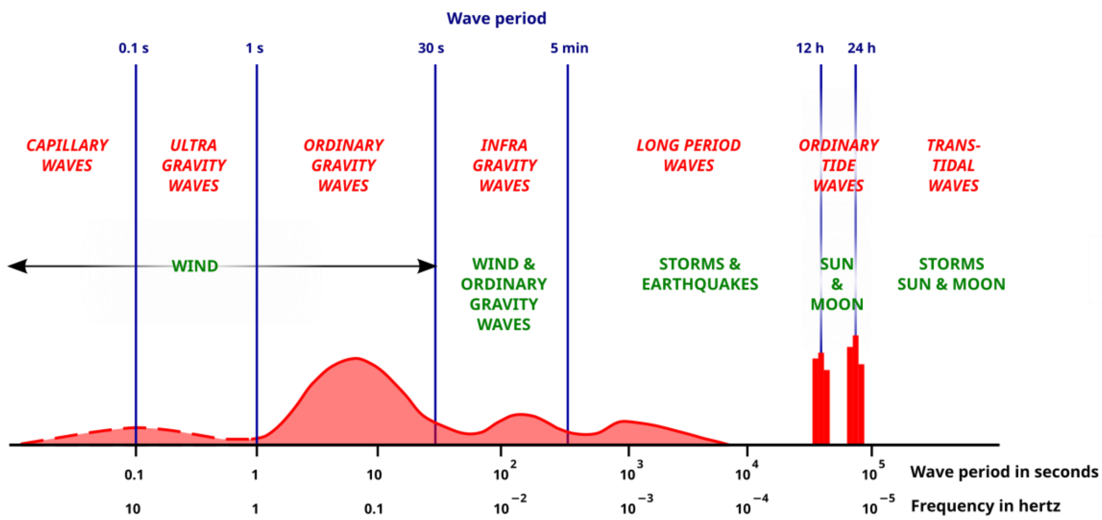

Fig. 1. Frequency spectrum of the oceans (Munk 1950). There are wave motions in oceans occurring over a wide range of frequencies. IG waves lie in between of a higher frequency band (forced by wind) and lower frequency band (forced by storms and celestial bodies). Unlike these other bands, they are primarily generated by nonlinear interactions in the nearshore regions, although many different deep water generation mechanisms also exist.

References

[1] Munk W., *Origin and generation of waves*, Proceedings 1st International Conference on Coastal Engineering, Long Beach, California. ASCE, pp. 1-4, 1950.

[2] Longuet-Higgins, et al., *Radiation stress and mass transport in gravity waves, with application to 'surf beats'*, Journal of Fluid Mechanics 13.4 (1962): 481-504.

[3] Fabrice A., et al., *A numerical model for free infragravity waves: Definition and validation at regional and global scales*, Ocean Modelling 77 (2014): 20-32.

[4] Bertin, X., et al. *Infragravity waves: From driving mechanisms to impacts*, Earth-Science Reviews 177 (2018): 774-799.

[5] Vrećica, T., et al., *Infragravity wave generation by wind gusts*, Geophysical Research Letters 46.16 (2019): 9728-9738.

10th International Congress of the Serbian Society of Mechanics
Niš, Serbia, June 18-20, 2025

B.14
Extended abstract

NUMERICAL SIMULATION OF ISOTHERMAL RAREFIED GAS FLOW BETWEEN TWO PLATES

Petar V. Vulićević[1], Snežana S. Milićev[1] [0000-0003-3055-5544], and Nevena D. Stevanović[1] [0000-0003-4385-3882]

[1]University of Belgrade, Faculty of Mechanical Engineering, Serbia, email: petar.vulicevic@protonmail.com, smilicev@mas.bg.ac.rs, nstevanovic@mas.bg.ac.rs

Abstract. The challenge of modelling flows in micro/nano flow domains arises due to violation of the continuum hypothesis. In order to determine whether the continuum hypothesis holds, a dimensionless number called the Knudsen number is introduced. It represents the ratio between the molecular mean free path length and the characteristic length $\mathrm{Kn} = \frac{\lambda}{h}$. In this study, we will analyse the gas flow in the slip ($0.001 < \mathrm{Kn} < 0.1$) and transition ($0.1 < \mathrm{Kn} < 10$) regimes. Generally, these problems can be solved both analytically and numerically; however, analytical solutions are available for a very limited number of problems with special geometries. Our aim here is to compare the analytical results obtained by treating this problem as one-dimensional (1D) [2] with the numerical results obtained by the commercial CFD code Ansys Fluent.

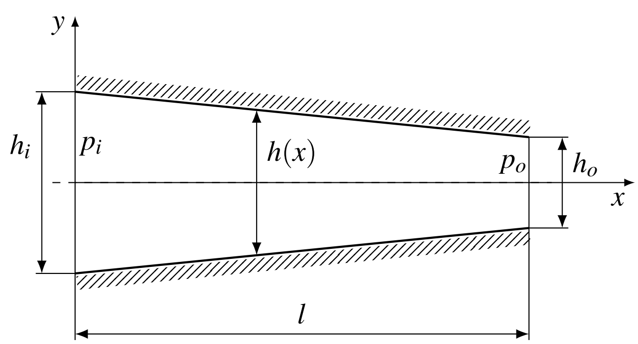

Figure 1: Flow domain

The problem analysed here is the compressible isothermal subsonic flow between two plates that form microchannels with constant, converging, or diverging cross sections (Figure 1). The variables in the inlet and outlet cross sections are denoted by the subscripts i and o, respectfully. The convergence or divergence of the plates is specified by dimensionless inlet height, defined as $\tilde{h}_i = h_i/h_o$, where $\tilde{h}_i > 1$ corresponds to convergent plates, while $\tilde{h}_i < 1$ to divergent plates. In the numerical procedure, we take the following steps. We start by specifying the ratio of the pressures at the inlet and outlet ($\Pi = p_i/p_o$), and set the outlet pressure so that the required outlet Knudsen number ($\mathrm{Kn_o}$) is achieved. Then, since the flow is isothermal, both wall temperatures, as well as the temperatures at the inlet and outlet, are set to a constant value. Additionally, a pressure-based solver is used, with the energy equation turned off, which is required to simulate an isothermal flow condition. Since we are simulating flows in the slip and transition flow regimes, we select the slip boundary conditions at the walls, which are already implemented in Fluent [3]. The momentum and energy accommodation coefficients were set to unity. The mesh with 120×600 elements was selected due to results obtained by mesh independence test.

In Figure 2 pressure and Mach number distributions are presented along the channel with parallel, convergent, and divergent plates in the slip ($\mathrm{Kn_o} = 0.1$) and transition ($\mathrm{Kn_o} = 1$) flow regimes for monatomic gas (Argon). In all results the outlet cross section height h_o and the microchannel length l are the same for all geometries, where the length l is specified by the small parameter $\varepsilon = h_o/l$. The pressure distributions for both flow regimes (Figures 2(a),2(c)) have almost perfect correspondence with 1D solutions [2]. However, there are slight discrepancies in the Mach number distributions between the numerical and 1D analytical results (Figures 2(b),2(d)), which can be attributed to the presence of a crosswise velocity component in numerical simulation. Nevertheless, despite the simplifications in the 1D theoretical analysis, it still provides accurate predictions.

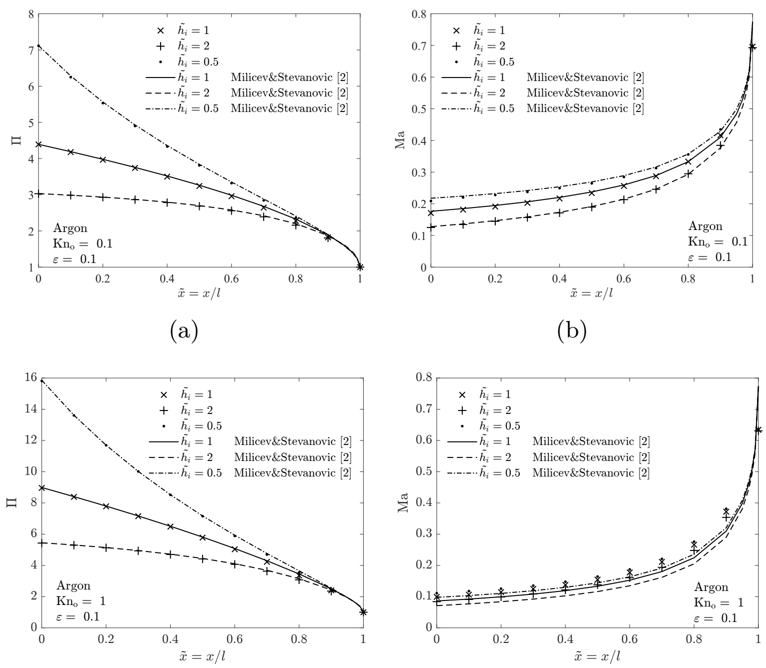

(a) (b)

(c) (d)

Figure 2: Pressure and Mach number distributions in slip and transition flow regimes for parallel, convergent, and divergent plates

Keywords: rarefied flow, compressible, isothermal, subsonic, numerical simulation

References

[1] Gad-El-Hak M., The MEMS Handbook, CRC Press, Boca Raton, Florida, 2002.

[2] Milićev S. S., & Stevanović N. D., Gas Flow in Microchannels and Nanochannels With Variable Cross Section for All Knudsen and All Mach Number Values, ASME. J. Fluids Eng., Vol. 143, February 2021.

[3] Ansys Fluent Theory Guide, Ansys, Inc., Canonsburg, January 2025.

C: Solid Mechanics

10th International Congress of the Serbian Society of Mechanics
Niš, Serbia, June 18-20, 2025
C.1
Original Scientific Paper

DOI: 10.46793/ICSSM25.118D

PHASE-FIELD MODELING OF CONCRETE: NUMERICAL SIMULATION AND EXPERIMENTAL VERIFICATION

Vladimir Lj. Dunić[1][0000-0003-1648-1745]**, Miroslav M. Živković**[1][0000-0002-0752-6289]**,**
Dragan M. Rakić[1][0000-0001-5152-5788]**, Vladimir P. Milovanović**[1][0000-0003-3071-4728]

[1] University of Kragujevac
Faculty of Engineering, Sestre Janjić 6, 34000 Kragujevac, Serbia
e-mail: dunic@kg.ac.rs, miroslav.zivkovic@kg.ac.rs, drakic@kg.ac.rs, vladicka@kg.ac.rs

Abstract:

Simulation of concrete structures behavior is very popular in engineering design, as the concrete is the most used the material in the world. The possibilities are related to the development of Finite Element Method (FEM) based software and the possibility to implement advanced constitutive models or computational mechanics methods which can provide satisfying results. The most popular concrete constitutive model available in many FEM software is Concrete Damage Plasticity (CDP) model which takes into account both tension and compression response, as well as damage field which can be considered as the level of stiffness decrease in the material. Another approach is a Phase-Field Damage Model (PFDM) which found application in recent years in modeling response of various materials exposed to extreme loading conditions. In this paper, the Drucker-Prager constitutive model is enhanced to compute a strain energy which produces damage in material under the certain conditions. The damage is considered as the additional degree of freedom in 3D solid element, where the threshold value of a critical total strain energy is declared as the limit quantity. The functionality of the proposed approach is considered by comparison of experimental and simulation results for uniaxial compression test.

Keywords: phase-field damage model, Drucker-Prager, concrete, uniaxial compression experiment

1. Introduction

Concrete structures are highly favored in civil engineering structural design due to the respectable strength and reliability. A modeling of the concrete structures behavior can offer the essential information necessary in a design procedure. The available EC standards as well as national standards offer the relations and limits based on concrete characteristics and mechanics laws, but complex structures often need specific loading and boundary conditions which are not covered by the standards. As a complementary solution, various software tools, usually based on Finite Element Method, are developed by researchers and engineers which can solve such problems. The specific behavior of concrete structures can be taken into account by implementing the appropriate constitutive model such as Concrete Damage Plasticity (CDP) model [1, 2]. This model includes both, tension and compression response, as well as a damage computation as local internal variable related to the plastic strain field. However, this model has some disadvantages such as mesh and step size sensitivity, large number of material parameters, and problems with local damage jump which can cause losing of convergence stability.

One alternative which can be considered is a Phase-Field Damage Model (PFDM) [3, 4], which is cutting-edge technique implemented in various FEM software, but it is still under the investigation and the improvements are constant in recent years. The most popular application of PFDM is for brittle and ductile modeling of fracture in metals [5-7], especially steel and aluminum, but also it is used for modeling of high and low cyclic fatigue in other materials such as Shape Memory Alloys [8]. Also, it is successfully used for application to the concrete structures by implementation into the Drucker-Prager (DP) constitutive model [9].

In this paper, the theory and implementation of PFDM into the Drucker-Prager model is given as it is done in the PAK-DAM software. The standard degradation function for brittle fracture is used, along with linear hardening of yield function in DP model. The standard cube specimens are experimentally investigated and the obtained force-displacement response is compared to the simulation results for the uniaxial compression test and the identified material parameters.

2. Phase-field damage model for Drucker-Prager model

2.1 Phase-field damage model based on critical total strain

In concrete, after the initial yield stress is achieved, a plastic strain can be observed as well as decrease of strength which is described by damage variable. The stress-strain response change the trend and nonlinear relationship can be observed. The PFDM considers the damage as additional degree of freedom, where the damage variable range is defined as $d \in [0,1]$. If $d = 0$, the material can be considered as intact, while opposite limit when $d = 1$ means totally destroyed material without any stiffness. This theory is based on a Griffith's theory [10]. Francfort and Marigo [11] proposed a regularized approach which minimize energy functional based on equilibrium of the surface and the bulk strain energy. For this purpose, a regularized crack functional valid for multi-dimensional problems is [12]:

$$G_l(d) = \int_V \gamma_l(d, \nabla d)\, dV \quad . \tag{1}$$

The crack surface density function per unit volume is defined as:

$$\gamma_l = \frac{1}{2l_c}\left(d^2 + l_c^2 |\nabla d|^2\right) , \tag{2}$$

where l_c is the characteristic length and ∇ is the gradient operator. A total strain energy consists of the elastic-plastic part and a fracture contribution [12, 13]:

$$\psi_{\text{int}} = \psi_{\text{ep}} + \psi_{\text{f}} \quad . \tag{3}$$

The elastic-plastic strain energy is defined in relationship to the constitutive relations of the material, while the fracture part comes from the phase-field. The elastic-plastic strain is:

$$\psi_{\text{ep}} = g(d)\left(\frac{1}{2}\boldsymbol{\sigma} : \boldsymbol{\varepsilon}_e + \sigma_0 \bar{\varepsilon}_p + \frac{1}{2} H \bar{\varepsilon}_p^2\right) , \tag{4}$$

where $g(d)=1-d^2$ is the degradation function, $\boldsymbol{\sigma}$ is the stress tensor, $\boldsymbol{\varepsilon}_e$ is the elastic strain tensor, σ_0 is the initial yield stress, $\bar{\varepsilon}_p$ is the equivalent plastic strain, and H is the linear hardening parameter. In the concrete structures, the damage does not occur immediately after the loading starts, so a threshold should be determined. This is straightforward from the work-density criterion defined by Miehe et al. [13], if the fracture surface energy density is:

$$\psi_f = G_v\left[d+\frac{l_c^2}{2}|\nabla d|^2\right]. \tag{5}$$

In the previous equation, a specific fracture energy per unit volume is defined as $G_v = G_c / l_c$ [6]. After the appropriate derivation of previous equations, the final term for the fracture strain energy density is:

$$\psi_f = \frac{G_v}{2}\left(1-g(d)\right)+G_v l_c \gamma_l . \tag{6}$$

Finally, the total internal potential energy can be calculated as:

$$P=\int_V \psi_{\text{int}} dV = \int_V \left(\psi_{\text{ep}}+\psi_{\text{f}}\right) dV . \tag{7}$$

Equilibrium of variation of the total internal potential energy δP and the external potential energy:

$$W_{\text{ext}} = \int_V \mathbf{b}\cdot\delta\mathbf{u} dV + \int_A \mathbf{h}\cdot\delta\mathbf{u} dA , \tag{8}$$

where $\mathbf{b}$ is a body force per unit volume V, $\mathbf{h}$ is a boundary traction per unit area A, and $\mathbf{u}$ is a displacement vector. Applying the appropriate math transformation, the equilibrium equation and the phase-field damage evolution law are [3, 6, 14]:

$$\begin{aligned} &Div[\boldsymbol{\sigma}]+\mathbf{b}=0 \\ &G_v\left[d-l_c^2\nabla^2 d\right]+g'(d)\psi_{\max}=0 , \end{aligned} \tag{9}$$

where $\psi_{\max} = \psi_{\text{ep}}/g(d) - G_v/2$.

2.2 Drucker-Prager constitutive model

The concrete behavior can be described by Drucker-Prager constitutive model with non-associative yield criterion. It can take into account both tensile and compression loading conditions. The yield condition is defined as [9]:

$$f=\alpha_p I_1+\sqrt{J_{2D}}-k_p \tag{10}$$

where the hardening is described by linear rule: $k_p=\sigma_0+H\bar{\varepsilon}_p$, α_p is the material parameter, I_1 is the first invariant and J_{2D} is the second invariant of deviatoric stress. The plastic potential is described by function:

$$g = \alpha_n I_1 + \sqrt{J_{2D}} - k_p \quad . \tag{11}$$

where α_n is the additional material parameter. The plastic strain increment is then:

$$\Delta \boldsymbol{\varepsilon}_p = \lambda_p \mathbf{n}_{DP} = \lambda_p \frac{\partial g}{\partial \boldsymbol{\sigma}} \quad , \tag{12}$$

where λ_p is the plastic multiplier and the equivalent plastic strain increment is:

$$\Delta \bar{\varepsilon}_p = -\lambda_p \frac{\partial g}{\partial k_p} = \lambda_p \quad . \tag{13}$$

3. Comparison of experimental and numerical uniaxial compression test

The experimental investigation of concrete specimens is realized by compression testing machine – MATEST ServoPlus Research + ServoStrain 2000kN. The standard [15] 150 mm cube specimens are tested. The loading is controlled by the displacement rate of 1mm/min. The maximum recorded compression strength is 49.975 MPa. The stress-strain response is recorded by the piston stroke and the force measured by the compression testing machine. The compression testing machine and the specimen are shown in Fig. 1.

Fig. 1. Experimental investigation of concrete specimen in compression testing machine

The simulation of the uniaxial compression test is modelled by one element example. One 3D element of size 150 x 150 x 150 mm, is constrained at one side, while the opposite side is loaded by prescribed displacements. The material parameters are fitted to achieve the stress-strain response of the experimental investigation. Only material parameters for the compression loading conditions are given in Table 1.

Yield stress σ_0[MPa]	Young modulus E [MPa]	Poisson's ratio [-]	Mat. parameter $\alpha_{p,n}$
49.975	9258	0.192	0.0

Table 1. Material parameters necessary for the simulation in PAK-DAM

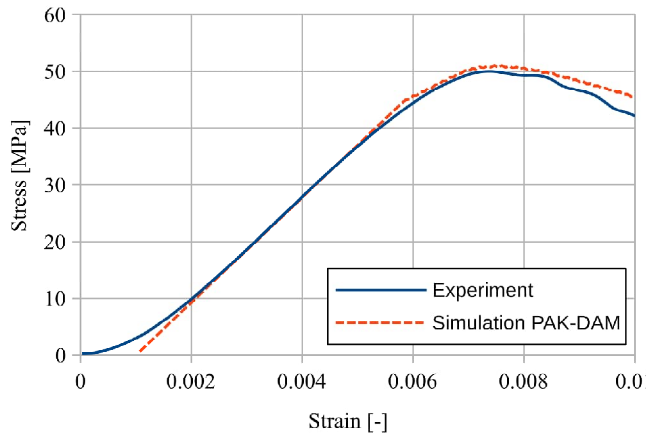

Fig. 2. Stress-strain response for the uniaxial compression test of standard cube specimen: experiment vs. simulation results

As it can be noticed from Fig. 2, the experimental stress-strain curve exhibits a non-linear behavior due to the several reasons, but the most important is the measurement of the strain by the piston displacement recorded by the compression machine. Such measurement of the strain includes the deformation of the entire testing machine, the elastic deflection of the compression plates, and the specimen slipping between the compression plates. Other reasons could be heterogeneous strain distribution in the specimen and effect of friction between the compression plates and the specimen. Also, this can cause reduced value of the Young modulus in comparison to the expected values. However, this paper does not tend to precisely capture the characteristics of the specific specimen, but the idea is to show the possibility to reproduce the behavior by the proposed simulation technique.

In this scope, the comparison of the experimental and the simulation results is given in Fig. 2. It can be observed that the experimental and the simulation curve are parallel in the elastic stage of loading, and when the plastic strain occurs, the linear hardening explained in Drucker-Prager constitutive model captured the response. The maximal strength of the specimen is achieved at the same strain level. After that point, the damage of the material occurs and the stress decreases according to the chosen degradation function.

4. Conclusions

The simulation of the concrete structures behavior is one of the most popular topics among the FEM software developers but also engineers and researchers. Specially, prediction of damage evolution in civil engineering concrete structures is essential for safety what increase the interest in this field at the highest level. Beside the classical concrete constitutive models which considers the damage as internal variable, the PFDM offers the possibility to predict the damage evolution as additional degree of freedom in various materials. The Drucker-Prager constitutive model can be modified and enhanced by PFDM to capture the response of the concrete structures in both tension and compression state of stress. For this purpose, DP model is implemented into the PAK-DAM software and the simulation response for the uniaxial compression loading is compared to the experimental investigation of standard specimen. The recorded results show very good functionality of the proposed implementation what is very promising for the further application in real engineering problems.

Acknowledgment

This research was supported by the Science Fund of the Republic of Serbia, #GRANT No 7475, Prediction of damage evolution in engineering structures - PROMINENT and by the Ministry of Science, Technological Development and Innovation, Republic of Serbia, Agreement No. 451-03-137/2025-03/200107.

References

[1] Lubliner J, Oliver J, Oller S, & Onate E (1989). *A plastic-damage model for concrete*. Int. Journal of Solids and Structures, Vol. 25, 299–326, 1989.
[2] Lee J, *Theory and implementation of plastic-damage model for concrete structures under cyclic and dynamic loading*. Berkeley, California: Department of Civil and Environmental Engineering, University of California, 1996.
[3] Miehe C., Hofacker M., Welschinger F., *A phase field model for rate-independent crack propagation: Robust algorithmic*. Comput. Methods Appl. Mech. Eng, 199, 2765–2778, 2010
[4] Alessi R., Marigo J., Maurini C., Vidoli, S. *Coupling damage and plasticity for a phase-field regularisation of brittle, cohesive and ductile fracture: One-dimensional examples*. Int. J. Mech. Sci., Vol. 149, 559–576, 2018
[5] Živković J., Dunić V., Milovanović V., Pavlović A., Živković M., *A Modified Phase-Field Damage Model for Metal Plasticity at Finite Strains: Numerical Development and Experimental Validation*, Metals, Vol. 11(1), 47, 2021
[6] Dunić V., Živković J., Milovanović V., Pavlović A., Radovanović A., Živković M., *Two-Intervals Hardening Function in a Phase-Field Damage Model for the Simulation of Aluminum Alloy Ductile Behavior*. Metals, Vol. 11(11), 1685, 2021
[7] Dunić V., Gubeljak N., Živković M., Milovanović V., Jagarinec D., Djordjevic N., *Experimental Characterization and Phase-Field Damage Modeling of Ductile Fracture in AISI 316L*, Metals, Vol. 14(7), 787, 2024
[8] Dunić V, Matsui R, Takeda K, Živković M. *Phase-field damage simulation of subloop loading in TiNi SMA*, International Journal of Damage Mechanics, 33(8), 577-604, 2024
[9] Schröder J., Pise M., Brands M., Gebuhr G. Anders S., *Phase-field modeling of fracture in high performance concrete during low-cycle fatigue: Numerical calibration and experimental validation*, Comput. Methods Appl. Mech. Eng., 398, 115181, 2022.
[10] Griffith A.A., *VI. The phenomena of rupture and flow in solids*. Philos. T. R. Soc A. 221, pp. 163–198, 1921.
[11] Francfort G., Marigo J.-J., *Revisiting brittle fracture as an energy minimization problem*, J. Mech. Phys. Solids. 46, 1319–1342, 1998
[12] Miehe C., Welschinger F., Hofacker M., *Thermodynamically consistent phase-field models of fracture: Variational principles and multi-field FE implementations*, Int. J. Numer. Methods Eng. 83, 1273–1311, 2010
[13] Miehe C., Hofacker M., Schanzel L.-M., Aldakheel F., *Phase field modeling of fracture in multi-physics problems. Part II.*, Comput. Methods Appl. Mech. Eng. 294, 486–522, 2015
[14] Kojić M., Bathe K.J. *Inelastic Analysis of Solids and Structures*, Springer: Berlin/Heidelberg, Germany, 2005
[15] Eurocode 2: Design of concrete structures, Part 1-1: General rules and rules for buildings. CEN, Brussels, EN 1992-1-1:2004.

10th International Congress of the Serbian Society of Mechanics
Niš, Serbia, June 18-20, 2025
C.2
Original Scientific Paper

DOI:10.46793/ICSSM25.124J

PREDICTION OF FREE-EDGE STRESSES IN COMPOSITE LAMINATES USING FULL-LAYERWISE-THEORY-BASED FINITE ELEMENTS

Emilija V. Jočić[1[0000-0001-9099-8983]], **Milica Z. Živković**[1[0009-0001-0629-544X]], **Miroslav S. Marjanović**[1[0000-0001-9790-912X]]

[1] Chair of Engineering Mechanics and Theory of Structures
University of Belgrade – Faculty of Civil Engineering,
Bulevar kralja Aleksandra 73, 11000 Belgrade, Serbia
e-mail: edamjanovic@grf.bg.ac.rs, mizivkovic@grf.bg.ac.rs, mmarjanovic@grf.bg.ac.rs.

Abstract:

This paper deals with the 3D analysis of free-edge stresses in laminated composite plates using Reddy's full-layerwise-theory-based finite element model (FLWT-FEM). The theory assumes a piece-wise linear variation of all displacement components and quadratic variation of interlaminar stresses within each layer. The free-edge effects are related to singular stress states at the interfaces between dissimilar layers along the free edges of the laminar composite. Stress concentrations at free edges can further lead to delamination and the significant drop in stiffness, with failure occurring at lower loads than expected.

Starting from the strong formulation of the FLWT, a family of layered finite elements has been derived and implemented in original object-oriented MATLAB code. Free-edge stress field under axial strain has been analyzed. A validation example of cross-ply composite has been presented, and the results are compared against the existing analytical solutions and those obtained using the commercial software. The accuracy of the model is verified, and the possibilities for the further improvement and applications are provided.

Key words: free-edge stresses, full layerwise theory, laminate, composite, plate.

1. Introduction

Because of their exceptional strength, stiffness and corrosion resistance, laminar composites have found an extensive application in construction of mechanical, aerospace, marine and automotive structures, typically demanding high reliability levels. When subjected to tension, they may fail through various scenarios, such as fiber breakage and pull out, matrix yielding and cracking, among others. Their ultimate strength and failure mechanisms depend on geometrical factors and material properties; therefore, a detailed study of their failure behavior is a crucial step towards the safe and reliable design of multilayer composite structures [1].

Several unique phenomena arising from the heterogeneous constitution of laminar composites motivated the researchers to derive complex computational models. For example, in localized regions where damage initiation is likely, refined plate theories are recommended, since the assessment of localized regions for potential damage initiation begins with the accurate determination of the 3D stress state at the ply level. The extensive review of refined laminate theories can be found in [2, 3], among others.

The displacement-based partial layerwise theories neglect the transverse normal stress σ_z (since the deflection is constant through the plate thickness). However, the incorporation of σ_z is important in modeling the localized effects, thus a full-layerwise theory should be considered [4]. In contrast to the equivalent-single-layer theories (ESL), the layerwise theories allow for the possibility of continuous transverse stresses at layer interfaces.

Different Poisson's ratios, elastic and shear moduli and thermal expansion coefficients cause different deformation of the adjacent layers in laminar composite. Since the layers cannot move independently, normal and shear stress concentrations occur to satisfy the conditions of displacement compatibility. These concentrations are pronounced at the free edges of a laminar composite, which can further lead to delamination, and consequently reduce the stiffness [5, 6]. This may cause a failure at loads significantly below the expected limit level.

In thin plates, the stress concentrations are more pronounced than in thick plates, since in thick plates there exists a certain interaction of internal fibers with edge ones, with a spreading of stresses over a larger surface area. The stress concentrations decrease with distance from the free edges of the plate, gradually diminishing to negligible values. Their magnitude is also a function of layer orientation, layer thickness, boundary conditions, and loading type, as well. Under axial strain, the stress concentrations at the free edges are generally lower when compared to laminar composites in bending or torsion [7, 8].

Various numerical and approximate analytical solutions have been derived so far to accurately identify and evaluate interlaminar stresses associated with the free-edge effect. A comprehensive review of different approaches for free-edge stress analysis can be found in [9, 10]. The earliest work on this topic was by Pipes and Pagano [11]. They formulated the problem of free edge effects in a symmetrically balanced laminar composite under uniform axial stress as a quasi-3D problem, and used the finite difference method to solve the equilibrium equations. A number of numerical solutions has been derived, as well, such as FEM-based solution proposed by Li et al. [12], that takes into account the 3D stress state at the free edges.

Exact analytical solutions for free-edge stress singularities are typically limited to simplified layups and loadings, becoming nontrivial for complex geometries and boundary conditions [13, 14]. Becker [15] proposed closed-form solutions using higher-order plate theory for free-edge stresses in cross-ply laminates. However, since ESL theories fail to accurately predict the out-of-plane stresses near free edges, Nosier and Bahrami [16] and Nosier and Maleki [17] applied improved first-order shear deformation theory (FSDT) and layerwise theory (LWT) to study free-edge effects in angle-ply and general laminates, incorporating reduced constitutive relations and traction-free boundary conditions. Tahani and Nosier [7] also used Reddy's full LWT to analyze stresses in symmetric and asymmetric laminates under uniform axial strain. FLWT was found to provide improved solutions for interlaminar stresses and stress singularities [18-21].

In the paper, the FLWT-based finite element model [4, 18] is used for the free-edge stress field assessment of the laminar composite under axial strain. The computational model is implemented within the MATLAB environment [22], while the GUI is developed using GiD [23, 24]. The results are compared against the existing analytical solutions and those obtained using the commercial software Abaqus CAE [25]. The accuracy of the model is verified, and the possibilities for the further improvement and applications are provided.

2. Formulation of the full-layerwise theory

In the paper, we consider laminated composite plate made of n orthotropic layers. The plate thickness is denoted as h (see Figure 1), while the thickness of the k^{th} lamina is denoted as h_k. The plate is supported along the portion Γ_u of the boundary Γ and loaded with loadings $q_t(x,y)$ and

$q_b(x,y)$ acting to either top or the bottom surface of the plate (S_t or S_b).

Piece-wise linear variation of all three displacement components is imposed, leading to the 3-D stress description of all material layers. The displacement field (u, v, w) of an arbitrary point (x,y,z) of the laminate is given as:

$$u=\sum_{I=1}^{N}U^{I}(x,y)\Phi^{I}(z),\quad v=\sum_{I=1}^{N}V^{I}(x,y)\Phi^{I}(z),\quad w=\sum_{I=1}^{N}W^{I}(x,y)\Phi^{I}(z)\quad , \tag{1}$$

where $U^{I}(x,y)$, $V^{I}(x,y)$ and $W^{I}(x,y)$ are the displacement components in the I^{th} numerical layer of the laminate in directions x, y and z, respectively, N is the number of interfaces between the layers including S_t and S_b, while $\Phi^{I}(z)$ are selected to be linear layerwise continuous functions of the z-coordinate (see [4], [26] for details).

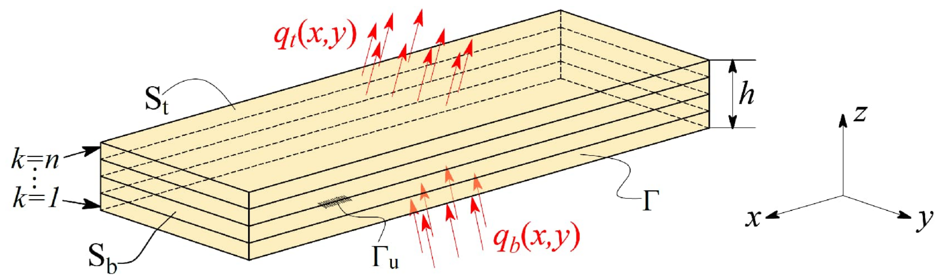

Fig. 1. Laminated composite plate with n material layers

The linear strain field associated with the previously shown displacement field can be derived in a straightforward manner [4]. It serves as the basis for the derivation of 3N governing differential equations which define the strong form of the FLWT. To reduce the 3D model to a 2D one, the z-coordinate is eliminated by the explicit integration of stress components multiplied with the corresponding functions $\Phi^{I}(z)$, introducing the appropriate stress resultants (see [4]).

The stresses in the k^{th} layer may be computed from the lamina 3-D constitutive equations:

$$\{\sigma_x \quad \sigma_y \quad \sigma_z \quad \tau_{yz} \quad \tau_{xz} \quad \tau_{xy}\}^{(k)T}=\left[\bar{C}_{ij}\right]^{(k)}\{\varepsilon_x \quad \varepsilon_y \quad \varepsilon_z \quad \gamma_{yz} \quad \gamma_{xz} \quad \gamma_{xy}\}^{(k)T} \tag{2}$$

where $\bar{C}_{ij\,(k)}$ are the transformed elastic coefficients in the (x,y,z) coordinates in the k^{th} layer, which are related to the elastic coefficients matrix in the material (1,2,3) coordinates $\mathbf{C}^{(k)}$ through the transformation matrix $\mathbf{T}^{(k)}$. All mentioned matrices can be found in [4]. The constitutive relations of the laminate can be derived in a usual manner by integrating the lamina constitutive equations through the thickness of the plate. The system of 3N Euler-Lagrange governing equations of motion for the FLWT are derived using the principle of virtual displacements, by satisfying the equilibrium of the virtual strain energy δU and the work done by the applied forces δV [24]. The primary variables of the problem are displacement components U^{I}, V^{I} and W^{I}.

3. Applied finite element models

3.1. Full-layerwise-theory-based model

Based on the FLWT formulation, the weak form is derived by substituting an assumed interpolation of the displacement field (1) into the equations of motion of the FLWT. The layered finite elements require only C^0 continuity of generalized displacements along element boundaries, because only translational displacement components are adopted as the nodal degrees of freedom. The formulation of the family of the 2D layered (plate) finite elements allows for the 2D type data structure similar to the FE models of the ESL theories, which provide a number of advantages against the conventional 3D models [26].

All displacement components are interpolated using the same level of interpolation:

$$U^I(x,y)=\sum_{j=1}^{m}U_j^I\psi_j(x,y),\qquad V^I(x,y)=\sum_{j=1}^{m}V_j^I\psi_j(x,y),\qquad W^I(x,y)=\sum_{j=1}^{m}W_j^I\psi_j(x,y) \tag{3}$$

where m is the number of nodes per 2D element, U_j^I, V_j^I, W_j^I are the nodal values of displacements U^I, V^I and W^I, respectively, in the j^{th} node of the 2-D element (representing the behaviour of the laminated composite plate in the I^{th} numerical interface), while $\psi_j(x,y)$ are the 2D Lagrangian interpolation polynomials associated with the j^{th} element node. The strain field is interpolated in the usual manner, by incorporating (3) in the kinematic relations of the FLWT.

In the paper, quadratic serendipity layered quadrilateral elements with reduced integration (FLWT Q8R), have been used (Figure 2a). After the derivation of the characteristic element matrices, the assembly procedure is done in a usual manner.

The assumed piecewise linear interpolation of displacement field through the laminate thickness provides discontinuous stresses across the interface between adjacent layers. Once the nodal displacements are obtained, the stresses can be computed from the constitutive relations. Since the interlaminar stresses calculated in this way does not satisfy continuous distribution through the laminate thickness, they are re-computed by assuming the quadratic distribution within each layer for every stress component, separately:

$$\left\{\tau_{xz}^k \quad \tau_{yz}^k \quad \sigma_z^k\right\}=a_s^k\bar{z}^2+b_s^k\bar{z}+c_s^k,\qquad 0\le\bar{z}\le h_k,\qquad k=1,2,...,N,\qquad s=xz,\ yz \text{ or } z. \tag{4}$$

The entire procedure is presented in detail in [27].

3.2. 3D models in Abaqus CAE

For model validation, two finite element types in Abaqus CAE have been used. The C3D8R element is a general-purpose linear brick element (8-noded), with reduced integration (1 integration point, in the middle of the element). This is a rotation-free element with three generalized displacements (translations) in every node (Figure 2b). In addition, the C3D10 element (Figure 2c) is a general-purpose quadratic tetrahedral rotation-free element (4 integration points). Three generalized displacements (translations) are defined in every node [28].

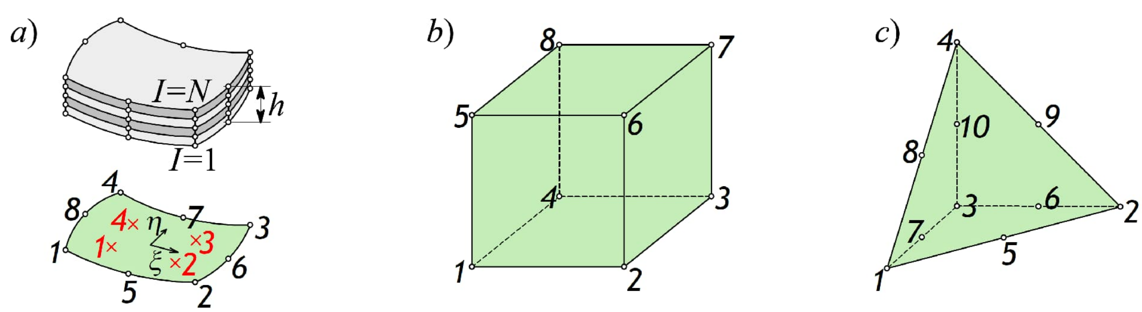

Fig. 2. (a) Serendipity FLWT-based Q8R layered finite element with marked reduced integration points; (b) C3D8R solid element in Abaqus CAE [28] (c) C3D10 finite element in Abaqus CAE [28]

4. Model validation

For model validation, two 4-layers rectangular laminated composite plates, with dimensions $a\times2b$, have been analyzed. Plate length is $a = 10h$, width is $b = 2h$, while layer thickness is $h_k = h/4$, where h is the total plate thickness. Each layer is a unidirectional reinforced composite made of material with the following properties in material coordinates: E_1 = 137.9 GPa, $E_2 = E_3$ = 14.48 GPa, $G_{12} = G_{13} = G_{23}$ = 5.86 GPa, while $\nu_{12} = \nu_{13} = \nu_{23}$ = 0.21.

Two cross-ply stacking sequences have been considered: $[0^o/90^o]_s$ and $[90^o/0^o]_s$.

All plate edges are free. The axial strain (tension) has been applied by applying the uniform displacement $\bar{U}$ in the x-direction along the plate edges: $u(a) = \bar{U}$ and $u(0) = -\bar{U}$ (see Figure 3).

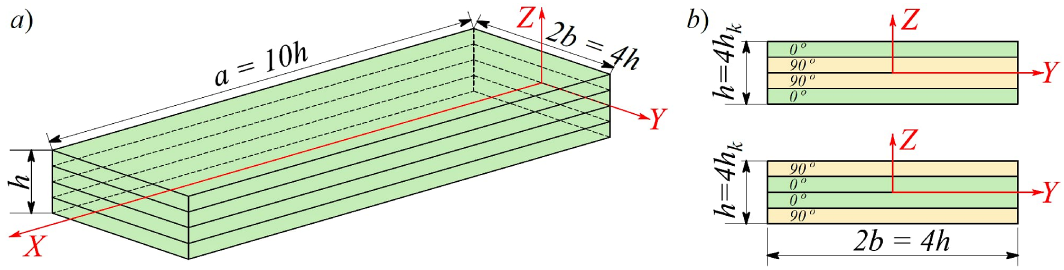

Fig. 3. Considered laminated composite plate (a) with two different stacking sequences (b)

For the through-the-thickness interpolation, three sub-laminate discretizations have been considered, including P=1, P=2 or P=4 sublayers through each material layer, respectively. This leads to the total of 4, 8 or 16 sublayers through the entire plate thickness. For the in-plane discretization, two mesh densities have been considered, including element sizes of $h/4$ (Mesh 1) and $h/8$ (Mesh 2). Due to the symmetry, only 1/8 of the plate has been modelled ($a/2\times b/2\times h/2$).

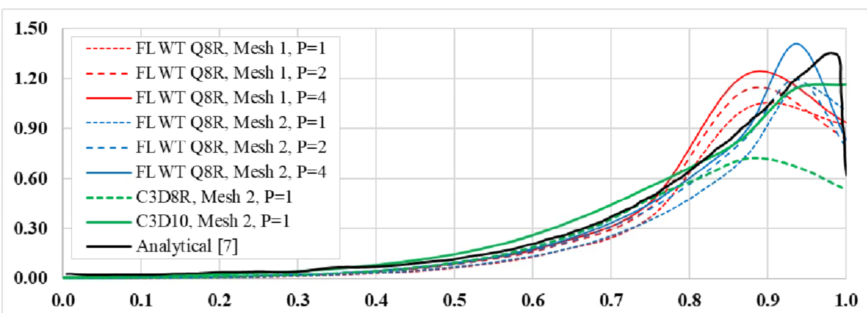

Fig. 4. Dimensionless interlaminar shear stress $(\tau_{yz} / \varepsilon_0)\times10^{-6}$ [kPa] distribution along the $0^o/90^o$ interface ($z = h_k$) of the $[0^o/90^o]$s laminate under uniform axial strain, considering different mesh densities, z-refinements and different computational models

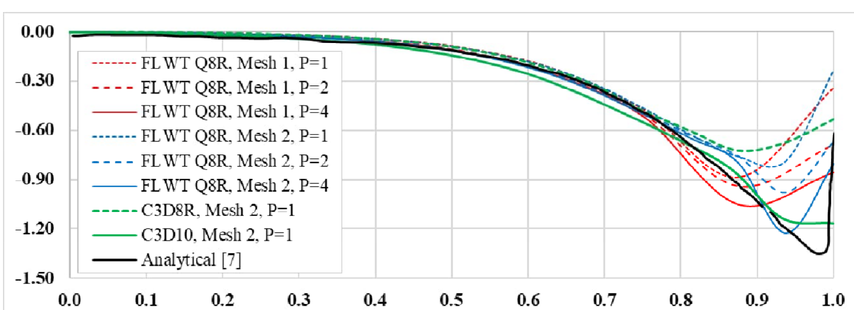

Fig. 5. Dimensionless interlaminar shear stress $(\tau_{yz} / \varepsilon_0)\times10^{-6}$ [kPa] distribution along the $90^o/0^o$ interface ($z = h_k$) of the $[90^o/0^o]$s laminate under uniform axial strain, considering different mesh densities, z-refinements and different computational models

The obtained results are compared against those obtained using the C3D8R and C3D10 finite elements in Abaqus CAE (Mesh 2, P=1), as well as against the analytical solution of the LWT, for the interlaminar stresses near the free edges [7].

Figure 4 shows the through-the-width distribution of the interlaminar shear stress τ_{yz} along the 0º/90º interface (z=h_k) of the [0º/90º]s laminate under uniform axial strain. FLWT-based finite elements are capable to accurately predict the τ_{yz} distribution, characterized with the increase of τ_{yz} towards the free edge and sudden drop at the free edge (Y = b). Both the in-plane and z-refinements resulted in the convergence of results to the analytical solution (black line). Finer in-plane mesh (blue lines) better predicts both the position and the value of the maximum interlaminar shear stress τ_{yz} when compared with the coarse mesh (red lines). Increasing the number of sublayers per lamina may improve the results, but τ_{yz} will never reach zero at the free edge, contrary to theoretical expectations, as indicated in [7].

When considering the solid-like finite element models in Abaqus CAE, C3D10 elements showed better accuracy against the C3D8R in predicting both the position and the value of the maximum interlaminar shear stress τ_{yz} (green lines).

Similar conclusions are derived for the interlaminar shear stress τ_{yz} distribution along the 90º/0º interface of the [90º/0º]s laminate under uniform axial strain, illustrated in Figure 5.

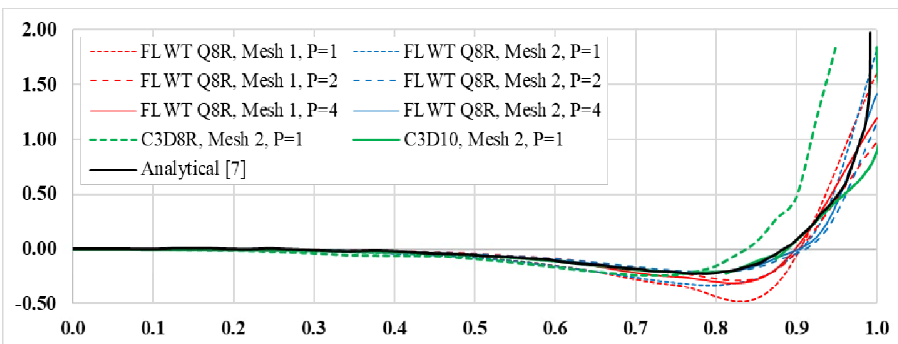

Fig. 6. Dimensionless interlaminar normal stress $(\sigma_z / \varepsilon_0)\times 10^{-6}$ [kPa] distribution along the 0º/90º interface (z = h_k) of the [0º/90º]s laminate under uniform axial strain, considering different mesh densities, z-refinements and different computational models

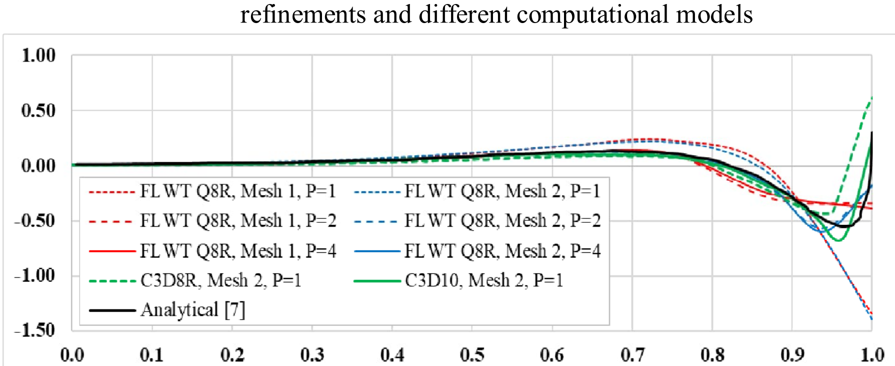

Fig. 7. Dimensionless interlaminar normal stress $(\sigma_z / \varepsilon_0)\times 10^{-6}$ [kPa] distribution along the 90º/0º interface (z = h_k) of the [90º/0º]s laminate under uniform axial strain, considering different mesh densities, z-refinements and different computational models

Figures 6 and 7 show the through-the-width distribution of the interlaminar normal stress σ_z along the z=h_k interfaces of the [0º/90º]s and [90º/0º]s laminates under uniform axial strain, respectively. Two different mesh densities of FLWT-based Q8R finite elements have been considered in combination with 3 different z-refinements. The numerical solutions showed good agreement against the analytical solution, except for the [90º/0º]s laminate, when only 1 sublayer is used for the z-refinement (see Figure 7).

Interlaminar normal stress σ_z reaches the maximum value along the free edge. For the [0º/90º]s laminate, mesh refinement leads to the increase of the σ_z along the free edge.

When considering the solid-like finite element models in Abaqus CAE, C3D10 elements showed better accuracy against the C3D8R in predicting both the position and the value of the maximum interlaminar normal stress σ_z.

5. Conclusions

Reddy's full-layerwise-theory-based finite element model (FLWT-FEM), previously implemented within the original object-oriented MATLAB code in conjunction with GiD, has been applied for the prediction of the 3D stress field in laminated composite plate. The focus of the analysis was related to the free-edge effects, i.e. interlaminar shear and normal stress distribution through the laminate width, under uniaxial extension.

A considered validation example of a cross-ply composite plate showed that the FLWT-based finite elements are capable to accurately predict both the τ_{yz} and σ_z distributions, when compared against the analytical solution of the FLWT. Both the in-plane and z- refinements resulted in the convergence of results to the analytical solution. However, similar to all FEM-based models, the FLWT-FEM has the limitations associated with deriving the zero-shear stress at the free edge.

When considering the solid finite elements in Abaqus CAE, C3D10 elements showed better accuracy against the C3D8R in predicting both the position and the value of the max interlaminar shear stress τ_{yz} and max interlaminar normal stress σ_z.

The scope for further analysis of free-edge effects is large, including the cases where the analytical solution does not exist: derivation of 3D stress fields under bending or torsional loads; considering more complex (i.e. arbitrary) plate geometries, among others.

Acknowledgments

The financial support of the Ministry of Education, Science and Technological Development of the Republic of Serbia, through the project 200092 is acknowledged.

References

[1] Jočić, E., Marjanović, M., *Progressive failure analysis of open-hole composite laminates using FLWT-SCB prediction model*, International Journal of Mechanical Sciences, Vol. 227, 107407, 2022.

[2] Carrera, E., *Theories and finite elements for multilayered, anisotropic, composite plates and shells*, Archives of Computational Methods in Engineering, Vol. 9, No. 2, 87-140, 2002.

[3] Liew, K. M., Pan, Z. Z., Zhang, L. W., *An overview of layerwise theories for composite laminates and structures: Development, numerical implementation and application*, Composite Structures, Vol. 216, 240-259, 2019.

[4] Reddy, J. N., *Mechanics of laminated composite plates and shells: theory and analysis*, CRC Press, Boca Raton, Florida, 2004.

[5] Mittelstedt, C., Becker, W., *Reddy's layerwise laminate plate theory for the computation of elastic fields in the vicinity of straight free laminate edges*, Materials Science and Engineering: A, Vol. 498(1-2), 76-80, 2008.

[6] Phillips, E. A., Herakovich, C. T., Graham, L. L., *Damage development in composites with large stress gradients*, Composites Science and Technology, Vol. 61(15), 2169–2182, 2001.

[7] Tahani, M., Nosier, A., *Free edge stress analysis of general cross-ply composite laminates under extension and thermal loading*, Composite Structures, Vol. 60, 91-103, 2003.
[8] Riepl, C., *FEM-Modeling of Composite Laminates considering Free Edge Effects*, Diploma Thesis, TU Wien, 2023.
[9] Mittelstedt, C., Becker, W., *Interlaminar stress concentrations in layered structures: part I – a selective literature survey on the free edge effect since 1967,* Journal of Composite Materials, Vol. 38(12), 1037–1062, 2004.
[10] D'Ottavio, M., Vidal, P., Valot, E., Polit, O., *Assessment of plate theories for free-edge effects*, Composites Part B: Engineering, Vol. 48, 111-121, 2013.
[11] Byron Pipes, R., Pagano, N. J., *Interlaminar Stresses in Composite Laminates Under Uniform Axial Extension*, Journal of Composite Materials, Vol. 4, 538, 1970.
[12] Li, D. H., Wu, P. X., Wan, A. S., *A three-scale layerwise multiscale analysis method for composite laminated plates*, Mechanics of Materials, Vol. 185, 104769, 2023.
[13] Savoia, M., Reddy, J. N., *A variational approach to three-dimensional elasticity solutions of laminated composite plates*, Journal of Applied Mechanics, Vol. 59(2S), 166–175, 1992.
[14] Liang, W. Y., Ju, S. H., Tarn, J. Q., *Analytic determination of stress fields in cross-ply symmetric composite laminates*, International Journal of Solids and Structures, Vol. 94-95, 87-99, 2016.
[15] Becker, W., *Closed-form solution for the free-edge effect in cross-ply laminates*, Composite Structures, Vol. 26(1), 39–45, 1993.
[16] Nosier, A., Bahrami, A., *Free-edge stresses in antisymmetric angle-ply laminates in extension and torsion*, International Journal of Solids and Structures, Vol. 43, 6800–6816, 2006.
[17] Nosier, A., Maleki, M., *Free-edge stresses in general composite laminates*, International Journal of Mechanical Sciences, Vol. 50(10), 1435–1447, 2008.
[18] Marjanović, M., Meschke, G., Damnjanović, E. *Object-oriented framework for 3D bending and free vibration analysis of multilayer plates: Application to cross-laminated timber and soft-core sandwich panels*, Composite Structures, Vol. 255, 112859, 2021.
[19] Gao, Y. S., Cai, C. S., Zhang, S. Q., *A compressible layerwise third-order shear deformation theory with transverse shear stress continuity for laminated sandwich plates*, Composite Structures, Vol. 338, 118108, 2024.
[20] Gao, Y., Zhang, S., Hu, W., Songyun, M. A., Markert, B., *Layerwise third-order shear deformation theory with transverse shear stress continuity for piezolaminated plates,* Chinese Journal of Aeronautics, Vol. 37(9), 490-505, 2024.
[21] Bouteiller, P., Bleyer, J., Sab, K., *Continuum damage analysis of delamination in composite laminates using a stress-based layerwise plate model*, International Journal of Solids and Structures, Vol. 246–247, 111611, 2022.
[22] MATLAB R2011b, The MathWorks, Inc., Natick, Massachusetts, USA.
[23] GiD Customization Manual. CIMNE – International Center for Numerical Methods in Engineering, 2016.
[24] https://github.com/miregrf/FLWTFEM
[25] ABAQUS User Manual 6.9. DS SIMULIA Corp., Providence, Rhode Island, USA, 2009.
[26] Damnjanović, E., Marjanović, M. *Three-dimensional stress analysis of laminated composite plates using FLWT-based finite elements*, 7th International Congress of Serbian Society of Mechanics, Sremski Karlovci, Serbia, June 24-26 2019.
[27] Marjanović, M., Marković, N., Damnjanović, E., Cvetković, R. *Three-dimensional stress analysis and design of cross-laminated timber panels using full-layerwise-theory-based finite element method*, Thin-Walled Structures, Vol. 157, 107156, 2020.
[28] Dhondt, G., *The Finite Element Method for Three-Dimensional Thermomechanical Applications*, Wiley, 2004.

10th International Congress of the Serbian Society of Mechanics
Niš, Serbia, June 18-20, 2025
C.3
Original Scientific Paper

DOI:10.46793/ICSSM25.132M

AN ESTIMATE OF PENETRATION DEPTH OF RIGID RODS THROUGH MATERIALS SUSCEPTIBLE TO MICROCRACKING: PART 1 - THEORY

S. Mastilovic[1[0000-0002-1856-626X]],

University of Belgrade
Institute for Multidisciplinary Research, Kneza Viseslava 1, 11030 Belgrade, Serbia
e-mail: misko.mastilovic@imsi.bg.ac.rs

Abstract:

The present study proposes an approximate model focused on a simplified estimate of depth of penetration of rigid projectiles into quasibrittle solids. Penetration at normal incidence of a slender, rigid rod into massive targets, made of materials predisposed to microcracking due to their inferior tensile strength and heterogeneous structure, is an event characterized by a high level of aleatory variability and epistemic uncertainty. This inherent stochasticity is incorporated into a model developed based on particle dynamics simulations that provide the key modeling ingredient – an estimate of the radial traction necessary to dynamically expand a cylindrical cavity. The penetration depth expressions are derived for the conical and ogive nose projectiles. The related theoretical considerations for spherical nose projectiles are developed to the point where using the cylindrical cavity approximation becomes debatable. The novel use of the power-law radial traction dependence upon the expansion rate yields equations of penetration resistance and penetration depth defined in terms of hypergeometric functions. These expressions are readily evaluated by modern tools for technical computing.

Key words: penetration depth, rigid projectile, quasibrittle materials, cylindrical cavity expansion

1. Introduction

Objectives of the studies of projectile penetration into geological targets are often limited to prediction and measurement of the penetration depth or deceleration history. Analytical modeling of the high-velocity projectile penetration through massive targets made of quasibrittle (damage tolerant) materials is plagued with inherent complexities coupled with a dearth of detailed experimental insight into salient physical mechanisms. A typical penetration is a catastrophic event (Fig. 1), characterized by large deformations at high strain rates, encompassing inertia effects, stress- and failure-wave propagation, mass transport and phase transitions; all taking place within a few micro-seconds. In the vicinity of the emerging tunnel, the target material is inundated by microcracks (and, given enough energy, ultimately pulverized and perhaps melted in the thin contact layer). The shattered material is transported away from the projectile path and the fragment cloud energetically ejected from the crater. The process is stochastic and, for all practical purposes, adiabatic. A penetration model must recognize these conspicuous features of the phenomena and incorporate their effects.

The solution technique used in this study belongs to the category of theoretical models that approximate the target response by cavity-expansion methods [1-3]. This approach is pioneered by Hopkins [3] and then employed by numerous authors to develop penetration models (e.g., [4-7]). The cavity expansion theories are constantly improved and adjusted to new target materials [8-10]. The present approach is unique to the extent that it uses particle dynamics simulations of the cylindrical cavity expansion (CCE) to model the functional dependence of the radial traction on the expansion rate. The approach originated by Mastilovic and Krajcinovic [11, 12] is extended in terms of both computational and analytical effort [13]. The details of the disordered, nonlinear particle dynamics model are only succinctly revisited here based on original articles [11, 13]. The material system is built by material points ("continuum" particles) that mimic basic texture cells on the mesoscale (a grain or an aggregate of a discontinuous and heterogeneous material system). Their mutual links capture the bonding effects of corresponding cementitious matrices. In the pristine state, each bulk particle is linked to its six nearest neighbors by "chemical" bonds nonlinear in compression and linear in tension. The crucial model feature in the context of the CCE simulation, which enables realistic capturing of to the low-energy micro-cracking and the concomitant flow of the shattered material, is the introduction of a "mechanical" compressive interaction between the particles (not chemically bonded initially) brought together by the mass transport accompanying the CCE. The approximation of the quasibrittle material by such system of particles was selected for a number of reasons. First, the random microstructure of the subject materials, characterized by morphological and structural disorder, is straightforwardly introduced. Second, the selection of the phenomenological load-transfer rules capturing the salient physical mechanisms can be, in principle, inferred from the molecular models (bottom-up approach). Finally, there is no need to develop ingenious, time-consuming computational techniques to track the material interfaces.

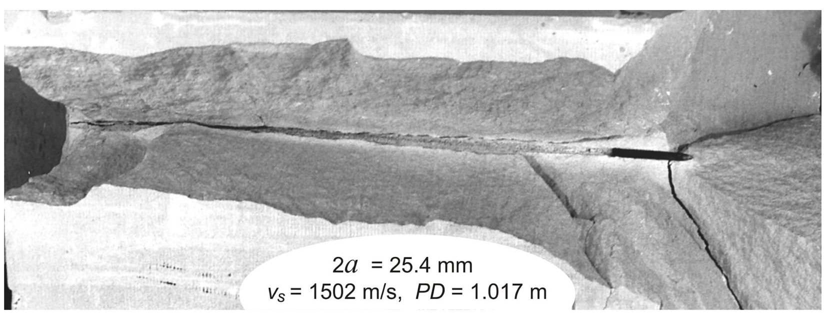

Fig. 1. A sectional view of a Salem limestone target penetrated by a 4340 steel projectile (adopted from [11]).

2. General expressions for the penetration resistance force

A slender rigid projectile (with conical, spherical or ogive nose (Fig. 2)) hits the target at normal incidence with the striking velocity v_s and continues to penetrate it with an ever-decreasing velocity v_z. For a rigid projectile, motion history and penetration depth can be calculated if the penetration resistance force is known. The derivation of this force is based herein on the target approximation by a stack of thin, independent layers of material perpendicular to the penetration direction (emphasized by the gray-shaded areas in Fig. 2), which facilitates the use of the CCE theory.

2.1 Penetration resistance for the conical-nose projectile

The conical nose with the cone angle 2ϕ (Fig. 2a) corresponds to the constant velocity CCE

$$v_r = v_z \frac{dr}{dz} \quad \Rightarrow \quad v_r = v_z \tan\phi \quad , \tag{1}$$

Eq. (1) reflects the constancy of the cone half-angle of the nose (Fig. 2a) that results in the constant radial velocity and, consequently, the constant radial traction σ_r along the generatrix. This simplifies the following analysis, which is the reason why the conical nose is addressed the first.

In the oncoming penetration-resistance derivation, the CCE approximation implies

$$dF_z = dF_r \frac{dr}{dz} \quad \Rightarrow \quad dF_z = dF_r \tan\phi = (\sigma_r\, 2r\pi\, dz)\tan\phi \tag{2}$$

where F_z is the penetration resistance force and F_r the radial force necessary for the CCE in an infinite material with the radial velocity v_r.

The frictional resistance is traditionally *added* to Eq. (2), if deemed necessary, by assuming that Coulomb friction formula $\sigma_t = \mu\, \sigma_r$ is applicable. Therefore,

$$dF_z = \sigma_r\,(2r\pi\, dz)\tan\phi + \mu\,\sigma_r\,(2r\pi\, d\xi)\cos\phi \tag{3}$$

In the first term of Eq. (3), the radial stress acting on the elementary surface $dA_r = 2\pi\, r\, dz$ ($0 \le z \le l = a / \tan\phi$) corresponds to the elementary force necessary for the CCE and thus enables the projectile penetration. In the second (superposed) term, the frictional force arises from the frictional traction ($\sigma_t = \mu\, \sigma_r$) acting on the elementary surface of the projectile nose $dA = 2\pi\, r\, d\xi$ ($0 \le \xi \le l = a / \sin\phi$). Obviously, since ϕ = const., the elementary integration yields

$$F_z = a^2\pi\left(1 + \mu/\tan\phi\right)\sigma_r\left(v_z\right) \tag{4}$$

In general, the radial traction $\sigma_r\,(v_z)$ necessary for the CCE is obtained from a one-dimensional, symmetric analysis (e.g., [5, 9]). A novel approach used in this study (following in the footsteps of [11, 13]) relies on the CCE particle dynamics simulations to provide guidance to $\sigma_r\,(v_r)$ modeling.

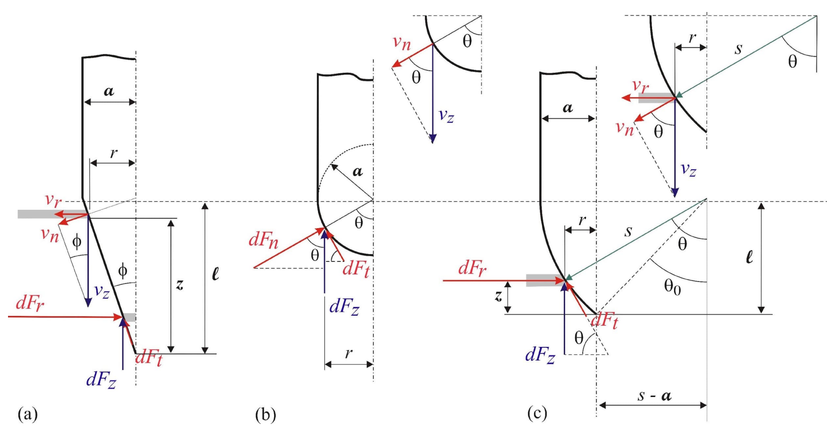

Fig. 2. Three different projectile-nose geometries: (a) conical, (b) spherical, (c) ogive, and corresponding parameters. Note the axial symmetry of the problem and the CCE approximation (v_r, F_r) with exception of (b) which emphasizes the spherical cavity expansion parameters (v_n, F_n).

2.2 Penetration resistance for the spherical-nose projectile

The derivation of the penetration resistance for the spherical nose is presented herein only briefly for the sake of completeness. The penetration of rigid, spherical-nose projectile cannot be realistically approximated by the CCE. The alternative, spherical cavity expansion leans naturally to this problem as indicated by the brief overview that follows.

The geometry of the spherical nose is defined by

$$\theta = arcsin(r/a) \quad \Rightarrow \quad r = a \ sin\theta \tag{5}$$

The elementary penetration resistance force (augmented by the friction contribution) is:

$$dF_z = dF_n \cos\theta + dF_t \sin\theta \tag{6}$$

as illustrated by Fig. 2b. Since the use of the spherical cavity expansion model is envisioned, the elementary surface corresponding to tractions is the same, $dA = 2\pi\ r\ a\ d\theta = 2\pi\ a^2 \sin\theta\ d\theta$. Thus,

$$dF_z = 2a^2\pi\ (\sigma_n \cos\theta + \sigma_t \sin\theta) \sin\theta\ d\theta \tag{7}$$

which finally leads to the penetration resistance force

$$F_z = a^2\pi\ (\sin 2\theta + 2\ \mu \sin^2\theta)\ \sigma_n(v_z, \theta)\ d\theta \tag{8}$$

As previously noted, the expression for the normal traction at the spherical nose is obtained from the spherical cavity expansion which is beyond the scope of the present article.

2.3 Penetration resistance for the ogive nose

The ogive nose geometry is defined by the caliber radius head

$$\psi = s/2a = \left[1 + (l/a)^2\right]/4 \tag{9}$$

where l is the projectile nose length, and a is the shank radius (Fig. 2c).

Within the CCE approximation, the target is *idealized* as a stack of thin independent layers of material, normal to the penetration direction. In every layer, in-plane cavity growth is taking place while the ogive nose of the projectile is perforating by passing through. The penetration resistance is, consequently, defined by the radial force necessary to dynamically open the cylindrical cavity. The equality of elementary works needed to perform those tasks provides Eq. $(10)_1$. The penetration resistance force that takes into account the frictional resistance is given by Eq. $(10)_2$

$$dF_z = dF_r \frac{dr}{dz} \quad \rightarrow \quad dF_z = \sigma_r\,(2\pi\, r\, dz)\frac{dr}{dz} + (\mu\,\sigma_r)(2\pi\, r\, sd\theta) sin\,\theta \tag{10}$$

From the ogive nose geometry, illustrated in Fig. 2c, it follows that

$$r = (a - s) + \sqrt{s^2 - (l - z)^2} \quad \Rightarrow \quad \frac{dr}{dz} = \frac{l - z}{\sqrt{s^2 - (l - z)^2}} \tag{11}$$

It is also convenient to introduce the following relationships:

$$\theta_0 = arcsin\,(1 - 1/2\psi) = arccos\left(\sqrt{4\psi - 1}/2\psi\right) \tag{12}$$

Consequently, Eq. $(10)_2$ could be expanded in the following form:

$$dF_z = 2\pi\,(a - s + \sqrt{s^2-(l-z)^2})\,\frac{l-z}{\sqrt{s^2-(l-z)^2}}\,\sigma_r(v_z,z)dz + \\ + 8a^2\pi\psi^2\mu\,(\sin\theta - \sin\theta_0)\sin\theta\,\sigma_r(v_z,\theta)\,d\theta \tag{13}$$

and integrated

$$F_z = 2\pi\int_0^l (a - s + \sqrt{s^2-(l-z)^2})\,\frac{l-z}{\sqrt{s^2-(l-z)^2}}\,\sigma_r(v_z,z)dz + \\ + 8a^2\pi\psi^2\mu\int_{\theta_0}^{\pi/2}(\sin\theta - \sin\theta_0)\sin\theta\,\sigma_r(v_z,\theta)\,d\theta \tag{14}$$

Similarly to the Eq. (4) and Eq. (8) the evaluation of integrals in Eq. (14) requires an analytical form of the traction at the rigid projectile nose, $\sigma_r(v_z, \theta)$. Usually, the analytical form of this traction is obtained from a one-dimensional, symmetric analysis of a cavity expansion (spherical or cylindrical). As already mentioned, in the present study the analytical form of the radial traction is deduced based on the results of CCE particle dynamics simulations.

3. CCE particle dynamics simulations: the radial traction dependence on the cavity expansion velocity

The CCE particle dynamics simulations provide a functional dependence of the radial traction on the cavity surface, σ_r, on the cavity expansion velocity, v_r, that is shown in Fig. 3.

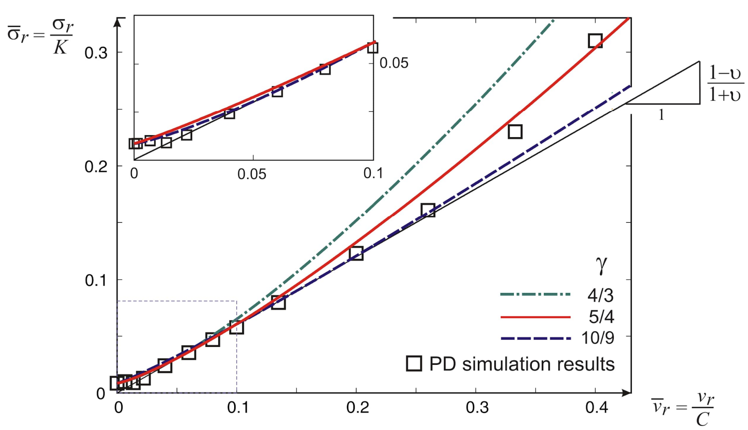

Fig. 3. Radial traction at the cavity surface vs. cavity expansion velocity (normalized by the bulk modulus and dilatational velocity, respectively). Squares mark CCE particle dynamics simulation results. The lines represent three analytical curves modeling data by the analytical approach presented later.

The set of simulation results shown in Fig. 3 represents a significant expansion [15] compared to the original set [11], with additional expansion rates applied to a larger particle dynamics model. The following observations can be made based on Fig. 3:

- Added simulations confirm the original observation of the practically linear $\bar{\sigma}_r = \sigma_r / K$ vs. $\bar{v}_r = v_r / C$ dependence in the medium-to-high CCE range ($\bar{v}_r \in$[0.0135, 0.20]) defined by the slope $(1 - \upsilon)/(1 + \upsilon)$ as illustrated in Fig. 3. (K, C and υ designate the bulk modulus, dilatational velocity, and Poisson's ratio, respectively.) The slope stems from the observed rule of thumb

$$\bar{\sigma}_r^{lb} = \frac{1}{3}\bar{\sigma}_r^F = \frac{1}{3}\left[\frac{3(1-\upsilon)}{(1+\upsilon)}\bar{v}_r\right] \quad \Rightarrow \quad \sigma_r^{lb} = \frac{1}{3}\sigma_r^F = \frac{1}{3}\sqrt{\frac{1-\upsilon}{(1+\upsilon)(1-2\upsilon)}E\,\rho}\; v_r \tag{15}$$

that relates the *stagnation* stress value ($\bar{\sigma}_r^{lb}$) with the radial stress at the elastic wave front at the cavity edge ($\bar{\sigma}_r^F$) derived by Kromm [2]. In Eq. $(15)_2$, E and ρ are the modulus of elasticity and density, respectively, and the square-root term is the wave impedance ($\rho{\cdot}C$) representing the ratio of the particle velocity (which in this case corresponds to the cavity expansion velocity v_r) and the radial stress (σ_r^F). Mastilovic and Krajcinovic [11] observed that $\bar{\sigma}_r^F$ captures with uncanny accuracy the peak value of the radial traction for the quasibrittle materials explored so far (Fig. 4).

● The additional simulations indicate that the stationary radial tractions deviate from the one-third rule of thumb (15) in the range of the highest expansion velocities ($v_r > 0.20{\cdot}C$). Consequently, pronounced nonlinearity of the functional dependence $\bar{\sigma}_r = f(\bar{v}_r)$ emerges, which is reminiscent of the pressure–particle velocity curves observed in the shock physics. (This is not just a coincidence because—within the present particle dynamics framework—σ_r and v_r indeed correspond to the internal pressure and the radial velocity of the particles located at the cavity rim.)

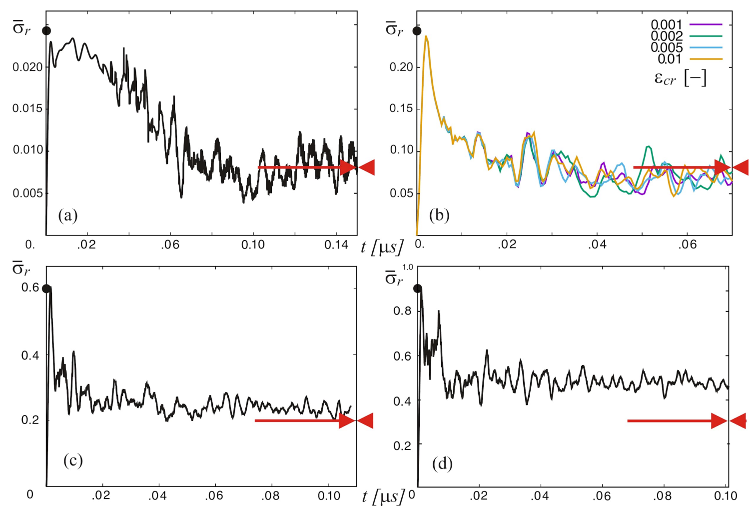

Fig. 4. $\bar{\sigma}_r$ time histories for four CCE velocities (v_r/C): (a) 0.0135, (b) 0.135, (c) 0.33 and (d) 0.50. The black circle on the ordinate designates the analytical solution of $\bar{\sigma}_r^F$ [2]. The thick red line with arrows on the right marks $\bar{\sigma}_r^F/3$ and approximates very well the stationary value of the radial traction in the medium-to-high CCE velocity range [0.0135, 0.20], represented by Eq. (15). For the highest expansion velocities, $v_r > 0.2{\cdot}C$, the stationary radial tractions deviate from the one-third rule of thumb and the functional dependence $\sigma_r = f(v_r)$ exhibits pronounced nonlinearity. The time on abscissa scales with the relative change of the cavity radius. (Note that four curves at the plot (b) demonstrate that the stationary values are not sensitive to an order of magnitude change of the link rupture strain, ε_{cr}, of the particle dynamics model.)

It cannot be overstated that the functional dependence $\bar{\sigma}_r = f(\bar{v}_r)$, captured by Fig. 3, is the key ingredient to the penetration resistance expressions (4) and (14) derived in the preceding section. Mastilovic and Krajcinovic [11] overlooked the nonlinearity in the high velocity range due to the narrower CCE velocity range explored. Thus, they analytically represented $\bar{\sigma}_r = f(\bar{v}_r)$ by two approximations: (i) the bilinear, and (ii) the second-order parabola. The former obviously underestimates the radial traction for the high expansion velocities ($v_r > 0.20{\cdot}C$). The problem with the later (that is commonly used in modeling) is that it might overestimate radial tractions for the larger expansion velocities if the characteristic slope in the medium-to-high expansion velocity range is to be emphasized.

In the present study, the functional dependence $\bar{\sigma}_r = f(\bar{v}_r)$ is assumed in the following form

$$\bar{\sigma}_r = \frac{\sigma_r}{K} = B + A \cdot \left(\frac{v_r}{C}\right)^{\gamma}, \quad \gamma \in \Re^+, \gamma > 1 \tag{16}$$

Based on the CCE particle dynamics results, the ansatz (16) should satisfy the four boundary conditions:

$$\begin{gathered} \bar{\sigma}_r \Big|_{\bar{v}_r=0} = (\bar{\sigma}_r)_{st}, \quad \frac{d\bar{\sigma}_r}{d\bar{v}_r}\Big|_{\bar{v}_r=0} = 0 \\ \bar{\sigma}_r \Big|_{\bar{v}_r=\alpha\cdot\bar{v}_r^*} = \left(\frac{1-\upsilon}{1+\upsilon}\right)\left(\alpha\cdot\bar{v}_r^*\right) \\ \frac{d\bar{\sigma}_r}{d\bar{v}_r}\Big|_{\bar{v}_r=\alpha\cdot\bar{v}_r^*} = \left(\frac{1-\upsilon}{1+\upsilon}\right) \end{gathered} \tag{17}$$

These boundary conditions require that

$$B = (\bar{\sigma}_r)_{st} = \sqrt{\frac{3}{2}\frac{(1-2\nu)}{(2-\nu)}}\,\bar{\sigma}_f, \quad A = \frac{\alpha^{1-\gamma}}{\gamma}\left(\frac{1-\upsilon}{1+\upsilon}\right)^{\gamma}(\bar{\sigma}_r)_{st}^{1-\gamma}, \quad \gamma = \frac{\alpha}{\alpha-1} \tag{18}$$

while the boundary condition $(17)_2$ is satisfied automatically by Eq. (16). The non-dimensional radial traction at the cavity surface for the static cavity expansion $(18)_1$, is derived for the elastic-cracked response in Appendix A of the accompanying article [14]. The derivation of parameters $\mathcal{A}$ and γ (18) is available in reference [13]. In short, $\mathcal{A}$ and γ are obtained from requirement that the radial traction curve (16) starts from the static value $(17)_1$ at zero slope $(17)_2$ and approaches from above the lower bound (15) at the abscissa value of $\alpha\cdot\bar{v}_r^*$ $(17)_3$ as illustrated in Fig. 5.

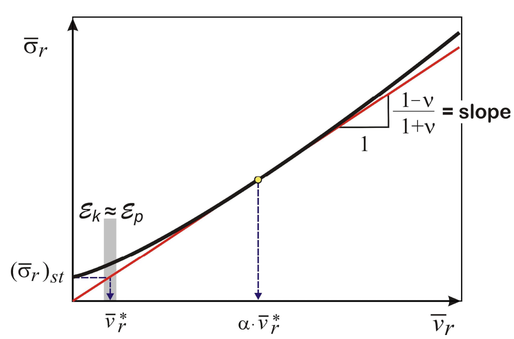

Fig. 5. Schematic representation of the radial traction at the cavity surface vs. the cavity expansion velocity. Note that the particle dynamics simulation results [13] fix $\bar{v}_r^*$ to 0.0143, which for the Salem limestone used in the accompanying article [14] corresponds to 60 m/s. (It has been noted in [11] that the narrow range of radial velocities centered on v_r^* is characterized by balance of kinetic and potential energies.)

Table 1 presents an example of the parameter values found in Eqs. (16) and (17).

α	γ	$\mathcal{A}$
2	2	10.5
3	3/2	1.94
4	4/3	1.17
5	5/4	0.928
10	10/9	0.670

Table 1. Five sets of parameters based on the particle dynamics inputs $\upsilon = 0.25$ and $(\bar{\sigma}_r)_{st} = 0.0086$. (Note that α is selected as the independent parameter. This role is interchangeable with γ.)

It is obvious from Fig. 3 that the larger values of the exponent γ better depict the nonlinearities in the the smallest- and the highest-velocity range. On the other hand, the smaller γ values naturally flatten the curve and tend to capture "quasi-linearity" in the medium-to-high velocity region. It is also evident that a compromise between these two conflicting requirements (the quasi-linearity in the medium-to-high, and the strong nonlinearity in the other two velocity regions) is needed for ansatz (16) to work. Therefore, Fig. 3 suggests that a reasonable overall agreement with the particle dynamics simulation results is achieved with exponent $\gamma = 5/4$ that departs from the observed radial traction at $\bar{v}_r = 0.5$ (which is over 2000 m/s for most quasibrittle materials of interest).

4. Calculations of the penetration resistance and the penetration depth based on the radial traction obtained from CCE particle dynamics simulations

The analytical form of the penetration resistance $F_z = f(\bar{v}_z)$ for the conical and the ogive projectile nose geometries is obtained by substitution of the radial traction expression, Eq. (16), into Eq. (4) and Eq. (14), respectively. (The spherical nose calculation is not performed herein since the CCE is an inadequate approximation for that geometry, as already noted.)

4.1 The conical-nose calculations

The conical nose is characterized by the constant radial tractions. Thus, upon the substitution of Eq. (16) into Eq. (4), the following expression for the penetration resistance is obtained

$$F_z = \alpha_{cc} + \beta_{cc}\, \bar{v}_z^{\gamma} \tag{19}$$

where

$$\alpha_{cc} = \lambda_{cc} \cdot (\bar{\sigma}_r)_{st}, \quad \beta_{cc} = \lambda_{cc} \cdot A \cdot (\tan\phi)^{\gamma}, \quad \lambda_{cc} = a^2 \pi (1 + \mu/\tan\phi) K.$$

Eq. (19) is then substituted into Newton's second law of motion

$$m_p \frac{dv_z}{dt} = -F_z \quad \Rightarrow \quad m_p C^2\, \bar{v}_z \frac{d\bar{v}_z}{dz} = -\left(\alpha_{cc} + \beta_{cc}\, \bar{v}_z^{\gamma}\right) \tag{20}$$

The penetration depth expression

$$PD = \frac{m_p v_s^2}{2\alpha_{cc}}\; {}_2\mathrm{F}_1\left(1, \frac{2}{\gamma}, 1 + \frac{2}{\gamma}, -\frac{\beta_{cc}}{\alpha_{cc}}\left(\frac{v_s}{C}\right)^{\gamma}\right) \tag{21}$$

is obtained by integration of Eq. $(20)_2$. In Eq. (21), m_p is the projectile mass, v_s – the striking velocity, and ${}_2\mathrm{F}_1$ $(a, b; c; z)$ – the hypergeometric function [15].

4.2 The ogive-nose calculations

The penetration resistance force acting on the ogive nose is defined by the integral expression (14). Thus, upon the substitution of Eq. (16) into Eq. (14), and evaluation of the integrals, the following expression for the penetration resistance is obtained [13]

$$F_z = \alpha_{co} + \beta_{co}\,\bar{v}_z^{\gamma}$$

$$\alpha_{co} = \lambda_{co}\left(\bar{\sigma}_r\right)_{st}\left[1 + 4\psi^2\,\mu\left(\pi/2 - \theta_0 + \sin 2\theta_0/2\right)\right],\quad \lambda_{co} = a^2\pi K, \tag{22}$$

$$\beta_{co} = 8\lambda_{co}\,\psi^2 A\,\mu\left\{\begin{array}{l}\dfrac{(cos\theta_0)^{\gamma+2}}{\gamma+2}\left[{}_2\mathrm{F}_1\left(\dfrac{\gamma}{2},1+\dfrac{\gamma}{2},2+\dfrac{\gamma}{2},cos^2\theta_0\right)-(1-\dfrac{1}{2\psi})\,{}_2\mathrm{F}_1\left(\dfrac{\gamma}{2},1+\dfrac{\gamma}{2},2+\dfrac{\gamma}{2},cos^2\theta_0\right)\right]+\\ +\mu\left[\begin{array}{l}\dfrac{(cos\theta_0)^{\gamma+1}}{\gamma+1}\left({}_2\mathrm{F}_1\left(\dfrac{1}{2},\dfrac{1+\gamma}{2},\dfrac{3+\gamma}{2},cos^2\theta_0\right)-sin\theta_0\right)-\\ -\dfrac{(cos\theta_0)^{\gamma+3}}{\gamma+3}\,{}_2\mathrm{F}_1\left(\dfrac{1}{2},\dfrac{3+\gamma}{2},\dfrac{5+\gamma}{2},cos^2\theta_0\right)\end{array}\right]\end{array}\right\}$$

The expressions for parameters α_{co} and β_{co} may appear cumbersome but they are uniquely determined by the material properties (K, υ, σ_f), the ogive nose geometry (a, ψ), and the friction coefficient (μ) and can be readily evaluated by software packages such as Wolfram Mathematica.

The penetration resistance (22) is then substituted into Eq. (20) which eventually yields

$$PD = \frac{m_p\,v_s^2}{2\,\alpha_{co}}\;{}_2\mathrm{F}_1\left(\frac{\gamma}{2},1,1+\frac{\gamma}{2},-\frac{\beta_{co}}{\alpha_{c0}}\left(\frac{v_s}{C}\right)^{\gamma}\right) \tag{23}$$

It is obvious from Eqs. (21) and (23) that the penetration depths for both conical and ogive noses are proportional to the kinetic energy of the striking projectile.

5. Summary

The present study is dedicated to analysis of the penetration depth of a slender rigid projectile into quasibrittle materials susceptible to microcracking (the damage-tolerant materials, primarily rocks). Three typical geometries of the projectile nose are considered with emphasis on the conical and ogive noses, which are better suited for the cylindrical cavity expansion approximation employed in this investigation. Specifically, the functional dependence of the radial traction at the cavity surface on the cavity expansion velocity is deduced based on particle dynamics simulation results. These results suggest the mildly nonlinear dependence ($\bar{\sigma}_r \propto \bar{v}_r^{\gamma}$, $\gamma >$ 1) composed of the nonlinear response in the range of extremely low (the quasistatic) and extremely high cavity expansion velocities and only a weakly nonlinear (practically quasi-linear) response in between. The described functional dependence is at the core of the proposed model. This analytical form results in penetration depth expressions in terms of hypergeometric functions. Accordingly, it could be argued that the simplicity of similar empirical formulas has not been maintained, which certainly would not be convenient for engineering applications. Nonetheless, as demonstrated in the accompanying article [14], the penetration depth expressions developed herein are easily evaluated by software systems with built-in libraries developed for modern technical computing (such as, as an example, Wolfram Mathematica). Last but not least, the resulting penetration depths for two nose geometries are proportional to the kinetic energy of the rigid projectile at the moment of impact.

(Discussion of the underlying assumptions of the proposed model, from the point of view of the impact on the accuracy of predictions, is left for the Conclusion of the accompanying article [14].)

References

[1] Bishop R.F., Hill R., Mott N.F., *The theory of indentation and hardness tests*, Proceedings of Physical Society, Vol. 57, 147–159, 1945.

[2] Kromm A., *Zur Ausbreitung von Stosswellen in Kreislochscheiben*, Zeitschrift fur Angewandte Mathematik und Mechanik (ZAAM), Vol. 28, 104-114, 1948.

[3] Hopkins H.G., *Dynamic expansion of spherical cavities in metals*, in: *Progress in Solid Mechanics* (Editors I.N. Sneddon and R. Hill), Vol. 1, 83-163. North-Holland, Amsterdam, 1960.

[4] Goodier J.M., *On the mechanics of indentation and cratering in solid targets of strain-hardening metal by impact of hard and soft spheres*, AIAA: Proceedings of the 7th Symposium on Hypervelocity Impact III, 215–259, 1965.

[5] Forrestal M.J., *Penetration into dry porous rock*, International Journal of Solids and Structures, Vol. 22, 1485-1500, 1986.

[6] Forrestal M.J., Luk V.K., *Dynamic spherical cavity-expansion in a compressible elastic-plastic solid*, Journal of Applied Mechanics, Vol. 55, 275-279, 1988.

[7] Warren T.L., Forrestal M.J., *Effects of strain hardening and strain-rate sensitivity on the penetration of aluminum targets with spherical-nosed rods*, International Journal of Solids and Structures, Vol. 35, 3737–3753, 1998.

[8] Kong X.Z., Wu H., Fang Q., et al., *Projectile penetration into mortar targets with a broad range of striking velocities: Test and analyses*, International Journal of Impact Engineering, Vol. 106, 18-29, 2017.

[9] Johnsen J., Holmen J.K., Warren T.L., Børvik T, *Cylindrical cavity expansion approximations using different constitutive models for the target material,* International Journal of Protective Structures, Vol. 9, 199-225, 2018.

[10] Zhang Y., Chen W., Cheng S., et al., *Penetration of rigid projectiles into concrete based on improved cavity expansion model*, Structural Concrete, Vol. 18, 974-985, 2017.

[11] Mastilovic S., *Dynamic Loading of Brittle Materials with Random Microstructure,* Arizona State University, Tempe, AZ, USA, 1999.

[12] Mastilovic S., Krajcinovic D., *Penetration of Rigid Projectiles Through Quasi-Brittle Materials*, Journal of Applied Mechanics, Vol. 66, 585-592, 1999.

[13] Mastilovic S. *A PD simulation-informed prediction of penetration depth of rigid rods through materials susceptible to microcracking,* Meccanica, Vol. 57 (12): 3051–3069, 2022.

[14] Mastilovic S., *An Estimate of Penetration Depth of Rigid Rods Through Materials Susceptible to Microcracking: Part 2 – Validation and Parameter Sensitivity*, Proceedings of the 10th International Congress of the Serbian Society of Mechanics, Nis, Serbia, 2025.

[15] Aomoto K., Kita M., *Theory of Hypergeometric Functions*, Springer, Heidelberg, 2011.

10th International Congress of the Serbian Society of Mechanics
Niš, Serbia, June 18-20, 2025

C.4
Original Scientific Paper

DOI:10.46793/ICSSM25.142M

AN ESTIMATE OF PENETRATION DEPTH OF RIGID RODS THROUGH MATERIALS SUSCEPTIBLE TO MICROCRACKING: PART 2 – VALIDATION AND PARAMETER SENSITIVITY

S. Mastilovic[0000-0002-1856-626X]

University of Belgrade
Institute for Multidisciplinary Research, Kneza Viseslava 1, 11030 Belgrade, Serbia
e-mail: misko.mastilovic@imsi.bg.ac.rs

Abstract:

A simple, approximate model aimed at estimating the penetration depth of slender rigid projectiles into massive targets made of quasibrittle solids is proposed in the companion article [1]. The key ingredient for that novel analytical approach—namely, the functional dependence of the radial traction at the cavity surface on the radial velocity of the cavity expansion—is provided by postprocessing of results of particle dynamics simulations. In this article, this model is validated using experimental results on the depth of penetration of long (virtually rigid) projectiles into Salem limestone targets. Salem limestone is a typical example of quasibrittle materials with random, discontinuous and heterogeneous micro/meso structure, inherently predisposed to microcracking, which is attributed to their inferior tensile strength. Such materials are known for their pronounced scatter of experimental data. This inherent stochasticity is explored in this paper through a comparative analysis of key model input parameters; primarily, the indirect (uniaxial) tensile strength and the coefficient of friction.

Key words: penetration depth, quasibrittle, stochasticity, parameter sensitivity, Salem limestone

1. Introduction

Penetration resistance of geological materials (primarily rocks, but also composites such as concrete and ceramics) is of great importance not only in defense applications but also in many other branches of industry. The solution technique proposed in the accompanying article [1] belongs to the category of models that approximate the target response by the theory of cylindrical cavity expansion (CCE). The succinct historical review of the key references is offered in [1, 2] together with specifics of the original contribution developed therein. Presently, it is deemed sufficient to recall that the novelty of the proposed approach rests on the approximation of a quasibrittle solid by an ensemble of “continuum” particles interacting via a nonlinear potential, selected for a number of reasons elaborated on in the original articles. The outcome of this strategy is the functional dependence of the radial traction at the cavity surface on the radial CCE velocity given in the power law form, $\sigma_r \propto v_r^\gamma$, where $\gamma > 1$ (see [1] for details). The particle dynamics simulation results suggest that this functional dependence is comprised of three distinctive regions: (i) the nonlinear in the extended quasistatic region, (ii) the weakly nonlinear ("quasi-linear") in the medium-to-high expansion velocity range ($0.01 < v_r / C < 0.25$), and (iii) increasingly nonlinear in the high velocity range. This relationship has been investigated by many authors (e.g., [2, 4, 5]); the novelty of this approach is that the highly-brittle responses of the materials susceptible to microcracking apparently favor smaller value of the exponent ($\gamma < 2$) to capture realistically the projectile resistance and largely linear response in the medium-to-high velocity range. Furthermore, the quasibrittle materials with random, discontinuous and heterogeneous micro/meso structure, inherently predisposed to microcracking attributed to their inferior tensile strength (such as rocks), are characterized by extremely large scatter of material properties (e.g., Table 1). The effect of this far-reaching stochasticity is explored herein.

Finally, it has been recognized from the very onset of development of penetration theories [6] that the friction coefficient has a large effect on the predictions of the rigid projectile motion upon impact. More often than not, it is assumed, for the sake of simplicity, that the friction coefficient, μ, is a velocity-independent constant (e.g., [7]). This assumption is investigated in the present study.

2. Numerical examples for the penetration depth of the rigid ogive-nose projectiles

The penetration depth expression for the ogive nose projectiles

$$PD = \frac{m_p v_s^2}{2\alpha_{co}} \, {}_2\mathrm{F}_1\left(\frac{\gamma}{2}, 1, 1+\frac{\gamma}{2}, -\frac{\beta_{co}}{\alpha_{c0}}\left(\frac{v_s}{C}\right)^\gamma\right) \tag{1}$$

is derived in the accompanying article [1]. In Eq. (1), m_p stands for the projectile mass, v_s – the striking velocity, C – the dilatational velocity, ${}_2\mathrm{F}_1$ (a, b; c; $f(z)$) – the hypergeometric functions (e.g., [8]), while the parameters are as follows

$$\alpha_{co} = \lambda_{co} (\bar{\sigma}_r)_{st} \left[1 + 4\psi^2 \mu \left(\frac{\pi}{2} - \theta_0 + \frac{1}{2} sin 2\theta_0\right)\right],$$

$$\beta_{co} = 8\lambda_{co}\psi^2 A \mu \left\{ \begin{array}{l} \dfrac{(cos\theta_0)^{\gamma+2}}{\gamma+2}\left[{}_2\mathrm{F}_1\left(\dfrac{\gamma}{2}, 1+\dfrac{\gamma}{2}, 2+\dfrac{\gamma}{2}, cos^2\theta_0\right) - (1-\dfrac{1}{2\psi})\,{}_2\mathrm{F}_1\left(\dfrac{\gamma}{2}, 1+\dfrac{\gamma}{2}, 2+\dfrac{\gamma}{2}, cos^2\theta_0\right)\right] + \\ + \mu \left[\begin{array}{l} \dfrac{(cos\theta_0)^{\gamma+1}}{\gamma+1}\left({}_2\mathrm{F}_1\left(\dfrac{1}{2}, \dfrac{1+\gamma}{2}, \dfrac{3+\gamma}{2}, cos^2\theta_0\right) - sin\theta_0\right) - \\ -\dfrac{(cos\theta_0)^{\gamma+3}}{\gamma+3}\,{}_2\mathrm{F}_1\left(\dfrac{1}{2}, \dfrac{3+\gamma}{2}, \dfrac{5+\gamma}{2}, cos^2\theta_0\right) \end{array} \right] \end{array} \right\}$$

$$\lambda_{co} = a^2 \pi K, \quad A = \frac{\alpha^{1-\gamma}}{\gamma}\left(\frac{1-\upsilon}{1+\upsilon}\right)^\gamma (\bar{\sigma}_r)_{st}^{1-\gamma}, \quad (\bar{\sigma}_r)_{st} = \sqrt{\frac{3}{2}\frac{(1-2\nu)}{(2-\nu)}\left(\frac{\sigma_f}{K}\right)}, \quad \theta_0 = arcsin\left(1 - \frac{1}{2\psi}\right) \tag{2}$$

The preceding penetration parameters, Eq. (2), are dependent upon:

- projectile information (m_p – projectile mass, a – shank radius, ψ - caliber radius head);
- material properties (K – bulk modulus, υ – Poisson ratio, σ_f – indirect tensile strength);
- the sliding friction coefficient (μ);

- the model parameter (α or γ).

2.1 A brief review of material properties for Salem limestone

As already mentioned, the physical and mechanical properties of quasibrittle materials are known for their extremely pronounced data scatter. This aleatory variability is illustrated in Table 1, which summarizes the limestone properties. The presented data show that mechanical properties of limestone can vary within an order of magnitude range, which is typical of brittle materials in general and rocks in particular. This variability is indeed far-reaching for model validation because researchers are unlikely to report all the inputs necessary for your model, while compiling material properties from different sources is an iffy endeavor in itself. Estimating ultimate tensile strength based on unconfined compressive strength introduces enough uncertainty to make any additional "guessing" of questionable use and the corresponding calculation results suspicious.

density, ρ [kg/m^3]	1.79 - 2.92
porosity, η [%]	2.6 - 20
modulus of elasticity, E [GPa]	10.0 - 80.0
compressive strength, σ_c [MPa]	13.8 - 255
tensile strength, ultimate σ_f [MPa]	5.0 - 25.0
modulus of rupture, R [GPa]	0.00340 - 0.0359

Table 1. Variability of the selected limestone properties

The material properties of Salem limestone used in the present study (K = 26.5 MPa, υ = 0.23, C = 4280 m/s, and $\sigma_f = \sigma_c/7$ = 9 MPa) are compiled from the penetration study by Frew at al. [9] and the triaxial compression experiments by Green [10]. It should be noted that the indirect uniaxial tensile strength σ_f is estimated herein based on the uniaxial compressive strength [10] out of necessity. The σ_f choice has a direct impact on results (which is discussed later) and the need to use this stochastic property, which is not an intrinsic material property and is known to be difficult to objectively determine experimentally, is among drawbacks of the proposed model. The uniaxial tensile strength of the quasibrittle materials is typically an order of magnitude inferior to their uniaxial compressive strength. The Salem limestone experimental data rarely even report σ_f and the available studies report values $\sigma_c/5$, $\sigma_c/7$. The latter is assumed herein as the more likely estimate but the effect of an even smaller tensile strength is explored henceforth.

Comparison of the penetration depth predictions obtained by the newly developed model (Eqs. (1) and (2)) and the Salem limestone experimental data [9] is presented in Table 2 and Fig. 1. The agreement between the experimental and computational results is less than 5% for the base case (3rd column in Table 2), which is considered very good. Actually, based on Fig. 1, it seems that the largest difference between results at a few striking velocities (notably, 939 m/s and 1098 m/s) is likely due to the experimental uncertainty rather than the predictions themselves. Nevertheless, the calculation results appear sensitive to some stochastic input parameters, which may cast a shadow on the model applicability if left unexplored.

2.2 Parametric sensitivity of calculation results

The sensitivity of the calculation results (the solid line in Fig. 1) to the choice of key model input parameters is explored in the last three columns of Table 2. First, the value of the exponent γ determines: (i) the "closeness" of the $\overline{\sigma}_r \left(\propto \overline{v}_r^{\gamma}\right)$ curve to the linear, inclined lower bound, and (ii) the degree of the nonlinearity in the high-velocity range (see Fig. 3 in the accompanying article [1]).

The selection of smaller value of the exponent, γ = 10/9, results in a less nonlinear $\overline{\sigma}_r = f(\overline{v}_r)$ and, consequently, a smaller penetration resistance for the higher striking velocities. Nonetheless, a more pronounced difference between two curves appears (according to Fig. 3 in [1]) only at high radial expansion velocities (v_r > 0.4 $C \approx$ 1600-1700 m/s for Salem limestone), which is beyond the velocity range used herein for validation and parametric sensitivity study.

Consequently, the comparison of the calculation results in the 3rd (corresponding to γ = 5/4) and 4th (γ = 10/9) columns of Table 2, shows that the difference becomes more pronounced only at the higher striking velocities (say, v_s > 1000 m/s, although the projectile size and mass affect this limit). Overall, the results are not too sensitive within the explored γ range. On the other hand, the one-third reduction of the tensile strength—from $\sigma_f = \sigma_c/7 \approx 9$ MPa (3rd column) to $\sigma_f = \sigma_c/10 \approx 6$ MPa (6th)—results in 14% increase of the penetration depth on average (Table 2). The difference in results is almost uniformly distributed over the entire explored velocity range (with the exception of the highest velocity). Such σ_f effect seems acceptable bearing in mind the overall uncertainty of the penetration depth estimate.

The model's tendency to overestimate the depth of penetration is discussed in the Conclusion.

v_s	PD^{exp}	$PD_{\substack{\gamma=5/4\\ \sigma_f=9MPa\\ \mu=0.08}}$	$PD_{\substack{\gamma=10/9\\ \sigma_f=9MPa\\ \mu=0.08}}$	$PD_{\substack{\gamma=5/4\\ \sigma_f=9MPa\\ \mu=0.02}}$	$PD_{\substack{\gamma=5/4\\ \sigma_f=6MPa\\ \mu=0.08}}$
[kg/m^3]	[m]	[m]	[m]	[m]	[m]
560	0.30	0.30	0.30	0.37	0.34
731	0.42	0.47	0.47	0.57	0.53
793	0.53	0.54	0.54	0.65	0.61
939	0.73	0.70	0.72	0.86	0.79
984	0.74	0.76	0.77	0.92	0.85
1098	0.79	0.90	0.93	1.10	1.01
1184	1.03	1.02	1.05	1.13	1.23

Table 2. Comparison of the experimental and computational results for penetration of a small-size ogive-nose projectile (m_p = 0.61 kg, $2a$ = 25.4 mm, ψ=3.0; Table 2 of ref. [9]) into Salem limestone target.

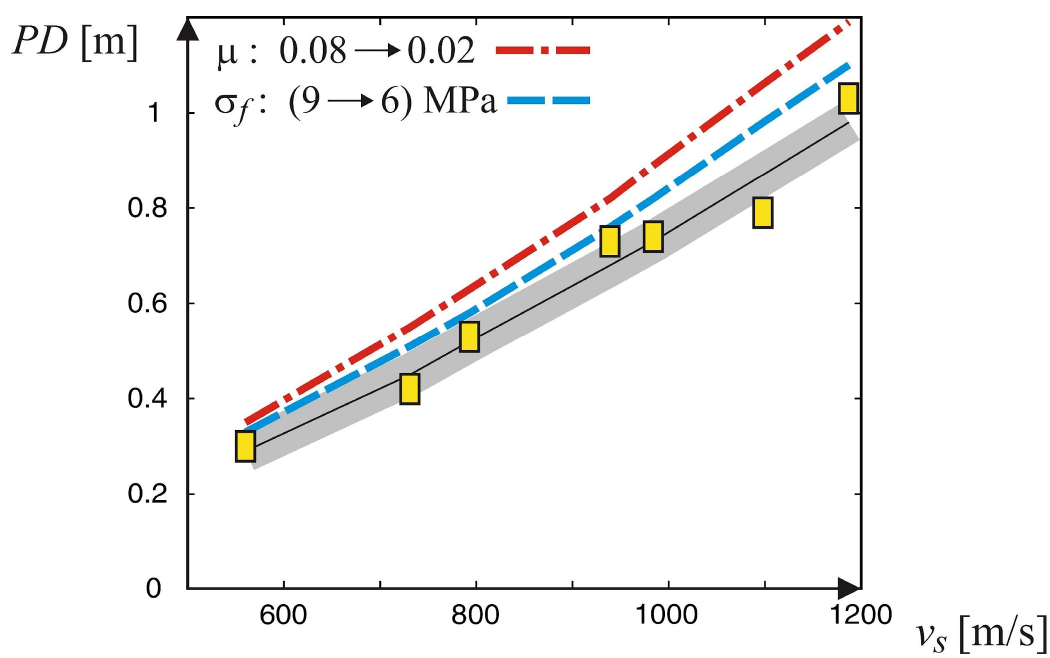

Fig. 1. Comparison of experimental (rectangles) and computational results for penetration of the ogive nose projectile into Salem limestone targets (Table 2). (Note that the thick gray line corresponds to the basic set of computational set of results - 3rd column in Table 2, while the dash-dotted red line and the dashed blue line correspond to the 5th and 6th columns, respectively, i.e. the indicated changes in input parameters.)

3. A numerical investigation of sliding friction effects

The obvious importance of the friction on the penetration depth is discussed from the very onset of the penetration studies [6] to the present (e.g., [7]). Early on, Forrestal and Grady [11], based on the data available at the time, set the friction coefficient value to $\mu = 0.08$. Not long after, Forrestal and coworkers [12] explored the friction coefficient values 0.02 and 0.10 for the rigid penetration into 6061-T651 aluminum targets.

Since then, the frictional resistance is sometimes completely neglected (e.g. [5, 14]), which is justified by the melting of the thin layer of the projectile in contact with the target. As an example, Jiang et al.'s investigation [13] of the role of friction for rigid penetration of concrete resulted in the conclusion that below a certain critical impact velocity the addition of friction improves agreement with test data; while, with the increase in impact speed, the effect of sliding friction weakens to the extent that it can be neglected.

Numerical results obtained from various engineering models developed in the last two decades ([13] and references therein) clarified this dependence and showed that the friction coefficient strongly affects the penetration depth in the case of high-speed penetration where the coefficient friction changes significantly.

3.1 Constant friction coefficient

In the present article the effect of the sliding friction coefficient is addressed twofold. Firstly, two relatively-small values of the friction coefficient are selected for this sensitivity study: μ=0.08 as the basic choice, and μ=0.02 as an alternative [16]. These values are then applied over the whole striking velocity range (Table 2; 3rd and 5th column, respectively). This μ reduction caused the penetration depth increase of 20% on average.[1] This difference may not be as alarming as it might seem at first look, bearing in mind the reduction of the friction coefficient by the factor of four. Nonetheless, since both used μ values are relatively small, the importance of this parameter choice should not be taken lightly. Moreover, as discussed above, with the increase of the striking velocity, the value of the sliding friction coefficient tends to zero, which implies that the model given by Eqs. (1) and (2) overestimates the penetration depth.

3.2 Sliding-velocity dependent friction coefficient

Secondly, it is recognized that the use of one constant friction coefficient throughout the *entire* penetration process is a questionable approach *regardless* of the value selected. On one side, penetration starts with the initial striking velocity ($v_z = v_s$) and ends with the projectile arrest ($v_z \equiv 0$). On the other side, at any moment of the penetration process, at any given penetration velocity, the sliding velocity varies from the minimum value at the tip of the projectile nose to the maximum at the nose-shank transition. For example, for v_z = 1000 m/s and the ogive nose with ψ = 3, the sliding velocity at the nose varies within the range [725, 1000] m/s. Thus, to capture the effect of this range of different velocities, a simplified analytical model is developed in reference [16], which includes the friction coefficient that changes with the sliding velocity. The comparison of the results corresponding to the fixed μ calculations (Fig. 2) indicate the difference

[1] The latter results is in reasonable agreement with observations reported in [11, 13, 16] that "a difference up to 25% was noticed when the friction coefficient was varied from 0.02 to 0.1" [13].

of approximately 20%, as already noted. On the other hand, the results for the calculation with the velocity-dependent friction coefficient obtained in [16] highlight a few salient points.

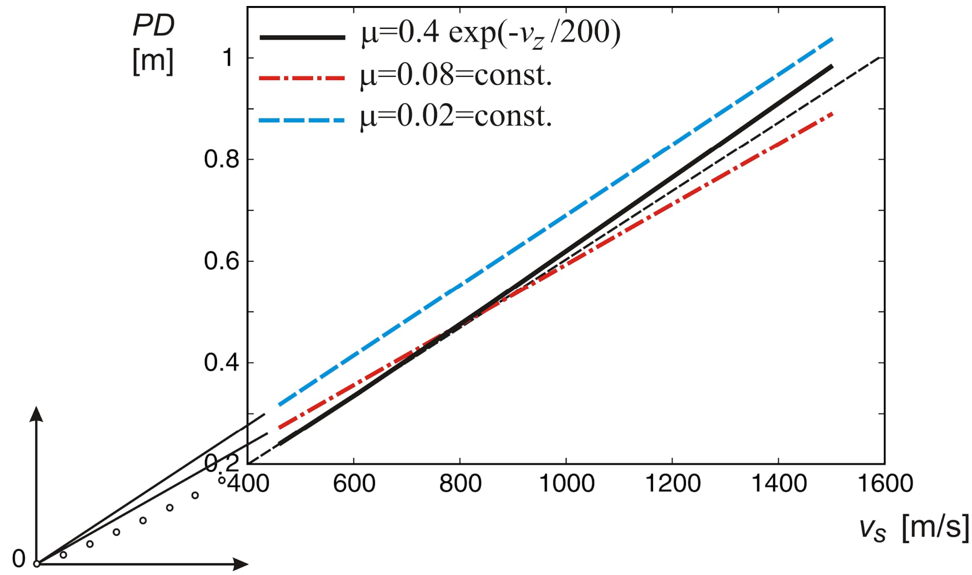

Fig. 2. Penetration depth vs striking velocity for three different friction coefficient treatments.

First, the penetration depth for the low striking velocities is smaller appreciably compared to the constant μ calculations. According to Fig. 2, at $v_s \approx 800$ m/s the cumulative effect of the friction coefficient exponential reduction results in equal penetration depth with the $\mu = 0.08$ calculation. (Interestingly, the crossover velocity, $v_s \approx 800$ m/s, corresponds to an order of magnitude smaller friction coefficient $\mu \approx 0.008$, according to [16].) Also, the penetration depth corresponding to the calculation with $\mu = 0.02 = const.$ consistently overestimates the results from the $\mu=f(v_s)$ calculation (the solid black line in Fig. 2); even for the highest striking velocities explored herein. This reveals the need to use the velocity-dependent friction coefficient in calculations instead of any fixed value. Moreover, the neglect of the frictional effects altogether (i.e., the use of $\mu \equiv 0$) is likely to result in the substantial overestimate of the penetration depth even for the highest striking velocities.

4. Conclusion

The approximate model presented—aimed to estimate the penetration depth of rigid projectiles impacting massive targets made of quasibrittle materials—is based on the key inputs from the particle dynamics simulation. The model is validated against experimental results for the Salem limestone targets. This comparison highlights the model's ability to predict penetration depth with reasonable accuracy, particularly considering the simplicity of the particle dynamics simulations and the fact that the predictions are based on just a few mechanical properties derived from *static* loading conditions. However, it is also recognized that the proposed model is based on some properties that are difficult to experimentally evaluate directly and/or exhibit a very pronounced variability. This data dispersion highlights the importance of understanding of the parametric sensitivity.

The case in point is the indirect (uniaxial) tensile strength, which is an extrinsic property, difficult to determine experimentally, and known for a large scatter. The investigation indicates that the one-third reduction of the tensile strength results in the 14% increase of the penetration depth, which is not insignificant. Furthermore, the choice the exponent γ, which defines the radial traction dependence on the expansion rate at the projectile nose, $\bar{\sigma}_r \propto (\bar{v}_r)^\gamma$, is proved to be robust in the relevant range, $0 < \gamma \leq 1.5$, as defined by the range of striking velocities that are of practical interest. Finally, arguably the most important parameters choice is that of the friction coefficient. The μ reduction from 0.08 to 0.02 results in the change of the prediction deviation from 4.7% to 25%, respectively. The study emphasizes benefits of the use of the velocity-dependent friction coefficient in the penetration modeling. The use of constant friction coefficient is an iffy proposition since every penetration event is a complex process that encompasses the entire range of sliding speeds that affect the friction coefficient value. The effect is cumulative and very difficult, if not impossible, to address with the sliding friction coefficient insensitive to the velocity.

The cause of the noted overestimates of the experimental data by the model predictions will be discussed only through three key points. Firstly, the assumption of the elastic-cracked response during the static CCE is questionable. Since the CCE begins from a zero initial radius, development of the global radial cracking (on the macroscopic scale) without crushing the material adjacent to the expanding cavity (i.e., the elastic-cracked-crushed response) is unlikely. Secondly, and more importantly, all CCE-based models overlook out-of-plane dissipation mechanisms by assuming plane strain conditions, whereas high-speed and X-ray imaging show that perforation involves significant out-of-plane deformation, damage, and fragmentation (e.g., petaling, bulging, ejection of fragments). Neglecting these dissipation effects (inherently unaccounted for due to the planar character of the CCE model) artificially increases the energy available for projectile penetration. Finally, in addition to these principal remarks, one should also note the neglect of the peak zone of the $\bar{\sigma}_r = f(\bar{v}_r)$ curve in the derivation of the penetration resistance (recall Fig. 4 of reference [1]).

References

[1] Mastilovic S., *An Estimate of Penetration Depth of Rigid Rods Through Materials Susceptible to Microcracking: Part 1 – Theory*, Proceedings of the 10th International Congress of the Serbian Society of Mechanics, Nis, Serbia, 2025.

[2] Mastilovic S., Krajcinovic D., *Penetration of Rigid Projectiles Through Quasi-Brittle Materials*, Journal of Applied Mechanics, Vol. 66, 585-592, 1999.

[3] Mayers, M.A., *Dynamic Behavior of Materials*, John Wiley, New York, 1994.

[4] Zhang Y., Chen W., Cheng S., Zou H., Guo Z., *Penetration of rigid projectiles into concrete based on improved cavity expansion model*, Structural Concrete, Vol. 18, 974-985, 2017.

[5] Johnsen J., Holmen J.K., Warren T.L., Børvik T, *Cylindrical cavity expansion approximations using different constitutive models for the target material,* International Journal of Protective Structures, Vol. 9, 199-225, 2018.

[6] Bishop R.F., Hill R., Mott N.F., *The theory of indentation and hardness tests*, Proceedings of Physical Society, Vol. 57, 147–159, 1945.

[7] Ölçmen S.M., Jones S.E., Weiner R.H., *A numerical analysis of projectile nose geometry including sliding friction for penetration into geological targets*, Proceedings of the Institution of Mechanical Engineers, Part C: Journal of Mechanical Engineering Science, Vol. 232, 284-304, 2018.

[8] Oberhettinger F., *Hypergeometric Functions*. Ch. 15 (pp. 555-566) in Handbook of Math. Functions, Abramowitz M. and Stegun I.A. (Eds.), 9th printing, New York, Dover, 1972.

[9] Frew D.J., Forrestal M.J., Hanchak S.J., Green M.L., *Penetration into Limestone Targets with Ogive-Nose Projectiles*, Proceedings of 14th Army Symposium on Solid Mechanics, Myrtle Beach, Battelle Press, SAND96-2494C, 1997.

[10] Green M.L., *Laboratory Test on Salem Limestone*, Waterways Experiment Station, Viksburg, MS, USA, 1992.

[11] Forrestal M.J., Grady D.E., *Penetration for Normal Impact into Geological Targets*, International Journal of Solids and Structures, Vol. 18, 229-234, 1982.
[12] Forrestal M.J., Okajima K., Luk V.K., *Penetration of 6061-T651 Aluminum Targets With Rigid Long Rods,* Journal of Applied Mechanics, Vol. 55, 755-760, 1988.
[13] Jiang N. Wu S.Hu Y.,Mu Z., Wu X.,Zhang W., *Investigations into the Role of Friction for Rigid Penetration into Concrete-Like Material Targets*, Materials 2020, 13, 4733.
[14] Chen, X.W., Li, Q.M., *Deep penetration of a non-deformable projectile with different geometrical characteristics*, International Journal of Impact Engineering, Vol. 27, 619–637, 2002.
[15] Forrestal M.J., Longcope D.B., *Target strength of ceramic materials for high-velocity penetration*, Journal of Applied Physics, Vol. 67, 3669-3672, 1990.
[16] Mastilovic S. *A PD simulation-informed prediction of penetration depth of rigid rods through materials susceptible to microcracking,* Meccanica, Vol. 57, 3051–3069, 2022.
[17] Feldgun V.R., Yankelevsky D.Z., Quasi-static spherical/cylindrical cavity expansion in a medium with an arbitrary equation of state and a shear strength plasticity envelope, International Journal of Solids and Structures Vol. 191–192, 146–156, 2020.

Appendix A – Static cavity expansion: elastic-cracked response

The problem considered is the static, radial CCE from a *zero initial radius* in an infinite, isotropic, brittle material under plane-strain conditions. Assuming that the CCE follows a response that combines elastic deformation and cracking (i.e., the elastic-cracked response), the expression for the radial traction at the cavity perimeter ($r = a$) can be derived by solving the boundary value problems that govern deformation in both the elastic and cracked regions of the material [15].

For the static cavity expansion, the material response in the elastic region ($r \geq e$) is governed by the equation of equilibrium (A1) and the corresponding boundary conditions.

$$\frac{\partial \sigma_{rr}}{\partial r} + \frac{1}{r}\left(\sigma_{rr} - \sigma_{\theta\theta}\right) = 0 \tag{A1}$$

The plane strain ($\varepsilon_z \equiv 0$), axisymmetric solution of the CCE in an *infinite* medium leads to

$$\sigma_r = \frac{A}{r^2} = -\sigma_\theta, \quad \sigma_z = 0; \quad \varepsilon_r = \frac{1+\nu}{E}\frac{A}{r^2} = -\varepsilon_\theta; \tag{A2}$$

where A is the integration constant. (Note the sign convention: stress and strain components are positive in compression ($A > 0$) and the radial displacement is positive outward.)

The boundary condition at the elastic-cracked interface, $\sigma_\theta\ (r = e) = -\sigma_f$, results in

$$\sigma_\theta(e) = -\frac{A}{e^2} = -\sigma_f \quad \Rightarrow \quad A = \sigma_f\, e^2 \tag{A3}$$

where σ_f represents the indirect tensile strength (i.e., the tensile strength corresponding to splitting under the far-field compression rather than tension; also known as, Brazilian tensile strength).

Consequently, expressions for stresses and particle displacement in the elastic region ($r \geq e$) are

$$\bar{\sigma}_r = \bar{\sigma}_f \left(\frac{e}{r}\right)^2 = -\bar{\sigma}_\theta\ , \quad u_r = \frac{1+\nu}{3(1-2\nu)}\left(\frac{e^2}{r}\right)\bar{\sigma}_f \tag{A4}$$

Hereinafter, the stress components with bar above correspond to non-dimensional counterparts normalized by the bulk modulus K (e.g., $\bar{\sigma}_r = \sigma_r / K$).

In the cracked region ($a \leq r \leq e$), the hoop stress is considered to be zero ($\sigma_\theta = 0$). The material behavior in this region is governed by the equation of equilibrium and the condition of radial stress continuity at the elastic-cracked interface. Thus, the radial traction acting on the cavity surface is:

$$(\bar{\sigma}_r)_{st} = \bar{\sigma}_r(a) = \bar{\sigma}_f \left(\frac{e}{a}\right) \tag{A5}$$

where the subscript *st* indicates the static solution.

Accordingly, in order to determine the radial traction at the cavity surface, it is necessary to determine (e/a). This is achieved by using the mass conservation equation in Eulerian form:

$$\frac{\partial}{\partial r}\left[(r-u)^2\right] = 2r\frac{\rho}{\rho_0} \tag{A6}$$

First, from the pressure-volumetric strain relation, $p = K\,\varepsilon_V = K\,(1 - \rho_0/\rho)$, it follows that

$$\frac{\rho}{\rho_0} = \left(1 - \frac{p}{K}\right)^{-1} = 1 + \frac{p}{K} = 1 + \frac{1}{3}\bar{\sigma}_f\left(\frac{e}{r}\right) \tag{A7}$$

With respect to Eq. (A7), it cannot be overemphasized that the CCE from a *zero initial radius* results in a huge compression (pressure buildup) and the consequent increase of material density.

Thus, by solving the mass conservation equation (A6), the aspect ratio is determined as follows

$$\left(\frac{e}{a}\right) = \frac{1-2\nu}{2(2-\nu)}\left[1 + \sqrt{1 + 6\left(\frac{2-\nu}{1-2\nu}\right)\frac{1}{\bar{\sigma}_f}}\right] \xrightarrow{\bar{\sigma}_f \ll 1} \left(\frac{e}{a}\right) = \sqrt{\frac{3}{2}\frac{(1-2\nu)}{(2-\nu)}\frac{1}{\bar{\sigma}_f}} \tag{A8}$$

A detailed procedure for solving Eq. (A6) is available, for example, in references [15, 17].

Finally, the dimensionless radial traction acting on the perimeter of the cylindrical cavity (for the elastic-cracked case) is obtained in the following form:

$$\sigma_r(a) = \sigma_f\left(\frac{e}{a}\right) \quad \Rightarrow \quad (\bar{\sigma}_r)_{st} = \left(\frac{\sigma_r}{K}\right)_{st} = \sqrt{\frac{3}{2}\frac{(1-2\nu)}{(2-\nu)}\left(\frac{\sigma_f}{K}\right)} \tag{A9}$$

10th International Congress of the Serbian Society of Mechanics
Niš, Serbia, June 18-20, 2025
C.5
Extended abstract

COMPARATIVE VIBRATION STABILITY ANALYSIS OF A COMPLEX MOVING OBJECT WITH TWO NOVEL STABILIZERS

Dunja Milić[1][0000-0002-8356-1553]

[1] Faculty of Mechanical Engineering
University of Niš, Aleksandra Medvedeva 14, 18000 Niš
e-mail: dunja1994milic@gmail.com, stojanovic.s.vladimir@gmail.com

Abstract

This study examines the dynamic stability of beam structures under moving loads, a key challenge in modern railway engineering. Using the D-decomposition method, two stabilization models are analyzed: one with a stabilizer attached to the car body and another with bogie-connected suspensions. The results indicate that car-body connected stabilizers provide larger stability regions, allowing greater variations in stiffness and damping with minimal impact on stability. In contrast, bogie-connected stabilizers are more sensitive to parameter changes, particularly in heavier car bodies. These findings contribute to optimizing railway systems for improved stability and performance.

Key words: Dynamic stability, Mechanical oscillator, Moving loads.

1. Introduction

The study of dynamic stability of beam structures under moving loads is crucial in modern railway engineering, particularly for optimizing high-speed train performance. When a train's velocity exceeds the propagation speed of elastic waves in the track, vibration instability can occur [1]. Previous research by Timoshenko [2] and Verichev and Metrikine [3] established foundational models for analyzing such instabilities. This study investigates the vibrational stability of a complex mechanical oscillator moving on an infinite continuous beam-foundation system, emphasizing the role of additional stabilizers in enhancing the stability of the standard moving system. The three-layer viscoelastic foundation is modeled using Reddy-Bickford beam theory, and stability is analyzed using the D-decomposition method and the argument principle to map stability regions. Understanding the effect of different stabilizer configurations is critical for optimizing both the stability and comfort of modern railway vehicles.

2. Results and Discussion

The considered complex coupled moving oscillator models, as shown in Fig. 1 and Fig. 3, illustrate two different stabilizer configurations—one attached to the car body and the other connected to the bogie suspension system—allowing for a comparative analysis of their effects on stability.

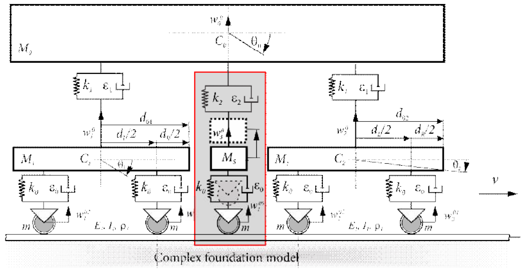

Fig. 1. Complex coupled moving oscillator with stabilizer attached to the car body

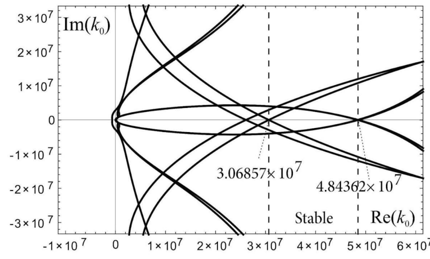

Fig. 2. D-decomposition curves for car body stabilizer (varying damping, constant stiffness)

Stability is assessed by analyzing the roots of the characteristic equation. If any root has a positive real part, the system is considered unstable. To simplify the analysis, the D-decomposition method and the argument principle are applied. The resulting curves (Fig. 2 and Fig. 4) are presented graphically for all considered cases, with a detailed examination of stable regions.

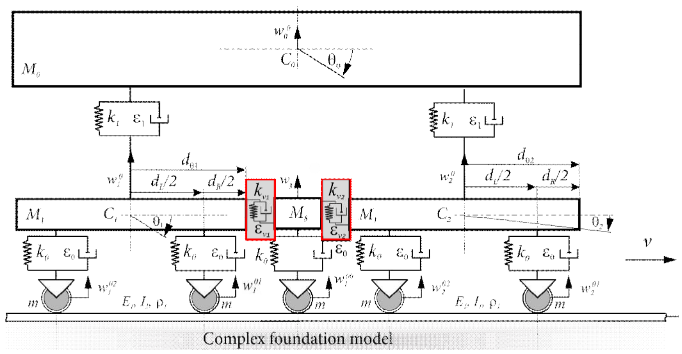

Fig. 3. Complex coupled moving oscillator with stabilizer attached to the bogies

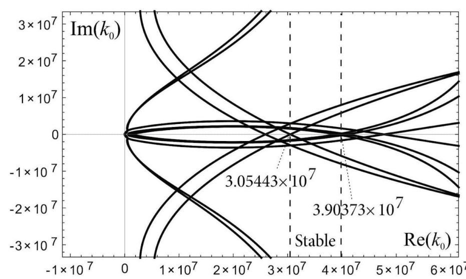

Fig. 4. D-decomposition curves for bogie stabilizer (varying damping, constant stiffness)

3. Conclusions

The stabilizer connected to the car body provided larger stability regions with minimal impact from changes in stiffness and damping, while the bogie-connected stabilizer showed smaller stability regions, with more significant effects from stiffness and damping, especially for heavier car bodies.

References

[1] Stojanović, V., Deng, J., Milić, D., Petković, M.D., *Dynamics of moving coupled objects with stabilizers and unconventional couplings*, Journal of Sound and Vibration, Vol. 570, 118020, 2024.
[2] Timoshenko, S., *Method of analysis of statical and dynamical stresses in rail*, Proceedings of the 2nd International Congress for Applied Mechanics, Zürich, Switzerland, 1-12, 1927.
[3] Verichev, S., Metrikine, A., *Instability of a bogie moving on a flexibly supported Timoshenko beam*, Journal of Sound and Vibration, Vol. 253, 653-668, 2002.

10th International Congress of the Serbian Society of Mechanics
Niš, Serbia, June 18-20, 2025
C.6

Extended abstract

ENERGY BASED FATIGUE DAMAGE MODEL

Zoran B. Perović[1[0000-0002-4633-954X]], **Stanko B. Ćorić**[1[0000-0002-7383-6154]], **Milica D. Koprivica**[1[0009-0005-3510-1877]]

[1] Faculty of Civil Engineering,
The University of Belgrade, Bulevar kralja Aleksandra 73, 11120 Belgrade
e-mail: zperovic@grf.rs , cstanko@grf.rs , mbendic@grf.rs

Abstract

This paper introduces material models for estimating of fatigue damage accumulation and fatigue life. The first - uniaxial material model is defined by connecting units (micro-elements), each with a different value of fracture energy. The unit element also represents an elastoplastic damage model with strain as an input function. By altering the distribution of dissipated energy limits of connected unit elements, various fatigue damage evolution laws are derived. The proposed uniaxial energy-based approach for accumulated damage can be effectively adapted to the multiaxial stress state – the second model. Data analysis from tubular specimens and multiple model parameters are used to establish correlations between fatigue damage and life estimation, highlighting the contributions of different cumulative measures in the critical plane and other material planes.

Key words: cumulative damage, fatigue failure, hysteresis, energy

1. Introduction

Cumulative damage models focus on quantifying and summing damage increments across different loading cycles while analyzing their potential interactions. The presented energy-based model for uniaxial stress state is determined from the unit (element *i* with fracture energy $Q_{f,i}$) based on a hysteretic operator that allows calculating hysteretic energy loss Q_{hys} [1]. In this paper, the total hysteretic energy loss at fracture is referred to as fracture energy, representing the energy released before a unit fractures. However, previous studies [2] have indicated a distinction between plastic energy and the dissipated hysteretic energy calculated using the proposed hysteretic operator. Plastic energy W_p, defined as the area of the hysteresis loop, can also serve as a controlling parameter for unit elimination. Calculating W_p often requires an approximation or numerical procedure which is herein used in the multiaxial stress state, in contrast to the proposed analytical solution for Q_{hys}.

2. Fatigue damage model

In the proposed uniaxial model, the evolution of the damage parameter D (Equation 1) is determined by dividing the number of fractured units (cells) by the total number of elements of the macro model. In Figure 1, n_{el} n_{el} represents a number of unit elements with identical fracture energy limits (maximum value is $Q_{f,max}$) according to the distribution of the corresponding probability density function (Weibull distribution). Since the number of active unit elements decreases through loading history, fatigue damage D at a particular time t of loading is defined by the corresponding value of the cumulative distribution function (*CDF*) for $Q_{el,i}(t) = Q_{f,i}$:

$$D = D(t) = CDF(Q_{el,i}(t) = Q_{f,i}) = 1 - e^{-\left(\frac{1}{\lambda}\cdot\frac{Q_{f,i}}{Q_{f,max}}\right)^{k}} \tag{1}$$

Where parameters of distribution λ and k can vary dynamically in function of loading parameters, enabling different types of damage evolution curves. Figure 1 illustrates the effect of mean stress on S355 steel under random loading, for different values of maximum strain amplitude $\Delta\varepsilon$. For the second model, the main goal is to reduce the complexity of a multiaxial stress state to an equivalent uniaxial damage field. In this case, both elastic and plastic energy is taken into account. Therefore, the evolution of different parameters in specific planes is the core of the presented multiaxial fatigue damage model.

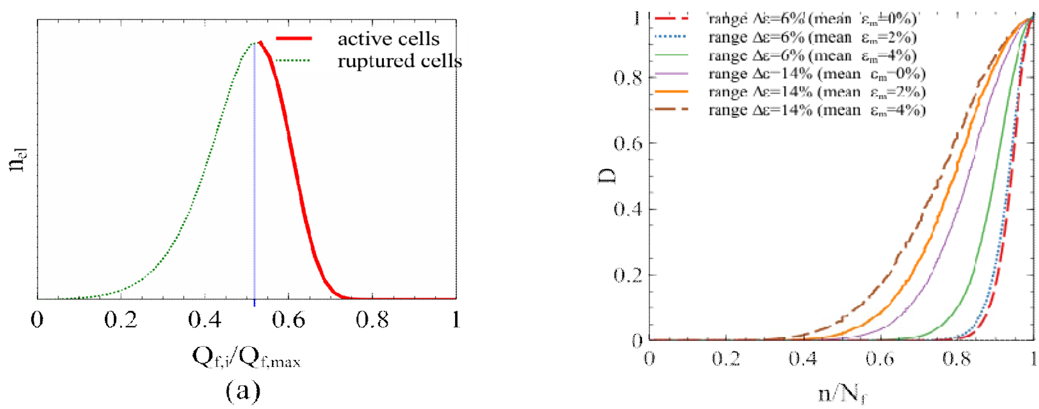

(a) (b)

Fig. 1. (a) Cells` fracture energy distribution; (b) S355 - damage evolution for random loading

3. Conclusions

The proposed model with different types of evolution curves indicates the possibility of modeling various evolution types while accurately predicting the fatigue life. Numerical models provided good agreement with experimental results [3], and the influence of various cumulative measures and on the critical plane and other material planes is highlighted as well.

References

[1] V. Lubarda, D. Sumarac, and D. Krajcinovic, "Hysteretic Response of Ductile Materials Subjected to Cyclic Loads," *Recent Adv. Damage Mech. Plast.*, vol. 123, pp. 145–157, 1992.

[2] D. Sumarac and Z. Perovic, "Cyclic plasticity of trusses," *Arch. Appl. Mech.*, vol. 85, pp. 1513–1526, 2015, doi: 10.1007/s00419-014-0954-7.

[3] N. Shamsaei, M. Gladskyi, K. Panasovskyi, S. Shukaev, and A. Fatemi, "Multiaxial fatigue of titanium including step loading and load path alteration and sequence effects," *Int. J. Fatigue*, vol. 32, no. 11, pp. 1862–1874, Nov. 2010, doi: 10.1016/j.ijfatigue.2010.05.006.

10th International Congress of the Serbian Society of Mechanics
Niš, Serbia, June 18-20, 2025

C.7

Extended abstract

VIBRATION CHARACTERISTICS OF 3D PRINTED STEPPED CANTILEVER BEAM

M. Pjević[1[0000-0002-4454-8663]], **A. Tomović**[1[0000-0002-8462-8086]], **M. Veg**[1[0000-0002-6702-6251]],
N. Zorić[1[0000-0001-5664-2924]], **V. M. Popović**[1[0000-0003-1836-6345]]

[1] Faculty of Mechanical Engineering,
The University of Belgrade, Kraljice Marije 16, 11120 Belgrade
e-mail: mpjevic@mas.bg.ac.rs, atomovic@mas.bg.ac.rs, mveg@mas.bg.ac.rs, nzoric@mas.bg.ac.rs, mpopovic@mas.bg.ac.rs

Abstract

This study aims to present the first three natural frequencies of a stepped 3D printed cantilever beam with an eccentrically placed rigid body at free end. Both, analytical and FEM approach are implemented, also an experiment is conducted. The first natural frequencies are computed to have the same values. The Euler-Bernoulli constitutive theory is implemented for modeling due to the characteristics of cantilever beams (L/D).

Key words: Euler-Bernoulli cantilever beam, natural frequencies, optimized shape.

1. Introduction

In this paper a straight, stepped elastic 3D printed beam of length $L = 600\ mm$ is considered. The undeformed condition is presented in Fig. 1. The first three natural frequencies are determined using experimental setup, finite element method and symbolic-numeric methods of initial parameters in differential form (SNMIP).

2. Problem statement

In Figure 1, the stepped cantilever beam of circular cross-sectional profile with constant diameters $d_1 = 12\ mm$, $d_2 = 10\ mm$ and $d_3 = 8\ mm$ with the following segment lengths $L_1 = L_2 = L_3 = 200\ mm$ is presented. The specimen is made of PLA material using FFF/FDM 3D printing technology. A rigid body is fixed at free end of the cantilever beam. The mass center of the body is eccentrically displaced with respect to the beam end. Longitudinal and transverse vibrations mode shapes are coupled based on the boundary conditions.

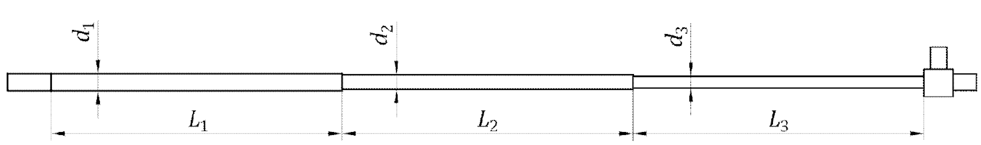

Fig. 1. Stepped cantilever beam with a tip rigid body

The partial differential equations for the transverse and longitudinal vibrations of the beam read respectively:

$$\frac{\square}{\partial z}[F_t(z,t)] - \rho(z)A(z)\frac{\partial^2 w(z,t)}{\partial t^2} = 0, \qquad \frac{\partial}{\partial z}[F_a(z,t)] - \rho(z)A(z)\frac{\partial^2 u(z,t)}{\partial t^2} = 0.\#(1)$$

Natural frequencies are presented in Table 1.

Source	f_1 [Hz]	f_2 [Hz]	f_3 [Hz]
Experiment	3.4	28.8	85.4
FEM	3.0072	27.355	78.577
SNMIP	3.1222	28.0281	77.4511

Table 1. First three frequencies of cantilever beam

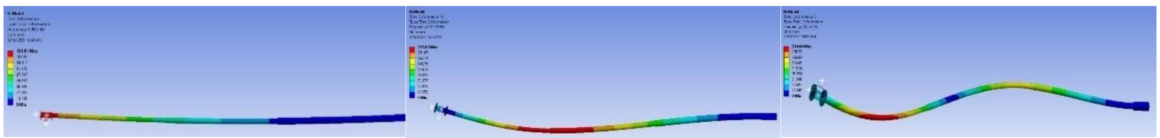

1. mode 2. mode 3. mode

Fig. 2. Mode shapes

Acknowledgement:

The research was funded by the Ministry of science, technological development and innovations of the Republic of Serbia, contract number 451-03-137/2025-03/ 200105.

References

[1] Šalinić S, Obradović A, Tomović A. Free vibration analysis of axially functionally graded tapered, stepped, and continuously segmented rods and beams. Compos Part B. 2018;150:135-143.
[2] Tomović A, Šalinić S, Obradović A, Zorić N, Mitrović Z. Coupled bending and axial vibrations of axially functionally graded Euler-Bernoulli beams. J Vibration Eng Technol. 2024;12:2987-3004. doi:10.1007/s42417-023-01027-y.
[3] Nikolić A. Free vibration analysis of a non-uniform axially functionally graded cantilever beam with a tip body. Arch Appl Mech. 2017;87:1227-1241.
[4] Tomović A. Influence of boundary conditions on natural frequencies of axially functionally graded Euler-Bernoulli cantilever beam with attached rigid body at the free end. In: Mathematics, Numerics and Applications, MNA 2022, Budva, Montenegro. University of Belgrade, Faculty of Mechanical Engineering; 2022 Jun 1-3.
[5] Veg M, Tomović A, Šiniković G, Dikić S, Zorić N, Šalinić S, Obradović A, Mitrović Z. Experimental and numerical approach to natural frequency of tapered 3D printed cantilever beam with a tip body. In: Proceedings of the 9th International Congress of the Serbian Society of Mechanics. Vrnjačka Banja, Serbia: Serbian Society of Mechanics; 2023 Jul 5-7. ISBN 978-86-909973-9-8.
[6] Tomović A, Šalinić S, Obradović A, Lazarević M, Mitrović Z. The exact natural frequency solution of a free axial-bending vibration problem of a non-uniform AFG cantilever beam with a tip body. In: Proceedings of the 7th International Congress of Serbian Society of Mechanics. Sremski Karlovci, Serbia; 2019 Jun 24-26. ISBN 978-86-909973-7-4. p. 1-10.
[7] Rao S. S., Vibration of Continuous Systems. Hoboken, New Jersey: John Wiley & Sons inc., 2007.

C.8

Extended abstract

VIBRATION CHARACTERISTICS OF AN OPTIMIZED CANTILEVER BEAM

A. Tomović[1][0000-0002-8462-8086], **M. Pjević**[1][0000-0002-4454-8663], **M. Veg**[1][0000-0002-6702-6251], **A. Obradović**[1][0000-0001-8808-6627], **Z. Mitrović**[1][0000-0002-7139-5658]

[1] Faculty of Mechanical Engineering,
The University of Belgrade, Kraljice Marije 16, 11120 Belgrade
e-mail: atomovic@mas.bg.ac.rs, mpjevic@mas.bg.ac.rs, mveg@mas.bg.ac.rs, aobradovic@mas.bg.ac.rs, zmitrovic@mas.bg.ac.rs

Abstract

This study aims to present the first three natural frequencies of 3D printed cantilever beams with eccentrically placed rigid bodies at free end. The analytical approach (the symbolic-numeric methods of initial parameters in differential form) is implemented and natural frequencies are computed from the characteristic equation. The first natural frequencies are computed to have the same values. The Euler-Bernoulli constitutive theory is implemented for modeling due to the characteristics of cantilever beams (L/D).

Key words: Euler-Bernoulli cantilever, in-plane vibrations, optimization

1. Introduction

In this paper straight elastic 3D printed beams of length $L = 250\,mm$ are considered. Their undeformed condition is presented in Figures 1 and 2. The first natural frequency of 9 Hz is the criterion for the computation of starting diameters of beams.

2. Problem Statement and Discussion of Results

In Figure 1, the cantilever beam of circular cross-sectional profile with constant diameter $d = 6.5\,mm$ is presented, while in Figure 2 the optimized beam is given.

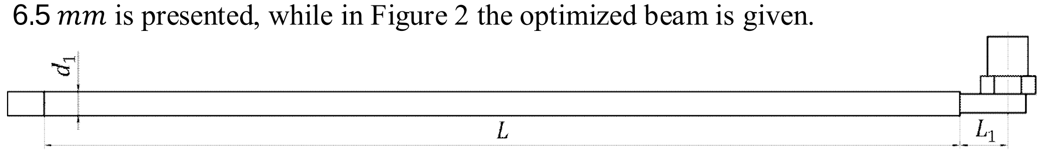

Fig 1. A cantilever beam with a tip placed rigid body

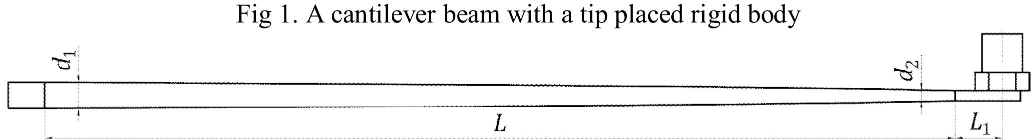

Fig 2. Optimized shape of a cantilever beam with a tip placed rigid body

Optimization criterion for the second beam is the minimal material consumption (mass minimization) in beam manufacturing in order to obtain the desired first natural frequency of 9 Hz. For manufacturing of the specimens, the PLA material is used with FFF/FDM 3D printing technology. A rigid body is fixed at the free end of the cantilever beam. The mass center of the rigid body is eccentrically displaced to the end of the beam, both axially and transversally. These eccentricities grant the coupling in longitudinal and transverse vibrations by boundary conditions.

The partial differential equations for the transverse and longitudinal vibrations of the beam read respectively:

$$\frac{\square}{\partial z}[F_t(z,t)] - \rho(z)A(z)\frac{\partial^2 w(z,t)}{\partial t^2} = 0, \qquad \frac{\partial}{\partial z}[F_a(z,t)] - \rho(z)A(z)\frac{\partial^2 u(z,t)}{\partial t^2} = 0. \#(1)$$

Optimization of beam shape using mass minimization is conducted using the Pontryagin's maximum principle. The following polynomial function is obtained by interpolation of diameter with a 5 mm step in axial direction:

$$D(z) = -1.148z^4 + 0.3683z^3 - 0.06043z^2 - 0.007329z + 0.00719. \#(2)$$

In Table 1, the natural frequencies are presented for both cantilever beams.

Diameter	f_1 [Hz]	f_2 [Hz]	f_3 [Hz]
Constant	9.00273	70.553	186.003
Optimized	8.99459	36.5187	119.976

Table 1. First three frequencies of cantilever beams

Acknowledgement:

The research was funded by the Ministry of science, technological development and innovations of the Republic of Serbia, contract number 451-03-137/2025-03/ 200105.

References

[1] Šalinić S, Obradović A, Tomović A. Free vibration analysis of axially functionally graded tapered, stepped, and continuously segmented rods and beams. Compos Part B. 2018;150:135-143.
[2] Obradović A, Jeremić B, Tomović A, Šalinić S, Mitrović Z. Mass minimization of axially functionally graded Euler–Bernoulli beams with coupled bending and axial vibrations. Mech Solids. 2024;59:1358–1375. doi:10.1134/S002565442460260X.
[3] A. Obradović, S. Šalinić, and A. Grbović, "Mass minimization of an Euler-Bernoulli beam with coupled bending and axial vibrations at prescribed fundamental frequency," Eng. Struct. 228, 111538 (2021) https://doi.org/10.1016/j.engstruct.2020.111538
[4] Tomović A, Šalinić S, Obradović A, Zorić N, Mitrović Z. Coupled bending and axial vibrations of axially functionally graded Euler-Bernoulli beams. J Vibration Eng Technol. 2024;12:2987-3004. doi:10.1007/s42417-023-01027-y.
[5] Veg M, Tomović A, Šiniković G, Dikić S, Zorić N, Šalinić S, Obradović A, Mitrović Z. Experimental and numerical approach to natural frequency of tapered 3D printed cantilever beam with a tip body. In: Proceedings of the 9th International Congress of the Serbian Society of Mechanics. Vrnjačka Banja, Serbia: Serbian Society of Mechanics; 2023 Jul 5-7. ISBN 978-86-909973-9-8.

10th International Congress of the Serbian Society of Mechanics
Niš, Serbia, June 18-20, 2025
C.9
Original Scientific Paper

DOI:10.46793/ICSSM25.159T

PREDICTIVE REANALYSIS IN STRUCTURAL DYNAMICS

Nataša R. Trišović[1][0000-0003-1043-5780]**, Tamas Mankovits**[2][0000-0001-7245-6443]**,**
Ana S. Petrović[1][0000-0002-5996-1485]

[1]Faculty of Mechanical Engineering, University of Belgrade, Serbia
e-mail: ntrisovic@mas.bg.ac.rs, aspetrovic@mas.bg.ac.rs,

[2]University of Debrecen, Department of Mechanical Engineering, Hungary
e-mail: tamas.mankovits@eng.unideb.hu

Abstract

Predictive reanalysis has emerged as a vital computational strategy in structural dynamics, enabling efficient updates of structural response predictions following minor modifications in geometry, material properties, or boundary conditions, without resorting to full re-computation. Traditionally rooted in finite element methods, reanalysis techniques have evolved through the integration of Artificial Intelligence (AI) models, offering unprecedented speed and adaptability in dynamic system assessments. This paper provides a comprehensive overview of predictive reanalysis approaches, with an emphasis on recent AI-assisted methodologies. The synergy between data-driven models such as neural networks, decision trees and ensemble learning and physics-based simulations enables more accurate prediction of structural behavior under varying operational scenarios. The application of machine learning has demonstrated significant potential in reducing computational costs, increasing adaptability and enhancing real-time monitoring capabilities in engineering systems. A numerical case study is presented, involving a cantilever beam discretized into five finite elements. The analysis explores how changes in cross-sectional properties at various segments affect the first natural frequency. Predictive AI models are employed to estimate frequency shifts and their performance is compared against classical empirical formulas. The results validate the ability of trained AI models to generalize the influence of structural variations and support decision-making in early design or maintenance phases. The study also highlights current challenges in predictive reanalysis, including data scarcity, model interpretability and integration with real-time monitoring systems. Future directions are outlined, focusing on hybrid modeling techniques, improved data acquisition strategies and the development of standardized benchmarks for AI-assisted structural reanalysis. Ultimately, this work contributes to the growing body of research bridging computational mechanics and machine intelligence, fostering more resilient, adaptive and efficient structural systems.

Keywords: natural frequency estimation, predictive reanalysis, artificial intelligence, FEM, structural dynamic

1. Introduction

In the context of modern engineering practice, structural systems are increasingly subjected to variable conditions throughout their service life, including alterations in load, damage accumulation, retrofitting interventions and changing boundary constraints. Under such circumstances, the ability to rapidly and accurately assess a structure's response becomes crucial for ensuring safety, performance and sustainability. Reanalysis methods have emerged as efficient computational tools that enable the prediction of a modified structure's response without the need to repeat the entire finite element (FE) analysis from scratch. These techniques leverage information from the original analysis to significantly reduce computational effort, particularly useful when iterative modifications are required during the design, optimization, or maintenance processes. With the advent of advanced data-driven techniques, Artificial Intelligence (AI) has increasingly been adopted to augment classical reanalysis approaches. AI models, particularly those based on machine learning and neural networks can learn from existing datasets and predict structural behavior under new conditions with high accuracy. This is especially valuable in dynamic analysis, where computational complexity and real-time constraints often pose limitations for traditional methods. This paper explores the integration of predictive reanalysis and AI in structural dynamics, providing a conceptual and practical foundation for future research and engineering applications.

2. Literature Review

2.1 Classical Approaches to Reanalysis

Traditional reanalysis methods have laid the groundwork for evaluating structural changes without re-solving the full system from scratch. These methods include direct stiffness modification, sensitivity analysis and the use of modal superposition techniques. While AI methods are rapidly evolving, traditional computational tools such as the Finite Element Method (FEM) remain essential for structural analysis, providing robust and accurate numerical solutions for evaluating stresses, deformations, and vibrations (Bathe, 1982). Sensitivity-based approaches, such as those developed by Sergeyev and Mroz (2000), focus on assessing how variations in structural parameters (e.g., cross-sectional dimensions, material properties) influence stress and frequency responses. Their work on 3D frame structures has significantly contributed to optimal structural design under multiple constraints. Similarly, studies on truss structures with frequency constraints have established the theoretical existence of solutions to such optimization problems, enabling more reliable and efficient designs (Tong et al., 2000). These classical methods emphasize deterministic formulations and linear or weakly nonlinear assumptions, which are efficient for engineering applications with limited design variations.

2.2 AI-Based Approaches to Reanalysis

Recent research highlights the growing application of artificial intelligence (AI) and machine learning (ML) techniques in structural engineering, particularly in areas such as design optimization, damage detection, and structural analysis. Neural networks have been successfully applied to predict the impact of preload location on the natural frequencies of cantilever beams, showcasing the ability of AI models to capture complex dynamic behavior in structural systems (Paridie et al., 2022). In parallel, convolutional neural networks (CNNs) and deep learning approaches have demonstrated powerful capabilities in pattern recognition tasks, such as image detection and classification, suggesting their potential utility in structural condition monitoring (Cynthia et al., 2022). Reinforcement learning methods are increasingly being explored for structural design tasks. For instance, recent studies have shown that reinforcement learning agents can autonomously learn to optimize structural layouts through iterative trial-and-error processes, offering promising directions for automated structural design (Rochefort-Beaudoin et al., 2024). Optimization techniques have also been a major area of focus, particularly for enhancing structural performance under specific constraints. The integration of AI with traditional engineering methods continues to expand, especially in performance prediction and classification tasks. Machine learning algorithms have been employed to classify and predict the behavior of reinforced masonry shear walls, enabling faster and more accurate assessments (Siam et al., 2019). Thai (2022) provided a comprehensive review emphasizing the broad applications of machine learning in structural engineering, including damage detection, health monitoring, and optimization processes. Beyond structural applications, machine learning models have proven valuable in environmental modeling, such as enabling smart downscaling of extreme precipitation events, illustrating the cross-disciplinary relevance of AI tools (Shi, 2020). Similarly, hybrid AI-physical modeling approaches have been used to correct penetration biases in radar-derived elevation models, showcasing the ability of AI to enhance the accuracy of remote sensing data (Mansour et al., 2025). Optimization of complex structures also benefits from combining AI algorithms with finite element simulations. For instance, genetic algorithms have been successfully utilized for the structural optimization of steel arch bridges, achieving material savings while ensuring performance (Feng et al., 2020). Deep reinforcement learning has been coupled with topology optimization to enhance the design of elementally discretized domains, enabling more efficient exploration of large design spaces (Brown et al., 2022). Nguyen and Tuan (2020) also explored the application of AI in structural optimization, highlighting how machine learning models can support the generation of optimal structural designs with improved efficiency. In the environmental domain, Zhou, Zhang, and Qiu (2024) reviewed the application of machine learning and optimization algorithms in evaluating the environmental effects of blasting, emphasizing the role of AI in complex environmental impact assessments. Finite Element Model Updating (FEMU) remains a critical technique for improving the accuracy of structural models, and recent reviews have systematically analyzed methods for model updating to enhance structural assessment accuracy (Ereiz et al., 2022). In particular, combining deep learning methods with FEMU has enabled more accurate structural damage detection, surpassing traditional approaches in terms of sensitivity and precision (Lee et al., 2023). Finally, the optimization of composite structures through multi-disciplinary design optimization (MDO) has been thoroughly reviewed, showing how integrated optimization strategies leveraging AI can lead to lighter, more efficient, and higher-performance composite designs (Ghadge et al., 2022). These developments collectively demonstrate that the fusion of AI techniques with traditional engineering analysis offers powerful tools for advancing the fields of structural optimization, health monitoring, and sustainable design.

Criteria	Classical Methods	AI-Based Methods
Theoretical Foundation	Based on physics-based models and deterministic formulations	Based on data-driven models, statistical learning and optimization
Accuracy	High for linear and well-defined problems	High for nonlinear, complex, or uncertain systems with sufficient data
Computational Efficiency	Generally efficient for small to medium-scale problems	Requires training time; efficient during inference
Scalability	Limited by complexity of analytical formulations	Scalable to high-dimensional problems
Interpretability	High interpretability due to physical basis	Often low; black-box nature (can be mitigated with explainable AI)
Flexibility	Limited adaptability to changes in boundary or material conditions	High flexibility; models can learn from changing data and conditions

Data Dependency	Low; relies on predefined equations and parameters	High; performance strongly depends on quality and quantity of training data
Typical Applications	Stress and frequency sensitivity, shape optimization, linear systems	Nonlinear dynamics, damage detection, predictive modeling

Table 1. Comparative Overview of Classical and AI-Based Reanalysis Approaches

3. Current Applications and Methods

Predictive reanalysis has become widely used in engineering, particularly in structural dynamics, enhancing the safety, durability, and performance of structures. Traditional reanalysis methods are increasingly supplemented by Artificial Intelligence (AI)-based techniques, offering more adaptive and scalable solutions.

3.1 Optimization of Structural Designs

Machine learning algorithms are now a key tool for optimizing structural designs, enabling engineers to efficiently explore complex design spaces and identify cost-effective, sustainable solutions. By integrating predictive reanalysis, AI methods improve the design workflow, helping to create safer structures. Genetic algorithms combined with finite element models (FEM) have been effectively used to minimize material usage while maintaining strength, iteratively evolving design configurations and simulating behavior under varying loads. Deep reinforcement learning has further advanced the optimization of large structures, such as high-rise buildings, by adaptively fine-tuning design parameters to balance efficiency and cost. Overall, AI-driven optimization reduces manual effort, speeds up design iterations, and offers deeper insight into performance predictions under various conditions.

3.2 Finite Element Method (FEM) Integration

FEM remains fundamental in structural analysis, but when combined with AI approaches, its potential expands significantly. AI models trained on FEM data such as displacement, stress, and natural frequencies enhance damage detection, optimization, and reanalysis, especially for non-linear systems. AI also improves FEM model calibration by automating the adjustment of parameters to align simulations with experimental data. Additionally, integrating machine learning with FEM strengthens structural health monitoring, allowing early and precise damage detection based on vibration or strain data. AI-based optimization further refines FEM applications by optimizing structural shapes and material layouts, leading to lighter and stronger designs. This synergy between FEM and AI is reshaping structural engineering, offering faster, more accurate, and intelligent solutions for complex challenges.

4. Challenges and Future Directions

The integration of Artificial Intelligence (AI) with traditional structural analysis methods such as Finite Element Method (FEM) has opened new avenues for the advancement of predictive reanalysis and optimization in structural engineering. However, despite the numerous benefits, there are still significant challenges to overcome before AI can be fully utilized in real-world applications. These challenges not only span technical limitations but also deal with data, model interpretability and the need for interdisciplinary expertise.

4.1 Challenges

The implementation of artificial intelligence in structural health monitoring and predictive reanalysis encounters several critical challenges. A primary concern is the limited availability and quality of data. Structural engineering often suffers from insufficient, noisy or incomplete datasets, hindering the development of robust AI models. Furthermore, the inherent complexity and limited interpretability of advanced models, such as deep neural

networks, present significant obstacles in safety-critical applications, where transparency and trust in predictions are essential. The integration of AI with established engineering systems also remains difficult, as it requires both technical adaptation and a shift from traditional methodologies. Finally, achieving model generalization across diverse structural types and varying environmental conditions poses an ongoing challenge, often necessitating extensive retraining to maintain predictive reliability.

4.2 Future Directions

Future advancements in structural engineering are expected to center around the development of hybrid AI and FEM models, combining data-driven approaches with physics-based methods to improve model generalization and interpretability. Techniques such as transfer learning and the inclusion of physical constraints offer promising strategies to address current limitations. Real-time structural health monitoring will become increasingly feasible as sensor technologies advance, enabling AI models to detect damage and predict maintenance needs with minimal human intervention. Furthermore, the integration of multimodal sensor data through data fusion techniques will enhance the robustness and reliability of predictive models. Progress in this field will also require stronger interdisciplinary collaboration between structural engineers, computer scientists and data scientists to ensure practical and effective AI solutions. Finally, the evolution of safety protocols and regulatory standards will be essential to support the responsible application of AI in critical infrastructure, ensuring that models are validated, transparent and trustworthy.

5. Numerical Example: Cantilever Beam with 5 Elements and Cross-Sectional Changes Impact on First Frequency

To illustrate the impact of cross-sectional changes on the first natural frequency of a cantilever beam, we analyze a beam divided into five finite elements. This example explores how modifications to the height of each section affect the first natural frequency. The beam's dynamic behavior is governed by stiffness and mass distribution along its length.

Element	Height Change (%)	Empirical Frequency (Hz)	Formula-Based Frequency (Hz)[1]
Element 1	+10%	165.87	161.66
Element 2	+10%	154.83	153.87
Element 3	+10%	147.00	145.00
Element 4	+10%	143.50	142.20
Element 5	+10%	142.50	142.00
Element 1	-10%	128.00	125.50
Element 2	-10%	134.50	133.00

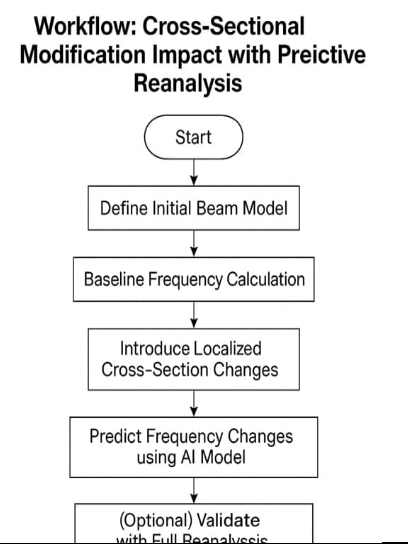

[1] Trišović, N, PhD Thesis, [18]

Element 3	-10%	138.00	137.00
Element 4	-10%	140.00	139.00
Element 5	-10%	140.90	140.50

Table 2. Influence of Height Modifications on Cantilever Beam Frequencies

Picture 1. Workflow: Cross-Sectional Modification Impact with Predictive Reanalysis

5.1 Beam Model Description

The cantilever beam is modeled with five finite elements, each with a potentially variable cross-sectional height. The first natural frequency is computed for different scenarios of localized height variation (both increases and decreases). The reference frequency for the unmodified beam is 141.91 Hz and the analysis will focus on how cross-sectional modifications influence this baseline (Table 2).

5.2 Interpretation of Results

The conducted analysis highlights how localized cross-sectional modifications along a cantilever beam influence its first natural frequency. Increasing the cross-section near the fixed support (Element 1) results in the most pronounced rise in the frequency. This outcome is expected, given that the fixed end of the cantilever experiences the highest bending moments and any enhancement in stiffness at this location greatly improves the beam’s dynamic response. Conversely, reducing the cross-sectional area at the fixed support leads to a significant decrease in the natural frequency, weakening the beam where it is most critical. Moving toward the first third of the beam (Element 2), increasing the height still positively affects the frequency, although the impact is somewhat less dramatic than at the fixed end. This section continues to carry substantial bending moments, meaning that changes here still play an important role in the overall stiffness and dynamic performance of the structure. At the mid-span (Element 3), modifications produce a moderate effect. While stiffness changes at this location influence the natural frequency, their impact is less pronounced compared to areas closer to the support, owing to the reduced bending moments in the beam's middle portion. Closer to the free end (Element 4), alterations in cross-sectional height cause only slight variations in the natural frequency. Since the bending moments here are relatively small, local changes in stiffness have limited influence on the global behavior of the beam. Finally, at the free end (Element 5), changes to the cross-section have minimal impact. Both mass and stiffness modifications at the tip do not significantly affect the beam’s first natural frequency, reflecting the cantilever's typical dynamic characteristics where the end is least sensitive to structural alterations.

5.3 Application of Predictive Reanalysis Using Artificial Intelligence

The results of localized cross-sectional modifications serve as an ideal basis for predictive reanalysis methodologies supported by artificial intelligence (AI). By training machine learning models on datasets that correlate geometric changes with resulting dynamic properties (such as natural frequencies), it becomes possible to predict the structural behavior of modified beams without performing full finite element reanalysis for each variation. In the context of the cantilever beam, AI algorithms such as neural networks, support vector machines, or regression-based models can be employed to: (a) Predict the first natural frequency based on the pattern and location of cross-sectional changes, (b) Identify critical regions where geometric modifications significantly influence dynamic behavior, (c) Suggest optimal modification strategies to achieve target frequency ranges without extensive computation.

This approach significantly reduces computational time and enables real-time sensitivity analysis and design optimization, which is particularly valuable in applications involving adaptive structures, maintenance planning and rapid prototyping. Furthermore, combining AI-driven predictions with classical mechanical models ensures both physical plausibility and computational efficiency, paving the way for intelligent frameworks in structural health monitoring and dynamic optimization. To improve the predictive analysis of cantilever beams, various AI models can be utilized. Artificial Neural Networks (ANNs) and Support Vector Machines (SVMs) capture complex relationships between geometry, material properties and natural frequencies. Random Forests (RF) offer robust predictions and feature importance insights, while Genetic Algorithms (GAs) enable design optimization. For time-dependent behavior, Recurrent Neural Networks (RNNs) and Long Short-Term Memory (LSTM) networks are effective. K-Nearest Neighbors (K-NN) provide simple predictions for moderate datasets and Gaussian Processes (GPs) offer valuable uncertainty estimates. Deep Reinforcement Learning (DRL) stands out for autonomous optimization of beam configurations through interaction and learning.

6. Concluding Remarks

This paper has explored the integration of artificial intelligence (AI) models into the reanalysis of structural systems, with a focus on cantilever beams and their dynamic behavior, particularly their natural frequencies. Through a combination of classical methods and advanced AI techniques, we have illustrated how the evolution of design parameters, such as cross-sectional changes and boundary conditions, impacts the structural performance of beams. The study demonstrated that AI models, including artificial neural networks (ANNs), support vector machines (SVMs), random forests (RF) and genetic algorithms (GA), offer significant improvements in predicting the dynamic characteristics of structures. These models excel in capturing complex, nonlinear relationships between design variables and output parameters, providing a more accurate and efficient means of structural reanalysis compared to traditional methods. Furthermore, the incorporation of AI techniques not only enhances predictive accuracy but also enables the optimization of structural designs and real-time monitoring through structural health monitoring (SHM) systems. Through the numerical example of a cantilever beam with five finite elements, the study highlighted how changes in cross-sectional properties influence the beam's first natural frequency. The results also illustrated the complex interplay between various design parameters, demonstrating the utility of AI models in identifying optimal configurations for improved structural performance. In addition to demonstrating the potential of AI in reanalysis, the paper discussed the challenges associated with AI model integration, such as the need for high-quality data, computational resources and model interpretability. It also pointed to future directions in the field, emphasizing the importance of combining AI with traditional engineering approaches for more holistic, efficient and sustainable design processes. The potential for real-time structural monitoring, optimization and decision-making through AI further adds to the transformative impact AI could have on the field of structural engineering. Ultimately, the combination of AI and structural reanalysis paves the way for more intelligent, adaptive and resilient engineering systems. As AI technologies continue to evolve, their role in the design, optimization and maintenance of critical infrastructure will only expand, driving advancements in the efficiency, safety and sustainability of engineering practices. The research presented here serves as a foundation for future studies and applications of AI in structural engineering, offering valuable insights for engineers, researchers and industry professionals interested in harnessing the power of AI for more accurate, cost-effective and optimized structural designs.

7. Acknowledgment

This research is supported by the Ministry of Science, Technological Development and Innovation of the Republic of Serbia, under the 2024 Agreement on Financing Scientific Research, No. 451-03-137/2025-03/200105, dated February 4, 2025, Serbian-Hungarian Bilateral Cooperation for the Years 2025-2026: Structural optimization of additively manufactured cellular titanium implant using artificial intelligence. Additional support provided by COST (European Cooperation in Science and Technology) CA21155, CA23138, CA23109 and CA21106.

8. References

[1] Paridie, A. M., Ene, N. M., Mohamed, Y. S. (2022). Using neural networks to predict the effect of the preload location on the natural frequencies of a cantilever beam. Heliyon, 8(11), e11242. https://doi.org/10.1016/j.heliyon.2022.e11242

[2] Cynthia, E. P., Ismanto, E., Arifandy, M. I., Sarbaini, S., Nazaruddin, N., Manuhutu, M. A., Akbar, M. A., Abdiyanto. (2022). Convolutional neural network and deep learning approach for image detection and identification. Journal of Physics: Conference Series, 2394(1), 012019. https://doi.org/10.1088/1742-6596/2394/1/012019

[3] Rochefort-Beaudoin, T., Vadean, A., Aage, N., Achiche, S. (2024). Structural design through reinforcement learning (arXiv:2407.07288). https://arxiv.org/abs/2407.07288

[4] Bathe, K. J. (1982). *Finite Element Procedures in Engineering Analysis*. Prentice-Hall.

[5] Sergeyev, O., Mroz, Z. (2000). Sensitivity analysis and optimal design of 3D frame structures for stress and frequency constraints. *Computers and Structures*, 75(2), 167–185.

[6] Tong, W. H., Jiang, J. S., Liu, G. R. (2000). Solution existence of the optimization problem of truss structure with frequency constraints. *International Journal of Solids and Structures*, 37(30), 4043–4060.

[7] Siam, A., Ezzeldin, M., El-Dakhakhni, W. (2019). Machine learning algorithms for structural performance classifications and predictions: Application to reinforced masonry shear walls. Structures, 22, 252–265. https://doi.org/10.1016/j.istruc.2019.06.017

[8] Thai, H.-T. (2022). Machine learning for structural engineering: A state-of-the-art review. Structures, 38, 448–491. https://doi.org/10.1016/j.istruc.2022.02.003

[9] Shi, X. (2020). Enabling smart dynamical downscaling of extreme precipitation events with machine learning. Geophysical Research Letters, 47(19), e2020GL090309. https://doi.org/10.1029/2020GL090309

[10] Mansour, I., Fischer, G., Haensch, R., Hajnsek, I. (2025). Hybrid AI-physical modeling for penetration bias correction in X-band InSAR DEMs: A Greenland case study. arXiv. https://doi.org/10.48550/arXiv.2504.08909

[11] Feng, Y., Wang, C., Briseghella, B., Fenu, L., Zordan, T. (2020). Structural optimization of a steel arch bridge with genetic algorithm. Structural Engineering International, 31(3), 347-356. https://doi.org/10.1080/10168664.2020.1773373

[12] Brown, N. K., Garland, A. P., Fadel, G. M., Li, G. (2022). Deep reinforcement learning for engineering design through topology optimization of elementally discretized design domains. Materials & Design, 218, 110672. https://doi.org/10.1016/j.matdes.2022.110672

[13] Nguyen, T.-H., Tuan, V. A. (2020). Application of artificial intelligence for structural optimization. In The International Conference on Modern Mechanics and Applications ICOMMA 2020 (pp. 82). https://doi.org/10.1007/978-981-16-3239-6_82

[14] Zhou, J., Zhang, Y., & Qiu, Y. (2024). State-of-the-art review of machine learning and optimization algorithms applications in environmental effects of blasting. Artificial Intelligence Review, 57(5). https://doi.org/10.1007/s10462-023-10636-8

[15] Ereiz, S., Duvnjak, I., & Jiménez-Alonso, J. F. (2022). Review of finite element model updating methods for structural applications. Structures, 41, 684–723. https://doi.org/10.1016/j.istruc.2022.05.041

[16] Lee, Y., Kim, H., Min, S., et al. (2023). Structural damage detection using deep learning and FE model updating techniques. Scientific Reports, 13, 18694. https://doi.org/10.1038/s41598-023-46141-9

[17] Ghadge, R., Ghorpade, R., & Joshi, S. (2022). Multi-disciplinary design optimization of composite structures: A review. Composite Structures, 280, 114875. https://doi.org/10.1016/j.compstruct.2021.114875

[18] Trišović, N. (2007). Developed procedure for dynamic reanalysis of structures. *PhD Thesis,* FMEUB, Belgrade

10th International Congress of the Serbian Society of Mechanics
Niš, Serbia, June 18-20, 2025
C.10

Extended abstract

MODE ORTHOGONALITY CONDITIONS OF SPATIAL VIBRATIONS OF AN EULER-BERNOULLI CANTILEVER BEAM WITH AN ECCENTRIC RIGID TIP LOAD

M. Veg[1][0000-0002-6702-6251], A. Tomović[1][0000-0002-8462-8086], A. Obradović[1][0000-0001-8808-6627], S. Šalinić[2][0000-0002-8146-5461], Yu. D. Selyutskiy[3][0000-0001-8477-6233]

[1] Faculty of Mechanical Engineering,
University of Belgrade, Kraljice Marije 16, 11120 Belgrade 35
e-mail: mveg@mas.bg.ac.rs, atomovic@mas.bg.ac.rs, aobradovic@mas.bg.ac.rs
[2] Faculty of Mechanical and Civil Engineering in Kraljevo,
University of Kragujevac, Dositejeva 19, 36 000 Kraljevo, Serbia
e-mail: salinic.s@mfkv.kg.ac.rs
[3] Institute of Mechanics, Moscow State University, Michurinskiy pr. 1, Moscow, 119192, Russia
e-mail: seliutski@imec.msu.ru

Abstract :

Presented here in matrix form are the orthogonality conditions for spatial vibrations of an Euler-Bernoulli cantilever beam with a variable circular cross-section, constructed from an axially functionally graded (AFG) material. An eccentrically positioned rigid body is fixed to its free end, thus leading to complete coupling of transverse vibrations in the two orthogonal planes, longitudinal and torsional vibrations.

Key words: Euler-Bernoulli cantilever, spatial vibrations, orthogonality conditions

1. Introduction

A problem of coupled linear bending vibrations in two planes $\left(w_2(z,t), w_1(z,t)\right)$, torsional □$(z,t)$ and longitudinal $\left(u(z,t)\right)$ vibrations is considered (Figure 1). The coupling is due to the effect of an eccentric rigid body attached at the free end of a cantilever beam of length L, with a variable diameter $d(z)$, made up of an axially functionally graded material (variable properties $\rho(z), E(z), G(z)$), where $\overrightarrow{O_1C} = \{e_x, e_y, e_z\}$. In similar problems in the available literature [1-4] this coupling is studied only partially, by analyzing the coupling of torsional vibrations and transverse vibrations in only one plane. In our work a complete coupling of vibrations is studied, which is induced by non-zero mass m and moment of inertia of the rigid body (the inertia tensor I). The appropriate orthogonality conditions are derived.

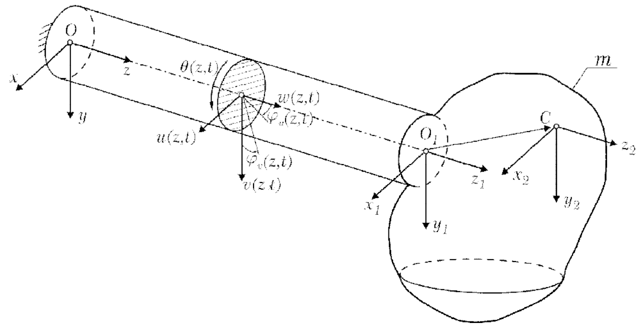

Fig. 1. Euler-Bernoulli AFG cantilever with an eccentric rigid tip load

2. Problem Statement and Discussion of Results

By using the extended Hamilton's principle [5] partial differential equations and boundary conditions are obtained at both ends of the cantilever beam. The coupling comes from the boundary conditions at the tip load, making the time function identical between all the differential equations when solving them by the method of separation of variables:

$$[w_2(z,t), w_1(z,t), u(z,t), w_1'(z,t), w_2'(z,t), \theta(z,t)]^T = X(z)e^{i\omega t},\ \ X(z) = [W_2(z), W_1(z), U(z), W_{d1}(z), W_{d2}(z), \Theta(z)]^T\,. \quad (1)$$

For each of the vibration types, the conventional method [5] for derivation of the orthogonality conditions of modes for different angular frequencies ω_α and ω_β, after summation and applying the boundary conditions, yields the following compact original matrix form:

$$\int_0^L \rho(z)\Big(A(z)\big(W_{1\alpha}(z)W_{1\beta}(z) + W_{2\alpha}(z)W_{2\beta}(z) + U_\alpha(z)U_\beta(z)\big) + I_0(z)\Theta_\alpha(z)\Theta_\beta(z)\Big)dz + +X_\alpha^T(L)K\,X_\beta^T(L) = 0,\ \ K = [m\ 0\ 0\ 0\ e_z m\ -e_y m\ 0\ m\ 0\ e_z m\ 0\ e_x m\ 0\ 0\ m\ -e_y m\ -e_x m\ 0\ 0\ e_z m\ -e_y m\ e_y^2 m + I_{xx} + e_z^2 m\ I_{xy} + e_x e_y m\ I_{xz} + e_x e_z m\ e_z m\ 0\ -e_x m\ I_{xy} + e_x e_y m\ e_x^2 m + I_{yy} + e_z^2 m\ -I_{yz} - e_y e_z m\ -e_y m\ e_x m\ 0\ I_{xz} + e_x e_z m\ -I_{yz} - e_y e_z m\ e_x^2 m + I_{zz} + e_y^2 m\,].\#(2)$$

To the best of the authors' knowledge, neither the orthogonality conditions in the case of complete coupling of all types of vibrations nor their matrix form have been published before.

Acknowledgement:

The research was funded by the Ministry of STDI of the Republic of Serbia, contract numbers 451-03-47/2023-01/200107 and 451-03-137/2025-03/200105, and bilateral project University of Belgrade, Faculty of Mechanical Engineering and Institute of Mechanics of Lomonosov MSU No.172/1.

References

[1] Oguamanam, D.,C.,D., *Free vibration of beams with finite mass rigid tip load and flexural-torsional coupling*, International Journal of Mechanical Sciences, Vol. 45, 963-979, 2003.

[2] Salarieh H., Ghorashi M., *Free vibration of Timoshenko beam with finite mass rigid tip load and flexural-torsional coupling*, International Journal of Mechanical Sciences, Vol. 48, 763-779, 2006.

[3] Zargarani A., Mahmoodi S.,N., *Flexural-torsional free vibration analysis of a double-cantilever structure*, Journal of Vibration and Acoustics, Vol. 144 (3), 031001, 2022.

[4] Zargarani A., O'Donnell J., Mahmoodi S.,N., *Coupled flexural–torsional forced vibration analysis of a piezoelectrically actuated double-cantilever structure*, Journal of Vibration and Acoustics, Vol. 144 (4), 4053714, 2022.

[5] Rao, S.,S., *Vibration of Continuous Systems*, John Wiley & Sons INC, New Jersey, 2007.

10th International Congress of the Serbian Society of Mechanics
Niš, Serbia, June 18-20, 2025

C.11

Extended abstract

FRICTION STIR WELDING – THERMO-MECHANICAL QUANTITIES AND ENERGY DISSIPATION FOR DIFFERENT JOINT SHAPES

Darko M. Veljić[1][0000-0002-0965-5500], **Bojan I. Međo**[2][0000-0001-8100-7519],
Nenad A. Radović[2][0000-0002-9521-6159], **Zoran M. Radosavljević**[3][0009-0005-6504-9475],
Dragana R. Mihajlović[2][0000-0003-3966-1909], **Aleksandar S. Sedmak**[4][0000-0002-5438-1895]

[1] Innovation Center of the Faculty of Technology and Metallurgy in Belgrade
Karnegijeva 4, 11000 Belgrade, Serbia

[2] Faculty of Technology and Metallurgy
University of Belgrade, Karnegijeva 4, 11000 Belgrade, Serbia
e-mail: bmedjo@tmf.bg.ac.rs

[3] Research and Development Institute Lola
Kneza Višeslava 70A, 11000 Belgrade, Serbia

[4] Faculty of Mechanical Engineering
University of Belgrade, Kraljice Marije 16, 11000 Belgrade, Serbia

Abstract:

In this work, influence of joint geometry on thermomechanical quantities in Friction Stir Welded (FSW) joints is analysed by using the finite element method. In addition to the standard butt joint, T-joints of aluminium alloy plates are considered. The material behaviour during the initial (plunge) stage of this non-melting process is modelled by Johnson-Cooke model. It is concluded that the T-shape of the joint gives different results when compared to the butt joint; the analysis of thermomechanical models enables determination of adequate welding parameters.

Key words: Friction stir welding, T-joint, Numerical simulation, Heat dissipation

1. Introduction, numerical model and results

Friction stir welding is a non-melting joining process which is used for Al alloys and many other metallic and polymer materials. The welding tool (Fig. 1) has two motions: rotation and translation; their speeds are the welding parameters of FSW. Before the welding, the tool must be plunged into the material; this has a key role, because the joint cannot be formed if proper thermomechanical conditions were not reached. In authors' previous studies, different aspects of FSW were analysed experimentally and numerically, e.g. [1]. Here, the influence of geometry is emphasized; T-joints are compared to typical butt joints. The main considered parameters are temperature, stress, strain, material velocity and generated heat amount during the plunge stage.

Fig. 1 contains the model of a T-joint (a), as well as temperature (b), slip rate (c) and equivalent von Mises stress (d) fields. The welding tool and backing tools are defined as rigid bodies, which is why they are not meshed. The joint is fabricated from Al alloy 2024 T3. Johnson-Cook material law is applied for modelling of material behaviour, [2]. Basically, this law defines dependence of the yield stress on temperature, strain and strain rate, which enables modelling of the material 'softening' during FSW. Some results (fields) are presented in Fig. 1, on T-joint; these quantities, along with the generated heat (from friction and plastic deformation) and the reaction force, enable determination of the influence of geometry on the joint formation.

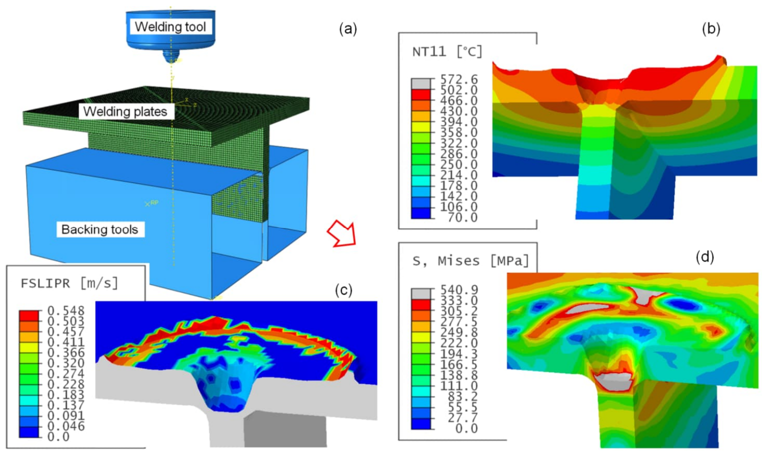

Fig. 1. Numerical model of a T-joint (welding plates, welding tool and backing tools) and results

The surface temperature distributions of the butt joint and T-joint are similar, because they are affected primarily by the tool geometry. In order to determine the adequate conditions for T-joint formation, it is especially important to analyse the temperature right below the tool pin. For successful welding, minimum temperature in the welding zone must be 80% of the solidus temperature (here: cca. 401 ºC). Variation of welding parameters enables determination of proper combination for each joint geometry; in addition to temperature, other thermomechanical quantities are also considered. For example, T-joint has higher amount of friction-generated heat and lower amount of plastic deformation generated heat, when compared to the butt joint.

2. Conclusions

Numerical simulation of the plunge stage of friction stir welding is considered. Based on the analysis of the thermomechanical quantities in the welding zone, the influence of the joint geometry is determined. In addition, these quantities are used to define the conditions for proper joint formation. Tools for fabrication of different T-joint geometries are currently being designed and fabricated, to enable experimental analysis and validation.

Acknowledgement

This work is dedicated to the memory of late Prof. Marko Rakin (1966–2023). It was supported by the Ministry of Science, Technological Development and Innovation of the Republic of Serbia (contracts 451-03-136/2025-03/ 200287 and 451-03-136/2025-03/200135).

References

[1] Veljić D., Rakin M., Sedmak A., Radović N., Međo B., Mrdak M., Bajić D., *Thermo-mechanical analysis of linear welding stage in friction stir welding - influence of welding parameters*, Thermal Science, Vol. 26/3A, 2125-2134, 2022.

[2] Johnson R.G., Cook W.H. *A constitutive model and data for metals subjected to large strains, high strain rates and high temperatures*, Proceedings of the 7th International Symposium on Ballistics, Hague, Netherlands, 541-547, 1983.

10th International Congress of the Serbian Society of Mechanics
Niš, Serbia, June 18-20, 2025
C.12
Extended abstract

GENERALIZED EINSTEIN TENSOR FOR EUCLIDEAN SURFACES WITH MECHANICAL POINT OF VIEW

Nenad O. Vesić[1] [0000-0002-7598-9058] and **Katarina V. Slavković**[2] [0009-0009-9231-2856]

[1]University of Belgrade, Mathematical Institute of Serbian Academy of Sciences and Arts, Serbia,
e-mail: n.o.vesic@outlook.com
[2]University of Belgrade, Mathematical Institute of Serbian Academy of Sciences and Arts, Serbia,
e-mail: katarina.slavkovic@mi.sanu.ac.rs

Abstract. In this paper, the transformation laws of the intrinsic geometry of a surface $\bar{r}=\bar{r}(u^1,u^2)$ into a surface $r=r(u^1,u^2)$, graphically expressed in $3D$-Euclidean space. The corresponding Christoffell symbols $\bar{\Gamma}^i_{jk}$ and Γ^i_{jk} of these surfaces are determined, and their difference $P^i_{jk}=\Gamma^i_{jk}-\bar{\Gamma}^i_{jk}$ is factorized in the form

$$P^i_{jk}=\Gamma^i_{jk}-\bar{\Gamma}^i_{jk}=\psi_k\delta^i_j+\psi_j\delta^i_k+\sigma_jF^i_k+\sigma_kF^i_j-\left(\bar{\sigma}_j\bar{F}^i_k+\bar{\sigma}_k\bar{F}^i_j\right).$$

The analogies of tensor F^i_j in previous factorization is recognized with respect to definitions presended in (Holzapfel, 2001).

Based on the factorization of the above presented tensor P^i_{jk}, and with respect to the methodology presented in (Vesić, Basic invariants of geometric mappings, 2020), we obtained the invariants for the last transformation of Thomas and Weyl type. Based on the basic invariant of Weyl type, whose components are $\mathscr{W}^i_{jmn}$, we obtained the invariant for this transformation as a monic linear function of Ricci tensor R_{ij}. The variation of integral $\int d^2x\sqrt{g}g^{ij}\mathscr{W}_{ij}$ with respect to metric tensor is vanished, from which we obtained the Einstein tensors for $3D$-surfaces.

As examples, we obtained generalized Einstein tensors for different surfaces in $3D$-space.

Keywords: surface, Riemannian space, Einstein tensor, variation, basic invariants, curvature tensor, Ricci tensor, scalar curvature.

1. Introduction

Let $D=(a,b)\subseteq\mathbb{R}$ be a continual interval. A vector function $r:(a,b)\times(a,b)\to\mathbb{R}^3$, $r=r(u^1,u^2)$ is a surface. The partial derivative of this surface by u^i, $i=1,2$, is vector $r_i=\dfrac{\partial r}{\partial u^i}$. The components of (covariant) metric tensor of the surface r are $g_{ij}=r_i\cdot r_j$, where "$\cdot$" denotes the inner product with respect to identical matrix of the type 2×2. We assume that is $\det[g_{ij}]\neq 0$. In this way, the components of contravatiant metric tensor are $\left[g^{ij}\right]=\left[g_{ij}\right]^{-1}$.

The Christoffell Symbols of second type for the surface r are [2]

$$\Gamma^i_{jk}=\frac{1}{2}g^{ip}\left(g_{jp,k}-g_{jk,p}+g_{kp,j}\right),\tag{1}$$

where comma denotes partial derivative, $g_{ij,k}=\partial g_{ij}/\partial u^k$ and Einstein summation convention is assumed for repeated indices, one covariant and one contravatiant.

The covariant derivative of a tensor a^i_j of the type $(1,1)$ with respect to Γ^i_{jk} is [2]

$$a^i_{j|k} = a^i_{j,k} + \Gamma^i_{pk} a^p_j - \Gamma^p_{jk} a^i_p. \tag{2}$$

The curvature tensor of surface r is [2]

$$R^i_{jmn} = \Gamma^i_{jm,n} - \Gamma^i_{jn,m} + \Gamma^p_{jm}\Gamma^i_{pn} - \Gamma^p_{jn}\Gamma^i_{pm}. \tag{3}$$

The Ricci tensor and scalar curvature of surface r are

$$R_{ij} = R^p_{ipj} \quad \text{and} \quad R = g^{pq} R_{pq}. \tag{4}$$

1.1 Invariants for transformation of surfaces

The reference configuration is given by surface $\bar{r} = \bar{r}(u^1, u^2)$, but the surface $r = \bar{r} + z$ corresponds to the current configuration. The components of corresponding metric tensors are $\bar{g}_{ij}$, $\bar{g}^{ij}$, g_{ij}, g^{ij}. The corresponding Christoffell symbols are $\bar{\Gamma}^i_{Jk}$ and Γ^i_{jk}, and their difference is

$$P^i_{jk} = \Gamma^i_{jk} - \bar{\Gamma}^i_{jk} = \psi_k \delta^i_j + \psi_j \delta^i_k + \rho^i_{jk} - \bar{\rho}^i_{jk}, \tag{5}$$

where $\rho^i_{jk} = \sigma_j F^i_k + \sigma_k F^i_j$ and $\bar{\rho}^i_{jk} = \bar{\sigma}_k \bar{F}^i_j + \bar{\sigma}_j \bar{F}^i_k$, and σ_j and F^i_j are tensor of the types $(0,1)$ and $(1,1)$, respectively.

Based on results presented in [1], we have that the invariants for the transformation determined by (5) are

$$\mathscr{T}^i_{jk} = \Gamma^i_{jk} - \frac{1}{3}\delta^i_j\big(\Gamma_k - \rho_k\big) - \frac{1}{3}\delta^i_k\big(\Gamma_j - \rho_j\big) - \rho^i_{jk}, \tag{6}$$

$$\begin{aligned}
\mathscr{W}^i_{jmn} = {} & R^i_{jmn} + \rho^p_{jm}\rho^i_{pn} - \rho^p_{jn}\rho^i_{pm} + \frac{1}{3}\delta^i_j\big(\rho_{m|n} - \rho_{n|m}\big) \\
& - \frac{1}{9}\delta^i_m\Big(3\big\{\Gamma_{j|n} - \rho_{j|n} - \rho^p_{jn}\big(\Gamma_p - \rho_p\big)\big\} + \big(\Gamma_j - \rho_j\big)\big(\Gamma_n - \rho_n\big)\Big) \\
& + \frac{1}{9}\delta^i_n\Big(3\big\{\Gamma_{j|m} - \rho_{j|m} - \rho^p_{jm}\big(\Gamma_p - \rho_p\big)\big\} + \big(\Gamma_j - \rho_j\big)\big(\Gamma_m - \rho_m\big)\Big).
\end{aligned} \tag{7}$$

2. Conclusion

In this research, we studied solids determined by $3D$-surfaces. With respect to the deformation tensor (5), we obtained the corresponding invariants of Thomas and Weyl types as in [1]. From the invariant $\mathscr{W}^i_{jmn}$, the generalized Einstein tensor for surface r was obtained. In this tensor, and with respect to definitions in [3], we recognized impacts of structures σ_j and F^i_k in our results.

References

[1] Vesić, N. O., *Basic invariants of geometric mappings*, Miskolc Mathematical Notes, Vol. 21, No. 1, pp. 473–487, 2020.

[2] Mikeš, J., *Differential Geometry of Special Mappings*, Palacky University, Olomouc, 1ed. 2015, 2ed. 2019.

[3] Holzapfel, G. A., *Nonlinear Solid Mechanics*: *A Continuum Approach for Engineering*, John Wiley & Sons Ltd, Chichester, 2001.

D: Applied Mechanics

10th International Congress of the Serbian Society of Mechanics
Niš, Serbia, June 18-20, 2025
D.1
Original Scientific Paper

DOI:10.46793/ICSSM25.174C

CRITICAL TEMPERATURE OF FGM PLATES RESTING ON ELASTIC FOUNDATIONS USING LAYERWISE FINITE ELEMENT

M. Cetkovic[1][0000-0001-8595-0424]

[1] University of Belgrade
Faculty of Civil Engineering, Bul. Kralja Aleksandra 73, 11000 Belgrade, Serbia
e–mail: cetkovicm@grf.bg.ac.rs

Abstract

It is known that many civil engineering structures are made from concrete, such as smart pavements, railways, bridges and building. Many of them may be exposed to severe environmental conditions during serviceability limit state. The temperature effects, as one of the environmental conditions, is often the cause of damage to concrete plates. By incorporated different agents and fibers to concrete mixture, the concrete structures may be monitored, controlled and healed against temperature damage. The material behavior of such mixture may generally be described by functionally graded materials (FGM) material models. To the author's best knowledge, there has been no study in the literature regarding thermal buckling of FGM plates resting on elastic foundations using LW theory of Reddy. Therefore, in this study the thermal buckling analysis of functionally graded plates resting on elastic foundation is modelled using one–parameter Winkler's and two–parameter Pasternak's model. The mathematical model, based on Layer wise theory of Reddy, assumes layer wise variation of in plane displacements and constant transverse displacement through the thickness, non–linear strain displacement relations (in von Karman sense) and isotropic nonhomogeneous thermo–mechanical material properties. The material properties of FGM plates are assumed to be constant in xy–plane and vary through the thickness by a power law function in terms of the volume fraction of the constituents. The principle of virtual displacement (PVD) is used to derive the weak form of linearized buckling problem. The weak form is discretized using 2D nine–node Lagrangian isoparametric finite element. The original MATLAB computer program is coded for finite element solution. The influence of different parameters, such as temperature distribution, side–to–thickness ratio b/h, aspect ratio a/b, power–low index n and elastic foundation parameters (k_w, k_s), are analyzed. The accuracy of the numerical model is verified by comparison with the available results from the literature and may be used in the design of smart concrete structures.

Key words: Thermal stability, elastic foundations, FGM plates, layer wise finite element; MATLAB computer program

1. Introduction

Many civil engineering structures may be exposed to extreme thermal environments, during the manufacturing or service life. This results in various types of thermal loads producing thermal stresses, which at certain level may cause the structure to buckle. The thermal buckling may be undesired design phenomenon in structures such as railroad tracks, pipelines and concrete roads, as well as nuclear reactors and aircrafts [1,2]. To reduce buckling temperature of such structures, new class on materials have been recently used, which are functionally graded materials (FGMs) [3]. The functionally graded materials (FGM) are high–performance heat–resisting materials, initially applied in Japan in mid–1980s for space plane project [4]. They are microscopically inhomogeneous materials, with smooth variation of mechanical properties from one surface to another, this eliminating interface problems of composite materials and achieving smooth stress

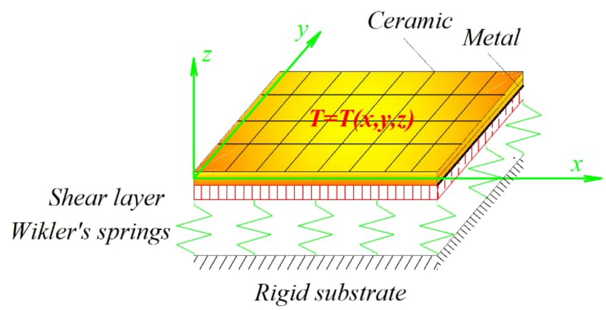

Fig. 1. Thermal buckling of rectangular FGM plate resting on elastic foundations under temperature field

distribution [5]. This is achieved by varying the volume fraction ratio of constituent materials. The constituent materials are usually metal and ceramics, where the ceramics serves for thermal resistance, while metal gives high toughness. Furthermore, a mixture of ceramic and metal with a continuously varying volume fraction can be easily manufactured [6].

The plates made of FGMs in highway and airfield pavement system are usually supported by surrounding soil or elastic foundations. The elastic foundations may be modelled using either: one–parameter or Winkler's model, two–parameter or Pasternak's model or using generalized foundation model. Since the one–parameter Winkler's model, described by linear elastic mutually independent vertical springs, is unable to take into account the continuity or cohesion of the soil, the two–parameter Pasternak foundation is suggested. The two–parameter Pasternak foundation enables the nonuniform deflection of foundation structure, and thus more realistic response.

The mathematical models for thermal buckling of FGM plates resting on elastic foundations are formulated using mostly equivalent single layer theories, which are Classical plate theory (CPT), First-order shear deformation plate theory (FPT) or Higher-order shear deformation plate theory (HSDT). Irwan et. al [7] used FSDT to investigate static, free vibration and thermal buckling of FGM plates. A finite element solution solution is derived, in order to study influence of various parameters like sandwich plate schemes, plate geometric parameters and power low index on deflections, stresses, frequencies and thermal buckling loads. Wafa et. al [5] used CPT and trigonometric shear deformation theory for thermal buckling of FGM plates resting on elastic foundations. The elastic foundation is modeled using two-parameter Pasternak's model. The analytical solution is presented for plates under various loading conditions, plate geometry, as well as foundation stiffness parameters.

After establishing the accuracy of the present LW model for linear and geometrically nonlinear bending, vibration and buckling analysis of perfect and imperfect laminated composite and sandwich plates subjected to thermo–mechanical load in authors previous papers [9–12], in this paper thermal buckling analysis of FGM plates resting on elastic foundations is further investigated. The mathematical model assumes layer wise variation of in–plane displacements and constant transverse displacement through the plate thickness, non–linear strain–displacement relations (in von Karman sense) and linear thermo-mechanical material properties. The material properties of FGM plates are assumed to be constant in xy–plane and vary through the thickness by a power law function in terms of volume fraction of the constituents. The effective materials properties are given by the rule of mixture. The governing finite element equations are derived using Principle of virtual displacements (PVD). A 2D nine-node Lagrangian finite element is used for the in-plane interpolation, while 1D two-node Lagrangian finite element is used for interpolation through the thickness. The original MATLAB program is coded for the finite element solution and is used to study the effects of side to thickness ratio, aspect ratio, power low index and foundation stiffness parameters on critical buckling temperature. The accuracy of the numerical model is verified by comparison with the available results from the literature.

2. Theoretical Formulation

A LW plate model may be composed of n layers, Figure 2. It is assumed that 1) layers have continuous variation of material properties from one surface to another, 2) material of each layer is isotropic and nonhomogeneous [8, 9, 10], 3) strains are small, 4) material is linear elastic, 5) inextensibility of normal is imposed.

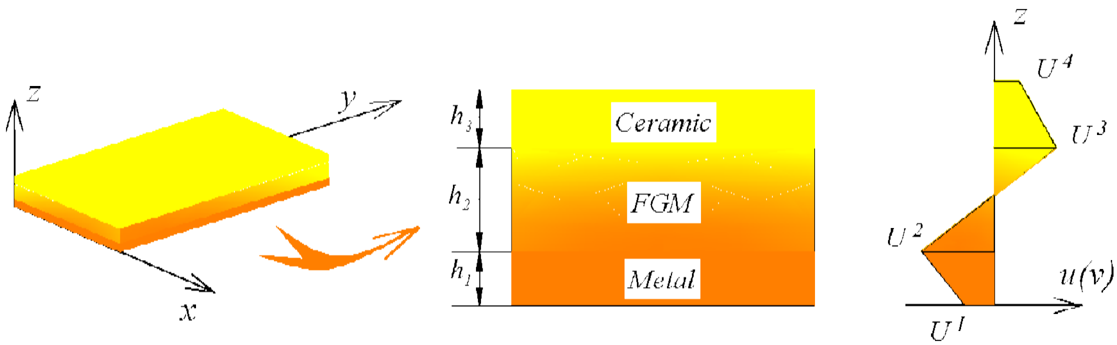

Fig. 2. Plate geometry and LW in–plane displacement field

2.1 Displacement field

The displacements components (u_1,u_2,u_3) at a point (x,y,z) of plate are expressed as [8]:

$$u_1(x,y,z)=u(x,y)+\sum_{I=1}^{N}U^I(x,y)\cdot\Phi^I(z),$$

$$u_2(x,y,z)=v(x,y)+\sum_{I=1}^{N}V^I(x,y)\cdot\Phi^I(z),$$

$$u_3(x,y,z)=w(x,y). \tag{1}$$

where (u,v,w) are displacements of a point $(x,y,0)$ on the reference plane, functions $\Phi^I(z)$ are 1D linear Lagrange interpolation functions of thickness coordinates, while (U^I,V^I) are the values of (u_1,u_2) at the I–th plane.

2.2 Strain–displacement relations

The strains associated with the displacement field (1) are given using von Karman's non–linear strain–displacement relations:

$$
\begin{aligned}
\varepsilon_{xx} &= \frac{\partial u}{\partial x} + \sum_{I=1}^{N} \frac{\partial U^I}{\partial x}\Phi^I + \frac{1}{2}\left(\frac{\partial w}{\partial x}\right)^2, \\
\varepsilon_{yy} &= \frac{\partial v}{\partial y} + \sum_{I=1}^{N} \frac{\partial V^I}{\partial y}\Phi^I + \frac{1}{2}\left(\frac{\partial w}{\partial y}\right)^2, \\
\gamma_{xy} &= \frac{\partial u}{\partial y} + \frac{\partial v}{\partial x} + \sum_{I=1}^{N}\left(\frac{\partial U^I}{\partial y} + \frac{\partial V^I}{\partial x}\right)\Phi^I + \frac{\partial w}{\partial x}\frac{\partial w}{\partial y}, \\
\gamma_{xz} &= \sum_{I=1}^{N} U^I \frac{d\Phi^I}{dz} + \frac{\partial w}{\partial x}, \\
\gamma_{yz} &= \sum_{I=1}^{N} V^I \frac{d\Phi^I}{dz} + \frac{\partial w}{\partial y}.
\end{aligned}
\tag{2}
$$

2.3 Constitutive equations

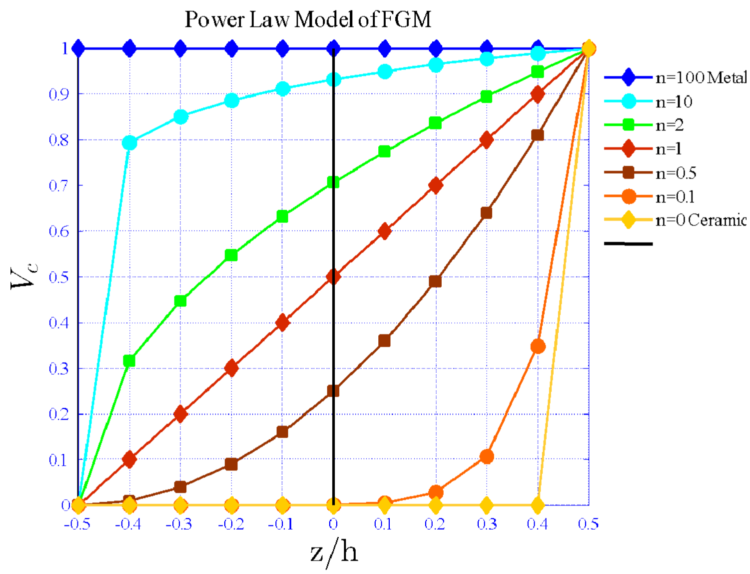

Fig. 3. Volume fraction V_c distribution along the plate thickness for different values of the volume fraction index n

The plate is made from a mixture of ceramic and metal, where the rule of mixture is defined as:

$$P_e = P_m + \left(P_c - P_m\right)V_c\left(z\right) \tag{3}$$

The P_e denotes the effective material properties of FGM plate, such as Young's modulus E and thermal expansion coefficient α, while Poisson's coefficient ν is assumed to be constant. The subscripts c and m denote the ceramic and metal, corresponding the material property of the lower and upper surface of the plate, respectively. The V_c is volume fraction of ceramic. The volume fraction is given by the power low distribution, in the thickness direction as, Figure 3:

$$V_c(z) = \left(\frac{z}{h} + \frac{1}{2}\right)^n \tag{4}$$

Where n denotes the power low index by which the gradation of the constituents is controlled and may take the values $[0, \infty]$. When the volume fraction exponent is 0 plate is fully made of ceramic, and when the volume fraction exponent is 1 the variation of the volume fraction is linear.

A linear elastic material behavior is considered. The stress–strain relations are given by the generalized Hook's law as:

$$\begin{Bmatrix} \sigma_{xx} \\ \sigma_{yy} \\ \tau_{xy} \\ \tau_{xz} \\ \tau_{yz} \end{Bmatrix} = \begin{bmatrix} Q_{11} & Q_{12} & Q_{13} & 0 & 0 \\ Q_{12} & Q_{22} & Q_{23} & 0 & 0 \\ Q_{13} & Q_{23} & Q_{33} & 0 & 0 \\ 0 & 0 & 0 & Q_{44} & 0 \\ 0 & 0 & 0 & 0 & Q_{55} \end{bmatrix} \times \begin{Bmatrix} \varepsilon_{xx} \\ \varepsilon_{yy} \\ \gamma_{xy} \\ \gamma_{xz} \\ \gamma_{yz} \end{Bmatrix} - \Delta T \begin{Bmatrix} \alpha_{xx} \\ \alpha_{yy} \\ 0 \\ 0 \\ 0 \end{Bmatrix}, \tag{5}$$

where Q_{ij} are elastic stiffness of FGM plate, given as:

$$Q_{11} = Q_{11} = \frac{(1-\nu)}{(1-2\nu)(1+\nu)} E(z), \quad Q_{12} = Q_{13} = Q_{23} = \frac{1}{(1-2\nu)(1+\nu)} E(z),$$
$$Q_{33} = Q_{44} = Q_{55} = \frac{1}{2(1+\nu)} E(z). \tag{6}$$

2.4 Temperature rise

The temperature rise analyzed in this paper, include nonlinear temperature rise for $\beta > 1$, given as:

$$\Delta T(z) = \frac{\Delta T}{h}\left(z + \frac{h}{2}\right)^{\beta} + T_{bott}, \tag{7}$$

where z is the coordinate variable in the thickness direction measured from the middle plane of the plate, β is nonlinear exponent and temperature difference is $\Delta T = T^{top} - T^{bott}$.

2.5 Equilibrium equations

The governing equations are derived using the principle of virtual displacements (PVD). By performing the integration in the thickness direction, the virtual work statement for thermal buckling problem of FGM plate resting on elastic foundations is given as:

$$\int_{\Omega} \left\{ \{\delta\varepsilon_{0L}\}^T \cdot \{N\} + \left\{\delta\varepsilon^I\right\}^T \cdot \left\{N^I\right\} + \{\delta\varepsilon_{0NL}\}^T \cdot \left\{N_T^0\right\} + \{\delta w\}^T (k_w \cdot w + k_s \nabla^2 w) \right\} d\Omega = 0 \tag{8}$$

3. Finite element solution

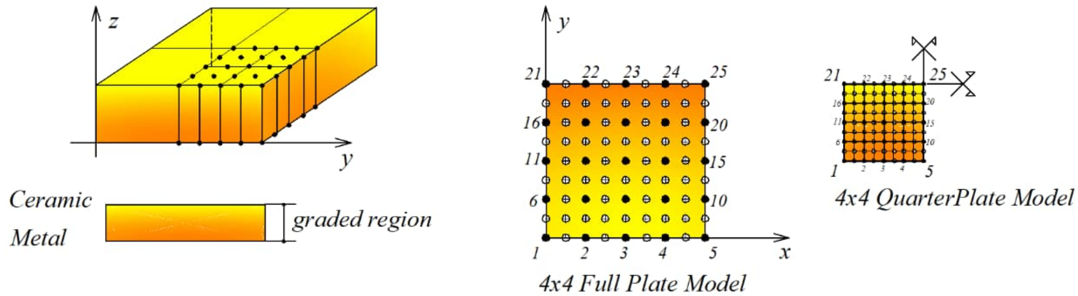

Fig. 4. Finite element model of FGM plate

3.1 Displacement field

The GLPT finite element consists of middle surface plane and $I = 1,N$ planes through the thickness of the plate, Figure 4. The element requires only the C^0 continuity of major unknowns, thus in each node only displacement components are adopted, that are (u, v, w) in the middle surface element nodes and (U^I, V^I) in the I-th plane element nodes. The generalized displacements over finite element Ω^e are expressed as:

$$\begin{Bmatrix} u \\ v \\ w \end{Bmatrix}^e = \begin{Bmatrix} \sum_{j=1}^{m} u_j \Psi_j \\ \sum_{j=1}^{m} v_j \Psi_j \\ \sum_{j=1}^{m} w_j \Psi_j \end{Bmatrix}^e = \sum_{j=1}^{m} \left[\Psi_j\right]^e \left\{\mathrm{d}_j\right\}^e \quad , \quad \begin{Bmatrix} U^I \\ V^I \end{Bmatrix}^e = \begin{Bmatrix} \sum_{j=1}^{m} U_j^I \Psi_j \\ \sum_{j=1}^{m} V_j^I \Psi_j \end{Bmatrix}^e = \sum_{j=1}^{m} \left[\bar{\Psi}_j\right]^e \left\{\mathrm{d}_j^I\right\}^e \tag{9}$$

where $\left\{\mathrm{d}_j\right\}^e = \left\{u_j^e \quad v_j^e \quad w_j^e\right\}^T, \left\{\mathrm{d}_j^I\right\}^e = \left\{U_j^I \quad V_j^I\right\}^T$ are displacement vectors in the middle plane and I-th plane, respectively, and Ψ_j^e are interpolation functions, for the j-th node of the element Ω^e, while $\left[\Psi_j\right]^e$ and $\left[\overline{\Psi}_j\right]^e$ are given in [13].

3.2 Finite element model

The governing finite element equations are obtained by substituting displacement field (9) into the virtual work statement (8). The set of homogeneous algebraic equations are solved as a solution of following eigenvalue problem:

$$\left(\left[K \right]^e + \left[K_F \right]^e - \Delta T_{cr} \left[K_G \right]^e\right) \times \{ d \}^e = \{ 0 \} \tag{10}$$

where element stiffness, geometric stiffness and foundation stiffness matrices $[\mathbf{K}]^e$, $[\mathbf{K}_G]^e$ and $[\mathbf{K}_F]^e$ are given in [12].

4. Numerical results and discussion

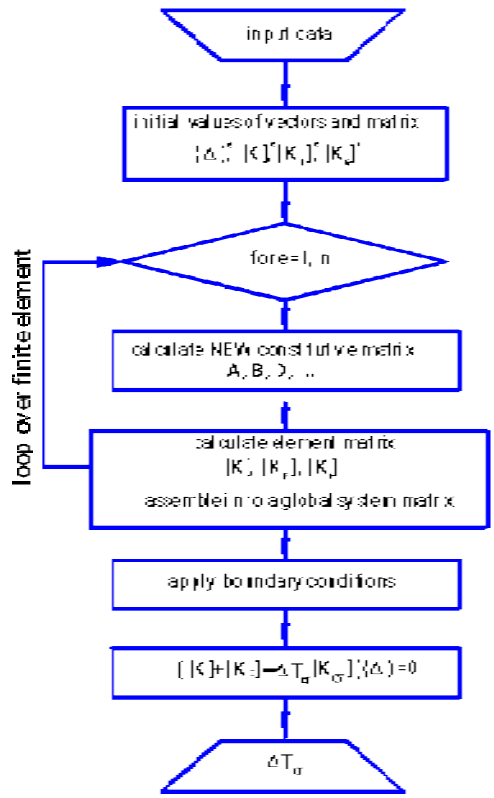

Fig. 5 Flowchart for finite element solution

Using previously derived FEM solutions, an original computer program is coded using MATLAB programming language Figure 5, for thermal buckling of simply supported FGM plate resting on elastic foundations. The plate is subjected to nonlinear buckling temperature rise ($\beta = 3$) and made of material:

Aluminum (Al): $E_m = 70\ GPa$, $\nu = 0.3$, $\alpha_m = 23 \cdot 10^{-6}\ 1/{}^0C$

Alumina (Al_2O_3): $E_c = 380\ GPa$, $\nu = 0.3$, $\alpha_c = 7.4 \cdot 10^{-6}\ 1/{}^0C$

The critical buckling temperature is presented in following form as $\Delta\bar{T}_{cr} = \Delta T_{cr} 10^{-3}$, while foundation stiffnesses are given as $\bar{k}_w = k_w a^4 / D_c$, $\bar{k}_s = k_w a^2 / D_c$.

The effects of plate geometry, given as side to thickness ratio a/h and aspect ratio a/b, is presented on Figure 6 and Figure 7. The Figures show that the increase, i.e. decrease of critical temperature of simply supported plate is due to increase i.e. decrease of plate stiffnesses. For thick plates CLPT overestimates critical temperature and maximum error compared to present an

HSDT model is 12% for a/h=4 and 24% for a/b=5. The reason for this may be neglection of transverse shear, as well as transverse normal stresses. As presented on Figure 8, the increase of power low index n decreases the critical temperature, as a result of decrease of ceramic constituent in plate mixture. The difference between the present and HSDT model is maximum 8% for $n=10$. Finally, the influence of foundation stiffness parameters $\bar{k}_w$ and $\bar{k}_s$, are presented on Figure 9, showing that two–parameter Pasternak's model, has greater effect on critical buckling temperature, compared to one–parameter Winkler's spring model.

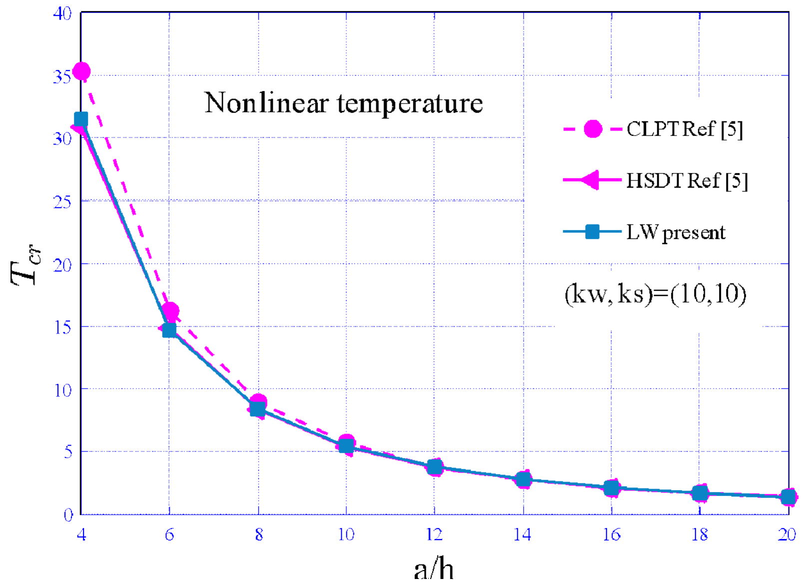

Fig. 6. Critical temperature for different values side to thickness ratio of a/h

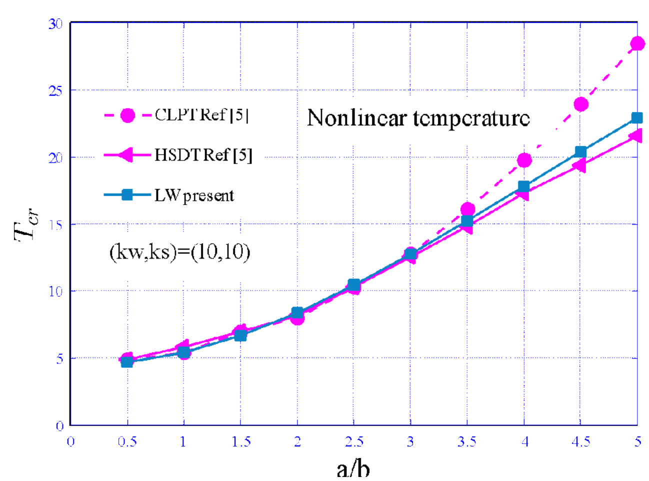

Fig. 7. Critical temperature for different values of aspect ratio a/b

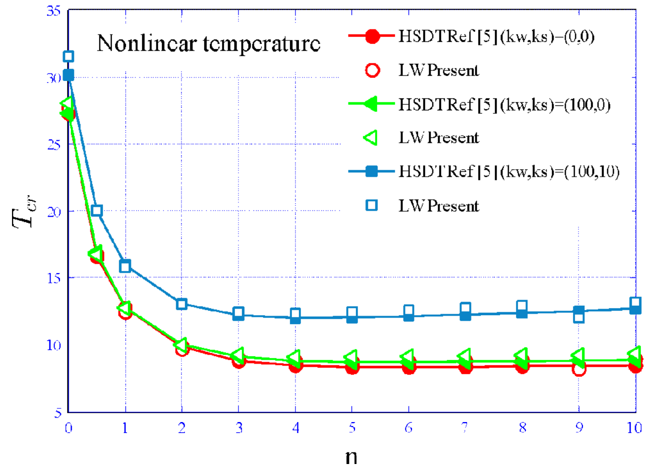

Fig. 8. Critical temperature for different values of the volume fraction ratio n

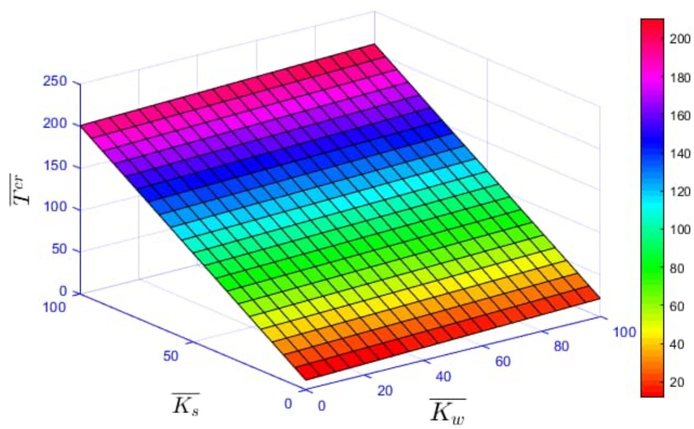

Fig. 9. Critical temperature surface for different values of foundation parameters ($\underline{k}_w$, $\underline{k}_s$)

5. Conclusion

Finite element solution is derived for thermal stability analysis of FGM plates resting on Pasternak-Winkler elastic foundations. The original MATLAB program is coded, based on numerical solution obtained using LW theory of Reddy. The results have shown close agreement with the results from the literature. The limitation of neglecting shear deformation in CLPT is verified. Also, the numerical model is shown that greater critical buckling load is obtained using Pasternak's model, compared to Winkler's foundation model. This may be due to the fact that soli-structure interaction is dominantly influenced by shear, reader than pure normal deformation modes.

Acknowledgment The author is thankful for the financial support received by the Ministry for Education, Science and Technology, Republic of Serbia, grant number 200092.

References

[1] Mokhtar B, Abedlouahed T, EL Abbas AB. *Buckling Response of Thick Functionally Graded Plates.* Journal of materials And Engineering Structures, Vol 1. 137–145, 2014.

[2] Hessameddin Y, Abdolhossein F. *Mechanical and thermal buckling analysis of functionally graded plates resting on elastic foundations: An assessment of a simple refined nth-order shear deformation theory*. Composites: Part B, Vol. 62,54–64, 2014.

[3] Shen HS. *Thermal post buckling behavior of shear deformable FGM plates with temperature-dependent properties*. International Journal of Mechanical Sciences, Vol. 49, 466–478, 2007.

[4] Javaheri R, Eslami MR. *Thermal Buckling of functionally graded plates based on higher order theory*. Journal of Thermal Stresses, Vol. 25, 603–625, 2002.

[5] Tebboune W, Benrahou KH, Houari SAH, Tounsi A. *Thermal buckling analysis of FG plates resting on elastic foundation based on an efficient and simple trigonometric shear deformation theory*. Steel and Composite Structures, Vol. 18(2), 443-465, 2015.

[6] Lanhe W. *Thermal buckling of a simply supported moderately thick rectangular FGM plate*. Composite Structures, Vol. 64, 211–218, 2004.

[7] Irwan K, Jean-Louis B, Susilo W, Hakim N, *The Q4γs plate finite element for three-layer FGM sandwich plates in deflection, stresses, vibration, and thermal buckling analysis,* Composite Structures, Vol. 338, 118098, 2024.

[8] Reddy JN, Barbero EJ, Teply JL, *A plate bending element based on a generalized laminated plate theory.* International Journal for Numerical Methods in Engineering, Vol. 28, 2275-2292, 1989.

[9] Yildizela SA, Tayehb BA, Calis G, *Experimental and modelling study of mixture design optimisation of glass fibre-reinforced concrete with combined utilisation of Taguchi and Extreme Vertices Design Techniques*, Journal of material research and technology, Vol. 92(2), 2093-2106, 2020.

[10] Zhizhong D, Wengui L, Wenkui D, Zhihui S, Jayantha K, Daichao S, *Multifunctional asphalt concrete pavement toward smart transport infrastructure: Design, performance and perspective*, Composites Part B, Vol 265, 110937, 2023.

[11] Cetkovic M. *Influence of initial geometrical imperfections on thermal stability of laminated composite plates using layer wise finite element*. Composite Structures, 291, 115547, 2022.

[12] Cetkovic M, *Mechanical buckling of FGM plates resting on elastic foundations using layer wise finite element.* 2nd International Conference on Mathematical Modelling in Mechanics and Engineering Mathematical Institute SANU, 12-14. Serbia, 2024.

[13] Cetkovic M. *Thermal Buckling of Laminated Plates Using Layer wise Displacement Model*. Composite Structures, Vol. 142, 238-253, 2016.

10th International Congress of the Serbian Society of Mechanics
Niš, Serbia, June 18-20, 2025
D.2
Original Scientific Paper

DOI:10.46793/ICSSM25.184D

A SYSTEM ENGINEERING APPROACH FOR ROBOT MANIPULATOR DESIGN USING GAME ENGINE SIMULATION AND COMPUTATIONAL MODELING

Andrija D. Dević[1][0000-0002-5773-1635]**, Jelena Z. Vidaković**[1][0000-0002-3363-8807]**,**
Nikola P. Slavkovic[2][0000-0003-1147-284X]**, Mihailo P. Lazarević**[2][0000-0002-3326-6636]**,**
Nikola Lj. Živković[1][0000-0002-2276-2933]

[1] Lola institute, Kneza Viseslava 70a, 11030 Belgrade, Serbia
e-mail: andrija.devic@li.rs, jelena.vidakovic@li.rs, nikola.zivkovic@li.rs
[2] Faculty of Mechanical Engineering,
The University of Belgrade, Kraljice Marije 16, 11120 Belgrade 35
e-mail: mlazarevic@mas.bg.ac.rs , nslavkovic@mas.bg.ac.rs

Abstract:

Modern game engine platforms are increasingly used in the field of robotics due to their built-in support for creating real-time simulation within an Extended Reality (XR) environment. This research investigates the integration of game engine platforms into systems engineering processes in the robotics domain. A novel method for the design of robotic manipulators, focusing on actuator selection, based on robot motion simulation within game engine platforms using integrated functionalities for joint torque calculation, is presented. The proposed robot model integration methodology involves the use of a CAD-based robot model, the game engine's physics engine, and MATLAB Simscape as an intermediate modeling environment. This approach enables appropriate actuator selection, verification of component dimensioning, and accelerates the design process. The proposed approach offers a cost-effective and flexible alternative to traditional simulation environments and offers enhanced immersive visualization of robotic systems through XR technologies. The simulated joint actuator torques are verified using MATLAB Simscape for a 6-DoF articulated robot model.

Key words: robot, design, game engine, Unity, actuator, dynamics.

1. Introduction

The number of technologies that employ industrial robots to increase the level of automation in production processes is constantly increasing [1]. Flexible robotic systems can adapt to a variety of tasks and products, making them particularly advantageous for high-mix, low-volume manufacturing [2]. There is a high demand for the development of robotics and automation solutions that are less expensive, safer, easier to install and re-program [3-4].

The development of robotic systems requires an iterative engineering approach with system simulation integrated as a part of this process. The numerical simulation of robot dynamics is widely diffused in research, industrial and education contexts, where it is used to support the design of new devices, trajectory validation, and comparison of different actuation and control systems [5]. 3D virtual simulators for robots are often used in the design and validation of robotic trajectories and are also integral to system engineering tasks. Dedicated robot simulation software can be categorized based on their functionality and integration level into: 1) frameworks and libraries that serve primarily as dynamics engines [6–7]; and 2) standalone simulators that offer complete simulation environments [8–9]. Although not a dedicated robot simulation tool, MATLAB Simscape [10] is a general-purpose physical modeling environment that has been extensively adopted for robotic system simulation due to its robust integration with MATLAB/Simulink and its ability to model complex multibody dynamics [5, 11-12].

The development of game engines and the enhancement of their computational and visualization features have led to their increasing usage in research involving robotics and multibody system simulation. Modern game engines such as Unity [13] and Unreal Engine [14] offer comprehensive toolsets and built-in features that enable the efficient development of real-time, immersive, and interactive robot simulation environments within the robotics domain [2-3, 15-16].

In this paper, a novel methodology for robot design based on the integration of a robot CAD model, MATLAB Simscape which serves as an intermediate environment for converting the robot dynamic model into a URDF format [17] compatible with Unity, and Unity's built-in physics engine is presented. The proposed model integration and motion simulation is used within the drive selection problem. The primary motivation for using the Unity software lies in its native support for Extended Reality (XR) development, which enables superior immersive visualization and interactive capabilities. 6DoF desktop articulated robot AD100 [18] is used for methodology verification.

2. Proposed methodology

The methodology proposed in this study aims to simulate the motion of an articulated robot and accurately compute the joint torques required to execute a predefined robot trajectory (addressing the robot inverse dynamics problem) in the Unity game engine based on the integration of a CAD model of a robot, and using Unity software's physics engine and its components. To facilitate the accurate transfer of robot geometry and physical parameters from the CAD environment to Unity, the robot model was processed through MATLAB Simscape software, and exported to Unity-compatible file format using the corresponding add-on.

Unity provides real-time feedback on the behavior of the robotic system via its physics engine. A physics engine is a software component or framework designed to simulate physical systems within a virtual environment. Physics engines are based on mathematical models that enable interactions between physical bodies in the virtual environment in a manner equivalent to those in the real world [19]. Unity's built-in physics engine is the Nvidia PhysX engine [20]. For the purpose of robotic research and with the intention of being used for realistic physical behaviors in the context of industrial applications simulation, in addition to standard rigid body dynamics, NVIDIA PhysX SDK offers the reduced coordinate articulations feature based on Featherstone's Articulation Body Algorithm (ABA) for forward dynamics computation [15, 21]. Its Articulation Body class [22] is used in this study for a robot's dynamic model integration, i.e. the configuration of a robot as an open kinematic chain consisting of rigid bodies and revolute joints. Articulation Body class enables the building of physics articulations such as robotic arms with GameObjects that are hierarchically organized.

Herein, the complementary simulation environment MATLAB Simscape is used as an intermediate environment for converting the model into a URDF format. URDF (Universal Robot Description Format) [17] is an open-source standard of XML type equipped with elements and attributes specific to robot kinematic and dynamic structure. The Articulation Body component in

Unity automatically retrieves all necessary kinematic and dynamic parameters from the URDF file, enabling accurate reconstruction of the robot model within the Unity environment.
SolidWorks [23] is used to design a 3D robot model as it allows model exportation to the URDF. Each link and joint is modeled with mass properties, dimensions, and constraints. Using the Simscape Multibody Link add-on [24], the mechanical assembly is exported directly to MATLAB Simscape in the form of an XML file with associated geometry, which ensures that the multibody system used for simulation maintains mechanical fidelity to the physical design, including link inertias, centers of masses, and joint configurations, Figure 1.

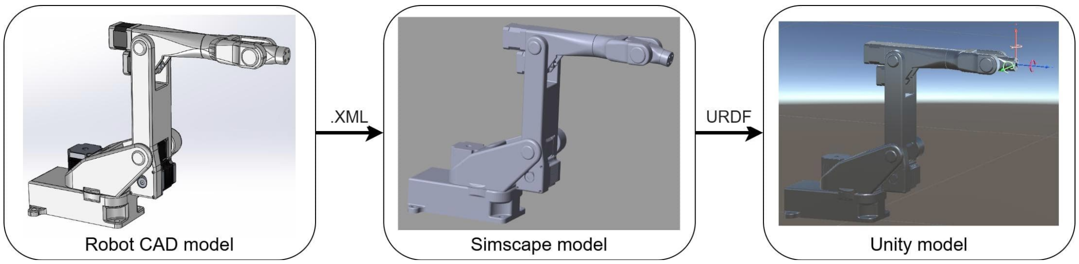

Fig. 1. Robot AD100 CAD model in SolidWorks, Simscape and Unity environment.

URDF file is generated from the MATLAB Simscape model and imported into Unity via the URDF Importer plugin [25]. The Articulation Body's function GetDriveForces [26] allows access to the torques generated by each joint during the robot's motion.

3. Simulation setup and results

3.1 Simulation setup

6DoF articulated robot AD100, Figure 2, is used for the proposed methodology verification used in this research. A detailed 3D model of the AD100 robotic arm was developed in SolidWorks, with particular emphasis on assigning appropriate material densities to the actuators and structural segments, ensuring that the model accurately reflects both geometric and physical parameters.

Given a sequence of target positions (robot program instructions), the motion trajectory of the robot's Tool Center Point (TCP) is generated by the robot's joint motions using a dedicated trajectory planning algorithm based on the solution of the inverse kinematics problem. The trajectory planning algorithm implemented within the Unity-based application for robot AD100 is described in [27]. The trajectory is generated using polynomial interpolation, providing smooth transitions with continuous velocity and acceleration profiles.

Articulation Body class integrates a built-in control algorithm via the XDrive variable [28]. Consequently, robotic motion in Unity is governed by applied torque values, rather than by specifying joint-space coordinates as in Simscape. The tuning method of XDrive control parameters is presented in [15]. The "GetDriveForces" function returns the torques applied by the joint drives in the Unity simulation environment. Since the robot motion simulation in Unity is executed in discrete steps, the joint torques obtained using the ArticulationBody.GetDriveForces function can exhibit high-frequency noise. To reduce this effect and obtain smoother torque profiles, a low-pass filter was applied to the raw data in this study.

Besides the intermediate environment for robot model integration into Unity, MATLAB Simscape is used in this research for methodology verification, i.e. for comparison of the obtained joint torques in Unity for the given robot trajectory. Using the Simscape toolbox within the Simulink environment, joint torques can be directly obtained based on predefined robot configurations. As the simulation progresses, MATLAB Simscape computes the required torques at each joint through inverse dynamics, accounting for gravitational forces, inertial effects, and internal constraints. The block diagram illustrating the system implementation is shown in Figure 3. The trajectory planner based on the inverse kinematics solution for the AD100 robotic arm [27] implemented within the Unity application was also used in the Simscape simulation setup.

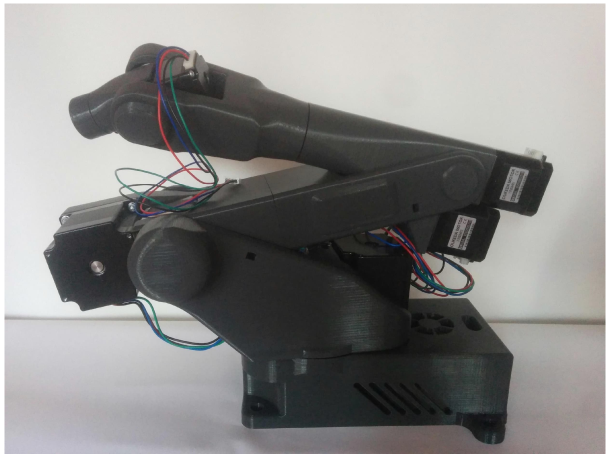

Fig. 2. 6DoF desktop robot arm AD100 [27]

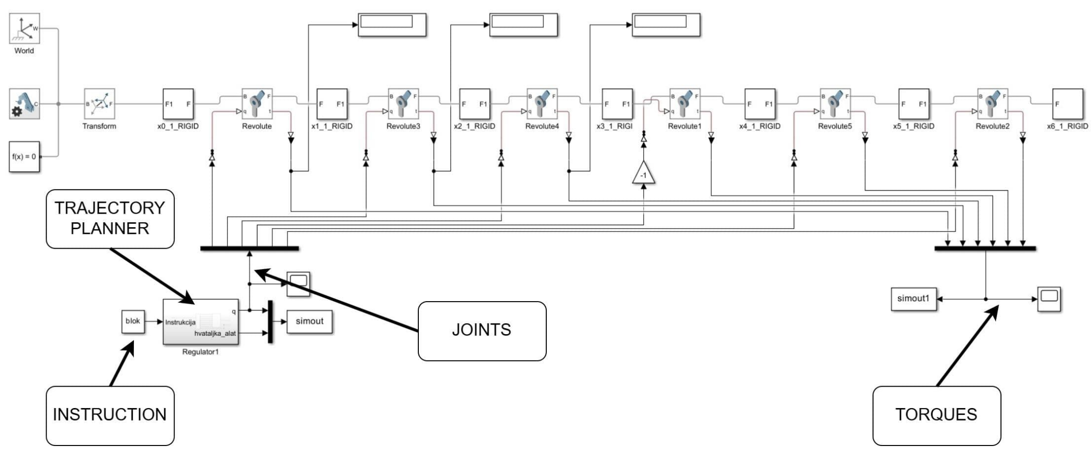

Fig. 3. Simulation block diagram in Simscape

The predefined robot motion, specified through motion instructions, and within the Unity software, is illustrated in Figure 4.

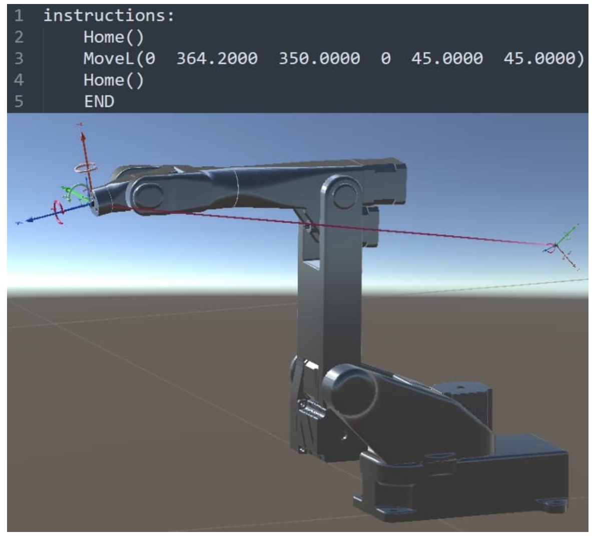

Fig. 4. Programmed robot motion

3.2 Simulation results

The dynamic simulation of the AD100 robot was conducted in both MATLAB Simscape and Unity using an identical joint-space trajectory, enabling a direct comparison between the torque results in the two simulation environments. Special attention was given to the torque behavior of Joint 2, which typically exhibits significant dynamic load due to its position within the kinematic chain. For programmed motion given in Figure 4, the trajectory of Joint 2 is given in Figure 5. Figure 6 shows a side-by-side comparison of the torque profiles for Joint 2 obtained from MATLAB Simscape (left) and Unity (right). The articulation drive forces from the Unity simulation setup exhibit an identical temporal structure to the MATLAB Simcape-computed torques. Key features, such as peak torque intervals and zero-crossing points, align closely between both simulations. This suggests that, when the robot dynamics parameters in Unity (links' centers of mass, inertias) are properly tuned using a CAD model-based URDF file, the simulation can serve as a practical tool for approximating torque demands.

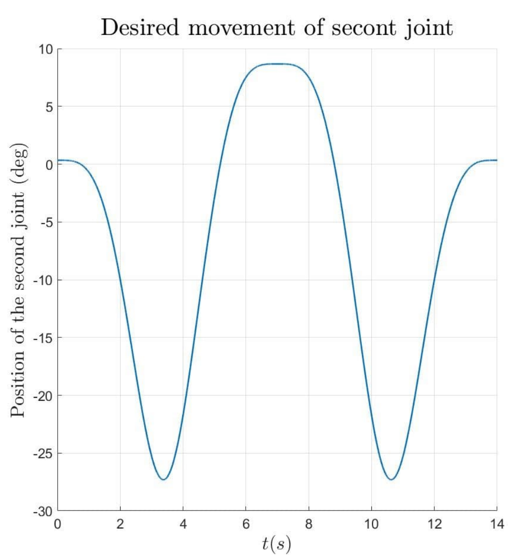

Fig. 5. Motion of the second joint based on given instructions

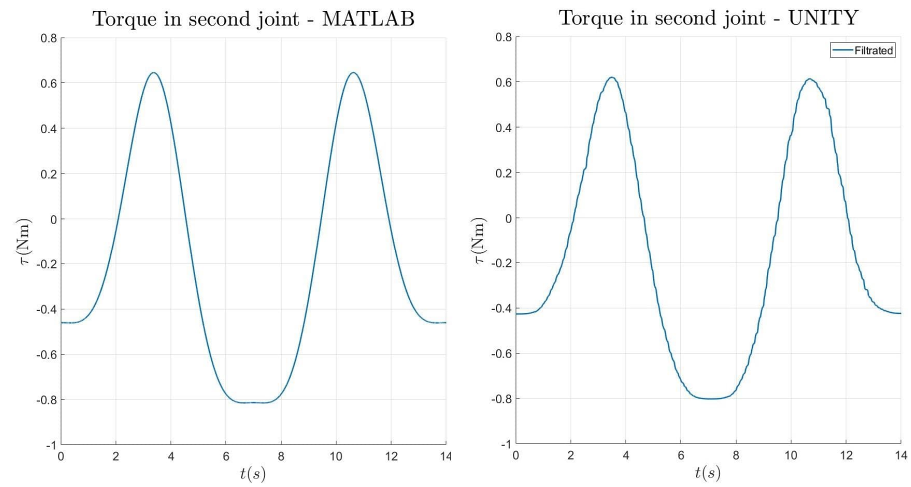

Fig. 6. Joint 2 torque obtained from MATLAB Simscape (left) and Unity (right)

4. Discussion

For the adequate dimensioning of the actuators and the robot links, information about the torques in the joints during movement is of essential importance. The presented approach demonstrates the potential of integrating game engine platforms for system engineering to support the design and early-stage evaluation of robotic manipulators. A key advantage of Unity and similar game engine platforms over conventional simulation environments lies in their native support for Extended Reality (XR), which enables advanced visualization features, for example, full-scale Augmented Reality (AR) representations of robots within their intended workspaces, Figure 7. It is possible to analyze the kinematic structure, robot motion, and workspace limitations before physical prototyping visually and spatially accurately in robots' workspace. The ability to iteratively test various configurations and robot designs in the game engine environment provides flexibility and reliability. This method particularly benefits early conceptual phases, where critical design decisions such as link lengths, joint ranges, or base configuration can be validated.

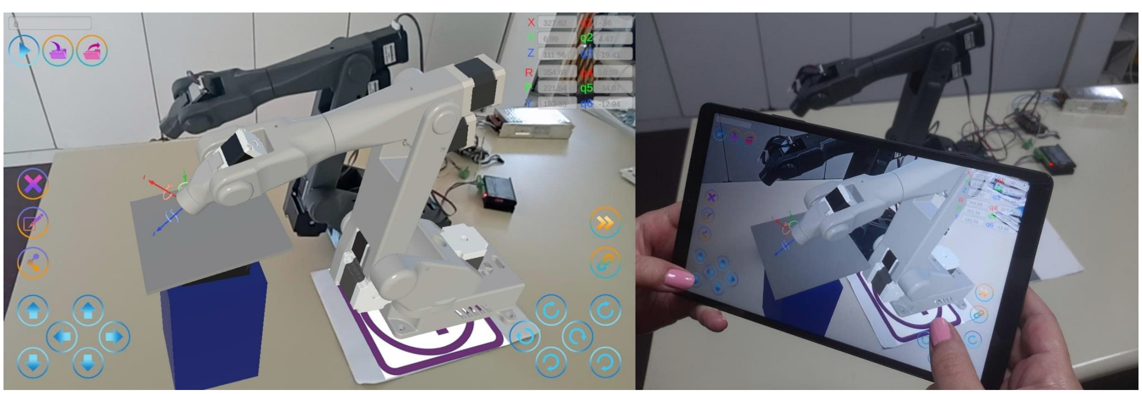

Fig. 7. Photo capture of augmented and real robot AD100 in designed robot programming Android app

Despite the growing interest in utilizing game engines for applications in robotics and multibody system simulation, the majority of existing resources are practice-oriented, with relatively few peer-reviewed scientific studies offering systematically defined methodologies and procedures for their integration into robotics research frameworks. This can be attributed to the free and open-source nature of the plugins, the multidisciplinary nature of such implementations, and the perception that game engines lack the scientific rigor required for high-precision robotic applications. However, this research shows that if an accurate robot model is imported into Unity (for which URDF file generated using MATLAB Simscape is used herein which allowed for precise transfer of geometric and physical parameters), Unity and its physics engine built-in functions can be used for reliable joint torque simulation, and consequently proper actuator selection.

5. Conclusions

This paper proposes a system engineering framework for the design of robotic manipulators and their actuator selection using interactive game engine platforms. The developed methodology integrates CAD modeling, MATLAB Simscape as an intermediate modeling environment, and Unity as a simulation platform that supports real-time robot motion simulation and immersive XR-based visualization. The use of MATLAB Simscape for importing the CAD model and converting it into a URDF file enabled the accurate transfer of mechanical properties into Unity. The native XR support in Unity enables full-scale visualization of the robot within its intended workspace, offering a distinct advantage over traditional simulation tools. The presented method supports the virtual verification of geometrical, kinematic, and dynamic properties and actuator selection, enabling early-stage decision-making in the development process and reduces the need for physical prototypes.

Acknowledgment

This research has been supported by the research grants of the Serbian Ministry of Science, Technological Development, and Innovations, Grant No. 451-03-137/2025- 424 03/200105 from 04.02.2025. and Grant No. 451-03- 425 136/2025-03/200066.

References

[1] Sobaszek, L., Gola, A., Varga, J. *Virtual designing of robotic workstations*. In Applied Mechanics and Materials. Vol. 844, pp. 31-37. Trans Tech Publications Ltd, 2016.
[2] Ong, S.K.; Yew, A.W.W.; Thanigaivel, N.K.; Nee, A.Y.C. *Augmented Reality-Assisted Robot Programming System for Industrial Applications*. Robot. Comput.-Integr. Manuf. 2020, 61, 101820.
[3] Fang, H. C., Ong, S. K., Nee, A. Y. C.: *Interactive robot trajectory planning and simulation using augmented reality*. Robotics and Computer-Integrated Manufacturing 28(2), 227-237, 2012
[4] Brogårdh, T.: *Present and future robot control development-An industrial perspective*. Annual Reviews in Control 31(1), 69-79, 2007.
[5] Pozzi, M., Achilli, G. M., Valigi, M. C., Malvezzi, M.. *Modeling and simulation of robotic grasping in simulink through simscape multibody*. Frontiers in Robotics and AI, 9, 873558, 2022.
[6] Todorov, E.; Erez, T.; Tassa, Y. MuJoCo: *A Physics Engine for Model-Based Control*. In Proceedings of the 2012 IEEE/RSJ International Conference on Intelligent Robots and Systems, Vilamoura-Algarve, Portugal, 7–12 October 2012; pp. 5026–5033.
[7] DART: Dynamic Animation and Robotics Toolkit. Available online: https://dartsim.github.io/ (accessed on 16 November 2023)
[8] Gazebo. Available online: https://gazebosim.org/home (accessed on 16 November 2024).
[9] Robot Simulator CoppeliaSim: *Create, Compose, Simulate, Any Robot-Coppelia Robotics*. Available online: https://www.coppeliarobotics.com/ (accessed on 16 November 2024).
[10] The MathWorks, Inc., *Simscape Multibody Link User's Guide*, Natick, MA, USA: MathWorks, 2023. [Online]. Available: https://www.mathworks.com/help/physmod/smlink/

[11] Boschetti, G., Sinico, T. *Designing digital twins of robots using simscape multibody*. Robotics, 13(4), 62, 2024.

[12] Bârsan, A., Racz, S. G., Breaz, R., & Crenganiș, M.. *Dynamic analysis of a robot-based incremental sheet forming using Matlab-Simulink Simscape™ environment*. Materials Today: Proceedings, 62, 2538-2542, 2022.

[13] Unity Real-Time Development Platform|3D, 2D, VR & AR Engine. Available online: https://unity.com (accessed on 23 November 2024).

[14] Unreal Engine|The Most Powerful Real-Time 3D Creation Tool. Available online: https://www.unrealengine.com/en-US/ (accessed on 23 November 2024)

[15] Devic, A., Vidakovic, J., Zivkovic, N.. *Development of Standalone Extended-Reality-Supported Interactive Industrial Robot Programming System*. Machines, 12(7), 480, 2024.

[16] Devic, A., Vidakovic, J., Zivkovic, N., Lazarevic, M.. *An Approach in the Design of an AR-Enhanced Robot Programming Platform for Educational Desktop Robot Arm*. In International Conference of Experimental and Numerical Investigations and New Technologies (pp. 121-128). Cham: Springer Nature Switzerland, 2024.

[17] URDF-ROS documentation. Available online: https://wiki.ros.org/urdf/XML/robot (accessed on February 2025).

[18] Dević, A., Vidaković, J., Živković, N., Lazarević, M.. *Systematic design of a desktop robot arm in solidworks and MATLAB Simulink*. In 9 th International Congress of Serbian Society of Mechanics Vrnjačka Banja, Serbia, July 5-7, 2023 (No. ID122, pp. 326-319). Belgrade: Serbian Society of Mechanics, 2023.

[19] Bennett, J.H. *How realistically can contemporary platoon-level infantry combat be simulated using First-Person Shooter (FPS) video games?*, Doctoral dissertation, King's College London, 2017.

[20] NVIDIA PhysX System Software. Available online: https://www.nvidia.com/en-gb/drivers/physx/physx-9-23-1019-driver/ (accessed on December 2024).

[21] Featherstone, R. *The Calculation of Robot Dynamics Using Articulated-Body Inertias*. Int. J. Robot. Res. 1983, 2, 13–30.

[22] Articulations-NVIDIA PhysX SDK 3.3.4 Documentation. Available online: https://docs.nvidia.com/gameworks/content/gameworkslibrary/physx/guide/3.3.4/Manual/Articulations.html?highlight=articulation (accessed on December 2024).

[23] 3D CAD Design Software|SOLIDWORKS. Available online: https://www.solidworks.com/media/solidworks-2020-improved-performance (accessed on December 2024).

[24] MATLAB Help Center-Solidworks. Available online: https://www.mathworks.com/help/smlink/solidworks.html (accessed on December 2024).

[25] URDF-Importer. Available online: https://github.com/Unity-Technologies/URDF-Importer/tree/main (accessed on February 2025).

[26] Unity Documentation - ArticulationBody.GetDriveForces. Available online: https://docs.unity3d.com/6000.0/Documentation/ScriptReference/ArticulationBody.GetDriveForces.html (accessed on December 2024).

[27] Devic, A.: *Design and control of a robotic system with six degrees of freedom*, Master thesis, Faculty of Mechanical Engineering Belgrade (2020).

[28] https://docs.unity3d.com/6000.0/Documentation/ScriptReference/ArticulationBody-xDrive.html

D.3

Extended abstract

BALLISTIC IMPACT OF FRAGMENT-SIMULATING PROJECTILES ON STEEL TARGETS: A MULTI-APPROACH STUDY

Predrag M. Elek[1][0000-0002-2927-019X], **Miloš D. Marković**[1][0000-0003-2217-9833], **Dejan T. Jevtić**[1][0000-0002-2228-1080], **Radovan V. Đurović**[1][0000-0001-6746-5468]

[1] Faculty of Mechanical Engineering,
The University of Belgrade, Kraljice Marije 16, 11120 Belgrade 35
e-mail: pelek@mas.bg.ac.rs, mdmarkovic@mas.bg.ac.rs, djevtic@mas.bg.ac.rs, rdjurovic@mas.bg.ac.rs

Abstract:

Penetration mechanics, a subfield of terminal ballistics, examines the impact of projectiles (penetrators) on targets (obstacles) [1–3]. This study investigates the ballistic impact of fragment-simulating projectiles (FSPs) on homogeneous steel plates, a topic relevant to assessing the efficiency of fragmentation warheads and projectiles, as well as target vulnerability and protection. Three complementary approaches—experimental, analytical, and numerical—are employed to analyze the penetration process.

Extensive experimental research has been conducted [4, 5] and supplemented with new results. Two steel target plates, 1.25 mm and 2.20 mm thick, were perforated using blunt, deformable cylindrical projectiles with a diameter of 4.70 mm and two distinct masses—1.090 g and 1.912 g. Given the geometric characteristics and material properties of both the penetrator and the target, the dominant penetration mechanism was identified as plugging. Impact and residual velocities of the FSPs were measured, alongside the geometric properties of deformed penetrators and perforation holes in the target plates.

Various analytical models describing the plugging perforation process were examined. Additionally, a numerical model was developed in Abaqus using a Lagrangian framework with explicit time integration. The Johnson-Cook constitutive and failure models were employed to characterize dynamic stress and material failure. The analytical and numerical results were validated against experimental data, showing good agreement. This validation enables key conclusions regarding the influence of penetrator mass on residual velocity and provides an evaluation of the ballistic limit velocity.

Key words: penetration mechanics, perforation, plugging, fragment simulating projectile, ballistic limit velocity, numerical simulation

References

[1] Walker, J.D., *Modern impact and penetration mechanics*, Cambridge University Press, Cambridge, 2021.
[2] Hazell, P.J., *Armour: Materials, Theory, and Design*, CRC Press, Boca Raton, FL, 2016.

[3] Crouch, I.G., *Science of Armour Materials*, Woodhead Publishing, 2016.

[4] Elek, P., Jaramaz, S., Micković, D.: Modeling of perforation of plates and multi-layered metallic targets, *International Journal of Solids and Structures,* 3-4/42, 2005, 1209-1224.

[5] Elek, P., Jaramaz, S., Micković, D., Miloradović, N.: Experimental and numerical investigation of perforation of thin steel plates by deformable steel penetrators, *Thin-Walled Structures*, Vol. 102, May 2016, 58-67.

D.4

Extended abstract

TRAPEZOIDAL CONTROL FOR PREVENTION OF UNWANTED VIBRATIONS OF MECHANICAL SYSTEMS

Alexander M. Formalskii[1], Yury D. Selyutskiy[1][0000-0001-8477-6233]

[1]Institute of Mechanics, Lomonosov Moscow State University, Michurinsky prosp. 1, 119192, Moscow, Russia, e-mail: formal@imec.msu.ru

Abstract:

A mechanical system with two DoFs is considered which contains two absolute rigid bodies. These bodies are connected by a weightless viscoelastic rod that can be stretched or compressed. Each body can move translationally along a fixed straight line parallel to the rod. A control force limited in magnitude is applied to one of these bodies. The force is directed along the rod. Time-continuous piecewise linear (trapezoidal) control is constructed that transfers the system from one equilibrium position to another within the time close to the minimum possible. The constructed control allows for avoiding unwanted vibrations in the system. Besides, it is robust in terms of the rod damping and stiffness parameters.

Key words: control, trapezoidal control, robustness, unwanted vibrations

1. Introduction

Time-optimal control of mechanical systems, as a rule, induces vibrations in these systems (sometimes, quite intensive) during the transient process. A vast literature (e.g., [1-3]) is dedicated to the problem of construction of a sub-optimal control that would allow for mitigation or prevention of such oscillations. In the present work, a method for construction of a time-continuous suboptimal control law is proposed that prevents occurrence of vibrations in mechanical systems of a certain type during the transient process.

2. Problem Statement and Results

Two rigid bodies can move along the abscissa axis. The bodies are connected with a weightless linear viscoelastic rod (Fig. 1). The control force **F** is applied to the first body and is limited in magnitude: $|\mathbf{F}| \le F_0$. The purpose of the control is to move the system from one equilibrium position to another without unwanted vibrations and quickly enough.

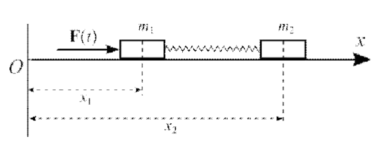

Fig. 1. Scheme of the considered system.

Instead of the time-optimal control, which in this case is of “bang-bang” type, we use a “trapezoidal” control (Fig. 2). The duration ϑ of the segments where the control F changes linearly with time equals to the natural period of vibrations of the system. Duration of segments where the control reaches maximum/minimum values is determined by the distance L between equilibrium positions. One can readily show that, in this situation, no vibrations appear during the transition process. Besides, the difference between the total time θ of the process and the time t_{opt} given by the time-optimal control is smaller than ϑ.

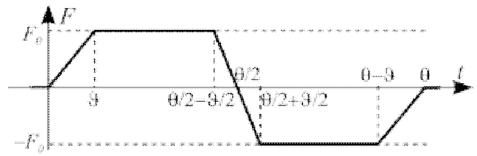

Fig. 2. Trapezoidal control.

An example of numerical simulation is shown in Fig. 2 for the case when there is no damping in the rod (red lines correspond to the trapezoidal control, and black ones, to the time-optimal control). Calculations are performed in normalized variables (the length of the non-deformed rod and the natural frequency of the rod were used for the normalization).

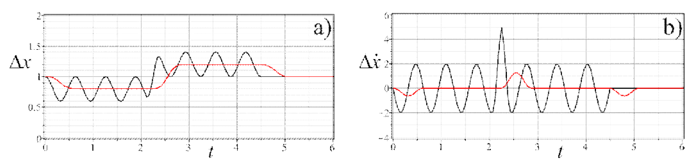

Fig. 3. Numerical example: a) normalized relative distance Δx between bodies vs. time; b) normalized relative speed $\Delta\dot{x}$ of bodies vs. time.

The proposed control allows for prevention of relative oscillations of bodies of the system. The process time is larger than the optimal one, but the difference is not very large.

In numerous works ([1-2], etc.), prevention of unwanted oscillations is ensured by discontinuous control law. The analysis of possibility to use alternative smooth control methods (such as MPC) remains an object for future research. Performed numerical calculations show also that the trapezoidal control is less sensitive to the variation of parameters of the system (such as stiffness and damping of the rod) than the time-optimal control.

3. Conclusions

The constructed “trapezoidal” control allows for mitigation of unwanted vibrations in some mechanical systems (both during the transition process and after its end) and is robust with respect to the change of values of system parameters. As a future work, it is planned to validate the proposed control approach experimentally.

References

[1] Prourzin V.A. *Control of elastic plant movement without excitation of eigen-oscillation*. Autom. Remote Control, Vol. 78, 2141-2153, 2017.

[2] Hoshino T., Fujiwara D. *Time-Suboptimal Trajectories for Vibration-Free Positioning of Undamped Flexible Systems*. IECON 2022, pp. 1-6.

[3] Budanov V.M., Selyutskiy Y.D., Formalskii A.M. *Prevention of oscillations of a spherical robot in longitudinal motion*. J. Comp. & Syst. Sci. Int., Vol. 61 (4), 567-580, 2022.

10th International Congress of the Serbian Society of Mechanics
Niš, Serbia, June 18-20, 2025
D.5
Original Scientific Paper

DOI:10.46793/ICSSM25.196I

MOTION ANALYSIS OF A VIBRATORY CONVEYOR'S TROUGH DURING ITS OPERATION

Uroš Lj. Ilić[1] [0000-0003-3955-8995], **Mihailo P. Lazarević**[2] [0000-0002-3326-6636], **Emil A. Veg**[2] [0000-0002-6702-6251], and **Željko V. Despotović**[1] [0000-0003-2977-6710]

[1]University of Belgrade, Institute Mihajlo Pupin, Volgina 15, Belgrade, Serbia

email: uros.ilic@pupin.rs

email: zeljko.despotovic@pupin.rs

[2]University of Belgrade, Faculty of Mechanical Engineering, Kraljice Marije 16, Belgrade, Serbia

email: mlazarevic@mas.bg.ac.rs

email: eveg@mas.bg.ac.rs

Abstract. This study investigates the dynamic behavior of a trough of a vibratory conveyor. The main focus is on modeling the motion of the trough, analyzing the forces acting on the system, and assessing the spring stiffness and deflections under operational conditions. Using theoretical modeling based on the theory of elasticity and rigid body mechanics mechanics, the dynamics of the system are described, and the differential equations of motion for a single-degree-of-freedom oscillator are derived. A finite element analysis inside Solidworks Simulation package is performed to observe the motion of the vibratory trough. Orthogonal displacements of the centre of mass of the vibratory trough were observed. Simulation results are provided and discussed accordingly at the end of this paper. The findings suggest that the axial displacement of the trough is couple orders of magnitude smaller than its transversal displacement, allowing for a simplification in further modeling. This study provides valuable insights into the design and operation of electromagnetic vibratory conveyors, contributing to the optimization of spring stiffness and system stability for industrial applications.

Keywords: Vibratory motion, Vibratory conveyor, Clamped beam, Composite leaf spring, FEA Simulation.

1. Introduction

Vibratory conveyors are advanced devices that utilize oscillatory motion to efficiently transport materials along predefined paths. These systems are widely used across various industrial sectors, including the food, pharmaceutical, chemical, mining, and materials processing industries [1]. For instance, Fig. (1(a)) illustrates how *KMG Systems* has addressed the challenge of internal material transport and precise dosing at the output [2]. These conveyors are particularly suitable for handling fine, granular, or powdery materials, as their vibrations facilitate a continuous and uniform flow without blockages.

A drawing of a vibratory conveyor is given in Fig. (1(b)), with its most significant elements annotated. The heaviest component is the massive base (Fig. (1(b)), 1), which is usually made of cast iron to further suppress vibrations originating from the actuator (Fig. (1(b)), 2). The vibratory actuator sets the vibratory trough (Fig. (1(b)), 3) into motion, propelling or sliding the conveyed material. The trough is connected to the massive base by a set of composite leaf springs (Fig. (1(b)), 4), which form an angle α with the vertical axis. This angle does not exceed 45°, but the vibratory process is most effective when it is around 20° [1]. The transverse motion of these leaf springs defines the vibratory motion of the trough, which is attached to their vibrating ends, Q and S. Their other ends, at points P and R, are clamped to the massive base, which is further supported by a set of viscoelastic damping elements (Fig. (1(b)), 5) that suppress vibrations and isolate the vibratory conveyor from its surroundings.

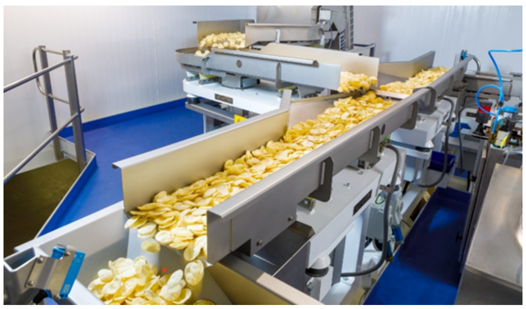

(a) A vibratory conveyor used in food industry

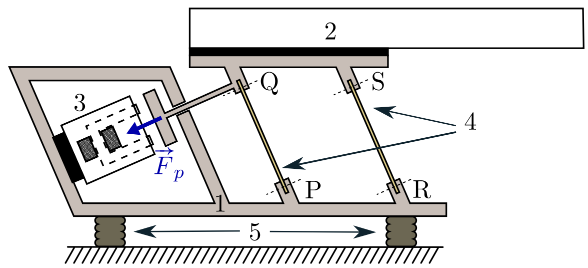

(b) An equivalent drawing of a vibratory conveyor with its most significant elements

Figure 1: A vibratory conveyor

There are two types of actuators: mechanical, which is driven by a camshaft, and electromagnetic. In modern applications, electromagnetic actuators are preferred because they offer better control and enable precise dosing of material. An electromagnet sets the armature into motion through electromagnetic force acting on it. Since the armature is rigidly connected to the vibratory trough, the trough is actuated in the same manner. Additionnally, electromagnetic actuators are more energy-efficient because they can be more easily tuned to the conveyor's natural frequency [1]. Additionally, electromagnetic vibratory actuators can be digitally controlled and tuned to excite the vibrating elements at specific times and/or positions. For example, the authors in [3] introduce a small impulse after each oscillation cycle, supplying just enough energy to maintain resonance, which minimizes energy dissipation. Moreover, various sensors can be attached to track the kinematic properties of the trough (displacement, velocity, and acceleration) and integrate complex control systems with feedback from sensor measurements [4].

To successfully implement a control algorithm, one must have a mathematical model of the desired machine. A vibratory conveyor is a complex system composed of various elastic and viscoelastic elements. Additionally, the effect of the transported load presents a complex challenge, as the conveyed material, which typically has a granular structure, must be modeled according to its vibro-rheological properties [5].

This paper focuses on the forces acting on the vibratory trough during its oscillatory motion. In the second section, its motion will be analyzed with the help of a free-body diagram. A discussion will be presented to explain the types of motion exhibited by the vibratory trough, along with the conditions required for each type. The corresponding differential equations of motion will also be provided. In the third section, a Finite Element Analysis (FEA) using SolidWorks simulation software will be conducted to assess the influence of forces acting along the length of the composite leaf springs. Simulation results will be presented at the end of the third section and discussed accordingly.

2. Motion Analysis of the Vibratory Trough

The vibratory trough from Fig. (1) is extracted, and its interactions with other components are replaced with the corresponding reaction forces and moments. Figure (2) represents a free-body diagram of the vibratory trough. Its mass is denoted as m_K, with the corresponding center of mass located at point K. The effect of gravity is represented by the gray vector $m_K\vec{g}$.

As stated in the introduction, modeling the conveyed medium is a complex task, and in the general case, its effect on the vibratory trough's surface cannot be expressed analytically. Typically, this effect is derived from experimental investigations or statistical mechanics [5]. Let us assume that the effect of the conveyed load is summarized by the main force vector $\vec{F}_R$ (purple), which acts at point R and has a time-dependent angle of attack β.

Electromagnetic vibratory conveyors are designed so that their excitation force vector $\vec{F}_E$ is perpendicular to the potential movement of the tip of the leaf springs. That is, it is collinear with the assumed rectilinear motion of the vibratory trough. Although the electromagnetic force acting on the electromagnet's armature is volumetric, its effect is represented as a force applied at point E, where the armature is rigidly connected to the trough. Due to the nature of electromechanical energy transduction, in a standard electromagnet configuration, this force is always attractive [6].

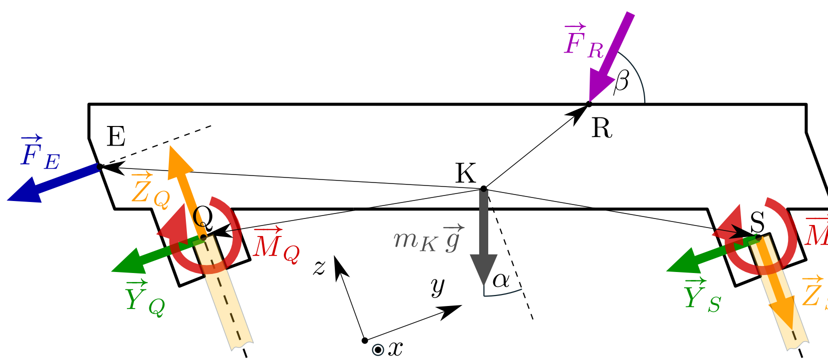

Figure 2: A free-body diagram of the vibratory trough during its vibratory motion

In the general case, the vibratory motion of the trough can be simplified to a two-dimensional planar motion. Leaf springs are clamped to the trough at points Q and S. Typically, their reactions can be expressed as a set of orthogonal reaction forces and a bending moment. Given that composite leaf springs can be represented as a transversely vibrating beam [3], the reaction forces and moments at these two points can be represented as vectors opposite to those experienced by the transversely vibrating beam at its foundation, i.e., its base.

For a coordinate system with axes as presented in Fig. (2), the directions of the reaction forces and moments are defined according to [7] and [8] for a potential positive displacement along the y-axis. The green vectors $\vec{Y}_Q$ and $\vec{Y}_S$ represent reactions along the y-axis, whose magnitudes correspond to the shear forces in the leaf springs at their vibrating ends Q and S. These forces tend to restore the system to its equilibrium position. Positioned orthogonally to them are the forces $\vec{Z}_Q$ and $\vec{Z}_S$ (orange), which correspond to the axial forces in the leaf springs at their respective moving ends Q and S. Additionally, since the moving ends of the leaf springs are clamped, they experience a bending moment at these points. Equal in magnitude but opposite in direction are the reaction moments $\vec{M}_Q$ and $\vec{M}_S$, which the vibratory trough experiences when displaced from its equilibrium (rest) position. These moments are oriented along the positive x-axis and are marked in red in Fig. (2). For the given set of forces, one can write the following vector equation:

$$m_K \vec{a}_K = m_K \vec{g} + \vec{F}_R + \vec{F}_E + \vec{Y}_Q + \vec{Y}_S + \vec{Z}_Q + \vec{Z}_S \ , \tag{1}$$

where $\vec{a}_K$ represents an acceleration of the point K. Also, one can write a moment equation around axis Kx, as follows:

$$[J_K]\,\vec{\varepsilon} = \overrightarrow{KR} \times \vec{F}_R + \overrightarrow{KE} \times \vec{F}_E + \overrightarrow{KQ} \times \vec{Z}_Q + \overrightarrow{KQ} \times \vec{Y}_Z + \overrightarrow{KS} \times \vec{Z}_S + \overrightarrow{KS} \times \vec{Y}_S + \vec{M}_Q + \vec{M}_S \ , \tag{2}$$

where $[J_K]$ represents tensor of inertia the vibratory trough and $\vec{\varepsilon}$ is angular acceleration of the vibratory trough. Furthermore, if the vector equation given by Eq. (1) is decomposed alongside y and z axis:

$$y: \quad m_K \ddot{y}_K = -m_K g \sin\alpha - F_R \cos\beta - F_E - Y_Q - Y_S \tag{3}$$

$$z: \quad m_K \ddot{z}_K = -m_K g \cos\alpha - F_R \sin\beta + Z_Q - Z_S \tag{4}$$

Given that the motion of the vibratory conveyor can be represented as a two-dimensional planar motion, hence the x-components of the positions vectors from Eq. (2) are set to zero. The vectors defining the positions of significant points relative to the trough's center of inertia have the following components in the $Kxyz$ coordinate system:

$$\overrightarrow{KR} = \begin{Bmatrix} 0 \\ \overline{KR}_y \\ \overline{KR}_z \end{Bmatrix} \qquad \overrightarrow{KE} = \begin{Bmatrix} 0 \\ \overline{KE}_y \\ \overline{KE}_z \end{Bmatrix} \qquad \overrightarrow{KS} = \begin{Bmatrix} 0 \\ \overline{KS}_y \\ \overline{KS}_z \end{Bmatrix} \qquad \overrightarrow{KQ} = \begin{Bmatrix} 0 \\ \overline{KQ}_y \\ \overline{KQ}_z \end{Bmatrix} \tag{5}$$

If we calculate the vector products from Eq. (2) and substitute the values from Eq. (5) into Eq. (2), the following scalar equation is obtained:

$$\begin{aligned} J_{Kx}\ddot{\varphi} = {} & \overline{KR}_z \cdot R\cos\beta - \overline{KR}_y \cdot R\sin\beta + \overline{KE}_z \cdot F_E \\ & + \overline{KQ}_z \cdot Y_Q - \overline{KS}_z \cdot Y_S - \overline{KQ}_y \cdot Z_Q - \overline{KS}_y \cdot Z_S - M_Q - M_S \ , \end{aligned} \tag{6}$$

where J_{Kx} represents the axial moment of inertia for the central x-axis, and $\ddot{\varphi}$ represents a component of angular acceleration $\vec{\varepsilon}$ along the x-axis. Consequently, the angle φ defines the angle of rotation of the vibratory trough during the operation of the vibratory conveyor.

In the general case, the vibratory trough, represented by a simple free-body diagram in Fig. 2, performs planar motion in the vertical plane. In other words, it is free to move along the y and z axes and rotate around the x-axis of the coordinate system $Kxyz$. A simplified version of the drawing from Fig. 1(b) is shown in Fig. 3(a).

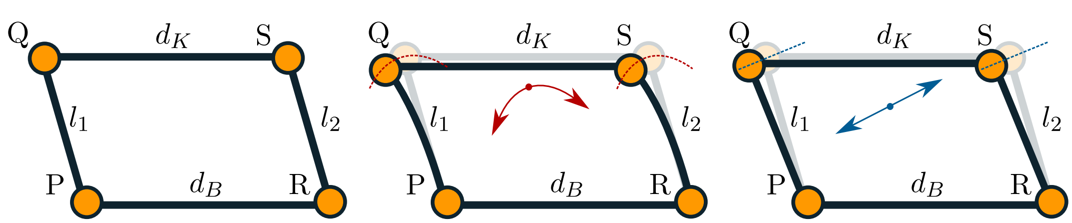

(a) Initial position of the conveyor (b) Translatory motion (c) Rectilinear motion

Figure 3: Different forms of motion of the vibratory trough

At the initial moment, this mechanical structure can be represented as a parallelogram with its vertices at points P, Q, R, and S. For simplicity, let us introduce the following notation for the lengths of the sides of the parallelogram:

$$\overline{PR} = d_B \qquad \overline{QS} = d_K \qquad \widehat{PQ} = l_1 \qquad \widehat{RS} = l_2 \;, \tag{7}$$

where $\overline{(\cdot)}$ denotes a straight line and $\widehat{(\cdot)}$ denotes the length of an arc, since composite leaf springs deform under transversal load. The physical interpretation of the lengths mentioned in Eq. (7) is as follows: l_1 and l_2 are the lengths of the composite leaf springs, while d_B and d_K represent the distances between their clamping points in the base and in the trough, respectively. Given that the base and the trough can be considered as rigid bodies, and that their strains can be assumed to be zero under standard forces experienced by the vibratory system during operation, it can be concluded that $d_B = d_K = \text{const.}$.

2.1 *Translatory motion of the vibratory trough*

Following on, considering that composite leaf springs are not rigid bodies, their shape (length) is defined by expressions from the theory of elasticity and/or continuum mechanics. The deflection of a transversely loaded beam is a function of its material characteristics, namely Young's modulus of elasticity E and density ρ, as well as its dimensions, namely length L and cross-sectional area $A = b \cdot h$ (from which the axial moment of inertia about the bending axis is also derived) [7]. Also, the deflection is a function of the transverse force that it experiences. Hence, the total length of the leaf spring is a function of all the physical quantities mentioned above. However, if we assume that these two bodies have the same mechanical characteristics (E and ρ), i.e., that they are made of the same material and that they are manufactured with the same dimensions (L, b, and h), and experience the same distribution of transverse force ($\vec{F}_E$), we can conclude that, for the purposes of this analysis, the lengths of the two springs, even in the deformed shape, can be assumed to be equal. Therefore, we can write that $l_1 = l_2$. Despite the fact that, in the general case, l_1 and l_2 are not straight lines, given that they share the same length, the *parallelogram* from Fig. (3(a)) keeps its horizontal sides parallel. Hence, it performs a translatory motion like the one depicted in Fig. (3(b)).

Given that the trough performs a translatory motion, it does not have an angular acceleration $\vec{\varepsilon}$, and Eq. (6) can be equated to zero. Furthermore, if we assume that the main reaction vector from the conveyed load $\vec{R}$ is known, we are left with eight unknowns: $\ddot{y}_K$, $\ddot{z}_K$, Y_Q, Y_S, Z_Q, Z_S, M_Q, and M_S (given that $\ddot{\varphi} = 0$). With only three equations, this system is undetermined. Even if we focus on the motion of the empty vibratory trough ($R = 0$), we are left with far more unknowns than equations. This form of motion can't be solved analytically, but it can be solved numerically using transient FEA simulations for small time increments.

In Fig. (3(b)), the red dashed curve represents the trajectory of the moving end of the composite spring. Taking into account that both springs perform identical motion and the trough is a rigid body, its center of mass will follow along a similar trajectory. The curvature of the trajectory is exaggerated to emphasize the fact that it is not a straight line. In real situations, the curvature is much smaller, so that under certain circumstances, the trajectory around the equilibrium points can be approximated with a straight line [3].

2.2 *Rectilinear motion of the vibratory trough*

Under normal working conditions, the optimal spring deflection (amplitude of vibration) does not exceed 1 mm for electromagnetic vibratory conveyors [9]. Given that the usual lengths of composite leaf springs used for vibratory conveyors exceed 100 mm [10], it can be approximated that

$l_1 = l_2 \approx$ const. Such approximations are also introduced for small deflections of beams ($y \ll l$), where the neutral line of the beam remains the constant length, but the ends of the beam are subjected to deformation [7], [8].

Motion of the trough relative to the base is considered to be rectilinear oscillatory [3]. Some authors go even further and approximate the whole vibratory system as a single degree-of-freedom oscillator [11]. Therefore, the motion of the vibratory trough can be represented as a rectilinear back-and-forth vibratory motion, like the one depicted in Fig. (3(c)), where the blue dashed line represents the trajectory of the moving end of the composite spring. Like in the previous case, the center of mass of the vibratory trough will follow along a similar trajectory.

For relatively small deflections, a composite leaf spring with high slenderness ratios can be modeled as an Euler-Bernoulli beam that has both of its ends clamped [12]. One can write expressions for bending moments and shear forces at its foundations, as a function of deflection $w(t)$ along the y axis. The forces and moments that the vibratory trough experiences are equal in intensity but have opposite directions. Therefore, the following expressions for the intensities of the reaction forces and moments at the clamping points Q and S are obtained from the literature [7]:

$$Y_Q = \frac{12EIw_Q(t)}{L^3} \quad M_Q = \frac{6EIw_Q(t)}{L^2} \quad Y_S = \frac{12EIw_S(t)}{L^3} \quad M_S = \frac{6EIw_S(t)}{L^2} \ , \tag{8}$$

where E is Young's modulus of elasticity, I is the axial moment of inertia for the bending axis, w_Q and w_S are the deflections along the y-axis at the corresponding points, and L is the length of the composite leaf spring. Following this, if we substitute the expressions from Eq. (8) into Eq. (3), we obtain the equation of motion for the center of mass of the vibratory trough:

$$m_K\ddot{y}_K = -m_K g \sin\alpha - F_R \cos\beta - F_E - \frac{12EI}{L^3}w_Q - \frac{12EI}{L^3}w_S \tag{9}$$

The last two terms in Eq. (9) indicate that the observed system comprises two parallel springs with equal stiffness. If the considered vibratory system has up to n composite leaf springs, the total stiffness of the system will be equal to $k_e = n \cdot \frac{12EI}{L^3}$, assuming that the springs are identical.

Taking into account that the trough moves in rectilinear motion, the deflections of points Q and S along the y-axis (w_Q and w_S) are equal to the y coordinate of the trough's center of mass in the $Kxyz$ coordinate system. Rearranging the elements from the previous equation, we obtain the final form of the differential equation of a single degree of freedom oscillator:

$$m_K\ddot{y}_K + \frac{24EI}{L^3}y_K = -m_K g \sin\alpha - F_R \cos\beta - F_E \ , \tag{10}$$

where the coefficient $\frac{24EI}{L^3}$ represents the total stiffness of the observed system, k_e. The left side of Eq. (10) then represents the external disruptive forces that act on the system. Following this, if the values from Eq. (8) are substituted into Eq. (4) and Eq. (6), and after rearranging the elements, given that $\ddot{z}_K = 0$ and $\ddot{\varphi} = 0$, the following system of equations is obtained:

$$Z_Q - Z_S = m_K g \cos\alpha + F_R \sin\beta \tag{11}$$

$$\begin{aligned} \overline{KQ}_y \cdot Z_Q + \overline{KS}_y \cdot Z_S = {} & F_R \left(\overline{KR}_z \cdot \cos\beta - \overline{KR}_y \cdot \sin\beta\right) + \overline{KE}_z \cdot F_E \\ & + \overline{KQ}_z \frac{12EI}{L^3}w_Q - \overline{KS}_z \frac{12EI}{L^3}w_S - \frac{6EI}{L^2}w_Q - \frac{6EI}{L^2}w_S \end{aligned} \tag{12}$$

From Eq. (11), it follows that:

$$Z_S = Z_Q - m_K g \cos\alpha - F_R \sin\beta \ , \tag{13}$$

and substituting Eq. (13) into Eq. (12), given that $w_Q \equiv w_S = y_K$, the following expression is obtained:

$$\overline{KQ}_y \cdot Z_Q + \overline{KS}_y \left(Z_Q - m_K g \cos\alpha - F_R \sin\beta\right) = F_R \left(\overline{KR}_z \cdot \cos\beta - \overline{KR}_y \cdot \sin\beta\right) + \overline{KE}_z \cdot F_E + \frac{12EI}{L^3}\left(\overline{KQ}_z - \overline{KS}_z - L\right) y_K \ , \tag{14}$$

from where it follows that:

$$Z_Q \left(\overline{KQ}_y + \overline{KS}_y\right) = F_R \left(\overline{KR}_z \cos\beta - \overline{KR}_y \sin\beta\right) + \overline{KE}_z \cdot F_E + \frac{12EI}{L^3}\left(\overline{KQ}_z - \overline{KS}_z - L\right) y_K + \overline{KS}_y \left(m_K g \cos\alpha + F_R \sin\beta\right) \ , \tag{15}$$

what leads to the final expression for the reaction in point Q along the z-axis:

$$Z_Q = \frac{1}{\overline{KQ}_y + \overline{KS}_y}\Bigg[F_R\Big(\overline{KR}_z \cos\beta + \left(\overline{KS}_y - \overline{KR}_y\right)\sin\beta\Big) + \overline{KE}_z \cdot F_E + \frac{12EI}{L^3}\left(\overline{KQ}_z - \overline{KS}_z - L\right) y_K + \overline{KS}_y m_K g \cos\alpha\Bigg]. \tag{16}$$

Substituting the expression from Eq. (16) into Eq. (13), after the simplification, leads to the final expression for the reaction in point S along the z-axis:

$$Z_S = \frac{1}{\overline{KQ}_y + \overline{KS}_y}\Bigg[F_R\Big(\overline{KR}_z \cos\beta - \left(\overline{KR}_y + \overline{KQ}_y\right)\sin\beta\Big) + \overline{KE}_z \cdot F_E + \frac{12EI}{L^3}\left(\overline{KQ}_z - \overline{KS}_z - L\right) y_K - \overline{KQ}_y m_K g \cos\alpha\Bigg] \ . \tag{17}$$

From expressions for Z_Q and Z_S given in Eq. (16) and Eq. (17), several conclusions can be drawn regarding the intensity of these two axial forces. Since the term $(\overline{KQ}_y - \overline{KS}_y)$ appears in the denominator, the proposed axial forces are inversely proportional to the distance between the springs' clamping points Q and S. As this distance increases, the magnitudes of these forces decrease proportionally. The numerator (inside the square brackets) consists of multiple components, leading to the following conclusions:

- Vertical component of the force $\vec{F}_R$ is proportionally split between axial forces, in accordance to the position of the attack point of the load's result vector relative to clamping Q and S.
- The effect of the excitation force $\vec{F}_E$ is identical in both forces and it's proportional to the vector's displacement from the trough's centre of mass.
- Given that composite leaf springs oscillate around the equilibrium point, their stiffness can be linearized around them. Hence the effect of the springs' stiffness on the axial forces is proportional to the trough's displacement y_K.
- The effect of the vibratory trough's weight is proportionally split between the axial forces, in accordance to corresponding forces' directions.

3. FEA Simulation

In order to assess the nature of motion of the vibratory trough, an FEA simulation was performed inside SolidWorks *Simulation* package. For the purpose of the simulation, a simplified CAD model of the vibratory trough was designed (Fig. 4(a)), with its most important components such as: 1) Massive base; 2) Vibratory trough; 3) Composite leaf springs. For the stationary massive base, the chosen material is standard cast iron, and the material of the trough is aluminum. The total mass of the trough is approx. 3.5 kg. Composite leaf springs resemble the ones found inside the laboratory of the Institute Mihajlo Pupin. The mechanical properties of the material that comprise the leaf springs used in the simulation are listed in Table (1). These values are taken from the manufacturer's web page [10] and used to generate a new material for the purposes of the FEA simulation. Dimensions of the springs are $b \times h \times L = 150 \times 5 \times 150$ mm.

Mechanical property	Value
Flexural strength [MPa]	932 ± 5%
Tensile strength [MPa]	800 ± 5 %
Compressive strength [MPa]	724 ± 5%
Modulus of elasticity [MPa]	28 000
Poisson's ratio	0.074
Mass density [g/cm^3]	1.8

Table 1: Mechanical properties of the *S-Ply Yellow* composite leaf spring

Constraints and external loads are also needed for the purpose of the simulation. Green arrows on Fig. (4(b)) represent translational constraints of the base. Given that the base is considered stationary, its motion is restricted in all three directions. The effect of the conveyed mass is modeled with the help of the *Remote Load/Mass* feature inside the SolidWorks Simulation interface. It is shown on Fig. (4(b)) with pink lines. The considered additional mass is equal to 500 g. Following on, blue lines on Fig. (4(b)) represent the electromagnetic excitation force that acts on the vibratory trough. For the purpose of the simulation, the force is modeled as an impulse with a magnitude of 1500 N, after which the trough continues to perform free vibrations. The effect of the gravitational forces is also taken into account. The direction of the gravitational pull is shown with a red vector on Fig. (4(b)).

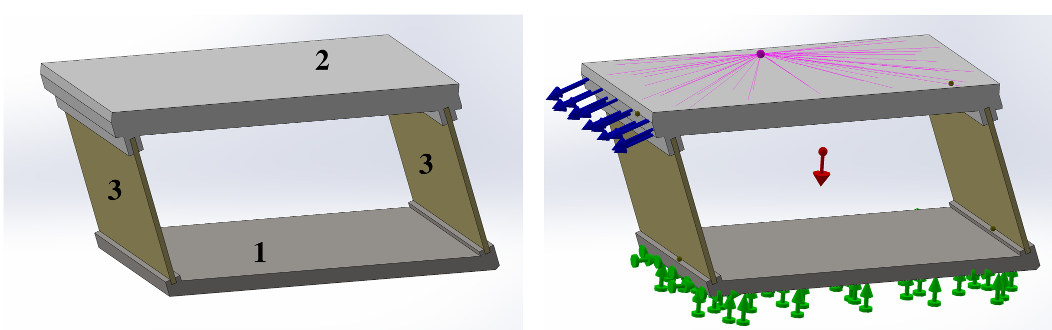

(a) Simplified CAD model used for FEA

(b) Constraints and External loads used for FEA

Figure 4: CAD modelling of the vibratory process

A chosen time step for this transient nonlinear dynamic analysis is 1 ms. With a total of 401 steps, the simulation lasts for up to only 0.4 s. Given that for each time step, the program needs to remesh the model and compute the forces, the total time needed for the final simulation to complete was around 1 hour. For the purpose of this research, the motion of the center of mass of the vibratory trough is observed. Figure (5) shows its displacements in the vertical plane. Its axial displacement (along the Kz axis) is shown on Fig. 5(a), while its transversal displacement (along the Ky axis) is shown on Fig. (5(b)). It can be observed that when the amplitude of the vibrations in the y direction falls below 1 mm, the displacement in the z direction falls below 0.005 mm. More precisely, the axial displacement (in the direction of leaf springs) of the vibratory trough is about 200 times smaller than the displacement perpendicular to the direction of leaf springs. Hence, in further evaluation and modeling, it is reasonable to neglect it, concluding that $z_K = \text{const.} = 0$.

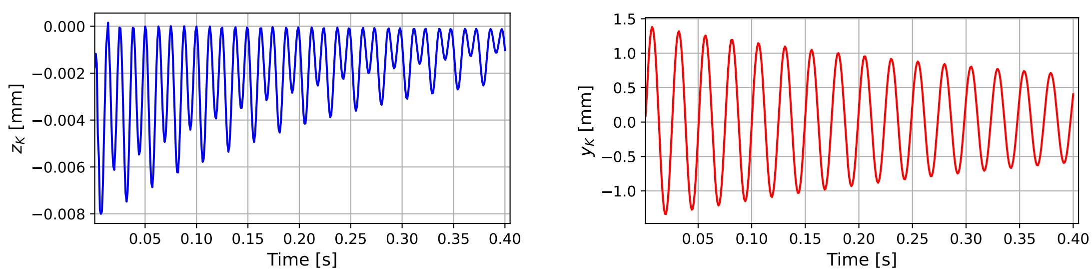

(a) Axial displacement of the vibratory trough

(b) Transversal displacement of the vibratory trough

Figure 5: Orthogonal displacements of the vibratory trough

4. Concluding remarks and Discussion

This study has presented an in-depth analysis of the dynamic behavior of a vibratory trough in an electromagnetic vibratory conveyor, focusing on the forces acting on the troigh during its motion. Through a combination of theoretical modeling and numerical simulations using FEA, the research demonstrated that the system behaves as a single-degree-of-freedom oscillator, with the vibrations primarily occurring in the vertical direction.

One of the key findings of this work is the negligible axial displacement of the trough compared to its vertical displacement, which simplifies further modeling of the system. Additionally. The results obtained from the FEA simulations were consistent with theoretical predictions, validating the modeling approach. Moreover, experimental validation of the simulation results is essential to confirm the accuracy of the model in real-world conditions.

Acknowledgement. Results presented in this paper are part of the research supported by the Ministry of Science, Technological Development and Innovation, Republic of Serbia, contracts' numbers 451-03-136/2025-03/200034 and 451-03-137/2025-03/200105 from 04.02.2025.

References

[1] Fayed M.E., Skocir T., *Mechanical Conveyors: Selection and Operation.*Technomic Publishing AG, Basel, Switzerland, 1996.

[2] KMGSystems: an image of vibratory conveyor, https://www.kmgsystems.com/machine/proportioning-control-vibratory-conveyors/ [last access 11. 03.2025.]

[3] Despotović Ž., Urukalo Dj., Lečić M., Ćosić A., *Mathematical modeling of resonant linear vibratory conveyor with electromagnetic excitation: simulations and experimental results*. Applied Mathematical Modelling, 41:1–24, 01 2017.

[4] Ribic A.I. , Despotovic Z.V., *High Performance Feedback Control of Electromagnetic Vibratory Feeder* , IEEE Transactions on Industrial Electronics, Vol.57, Issue IX, pp.3087-3094, September 2010.

[5] Goncharevich I. F., Frolov K. V., Rivin E. I.,. *Theory of Vibratory Technology*. Hemisphere Publishing Corporation, New York, 2nd edition, 1990.

[6] Gourishankar V., Donald H. K.,*Electromechanical energy conversion*, In: Intext Educational Publishers, New York, 2. ed., 1973

[7] Balachandran B, Magrab E. B. *Vibrations*. Cengage Learning, Australia, 2nd ed edition, 2009. OCLC: ocn181603380

[8] Megson T.H.G., *Deflection of Beams*. In: Structural and Stress Analysis, pages 337–388. Elsevier, 2014

[9] Parameswaran M.A., Ganapahy S., *Vibratory Conveying-Analysis and Design: A Review*, Mechanism and Machine Theory, Vol.14, No.2, pp. 89-97, April 1979

[10] Prause Durotec Leaf Spring: https://www.prause-durotec.de/en/service/data-sheets, [last access 11. 03.2025.]

[11] Chandravanshi, M. L., A. K. Mukhopadhyay. *Dynamic Analysis of Vibratory Feeder and Their Effect on Feed Particle Speed on Conveying Surface* Measurement 101 (2017): 145-156. https://doi.org/10.1016/j.measurement.2017.01.031.

[12] Heyliger P. R. *When beam theories fail*. Journal of Mechanics of Materials and Structures, 8(1), pp.15–35, March 2013

10th International Congress of the Serbian Society of Mechanics
Niš, Serbia, June 18-20, 2025
D.6
Original Scientific Paper

DOI:10.46793/ICSSM25.206M

PSO-BASED RESONANT CONTROLLER FOR TRAJECTORY TRACKING OF ROBOT MANIPULATOR

Petar D. Mandić[1][0000-0001-7004-2087], **Mihailo P. Lazarević**[1][0000-0002-3326-6636], **Tomislav B. Šekara**[2][0000-0001-8031-3135]

[1] University of Belgrade, Faculty of Mechanical Engineering,
Kraljice Marije 16, 11120 Belgrade 35
e-mail: pmandic@mas.bg.ac.rs, mlazarevic@mas.bg.ac.rs

[2] University of Belgrade, School of Electrical Engineering,
Bulevar kralja Aleksandra 73, 11120 Belgrade 35
e-mail: tomi@etf.rs

Abstract:

This paper addresses the problem of path following for robotic systems. Specifically, a robot manipulator with three degrees of freedom must consecutively track an elliptic curve in space while adhering to a prescribed velocity law. Given that robots are highly nonlinear mechanical systems, achieving this objective is a complex task. Therefore, the mathematical model of the robot manipulator is transformed into a more manageable linear form, based on the actuator dynamics. To achieve high-accuracy path following, a model-based resonant controller is proposed. While this type of controller is not novel within the control community, its application in robotics remains relatively unexplored. To minimize tracking error, a particle swarm optimization (PSO) algorithm is employed, with an appropriate objective function designed to achieve the desired goal. The primary contribution of this paper lies in the integration of this metaheuristic algorithm with the complex resonant controller. Extensive simulations are conducted for various velocities of the robot's end-effector, and the results are consistent with the expected dynamic behavior.

Key words: robot manipulator, resonant controller, path following, PSO algorithm

1. Introduction

The control of robotic manipulators remains an active research area, and due to their complex, coupled, nonlinear dynamics, it presents a significant challenge for the design of high-performance control systems [1]. Various control approaches have been proposed in the literature for designing tracking controllers for robotic manipulators. Representative approaches include designs based on proportional-integral-derivative (PID) control [2,3], H-infinity control [4], Lyapunov-based theory [5], variable structure control [6], optimal control [7], robust feedback linearization (FL) [8], neural networks [9], and fuzzy logic [10]. An exhaustive survey of the various strategies proposed for the design of robust controllers for robotic manipulators can be found in [11,12].

This paper focuses on the problem of repetitive following of closed trajectories in three-dimensional (3D) space, which is relevant to many robotic tasks in industrial environments. For instance, during processes such as welding or painting, the manipulator must follow a closed trajectory multiple times in succession. A standard solution typically involves a PID controller, which is the most widely used algorithm in industry [13–16]. This type of control provides satisfactory results when the robot tip moves slowly, allowing sufficient time for the control action to compensate for tracking errors. However, at higher velocities, a resonant controller would be a more suitable choice, as it is specifically designed for such tasks. While this solution involves a more complex algorithm, the performance benefits justify the additional complexity. One key advantage of a resonant controller is its structural term, which corresponds to the fundamental frequency of the desired end-effector trajectory. Resonant controllers are widely employed in the control of electrical grids and similar applications, but their use in robotics and motion control has largely been overlooked. To the best of the authors' knowledge, this paper represents one of the few studies addressing this topic in the context of robot control [17].

In addition to resonant controllers, other potential solutions include fractional-order controllers [18], PID controllers with double derivative terms [19], or intelligent control strategies such as iterative learning control (ILC) techniques [20,21]. These areas of research have been significantly explored in the literature and will not be addressed in this study.

The remainder of the paper is organized as follows. First, a mathematical model of the robot manipulator is derived. Due to the high gear reduction ratio, a linear model is obtained based on the dynamics of a direct current (DC) motor. Next, a resonant controller is designed to address the problem of following a closed curve in space. The optimal parameters of the controller are determined using a particle swarm optimization algorithm. In the fourth section, numerical simulations of the robot manipulator are conducted, and the results are briefly discussed and analyzed. Finally, concluding remarks are provided, along with recommendations for future work.

2. Mathematical model

Mathematical model of robot manipulator can be given in the following matrix form:

$$A(\boldsymbol{q})\ddot{\boldsymbol{q}} + C(\boldsymbol{q},\dot{\boldsymbol{q}})\dot{\boldsymbol{q}} - \boldsymbol{Q}^{g} = \boldsymbol{Q}^{m} \tag{1}$$

In this study, a three-degree-of-freedom (DOF) robot manipulator is considered as a simplified version of the more complex NeuroArm robot [22], which is an integral part of the Laboratory of Applied Mechanics at the Faculty of Mechanical Engineering in Belgrade (Figure 1).

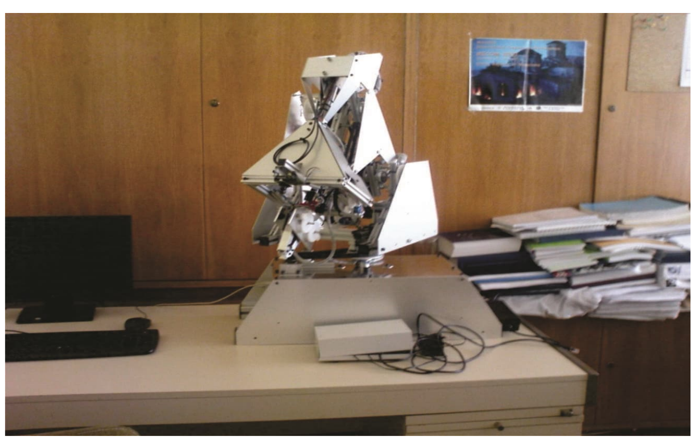

Fig. 1. NeuroArm robotic manipulator with 7 DOFs

The robot manipulator features three revolute joints, representing the minimum configuration required for solving three-dimensional (3D) position control tasks. In above equation, $\boldsymbol{q} \in R^3$ denotes vector of generalized coordinates, $A(\boldsymbol{q}) \in R^{3\times3}$ represents basic metric tensor (or inertia matrix), $C(\boldsymbol{q},\dot{\boldsymbol{q}}) \in R^{3\times3}$ is a matrix that includes centrifugal and Coriolis effects, $\boldsymbol{Q}^{\boldsymbol{g}} \in R^3$ and $\boldsymbol{Q}^{\boldsymbol{m}} \in R^3$ are gravity term and torque vectors applied to the joints, respectively. For more detailed analysis of Eq.(1), reader is referred to [23].

Typically, robotic segments are driven by electrical actuators, such as DC motors. Since the operating conditions of the motor involve high angular speed and low torque, contrasted with the low speed and high torque required for the movement of the robot links, it is necessary to include a transmission gear between the motor and the robot links. Let $\boldsymbol{q}_m$ denote the vector of angular displacements of the motors, then the following relationship can be written:

$$\boldsymbol{q}_m = N\boldsymbol{q},\ \ \boldsymbol{Q}^{\boldsymbol{m}} = N\boldsymbol{\tau}_l, \tag{2}$$

wherein N represents diagonal matrix of gear ratios. Vector $\boldsymbol{\tau}_l$ can be regarded as a disturbance vector acting on the motor shafts. It can be shown that the following relation holds [24]:

$$\tau_l = \left(N^2\right)^{-1}\left(A(\boldsymbol{q})\ddot{\boldsymbol{q}}_m + C(\boldsymbol{q},\dot{\boldsymbol{q}})\dot{\boldsymbol{q}}_m\right) - N^{-1}\boldsymbol{Q}^g \tag{3}$$

This key expression enables the simplification of robot dynamics by neglecting nonlinear effects in cases involving high gear ratios. Specifically, instead of using the highly nonlinear equation (1), a linear model of the DC motor can be employed, as discussed in [25]. A block diagram of the robotic system based on a standard DC motor is presented in Figure 2. The resistance of the armature circuit is denoted by R, while L represents armature inductance. The linear relationship between motor torque τ_m and the current i is defined by the torque constant K_t. The mechanical behavior of the DC motor is characterized by the motor's moment of inertia J_m and the viscous friction coefficient B_m. The input motor voltage u is proportional to the motor's angular velocity via the back electromotive force (EMF) constant K_e.

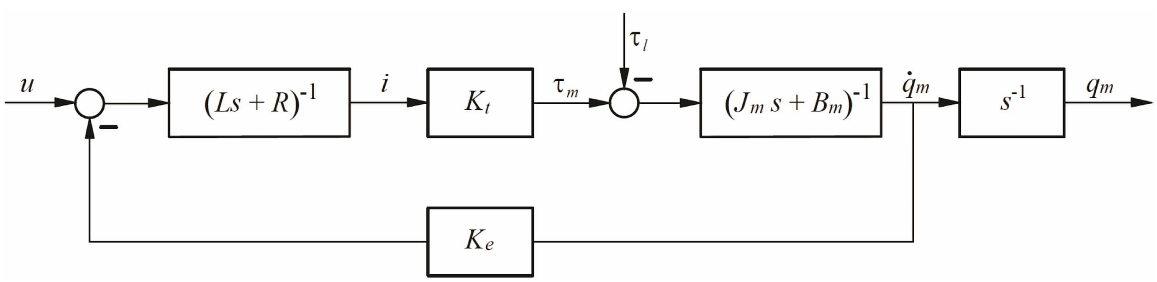

Fig. 2. Linear robot model representation based on actuator dynamics

In our study, the robot manipulator employs three identical Maxon motors to actuate the robot's links. Based on the specifications provided in the datasheet [24], which indicate $L \ll R$ and $B_m \approx 0$, the transfer function of the DC motor can be derived as follows:

$$G_{\mathrm{m}}(s)=\frac{K}{s(Ts+1)}. \tag{4}$$

wherein K=22.515 and $T=0.0056409$. In conclusion, the high gear ratio matrix (in our case $N=\operatorname{diag}\{185,632,140\}$) enables the transformation of the nonlinear system described by Eq. (1) into three linear, decoupled subsystems. Each of these subsystems can be represented by the corresponding motor transfer function $G_{\mathrm{m}}(s)$.

3. Controller design

The objective of this paper is to design a controller capable of accurately tracking a closed trajectory in three-dimensional space. Specifically, the robot's end effector is required to repeatedly follow a predefined spatial curve in accordance with a known velocity profile. An appropriate solution to this problem can be achieved using a resonant controller. The transfer function of such a controller is given by:

$$C(s)=\frac{(Ts+1)\left(a_3s^3+a_2s^2+a_1s+1\right)}{s(s^2+\omega_0^2)(b_1s+b_0)} \tag{5}$$

wherein

$$\begin{aligned}
a_3&=T\left(\left(1-\lambda^2\omega_0^2\right)T^2+6T\lambda+3\lambda^2\right),\\
a_2&=\left(-2T^3\lambda\omega_0^2+\left(3-3\lambda^2\omega_0^2\right)T^2+6T\lambda+\lambda^2\right),\\
a_1&=3T+2\lambda,\ b_0=KT^2\lambda\left(2T+3\lambda\right),\ b_1=KT^3\lambda^2
\end{aligned} \tag{6}$$

In the above expression, ω_0 is the fundamental frequency. If T_0 represents the time required for the end-effector to complete one full traversal of the desired closed trajectory in space, then $\omega_0=2\pi/T_0$. The adjustable parameter λ can be tuned by the control designer to achieve an acceptable trade-off between performance and robustness of the closed loop system. A more detailed controller design procedure is provided in [17], while the block diagram of the closed loop system is shown in Figure 3.

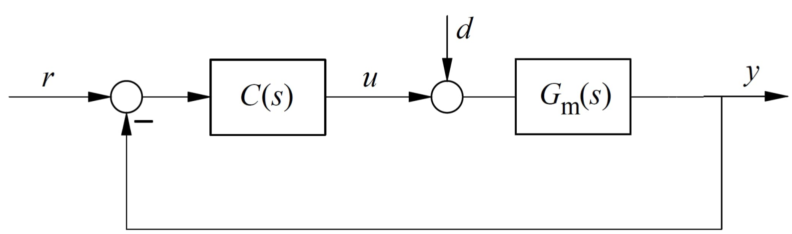

Fig. 3. Block diagram of a closed-loop system

Since the manipulator consists of three robotic links, each actuated by an individual DC motor, it is necessary to control the motion of each link independently. In other words, three separate resonant controllers $C_i(s),\ i=1,2,3,$ must be designed. The adjustable parameters $\lambda_i,\ i=1,2,3$, associated with each controller should be selected based on a well-defined design criterion. In this paper, the following objective (cost) function is adopted:

$$J(\lambda_1,\lambda_2,\lambda_3)=\frac{1}{T_0}\int_0^{T_0}\Delta(\lambda_1,\lambda_2,\lambda_3,t)\,dt$$
$$=\frac{1}{T_0}\int_0^{T_0}\sqrt{\left(x_d(t)-x(\lambda_1,\lambda_2,\lambda_3,t)\right)^2+\left(y_d(t)-y(\lambda_1,\lambda_2,\lambda_3,t)\right)^2+\left(z_d(t)-z(\lambda_1,\lambda_2,\lambda_3,t)\right)^2}\,dt \tag{7}$$

wherein $x_d(t)$, $y_d(t)$ and $z_d(t)$ represent the Cartesian coordinates of the desired spatial trajectory at time t, while $x(\lambda_1,\lambda_2,\lambda_3,t)$, $y(\lambda_1,\lambda_2,\lambda_3,t)$ and $z(\lambda_1,\lambda_2,\lambda_3,t)$ denote the actual coordinates of the robot's end-effector at the same time instant. The criterion J can be interpreted as the average positional error of the end-effector from the desired trajectory during the first traversal. The objective is to determine the optimal values of the free parameters $\lambda_i,\ i=1,2,3$ in order to minimize the cost function J, thereby ensuring that the deviation between the actual and desired trajectories is minimized. Due to the highly nonlinear nature of the cost function $J(\lambda_1,\lambda_2,\lambda_3)$, it is not feasible to derive an analytical solution. Therefore, in this work, we propose the use of the particle swarm optimization algorithm to address this complex optimization problem.

PSO is one of the most widely recognized swarm-based metaheuristic algorithms in the literature. It is a computational technique that solves optimization problems by iteratively improving a set of candidate solutions with respect to a defined cost function. The algorithm maintains a population of candidate solutions, referred to as particles, which explore the search space based on simple mathematical rules that incorporate both individual and collective experience. In the following section, we demonstrate the effectiveness of the PSO algorithm in solving the optimization problem associated with the robot trajectory tracking task.

4. Simulation results

In this study, the robot manipulator is required to follow an elliptical trajectory by moving its end-effector along the path at a constant speed V. The ellipse, illustrated in Figure 4, is centered at the point $(0.1,\ 0.35,\ 0.47)\,\mathrm{m}$ with respect to a fixed Cartesian coordinate system. The lengths of the semi-major and semi-minor axes are $a=0.2\ \mathrm{m},\ b=0.1\ \mathrm{m}$, respectively.

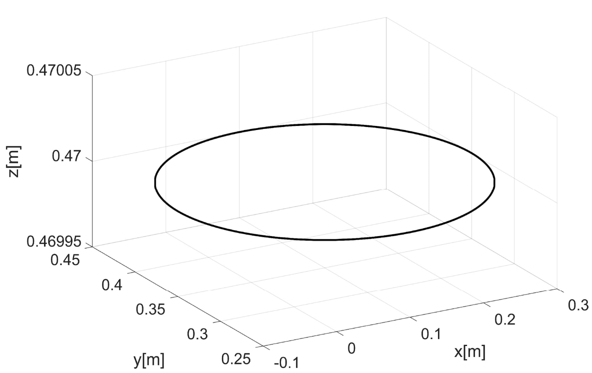

Fig. 4. Reference trajectory of the end-effector

For a fixed velocity V, the PSO algorithm is used to determine the optimal values of the free parameters of the resonant controllers $\lambda_i,\ i=1,2,3,$ based on the specified criterion (7). The end-effector follows the desired trajectory multiple times consecutively; however, the cost function is evaluated only during the first traversal. The optimization procedure is repeated for different velocity values, namely $V = 0.1j\ [\mathrm{m/s}]$, $j = 1,2,\ldots,10$. The range of the free parameters is selected as:

$$\lambda_i \in [T,\ 15T],\ i = 1,2,3, \tag{8}$$

where T is the time constant of the DC motor mentioned above. The range of these parameters is selected to achieve a good trade-off between the robustness and performance of the closed-loop system. The PSO algorithm parameters are configured as follows [26]: swarm size $N_{SW} = 30$,"Self Adjustment Weight" $y_1 = 1.9$, "Social Adjustment Weight" $y_2 = 2.12$, "Inertia" weight $W = -0.1618$, maximum number of iterations $N_I = 100$, maximum number of stall iterations $N_{ST} = 30$ and the minimum neighbor fraction "MinNeighborsFraction" $c = 0.4$.

The results of the simulations are summarized in Table 1. The parameter $\Delta_{\max}$ denotes the maximum distance of the end-effector's path from the desired trajectory, i.e. $\Delta_{\max}(\lambda_1,\lambda_2,\lambda_3) = \max\limits_{[0,\ T_0]} \Delta(\lambda_1,\lambda_2,\lambda_3,t)$. The values of the cost function J during the end-effector's second loop, third loop, and subsequent loops are labeled as $J_2,\ J_3,\ldots$. It is reasonable to expect that the values of $J_n,\ n = 2,3,\ldots,$ will decrease compared to J since the effects of non-nominal initial conditions at the beginning of the first loop are effectively eliminated in the subsequent loops. Graphical representations of the results presented in Table 1 are shown in Figures 5 and 6.

$V\,[\mathrm{m/s}]$	$\lambda_1 \times 100$	$\lambda_2 \times 100$	$\lambda_3 \times 100$	$J \times 10^{-5}\,[\mathrm{m}]$	$\Delta_{\max} \times 10^{-3}\,[\mathrm{m}]$	$J_2, J_3, \ldots \times 10^{-5}\,[\mathrm{m}]$
0.1	8.19	2.78	2.85	0.596	0.227	0.499
0.2	7.31	3.19	3.20	1.431	0.486	1.001
0.3	4.10	3.71	3.69	2.640	0.782	1.507
0.4	2.96	3.85	3.82	4.297	1.076	2.149
0.5	3.15	3.68	3.74	6.570	1.360	3.176
0.6	3.50	3.62	3.68	9.690	1.648	4.828
0.7	3.96	3.60	3.68	13.907	1.942	7.412
0.8	4.42	3.61	3.69	19.420	2.247	11.075
0.9	5.00	3.68	3.79	26.292	2.566	16.094
1.0	5.56	3.86	3.96	34.720	2.909	22.605

Table 1. Optimisation results for different end-effector velocities

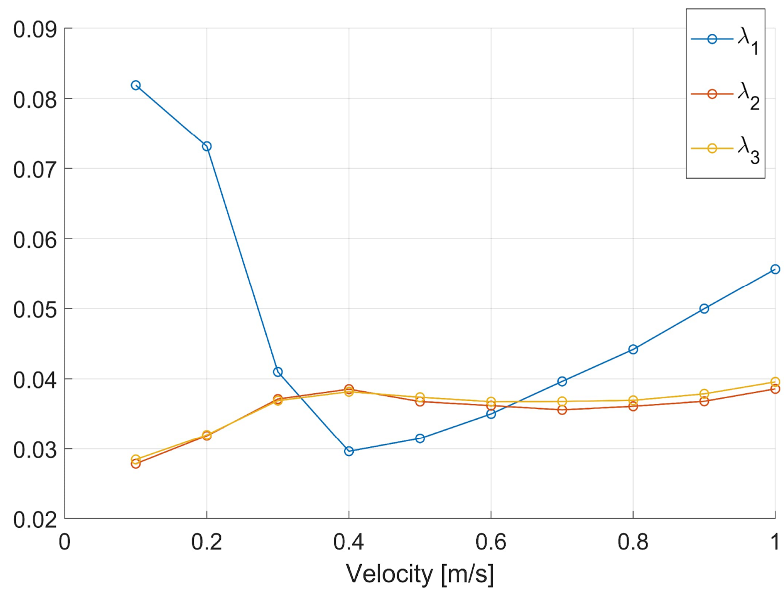

Fig. 5. Change in free parameters $\lambda_i,\ i=1,2,3$ for different values of end-effector velocity

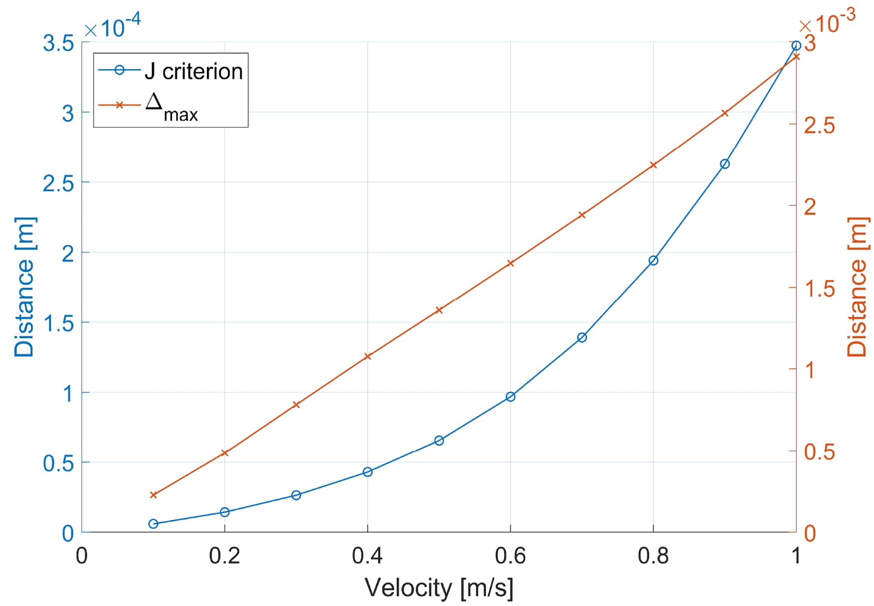

Fig. 6. Average and maximum errors during the first loop of trajectory tracking

Figure 7 illustrates the relationship between the maximum value of torque τ_l, as given by Eq.(3), and the end-effector velocity V. Since τ_l can be considered a disturbance torque acting on the motor shafts, its impact on motor dynamics increases as V rises This is a logical conclusion, as an increase in velocity directly amplifies the nonlinear effects of the robot dynamics, such as centrifugal and Coriolis forces. This explains why both the average and maximum errors $(J$ and $\Delta_{max})$ increase with the end-effector's velocity, as shown in Figure 6.

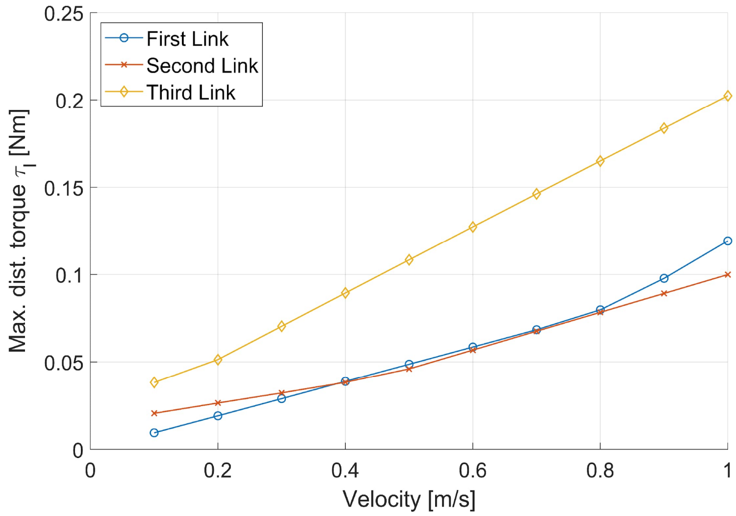

Fig. 7. Maximum disturbance torque values for three robotic links

Figures 8 and 9 illustrate the end-effector's trajectory at different moving speeds along the path. It is visually evident that the deviation between the actual and desired path increases as V grows, which has already been stated and confirmed by the data in Table 1 and Fig. 6.

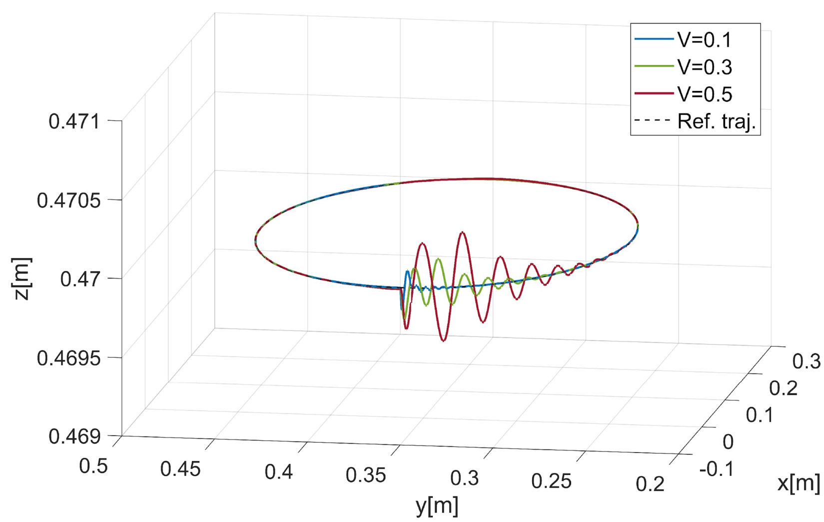

Fig. 8. End-effector's trajectory for velocity values $V = \{0.1,\ 0.3,\ 0.5\}[\mathrm{m/s}]$

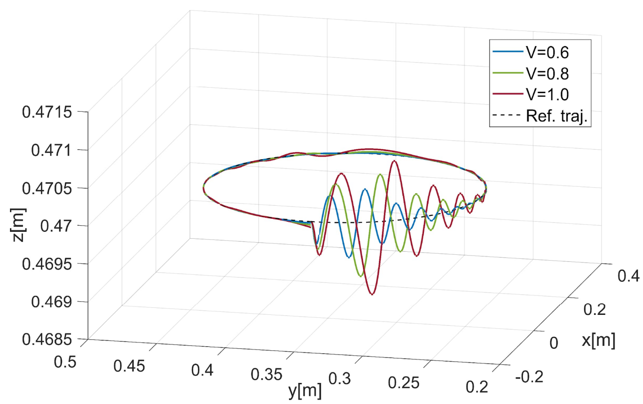

Fig. 9. End-effector's trajectory for velocity values $V = \{0.6,\ 0.8,\ 1.0\}\,[\mathrm{m/s}]$

5. Conclusions

In this paper, a particle swarm optimization algorithm was applied to solve the optimization problem related to the trajectory control of a 3-DOF robot manipulator. An analytically designed resonant controller was used to stabilize the closed-loop system and ensure the fast convergence of the end-effector trajectory to the desired path. The cost function was selected to minimize the average distance between the actual and reference trajectories. Simulations were conducted for various moving speeds of the robot tip along the desired path. The results indicate that as the velocity increases, the deviations of the end-effector from the reference trajectory also grow. This conclusion was supported by extensive simulation data, presented in both tabular and graphical formats. Future work will extend this approach to other types of desired trajectories, including those with time-varying velocity profiles, and will explore more advanced controllers, such as those based on iterative learning algorithms.

Acknowledgment. Authors gratefully acknowledge the support of Ministry of Education, Science and Technological Development of the Republic of Serbia under the contract 451-03-137/2025-03/200105 from 04.02.2025 (P.D.M and M.P.L.), and 451-03-137/2025-03/200103 (T.B.Š.)

References

[1] B. Siciliano, L. Sciavicco, L. Villani, G. Oriolo, *Robotics*, London: Springer-Verlag, 2009.
[2] Dawson DM, Qu Z, Lewis FL, Dorsey JF. *Robust control for the tracking of robot motion.* International Journal of Control 1990; 52(3):581–595.
[3] Alvarez-Ramirez J, Cervantes I, Kelly R. *PID regulation of robot manipulators: stability and performance.* Systems and Control Letters 2000; 41(2):73–83.
[4] Stout WL, Sawan ME. *Application of H-infinity theory to robot manipulator control*. Proceedings of the IEEE Conference on Control Applications, Dayton, OH, USA, 13–16 September 1992; 148–153.
[5] Spong MW. *On the robust control of robot manipulators*. IEEE Transactions on Automatic Control 1992; 37(11):1782–1786.
[6] Stepanenko Y, Cao Y, Su C-Y. *Variable structure control of robotic manipulator with PID sliding surfaces*. International Journal of Robust and Nonlinear Control 1998; 8(1):79–90.

[7] Lin F, Brandt RD. *An optimal control approach to robust control of robot manipulators*. IEEE Transactions on Robotics and Automation 1998; 14(1):69–77.
[8] Kolhe JP, Shaheed M, Chandar TS, Talole SE. *Robust control of robot manipulators based on uncertainty and disturbance estimation*. Int. J. Robust. Nonlinear Control, 23(1), 104-122, 2011.
[9] Lewis FL. *Neural network control of robot manipulators*. IEEE Expert Magazine 1996; 11(3):64–75
[10] Ham C, Qu Z, Johnson R. *Robust fuzzy control for robot manipulators*. IEE Proceedings - Control Theory and Applications 2000; 147(2):212–216.
[11] M. C. Chou and C. M. Liaw, *Development of Robust Current 2-DOF Controllers for a Permanent Magnet Synchronous Motor Drive With Reaction Wheel Load*, in *IEEE Transactions on Power Electronics*, vol. 24, no. 5, pp. 1304-1320, May 2009.
[12] Abdallah C, Dawson D, Dorato P, Jamshidi M. Survey of robust control for rigid robots. IEEE Control Systems Magazine 1991; 11(2):24–30
[13] T.B. Šekara, M.R. Mataušek, *Optimization of PID Controller Based on Maximization of the Proportional Gain Under Constraints on Robustness and Sensitivity to Measurement Noise*, IEEE Trans Automat Contr, vol. 54, pp. 184-189, 2009.
[14] T.B. Šekara, M.R. Mataušek, (2010). *Revisiting the Ziegler-Nichols process dynamics characterization*. Journal of Process Control, 20(3), 360–363.
[15] T.B. Šekara, M.R. Mataušek, (2011). *Classification of dynamic processes and PID controller tuning in a parameter plane.* Journal of Process Control, 21(4), 620–626.
[16] M.R. Mataušek, T.B. Šekara, (2011). *PID controller frequency-domain tuning for stable, integrating and unstable processes, including dead-time*. Journal of Process Control, 21(1), 17–27.
[17] P.D. Mandić, T.B. Šekara, M.P. Lazarević, *Analytical design of resonant controller applied for solving robot arm tracking problem*, 9th International Congress of Serbian Society of Mechanics, Vrnjacka Banja, Serbia, July 5-7, 2023.
[18] P.D. Mandić, T.B. Šekara, M.P. Lazarević, M.Č. Bošković. *Dominant pole placement with fractional order PID controllers: D-decomposition approach*, 67, 76-86, 2017.
[19] P.D. Mandić, M.Č. Bošković, T.B. Šekara, M.P. Lazarević, *A new optimisation method of PIDC controller under constraints on robustness and sensitivity to measurement noise using amplitude optimum principle*, International Journal of Control, 97(1), 36-50,2024.
[20] M.P. Lazarević, P.D. Mandić, S.Ostojić, *Further results on advanced robust iterative learning control and modeling of robotic systems*, Proc IMechE Part C: J Mechanical Engineering Science, pp. 1-16, 2020.
[21] B.P. Cvetković, M.P. Lazarević, P.D. Mandić, T.B. Šekara, *Open closed loop PD^{μ}/PD type ILC control of NeuroArm robotic system*, 8th International Congress of Serbian Society of Mechanics, Kragujevac, Serbia, June 28-30, 2021.
[22] P.D. Mandić, M.P. Lazarević, Z. Stokić, T.B. Šekara, *Dynamic Modelling and Control Design of Seven Degrees of Freedom Robotic Arm*, 6th International Congress of Serbian Society of Mechanics, Tara, Serbia, June 19-21, 2017.
[23] V. Čović, M.P. Lazarević, *Robot Mechanics*, Faculty of Mechanical Engineering, Belgrade, Serbia, 2009.
[24] P.D. Mandić, *Advanced modeling of complex robotic systems and mechanisms and applications of modern control theory*, PhD Dissertation, Faculty of Mechanical Engineering, 2019.
[25] P.D. Mandić, P. Lino, G. Maione, M.P. Lazarević, T.B. Šekara, *Design of fractional order lag network and fractional order PI controller for a robotic manipulator*, IFAC PapersOnLine, 53(2), 3669-3674, 2020.
[26] https://www.mathworks.com/help/gads/particleswarm.html

10th International Congress of the Serbian Society of Mechanics
Niš, Serbia, June 18-20, 2025

D.7

Extended abstract

COMPUTATIONAL MODELING OF DRUG TRANSPORT FROM DRUG COATED BALLONS (DCB)

Miljan Milošević[1,2,3][0000-0003-3789-2404], Bogdan Milićević[1,2][0000-0002-0315-8263], Vladimir Simić[2,3][0000-0001-7842-8902], Aleksandar Nikolic[1][0000-0002-7052-7444], Nenad Filipović[2,3][0000-0001-9964-5615] and Miloš Kojić[2,4,5][0000-0003-2199-5847]

[1] Institute for Information Technologies, University of Kragujevac, Kragujevac 34000, Serbia, e-mail: miljan.m@kg.ac.rs, vsimic@kg.ac.rs, bogdan.milicevic@uni.kg.ac.rs
[2] Bioengineering Research and Development Center (BioIRC), Kragujevac 34000, Serbia. e-mail: mkojic42@gmail.com
[3] Belgrade Metropolitan University, Belgrade 11000, Serbia.
[4] Faculty of Engineering, University of Kragujevac, Kragujevac 34000, Serbia. e-mail: fica@kg.ac.rs
[5] Serbian Academy of Sciences and Arts, Belgrade 11000, Serbia.

Abstract

Balloon angioplasty remains a standard treatment of stenosis in peripheral artery disease (PAD); however, the mechanical dilation often causes arterial wall injury, triggering tissue hyperplasia and subsequent restenosis. To address this limitation, drug-coated balloons (DCBs) have emerged as a promising alternative, enabling localized drug delivery without permanent stent implantation. Computational modeling offers a powerful tool for optimizing DCB performance by simulating drug transport dynamics post-delivery. This study introduces a novel 2D multiphysics model capable of concurrently analyzing fluid flow, solid mechanics, and drug release kinetics. The fluid dynamics component evaluates drug washout effects following balloon deflation, while the solid mechanics module captures the interaction between the expanding balloon and the arterial wall. The balloon is represented as a deformable structure using a linear elastic material approximation, compressing both plaque and healthy arterial segments upon inflation. Simultaneously, the model tracks drug diffusion and absorption into the vascular tissue. The proposed framework serves as a foundation for future extensions, including modules for inflammatory response, atherosclerotic plaque progression, and tissue rupture mechanics.

Key words: atherosclerosis, drug coated balloons, computational modeling, fluid-solid interaction, drug transport

1. Introduction

Peripheral artery disease (PAD) is a major global health concern, affecting over 200 million adults aged 25 and above [1]. The disease primarily stems from arterial stenosis, where balloon angioplasty is frequently employed to restore perfusion by inflating a balloon catheter to compress the obstructive plaque. However, this mechanical intervention induces arterial wall injury, triggering pathological remodeling, endothelial regrowth, and ultimately restenosis. Drug-coated balloons (DCBs) have emerged as a promising alternative, delivering antiproliferative agents directly to the lesion site to mitigate restenosis. While computational modeling has proven valuable in evaluating DCB efficacy, existing studies remain limited in scope. Prior work has largely focused on simplified 2D geometries [2,3], neglecting complex hemodynamic interactions in anatomically realistic vessels, such as the superficial femoral artery (SFA). To bridge this gap, we propose an advanced computational framework capable of simulating multiple DCB deployment phases, including balloon expansion, arterial wall interaction, and controlled drug release kinetics.

2. Methodology

The computational model was developed using the high-performance finite element analysis (FEA) software PAK. A parametric 2D axisymmetric representation of the artery and balloon was designed via CAD Field & Solid, incorporating four key components: capillary lumen, expandable balloon, calcified plaque, and healthy arterial wall segments.

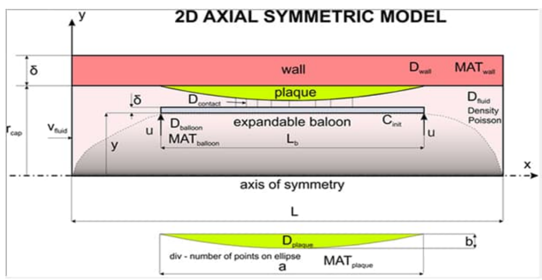

Fig. 1. 2D axisymmetric model of a stenotic capillary with an inserted balloon and adherent plaque.

The framework couples fluid-structure interaction (FSI) to simulate balloon inflation, plaque compression, and drug washout dynamics, while solving advection-diffusion equations for drug transport

3. Conclusions

This study presents a versatile computational platform for DCB optimization, with potential applications in patient-specific geometries derived from medical imaging. Future extensions will incorporate plaque fracture mechanics, inflammatory tissue growth models, and drug-tissue interaction effects on restenosis progression. Such advancements could refine DCB design and deployment strategies, improving clinical outcomes in PAD management.

References

[1] Colombo M, Corti A, Berceli S,Migliavacca F, McGinty S, Chiastra C (2021) *3D modelling of drug-coated balloons for the treatment of calcified superficial femoral arteries.* PLoS ONE 16(10): e0256783. https://doi.org/10.1371/journal.pone.0256783.
[2] Anbalakan K, Toh HW, Ang HY, Buist ML, Leo HL. Assessing the influence of atherosclerosis on drug coated balloon therapy using computational modelling. Eur J Pharm Biopharm. 2021;158: 72–82. doi: 10.1016/j.ejpb.2020.09.016.
[3] Kolandaivelu K, O'Brien CC, Shazly T, Edelman ER, Kolachalama VB. Enhancing physiologic simulations using supervised learning on coarse mesh solutions. J R Soc Interface. 2015;12: 1–10. doi: 10.1098/rsif.2014.1073

10th International Congress of the Serbian Society of Mechanics
Niš, Serbia, June 18-20, 2025
D.8

Extended abstract

DATA-DRIVEN NONLINEAR MODELLING OF RECYCLED AGGREGATE CONCRETE-FILLED STEEL TUBE COLUMNS

Jelena Nikolić[1[0000-0002-5770-897X]], **Nikola Tosić** [2[0000-0003-0242-8804]], **Svetlana M. Kostić**[1[0000-0001-7978-3332]]

[1] Faculty of Civil Engineering
The University of Belgrade, Bul. kralja Aleksandra 73, 11000 Belgrade, Serbia
e-mail: jnikolic@grf.bg.ac.rs, svetlana@grf.bg.ac.rs
[2] Universitat Politècnica de Catalunya – BarcelonaTech (UPC), Civil and Environmental Engineering Depart-ment, Jordi Girona 1–3, 08034 Barcelona, Spain;
e-mail: nikola.tosic@upc.edu

Abstract:

Recycled aggregate concrete-filled steel tube columns represent sustainable solutions for column members. However, as a relatively new option, there are currently no clear design guidelines available for their design and modelling. The second generation of Eurocode 2 presents a proposal for the recycled aggregate concrete material model. Yet, due to the specific 3D stress state of the concrete portion within the steel tube, this model cannot be directly applied to the numerical modelling of recycled aggregate concrete-filled steel tube columns. Therefore, this study aims to develop a highly reliable nonlinear numerical model for the structural analysis of these columns. An advanced data-driven numerical procedure employs the Bayesian optimisation algorithm for the calibration of concrete material parameters. The database used for calibration consists of 182 experimental results of axially loaded stub columns. The benefits of the presented approach, which can be applied to a wide range of loading conditions, are demonstrated through the optimised axial force-axial displacement curves.

Key words: composite structures, recycled aggregate concrete, concrete-filled steel tube, Bayesian optimisation, Machine learning

1. Introduction

This study addresses the computational procedure for development of a stress–strain model for confined recycled aggregate concrete (RAC) in composite columns. Recycled Aggregate Concrete-Filled Steel Tube (RACFST) columns enhance RAC mechanical performance due to confinement. The high–fidelity 3D FEM numerical models in ABAQUS [1] accurately capture material and geometric nonlinearities in column behaviour [2]. However, the existing numerical models lack calibration on large datasets and standardized stress-strain formulations [3]. For these reasons, the numerical procedure presented in this paper is developed for the reliable calibration of material model parameters on large datasets and to improve the prediction of the RACFST column response.

2. Computational Procedure

A database of RACFST columns was compiled from over 35 studies, focusing on 182 circular stub specimens (L/D ≤ 4.0) with carbon steel tubes. Key geometric and material parameters, along with axial strength and load–load-displacement data, were extracted. The optimisation process, illustrated in Fig. 1, begins in the MATLAB environment using Bayesian optimisation with initial parameter values. In each iteration, a Python script executes a 3D ABAQUS model analysis using input data from the RACFST column experimental database. The numerical simulation incorporates both the steel and concrete material models with their respective parameters. The resulting axial load–displacement curve *(N–δ)* from the simulation is then compared to the experimental curve in every iteration. The normalized root means square error (NRMSE) is calculated using the expression provided in Fig. 1, where $N_{(i)}$ and $\delta_{(i)}$ represent the axial force and axial displacement at the i-th point of the numerical curve, respectively, and $N_{exp(i)}$ and $\delta_{exp(i)}$ are the corresponding values from the experimental curve. This loop runs for 30 iterations, yielding calibrated material model parameters that correspond to the minimal value of the adopted error measure.

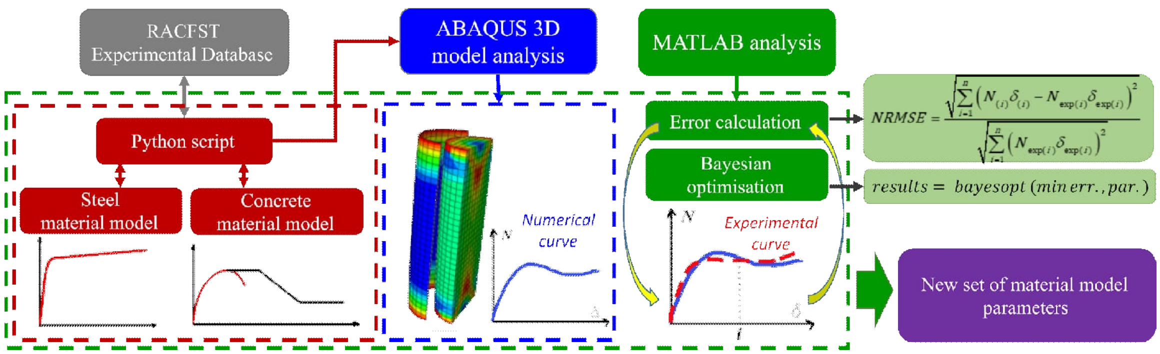

Fig. 1. Computational procedure flowchart

After obtaining the optimised dataset of material model parameters, the regression analysis is performed to define the expressions for parameters of a concrete material model that can be used in numerical modelling of arbitrary RACFST columns.

3. Conclusion

The study presents a data-driven numerical procedure for developing a calibrated stress-strain model for recycled aggregate concrete within steel tubes. The procedure is based on Bayesian optimisation to find the material model parameters that optimise the column's axial load-displacement response curve. However, the presented approach is general and can be applied to a wide range of problems and loading conditions.

Acknowledgement This research was funded by the Ministry of Education, Science and Technological Development, Republic of Serbia, grant number 200092.

References

[1] Corp. DS. ABAQUS User Manual 6.9. . Providence, Rhode Island, USA; 2009
[2] Nikolić J, Kostić SM, Stošić S. *Numerical modelling of concrete-filled steel tubular short columns under axial compression. Building Materials and Structures*. 2023;66. 10.5937/GRMK2300004N
[3] Nikolić J, Tošić N, Murcia-Delso J, Kostić SM. *Comprehensive review of the structural behaviour and numerical modelling of recycled aggregate concrete-filled steel tubes. Engineering Structures*. 2024;303:117514. 10.1016/j.engstruct.2024.117514

10th International Congress of the Serbian Society of Mechanics
Niš, Serbia, June 18-20, 2025
D.9
Original Scientific Paper

DOI:10.46793/ICSSM25.220R

DESIGN AND EXPERIMENTAL VERIFICATION OF THE COMPOSITE BLADE OF THE MAIN ROTOR OF AN UNMANNED HELICOPTER

Radoslav Radulovic[1][0000-0002-9345-919X], Milica Milic[1]

[1] Faculty of Mechanical Engineering,
The University of Belgrade, Kraljice Marije 16, 11120 Belgrade 35
e-mail: rradulovic@mas.bg.ac.rs , mmilic@mas.bg.ac.rs

Abstract:

The increasing use of unmanned aerial vehicles (UAVs) across various industries worldwide dictates new design rules and standards for their structures and systems. The reliability and durability of these structures are achieved through the application of advanced materials. Each structure must be designed in accordance with mission requirements to withstand the necessary aerodynamic and mechanical loads. The development of an unmanned helicopter presents a significant engineering challenge, particularly in the design of the main rotor, which requires a multidisciplinary approach and the coupling of aerodynamic, aeroelastic, and structural phenomena. This helicopter has a maximum takeoff weight of 750 kg, classifying it as a light helicopter. This research presents a comprehensive approach to the design, numerical analysis, and experimental validation of a composite helicopter rotor blade, in accordance with predefined operational requirements. The key specifications include maintaining an identical geometry compared to an existing model, precisely defining the blade mass at 11.5 kg, utilizing composite materials, and ensuring that the blade root can withstand an axial load of 40 tons. Additionally, aerodynamic efficiency is optimized by maintaining the LOCK number within the range of 5–7.
The blade design is based on composite prepreg materials due to their high specific strength, excellent fatigue resistance, and superior damage tolerance. The structural configuration has been developed to achieve an optimal balance of weight, strength, and aerodynamic performance.

Key words: *UAV, unmanned helicopter, composite materials*

1. **Introduction**

The rapid development of unmanned aerial vehicles (UAVs) in recent decades has led to significant technological advancements in the field of aeronautical engineering. These advancements have imposed new requirements regarding the design, performance, and reliability of UAV components. Among the critical structural elements of unmanned helicopters, the main rotor plays a pivotal role, as its design presents a complex engineering challenge due to the combined effects of aerodynamic, structural, and dynamic loads during operation [1]. Traditionally, helicopter blades were manufactured from metallic alloys; however, the introduction of composite materials has enabled substantial improvements in terms of specific strength, fatigue resistance, and the ability to optimize mechanical properties through precise control of fiber orientation and layer arrangement [2]. The application of composite materials provides opportunities for weight reduction, enhancement of aerodynamic performance, and increased structural reliability of rotor blades, which are essential factors for the efficiency and operational lifespan of UAVs. This study presents a comprehensive approach to the design of a composite helicopter main rotor blade, including numerical analysis and experimental validation in accordance with predefined operational requirements [3,4]. The primary objective of the research is to develop a rotor blade structure with a strictly controlled mass of 11.5 kg while ensuring optimal structural characteristics that enable safe operation under extreme loading conditions. A particular challenge lies in the dimensioning of the blade root to withstand an axial force of 40 tons, as well as achieving a LOCK number within the range of 5–7 to ensure adequate aerodynamic efficiency.

To achieve these objectives, a methodology was applied that combines numerical analysis using the finite element method (FEM) and experimental testing. FEM simulations allowed for the evaluation of stress distribution, deformations, and modal characteristics of the blade, enabling the identification of critical structural points and optimization of the composite layer arrangement. After completing the numerical analyses, a physical prototype of the blade was fabricated and subjected to experimental tests to validate the designed performance and assess mechanical behavior under real operational loads [5]. The research findings provide valuable insight into the behavior of composite rotor blades under various operational loading conditions and contribute to the improvement of methodologies for their design. The experimental testing was conducted according to predefined bending loads, and the corresponding bending stiffness was determined analytically using deflection equations to verify the FEM model [6,7]. The results of this study offer a foundation for further optimization, particularly in terms of improving fatigue resistance, reducing mass, and enhancing structural reliability, which are critical for their application in modern helicopter technology.

2. **Methodology**

The design and validation process of the helicopter composite blade included several key phases: requirement definition, numerical analysis using the finite element method (FEM), physical prototype manufacturing, and experimental testing. This methodology enabled the optimization of the structure to achieve the required mass, structural reliability, and aerodynamic performance[1,2].

2.1 *Load estimation*

The load estimation of the main rotor composite blade was carried out using an analytical approach. Based on the blade's geometry and structure, the known values are:

the principal moments of inertia of the blade's cross-section (given by Equation 1).

$$I_x = 1.1497 \cdot 10^{-7}\,\mathrm{m}^4, \quad I_y = 7.6421 \cdot 10^{-6}\,\mathrm{m}^4 \tag{1}$$

and the cross-sectional area.

$$A = 0.00337\,\mathrm{m}^2 \tag{2}$$

The deflection of the blade at the free end is determined using the Maxwell-Mohr integration method.

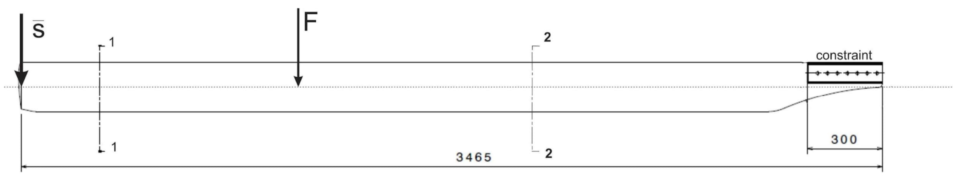

Figure 2.1. Defined boundary conditions for deriving the deflection equation of the blade.

The laws of variation of bending moments in sections I and II (as shown in Figure 2.1) due to force *F*, acting at a distance *a* from the clamping, as well as due to a unit concentrated force $\overline{S}=1$, acting at the free end of the blade, are:

$$M_{1-1}^{F}(z_1)=0,\quad M_{2-2}^{F}(z_2)=F z_2$$
$$\overline{M}_{1-1}^{\overline{S}}(z_1)=\overline{S} z_1,\quad \overline{M}_{2-2}^{\overline{S}}(z_2)=\overline{S}(b+z_2) \tag{3}$$

The deflection at the free end is obtained as follows:

$$\vartheta_B=\frac{1}{EI_x}\sum_{i=1}^{2}\int_{z_{i0}}^{z_{i1}} M_{i-i}^{F}(z_i)\overline{M}_{i-i}^{\overline{S}}(z_i)dz_i=\frac{1}{EI_x}\left(\int_0^a F z_2(b+z_2)dz_2\right)=\frac{Fa^2}{6EI_x}(3L-a) \tag{4}$$

From Equation (4), the equation for the modulus of elasticity follows:

$$E=\frac{Fa^2}{6\vartheta_B I_x}(3L-a) \tag{5}$$

Based on the derived expression, the value of the equivalent modulus of elasticity for the composite blade is:

$$E=30\text{GPa} \tag{6}$$

In order to analytically determine the required estimation, the equivalent modulus of elasticity for the entire laminate must be used, so that each layer is not considered individually, given that the stacking has the same character and the same stacking orientation angle [3].
After determining the modulus of elasticity, it is possible to approximate the stress analysis in the isolated cross-section.
The cross-section A-A is an airfoil NACA 23012 with a chord length of 200 mm. This cross-section remains constant along the entire blade, which has a length of $L=3.205\text{m}$ and is shown in Figure 2.1.
The elemental centrifugal force acting on the blade is determined as:

$$dF_c=r\omega^2 dm \tag{7}$$

The elementary mass of the blade is:

$$dm=\rho dV=\rho A dr \tag{8}$$

Assuming that the cross-sectional area of the blade is constant and equals *A*, while the equivalent density of the material is ρ, after substituting the expression for the elemental mass of the blade into the expression for the centrifugal force, the following is obtained:

$$dF_c = \rho A \omega^2 r dr \tag{9}$$

The termsand ρ, A and ω in the previous expression are constants, so after integration, the following is obtained:

$$F_c = \rho A \omega^2 \int_{R_0}^{R_1} r dr = \frac{\rho A \omega^2}{2}\left(R_1^2 - R_0^2\right) \tag{10}$$

The position of the center of mass of the blade is determined by the following expression:

$$r_c = \frac{1}{m}\int r dm = \frac{\rho A}{m}\int r dr \Rightarrow \rho A \int r dr = m r_c \tag{11}$$

While the final form of the centrifugal force is:

$$F_c = m \omega^2 r_c \tag{12}$$

The angular velocity at which the main rotor rotates is:

$$\omega = \frac{n\pi}{30} = \frac{500\pi}{30} = 52.36 \mathrm{s}^{-1} \tag{13}$$

the value of the centrifugal force is:

$$F_c = m r_c \omega^2 = 11.5 \cdot 1.82 \cdot 52.36^2 = 57.38 \mathrm{kN} \tag{14}$$

The normal stress due to tension in the cross-section A-A, caused by the action of the centrifugal force, is:

$$\sigma_{1-1}\left(F_c\right) = \frac{F_c}{A_{1-1}} = \frac{57.38 \cdot 10^3}{0.00337} = 17.03 \mathrm{MP_a} \tag{15}$$

After analyzing the stress state and approximating the centrifugal force, based on the elemental lift force, an expression for the aerodynamic lift force of the considered blade can be derived. The elemental lift force is defined as:

$$dR_z = \frac{1}{2}\rho V^2 C_z dS \tag{16}$$

Where dS is the elemental lift surface of the blade. Since the lift surface of the blade is in the shape of a rectangle, with the chord length c, the elemental lift surface is calculated using the following expression:

$$dS = c dr \tag{17}$$

On the other hand, the velocity of the elemental lift surface of the blade, in the case of pure rotation without horizontal movement of the helicopter, is:

$$V = r\omega \tag{18}$$

the expression for the elemental lift force takes the following form:

$$dR_z = \frac{1}{2}\rho C_z c \omega^2 r^2 dr \tag{19}$$

After integrating the previous expression, the following is obtained:

$$R_z = \frac{1}{6}\rho C_z c \omega^2 \left(R_1^3 - R_0^3\right) \tag{20}$$

The lift coefficient of the airfoil can be determined by the expression:

$$C_z = a\left(\alpha - \alpha_n\right) \tag{21}$$

The final form of the aerodynamic force expression is:

$$R_z = \frac{1}{6}\rho c\omega^2 a\left(\alpha - \alpha_n\right)\left(R_1^3 - R_0^3\right) \tag{22}$$

The value of the maximum lift force of the main rotor on the ground is:

$$R_z = 2\cdot\frac{1}{6}\cdot 1.225\cdot 0.202\cdot 52.36^2\cdot 0.1\cdot\left(9.2+1.4\right)\cdot\left(3.465^3 - 0.435^3\right) = 9.95\text{kN} \tag{23}$$

The measured value of the lift force in the helicopter test, for the same angle of attack, is:

$$R_z = 9.205\text{kN} \tag{24}$$

Considering that the analytical and actual values of the aerodynamic force differ by 8%, it can be assumed that for quicker approximations of the load in the initial stages of blade design, the analytical method can be used as valid. The lift force per blade is:

$$R_z = \frac{1}{6}\cdot 1.225\cdot 0.202\cdot 52.36^2\cdot 0.1\cdot\left(9.2+1.4\right)\cdot\left(3.465^3 - 0.435^3\right) = 4.98\text{kN} \tag{25}$$

In addition to the lift force, for the structure sizing, it is necessary to determine the bending moment from the aerodynamic lift force. In order to determine the bending moment, it is necessary to analytically determine the position of the point of attack of the resultant force. The elemental value of the bending moment from the lift force is:

$$dM_0 = dR_z r = \frac{1}{2}\rho C_z c\omega^2 r^3 dr \tag{26}$$

After integrating the previous expression, the following is obtained:

$$M_0 = \frac{1}{8}\rho c\omega^2 a\left(\alpha - \alpha_n\right)\left(R_1^4 - R_0^4\right) \tag{27}$$

On the other hand, the moment from the lift force can be represented by the following expression:

$$M_0 = R_z R^* = \frac{1}{6}\rho c\omega^2 a\left(\alpha - \alpha_n\right)\left(R_1^3 - R_0^3\right)R^* = \frac{1}{8}\rho c\omega^2 a\left(\alpha - \alpha_n\right)\left(R_1^4 - R_0^4\right) \tag{28}$$

where R^* is the position of the point of attack of the lift force from the axis of rotation. Considering the previous expressions, the position of the attack line of the lift force can be determined:

$$R^* = \frac{3}{4}\frac{R_1^4 - R_0^4}{R_1^3 - R_0^3} = 2{,}603\text{m} \tag{29}$$

2.2 *FEM analysis and experimental validation*

The total calculated mass of the blade is 11.254 kg. To this mass, the balancing mass possessed by the actual blade must be added. The alignment has been determined and verified by a numerical model based on measurements of the same quantities as those in the experimental testing. The deflection result obtained through numerical calculation is provided in the table, along with the modulus of elasticity for the equivalent laminate under maximum load [4,5,6]. (According to the maximum stress criterion, not considering elements with singularities, or the origin of numerical errors) [7,8,9]. Measurements were performed for four different loading cases F_1, F_2, F_3 and F_4 corresponding to the deflections of the blade at the free end $\vartheta_{B1}, \vartheta_{B2}, \vartheta_{B3}$ and ϑ_{B4} respectively. The measurement results are presented in tabular form in Table 2.1.

F_1	9.633	N

F_2	56.898	N
F_3	105.948	N
F_4	204.048	N
θ_{B1}	0.0093	m
θ_{B2}	0.055	m
θ_{B3}	0.102	m
θ_{B4}	0.195	m

Table 2.1. Results of the experimental testing.

Comparison of the numerical results for the selected loading case F_4 is presented in tabular form and in the figure.

F_4	204.048	N
θ_{B4}	0.19224	m
E	30.1	GPa

Table 2.2. Numerical analysis results.

a)

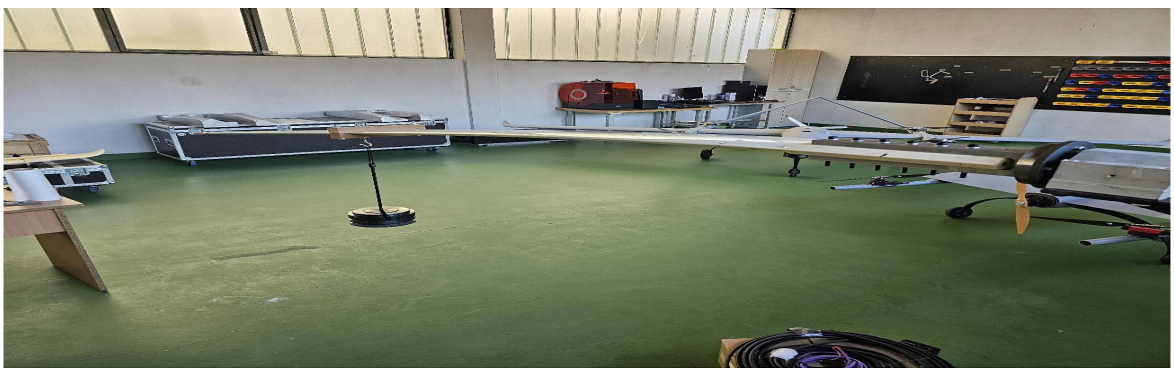

b)

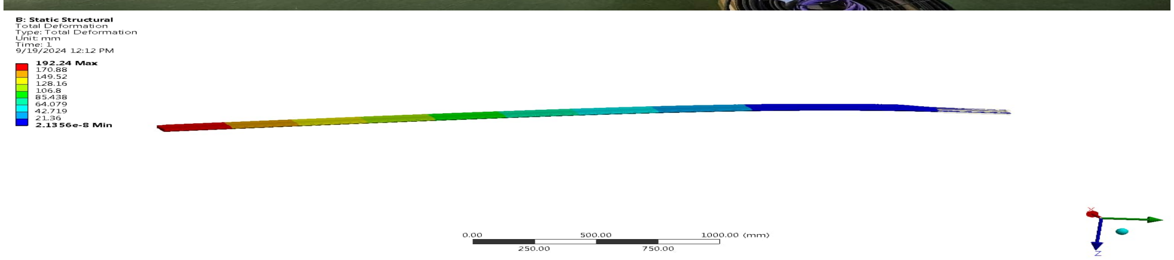

Figure 2.1 a) Experimentally obtained elastic bending line of the blade due to the action of force F_4
b) Numerically obtained elastic bending line due to the action of force F_4

3. Lock number

The Lock number is a dimensionless parameter used in the analysis of the dynamic response of helicopter blades. It represents the ratio between aerodynamic and inertial forces, allowing for the assessment of rotor stability and performance[1,6]. A higher Lock number indicates that aerodynamic forces dominate over inertial forces, which is usually desirable in operation. On the other hand, a lower Lock number means that inertial forces are dominant, which can lead to less stability and different dynamic behaviors[9,10].
The Lock number is calculated using the following expression:

$$\gamma = \frac{\rho c a R^4}{I} \tag{30}$$

where:

γ – Lock number, ρ – air density (kg/m³), c – mean aerodynamic chord of the blade (m), a – slope of the lift coefficient (linear aerodynamic coefficient), R – rotor radius (m), I – moment of inertia of the blade relative to its hub (kgm²).

The values of the required quantities for calculating the Lock number are:
$\rho = 1.225\ \mathrm{kg/m^3}$, $c = 0.202\ \mathrm{m}$, $a = 5.7\ \mathrm{rad}$, $R = 3.465\ \mathrm{m}$.

The moment of inertia II for the blade axis relative to its hub is expressed through the Huygens-Steiner theorem. The mathematical expression of the theorem is:

$$I = I_c + md^2 \tag{31}$$

where:

I is the moment of inertia relative to the new axis, I_c is the moment of inertia relative to the central axis (the axis through the center of mass), m is the mass of the body, d is the distance between the central axis and the new axis

In accordance with Eq.31:

$$I = 11.623 + 11.5 \cdot 1.576^2 = 40.18\ \mathrm{kgm^2}$$

The Lock number for this blade is $\gamma = 5.06$.Examples of Lock numbers for light helicopters in which the Hornet helicopter is included:

1. Robinson R44: Lock number is around 4.5.
2. Schweizer 300C: Lock number is around 3.8. This light helicopter uses a simple rotor, resulting in a lower Lock number.
3. Guimbal Cabri G2: Lock number is around 5. The Cabri G2 is a modern light helicopter with a relatively efficient rotor system, so it has a slightly higher Lock number compared to traditional training helicopters.
4. Enstrom F-28: Lock number is around 4. The helicopter is known for its simple design and reliable rotor system, but its Lock number remains in the lower range for light helicopters.
5. Hughes 500 (MD 500): Lock number is around 5.2. Despite being small, this helicopter uses an advanced rotor design with relatively efficient blades, resulting in a somewhat higher Lock number compared to many light helicopters.

Small and light helicopters typically have Lock numbers ranging from 3.5 to 5.5, depending on the blade design, rotor, and aerodynamic properties. Therefore, it can be concluded that the structure of the blade is well-dimensioned and meets the required specifications.

4. **Conclusions**

This paper presents the methodology for designing the composite blade of a light helicopter's main rotor. The methodology integrates both analytical and numerical approaches for approximating loading conditions. This methodology has been experimentally verified and demonstrates that the analytical approach can be used in the early stages of design for quicker approximations. The verified approach saves time and does not require high computational power. By combining both approaches, the methodology ensures a balance between accuracy and efficiency, enabling rapid design iterations without compromising the quality of the results. The integration of analytical calculations with numerical simulations allows for a comprehensive understanding of the structural behavior and performance characteristics of the rotor blades under various loading conditions. This facilitates optimization of the blade design, ensuring it meets the required aerodynamic and mechanical criteria while keeping development costs and time to a minimum. The experimental verification further strengthens the reliability of the methodology, confirming its practical applicability in real-world design scenarios. This approach proves particularly valuable in the conceptual design phase, where rapid decision-making and iterative testing are crucial. It also provides an effective means of preliminary performance evaluation, enabling designers to identify potential issues early in the development process.T he presented methodology not only enhances the speed and accuracy of the design process for composite rotor blades but also contributes to the broader goal of optimizing helicopter performance and safety. It provides a robust framework that can be applied to various helicopter models, particularly light helicopters, where efficient design and reduced computational demands are essential.

References

[1] Venkatesan, C., *Fundamentals of Helicopter Dynamics*, CRC Press, Boca Raton, FL, 2014, ISBN: 9781466566347.

[2] Kindervater, C., Deletombe, E., *Composite Helicopter Structural Crashworthiness: Progress in Design and Crash Simulation Approaches*, 2nd ONERA-DLR Aerospace Symposium, ODAS 2000, Berlin, 15-16 June 2000.

[3] Torpan, R., Zaharia Sebastian-Marian, *Manufacturing Process of Helicopter Tail Rotor Blades from Composite Materials Using 3D-Printed Moulds*, Appl. Sci. 2024, *14*(3), 972; https://doi.org/10.3390/app14030972

[4] Rasuo, B. *Helicopter Tail Rotor Blade from Composite Materials*: An Experience. SAE Int. J. Aerosp. 2011, 4, 828–838.

[5] Euler, A.H.L.; Beziac, G.F.A. *Method of Manufacturing a Helicopter Rotor Blade*. U.S. Patent 4,298,417, 3 November 1981.

[6] Filippi, M.; Zappino, E.; Carrera, E.; Castanie, B. *Effective Static and Dynamic Finite Element Modeling of a Double Swept Composite Rotor Blade*. J. Am. Helicopter Soc. 2020, 65, 1–12.

[7] Debski, H.; Ostapiuk, *M. Numerical FEM analysis for the part of composite helicopter rotor blade*. J. Kones 2012, *19*, 71–77.

[8] Falkowicz, K. *Experimental and numerical failure analysis of thin-walled composite plates using progressive failure analysis. Compos. Struct.* **2023**, *305*, 116474.

[9] Yu, G.; Li, X.; Huang, W. *Performance and Damage Study of Composite Rotor Blades under Impact*. Polymers 2024, *16*, 623. https://doi.org/10.3390/polym16050623

[10] Tobias Pflumm, *Numerical and Experimental Structural Beam Analysis for the Development of Helicopter Rotor Blades*, Doctoral dissertation, Technical University of Munich, 2022. [Online]. Available: https://mediatum.ub.tum.de/doc/1656540/1656540.pdf

10th International Congress of the Serbian Society of Mechanics
Niš, Serbia, June 18-20, 2025

D.10
Original Scientific Paper

DOI:10.46793/ICSSM25.228R

DIFFERENT TYPES OF THE DEFORMED EXPONENTIAL FUNCTIONS IN THE STATISTICAL MECHANICS

Predrag M. Rajković[1] [0000-0002-2914-0985], Sladjana D. Marinković[2] [0000-0002-7752-4393], and Miomir S. Stanković[3] [0009-0002-8504-6966]

[1]University of Niš, Faculty of Mechanical Engineering, e-mail: predrag.rajkovic@masfak.ni.ac.rs

[2]University of Niš, Faculty of Electronic Engineering, , e-mail: sladjana.marinkovic@elfak.ni.ac.rs

[3]University of Niš, Faculty of Ocupational Safety, e-mail: miomir.stankovic@gmail.com

Abstract. In recent developments in various sciences, the need is noted to define and use deformed versions of the exponential function. In this paper, the consideration of such functions has two purposes: to have the exponential function as their special case, and, even more, to acquit their inauguration from a mathematical point of view. Starting from well-known Tsallis and Kaniadakis versions, we proposed our own deformed versions and connect them with others. It leads to definition of the deformed numbers and operators. We find their series expansions and derived differential and difference properties. They are important in forming and explaining continuous and discrete models of numerous phenomena in statistical mechanics, thermostatics, information theory, cybernetics, control theory, etc. We illustrate it by analyzing of the different versions of Malthus model in population dynamics. Also, we look back on the well-known law of composed interest in the economy by the deformed exponential function.
Keywords: Exponential function, differential operator, difference operator, Malthus model.

1. Introduction

The exponential function $y = e^x$ is one of the most important functions with applications in many sciences such as mathematics, statistics, natural sciences, and economics. The exponential function arises whenever a quantity grows or decays at a rate proportional to its current value. One such situation is continuously compounded interest, and in fact, it was this that led Jacob Bernoulli in 1683. to the number e and Johann Bernoulli in 1697. to the exponential function (see [1]):

$$\lim_{n\to\infty}\left(1+\frac{1}{n}\right)^n = e \approx 2.71828, \quad e^x = \exp(x) = \lim_{n\to\infty}\left(1+\frac{x}{n}\right)^n.$$

New circumstances and challenges in the twentieth century required generalizations and deformations of the exponential function.

Deformations of the exponential functions are considered in three main (complementary) directions:

1. Formal mathematical developments;

2. Observation of consistent concordance with experimental (or natural) behavior;
3. Theoretical physical developments.

One-parameter deformation of the exponential function was proposed by C. Tsallis in 1988. in the context of nonextensive statistic mechanics [2]:

$$e_q^x = \big(1+(1-q)x\big)^{1/(1-q)}. \tag{1}$$

Afterwards, considering a connection between the generalized entropy and theory of quantum groups, S. Abe [3] in 1998. introduced another deformation by

$$e_p^{(A)}(y) = p^{y/(p-1)}. \tag{2}$$

In 2001, G. Kaniadakis [4] proposed a one-parameter deformation for the exponential function in the context of special relativity:

$$\exp_{\{\kappa\}}(x) = \big(\sqrt{1+\kappa^2x^2}+\kappa x\big)^{1/\kappa}. \tag{3}$$

Using a formal mathematical approach, we introduce two variants of the deformed exponential function of two variables to express discrete and continuous behavior using one model. They have such differential i difference properties that allow us to do it. In these functions someone can recognize well-known generalizations and deformations as the special cases [6].

2. Powers and differences

Let $h\in\mathbb{R}\setminus\{0\}$. The generalized integer powers of real numbers have an important role in modern theoretical considerations. In that manner, we first introduce the backward and forward integer powers given by

$$z^{(0,h)}=1,\quad z^{(n,h)}=\prod_{k=0}^{n-1}(z-kh),\qquad z^{[0,h]}=1,\quad z^{[n,h]}=\prod_{k=0}^{n-1}(z+kh)\qquad (n\in\mathbb{N}).$$

The central integer power is defined as

$$z^{\langle 0,h\rangle}=1,\quad z^{\langle n,h\rangle}=\begin{cases}\prod\limits_{k=0}^{m-1}(z-2kh)(z+2kh) & (n=2m,\ m\in\mathbb{N}),\\ z\prod\limits_{k=0}^{m-1}\big(z-(2k+1)h\big)\big(z+(2k+1)h\big) & (n=2m+1,\ m\in\mathbb{N}_0).\end{cases}$$

For $n\in\mathbb{N}$, a relationship with the previously defined generalized powers is given by

$$z^{(n,h)}=z^{[n,-h]},\qquad z^{\langle n,h\rangle}=z^{\langle n,-h\rangle},$$

$$z^{\langle n,h\rangle}=\begin{cases} z^{(m,2h)}\ z^{[m,2h]} & (n=2m,\ m\in\mathbb{N}),\\ z\ (z-h)^{(m,2h)}(z+h)^{[m,2h]} & (n=2m+1,\ m\in\mathbb{N}_0).\end{cases}$$

Also, the following is valid:

$$z^{\langle n,h\rangle}=\ z\big(z+(n-2)h\big)^{(n-1,\ 2h)},\quad z^{\langle 2m,h\rangle}z^{\langle 2m+1,h\rangle}=z\ z^{(2m,h)}\ z^{[2m,h]}.$$

Consider the h–difference operators:

$$\Delta_{z,h}f(z)=\frac{f(z+h)-f(z)}{h}\ ,\quad \nabla_{z,h}f(z)=\frac{f(z)-f(z-h)}{h}\ ,\quad \delta_{z,h}f(z)=\frac{f(z+h)-f(z-h)}{2h}\ .$$

Notice that

$$\nabla_{z,h}f(z)=\Delta_{z,-h}f(z)=\Delta_{z,h}f(z-h),\quad \delta_{z,-h}f(z)=\delta_{z,h}f(z).$$

We can prove that their acting on integer generalized powers is given by:

$$\Delta_{z,h}\,z^{(n,h)}=nz^{(n-1,h)},\quad \nabla_{z,h}\,z^{[n,h]}=nz^{[n-1,h]},\quad \delta_{z,h}\,z^{\langle n,h\rangle}=nz^{\langle n-1,h\rangle}. \tag{4}$$

3. The deformed exponential function of the Tsallis type

Let $h \in \mathbb{R} \setminus \{0\}$. We define a function $(x,y) \mapsto e_h(x,y)$ by

$$e_h(x,y) = (1+hx)^{y/h} \qquad (x \in \mathbb{C} \setminus \{-1/h\},\ y \in \mathbb{R}). \tag{5}$$

Since

$$\lim_{h \to 0} e_h(x,y) = e^{xy} \ ,$$

this function can be viewed as an one-parameter deformation of the exponential function of two variables.

If $h = 1-q$ $(q \neq 1)$ and $y = 1$, the function (5) becomes

$$e_{1-q}(x,1) = \big(1+(1-q)x\big)^{1/(1-q)},$$

i.e., $e_{1-q}(x,1) = e_q^x$, where e_q^x is Tsallis q–exponential function defined by (1).

If $h = p-1$ $(p \neq 1)$ and $x = 1$, the function (5) becomes

$$e_{p-1}(1,y) = p^{y/(p-1)} = e_p^{(A)}(y),$$

i.e. function defined by (2) and considered for a generalization of the standard exponential function in the context of quantum group formalism.

The function $e_h(x,y)$ can be viewed as the scaled Tsallis exponential function:

$$e_h(x,y) = e_{q'}^{x'} \quad \text{with} \quad x' = xy \quad \text{with} \quad q' = 1 - h/y.$$

Notice that function (5) can be written in the form

$$e_h(x,y) = \exp\Big(\frac{y}{h}\ \ln(1+hx)\Big).$$

If we introduce a deformation of number $x \mapsto \{x\}_h$ by

$$\{x\}_h = \frac{1}{h}\ \ln(1+hx) \qquad (x \in \mathbb{C} \setminus \{-1/h\}), \tag{6}$$

then we can represent the function (7) as follows

$$e_h(x,y) = e^{\{x\}_h\, y}. \tag{7}$$

We can show that the function (5) preserves some basic properties of exponential function. For $x \in \mathbb{C} \setminus \{-1/h\}$ and $y \in \mathbb{R}$ the following holds:

$$e_h(x,y) > 0 \qquad (x < -1/h \ \text{ for } \ h < 0 \quad \vee \quad x > -1/h \ \text{ for } \ h > 0),$$
$$e_h(0,y) = e_h(x,0) = 1, \qquad e_{-h}(x,y) = e_h(-x,-y), \qquad e_h(x,y_1+y_2) = e_h(x,y_1)e_h(x,y_2).$$

The last formula confirms that the additive property is true with respect to the second variable. However, with respect to the first variable, the following holds:

$$e_h(x_1,y)e_h(x_2,y) = e_h\big(x_1+x_2+hx_1x_2,y\big)\ .$$

This equality suggests us to introduce a generalization of the addition:

$$x_1 \oplus_h x_2 = x_1 + x_2 + hx_1x_2\ . \tag{8}$$

This operation is commutative, associative and 0 is its identity. For $x \neq -1/h$, the $\oplus_h$–inverse exists as

$$\ominus_h x = \frac{-x}{1+hx},$$

such that $x \oplus_h (\ominus_h x) = 0$ is valid. Hence, $(I, \oplus_h)$ is an Abelian group, where $I = (-\infty, -1/h)$ for $h < 0$ or $I = (-1/h, +\infty)$ for $h > 0$. In this way, the $\ominus_h$–subtraction can be defined by

$$x_1 \ominus_h x_2 = x_1 \oplus_h (\ominus_h x_2) = \frac{x_1 - x_2}{1+hx_2} \qquad \left(x_2 \neq -\frac{1}{h}\right). \tag{9}$$

Due to (6), we can prove the next equality:

$$\{x_1\}_h + \{x_2\}_h = \{x_1 \oplus_h x_2\}_h \qquad (x_1, x_2 \in I). \tag{10}$$

The operation (8) allows us to observe the deformed addition property of the function (5) with respect to the first variable. For $x_1, x_2 \in \mathbb{C} \setminus \{-1/h\}$ and $y \in \mathbb{R}$, the following is valid:

$$e_h(x_1 \oplus_h x_2, y) = e_h(x_1, y) e_h(x_2, y), \qquad e_h(x_1 \ominus_h x_2, y) = e_h(x_1, y) e_h(x_2, -y).$$

The function $e_h(x,y)$ determines a surface shown in Figure 1. Bold-emphasized line is e^x in the part 1(a), and e^y in the part 1(b).

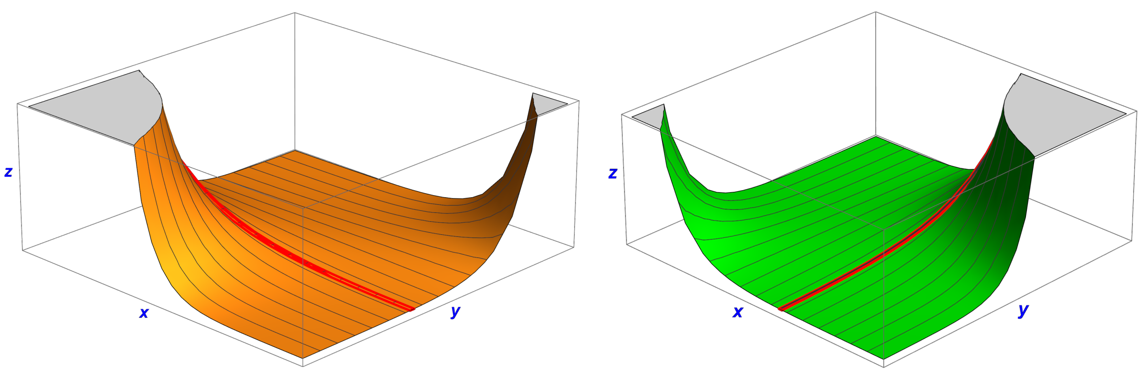

(a) $y =$const. (b) $x =$const.

Figure 1: The behavior of $z = e_h(x,y)$ for $h = 0.05$.

4. The deformed exponential functions of Kaniadakis type

Let us define a function $(x,y) \mapsto \exp_h(x,y)$ by

$$\exp_h(x,y) = \left(hx + \sqrt{1+h^2x^2}\right)^{y/h} \qquad (x \in \mathbb{C},\ y \in \mathbb{R}). \tag{11}$$

Since

$$\lim_{h \to 0} \exp_h(x,y) = e^{xy},$$

this function can be viewed as an one–parameter deformation of the exponential function with two variables.

If $h=\kappa$ and $y=1$, the function (11) becomes κ–exponential function (3) introduced by Kaniadakis. The function $\exp_h(x,y)$ can be viewed as a scaled Kaniadakis exponential:

$$\exp_h(x,y)=\exp_{\{\kappa'\}}(x') \quad \text{with} \quad x'=xy \quad \text{and} \quad \kappa'=h/y.$$

Since

$$\operatorname{arcsinh}(hx)=\ln(hx+\sqrt{1+h^2x^2}), \tag{12}$$

the function (11) can be written in the form

$$\exp_h(x,y)=\exp\Big(\frac{y}{h}\operatorname{arcsinh} hx\Big).$$

By introducing the deformed number $x\mapsto\{x\}^h$ defined as

$$\{x\}^h=\frac{1}{h}\operatorname{arcsinh} hx \qquad (x\in\mathbb{C}). \tag{13}$$

the function (11) can be written as

$$\exp_h(x,y)=e^{\{x\}^h y}. \tag{14}$$

For $x\in\mathbb{C}$ and $y\in\mathbb{R}$ the following holds:

$$\begin{gathered}\exp_h(x,y)>0 \quad (x\in\mathbb{R}), \quad \exp_h(0,y)=\exp_h(x,0)=1,\\ \exp_{-h}(x,y)=\exp_h(x,y), \quad \exp_h(x,y_1+y_2)=\exp_h(x,y_1)\exp_h(x,y_2).\end{gathered}$$

This function preserves additive property with respect to the second variable only. However, according to (12) we have:

$$\exp_h(x_1,y)\exp_h(x_2,y)=\exp_h\Big(x_1\sqrt{1+h^2x_2^2}+x_2\sqrt{1+h^2x_1^2},y\Big).$$

This suggests that we can introduce another generalization of addition:

$$x_1\oplus^h x_2=x_1\sqrt{1+h^2x_2^2}+x_2\sqrt{1+h^2x_1^2}\ . \tag{15}$$

The operation $\oplus^h$– sum is commutative, associative, its identity is 0 and $\oplus^h$– inverse for $x\in\mathbb{R}$ is $-x$. Thus, $(\mathbb{R},\oplus^h)$ is an Abelian group, and $\ominus^h$– subtraction can be defined by

$$x_1\ominus^h x_2=x_1\oplus^h(-x_2)=x_1\sqrt{1+h^2x_2^2}-x_2\sqrt{1+h^2x_1^2}\ . \tag{16}$$

Related to (13), we can prove the next equality:

$$\{x_1\}^h+\{x_2\}^h=\{x_1\oplus^h x_2\}^h.$$

We are now able to observe the deformed addition property. For $x_1,x_2\in\mathbb{C}$ and $y\in\mathbb{R}$, the following is valid:

$$\begin{aligned}&\exp_h(x_1\oplus^h x_2,y)=\exp_h(x_1,y)\exp_h(x_2,y),\\ &\exp_h(x_1\ominus^h x_2,y)=\exp_h(x_1,y)\exp_h(-x_2,y)=\exp_h(x_1,y)\exp_h(x_2,-y).\end{aligned}$$

The surface determined by $\exp_h(x,y)$ for very small h is shown on Figure 2. The bold–emphasized curve is e^x in the first, and e^y in the second part of the figure.

The relationship between functions (5) and (11) is given by

$$\exp_h(x,y)=e_h\Big(x-\frac{1-\sqrt{1+h^2x^2}}{h}\ ,\ y\Big).$$

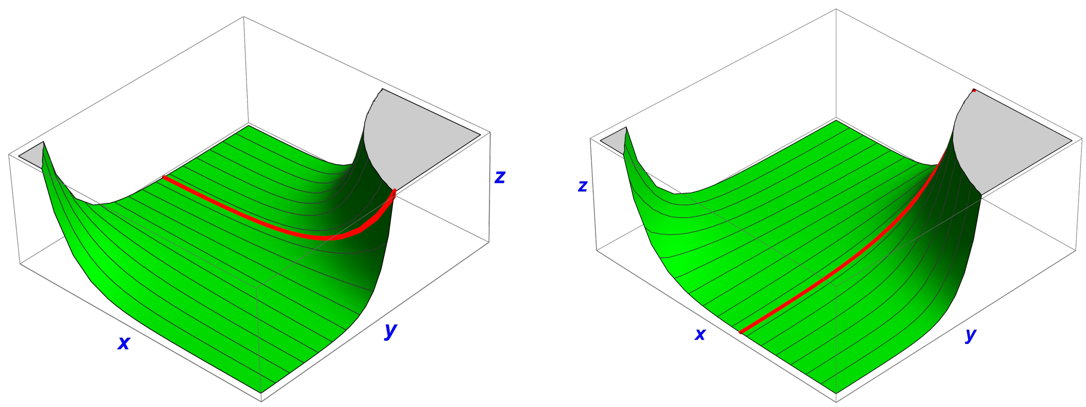

(a) $y =$const. (b) $x =$const.

Figure 2: The behavior of $\exp_h(x,y)$ for $h = 0.01$

5. Expansions into series, difference and differential properties

In this section, we consider the expansions of the introduced deformed exponential functions. Related to these expansions, we show that the functions $e_h(x,y)$ and $e_{-h}(x,y)$ are eigenfunctions of the operators $\Delta_{y,h}$ and $\nabla_{y,h}$ with the eigenvalue x. In addition, the function $\exp_h(x,y)$ is an eigenfunction of operator $\delta_{y,h}$ with eigenvalue x.

For the functions $(x,y) \mapsto e_h(x,y)$ and $(x,y) \mapsto e_{-h}(x,y)$, the following representations hold respectively:

$$e_h(x,y) = \sum_{n=0}^{\infty} \frac{1}{n!} x^n y^{(n,h)}\ , \qquad e_{-h}(x,y) = \sum_{n=0}^{\infty} \frac{1}{n!} x^n y^{[n,h]} \qquad (|hx| < 1). \tag{17}$$

Really,

$$e_h(x,y) = (1+hx)^{y/h} = \sum_{n=0}^{\infty} \binom{y/h}{n} h^n x^n = \sum_{n=0}^{\infty} \frac{y(y-h)\cdots\big(y-(n-1)h\big)}{h^n\ n!} h^n x^n = \sum_{n=0}^{\infty} \frac{y^{(n,h)}}{n!} x^n.$$

Also, the function $(x,y) \mapsto \exp_h(x,y)$ can be represented as (see [6])

$$\exp_h(x,y) = \sum_{n=0}^{\infty} \frac{1}{n!} x^n y^{\langle n,h \rangle} \tag{18}$$

Notice that in expressions (7) and (14) the deformations of variable x appear, but, contrary to that in expansions (18), the deformations of the powers of y are present.

Using the above expansions and relations (4) we can prove that the functions $y \mapsto e_h(x,y)$, $y \mapsto e_{-h}(x,y)$ and $y \mapsto \exp_h(x,y)$ are eigenfunctions of operators $\Delta_{y,h}$, $\nabla_{y,h}$ and $\delta_{y,h}$ respectively, with eigenvalue x:

$$\Delta_{y,h}\ e_h(x,y) = x\ e_h(x,y), \qquad \nabla_{y,h}\ e_{-h}(x,y) = x\ e_{-h}(x,y), \qquad \delta_{y,h}\ \exp_h(x,y) = x\ \exp_h(x,y).$$

Here, the proof of only the first equality will be presented, as the other two are proven similarly.

$$\Delta_{y,h}\ e_h(x,y) = \Delta_{y,h}\left(\sum_{n=0}^{\infty}\frac{1}{n!}x^n y^{(n,h)}\right) = \sum_{n=0}^{\infty}\frac{1}{n!}x^n \Delta_{y,h} y^{(n,h)} = \sum_{n=1}^{\infty}\frac{1}{(n-1)!}x^n y^{(n-1,h)}$$
$$= x\sum_{n=0}^{\infty}\frac{1}{n!}x^n y^{(n,h)} = x\ e_h(x,y).$$

After deformed numbers and deformed addition operations, it is also possible to introduce deformed differential operators. In this sense we can define deformed h–differential and h–derivative accordingly with operation (9) (see [7]):

$$d_h z = \lim_{u\to z} z\ominus_h u, \quad \frac{df(z)}{d_h z} = \lim_{u\to z}\frac{f(z)-f(u)}{z\ominus_h u} = (1+hz)\frac{df(z)}{dz}\ .$$

The function $x\mapsto e_h(x,y)$ is an eigenfunction of operator $\dfrac{d}{d_h x}$ with eigenvalue y:

$$\frac{d}{d_h x}\ e_h(x,y) = y\ e_h(x,y).$$

Really,

$$\frac{d}{d_h x}\ e_h(x,y) = (1+hx)\frac{d}{dx}\left(e_h(x,y)\right) = (1+hx)\frac{d}{dx}\left((1+hx)^{y/h}\right)$$
$$= y(1+hx)^{y/h} = y\ e_h(x,y).$$

In [4], the deformed h–differential and h–derivative were defined accordingly to operation (16):

$$d^h z = \lim_{u\to z} z\ominus^h u, \quad \frac{df(z)}{d^h z} = \lim_{u\to z}\frac{f(z)-f(u)}{z\ominus^h u} = \sqrt{1+h^2z^2}\ \frac{df(z)}{dz}\ .$$

The function $x\mapsto \exp_h(x,y)$ is an eigenfunction of operator $\dfrac{d}{d^h x}$ with eigenvalue y:

$$\frac{d}{d^h x}\ \exp_h(x,y) = \sqrt{1+h^2x^2}\ \frac{d}{dx}\left(\exp_h(x,y)\right) = \sqrt{1+h^2x^2}\ \frac{d}{dx}\left(\left(hx+\sqrt{1+h^2x^2}\right)^{y/h}\right)$$
$$= y\left(hx+\sqrt{1+h^2x^2}\right)^{y/h} = y\ \exp_h(x,y).$$

Finally, let us consider the behavior of deformed exponential functions related to differentiation over the second variable. We conclude that they are eigenfunctions of the operator $\partial/\partial y$ with deformed numbers as eigenvalues:

$$\frac{\partial}{\partial y}e_h(x,y) = \{x\}_h\ e_h(x,y), \qquad \frac{\partial}{\partial y}\exp_h(x,y) = \{x\}^h\ \exp_h(x,y).$$

6. Applications

In this section, we will note the presence and potential of deformed exponentials in growth models.

Firstly, their applications in the population dynamics can be found in the papers of S. de Andreis and P.E. Ricci [9] and G. Bretti and P.E. Ricci [10] and in our papers [5] and [6].

Consider the number $N(t)$ of individuals in the population at the time t with initial value $N(0) = N_0$. The model assumes that the increment of population in time period δt is proportional to $N(t)$, i.e. the next difference equation is satisfied

$$\Delta_{t,\delta t} N(t) = rN(t), \tag{19}$$

where r is called the intrinsic growth rate. The function $t \mapsto e_{\delta t}(r,t)$ is an eigenfunction of the difference operator $\Delta_{t,\delta t}$ with eigenvalue r.

Hence, the solution of equation (19) can be expressed by the deformed exponential function in the form

$$N(t) = N_0 e_{\delta t}(r,t) = N_0(1 + r\delta t)^{t/\delta t}. \tag{20}$$

When $\delta t \to 0$, we get the Malthus model in population dynamics described by equation (see [11])

$$\frac{d}{dt}N(t) = rN(t), \qquad N(0) = N_0,$$

whose solution is

$$N(t) = N_0 e^{rt}.$$

Obviously, $N(t) \to +\infty$ when $t \to +\infty$ with $r > 0$, it means that the species population is to explode in a process of long-time evolution. Because the resources of the surrounding environment in nature are always limited, therefore, unlimited population growth is impossible when the species population is numerous.

In [10], the equation

$$\frac{d}{dt}t\frac{d}{dt}N(t) = rN(t), \qquad N(0) = N_0,\ N'(0) = N_1 = rN_0,$$

which describes the L–Malthus model, is discussed. In this case, population growth increases according to the function $e_1(x)$, where

$$e_k(t) = \sum_{n=0}^{\infty} \frac{t^n}{(n!)^{k+1}} \qquad (k = 0, 1, \ldots).$$

Thus, the relevant increase is slower with respect to the classical Malthus model.

Consider a deformed h–Malthus model described by equation

$$\frac{d}{d_h t}N(t) = rN(t), \qquad N(0) = N_0.$$

Its solution is

$$N(t) = N_0 e_h(t,r) = N_0(1 + ht)^{r/h}.$$

With appropriate choice of the constant $h > 0$, we can obtain an arbitrary level of population growth increase. Similarly, the second deformed h-Malthus model can be described by the equation

$$\frac{d}{d^h t}N(t) = rN(t), \qquad N(0) = N_0,$$

Year	1980	1985	1990	1995	2000	2005	2010	2015	2020	2025
Population	4.454	4.850	5.276	5.686	6.079	6.449	6.870	7.470	7.887	?

Table 1: The world population from the year 1980 til 2020.

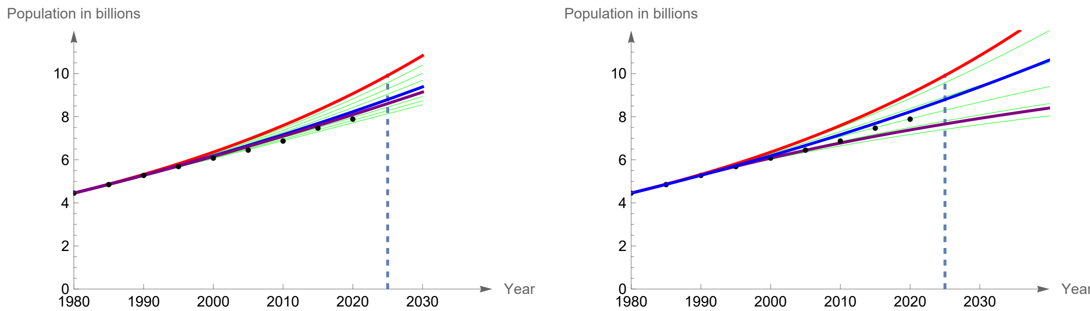

(a) $N(t) = N_0 e_h(t,r)$ (b) $N(t) = N_0 \exp_h(t,r)$

Figure 3: The Malthus, L–Malthus and h–Malthus models

and its solution

$$N(t) = N_0 \exp_h(t,r) = N_0 \left(ht + \sqrt{1+h^2t^2}\right)^{r/h}.$$

Here we will use data from Table 1 in order to predict the world population in 2025.

We will compare the functions which appear in the Malthus, L–Malthus and h–Malthus models. Here, the upper bold-emphasized (red) function is $N(t) = N_0 e^{rt}$ and the lower (blue) is $N(t) = N_0 e_1(rt)$. The Estimation for the year 2025 by Malthus model is $9.91434 \cdot 10^9$.

Thin green lines are provided for $h = 0.01(0.01)0.08$.

The optimal function with $e_h(x,y)$ is provided for $h = 0.0507207$, and estimation of the world population for the year 2025 is $8.61017 \cdot 10^9$. But, the optimal function with $\exp_{\{h\}}(x,y)$ s provided for $h' = 0.259719$ and estimation of the world population for the year 2025 is $7.66321 \cdot 10^9$. Such big difference in the estimation comes from the fact that we use initial points which are very far away from the required to be estimated. The optimal functions are drawn as thick purple lines.

Using the same model as in (19) in the economy, we can express the well-known law of composed interest by the deformed exponential function as

$$A(t) = P\left(1+\frac{r}{n}\right)^{nt} = Pe_{1/n}(r,t),$$

where $A(t)$ is the final amount, P is the initial investment, r is the annual nominal interest rate, n is the number of times the interest is compounded per year and t is the number of years.

Other interesting examples in the other sciences can be found, for example, in [8] and [12].

7. Concluding remarks

Besides the classical statistical theories in which most distribution functions are based on the exponential function and the entropy is based on the logarithm function, a few new theories appeared which required generalizations and deformations of well-known classical functions. We wanted to point to the properties of these functions and their applications, not only in statistical mechanics and thermostatics, nevertheless it might be of some interest in the frame of information theory, cybernetics, control theory, etc.

Acknowledgement. We wish to express our gratitude to the editor and unknown referees for careful reading of the manuscript and very useful suggestions which had the influence on its improvement.

This work was supported by the Ministry of Science, Technological Development and Innovation of the Republic of Serbia [grants No. 451-03-65/2024- 03/200102 and No. 451-03-66/2024-03/200109].

References

[1] Bernoulli, J., Opera omnia, Vol. 3, 1697.

[2] Tsallis, C., Possible generalization of Boltzmann-Gibbs statistics, Journal of Statistical Physics, Vol. 52, 479-487,1988.

[3] Abe, S., Nonextensive statistical mechanics of q–bosons based on the q–deformed entropy, Physics Letters A, Vol. 224, 229-236, 1998.

[4] Kaniadakis, G., Non–linear kinetics underlying generalized statistics, Physica A, Vol. 296, 405-425, 2001.

[5] Stanković, M.S., Marinković, S.D., Rajković, P.M., The deformed and modified Mittag–Leffler polynomials, Mathematical and Computer Modelling, Vol. 54, 721-728, 2011.

[6] Stanković, M.S., Marinković, S.D., Rajković, P.M., The deformed exponential functions of two variables in the context of various statistical mechanics, Applied Mathematics and Computation, Vol. 218, 2439-2448, 2011.

[7] Borges, E., A possible deformed algebra and calculus inspired in nonextensive thermostatics, Physica A, Vol. 340, 95-101, 2004.

[8] Kaniadakis, G., Maximum entropy principle and power-law tailed distributions, The European Physical Journal B, Vol. 70, No 3, 3-13, 2009.

[9] Andreis, S. de, Ricci, P.E., Modelling Population Growth via Laguerre-Type Exponentials, Mathematical and Computer Modelling, Vol. 42, 1421-1428, 2005.

[10] Bretti, G., Ricci, P.E., Laguerre-type special functions and population dynamics, Applied Mathematics and Computation, Vol. 187, 89-100, 2007.

[11] Malthus, T.R., Principle of Population, Penguin, Harmondsworth, England, 1798.

[12] Murray, J., Mathematical Biology, Springer-Verlag, Berlin, 1989.

10th International Congress of the Serbian Society of Mechanics
Niš, Serbia, June 18-20, 2025
D.11
Original Scientific Paper

DOI:10.46793/ICSSM25.238R

TRUSS STRUCTURE OPTIMIZATION USING PARTICLE SWARM OPTIMIZATION WITH DIRECT FEM COUPLING

Ognjen Ristić[1] [0009-0004-3867-5625] and **Nataša Trišović**[2] [0000-0003-1043-5780]

[1]Institut Mihajlo Pupin: Belgrade, Central Serbia, email: risticognjen94@gmail.com

[2]University of Belgrade, Faculty of Mechanical Engineering, Serbia, e-mail: ntrisovic@mas.bg.ac.rs

Abstract. This paper presents a methodology for the mass optimization of truss structures using Particle Swarm Optimization (PSO) coupled with Finite Element Method (FEM) analysis. The approach allows for the modification of nodal coordinates while maintaining structural integrity under specified loading conditions. The results indicate that the PSO algorithm effectively navigates the design space to identify optimal node positions that minimize structural mass while maintaining performance requirements. This methodology offers a promising approach for structural design in engineering applications where displacement reduction is critical.

Keywords: Particle Swarm Optimization, Truss Structures, Topology Optimization, Finite Element Method, Direct Coupling.

1. Introduction

Structural optimization is an area in engineering design that aims to find the most efficient configuration of a structure while satisfying various performance constraints. Truss structures are widely used in engineering applications due to their efficiency in load-bearing capabilities and material usage. Optimizing these structures can lead to significant material savings, reduced construction costs, and improved performance. Topology optimization of truss structures has traditionally been approached through mathematical programming methods, which often require sensitivity analysis and can be computationally expensive for complex structures. Shape optimization, which involves modifying the geometric configuration of the structure, offers additional opportunities for mass reduction by allowing the structure to adapt its form to the specific loading conditions [1]. Particle Swarm Optimization (PSO), first introduced by Kennedy and Eberhart [2], is a population-based stochastic optimization technique inspired by social behavior of bird flocking or fish schooling. PSO has shown promising results in various engineering optimization problems due to its simplicity and efficiency [3]. However, its application to truss structure optimization, especially with direct coupling to Finite Element Analysis, has not been extensively explored. Initial efforts by Tang et al. [4] and Fourie and Groenwold [5] demonstrated the potential of PSO for structural optimization, but their approaches typically relied on separate FEM solvers rather than direct coupling. This paper presents an approach that directly couples PSO with Finite Element Method (FEM) for optimizing truss structures. The proposed method modifies the nodal coordinates of a truss structure while maintaining connectivity to achieve displacement reduction while satisfying stress constraints.

2. Problem Formulation

2.1 Truss Structure Optimization

The truss structure optimization problem can be formulated as a constrained optimization problem:

$$
\begin{aligned}
\min_{\mathbf{x}} \quad & M(\mathbf{x}) \\
\text{s.t.} \quad & \sigma_{\max}(\mathbf{x}) \leq \sigma_{\text{allow}} \\
& u_{\max}(\mathbf{x}) \leq u_{\text{allow}} \\
& L_{\min} \leq L_i(\mathbf{x}) \\
& \mathbf{x}_{LB} \leq \mathbf{x} \leq \mathbf{x}_{UB}
\end{aligned}
\tag{1}
$$

where $M(\mathbf{x})$ is the mass of the structure, $\sigma_{\max}(\mathbf{x})$ is the maximum stress in any element, $u_{\max}(\mathbf{x})$ is the maximum displacement at any node, $L_i(\mathbf{x})$ is the length of the i-th element, and $\mathbf{x}$ represents the design variables, which in this case are the coordinates of the movable nodes.

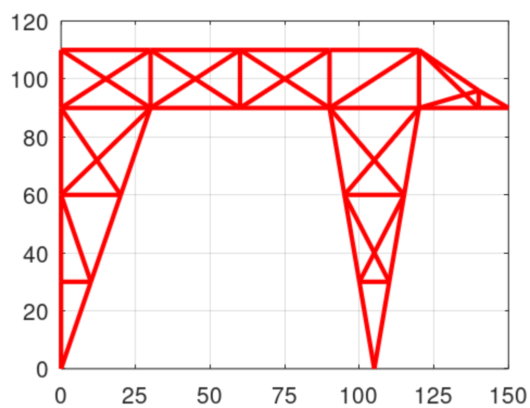

Figure 1: Truss structure

The constraints ensure that the maximum stress and displacement remain below allowable values, that all member lengths remain above a minimum value, and that all design variables remain within their bounds. The truss structure is presented in Figure 1.

2.2 Finite Element Formulation

For a truss element with nodes i and j, the element stiffness matrix in the local coordinate system is given by:

$$
\mathbf{k}_l = \frac{EA}{L} \begin{bmatrix} 1 & -1 \\ -1 & 1 \end{bmatrix} \tag{2}
$$

where E is the Young's modulus, A is the cross-sectional area, and L is the element length. The transformation matrix from local to global coordinates is:

$$
\mathbf{C} = \begin{bmatrix} \cos\theta & \sin\theta & 0 & 0 \\ 0 & 0 & \cos\theta & \sin\theta \end{bmatrix}^T \tag{3}
$$

where θ is the angle between the element and the global x-axis. The element stiffness matrix in global coordinates is then:

$$\mathbf{k}_g = \mathbf{C}^T \mathbf{k}_l \mathbf{C} \tag{4}$$

The global stiffness matrix $\mathbf{K}$ is assembled from the element stiffness matrices using connectivity information, [7]. The displacement vector $\mathbf{u}$ is obtained by solving:

$$\mathbf{K}\mathbf{u} = \mathbf{F} \tag{5}$$

where $\mathbf{F}$ is the applied load vector, [6]. Once displacements are determined, element stresses can be calculated using:

$$\sigma_i = E \cdot \mathbf{B}_i \cdot \mathbf{u}_i \tag{6}$$

where $\mathbf{B}_i$ is the strain-displacement matrix for element i, and $\mathbf{u}_i$ is the displacement vector for the nodes of element i, [7].

3. Particle Swarm Optimization

3.1 PSO Algorithm

The PSO algorithm maintains a population of particles (potential solutions) that move through the search space according to simple mathematical formulae, [8]. Each particle's movement is influenced by its local best-known position and the global best-known position discovered by any particle in the swarm [9]. For each particle i, the position update is governed by:

$$\begin{aligned} \mathbf{v}_i^{t+1} &= w\mathbf{v}_i^t + c_1 r_1(\mathbf{p}_i - \mathbf{x}_i^t) + c_2 r_2(\mathbf{g} - \mathbf{x}_i^t) \\ \mathbf{x}_i^{t+1} &= \mathbf{x}_i^t + \mathbf{v}_i^{t+1} \end{aligned} \tag{7}$$

Where: $\mathbf{v}_i^t$ is the velocity of particle i at iteration t, $\mathbf{x}_i^t$ is the position of particle i at iteration t, w is the inertia weight, c_1, c_2 are acceleration coefficients, r_1, r_2 are random numbers between 0 and 1, $\mathbf{p}_i$ is the best position found by particle i (personal best), $\mathbf{g}$ is the best position found by any particle (global best). In this implementation, a linearly decreasing inertia weight strategy is employed to balance exploration and exploitation:

$$w = w_{max} - (w_{max} - w_{min}) \times \frac{t}{t_{max}} \tag{8}$$

Where $w_{max} = 0.9$, $w_{min} = 0.4$, and t_{max} is the maximum number of iterations.

3.2 Fitness function

The fitness function guides the PSO algorithm toward optimal solutions [4]. A penalty approach is used:

$$f = M_{initial}\left(1 + \left(\frac{\delta_{max}}{\delta_{allow}}\right)^2 + \left(\frac{\sigma_{max}}{\sigma_{allow}}\right)^2\right) \tag{9}$$

This formulation heavily penalizes constraint violations, steering the search toward feasible regions.

4. Direct PSO-FEM Coupling

A key contribution of this work is the direct coupling between PSO and FEM. Rather than calling an external solver for each fitness evaluation, the FEM analysis is integrated directly into the optimization loop, [7].

The direct coupling is implemented through the following steps: Pre-compute Initial FEM Matrices(Before the optimization loop, the initial stiffness matrix $\mathbf{K_0}$ and load vector $\mathbf{F}$ are computed for the original geometry), efficient Update of stiffness Matrix, the sparsity pattern of the stiffness matrix remains constant, allowing for efficient memory allocation and computation, the FEM analysis operations are vectorized where possible to improve computational performance.

The pseudocode for the direct coupling is shown in Algorithm 1.

Algorithm 1: Direct PSO-FEM Coupling

1. Precompute K_0 and F for original geometry;
2. Initialize particles with random positions within bounds;
3. For each iteration t = 1 to t_{max}:
4. For each particle $i = 1$ to $n_{particles}$:
5. Update geometry based on particle position
6. Efficiently update K from K_0 using new geometry
7. Solve $Ku = F$ for displacements
8. Calculate stresses, mass, and constraints
9. Evaluate fitness with penalties
10. Update personal best and global best
11. End For
12. Update particle velocities and positions
13. Adapt inertia weight w based on iteration
14. End For
15. Return best geometry and performance metrics

5. Implementation

The implementation of the proposed method was carried out in MATLAB. Problem Data Structure: The truss structure is represented by nodal coordinates (geom), element connectivity (connec), material properties (prop), nodal degrees of freedom (nf), and applied loads (load). The FEM analysis includes efficient assembly of the global stiffness matrix, solution of the linear system for displacements, and calculation of element stresses. The fitness function evaluates the mass of the structure, checks for constraint violations, and applies penalties as needed. The results are visualized through comparisons of the original and optimized geometries, as well as stress distributions.

5.1 Model description

The methodology is applied to a 23-node, 50-member planar truss structure. The initial configuration, shown in Figure 1, represents a typical bridge-like structure with dimensions spanning approximately 150cm in length and 110cm in height. Material properties and constraints: Young's modulus: 210 GPa (steel), Density: 7850 kg/m^3, Cross-sectional area: 0.001 m^2. Loading conditions consist of vertical downward forces applied at nodes 11 (10 kN) and 15 (20 kN), simulating typical structural loading scenarios.

The PSO algorithm was configured with the following parameters: Population size: 30 particles, Maximum iterations: 20, Acceleration coefficients: $c_1 = c_2 = 2.5$, Initial inertia weight: 0.9 (decreasing linearly to 0.4)

6. Numerical Results

To demonstrate the effectiveness of the proposed method, a truss structure optimization problem was solved. The initial structure consisted of 23 nodes and multiple elements, with fixed nodes at the two support points.

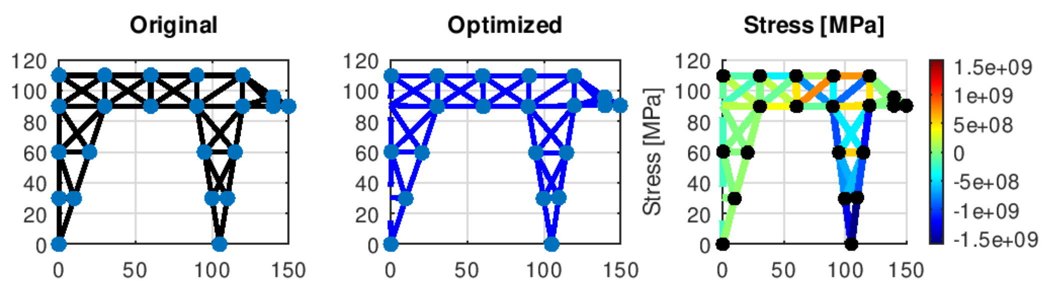

Figure 2: After PSO

The graphical representation of the results is presented in the Fig 3.

6.1 Optimization Results

The optimization was run for 20 iterations with 30 particles. Comparison of the original and optimized geometries is presented in Figure 2. The optimized structure maintains the overall connectivity pattern but with modified node positions that result in a more efficient load path, and illustrates the stress distribution in the original structure.

The exaggerated geometrical difference of the original and optimized structure is presented in Figure 3. The comparison of the displacements of the structure before and after PSO optimization are presented in the table 1.

7. Discussion

The results demonstrate that the proposed method is effective for optimizing truss structures. The direct coupling between PSO and FEM provides computational efficiency, while the modified PSO algorithm with dynamic parameter adaptation and constraint handling ensures robust convergence to feasible solutions.

Several key observations can be made from the results:

1. All X-displacement values in File 2 are smaller than in File 1, with differences ranging from -8.28 % to -23.79 % .

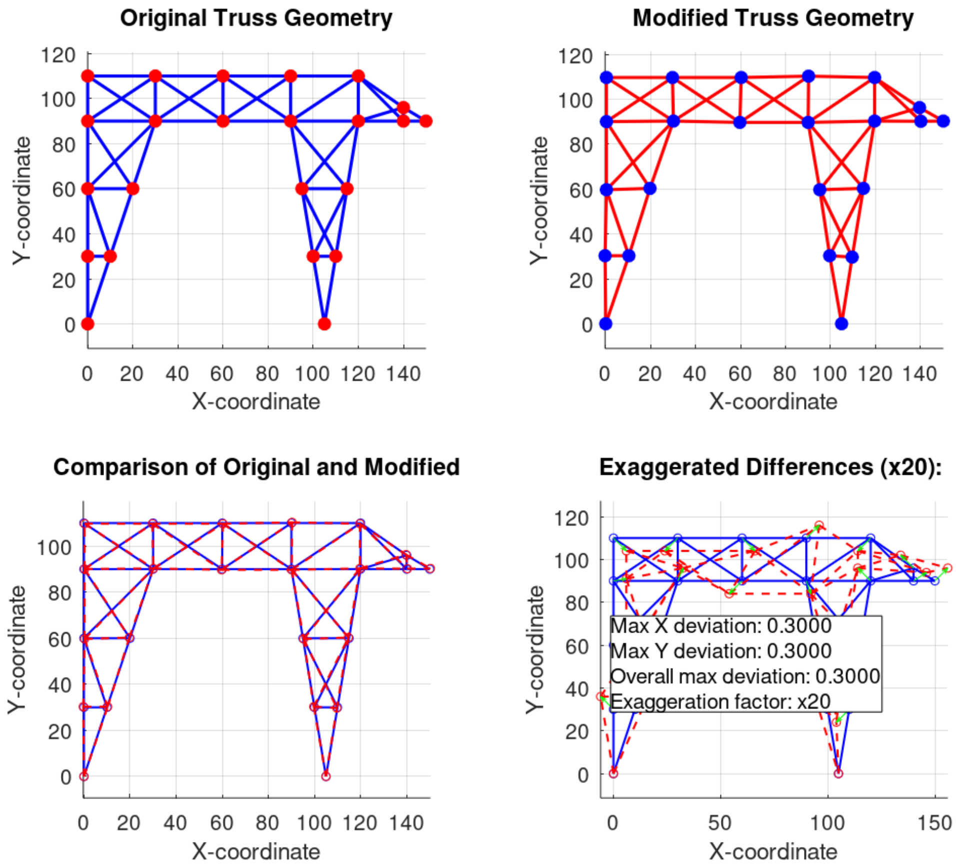

Figure 3: Comparison of the structures

2. The Y-displacement differences vary, with some values increasing and others decreasing in File 2 compared to File 1.
3. The largest X-displacement differences occur at nodes 18 and 19 (-23.79 % and -22.64) %.
4. The largest Y-displacement differences occur at nodes 2 and 4 (8.17 % and -9.90 %).
5. Nodes 1 and 20 show no displacement in both files, as they are fixed support points.

8. Concluding Remarks

This paper presented a novel approach for topology optimization of truss structures using Particle Swarm Optimization directly coupled with Finite Element Method. The proposed method optimizes the nodal coordinates of a truss structure to minimize mass while satisfying stress and displacement constraints.

The key contributions of this work include:

1. A direct coupling strategy between PSO and FEM that eliminates the need for external solver calls and improves computational efficiency.
2. A modified PSO algorithm with dynamic inertia weight adaptation and constraint handling tailored for truss structure optimization.

Table 1: Comparison of Node Displacements Between Analysis Results

Node	X Displacement			Y Displacement		
	File 1	File 2	Diff (%)	File 1	File 2	Diff (%)
1	0.00	0.00	0.00	0.00	0.00	0.00
2	5.79	5.18	-10.59	-0.31	-0.34	8.17
3	5.79	5.17	-10.64	-1.80	-1.70	-5.80
4	9.32	8.35	-10.41	-0.62	-0.56	-9.90
5	9.33	8.42	-9.69	-2.86	-2.68	-6.23
6	12.22	11.12	-8.96	-0.93	-0.90	-3.87
7	12.46	11.28	-9.48	-3.77	-3.50	-7.21
8	13.90	12.65	-8.94	-1.03	-0.99	-4.65
9	13.67	12.52	-8.47	-3.76	-3.50	-6.93
10	12.99	11.87	-8.64	-4.80	-4.65	-3.17
11	13.06	11.86	-9.17	-5.24	-5.10	-2.66
12	13.12	12.01	-8.51	-2.93	-2.97	1.47
13	12.94	11.77	-8.99	-2.51	-2.55	1.36
14	14.19	13.01	-8.28	-7.15	-7.02	-1.91
15	13.63	12.48	-8.45	-7.62	-7.49	-1.65
16	8.04	7.05	-12.25	-1.84	-1.93	4.60
17	8.55	7.54	-11.82	-5.06	-4.98	-1.56
18	3.55	2.71	-23.79	-1.42	-1.47	3.51
19	3.73	2.89	-22.64	-2.86	-2.79	-2.50
20	0.00	0.00	0.00	0.00	0.00	0.00
21	13.71	12.55	-8.45	-7.79	-7.62	-2.12
22	13.61	12.46	-8.48	-7.78	-7.62	-2.13
23	13.61	12.46	-8.48	-7.94	-7.77	-2.21

3. A comprehensive implementation that includes efficient matrix operations, error handling, and visualization capabilities.

The numerical results demonstrate that the method can achieve significant mass reductions while maintaining structural integrity. The optimized structures exhibit improved efficiency in load transfer, resulting in material savings without compromising performance.

Future work could explore the extension of the method to three-dimensional truss structures, consideration of additional constraints such as buckling, and integration with multi-objective optimization approaches to balance multiple competing objectives.

References

[1] Rozvany, G.I.N., "A critical review of established methods of structural topology optimization," Structural and Multidisciplinary Optimization, Vol. 37, 217-237, 2009.

[2] Kennedy, J., Eberhart, R., "Particle swarm optimization," Proceedings of ICNN'95 - International Conference on Neural Networks, Vol. 4, 1942-1948, 1995.

[3] Brandon, J. A., "Strategies for Structural Dynamic Modification," John Wiley & Sons INC, New York, 1990.

[4] Tang, W., Tong, L., Gu, Y., "Improved genetic algorithm for design optimization of truss structures with sizing, shape and topology variables," International Journal for Numerical Methods in Engineering, Vol. 62, 1737-1762, 2005.

[5] Fourie, P.C., Groenwold, A.A., "The particle swarm optimization algorithm in size and shape optimization," Structural and Multidisciplinary Optimization, Vol. 23, 259-267, 2002.

[6] Bathe, K.J., "Finite Element Procedures," Prentice Hall, 2nd Edition, 2014.

[7] Khennane, A., "Introduction to Finite Element Analysis Using MATLAB® and Abaqus," Taylor & Francis, Boca Raton, 2013.

[8] Miljković, Z., and Petrović, M., "Inteligentni tehnološki sistemi sa izvodima iz robotike i veštačke inteligencije," Univerzitet u Beogradu, Mašinski fakultet, Belgrade, 2021.

[9] Rapaić, M., Kanović, Ž., and Jeličić, Z., "Discrete Particle Swarm Optimization Algorithm for Solving Optimal Sensor Deployment Problem," *Journal of Automatic Control*, vol. 18, no. 1, pp. 9–14, 2008.

10th International Congress of the Serbian Society of Mechanics
Niš, Serbia, June 18-20, 2025
D.12
Extended abstract

MOTION CONTROL OF A COPTER WITH A SLUNG LOAD PARTIALLY FILLED WITH LIQUID

Yury D. Selyutskiy[1][0000-0001-8477-6233], Boris Y. Lokshin[1][0000-0002-0643-3822], Andrei P. Holub[1]

[1]Institute of Mechanics, Lomonosov Moscow State University, Michurinsky prosp. 1, 119192, Moscow, Russia; e-mail: seliutski@imec.msu.ru

Abstract:

The motion of a copter with a suspended payload in a vertical plane is considered. The payload has a spherical shape and contains a concentric spherical cavity partially filled with ideal liquid. The system is in a horizontal steady wind. The aerodynamic load on the payload is described using the quasi-steady approach. The dynamics of the liquid is simulated using the modified phenomenological pendulum model. The controllability and observability of a stationary flight of a copter with the payload are studied. A control strategy is proposed aimed at bringing the system from a certain initial state to a certain final state, so that the center of mass of the copter moves along a given sufficiently smooth curve. The control is designed in such a way as to ensure the suppression of oscillations of the liquid along the entire trajectory.

Key words: copter; slung load; liquid filling; dynamics; control

1. Introduction

The study of the dynamics of suspended loads and the development of effective control laws for them has high practical importance for various fields (in particular, in relation with the manipulation of loads using copters). The internal structure of the load can be rather complicated. For example, it can contain a cavity partially filled with liquid. Fluctuations of the liquid under certain circumstances have a noticeable effect on the behavior of the load, and this should be taken into account when constructing the control. Multiple papers deal with various aspects of this problem (e.g., [1-3]).

In the present work, the motion of a quadcopter with a slung spherical load that contains a spherical cavity partially filled with ideal liquid is considered taking into account the aerodynamic drag (including due to the wind). A control strategy is proposed aimed at tracking of a given trajectory (provided that it is sufficiently smooth) and preventing large oscillations of the liquid inside the cavity.

2. Problem Statement and Results

A mechanical system is considered that consists of a copter and a load. The load has a spherical shape and is slung to the center of mass G of the copter with an inextensible weightless string. The center of mass of the load coincides with the center of its spherical shell. Inside the load, there is a spherical cavity with the center. The cavity is partially filled with ideal fluid (Fig. 1). It is supposed that the aerodynamic load (taking into account, in particular, the horizontal steady wind) onto the sphere is reduced to the drag force. This force is described using the quasi-steady approach. In order to simulate the oscillations of the liquid in the cavity, the known phenomenological pendulum model is used with some modifications.

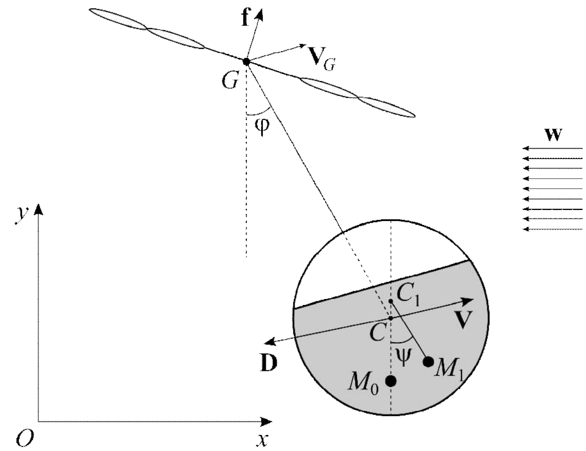

Fig. 1. Scheme of the system.

It is shown that the system is controllable and observable in the vicinity of the steady rectilinear flight when only positions and speeds of the copter and load are measured. Estimations are given for the maximum acceleration of the copter, such that the liquid oscillations remain within the specified range. An algorithm for construction of the control of the copter thrust **f** is proposed that ensures the motion of the copter from the rest at the starting point to the rest at end point along the target trajectory (which is supposed smooth enough) with the specified cruising speed in such a way that the amplitude of oscillations of the liquid in the cavity remains within the specified limits. Numerical simulations show that the proposed algorithm is efficient in a wide enough range of parameters of the system and characteristics of the target trajectory.

3. Conclusions

The proposed strategy for controlling the copter with a slung load partially filled with fluid ensures such motion of the copter center of mass along the prescribed smooth enough trajectory that the amplitude of oscillations of fluid inside the payload remains within the specified limits. The control takes into account the aerodynamic drag force acting on the payload (including due to the presence of horizontal wind).

The future work could involve addressing the effects of uncertainties in system parameters. This could require the use of alternative control approaches, such as model predictive control or reinforcement learning-based methods.

References

[1] Moriello, L., Biagiotti, L., Melchiorri, C., Paoli, A. *Manipulating liquids with robots: a sloshing-free solution*. Control Eng. Pract., Vol. 78, 129-141, 2018.

[2] Sayyaadi, H., Soltani, A. *Modeling and control for cooperative transport of a slung fluid container using quadrotors*. Chin. J. Aeronaut., Vol. 31 (2), 262-272, 2018.

[3] Zhu, K., Huang, J., Gnezdilov, S. *Attitude-Pendulum-Sloshing Coupled Dynamics of Quadrotors Slung Liquid Containers*. Proc. Inst. Mech. Eng., Part G., Vol. 236, 2022.

10th International Congress of the Serbian Society of Mechanics
Niš, Serbia, June 18-20, 2025
D.13
Abstract

COMPUTATIONAL MODELING AND PARAMETRIC STUDY OF CIRCULATING TUMOR CELLS MOTION THROUGH CAPILLARIES AND INTERACTION WITH NON/ THROMBIN ACTIVATED PLATELETS

Vladimir Simic[1,2][0000-0001-7842-8902], **Miljan Milosevic**[1,2,5][0000-0003-3789-2404], **Aleksandar Nikolic**[1][0000-0002-7052-7444], **Shao Ning**[4][0000-0003-2625-4546], **Fransisca Leonard**[4], **Xuewu Liu**[4][0000-0002-8702-0295] **and Milos Kojic**[2,3,4*][0000-0003-2199-5847]

[1] Institute for Information Technologies, University of Kragujevac, Jovana Cvijića bb, 34000 Kragujevac, Serbia. e-mail: vsimic@kg.ac.rs, miljan.m@kg.ac.rs, dziga@kg.ac.rs
[2] Bioengineering Research and Development Center BioIRC Kragujevac, Prvoslava Stojanovica 6, 3400 Kragujevac, Serbia. e-mail: mkojic42@gmail.com
[3] Serbian Academy of Sciences and Arts, Knez Mihailova 35, 11000 Belgrade, Serbia.
[4] Houston Methodist Research Institute, The Department of Nanomedicine, 6670 Bertner Ave., R7 117, Houston, TX 77030. email: nshao@houstonmethodist.org, xliu@houstonmethodist.org, fleonard@houstonmethodist.org
[5] Belgrade Metropolitan University, Tadeuša Košćuška 63, 11000 Belgrade, Serbia.

Abstract:

Metastasis is a multistep process in which circulating tumor cells (CTCs) shed from the primary tumor, enter the circulatory system, and interact with host cells before colonizing target organs. Adhesive interactions with platelets, leukocytes, and endothelial cells play a crucial role in CTC survival and extravasation. Platelets, in particular, enhance CTC survival in the bloodstream and exacerbate metastasis by adhering to CTCs. To study the biomechanical conditions for CTC arrest, we have developed a custom-built computational platform within the PAK software combining 2D axisymmetric and solid-fluid models. These models serve to evaluate the limiting conditions for CTC passage through capillaries under physiological conditions and explore the relationship between capillary pressure gradients, CTC size, stiffness, and platelet size. Our parametric study also investigates the impact of platelet number, CTC size, stiffness, and ligand-receptor stiffness on CTC trajectory, axial position, and wall attachment. Both resting and activated platelets were considered to quantify their effect on metastasis. Experimental data on platelet-CTC adhesion forces—both with non-activated and thrombin-activated platelets—were integrated into the model using a 1D finite element truss element for simulating active ligand-receptor bonds. Relationships between CTC and platelet properties, ligand-receptor interaction strength, and biomechanical conditions necessary for CTC arrest were established, contributing to predictive capabilities for metastasis initiation and progression, further advancing our understanding of metastasis dynamics.

Key words: metastasis, circulating tumor cells, platelets, adhesive forces, ligand-receptor bonds, platelets activation

10th International Congress of the Serbian Society of Mechanics
Niš, Serbia, June 18-20, 2025
D.14

Extended abstract

KINEMATICS MODELING OF COMPLIANT AND EXTENSIBLE STEWART-LIKE PLATFORM

Nemanja O. Tanasković[1][0009-0008-0129-2611], **Mihailo P. Lazarević**[1][0000-0002-3326-6636], **Damir Krklješ**[2][0000-0003-2279-4545]

[1] Faculty of Mechanical Engineering
The University of Belgrade, Kraljice Marije 16, 11120 Belgrade 35, Serbia
e-mail: d11-2023@studenti.mas.bg.ac.rs, mlazarevic@mas.bg.ac.rs
[2] BioSense Institute,
Dr Zorana Đinđića 1, 21000 Novi Sad,
e-mail: dkrkljes@biosense.rs

Key words: *compliance, extensible robots, robotics, kinematics, scissor mechanism, Stewart platform*

Abstract:

Labor shortages, sustainability challenges, and the limitations of conventional robotic systems for delicate tasks like crop harvesting drive the need for innovative solutions. This paper introduces a low-cost, modular robotic platform that combines passive compliance with extensibility, enabling safe human–robot collaboration and scalable operation in dynamic agricultural, medical or industrial environments. The proposed hybrid Stewart-like platform (SLP) integrates a parallel kinematic structure with scissor mechanisms, using lightweight, 3D-printed components for rapid prototyping. This study provides detailed design and kinematic analysis.

1. Introduction

Labor shortages and sustainability challenges in agriculture highlight the need for affordable, adaptable robotic systems capable of handling delicate tasks like crop harvesting. Conventional robotic solutions often lack the compliance and scalability required for safe human–robot collaboration in dynamic environments [1]. This paper presents a hybrid Stewart-like platform (SLP), show in the Figure 1. a), that combines a parallel kinematic structure with scissor mechanisms. The design uses lightweight, 3D-printed components for cost-effective prototyping and includes built-in springs and spherical joints for passive compliance, essential for handling crops. Its modular design supports additional devices, such as grippers and cameras, expanding functionality.

2. Design and Kinematic Analysis of a Hybrid Stewart-Like Robotic Platform

Kinematic analysis confirms the platform's suitability for agricultural tasks, with three degrees of freedom validated using Grübler's equation [2]. Actuator positions are evenly

The base platform houses actuators and springs, while the upper platform, supported by springs and a scissor mechanism, can hold various end-effectors. While this study provides a detailed design and kinematic analysis, it does not include result validation or quantitative comparisons with simulations or experimental benchmarks. These aspects are planned for future work to enhance the credibility and applicability of the proposed design.

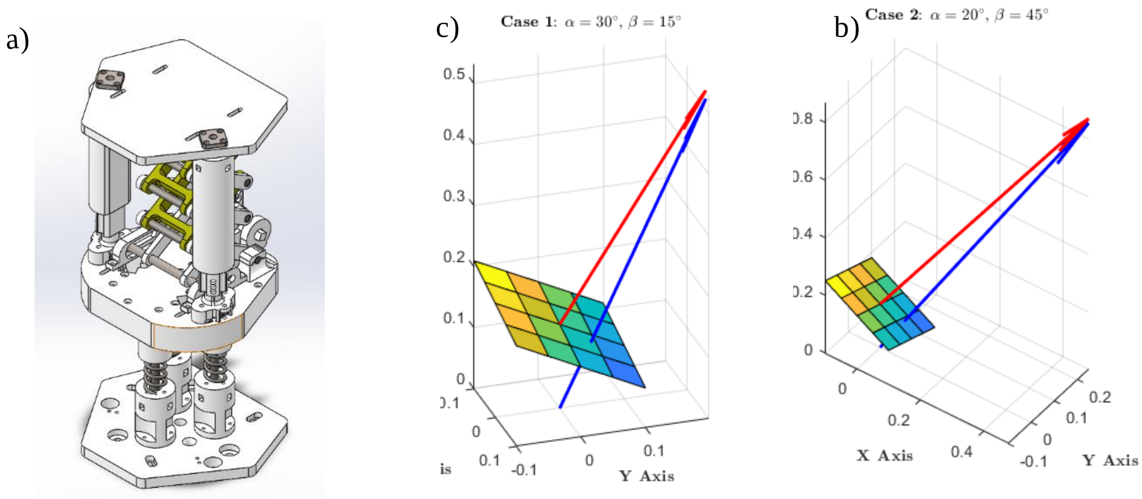

Fig. 1. a) our SLP, b) and c) Sequence of transitions from the start to the endpoint

3. Conclusion

In summary, this work shows that compliant, extensible robotic systems can effectively bridge the gap between affordability and advanced functionality, offering small-scale farmers adaptable, efficient, and safe solutions for modern agricultural, medical, industrial applications.

Acknowledgments

We are grateful to Marko Popović, who was a dedicated researcher at the BioSens Institute, whose insightful contributions and unwavering support have been invaluable throughout this research endeavor.

This research has been supported by the research grant of the Serbian Ministry of Science, Technological Development and Innovations, grant No. 451-03-137/2025-03/ 200105 from 04.02.2025.

References

[1] S. Robla-Gómez, V. M. Becerra, J. R. Llata, E. González-Sarabia, C. Torre-Ferrero, and J. Pérez-Oria, “Working Together: A Review on Safe Human-Robot Collaboration in Industrial Environments,” *IEEE Access*, vol. 5, pp. 26754–26773, 2017, doi: 10.1109/ACCESS.2017.2773127.

[2] J. M. McCarthy and G. S. Soh, “Analysis of Spatial Chains,” in *Geometric Design of Linkages*, J. M. McCarthy and G. S. Soh, Eds., New York, NY: Springer, 2011, pp. 253–279. doi: 10.1007/978-1-4419-7892-9_11.

[3] V.Čović, M.Lazarević, " Robot mechanics", University of Belgrade, Faculty of Mechanical Engineering, 2021, pp. 232, (in Serbian)

10th International Congress of the Serbian Society of Mechanics
Niš, Serbia, June 18-20, 2025
D.15
Original Scientific Paper

DOI:10.46793/ICSSM25.251T

INVERSE KINEMATICS SOLUTIONS OF ROBOTIC MANIPULATORS USING PADEN-KAHAN SUBPROBLEMS AND SCREW THEORY

Vuk Todorović[1], **Nikola Nešić**[2] [0000-0001-6237-4735], and **Mihailo Lazarević**[3] [0000-0002-3326-6636]

[1,2]University of Pristina in Kosovska Mitrovica, Faculty of Technical Sciences, Serbia [3]University of Belgrade, Faculty of Mechanical Engineering, Serbia

[1]email: vuk.todorovic01@gmail.com
[2]email: nikola.nesic@pr.ac.rs
[3]email: mlazarevic@mas.bg.ac.rs

Abstract. In this paper, we used the Paden-Kahan subproblems and their extensions in the context of screw theory to solve the inverse kinematics of common robot manipulators: RR, RRR, RPR planar, and RPP spatial robot models. The inverse kinematics problem of a robot is fundamental to determining a robot's mechanics, and among the different ways to solving it, we chose the Paden-Kahan subproblems approach for its effectiveness and simplicity. The canonical subproblems have been significantly extended and of particular interest to us are the inclusion of solutions to parallel screw axes for the second subproblem and prismatic joints instead of only revolute joints, also known as Pardos-Gotor subproblems, After solving the inverse kinematics of each robot model and representing the solutions via graphs, we then proceeded to demonstrate the correctness of our solutions against the desired configuration and found that the orientational and positional errors between the desired configuration and our solution were in the range of floating-point arithmetic errors. Taking into account the simplicity during solving the inverse kinematics and the number of operations performed, we concluded that, at least where applicable, the Paden-Kahan subproblems and their extensions provide significant advantages to other methods.

Keywords: Inverse kinematics, Paden-Kahan subproblems, Pardos-Gotor subproblems, RR Robot, RRR Robot, RPR Robot, RPP Robot.

1. Introduction

The inverse kinematics (IK) problem of robot mechanics is an active research area that consists of determining the set of joint values of a robot corresponding to a given configuration. This is in contrast to the inverse problem, that is, determining the configuration that corresponds to a given set of joint values. This is known as the forward kinematics (FK) problem. There are also a couple of different frameworks under which we solve such problems, in this work we will be using the screw theory approach [1, 2], whose roots lie in the Mozzi-Chasles theorem [3] where rigid-body motion is decomposed into a rotational and translational part about a screw axis.

Multiple methods for solving a robot's IK were developed. The more notable ones include using the Newton-Raphson numerical method [1], dialytical elimination for 6R robots by Manocha and Canny [2, 4], and the Paden-Kahan (PK) subproblems [2]. Among these, we will use the three PK subproblems, developed independently by Paden [5] and Kahan [6], which rely on the geometric aspects of the mechanical structure of a robot to find closed-form analytical solutions. Several extensions to the canonical form of the subproblems have been developed that further increase the number of robot models solvable by these subproblems. Here, we will use the extended second subproblem from [7] and the extended second and third subproblems to prismatic joints [8], also known as the second and third Pardos-Gotor (PG) subproblems (the original subproblems apply only to revolut joints).

Here, we aim to show the effectiveness of the PK subproblems and their extension in solving the IK of common manipulator planar models, including RR, RRR, RPR robots, and an RPP spatial robot model. As a result, for all the mentioned robot models, we started from the robots FK equation and have reduced them to forms solvable by either the PK or PG subproblems.

In the next chapter, we will present the kinematic models of the robots and some key mechanical specifications necessary for solving the robots IK problems. Afterward, we will briefly define the canonical PK subproblems, its extension relevant to our case (we will only need the extension of the second subproblem related to parallel screw axes), and the relevant PG subproblems. Then, in the main part of the paper, we explain the steps to solve the problem and present the results. Lastly, we perform a numerical tests where we check whether our results are correct for certain joint coordinates. We will end with a discussion and conclusion of our findings.

2. Robotic Manipulator Models

The robotic manipulator models are presented in Figure 1. Based on this, their screw axes and home configuration are shown in tables 1 and 2 respectively.

Index	RR	RRR	RPR	RPP
1	$\begin{bmatrix}0 & 0 & 1 & 0 & 0 & 0\end{bmatrix}$	$\begin{bmatrix}0 & 0 & 1 & 0 & 0 & 0\end{bmatrix}$	$\begin{bmatrix}0 & 0 & 1 & 0 & 0 & 0\end{bmatrix}$	$\begin{bmatrix}0 & 0 & 1 & 0 & 0 & 0\end{bmatrix}$
2	$\begin{bmatrix}0 & 0 & 1 & 0 & -L_1 & 0\end{bmatrix}$	$\begin{bmatrix}0 & 0 & 1 & 0 & -L_1 & 0\end{bmatrix}$	$\begin{bmatrix}0 & 0 & 0 & 0 & 1 & 0\end{bmatrix}$	$\begin{bmatrix}0 & 0 & 0 & 0 & 0 & 1\end{bmatrix}$
3	None	$\begin{bmatrix}0 & 0 & 1 & 0 & -L_{12} & 0\end{bmatrix}$	$\begin{bmatrix}0 & 0 & 1 & 0 & -L_{12} & 0\end{bmatrix}$	$\begin{bmatrix}0 & 0 & 0 & 0 & 1 & 0\end{bmatrix}$

Table 1: The transposed screw axes of the robots in the space frame $\mathcal{S}_i^T = (\boldsymbol{\omega}_i^T, \mathbf{v}_i^T) \in \mathbb{R}^6$ (based on Figure 1) where the index i corresponds to the i-th joint, $\boldsymbol{\omega}_i$ is the screw axis' angular velocity and $\mathbf{v}_i$ is the screw axis' linear velocity. The notation L_{ij} is the sum of the lengths from the i-th to the j-th link, $L_{ij} = \sum_{k=i}^{j} L_k$

RR	RRR	RPR	RPP
$\begin{bmatrix}1 & 0 & 0 & L_{12}\\ 0 & 1 & 0 & 0\\ 0 & 0 & 1 & 0\\ 0 & 0 & 0 & 1\end{bmatrix}$	$\begin{bmatrix}1 & 0 & 0 & L_{13}\\ 0 & 1 & 0 & 0\\ 0 & 0 & 1 & 0\\ 0 & 0 & 0 & 1\end{bmatrix}$	$\begin{bmatrix}1 & 0 & 0 & L_{13}\\ 0 & 1 & 0 & 0\\ 0 & 0 & 1 & 0\\ 0 & 0 & 0 & 1\end{bmatrix}$	$\begin{bmatrix}1 & 0 & 0 & 0\\ 0 & 1 & 0 & L_3\\ 0 & 0 & 1 & L_{12}\\ 0 & 0 & 0 & 1\end{bmatrix}$

Table 2: The home configurations $\mathbf{M} \in SE(3)$ of the robots based on Figure 1

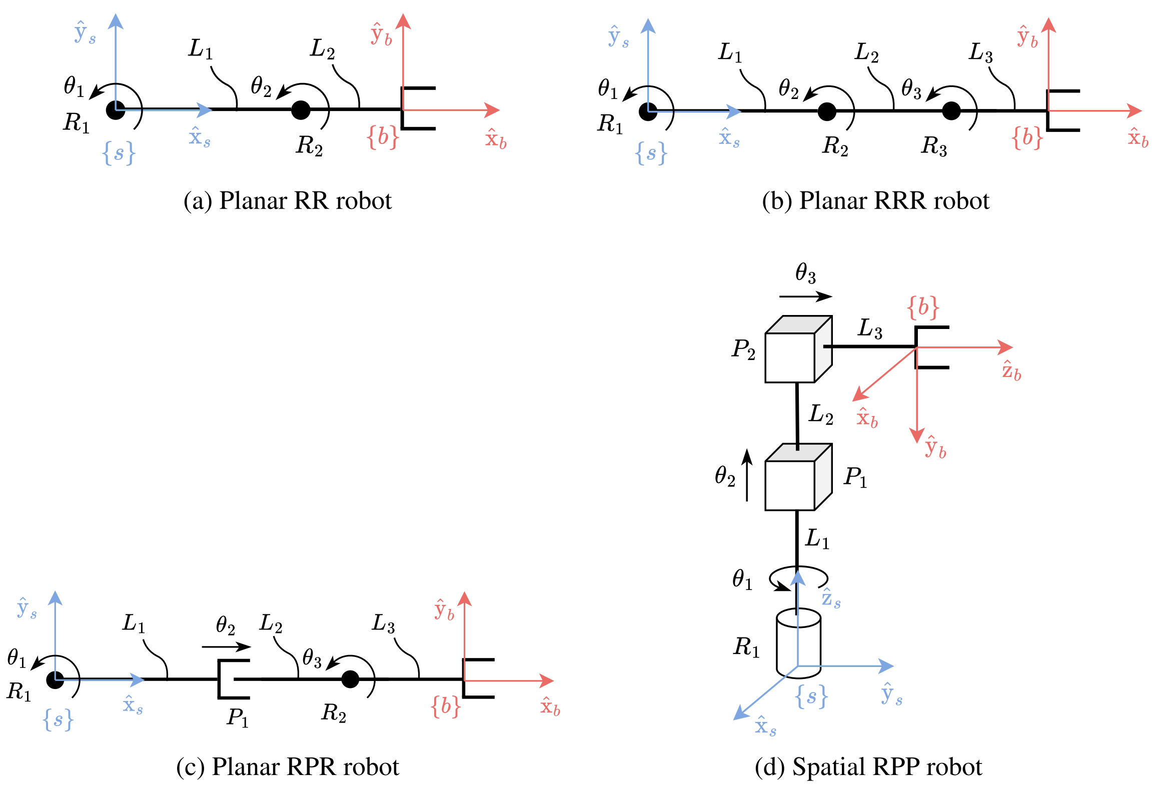

(a) Planar RR robot

(b) Planar RRR robot

(c) Planar RPR robot

(d) Spatial RPP robot

Figure 1: Kinematic models of the manipulators where: $\{s\}$–space frame, $\{b\}$–body frame, L_i–i-th link length, R_i–i-th revolute joint, P_i–i-th prismatic joint, θ_i–i-th joint coordinate, $\hat{x}_s, \hat{y}_s, \hat{z}_s$–unit vectors in the space frame, and $\hat{x}_b, \hat{y}_b, \hat{z}_b$–unit vectors in the body frame.

3. Paden-Kahan and Pardos-Gotor subproblems

Here, we will only state the PK subproblems and their extension. The number of solutions, the form of the solution and its existence are available at [2] for the canonical PK subproblems, [7] for the extension of the second subproblem, and [8] for the extension of the canonical subproblems to prismatic joints.

The canonical PK subproblems are stated as follows:

PK 1. Let $\mathcal{S}$ be a zero-pitch screw axis, and $\mathbf{p},\mathbf{q} \in \mathbb{R}^3$ two points, find the joint coordinate θ such that

$$e^{[\mathcal{S}]\theta}\mathbf{p} = \mathbf{q}. \tag{1}$$

PK 2. Let $\mathcal{S}_1$ and $\mathcal{S}_2$ be two intersecting zero-pitch screw axes, and $\mathbf{p},\mathbf{q} \in \mathbb{R}^3$ two points, find the joint coordinates θ_1 and θ_2 such that

$$e^{[\mathcal{S}_1]\theta_1}e^{[\mathcal{S}_2]\theta_2}\mathbf{p} = \mathbf{q}. \tag{2}$$

PK 3. Let $\mathcal{S}$ be a zero-pitch screw axis, $\mathbf{p},\mathbf{q} \in \mathbb{R}^3$ two points, and $\delta \in \mathbb{R}^+$, find the joint coordinate θ such that

$$||e^{[\mathcal{S}]\theta}\mathbf{p} - \mathbf{q}|| = \delta. \tag{3}$$

The extended second subproblem presented in [7] is stated as the second canonical PK, but the screw axes need not intersect.

The first three PG subproblems are stated as the canonical PK subproblems, with the screw axes being infinite-pitch rather than zero-pitch.

In the following chapters, we will use PKi φ_j : "expression", where $i \in \{1,3\}$, to specify that the solution to the j-th joint variable determined using the i-th PK subproblem with parameters defined by the expression (e.g. PK1 φ_3 : $e^{[\mathcal{S}_3]\varphi_3}\mathbf{m} = \mathbf{n}$ means that we can solve the expression by using the first PK subproblem with $\mathbf{m}$ and $\mathbf{n}$ corresponding to $\mathbf{p}$ and $\mathbf{q}$ respectively in Equation (1)). In the case of the second subproblem, we will write PK3 (φ_j, φ_k) : expression to specify that we used the third PK subproblem to solve for a pair of solution coordinates, i.e. for the j-th and k-th joint variable. The same goes for PGi φ_j : expression and PGi (φ_j, φ_k) : expression which is the same as PKi φ_j and PKi (φ_j, φ_k) : expression respectively but using the i-th PG subproblem instead of the i-th PK subproblem.

4. Determining the Inverse Kinematics of the Robot Models

For these robot models, their FK can be expressed using the product of exponentials formula [1, 2] as

$$\prod_{i=1}^{n} e^{[\mathcal{S}_i]\theta_i}\mathbf{M} = \mathbf{T}_d(\boldsymbol{\theta}) \tag{4}$$

where n–number of joints, $[\mathcal{S}_i]$–$se(3)$ representation of the i-th screw axis $\mathcal{S}_i$, $\boldsymbol{\theta} = \begin{bmatrix}\theta_1 & \cdots & \theta_n\end{bmatrix}^T \in \mathbb{R}^n$–coordinate vector, and $\mathbf{T}_d(\boldsymbol{\theta}) \in SE(3)$–desired configuration. Another form of equation (4), where we separate the known and unknown matrices, will prove to be useful:

$$\prod_{i=1}^{n} e^{[\mathcal{S}_i]\theta_i} = \mathbf{T}_d\mathbf{M}^{-1} = \mathbf{T}_1 \tag{5}$$

Some additional notation that will be used is: $\mathbf{r}_i \in \mathbb{R}^3$–position vector pointing to the i-th screw axis, $\mathbf{p}_i$–any vector other than $\mathbf{r}_i$, i.e. $\mathbf{p} \in \mathbb{R}^3 \setminus \{\mathbf{r}_i\}$, $\boldsymbol{\varphi} = \begin{bmatrix} \varphi_1 & \cdots & \varphi_n \end{bmatrix}^T \in \mathbb{R}^n$–unknown solution vector, $\boldsymbol{\theta} = \begin{bmatrix} \theta_1 & \cdots & \theta_n \end{bmatrix}^T \in \mathbb{R}^n$–known coordinate vector and $\mathbf{Tx} = \mathbf{Rx} + \mathbf{p}$–shorthand notation for multiplying $\mathbf{T} = (\mathbf{R}, \mathbf{p}) \in SE(3)$, where $\mathbf{R} \in SO(3)$ and $\mathbf{p} \in \mathbb{R}^3$, with a three-vector $\mathbf{x} \in \mathbb{R}^3$.

Some useful expressions that will be used include:

$$\mathbf{Tr} = \mathbf{r}, \quad \mathbf{r} \in \mathbb{R}^3 \setminus \{\mathbf{0}\}, \quad \mathbf{T} \in SE(3), \tag{6}$$

where $\mathbf{r}$ points to the screw axis of $\mathbf{T}$, taken from [2],

$$\|\mathbf{Tx} - \mathbf{Ty}\| = \|\mathbf{x} - \mathbf{y}\|, \quad \mathbf{x}, \mathbf{y} \in \mathbb{R}^3, \quad \mathbf{T} \in SE(3), \tag{7}$$

taken from [1], and

$$e^{[\mathcal{S}]\theta}\mathbf{x} = \theta\mathbf{v} + \mathbf{x}, \quad e^{[\mathcal{S}]\theta} \in SE(3), \quad \mathcal{S} = (\mathbf{0}, \mathbf{v}) \tag{8}$$

where $\mathcal{S}$ is an infinite-pitch screw axis. This expression is a direct result of the Mozzi-Chasles theorem, i.e. for an inifnite-pitch screw axis $\mathcal{S} = (\mathbf{0}, \mathbf{v})$, the theorem states that [1]

$$e^{[\mathcal{S}]\theta} = \begin{bmatrix} \mathbf{I} & \theta\mathbf{v} \\ \mathbf{0}^T & 1 \end{bmatrix}. \tag{9}$$

Based on this, we have solved the inverse kinematics of the robot models in the following manner:

RR. Starting from Equation (5) where $n = 2$ and multiplying both sides with the position vector of the second screw axis, we get

$$\text{PK1 } \varphi_1 : e^{[\mathcal{S}_1]\varphi_1}\mathbf{r}_2 = \mathbf{T}_1\mathbf{r}_2, \quad \mathbf{r}_2 = \begin{bmatrix} L_1 \\ 0 \\ 0 \end{bmatrix}, \tag{10}$$

where we applied $e^{[\mathcal{S}_2]\varphi_2}\mathbf{r}_2 = \mathbf{r_2}$ (Equation (6)). Now, given the joint coordinate φ_1 from the previous equation, we separate the knowns from the unknowns in Equation (5) and multiply by a vector $\mathbf{p}_2$ on both sides such that

$$\text{PK1 } \varphi_2 : e^{[\mathcal{S}_2]\varphi_2}\mathbf{p}_2 = e^{-[\mathcal{S}_1]\varphi_1}\mathbf{T}_1\mathbf{p}_2. \tag{11}$$

RRR. Starting from Equation (5) where $n = 3$ and multiplying both sides with the position vector of the third screw axis, we get

$$\text{PK2 } (\varphi_1, \varphi_2) : e^{[\mathcal{S}_1]\varphi_1}e^{[\mathcal{S}_2]\varphi_2}\mathbf{r}_3 = \mathbf{T}_1\mathbf{r}_3, \quad \mathbf{r}_3 = \begin{bmatrix} L_{12} \\ 0 \\ 0 \end{bmatrix}. \tag{12}$$

Now that we know the first two joint coordinates, we can determine the last joint coordinate as

$$\text{PK1 } \varphi_3 : e^{[\mathcal{S}_3]\varphi_3}\mathbf{p}_3 = e^{-[\mathcal{S}_2]\varphi_2}e^{-[\mathcal{S}_1]\varphi_1}\mathbf{T}_1\mathbf{p}_3. \tag{13}$$

RPR. Starting from Equation (5) where $n = 3$ and multiplying both sides with the position vector of the third screw axis, we get

$$e^{[\mathcal{S}_1]\varphi_1}e^{[\mathcal{S}_2]\varphi_2}\mathbf{r}_3 = \mathbf{T}_1\mathbf{r}_3, \quad \mathbf{r}_3 = \begin{bmatrix} L_{12} \\ 0 \\ 0 \end{bmatrix}, \tag{14}$$

which cannot be readily solved because the screw axes don't have the same pitch. Now subtract from both sides of the equation the position vector of the third screw axis and take the norm

$$\|e^{[\mathcal{S}_1]\varphi_1}e^{[\mathcal{S}_2]\varphi_2}\mathbf{r}_3-\mathbf{r}_1\|=\|\mathbf{T}_1\mathbf{r}_3-\mathbf{r}_1\|,\quad \mathbf{r}_1=\begin{bmatrix}0\\0\\r_1\end{bmatrix},\quad r_1\in\mathbb{R}\setminus\{0\},\tag{15}$$

and simplifying the left-hand side by using Equations (6) and (7) to get

$$\text{PG3 } \varphi_2:\|e^{[\mathcal{S}_2]\varphi_2}\mathbf{r}_3-\mathbf{r}_1\|=\|\mathbf{T}_1\mathbf{r}_3-\mathbf{r}_1\|.\tag{16}$$

Going back to Equation (14) and using the now known joint coordinate φ_2,

$$\text{PK1 } \varphi_1: e^{[\mathcal{S}_1]\varphi_1}(\varphi_2\mathbf{v}_2+\mathbf{r}_3)=\mathbf{T}_1\mathbf{r}_3.\tag{17}$$

Now that we know the first two joint coordinates, we can determine the last joint coordinate as

$$\text{PK1 } \varphi_3: e^{[\mathcal{S}_3]\varphi_3}\mathbf{p}_3=e^{-[\mathcal{S}_2]\varphi_2}e^{-[\mathcal{S}_1]\varphi_1}\mathbf{T}_1\mathbf{p}_3.\tag{18}$$

RPP. Starting from Equation (5) where $n=3$ and taking the inverse of both sides,

$$e^{-[\mathcal{S}_3]\varphi_3}e^{-[\mathcal{S}_2]\varphi_2}e^{-[\mathcal{S}_1]\varphi_1}=\mathbf{M}\mathbf{T}_d^{-1}=\mathbf{T}_1^{-1},$$

which is the same as

$$e^{[\mathcal{S}_3](-\varphi_3)}e^{[\mathcal{S}_2](-\varphi_2)}e^{[\mathcal{S}_1](-\varphi_1)}=\mathbf{T}_1^{-1},$$

therefore we may multiply both sides by the position vector of the first screw axis,

$$\text{PG2 } (-\varphi_3,-\varphi_2): e^{[\mathcal{S}_3](-\varphi_3)}e^{[\mathcal{S}_2](-\varphi_2)}\mathbf{r}_1=\mathbf{T}_1^{-1}\mathbf{r}_1,\quad \mathbf{r}_1=\begin{bmatrix}0\\0\\r_1\end{bmatrix},\quad r_1\in\mathbb{R}\setminus\{0\}.\tag{19}$$

Now we may derive the solution to the first joint coordinate using Equation (5) as such,

$$\text{PK1 } \varphi_1: e^{[\mathcal{S}_1]\varphi_1}\mathbf{p}_1=\mathbf{T}_1e^{[\mathcal{S}_3](-\varphi_3)}e^{[\mathcal{S}_2](-\varphi_2)}\mathbf{p}_1.\tag{20}$$

5. Numerical Testing Results

This section consists of testing the solutions from Section 4 by choosing specific parameters and finding the positional and orientational error from the obtained results against the desired results.

The test was performed for each robot model separately in the following algorithmic manner:

Step 1. **Parameter selection:** L_i–link lengths, $\boldsymbol{\theta}\in\mathbb{R}^n$–vector of joint coordinates where $n=2$ for the RR robot model and $n=3$ for all other models, $\mathbf{r}_i$–screw axes position vectors that are not fully defined by the parameters L_i, and $\mathbf{p}_i\in\mathbb{R}^3\setminus\{\mathbf{r}_i\}$–3-vectors where $\mathbf{r}_i$ is a point on the i-th screw axis of a robot. The vectors $\mathbf{p}_i$ must be linearly independent of $\mathbf{r}_i$, because this implies that $\mathbf{p}_i\neq\mathbf{r}_i$. If they were equal to each other, then they would be scalar multiples of each other, hence linearly dependent, which is against our assumption that they are linearly independent.

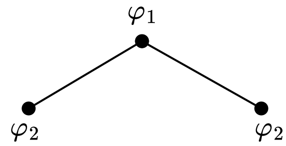

Figure 2: Solution vectors graph. The nodes refer to all possible joint coordinates, and the links constitute different solution vectors. The solution vector elements are computed via the links from top to bottom

Step 2. **Parameter computation:** Based on the chosen parameters, compute: the screw axes based on Table 1, the home configurations based on Table 2, the position vectors $\mathbf{r}_i$ defined by equations (10), (12), (14), (15), and (19) depending on the robot model we are testing, the desired configuration $\mathbf{T}_d(\boldsymbol{\theta})$ from Equation (4), and accordingly the homogeneous transformation matrix $\mathbf{T}_1$ from Equation (5).

Step 3. **Determining the solution set:** Each PK and PG subproblem can have zero or one solution for a specific coordinate, but some subproblems may produce two solutions for a specific coordinate. Thus, if a joint value or a pair of joint values have multiple solutions, we need to combine each of these solutions with the rest of the singular solutions to obtain multiple solution vectors $\boldsymbol{\varphi}_i$. The number of solution vectors for a desired configuration is based on the way we solve the robots' IK and the robots' mechanical specification. We group all of these solution vectors in the set

$$\Phi = \{\boldsymbol{\varphi}_i \mid \mathbf{T}_s(\boldsymbol{\varphi}_i) \approxeq \mathbf{T}_d(\boldsymbol{\theta})\}. \tag{21}$$

For example, if we solve a robot's IK by first finding the coordinate φ_{11} (and φ_{12}, if it exists) using the third PK subproblem, and then find φ_2 using the first PG subproblem, we may get up to two solution vectors $\boldsymbol{\varphi}_1 = \begin{bmatrix}\varphi_{11} & \varphi_2\end{bmatrix}^T$ and $\boldsymbol{\varphi}_2 = \begin{bmatrix}\varphi_{12} & \varphi_2\end{bmatrix}^T$ (if φ_{12} exists). This is because the second PK subproblem may give two solutions $(\varphi_{11}, \varphi_{12})$ for the first joint coordinate. The set of solutions Φ can be represented by a graph, as in Figure 2 for the previous example.

Step 4. **Computing the homogeneous solution matrices, orientational errors and positional errors:** For each solution vector from the set of solutions Φ, compute the resulting solution configurations $\mathbf{T}_{s,i}(\boldsymbol{\varphi}_i)$ based on Equation (4). To find the orientational e_r and positional e_p errors, we split each solution matrix's $\mathbf{T}_{s,i} = (\mathbf{R}_{s,i}, \mathbf{p}_{s,i})$ and desired configuration $\mathbf{T}_d = (\mathbf{R}_d, \mathbf{p}_d)$ into its rotation matrix and position vector, and determine the errors as such:

$$e_r = \frac{1}{\operatorname{card}\Phi} \sum_{i=1}^{\operatorname{card}\Phi} \sqrt{\operatorname{tr}[(\mathbf{R}_d - \mathbf{R}_{s,i})^T(\mathbf{R}_d - \mathbf{R}_{s,i})]}, \tag{22}$$

$$e_p = \frac{1}{\operatorname{card}\Phi} \sum_{i=1}^{\operatorname{card}\Phi} \sqrt{(\mathbf{p}_d - \mathbf{p}_{s,i})^T(\mathbf{p}_d - \mathbf{p}_{s,i})}, \tag{23}$$

i.e. e_r is equal to the arithmetic mean of the Frobenius norm of the difference between the desired and solution rotation matrices, and e_p is equal to the arithmetic mean of the Euclidean norm of the difference between the desired and solution position vectors. The notation $\operatorname{card}\Phi$ represents the cardinality of the set Φ, and $\operatorname{tr}\mathbf{A}$ is the trace of an $n \times n$ matrix $\mathbf{A}$.

The parameters chosen for the tests are available in Table 3, the solution graphs in Figure 3, and the results of the tests in Table 4. For the test, we used the Python programming language[1], version `3.12.5`. In it, we used the NumPy library [9], version `2.2.4`, and Mehanika robota library [10], version `2025.3.28`, which also contains the code for the tests in the "eksperimenti" subfolder under the names `icssm10_rr.py`, `icssm10_rrr.py`, `icssm10_rpr.py`, and `icssm10_rpp.py`. In NumPy, we used double-precision floating points, i.e., `numpy.float64` numbers for all relevant computed variables.

Parameter	Unit	RR	RRR	RPR	RPP
L_i	m	$\{0.2, 0.2\}$	$\{0.6, 0.4, 0.2\}$	$\{0.1, 0.2, 0.1\}$	$\{0.3, 0.3, 0.1\}$
$\boldsymbol{\theta}$	m or rad*	$\begin{bmatrix} \pi/6 \\ -\pi/3 \end{bmatrix}$	$\begin{bmatrix} -\pi/6 \\ \pi/2 \\ -\pi/3 \end{bmatrix}$	$\begin{bmatrix} 0 \\ 0.1 \\ -3\pi/2 \end{bmatrix}$	$\begin{bmatrix} \pi \\ 0.05 \\ 0.1 \end{bmatrix}$
$\mathbf{r}_i$	m	None	None	$\mathbf{r}_1 = \begin{bmatrix} 0 \\ 0 \\ 0.1 \end{bmatrix}$	$\mathbf{r}_1 = \begin{bmatrix} 0 \\ 0 \\ 0.1 \end{bmatrix}$
$\mathbf{p}_i$	m	$\mathbf{p}_2 = \begin{bmatrix} 0 \\ 0.1 \\ 0 \end{bmatrix}$	$\mathbf{p}_3 = \begin{bmatrix} 0 \\ 0.1 \\ 0 \end{bmatrix}$	$\mathbf{p}_3 = \begin{bmatrix} 0 \\ 0.1 \\ 0 \end{bmatrix}$	$\mathbf{p}_1 = \begin{bmatrix} 0 \\ 0.1 \\ 0 \end{bmatrix}$

* coordinate elements θ_i that define distance for prismatic joints have their units in meters, while those that define angle coordinates for revolut joints have their units in radians.

Table 3: Parameters chosen for the tests

Robot Model	e_r(rad)	e_p(m)
RR	$2.355\,138\,688\,025\,662\,4 \times 10^{-16}$	0.0
RRR	$4.793\,457\,360\,479\,470\,5 \times 10^{-17}$	$1.180\,065\,049\,725\,794\,5 \times 10^{-16}$
RPR	$7.540\,531\,475\,574\,731 \times 10^{-17}$	$2.775\,557\,561\,562\,891\,4 \times 10^{-17}$
RPP	0.0	0.0

Table 4: Test results

6. Discussion

In Section 4, we determined the IK of the selected robot models. Although the calculations were rather simple for our selected model, this might not always be the case. Especially for, e.g., 6R robots, which are also common in practice, the FK equation has six unknown coordinates, and solving its IK using subproblems can be achieved with a somewhat narrow set of geometries.

[1] `http://www.python.org`

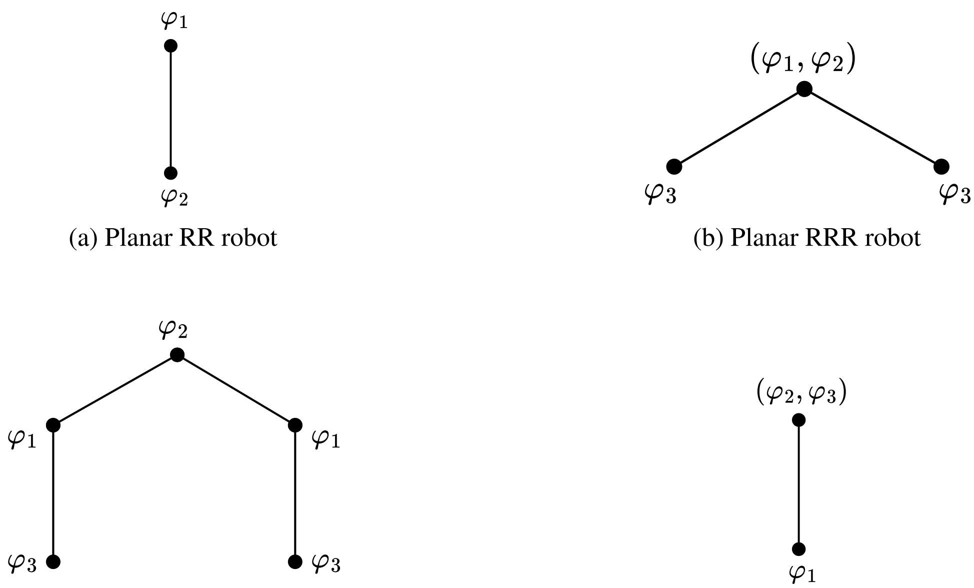

(a) Planar RR robot

(b) Planar RRR robot

(c) Planar RPR robot

(d) Spatial RPP robot

Figure 3: Solution graphs of the common robot models according to the solutions from Section 4

In the test results (Table 4), we see that the magnitude of the error is so low that it is justified as errors occurred during floating-point arithmetic. This justification is due to double precision floatings having between 15 and 17 significant digits, and other than the exact results being null, the small errors have significant digits within that range. The tests that were performed are in no way exhaustive, for that we would need to test against numerous joint coordinates $\boldsymbol{\theta}$; rather, it is used to demonstrate the effectiveness of using PK subproblems.

7. Conclusion

The simple and small number of calculations performed to solve each robot manipulator, compared to, e.g., the Newton-Raphson method and dialytical elimination for 6R robots by Manocha and Canny, is the main strength of employing PK subproblems and their extension to solve a robot's IK. The results from Table 4 further reinforce the precision of such analytic results, albeit they only serve as a demonstration. The main drawback of such a method is the geometry of a robot and the number of joints. Hence, while the subproblems can be applied to various robot models, they are not always applicable.

Acknowledgement. This research has been supported by the research grant of the Serbian Ministry of Science, Technological Development and Innovations, grant No. 451-03-137/2025-03/ 200105 from 04.02.2025.

References

[1] Lynch K., & Park F., *Modern Robotics: Mechanics, Planning, and Control*, Cambridge University Press, UK, 2017.

[2] Murray R., Li Z., & Sastry S., *A Mathematical Introduction to Robotic Manipulation*, CRC Press, USA, 1994.

[3] Ceccarelli M., *Screw Axis Defined by Giulio Mozzi in 1763 and Early Studies on Helicoidal Motion*, Mechanism and Machine Theory 35(6), 761-770, 2000.

[4] Manocha D., & Canny J. F., *Real Time Inverse Kinematics for General 6R Manipulators*, IEEE International Conference on Robotics and Automation, 383-389, 1992.

[5] Paden B., *Kinematics and Control of Robot Manipulators*, PhD thesis, Department of Electrical Engineering and Computer Sciences, University of California, USA, 1986.

[6] Kahan W., *Lectures on Computational Aspects of Geometry*, Unpublished, 1983.

[7] Dimovski I., Trompeska M., Samak S., Dukovski V., & Cvetkoska D., *Algorithmic Approach to Geometric Solution of Generalized Paden-Kahan Subproblem and its Extension*, International Journal of Advanced Robotic Systems 15(1), 2018.

[8] Pardos-Gotor J., *Screw Theory in Robotics: an Illustrated and Practicable Introduction to Modern Mechanics*, CRC Press, USA, 2022.

[9] Oliphant T., url: *https://numpy.org*, 2005.

[10] Todorovic V., url: *https://github.com/VuckoT/mehanika_robota*, 2024.

10th International Congress of the Serbian Society of Mechanics
Niš, Serbia, June 18-20, 2025
D.16
Original Scientific Paper

DOI:10.46793/ICSSM25.261T

ANALYSIS OF STEEL PLATE GIRDERS SUBJECTED OF PATCH LOADING WITH GEOMETRICAL AND STRUCTURAL IMPERFECTIONS

Turnić Dragana[1][0000-0001-7494-8257], **Spasojević Šurdilović Marija**[1][0000-0003-3376-1909], **Živković Srđan**[1][0000-0002-7726-4149], **Petrović Žarko**[1][0000-0003-3025-8259], **Petronijević Predrag**[1][0000-0003-4601-5825]

[1] Faculty of Civil Engineering and Architecture,
The University of Niš, Aleksandra Medvedeva 14, 18000 Niš, Serbia
e-mail: dragana.turnic@gaf.ni.ac.rs
e-mail: marija.spasojevic.surdilovc@gaf.ni.ac.rs, zarko.petrovic@gaf.ni.ac.rs, predrag.petronijevic@gaf.ni.ac.rs

Abstract:

The behavior of welded steel I-girders presents a complex stability and elastic-plastic problem. The girders are loaded over a short length of the flange and within the plane of the web, under either concentrated or uniformly distributed loads, commonly referred to as patch loading. This study analyzes welded steel I-girders both with and without longitudinal web stiffening. The girders, or sections of the girders, are not perfectly flat in terms of their geometry, and the materials from which the girders are made exhibit certain deviations, referred to as geometric and structural imperfections. These imperfections can influence the behavior of the girders, and they are accounted for in this research. The load was progressively increased until the ultimate load capacity was reached, which was characterized by the buckling of the web. The analysis was conducted using the ANSYS software package, and the results were compared with experimental data from the literature.

Key words: steel I girders, patch loading, ultimate load capacity, imperfections

1. Introduction

The behavior of welded plate girders subjected to patch loads or partially distributed loads on the flange in the plane of the web presents a complex stability and elastic-plastic problem.

The complexity of this problem arises from the fact that, on one hand, there is localized buckling of the girder in the web, while, on the other hand, the load due to buckling does not coincide with the limit load. In practice, this situation is encountered during bridge assembly, specifically during the process of launching the bridge into its final position over temporary or permanent supports.

The influences that occur may exceed the load capacity of the structure at certain points due to patch loading. Since a complete theoretical solution to this problem has not yet been found, a more detailed analysis is needed. To address such problems and perform the design, it is essential to consider both the geometry of the girders and the characteristics of material from which they are made [1]. Solving this problem requires a combination of experimental research and numerical analysis, with particular emphasis placed on this approach in the present paper. In numerical simulations, where models are developed, it is crucial to incorporate imperfections in the girders. Numerous studies over the past decades have identified key parameters influencing the behavior of plate girders subjected to patch loading, including the thickness of the web, flange size, spacing of vertical and longitudinal stiffeners, yield stresses of girder components, load distribution length, and the value of the bending moment [2], [3], [4].

Both geometric and material non-linearities play a significant role in the girder's behavior. Initially, when analyzing the behavior of plate steel girders, models were composed of ideally flat plates. However, it is evident that real structures are not perfectly flat and exhibit initial imperfections before the load is applied. These irregularities have become an essential consideration in the analysis, and it has been demonstrated that, in some cases, their impact is significant [5], [6].

The importance of this issue is highlighted by the fact that European regulations, such as EN1993-1-5 in Annex C [7], provide recommendations for determining initial imperfections. However, studies addressing the impact of real imperfections on the magnitude of the limit load are relatively limited in the literature.

The analysis of the girders was conducted using the ANSYS program [8]. Both girders without longitudinal stiffeners and those with a longitudinal stiffener near the loaded upper flange were examined. The influence of the length of the uniformly distributed load on the loaded flange and in the web plane, the girder's behavior in the nonlinear domain, and the ultimate load (characterized by a progressive increase in deformations of the flanges and web, with strains continuing to increase without a corresponding rise in force) were investigated. Numerical simulations were performed to evaluate the behavior of the girder model and the ultimate load values for different material models in the plastic domain, with the goal of selecting the model that provides results most closely aligned with the real structure [9], [10], [11].

Recently, there have been particularly interesting works that use artificial neural networks to predict patch loading [12], [13].

2. Model characteristics

The models of the girders analyzed and their geometry were selected from the literature. It should be noted that while the literature contains a large number of girders with varying dimensions, this study focuses on girders that are part of the experimental results of Dr. Marković [14]. These results were used as the model for numerical simulations, as they were available to the authors. These models represent a portion of larger girders, with the emphasis placed on the girder surface affected by patch loading.

Regarding the geometry, four types of girders were analyzed. All girders have dimensions of 500x500 cm, with two girders featuring a longitudinal stiffener at one-fifth of the height from the loaded flange, while the other two girders are without longitudinal stiffener. Additionally, two girders are subjected to a patch load with a width of 50 cm, and the other two girders are subjected to a patch load with a width of 150 cm. In this way, four distinct cases are considered, as shown in Figure 1. The girders are labeled Series A.

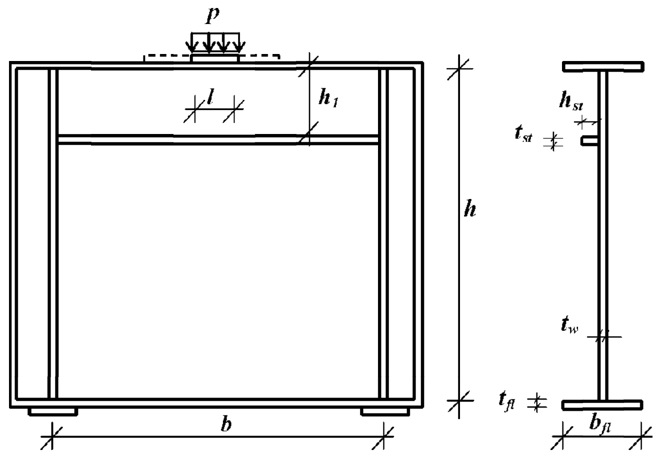

Fig.1. Model sketch with geometry

Table 1 presents the geometric characteristics for each of the girders.

Girders (mm)	**A1**	**A2**	**A3**	**A4**
s	500	500	500	500
h	500	500	500	500
t_w	4	4	4	4
bfl	120	120	120	120
tfl	8	8	8	8
l	50	150	50	150
hst	-	-	30	30
tst	-	-	8	8
s	-	-	100	100

Table 1. Geometric characteristics of the girders model

During the experimental investigation, the girders were subjected to testing within a specially designed closed frame, with the load being applied by a press connected to a hydraulic pump. Initially, the force was increased in large increments, followed by smaller load increments in subsequent stages.

In patch loading experiments, there is a wide range of load control methods that can be applied, depending on the research goals, loading dynamics, and specific requirements for controlling stability, vibrations, and stress distribution. Some of them are: ramp control, sine wave control, step control, constant force control, proportional-integral-derivative, trapezoidal control, adaptive control, feedback control etc. In further research, it would be useful to compare the results obtained with different load application methods.

Throughout the testing process, lateral displacements were recorded at key points along the web, and deflections were measured at the midpoint of both the top and bottom flanges. Strains were monitored at selected points on both the web and flanges, and lateral displacements were measured at the mid-span cross-section of the web following each load variation.

The load was gradually increased until the ultimate load was reached. At this point, the ultimate load was characterized by a progressive increase in the deformations of the flanges and the web, as well as strains, without a further increase in applied force. During this process, visible buckling of the web occurred below the zone where the load was applied. In girders with longitudinal stiffeners, buckling was most prominent between the loaded flange and the longitudinal stiffener.

After the maximum load was maintained for a specified duration (which varied across the individual tests), the girders were unloaded, and the residual deformations of the web and loaded flanges were measured.

2.1 Geometrical imperfections

The aim of this research is, among other objectives, to examine the influence of real geometric imperfections in the girder web on the ultimate load, with the girder models for computer simulations being represented as girders with imperfections [15].

The initial shape of the girder for the numerical model was defined based on the precise geometry of the examined experimental model. In the experimental setup, the initial geometric imperfections of the web were measured at multiple points using a measuring device. Imperfections in the flanges and stiffeners were not considered. Figure 2 illustrates the shape of the initial geometric imperfections of web before load application, with the values magnified to emphasize the imperfections.

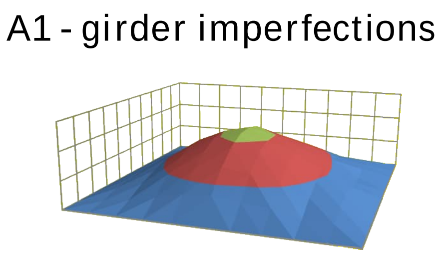

Fig.2a girder imperfections A1

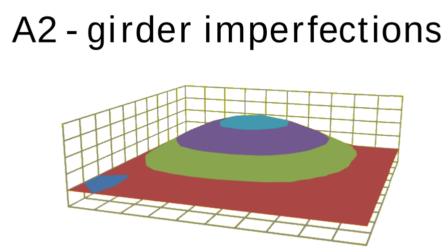

Fig.2b girder imperfections A2

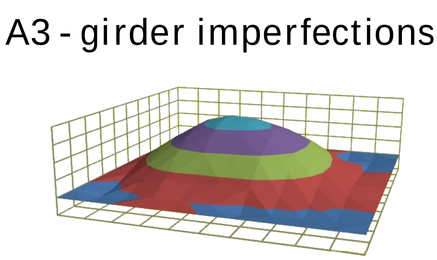

Fig.2c girder imperfections A3

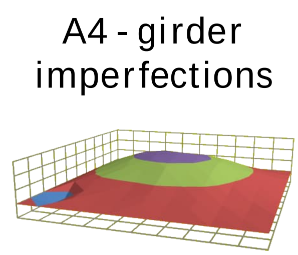

Fig.2d girder imperfections A4

Fig.2. The shape of the initial geometric imperfections of web, for all type of girders

2.2 Material imperfections

Assigning the appropriate material behavior parameters is crucial for obtaining relevant data through numerical analysis. For the steel girder under consideration, its mechanical properties are defined by the modulus of elasticity, Poisson's ratio, and both compressive and tensile yield strengths. It is assumed that the material is isotropic, exhibiting identical mechanical properties in all directions.

To obtain the most accurate data possible, steel coupons were extracted from the girder webs and tested. Each coupon had a width of 12.5 mm and a length of 65 mm. The test results were then used to develop simplified material models of the σ-ε curves [14]. The tests confirmed that the material corresponds to steel grade S275. In cases where a more realistic representation is required, the material curve can be approximated as a multilinear curve, which will better represent the material characteristics if such data are available. The σ-ε diagram representing the material characteristics of one of the coupons is shown as “multilinear curve” in Fig. 3.

Recommendations for design in EN-1993-1-5 Annex C [16] also address material property considerations. The behavior of structural steels is elasto-plastic. Once the yield point f_y is reached, the material no longer behaves in a linear-elastic manner but becomes plasticized and strengthened, meaning material non-linearity occurs. Depending on the accuracy and availability of data, the following material models are proposed: a bilinear stress-strain curve, where material data are unavailable, with yield assumed as a horizontal line or with a slope defined by $E/10000$; alternatively, the curve may be approximated with a slope of $E/100$, accounting for material strengthening.

According to BSK07, Swedish standards [17], a multilinear curve obtained by calculation, as shown in Fig. 3. is recommended. In this study, bilinear curves with tangent modulus $E_t=E/10000$E, $E_t=E/100$, and in additional analyses with $E_t=E/1000$ will be used, as specified in the European standard EN1993-1-5.

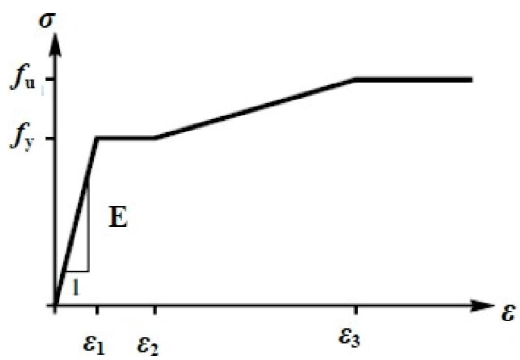

$$\varepsilon_1 = \frac{f_y}{E}$$

$$\varepsilon_2 = 0.025 - 5\frac{f_y}{E}$$

$$\varepsilon_3 = 0.02 + 50\frac{f_u - f_y}{E}$$

Fig.3 σ-ε multilinear curve according to the BSK07 standard

The material's modulus of elasticity is 210 MPa, and the Poisson's ratio is ν=0.3\nu = 0.3ν=0.3. The material models used are based on the isotropic assumption and the Von Mises plasticity theory.

During the non-linear analysis, the values of strains were calculated based on various material models in the elastic-plastic region [18]. For example, for Model A3, a numerical simulation was performed on the same girder using five different material behavior models during loading until failure, as follows:

- EN1993-1-5: Multilinear curve corresponding to the real material curve.
- BSK07 (Swedish standard): multilinear curve, Fig.3.
- EN1993-1-5: Bilinear curve with tangent modulus $E_t=E/10000$E.
- Bilinear curve with tangent modulus $E_t=E/1000$ for additional analysis.
- EN1993-1-5: Bilinear curve with tangent modulus $E_t=E/100$.

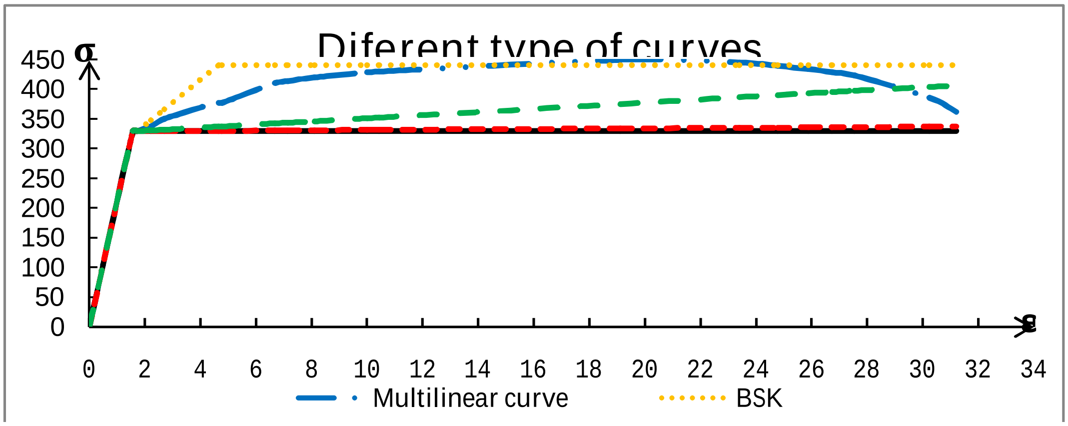

Fig.4 σ-ε curves used in numerical modeling

3. Modeling of the girders

To obtain the most accurate results, the girder model was fully adapted to the experimental setup. The numerical modeling was performed using the ANSYS software [10].

The girder modeling process included the following steps: defining material properties, specifying the appropriate geometry of the girder, incorporating geometric imperfections of the ribs, applying boundary conditions, assigning loads based on the experimental models, selecting an appropriate finite element mesh size, and setting other relevant parameters for the analysis [19]. The numerical models were developed to closely replicate the experimental models.

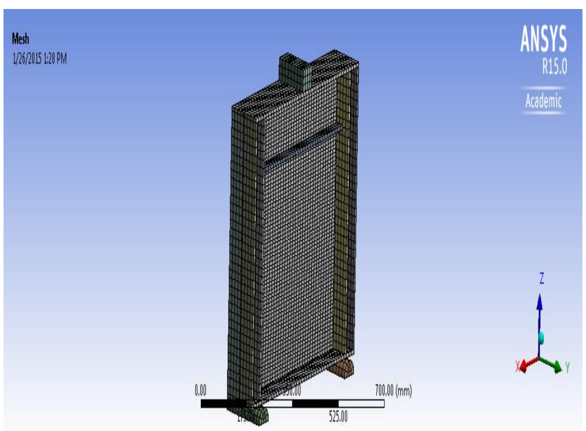

Fig.5 Numerical model in ANSYS

The geometry of the girders with initial deformations, along with the material characteristics and models, was presented in the previous section. The loading was applied to the girder in the same manner as in the experiment.

The load was applied in six increments. For each type of girder, the load increment varied according to the expected ultimate load value, as determined by the experimental data. This approach allowed for monitoring the variation in the stress and strain state of the girder throughout the loading process.

Starting with the finite element mesh size, we selected a specific element size. As the elements were made progressively smaller and the mesh refined, the computed solution converged towards the true solution. The criterion for convergence was a difference of less than 5% between two iterations. This approach allowed for effective discretization of the finite element mesh. The chosen finite element size was 1.5 cm. The finite elements used were of type 'SOLID 186,' defined by twenty nodes, making them well-suited for nonlinear analysis [19].

One of the primary objectives of this modeling is the determination of the girder's ultimate load capacity. This section presents the determination of the ultimate load for four types of girders with six different material models. The obtained results are compared with experimental data, and an analysis of these results is conducted. The increase in ultimate load capacity with both the length of the loading and the influence of stiffeners is discussed.

In the numerical analysis, the criterion for determining the ultimate load is the point at which the solutions begin to diverge, and the girder starts to lose stability, exhibiting a sudden increase in deformations.

The analysis of the ultimate load values was performed for all types of girders and different material models: the σ-ε curve based on experimental data, the σ-ε curve according to the experimental model and BSK07 standard [17], and bilinear curves with tangent moduli E_t=E/100, E_t=E/1000 and E_t=E/100000. The calculated ultimate loads were compared with the experimentally obtained ultimate loads [20]. The analysis of ultimate load values for all types of girders and various material models was conducted by comparing these results with the experimental outcomes. The ultimate load capacities, expressed in kN, for all four types of girders (A1, A2, A3, and A4) are presented in Table 2.

Material models	**A1**	**A2**	**A3**	**A4**	Averagevalue (%)
Experiment (kN)	165	215	183	255	-
***Multi. EN* (kN)**	178,174	216,9275	188,5	274	-
***Δ* (%)**	7,98	0,90	3,01	7,45	**4,84**
***BSK* (kN)**	162	196,297	164,472	262	-
***Δ* (%)**	−1,82	−8,70	−10,12	2,75	5,85
***E*/10000 (kN)**	172	235,406	176,962	299,407	-
***Δ* (%)**	4,24	9,49	−3,30	17,41	8,61
***E*/1000 (kN)**	174	235,642	177,396	302,591	-
***Δ* (%)**	5,45	9,60	−3,06	18,66	9,19
***E*/100 (kN)**	180,5	238,637	185,5	302,438	-
***Δ* (%)**	9,39	10,99	1,37	18,60	10,09

Table 2. The values of ultimate load capacity

3. Results

Numerical analysis was performed to obtain the limit load results for different material models. As shown in Table 2, all material models provided satisfactory congruence. The best match was observed with the material model using the multilinear curve according to experimental data, which exhibited an average deviation of 4.84% across all girder types.

The analysis of the results revealed the increase in ultimate load capacity when a longitudinal stiffener is added to the girder. The increase in ultimate load capacity for girders with a patch loading length of 50 mm (A1 and A3) and 150 mm (A2 and A4) for different material models is presented in Fig. 6.

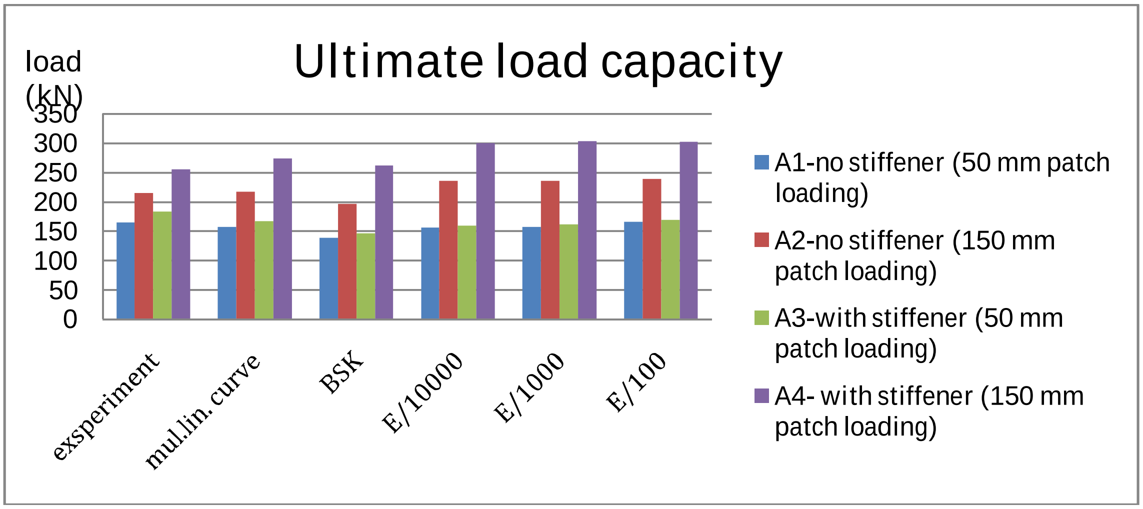

Fig.6. Increase in ultimate load for different patch loading lengths

The same diagram also shows the increase in ultimate load capacity when the patch loading length is increased from 50 mm to 150 mm. The girders without longitudinal stiffeners (A1 and A2) and the girders with longitudinal stiffeners (A3 and A4) are presented for different material models.

	With and without stiffener (%)		Length of patch loading is increased from c=50÷150 mm (%)	
	c=50 mm A1and A3(%)	c= 150 mm A2 and A7(%)	Without stiffener A1 and A2(%)	With stiffener A3 and A7(%)
Experiment	9,84	15,69	23,26	31,20
Multi. EN	5,8	20,83	17,86	59,66
BSK	1,53	25,08	17,47	37,22
E/10000	2,88	21,38	26,93	40,90
E/1000	1,95	22,13	26,16	41,37
E/100	2,77	21,10	24,36	38,67
Average value	2,99	22,10	22,56	43,56

Table 3. Increase of ultimate load capacity when the length of patch loading is increased and longitudinal stiffener is present, expressed in percents

Table 3 presents an analysis of the increase in ultimate load capacity. The first two columns show the percentage increase in ultimate load capacity when a longitudinal stiffener is added to the girder. The first column presents the girders with a patch loading length of 50 mm, while the second column presents those with a patch loading length of 150 mm. The third and fourth columns show the increase in ultimate load capacity when the patch loading length is increased from 50 mm to 150 mm. The third column presents the girders without stiffeners, and the fourth column presents the girders with stiffeners.

4. Conclusions

This paper develops appropriate numerical models using the ANSYS software package, which best represent the experimental models. The objective of this research is to obtain results that can be used in practical applications to select the most suitable material model for analysis, in accordance with European standards.

Upon analyzing the obtained results, it was concluded that all material behavior curves provided satisfactory outcomes. The material model corresponding to the multilinear curve of the real material based on experimental data, showed the best agreement with the experimental results, with an average deviation of 4.84% for all types of girders.

When analyzing the results, the following considerations must be taken into account: initial geometric imperfections are assumed to be present only in the web; the material characteristics for the real curve, as well as the yield stress f_y and tensile strength f_u, are assumed to be the average values from the tested coupons; the material properties of the flanges and webs are assumed to be identical (which was not the case in the experiment); the impact of welds and initial geometric imperfections in the flanges and stiffeners is neglected; and accurately defining boundary conditions is not possible, among other factors.

Taking these factors into account, it can be concluded that satisfactory agreement was achieved between the results obtained experimentally and those from the numerical analysis.

The behavior of plate girders under patch loading is highly complex and depends on various parameters. As demonstrated, the resulting deformations need not be significant. Plasticization begins at the most heavily loaded section of the web, initially occurring at the surface and then progressively spreading through the thickness of the web.

This suggests that two combinations should be analyzed for each structure: a girder made of high-grade steel with a higher yield strength and a slender web, or a girder made of low-grade steel with a thicker web. The parameters leading to an increase in the ultimate load were analyzed, and the conclusion is that the ultimate load increases more significantly with an increase in the length of the applied load from 50 mm to 150 mm than with the addition of a longitudinal stiffener to the girder.

This conclusion has practical applications. In bridge assembly, when a bridge is being slid into its designed position over temporary or permanent supports, it is beneficial to increase the contact surface between the girder and the support, thereby enhancing the ultimate strength of the girders.

Acknowledgement

This research was supported by the Ministry of Science, Technological Development and Innovation of the Republic of Serbia under the Agreement on the Implementation and Financing of Scientific Research Work of the NIO in 2025 - Registration number: 451-03-136/2025-03/ 200095 dated 04/02/2025.

References

[1] Markovic N., Hajdin N, *A Contribution to the Analysis of the Behaviour of Plate Girders subjected to Patch Loading*, Journal of Constructional Steel Research. Vol. 21, pp. 163-173, 1992.

[2] Bergfelt A., *Patch loading on a slender web. Influence of horizontal and vertical web stiffeners on the load carrying capacity*, Department of Structural Engineering, Chalmers University of Technology, Publication S79, Goteborg, 1979.

[3] Braun B., *Stability of steel plates under combined loading*, Doctoral Thesis, Nr 2010-3, Institut für Konstruktion und Entwurf Stahl-Holz- und Verbundbau, Universität Stuttgart, Germany 2010.

[4] Davaine L., *Formulations de la réststance au lancement d'une âme métallique de pont raide longitudinalement*, Doctoral Thesis D05-05, INSA de Rennes, France, 2005.

[5] Ceranic A., Bendic M., Kovacevic S., Salatic R., Markovic N., *Influence of patch load length on strengthening effect in steel plate girders*, Journal of Constructional Steel Research, Vol.

195, pp. 107348, Elsevier, 2022.

[6] Graciano C., Kurtoglu A., Kövesdi B., Casanova E., *Patch loading resistance prediction of plate girders with multiple longitudinal stiffeners using machine learning*, Steel & Composite Structures: An International Journal, Vol. 49, No. 4, pp. 419-430, Techno-press, 2023.

[7] EN1993-1-5:2006 Eurocode3: Design of steel structures, Part1-3: Plated structural elements, November 2006, ISBN 0580496678.

[8] ANSYS 15, LS-DYNA Keyword user`s manual, Vol I, II, III, February 2013, Version R7.0, Livermore Software Technology Corporation.

[9] Casanova E., Graciano C., Chacón R., *Patch loading resistance of steel plate girders stiffened with triangular cell flanges*, Structures, Vol. 38, pp. 993-1004, Elsevier, 2022.

[10] Kovacevic S., Markovic N., *Experimental study on the influence of patch load length on steel plate girders*, Thin-Walled Struct. 151, pp. 106733, 2020.

[11] Rogač M., Aleksić S., Lučić D., *Influence of patch load length on the ultimate resistance of I-girders: state-of-the-art review*, Conference: Association of Structural Engineers of Serbia, pp.174-183, Vrnjačka Banja, 2024.

[12] Sy Hung Mai, Viet-Linh Tran, Duy-Duan Nguyen, Viet Tiep Nguyen and Duc-Kien Thai, *Patch loading resistance prediction of steel plate girders using a deep artificial neural network and an interior-point algorithm*, Steel and Composite Structures, Vol. 45, No 2, pages 159-173, 2022.

[13] Kumar S. A., Sofi F. A., Bhat J. A., *Estimation of patch-loading resistance of steel girders with unequal trapezoidal web-corrugation folds using nonlinear FE models and artificial neural networks*, Structures, Vol. 48, p.p. 16551-1669, 2023.

[14] Marković N., *Izbočavanje limenih nosača pod dejstvom lokalnog opterećenja*, Doktorska disertacija, Građevinski fakultet u Beogradu, 2003.

[15] Turnić D., Živković S., Spasojević Šurdilović M., Milošević M., Igić A., *Influence of Geometrical and structural imperfections of steel plate girders*, Facta Universitatis, Series: Architecture and Civil engineering, Vol. 19, No 2, 2021, pp.171-182, ISSN: 2406-0860.

[16] Johansson B., Maquoi R., Sedlacek G., Müller C., Beg D., *Commentary and worked examples to EN1993-1-5, Plated structural elements*, JRT Scientific and Technical Reports, 2007.

[17] BSK07, Boverkets handbok om stålkonstruktioner BSK 07, ISSN: 1400-1012 (in Sweden), 2007.

[18] Turnić D., Marković N., Igić T., *Stress analysis of steel plate girders subjected to patch loading in elastoplastic domain*, Tehnički vjesnik, Vol.28. No.4, 2021., ISSN 1330-3651.

[19] Turnić D., *Nelinearno ponašanje i granična nosivost limenih nosača opterećenih lokalizovanim opterećenjem*, doktorska disertacija GAF Niš, 2016.

[20] Turnić D., Marković N., Igić T., Nikolić V., Spasojević Šurdilović M., *Analysis of material non-linearity of steel girders subjected to patch loading*, Tehnički vjesnik, 2017, vol.24. No.6, p.p. 1991-1998.

10th International Congress of the Serbian Society of Mechanics
Niš, Serbia, June 18-20, 2025
D.17
Original Scientific Paper

DOI:10.46793/ICSSM25.271Z

ILC-MPC CONTROLLER FOR ROBOTIC MANIPULATORS BASED ON THE ULTRA-LOCAL MODEL

Nikola LJ. Živković[1] [0000-0002-2276-2933], **Mihailo P. Lazarević**[2] [0000-0002-3326-6636], **Jelena Z. Vidaković**[1] [0000-0002-3363-8807], and **Petar D. Mandić**[2] [0000-0001-7004-2087]

[1]Lola Institute Ltd., Belgrade, Serbia, email: nikola.zivkovic@li.rs
[2]University of Belgrade, Faculty of Mechanical Engineering, e-mail: mlazarevic@mas.bg.ac.rs

Abstract. This research explores the possibility of simplifying model predictive control strategy for robotic manipulators and improving the control system's performance with data-driven learning controllers. The main goal is to synthesize a controller that will be feasible for embedded hardware. Simplifying the robot dynamics is done using the ultra-local model method, and then new equations of motion are used to solve a nonlinear optimization problem in model predictive control. An iterative learning controller with a serial structure is added for increased performance when the given task is repetitive. Test simulation is carried out in Matlab to verify the feasibility of the proposed control system. Results of the simulation show that the proposed controller indeed manages to attenuate external disturbances and improve performance through the learning process.

Keywords: Model Predictive Control, Ultra-local model, Iterative Learning Control, Robotics, Trajectory tracking.

1. Introduction

Trajectory tracking is one of the key elements of robot control system design. Achieving accurate trajectory tracking under disturbances, unmodeled dynamics, and parametric uncertainties is challenging for multiple Degree of Freedom (DoF) mechanisms such as robotic manipulators. Various control approaches are used to address trajectory tracking problems for robotic manipulators, from simple PID controllers to advanced controllers such as Inverse Dynamics, Sliding Mode Control, Adaptive Control, Robust Control, Fuzzy Control, and Model Predictive Control (MPC) [1, 2, 3, 4, 5, 6, 7]. Most advanced control strategies for robotic manipulators are model-based, meaning that a model of the robot manipulator dynamics is required to satisfy controller performance.

Model Predictive Control is one of the few model-based control strategies extensively used in industry, especially the petrochemical industry [8]. MPC also found its applications in the field of robotics [9, 10]. Robot manipulators' dynamics are inherently nonlinear and strongly coupled, especially in robots with three or more degrees of freedom. The concept of simplified dynamics model under the term *ultra-local model* from [11] is investigated in [12] for mobile robots MPC.

Further improvement of the control system performance can be made by incorporating a feedforward controller to compensate for any known disturbances, reduce delay in the response signal, etc. A control strategy suitable for trajectory tracking problems for systems executing repetitive tasks is Iterative Learning Control (ILC) [13]. The ILC is an intelligent, data-driven control method aimed at improving the trajectory-tracking performance of the system that operates repetitively over a fixed time interval [14]. Few papers tackle improving the MPC performance with iterative learning controllers [15, 16].

This research presents the integration of MPC and ILC using a control scheme consisting of a serial ILC and MPC controller based on an ultra-local model for position control of the robot manipulator. The UL-MPC controller is based on the simplified dynamics model via an ultra-local representation that is updated at every time step. The motivation for the serial ILC structure is modularity and ease of implementation.

The remainder of this paper consists of Section 2. which describes the concept of the ultra-local model; Section 3. which presents the proposed control system design; Section 4. which displays simulation results; and Section 5. gives concluding remarks.

2. Ultra-local model

The n-degree of freedom robot manipulator equations of motion are:

$$\mathbf{A}(\mathbf{q}(t))\ddot{\mathbf{q}}(t)+\mathbf{C}(\mathbf{q}(t),\dot{\mathbf{q}}(t))\dot{\mathbf{q}}(t)+\mathbf{Q_g}(\mathbf{q}(t))=\mathbf{Q_a}(t), \tag{1}$$

where $\mathbf{q}(t)\in\mathbb{R}^{n\times 1}$, $\dot{\mathbf{q}}(t)\in\mathbb{R}^{n\times 1}$, and $\ddot{\mathbf{q}}(t)\in\mathbb{R}^{n\times 1}$ are vectors of generalized coordinates $q_j(t)$, $\dot{q}_j(t)$, $\ddot{q}_j(t),(j=1,...,n)$ representing joint positions, speeds and accelerations, respectively, term $\mathbf{A}(\mathbf{q}(t))\in\mathbb{R}^{n\times n}$ is the inertia matrix, term $\mathbf{C}(\mathbf{q}(t),\dot{\mathbf{q}}(t))\in\mathbb{R}^{n\times n}$ is the Coriolis and centrifugal forces matrix, and $\mathbf{Q^g}(\mathbf{q}(t))\in\mathbb{R}^{n\times 1}$ is a vector of generalized forces due to gravity, $\mathbf{u}(t)\in\mathbb{R}^{m\times 1}$ is a vector of generalized joint actuation torques, where m is a number of actuated joints. Let the (1) be expressed in the following general form:

$$\mathbf{q}^{(\nu)}(t)=f(\mathbf{q}^{(\nu-1)}(t),\ldots,\mathbf{q}(t),\mathbf{u}(t)), \tag{2}$$

where $\mathbf{q}(t)\in\mathbb{R}^{n\times 1}$ is vector of system outputs and its time derivatives up to ν^{th} order, and $\mathbf{u}(t)\in\mathbb{R}^{m\times 1}$ is vector of control input, in this case we adopt that $n=m$. The equations of motion (2) can be represented as an ultra-local model (ULM) for a MIMO (Multiple Input Multiple Output) system with the following equation:

$$\mathbf{q}^{(\nu)}(t)=\mathbf{f}(t)+\mathbf{B}\mathbf{u}(t), \tag{3}$$

where $\mathbf{q}^{(\nu)}(t)$ is the ν^{th} derivative of the system output vector $\mathbf{q}\in\mathbb{R}^{n\times 1}$ at time t, $\mathbf{B}\in\mathbb{R}^{n\times m}$ is the positive diagonal square gain matrix chosen by trial and error, $\mathbf{u}(t)\in\mathbb{R}^{m\times 1}$ is the control input vector. The vector $\mathbf{f}(t)\in\mathbb{R}^{n\times 1}$ is a differentiable continuous vector function comprising non-modeled dynamics and external disturbances. The procedure for establishing an ultra-local model is following:

- Find $\mathbf{q}^{(\nu)}(t)$. The value of derivative order ν can be both integer or fractional $\nu\in\mathbb{R}$, but in case of robotic manipulator $\nu=2$;
- To obtain the estimated value $\hat{\mathbf{f}}(t)$ of $\mathbf{f}(t)$, substitute the ν^{th} order derivative of the system output $\mathbf{q}^{(\nu)}(t)$ and control input at the previous time step $\mathbf{u}(t-T)$ (T is the sampling period) into following equation:

$$\hat{\mathbf{f}}(t)=\mathbf{q}^{(\nu)}(t)-\mathbf{B}\mathbf{u}(t-T), \tag{4}$$

- Finally, establish ultra-local model by substituting $\hat{\mathbf{f}}(t)$ into (3):

$$\mathbf{q}^{(\nu)}(t)=\hat{\mathbf{f}}(t)+\mathbf{B}\mathbf{u}(t), \tag{5}$$

where estimated function $\hat{\mathbf{f}}(t)$ is a piecewise constant function.

3. Serial ILC-UL-MPC controller design

This control scheme consists of a nonlinear UL-MPC controller based on the ultra-local representation of robot dynamics and a serial ILC controller (Figure 1). Given that $\nu = 2$ for robot manipulator, the ultra-local model system of equations is:

$$\ddot{\mathbf{q}}(t) = \hat{\mathbf{f}}(t) + \mathbf{A}^{-1}(\mathbf{q}(t))\mathbf{u}(t). \tag{6}$$

Ultra-local model (6) in a discrete state-space form is:

$$\mathbf{x}(k+1) = \begin{bmatrix} \mathbf{x}_2(k) \\ \hat{\mathbf{f}}(k) + \mathbf{B}\mathbf{u}(k) \end{bmatrix}, \tag{7}$$

where $k = 0, \ldots, N$ is the time step index, N is the total number of time steps, and $\mathbf{x}(k) = [\mathbf{x}_1(k),\ \mathbf{x}_2(k)]^T$, $\mathbf{x}_1(k) = \mathbf{q}(k), \mathbf{x}_2(k) = \dot{\mathbf{q}}(k)$ is the state vector.

The basis of the Model Predictive Control is to define and solve optimization problems according to the imposed constraints and defined objective function. Equations (7) are being used to solve nonlinear optimization problems for a specified time interval called the horizon. The general form of the nonlinear optimization problem reads:

$$\min f(\mathbf{x}),\ g(\mathbf{x}) \leq 0,\ h(\mathbf{x}) = 0,\ \mathbf{x} \in \mathbf{X}, \tag{8}$$

where $f(\mathbf{x})$ is objective function, $g(\mathbf{x})$ are inequality constraint, $h(\mathbf{x})$ are equality contraints and $\mathbf{X}$ is set of values which vector $\mathbf{x}$ can have. The proposed UL-MPC controller defines optimization problem as:

$$\min f(\mathbf{x},\mathbf{u}) = \sum_{k=0}^{N} \mathbf{e}^T(k)\mathbf{W}\mathbf{e}(k) + \mathbf{u}^T(k)\mathbf{R}\mathbf{u}(k);\ \mathbf{W} = \begin{bmatrix} \mathbf{W^p} & \mathbf{0} \\ \mathbf{0} & \mathbf{W^v} \end{bmatrix}, \tag{9}$$

$$\mathbf{x}(k+1) - f(\mathbf{x}(k),\mathbf{u}(k)) = 0;\ f(\mathbf{x}(k),\mathbf{u}(k)) = \begin{bmatrix} \mathbf{x}_2(k) \\ \hat{\mathbf{f}}(k) + \mathbf{B}\mathbf{u}(k) \end{bmatrix}, \tag{10}$$

$$\mathbf{x} \in \mathbf{X}, \mathbf{u} \in \mathbf{U} \tag{11}$$

where $\mathbf{W}$ and $\mathbf{R}$ are weighting matrices (matrix $\mathbf{W}$ consists of two sub-matrices $\mathbf{W^p}$ and $\mathbf{W^v}$ that are representing position and velocity states weights, respectively), $\mathbf{e}(k) = \delta\mathbf{x}^d(k) - \mathbf{x}(k)$ is errors

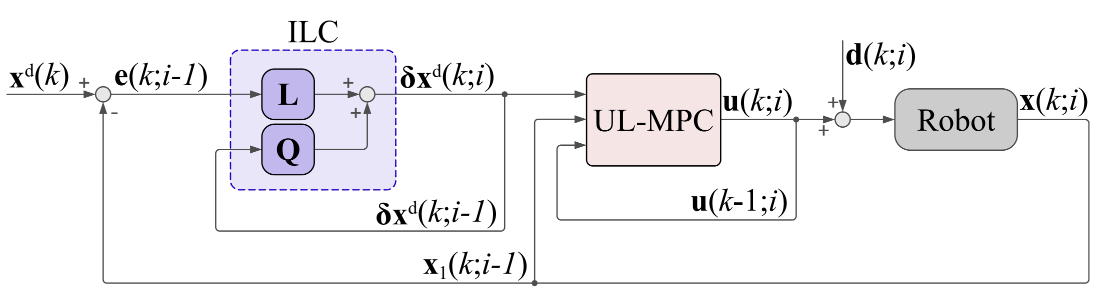

Figure 1: Control scheme of the proposed serial ILC-UL-MPC controller. Indices k and i denote time step and iteration index, respectively.

vector, $\mathbf{u}(k)$ is control inputs vector, and $\mathbf{X}$ and $\mathbf{U}$ are sets of all possible values vectors $\mathbf{x}$ and $\mathbf{u}$ can have. The problem defined by (9), (10) and (11) is solved for each time step k over the period defined by a horizon of time samples N_H and from the obtained optimal control signal $\mathbf{u}^{opt}(kN_H)$ only the first value $\mathbf{u}(k) = \mathbf{u}^{opt}(1)$ is applied as a control input. The same procedure is repeated for all time steps kN.

The reference signal $\delta\mathbf{x}^d(k)$ for the UL-MPC can be controlled to achieve better performance by applying ILC. Since ILC controllers add iteration dimension beside time to the control problem, the notation for iteration-varying vectors is adopted as $\mathbf{x}(k;i)$ where i denotes the iteration index. The controller structure where the output from the ILC is used as a reference for the next stage controller is usually named serial, indirect, or cascaded. This contribution adopts the term serial as a naming convention. Let the reference to UL-MPC be defined as:

$$\delta\mathbf{x}^d(k;i) = \mathbf{Q}\left(\delta\mathbf{x}^d(k;i-1) + \mathbf{L}\mathbf{e}(k;i-1)\right) \tag{12}$$

where $\mathbf{L}$ is the learning gains matrix and $\mathbf{Q}$ is the robustness gains matrix. Matrices $\mathbf{L}$ and $\mathbf{Q}$ are divided in sub-matrices as:

$$\mathbf{Q} = \begin{bmatrix} \mathbf{Q^p} & \mathbf{0} \\ \mathbf{0} & \mathbf{Q^v} \end{bmatrix}, \; \mathbf{L} = \begin{bmatrix} \mathbf{L^p} & \mathbf{0} \\ \mathbf{0} & \mathbf{L^v} \end{bmatrix}. \tag{13}$$

where superscripts $\mathbf{p}$ and $\mathbf{v}$ denote relation to position $\mathbf{x}_1$ and velocity $\mathbf{x}_2$ parts of the state vector $\mathbf{x}$, respectively. Equation (12) represents ILC update law.

4. Simulation setup and results

The simulation is conducted to verify and test the proposed controller on a three-degree-of-freedom robot manipulator - NeuroArm (Figure 2). The robot's desired trajectory is defined in joint space as a cubic polynomial, with velocity and acceleration determined as its first and second time derivatives. The control system is simulated in Matlab and Simulink with a uniform sampling period of T = 0.01s, and the horizon for UL-MPC is chosen to be $N_H = 5$ time steps. The joint position, speed, and torque limits are given in Table 1, and parameters for the proposed ILC-UL-MPC controller are shown in Table 2. The performance of the ILC controller in the iteration domain is measured using the infinite norm of the error - $\|e_j\| = \max_k |e_j(k)|$. Each robot joint is subjected to a disturbance torque in the form of a step function defined as:

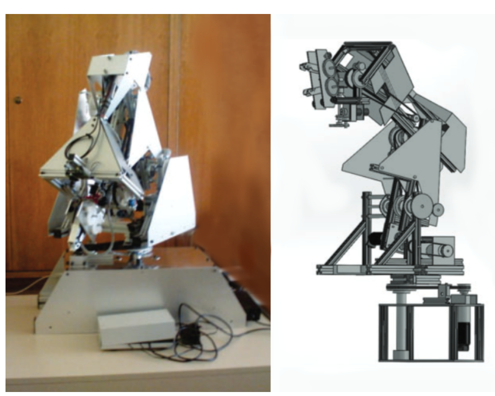

Figure 2: NeuroArm robot manipulator.

Joint j	q_j^{lb}(deg)	q_j^{ub}(deg)	$\dot{q}_j^{lb}$(deg/s)	$\dot{q}_j^{ub}$(deg/s)	u_j^{lb}(Nm)	u_j^{ub}(Nm)
1	-90	90	-5	5	-20	20
2	-90	90	-5	5	-20	20
3	-90	90	-5	5	-20	20

Table 1: Lower (index - lb) and upper (index - ub) bounds of state and actuation variables.

Joint j	$W^p{}_{jj}$	$W^v{}_{jj}$	R_{jj}	$L^p{}_{jj}$	$L^v{}_{jj}$	$Q^p{}_{jj}$	$Q^v{}_{jj}$
1	10	0.1	0.001	1	0	0.85	1
2	100	0.1	0.001	1	0	0.85	1
3	45	0.1	0.001	1	0	0.85	1

Table 2: Control parameters for UL-MPC and ILC controllers.

$$d(k) = \begin{cases} 0, & k \leq 100 \\ D, & k > 100 \end{cases}, \; D = 5\text{Nm}. \tag{14}$$

Simulation results have shown that the proposed controller improves the trajectory-tracking performance of all three DoFs (Figure 3). Data in Figure 3 indicates that the ILC update law successfully improves the performance of the UL-MPC controller. The infinite norm of the errors converges as iterations progress, and after approximately six iterations, the learning process is finished. Figure 5 shows an error in the time domain at the 10th iteration, where disturbance attenuation can be observed at $t = 1s$. A similar observation can be seen in Figure 6, at $t = 1s$, as actuators react to a disturbance torque. Measured vs desired joint positions in Figure 4 illustrate the satisfying performance of the proposed controller, as actual joint positions successfully track given desired positions.

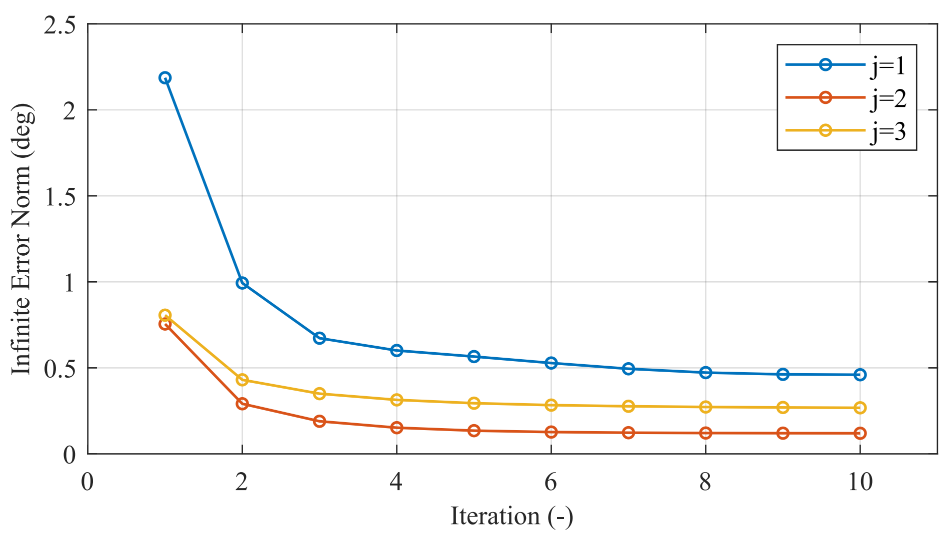

Figure 3: Infinite norm convergence of the error signal for all three joints, j denotes joint index.

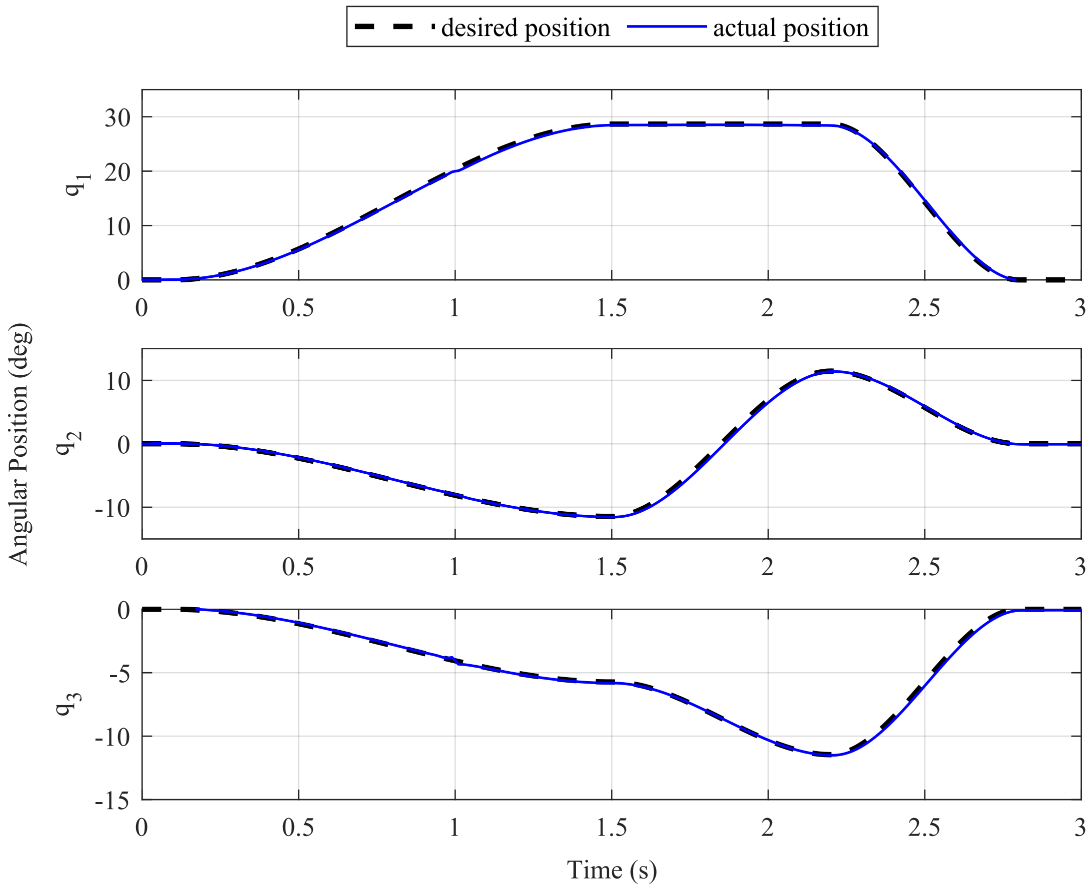

Figure 4: Desired vs actual joint positions at 10^{th} iteration, j denotes joint index.

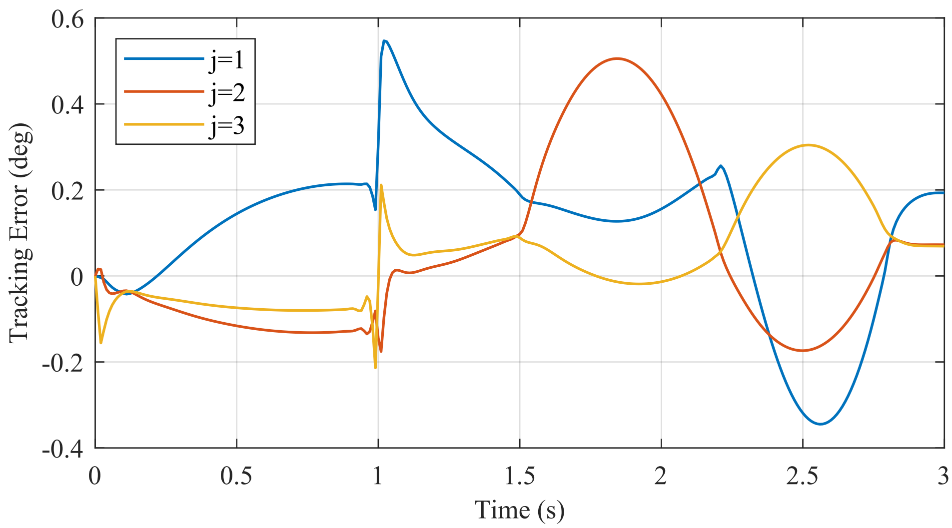

Figure 5: Errors for all three joints at 10^{th} iteration, j denotes joint index.

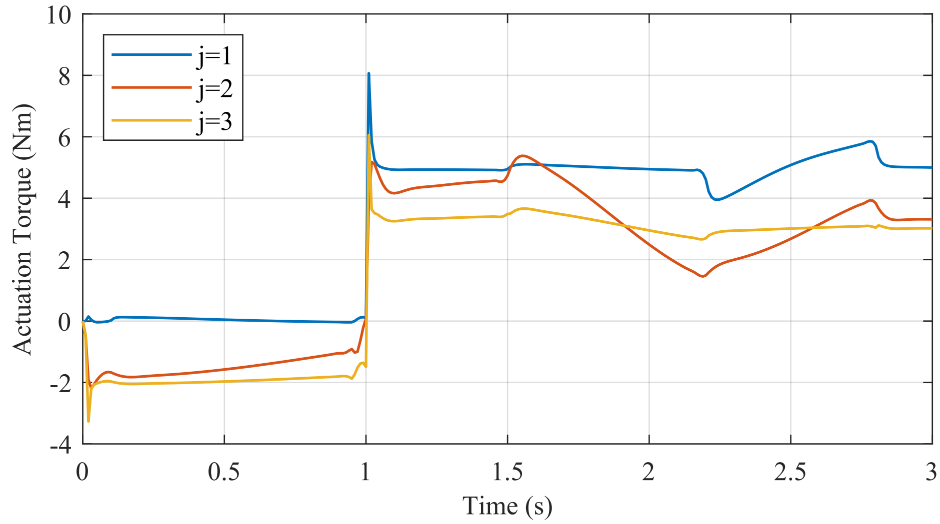

Figure 6: Control efforts for all three joints at 10^{th} iteration, j denotes joint index.

5. Concluding remarks

The research presented in this contribution proposes a controller for robot manipulators using the model predictive control and iterative learning control strategies. The test simulation confirms that the proposed controller's implementation of the simplified dynamics model is successful. The UL-MPC controller successfully attenuates external disturbances, and the addition of serial ILC improves performance after a learning process of ten iterations. Errors at the end of the learning process were under 0.5°, which is acceptable for robotic manipulator systems.

Acknowledgement. This research has been supported by the research grants of the Serbian Ministry of Science, Technological Development, and Innovations, Grant No. 451-03-137/2025-03/200105 from 04.02.2025. and Grant No. 451-03-136/2025-03/200066.

References

[1] Luh, J.,Y.,S., *Conventional controller design for industrial robots—a tutorial*, IEEE Transactions on Systems, Man, and Cybernetics, Vol. SMC-13, No. 3, 298-316, 1983.

[2] Cervantes, I., Alvarez-Ramirez, J., *On the PID tracking control of robot manipulators*, Systems & Control Letters, Vol. 42, No. 1, 37-46, 2001.

[3] Kreutz, K., *On manipulator control by exact linearization*, *IEEE Transactions on Automatic Control*, Vol. 34, 763–767, 1989.

[4] Slotine, J.-J.,E., *The robust control of robot manipulators*, International Jorunal of Robotics Research, Vol. 4, No. 2, 49–64, 1985.

[5] Shafiqul, I., Liu, X.,P., *Robust sliding mode control for robot manipulators*, *IEEE Transactions on industrial electronics*, Vol. 58, No. 6, 2444-2453, 2010.

[6] Dai, L., Yu, Y., Zhai, D.,H., Huang, T., Xia, Y., *Robust model predictive tracking control for robot manipulators with disturbances*, IEEE Transactions on industrial electronics, Vol. 68, No. 5, 4288-4297, 2021.

[7] Wang, H., *Adaptive control of robot manipulators with uncertain kinematics and dynamics*, IEEE Transactions on Automatic Control, Vol. 62, No. 2, 948-954, 2016.

[8] García, C.,E., Prett, D.,M., Morari, M., *Model predictive control: Theory and practice—A survey*, Automatica, Vol. 25, No. 3, 335-348, 1989.

[9] Erez, T., Lowrey, K., Tassa, Y., Kumar, V., Kolev S., Todorov, E., *An integrated system for real-time model predictive control of humanoid robots*, 2013 13th IEEE-RAS International Conference on Humanoid Robots (Humanoids), Atlanta, GA, USA, 292-299, 2013.

[10] Carron, A., Arcari, E., Wermelinger, M., Hewing, L., Hutter M., Zeilinger, M.,N., *Data-Driven Model Predictive Control for Trajectory Tracking With a Robotic Arm*, IEEE Robotics and Automation Letters, Vol. 4, No. 4, 3758-3765, 2019.

[11] Fliess, M., Join, C., *Model-free control*, International Journal of Control, Vol. 86, No. 12, 2228-2252, 2013.

[12] Wang, Z., Wang, J., *Ultra-local model predictive control: A model-free approach and its application on automated vehicle trajectory tracking*, Control Engineering Practice, Vol. 101, 104482, 2020.

[13] Arimoto, S., Kawamura, S., Miyazaki, F., *Bettering operation of robots by learning*, Journal of Robotic systems, Vol. 1, No. 2, pp. 123-140, 1984.

[14] Moore, K.,L., *Iterative Learning Control for Deterministic Systems*, Springer-Verlag, London, 1993.

[15] Li, D., He, S., Xi, Y., Liu, T., Gao, F., Wang, Y., Lu, J., *Synthesis of ILC–MPC Controller With Data-Driven Approach for Constrained Batch Processes*, IEEE Transactions on Industrial Electronics, Vol. 67, No. 4, 3116-3125, 2020.

[16] Chen, X., Yang, C., Cheng, J., Hu, H., Shao, G., Gao, Y., Zhu, Q., *A Novel Iterative Learning-Model Predictive Control Algorithm for Accurate Path Tracking of Articulated Steering Vehicles*, IEEE Robotics and Automation Letters, Vol. 9, No. 8, 7373-7380, 2024.

Mini-Symposia 1: Mechanical Metamaterials

Organizers:

Milan Cajić (Mathematical Institute of Serbian Academy of Sciences and Arts, Serbia),
Danilo Karličić (Mathematical Institute of Serbian Academy of Sciences and Arts, Serbia),
Ji Lin (Hohai University, China),
Hong Guang Sun (Hohai University, China).

10th International Congress of the Serbian Society of Mechanics
Niš, Serbia, June 18-20, 2025
M.1.1

Extended abstract

AN OVERVIEW OF COUPLED MECHANICAL PROBLEMS INCLUDING CONTACT PHENOMENA SOLVED BY FEA

Ivana D. Atanasovska[0000-0002-3855-4207]

Mathematical Institute of the Serbian Academy of Sciences and Arts
Kneza Mihaila 36, 11000 Belgrade, Serbia
e-mail: iatanasovska@mi.sanu.ac.rs

Abstract:

Almost all mechanical systems operate under conditions of coupled mechanical problems, most often nonlinear. One of the primary sources of nonlinearity is the contact phenomenon, which is present in a large number of complex mechanical systems used, for example, in engineering and biomedicine. So far, no exact analytical methods exist for solving the response of bodies in contact in solid mechanics. To achieve this, the Finite Element Analysis (FEA) is employed, whose accuracy largely relies on properly chosen initial and boundary conditions, as well as the contact parameters, especially the contact stiffness. However, when the contact is coupled with other phenomena within the same mechanical problem, solving this task becomes far more complex. This is especially the case with engineering mechanical systems, where other phenomena, such as dynamics, impact, material elastoplastic characteristics, thermal strains, geometric nonlinearities, and multiple contacts, often appear as also nonlinear and can only be reduced to linear ones by introducing appropriate simplifications and assumptions. Nowadays, high accuracy in predicting the operating conditions and behavior of contemporary mechanical systems is also required. This leads to further complexity of models and simulations of the investigated complex mechanical systems. From the perspective of using validated approximate methods, such as FEA, the required knowledge of both the modeled systems and the modeling approaches is exceptionally high. To illustrate the problems that may arise when modeling such systems, as well as the approaches developed for solving complex mechanical problems with coupled nonlinear phenomena, including contact, this paper presents and discusses various case studies that the author has solved in previous years [1-4], as shown in Figure 1. An original approach in developing highly accurate and less time-consuming models for FEA based on controlled and precisely tailored models built from the bottom-up will be presented, meaning that FEA models are bottom-up developed to ensure accuracy, fidelity, and efficiency, and simultaneously adapted to the planned simulations from the very beginning.

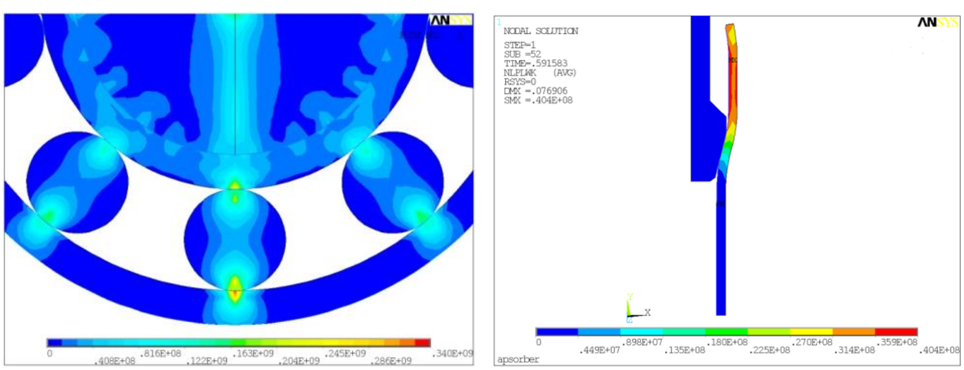

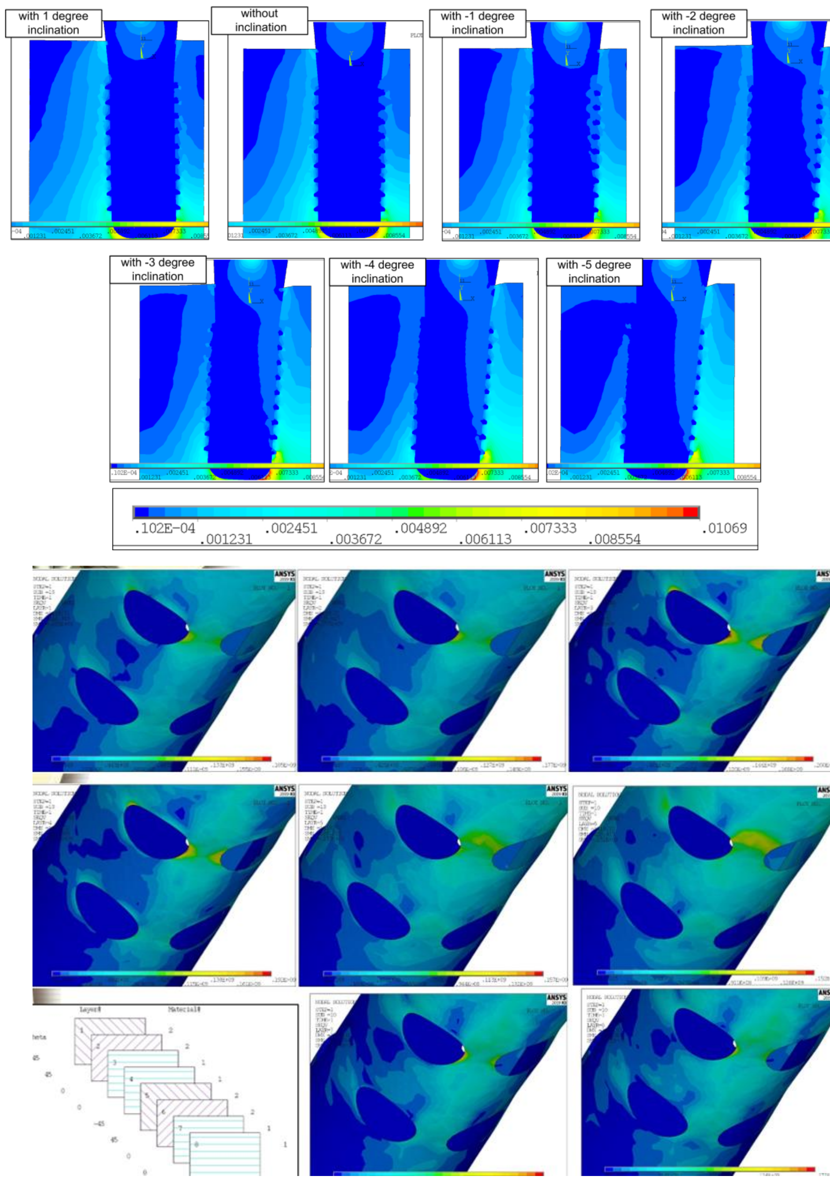

Fig. 1. Von Mises stress distribution for coupled nonlinear mechanical problems including contact – case studies

Key words: coupled problems, solid mechanics, nonlinearity, contact phenomena, FEA

References

[1] Atanasovska I. et al., *Damage Factor Calculation for Condition Monitoring of Rolling Bearings*, Arabian Journal for Science and Engineering, Vol. 48, 3181–3194, 2023.

[2] Atanasovska I., *The Mathematical Phenomenological Mapping in Nonlinear Dynamics of Spur Gear Pair and Radial Ball Bearing due to the Variable Stiffness*, International Journal of Non-linear Mechanics, Vol. 73, 114-120, 2015.

[3] Sarac D., Atanasovska I. et al., *Numerical Study of the Effect of Dental Implant Inclination*, Journal of the Serbian Society for Computational Mechanics, Vol. 11, 63-79, 2017.

[4] Milic M. et al., *Mathematical modeling and experimental investigation of a composite beam failure - Case study*, Proc.IMEng, Part C: J. Mech Eng Sci, Vol 238 (3), 654-665, 2024.

10th International Congress of the Serbian Society of Mechanics
Niš, Serbia, June 18-20, 2025

M.1.2
Extended abstract

SHEAR STRIPING PHENOMENA IN VISCOELASTIC LIQUID CRYSTAL ELASTOMERS

Milan Cajić[1] [0000-0001-5513-0417], **Danilo Karličić**[1] [0000-0002-7547-9293], and **Stepa Paunović**[1] [0000-0001-9785-4851]

[1] Mathematical institute of the SASA, Serbia, email: mcajic@mi.sanu.ac.rs

Abstract. Liquid crystal elastomers (LCEs) are unique materials that exhibit distinctive properties due to their dual nature—combining the orientational characteristics of liquid crystals with the elasticity of polymers. In monodomain samples, the mesogens, which are attached to polymer chains and modeled as a unit nematic director, align along a single preferred direction. A key feature of LCEs is their response to mechanical stretching, displaying semi-soft elasticity and the formation of stripe domains under specific conditions. Experimental observations indicate that in stripe domain patterns, mesogens in adjacent stripes rotate by the same angle but in opposite directions. This study seeks to model the formation of stripe domains in viscoelastic nematic LCEs subjected to mechanical stretch and high strain rates. The approach employs a dynamic three-dimensional mixed finite element formulation in the FeniCSx environment.

Keywords: Shear striping; Nematic LCEs; Viscoealsticity; Semi-soft elasticity;

1. Model formulation and numerical results

Nematic liquid crystal elastomers form an important class of highly responsive multifunctional materials combining the anisotropy and self-organisation of liquid crystal mesogens with the flexibility of cross-linked polymeric networks [1]. To observe shear stripes and semi-soft elasticity one needs to adopt improved models acounting both of these phenomena.To define an incompressible model of viscoelastic nematic LCE we adopt the next additive strain-energy function [2]:

$$\Psi_R = \Psi_R^{lce+fra+neq} = \frac{\mu_1}{2}\left(\mathrm{tr}\overline{\mathbf{C}}-3\right) + \sum_{\alpha}\frac{1}{2}\mu_{neq}^{(\alpha)}\left(\mathrm{tr}\bar{\mathbf{C}}^{e(\alpha)}-3\right) + \tag{1}$$

$$\frac{\mu_2}{2}\left(\mathbf{A}:\mathbf{A}-3\right) + \frac{JK_f}{2}\|\nabla\mathbf{n}\mathbf{F}^{-1}\|^2 + \frac{K}{2}(\mathrm{J}-1)^2,$$

where $\alpha = 1,2,3$, $\mu_{1,2}$ are equilibrium shear coefficents, $\mu_{neq}^{(\alpha)}$ are non-equilibrium shear coefficents, $\mathbf{F}$ is the deformation gradient, $\overline{\mathbf{C}}$ is isochoric part of the right Cauchy-Green deformation tensor, $\mathbf{A} = \mathbf{G}^{-1}\mathbf{F}\mathbf{G}_0$ with natural deformation tensor $\mathbf{G}$ defined as $\mathbf{G} = a^{-1/6}\mathbf{I} + \left(a^{1/3} - a^{-1/6}\right)\mathbf{n}\otimes\mathbf{n}$, $\mathbf{n} = [\sin\theta, \cos\theta, 0]$ is the director field vector defining the orientation of LCE mesogens as a function of angle θ (see Fig. 1(a)) , $\mathbf{G}_0$ is the natural deformation tensor for the initial nematic state.

The weak form of the system equations implemented in FEniCSx are obtained as:

$$\int_{\mathbf{V}_R}\left(\mathbf{P}^{\mathrm{tot}} - pJ\mathbf{F}^{-T}\right) : Grad\mathbf{w}_1 dv_R = 0, \tag{2}$$

$$\int_{\mathbf{V}_R} -\Sigma : Grad\mathbf{w}_2 + \phi\cdot\mathbf{w}_2 dv_R = 0, \quad \int_{\mathbf{V}_R}(J-1)\, w_4 dv_R = 0. \tag{3}$$

where $\mathbf{P}^{\text{tot}}$ is the total first Piola–Kirchhoff stress tensor, Σ is the couple stress tensor, ϕ is the internal orientation body force and $(\mathbf{w}_1, w_2, w_3)$ are test function corresponding to known field variables $(\mathbf{u}_1, p, \theta)$.

Figure 1a shows a 2D liquid crystal elastomer (LCE) model in the nematic state subjected to quasi-static uniaxial stretching perpendicular to the nematic director orientation. Figure 1b depicts the formation of multiple stripe domains after finite deformation of the LCE sample, where the red and blue regions represent distinct values of the director angle θ, illustrating the striping pattern. The implemented model in FEniCSx demonstrates the ability to capture both stripe formation and semi-soft elasticity. However, these combined elastic and micro-structural instabilities can lead to numerical convergence issues. By incorporating a viscoelastic model, we achieve two key improvements: (1) a more realistic representation of the elastomer matrix's viscoelastic behavior and (2) enhanced stability in the finite element method (FEM) simulations.

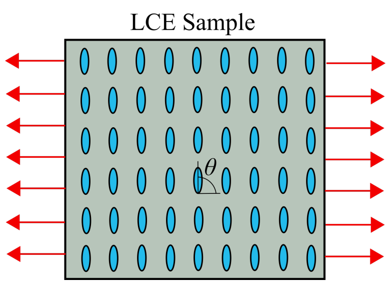

(a) Illustration of uniaxial stretch

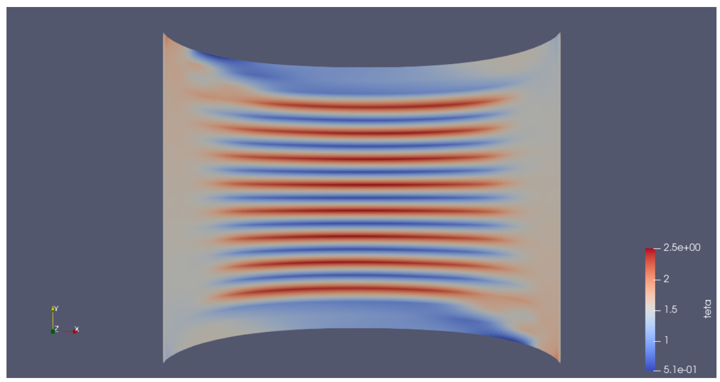

(b) Formaton of stripe domains

Figure 1: (a) Schematic representation of the 2D nematic LCE model, illustrating mesogen alignment and the definition of characteristic angles. (b) Visualization of the shear striping phenomenon in the 2D LCE model, highlighting regions of localization.

2. Concluding remarks

In conclusion, the developed viscoelastic-nematic LCE model successfully captures both the striping and semi-soft elasticity phenomena characteristic of nematic LCEs. The implemented FEM framework in FEniCSx exhibits robust stability and convergence, even under large deformation increments and coarse mesh discretizations. These results are promising for future studies on more complex phenomena, such as dynamic wrinkling and creasing deformations in nematic LCEs.

References

[1] Concas, F.& Groß, M. Analysis of stripe domains in nematic LCEs by means of a dynamic numerical framework. *C*ontinuum Mechanics and Thermodynamics. **37** pp. 1-16 (2025)

[2] Poudel, R., Sengül, Y. & Mihai, L.A. Deformation localisation in stretched liquid crystal elastomers. *M*echancis of Soft Materials. **6**, pp. 1-14 (2024)

M.1.3

Abstract

MACHINE-LEARNING-BASED OPTIMIZATION DESIGN OF COMBINED SEISMIC METAMATERIALS

Zhuojia Fu [1[0000-0002-3231-1597]], **Yu Ding**[1], **Hanshu Chen**[1]

[1] College of Mechanics and Engineering Science,
Hohai University, Nanjing 211100, China
e-mail: paul212063@hhu.edu.cn

Abstract:

Seismic metamaterials represent artificially engineered periodic structures capable of effectively suppressing Rayleigh waves that threaten building integrity, demonstrating significant potential in seismic protection applications. However, the rapid inverse design of low-frequency broadband bandgaps remains a critical challenge for engineering implementation. This study develops a collaborative optimization framework integrating Q-Learning algorithms and Kriging surrogate models, successfully overcoming performance limitations in low-frequency and broadband scenarios while achieving precise co-regulation of first bandgap width and initial frequency. Considering the inherent uncertainties in geological parameters, material property variations, and structural complexity, we introduce a multi-source stochastic factor coupling analysis technique to systematically evaluate the reliability of metamaterial systems.

Key words: seismic metamaterials; inverse design; structural reliability analysis

10th International Congress of the Serbian Society of Mechanics
Niš, Serbia, June 18-20, 2025
M.1.4
Extended abstract

A FINITE ELECTRO-VISCOELASTIC MODEL FOR NEMATIC LIQUID CRYSTAL ELASTOMERS

Danilo Karličić[1] [0000-0002-7547-9293], **Milan Cajić**[2] [0000-0001-5513-0417], and **Stepa Paunović**[3] [0000-0001-9785-4851]

[1]Mathematical institute of the SASA, Serbia, email: danilok@mi.sanu.ac.rs
[2]Mathematical institute of the SASA, Serbia, email: mcajic@mi.sanu.ac.rs
[3]Mathematical institute of the SASA, Serbia, email: stepa.paunovic@mi.sanu.ac.rs

Abstract. This work is dedicated to the computational implementation of a finite strain model of electro-viscoelastic interactions occurring in dielectric Nematic Liquid Crystal Elastomers (NLCEs), including key phenomena such as Maxwell's stress, director rotation, deformations, the electric Fréedericksz transition, and dissipation. By integrating the framework of continuum mechanics and Maxwell's equations, the governing equations for dielectric NLCEs are systematically derived. This approach ensures the formulation of thermodynamically consistent constitutive relations, capturing the coupled electro-mechanical behavior and time-dependent viscoelastic response. Special attention is given to the finite element implementation in the FEniCSx software, focusing on the electro-viscoelastic defomations and instabilities. The study explores various deformation modes that may emerge during Fréedericksz transition phenomena, with particular focus on the bending actuation of a bilayer sample.

Keywords: Nematic elastomers; Visco-hyperelasticity; Finite deformation; Fréedericksz transition;

1. Model formulation, numerical results and conclusions

In order to develop continuum model of LCE with included nematic micro-structure which depend on director filed, we adopt principle of virtual power [1], where following equations represent balance laws in material description:

$$\mathrm{Div}\mathbf{P}+\mathbf{b}_R=\rho_R\ddot{\mathbf{u}},\quad \mathrm{Div}\Sigma+\pi=\mathbf{0},\quad \mathrm{Skw}\left(\mathbf{P}\mathbf{F}^T-\pi\otimes\mathbf{n}+\Sigma(\nabla\mathbf{n})^T\right)=\mathbf{0}, \tag{1}$$

in which $\mathbf{P}$ is the first Piola-Kirchhoff stress tensor, $\mathbf{u}$ is the displacement vector, Σ is the couple stress tensor, π is the internal orientation body force, $\mathbf{n}$ is the director field vector and $\mathbf{F}$ is the deformation gradient. To complete the system of governing equations we include Maxwell's equations, $Div\tilde{\mathbf{D}}=\mathbf{0}$ and $Curl\tilde{\mathbf{E}}=\mathbf{0}$. Applying the second law of thermodynamics and assuming the additive property of Helmholtz free energy function ψ_R, the constitutive equations are [2]:

$$\mathbf{P}=J\left[\sum_{\alpha=0}^{M}J^{e(\alpha)-1}\frac{\partial\psi_R^{(\alpha)V-E}}{\partial\mathbf{F}^{e(\alpha)}}\mathbf{F}^{e(\alpha)T}\right]\mathbf{F}^{-T}+\frac{\partial\psi_R^{NC}}{\partial\mathbf{F}}+\frac{\partial\psi_R^{Frank}}{\partial\mathbf{F}}+\frac{\partial\psi_R^{MW}}{\partial\mathbf{F}}, \tag{2}$$

$$\pi=\frac{\partial\psi_R}{\partial\mathbf{n}},\quad \Sigma=\frac{\partial\psi_R}{\partial\nabla\mathbf{n}},\quad \tilde{\mathbf{E}}=\frac{\partial\psi_R}{\partial\tilde{\mathbf{D}}},$$

and dissipation inequality as $\sum_{\alpha=1}^{M}\mathbf{M}^{e(\alpha)}:\mathbf{D}^{v(\alpha)}\geq 0$, where $\mathrm{J}=\det\mathbf{F}$ and $J^{e(\alpha)}=\det\mathbf{F}^{e(\alpha)}$. The term $\tilde{\mathbf{E}}=-\nabla\phi$ represents the electric field and $\tilde{\mathbf{D}}=\det(\mathbf{F})\mathbf{F}^{-1}\mathbb{D}_n\mathbf{F}^{-T}\tilde{\mathbf{E}}$ is the electric displacement, ϕ is the electrostatic field, all given in the referential configuration.

The numerical implementation of the weak form of our system equations [1] and [2] is performed in FEniCSx, where weak form equations are given as

$$\int_{\mathscr{P}} \left(\mathbf{P} - pJ\mathbf{F}^{-T}\right) : \mathrm{Grad}\mathbf{w}_1 + \rho_R \ddot{\mathbf{u}} dv_R = 0, \quad \int_{\mathscr{P}} -\Sigma : \mathrm{Grad}\mathbf{w}_2 + \pi \cdot \mathbf{w}_2 dv_R = 0, \tag{3}$$

$$\int_{\mathscr{P}} \tilde{\mathbf{D}} \cdot \mathrm{Grad} w_3 dv_R = 0, \quad \int_{\mathscr{P}} \left(J - 1 + \frac{p}{K}\right) w_4 dv_R = 0,$$

and evolution equation for viscoelastic flow $\dot{\mathbf{C}}^{v(\alpha)} = \frac{1}{\tau^{\alpha}} J^{-2/3} \left[\mathbf{C} - \frac{1}{3}(\mathbf{C} : \mathbf{C}^{v(\alpha)-1})\mathbf{C}^{v(\alpha)}\right]$.

Figure 1 depicts the electro-mechanical deformations of the 2D NLCE sample, highlighting the electric Fréedericksz transition and finite bending deformation. The initial director field is assumed to be perpendicular to the applied electrostatic field. Fig. 1a shows how an increasing electric field intensity causes a rotation of mesogen directors, which all gradually aligns with the electric field direction, leading to the sample contraction [3]. This Fréedericksz transition is particularly useful for actuation devices, especially in bilayer structures. The bending actuation mode, depicted as a cantilever beam in Fig. 1 b), reveals how a weak electric field can trigger substantial deformation.

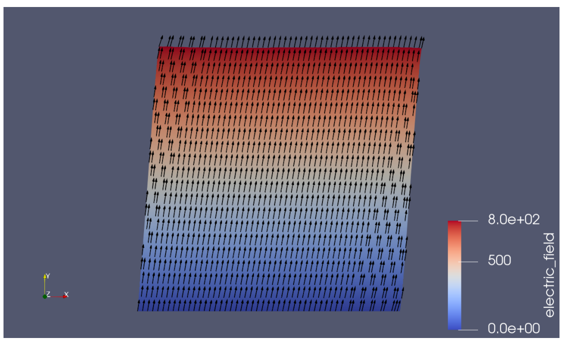

(a) Electric Fréedericksz transition

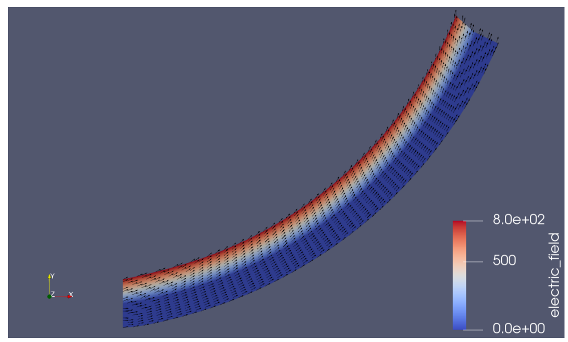

(b) Bending deformation of DLCE

Figure 1: Snapshots of the finite electro-viscoelastic deformation of the 2D DLCE sample, with director field reorientation and distribution of electic potential. The results are visualized in ParaView.

To summarize the results of this study, we have: (i) developed a thermodynamically consistent model of viscoelastic NLCEs subjected to an electrostatic field, (ii) demonstrated the electric Fréeder- icksz transition, and (iii) analyzed the finite bending actuation mode in a bilayer sample.

References

[1] Wang, Z., Chehade, A., Govindjee, S. & Nguyen, T. *A nonlinear viscoelasticity theory for nematic liquid crystal elastomers*. Journal Of The Mechanics And Physics Of Solids, **163** pp. 104829, 2022.

[2] Li, D., Peng, Z., Chen, Y. & Huo, Y. *An extended neo-classical model for nematic elastomers with transversely isotropic semisoft elasticity.* Journal Of The Mechanics And Physics Of Solids, **199** pp. 106077, 2025.

[3] Jiang, Z., Liu, Q., Xiao, Y. & Zhao, Y. *Liquid crystal elastomers for actuation: A perspective on structure-property-function relation.* Progress In Polymer Science, pp. 101829, 2024.

10th International Congress of the Serbian Society of Mechanics
Niš, Serbia, June 18-20, 2025

M.1.5
Extended abstract

SIMULATION OF THERMAL FIELD IN MASS CONCRETE STRUCTURES WITH COOLING PIPES BY THE LOCALIZED MESHLESS METHOD

J. Lin[1] [0000-0002-9596-9601] and **Y.X. Hong**[2] [0000-0001-9077-4808]

[1]Hohai University, College of Mechanics and Engineering Science, China, email: linji@hhu.edu.cn

[2]Hohai University, Department of Mechanical and Electrical Engineering, China, e-mail: hongyxg@126.com

Abstract. During the construction of mass concrete structures, embedded water pipe cooling systems are critical for mitigating thermal cracking and ensuring structural integrity. Accurate prediction of the thermal field within these structures is essential for optimizing cooling system design and minimizing thermal stress risks. In this study, a localized meshless collocation method based on multiquadric radial basis functions (MQ-RBF) is proposed to simulate the thermal field evolution in concrete structures integrated with water pipe cooling systems. The method introduces a novel adaptive strategy for dynamically determining shape parameters in MQ-RBF, enhancing numerical stability and spatial discretization accuracy. By employing a localized domain discretization scheme, the algorithm generates sparse coefficient matrices, significantly reducing memory requirements by compared to global meshless methods while maintaining computational precision. The framework is rigorously validated through benchmark cases, including a complex 2D scenario with five cooling pipes and a 3D simulation incorporating time-dependent boundary conditions. Some results can be seen in Figure 1 and Figure 2.

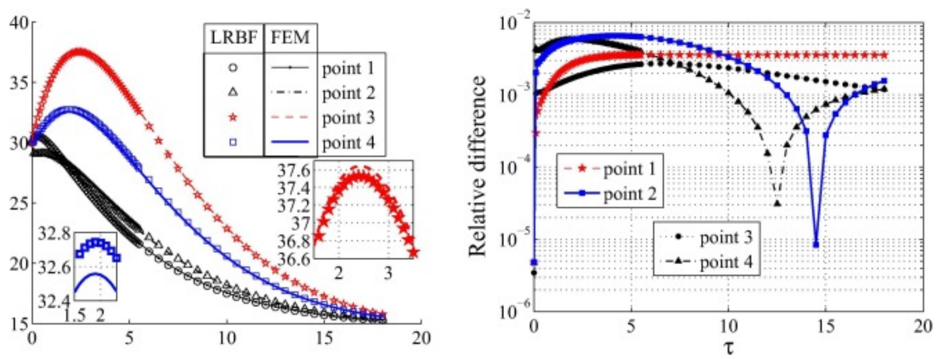

Figure 1: Comparison of the numerical solutions obtained by the proposed LRBFCM and the FEM, where the FEM contains 10813 degrees of freedom

In all examples[1, 2], the Neumann boundary conditions are taken into account. We have found that the results in the sub-domain of Neumann boundary parts should be simulated by using more points. Usually, the local points should be more than 20 for two-dimensional problems and a bit more for three-dimensional problems. Compared with the analytical results or the results obtained by the FEM, all tested examples demonstrate that the proposed LRBFCM could provide accurate

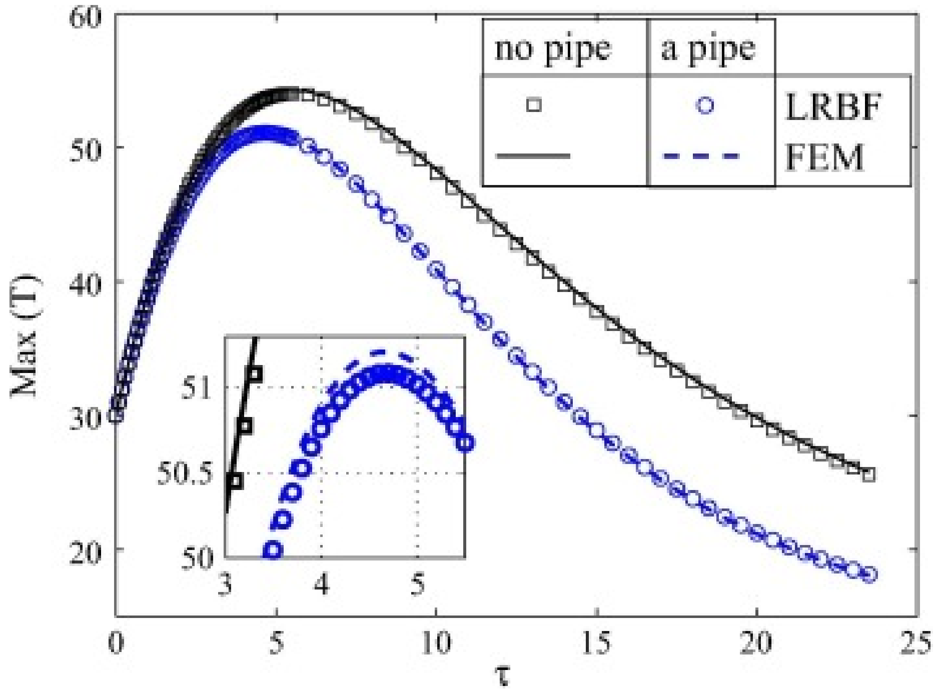

Figure 2: The numerical solutions of max(T) versus time with a pipe or no pipe obtained by the proposed LRBFCM.

predictions. The convergence, stability and efficiency of the present scheme also are presented in these examples. The obtained numerical results indicate that the proposed LRBFCM has great potential for the design of the water pipe cooling system.

Keywords: Mass concrete; Cooling system; Localized method

References

[1] Hong Y., Lin J., Chen W., *Simulation of thermal field in mass concrete structures with cooling pipes by the localized radial basis function collocation method*, International Journal of Heat and Mass Transfer, Vol. 129, 449-459, 2019.

[2] Hong Y., Lin J., Chang A., *Numerical analysis of heat transfer in mass concrete embedded with multi-pipes via a fast double-layer model based on generalized finite difference method*, International Communications in Heat and Mass Transfer, Vol. 158, 107911, 2024.

10th International Congress of the Serbian Society of Mechanics
Niš, Serbia, June 18-20, 2025

M.1.6
Extended abstract

APPLICATION OF SOFT MREs FOR MAGNETICALLY INDUCED ACTUATION WITH IMPLEMENTATION IN FEniCSx

Stepa Paunović[1] [0000-0001-9785-4851], **Danilo Karličić**[1] [0000-0002-7547-9293], and **Milan Cajić**[1] [0000-0001-5513-0417]

[1]Mathematical institute of the SASA, Serbia, email: stepa.paunovic@mi.sanu.ac.rs

Abstract. In this contribution a model for a soft magnetic magnetorheological elastomer material is derived and numerically applied for magnetically induced actuation of a polymeric cantilever beam. The model encompasses both microstructural details and macroscopic behaviour of MREs through continuum mechanics framework, including nonlinear visco-elasticity and full magneto-mechanical coupling, accounting for complex material phenomena such as magnetostriction. The governing equations are derived following standard thermodynamically consistent procedure, by applying the virtual power principle for an isothermal case, arriving at the suitable free energy expressions and the corresponding constitutive relations for magneto-active materials. The model is validated against the results from the literature, and then applied to analyse actuation of a polymeric cantilever beam by introducing soft-MRE patches and varying the surrounding magnetic field. The results show that soft-MREs are highly suitable for magnetic actuation and soft-robotic applications.

Keywords: Magnetoactive actuators, Magnetorheological elastomers, Finite magneto-viscolasticity.

1. Introduction and problem statement

If small particles of a magnetic material are embedded in elastomeric matrix, such compound materials exhibits large magnetostriction effect and are knows as magnetorheological elastomers (MRSs). Depending on the magnetic particles used, MREs can be ”soft-magnetic” and ”hard-magnetic”. Soft-magnetics have narrow magnetic hysteresis loop and are highly responsive to variations in the surrounding magnetic field, while hard-magnetics have much wider magnetic hysteresis loop and require higher magnetic field intensity changes to modify their magnetization. Therefore, hard-MRSs are better applied in structures with magnetically-dependent shape, while soft-MREs are more suitable for actuation purposes. In this contribution, a mathematical model for a soft-MRE actuator is derived and numerically implemented to illustrate its robustness in application practice.

2. Mathematical and numerical modelling

Material model is developed using the continuum mechanics framework, by assuming nonlinear viscoelastic properties with full magneto-mechanical coupling, thus obtaining a macroscopically homogeneous material, while accounting for soft-MRE microstructure. The governing equations are derived following the thermodynamics constitutive methodology [1], by applying the virtual power principle for an isothermal case, while also including inertial effects, since these are vital when dealing with actuation applications. The viscoelastic model proposed by Anand et. al. [2] has been adopted, with $\alpha = 1, \ldots, M$, $M = 3$ dissipation branches. With $\mathbf{G}$ as the shear modulus, K the bulk modulus, $J = \det(\mathbf{F})$, $\mathbf{C} = \mathbf{F}^T\mathbf{F}$, $I_1 = \mathrm{tr}(\mathbf{C})$, μ_0 the magnetic permeability, $\mathbf{h}$ the magnetic field,

m_s the magnetization saturation limit and χ the magnetic susceptibility, the total free energy ψ_R of the material can be expressed in the following form:

$$\psi_R = \psi_R^{elastic} + \psi_R^{visco} + \psi_R^{field} + \psi_R^{magnetization} = \frac{\mathbf{G}_{eq}}{2}(\bar{I}_1 - 3) + \frac{1}{2}K(J-1)^2$$
$$+ \sum_{\alpha=1}^{M} \frac{\mathbf{G}_{neq}^{(\alpha)}}{2}(\bar{I}_1^{e(\alpha)} - 3) + J\left(-\mu_0 \frac{1}{2}\mathbf{h}_R \cdot \mathbf{C}^{-1}\mathbf{h}_R\right) + J\left(-\mu_0\left[\frac{m_s^2}{\chi}\ln\left(\cosh\left(\frac{\chi}{m_s}\sqrt{\mathbf{h}_R \cdot \mathbf{C}^{-1}\mathbf{h}_R}\right)\right)\right]\right) \tag{1}$$

The appropriate constitutive relations were derived and the model was also validated against other recent numerical models [3], which were verified with experimental results from the literature. This material model has been numerically implemented in FEniCSx software to analyse a polymer cantilever beam actuated by two soft-MRE patches connected to it from both sides. The actuation is achieved through varying the surrounding magnetic field and the results are shown in Figure 1.

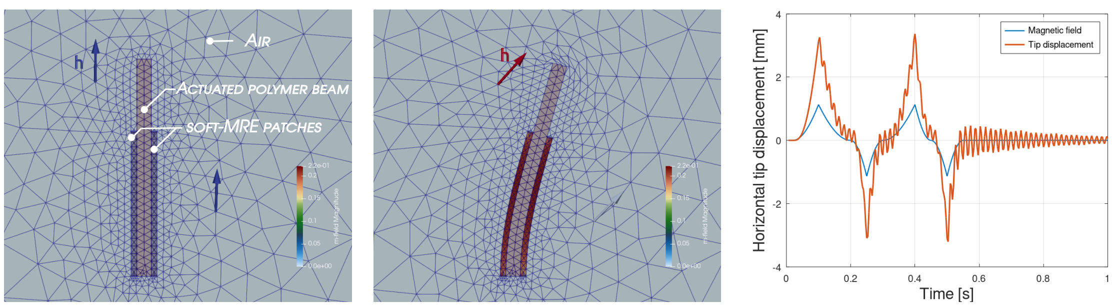

(a) Numerical model - initial state (b) Actuation by magnetic field (c) Time response of the actuated beam

Figure 1: Soft-MRE actuator. a) FEM model of a polymer cantilever with MRE patches, b) beam actuation through the varying magnetic field c) Horizontal tip displacement of the actuated beam

3. Concluding remarks

In this contribution we have derived a mathematical model for a viscoelastic soft-magnetic MRE material and applied it to analyse of a magnetic actuator of a polymeric beam. The results show that soft-MREs are very responsive to magnetic field changes and that MRE patches can be readily used for actuation purposes. Special attention should be given to problem of control and mitigating inertial effects, but this is beyond the scope of the presented contribution and is left for future studies.

References

[1] Danas, K., *A unified theoretical modeling framework for soft and hard magnetorheological elastomers*, In: Electro-and Magneto-Mechanics of Soft Solids: Constitutive Modelling, Numerical Implementations, and Instabilities, Cham: Springer Nature Switzerland, 2024.

[2] Stewart, E.M. and Anand, L., *A large deformation viscoelasticity theory for elastomeric materials and its numerical implementation in the open-source finite element program FEniCSx*, International Journal of Solids and Structures, Vol. 303, 113023, 2024.

[3] Stewart, E. M., and Anand, L., *Magnetostriction of soft-magnetorheological elastomers*, Journal of the Mechanics and Physics of Solids, Vol. 194, 105934, 2025.

10th International Congress of the Serbian Society of Mechanics
Niš, Serbia, June 18-20, 2025

M.1.7
Extended abstract

Inertial Amplification Effects on Wave Dispersion in Metastructures with Elastic and Rigid Segments

Nevena Rosić[1] [0000-0002-9683-3079], **Danilo Karličić**[2] [0000-0002-7547-9293], and **Mihailo Lazarević**[1] [0000-0002-3326-6636]

[1]University of Belgrade, Faculty of Mechanical Engineering, email: nrosic@mas.bg.ac.rs,mlazarevic@mas.bg.ac.rs

[2]Mathematical Institute of the Serbian Academy of Sciences and Arts, e-mail: danilok@mi.sanu.ac.rs

Abstract. We investigate a metastructure made from unit cells with coaxial Timoshenko beams and rigid bodies, and an inertial amplifier attached at the left end. The inertial amplification mechanism is consisted of two auxiliary masses which are connected with rigid bars to both the beam and main mass. Using a combination of the transfer matrix method and the spectral element method, we examine how changing one design parameter affects the dispersion properties. Inertial amplification induces low-frequency wave attenuation without increasing system mass, which is one of the key challenges in metastructure design. These findings offer an effective strategy for wave control in periodic structures composed of elastic and rigid segments, with potential applications in lightweight acoustic insulation and seismic isolation for structures such as buildings and bridges.

Keywords: inertial amplifier, periodic structure, frequency band structure, spectral element method, transfer matrix method

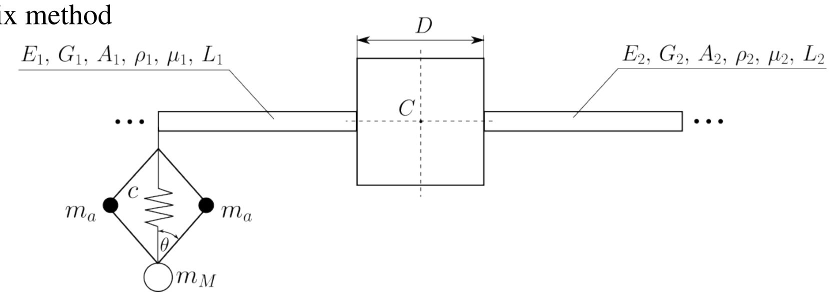

Figure 1: Unit cell consisted of two coaxial beams with a rigid body between them, and an inertial amplifier attached at the left end.

The point force resulting from the inertial amplifier (IA) acting at the attachment point is [1]:

$$f = -\frac{(c - b\omega^2)m_M\omega^2}{c - b\omega^2 - m_M\omega^2}w, \quad b = m_0\frac{\cot^2\theta - 1}{2}, \tag{1}$$

where w is the transverse displacement of the beam at the attachment point, m_M is the main mass of IA, c is the spring stiffness, ω is angular frequency, b is equivalent inertance, m_0 is auxiliary mass and θ is the angle between the spring and a rigid bar, as depicted in Fig. 1. By using the transfer matrix method and applying the Floquet-Bloch theorem to two consecutive unit cells, we obtain the dispersion relation (EIP) [2], a function of dimensionless wavenumber and frequency $f(\tilde{\kappa}, \Omega) = 0$.

The EIP is solved over a range of frequencies to obtain the dispersion diagram [2]. By employing the spectral element method for a system of 20 unit cells with a unit force acting at one end, and solving for displacements, we also obtain the frequency response function (FRF), in logarithmic scale [3]. The results shown in Fig. 2 indicate that attenuation bands due to Bragg scattering (BSBGs) can be expanded by up to 50% across all frequency ranges. Furthermore, we observe a local resonance band gap (LRBG) at a lower frequency range, controlled by the chosen design parameter instead of system mass. A near-coupling effect between local resonance and Bragg scattering band gaps can also be achieved, leading to the formation of a wider low-frequency band gap.

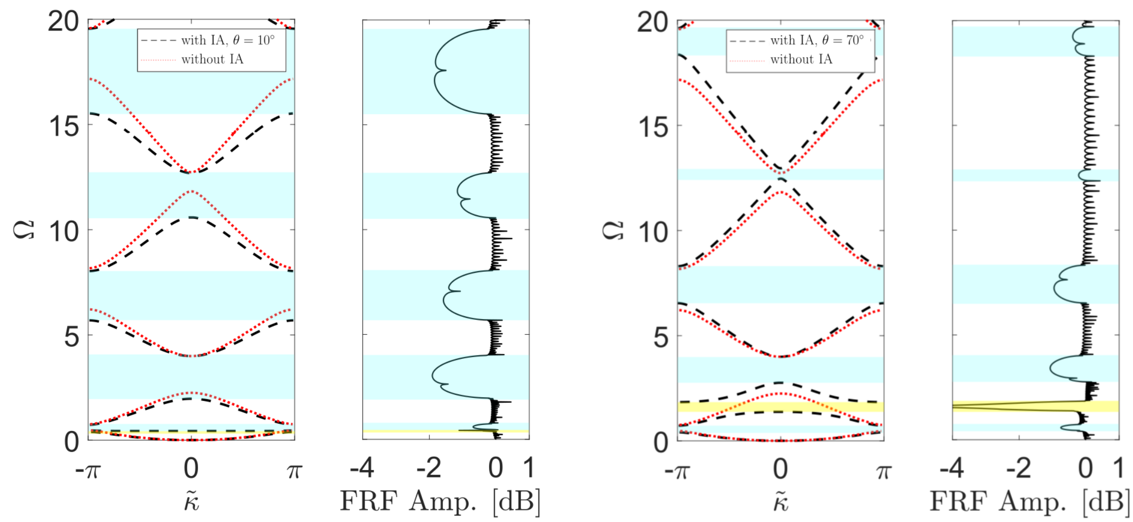

(a) (b)

Figure 2: Dispersion diagram (red, dotted) and frequency responce function, when: a) $\theta = 10^\circ$, b) $\theta = 70^\circ$, compared to results derived without the inertial amplifier (black, dashed line). BSBGs are designated in blue and LRBGs are desgnated in yellow.

Acknowledgement. This research has been supported by the research grant of the Serbian Ministry of Science, Technological Development and Innovations, through the Mathematical Institute SANU and grant No. 451-03-137/2025-03/200105 from 4.2.2025. This support is gratefully acknowledged.

References

[1] Frandsen M.M.N., Bilal R.O., Jensen S.J., Hussein I.M., *Inertial amplification of continuous structures: Large band gaps from small masses*, Journal of Applied Physics, Vol. 119, 124902, 2016.

[2] Rosic N., Karlicic D., Cajic M., Adhikari S., Lazarevic M., *Wave propagation in tailored metastructures consisting of elastic beams and rigid bodies*, Philosophical Transactions of the Royal Society A, Vol. 382, 20230362, 2024.

[3] Wang Z.-C., Yang W.-J., Yung K.-V., *A transfer matrix method-based closed-form solution of sensitivities of dynamic properties and FRF for multi-span pipes under complex boundary conditions*, Mechanical Systems and Signal Processing, Vol. 198, 110428, 2023.

10th International Congress of the Serbian Society of Mechanics
Niš, Serbia, June 18-20, 2025
M.1.8

Extended abstract

UPSCALING ANOMALOUS TRANSPORT IN FRACTURED MEDIA USING FRACTIONAL ADVECTION-DISPERSION EQUATION MODEL

HongGuang Sun[1][0000-0002-8422-3871]

[1] The National Key Laboratory of Water Disaster Prevention, College of Mechanics and Engineering Science, Hohai University, Nanjing, China
e-mail: shg@hhu.edu.cn

Abstract:

This study develops a physical model to predict how pollutants move through fractured aquifers, particularly focusing on the behavior of solutes in fractures that trap water. We combine detailed simulations and simplified models to predict pollutant behavior in fractured rock systems. This is a first step toward improving how we predict pollutant transport in real-world fractured aquifer systems.
Key words: Upscaling method, Anomalous diffusion, Fractal fracture, Fractional derivative

1. Main content

Complex structures in fractures and the rock matrix, which are difficult to map exhaustively at the local scale, can dominate contaminant transport in fractured aquifers. An upscaled model is therefore needed to effectively characterize solute transport in a heterogeneous fracture-matrix system on a large spatiotemporal scale. Most existing upscaling methods, however, do not specifically quantify the influence of matrix diffusion and fracture surface roughness on solute transport, and their upscaling parameters are usually difficult to obtain. To fill this knowledge gap, first, a time fractional advection-dispersion equation (t-FADE) model, which can accurately describe solute transport in straight fractured media, is proposed. Next, the influence of local roughness and tortuosity of fractures on transport is comprehensively considered by introducing trend lines. The t-FADE is used to characterize solute transport in each segment of rough fractures, and an upscaled model describing solute transport in rough fractures is established by averaging the governing equations of each segment. Finally, a time dependent attenuation function is introduced into the convolutional function of the upscaled model to overcome the error caused by overlapping diffusion regions. Model comparison and analysis reveal that the rough wall of fractures strengthens matrix retention capacity, leading to a delayed peak of the breakthrough curve (BTC) with a lower peak concentration, which can be quantitatively characterized by the ratio of the actual fracture length to its longitudinal length; however, the fracture structure does not affect the solute BTC's trailing concentration at the constant fracture mean flow velocity without considering mechanical dispersion, so the relatively simple straight fracture model can be used to describe the trailing stage of transport in rough-walled fracture media.

Pollutant transport in discrete fracture networks (DFNs) exhibits complex dynamics that challenge reliable model predictions, even with detailed fracture data. To address this issue, this study derives an upscaled integral-differential equation to predict transient anomalous diffusion in two-dimensional (2D) DFNs. The model includes both transmissive and dead-end fractures (DEFs), where stagnant water zones in DEFs cause non-uniform flow and transient sub-diffusive transport, as shown by both literature and DFN flow and transport simulations using COMSOL. The upscaled model's main parameters are quantitatively linked to fracture properties, especially the probability density function of DEF lengths. Numerical experiments show the model's accuracy in predicting the full-term evolution of conservative tracers in 2D DFNs with power-law distributed fracture lengths and two orientation sets. Field applications indicate that while model parameters for transient sub-diffusion can be predicted from observed DFN distributions, predicting parameters controlling solute displacement in transmissive fractures requires additional field work, such as tracer tests. Parameter sensitivity analysis further correlates late-time solute transport dynamics with fracture properties, such as fracture density and average length. Potential extensions of the upscaled model are also discussed. This study, therefore, proves that transient anomalous transport in 2D DFNs with DEFs can be at least partially predicted, offering an initial step toward improving model predictions for pollutant transport in real-world fractured aquifer systems.

References

[1] Sun H.G., Lei D., Zhang Y., Qian J., and Yu X. *Predicting transient anomalous transport in two-dimensional discrete fracture networks with dead-end fractures,* Water Resources Research, Vol. 61, e2024WR038731, 2025.

[2] Lei D., Sun H.G., Zhang Y., Blaszczyk T., and Yu Z. *Upscaling solute transport in rough single-fractured media with matrix diffusion using a time fractional advection-dispersion equation*. Journal of Hydrology, Vol. 627, 130280, 2023.

M.1.9

Extended abstract

Data-driven diffusion law for multiscale dynamics in granular materials via an improved deep physical symbolic regression

Shengjie Yan[1][0009-0000-4426-9149], **Yingjie Liang**[1][0000-0002-3201-6969]

[1] College of Mechanics and Engineering Science, Hohai University, Nanjing, China

e-mail: liangyj@hhu.edu.cn

Abstract:
Symbolic regression (SR) is an alternative approach to unveil a suitable symbolic expression for diffusion law, connecting the experimental measurement, which has been used in engineering, economy, psychology, physics, chemistry, to derive mathematical and physical expressions. In granular cemented paste materials, diffusion dynamics no longer follows a simple diffusion law, but transfers to a two-stage multiscale diffusion process. In this study, the two-stage diffusion law, i.e., mean squared displacement (MSD) is estimated to characterize water and chloride diffusion in Friedel's salt without any empirical assumptions via an improved deep physical symbolic regression model, which combines the recurrent neural networks with the physical symbolic regression method. The MSD and time-averaged MSD are simulated to evaluate non-ergodicity of the multiscale diffusion in terms of the scaled Brownian motion, where the Fokker-Planck equation has a time dependent diffusion coefficient. The established two-stage diffusion law is verified by using the molecular dynamics simulated data of water and chloride diffusion in Friedel's salt under increasing hydration time and temperatures. This study provides an artificial intelligent method to detect the physical properties of granular cemented paste materials from the perspective of multiscale diffusion.

Key words: Recurrent neural network, Physical symbolic regression, Multiscale diffusion, Mean squared displacement, Ultraslow diffusion, Friedel's salt

Main results:

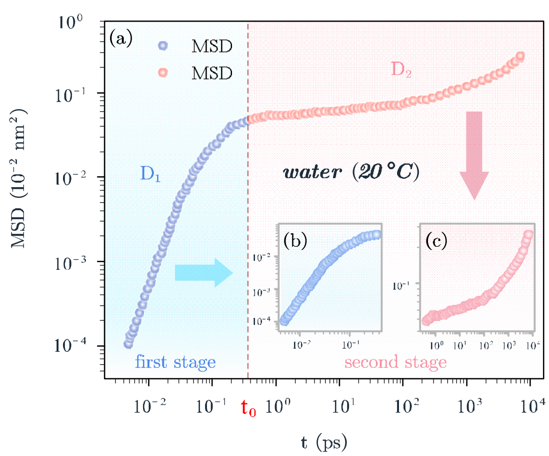

Fig. 1 Two stages of the MSD data in Friedel's salt.

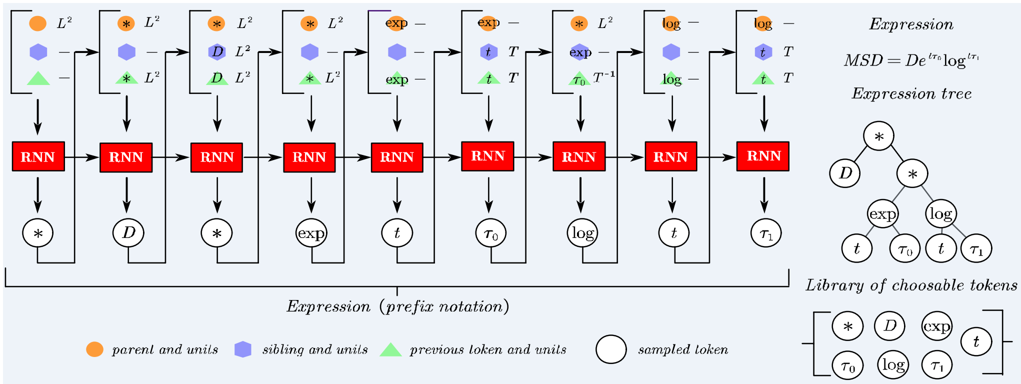

Fig. 2 Expression generation sketch at the first-stage diffusion process.

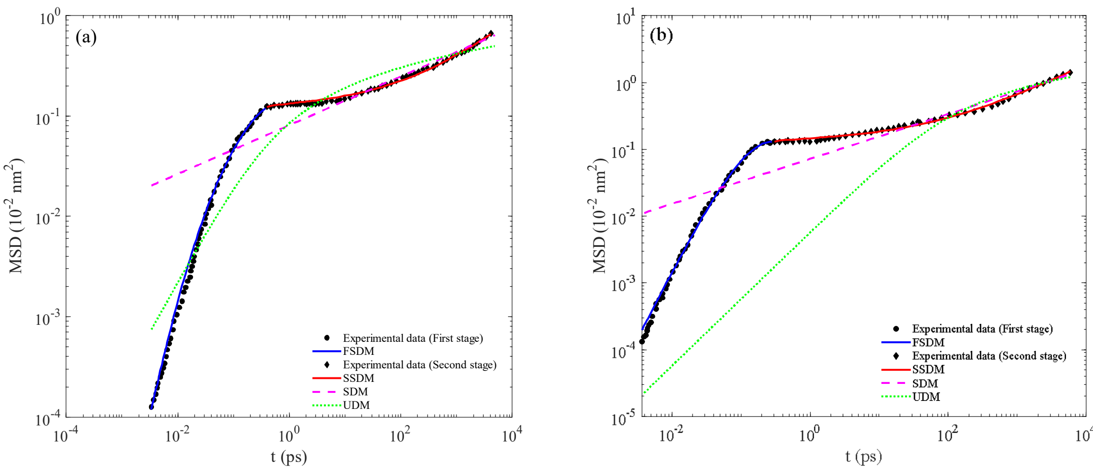

Fig. 3(a) Plots of subdiffusion model (SDM), ultraslow diffusion model (UDM), first-stage diffusion model (FSDM), and second-stage diffusion model (FSDM) in fitting the entire diffusion processes of water at 20 °C and Fig. 3(b) entire diffusion processes of water at 40 °C.

References

[1] Chen Z., Wang N. *Learning dynamics from coarse/noisy data with scalable symbolic regression*, Mech. Syst. Signal Pr. 2023 (190) 110147.

[2] Muller T., Hernandez A., Wang C. *Machine learning for interatomic potential models*, J. Chem. Phys. 2020 (152) (5) 050902.

[3] Schneider M., Beeres K., Coban L., et al. *Associations of non-symbolic and symbolic numerical magnitude processing with mathematical competence: a meta-analysis*, Developmental Sci. 2017 (20) (3) e12372.

[4] Chen J., Wang B., Zhang W., et al. *Study a decay and proton emission based on data-driven symbolic regression*, Comput. Phys. Commun. 2024 (304) 109317.

[5] Tenachi W., Ibata R., I.Diakogiannis F., *Deep symbolic regression for physics guided by units constraints: Toward the automated discovery of physical laws*, Astrophys. J. 2023 (959) (2) 99.

[6] Udrescu S., Tegmark M., *AI Feynman: A physics-inspired method for symbolic regression*, Sci. Adv. 2020 (6) (16) eaay2631.

Mini-Symposia 2: Turbulence

Organizer:
Đorđe Čantrak (Faculty of Mechanical Engineering, University of Belgrade, Serbia).

10th International Congress of the Serbian Society of Mechanics
Niš, Serbia, June 18-20, 2025
M.2.1
Extended abstract

PIV experiment in a scaled operating room with laminar airflow ventilation

Tani Angiero*[1] [0009-0003-9291-6314], **Stefano Discetti**[1] [0000-0001-9025-1505], and **Andrea Ianiro**[1] [0000-0001-7342-4814]

[1]Department of Aerospace Engineering, Universidad Carlos III de Madrid, Spain
e-mail: tangiero@ing.uc3m.es, sdiscett@ing.uc3m.es, aianiro@ing.uc3m.es

Extended Abstract.

Surgical site infections (SSIs) represent a significant concern in healthcare, contributing to patient morbidity and mortality during and after surgery. The operating room (OR) environment, particularly the performance of its ventilation system, plays a vital role in minimizing the risk of these infections. Laminar airflow (LAF) systems are commonly implemented in ORs to deliver clean air and reduce contamination risks. Nevertheless, even though the system is referred to as *laminar*, the airflow is turbulent, even over the surgical table, which could not guarantee the desired sterile and clean air flow required for optimal conditions. Airflow behavior in these settings - especially under the influence of thermal plumes produced by hotter human bodies and physical obstructions due for instance to the presence of lamps or other objects - remains insufficiently understood due to the complexity of fluid dynamics and the influence of multiple unpredictable factors. Capturing the intricate fluid dynamic structures involved through numerical simulation is not feasible in this case, and performing experiments in a full-sized operating room for practical reasons is also not possible.

To investigate this, a scaled-down model of an operating room with a LAF ventilation system has been designed and is currently being manufactured. The model includes critical elements, such as five manikins representing OR staff and one recumbent manikin simulating a patient on the surgical table. To ensure dynamic similarity, the model and ventilation system are designed to maintain Richardson and Reynolds numbers consistent with those of a full-sized operating room. Based on these considerations, water was chosen as the experimental medium, and the model dimensions are $87.5 \times 87.5 \times 37.5\ cm$, with a LAF outlet velocity of $0.066\ m/s$. Thermal plumes generated by heated manikins, along with obstruction elements like ceiling-mounted surgical lights, are incorporated to replicate real-life conditions.The 3D model of the operating room is shown in Figure 1.

The velocity field within the surgical zone will be measured with Particle Image Velocimetry (PIV). This method will allow for the identification of flow distribution patterns and the detection of potential instabilities that may affect the safety and well-being of patients and staff in the OR. The findings are expected to deliver valuable insights into the velocity field of air in ORs equipped with LAF systems, contributing to the optimization of ventilation design and enhancing the quality of the surgical environment.

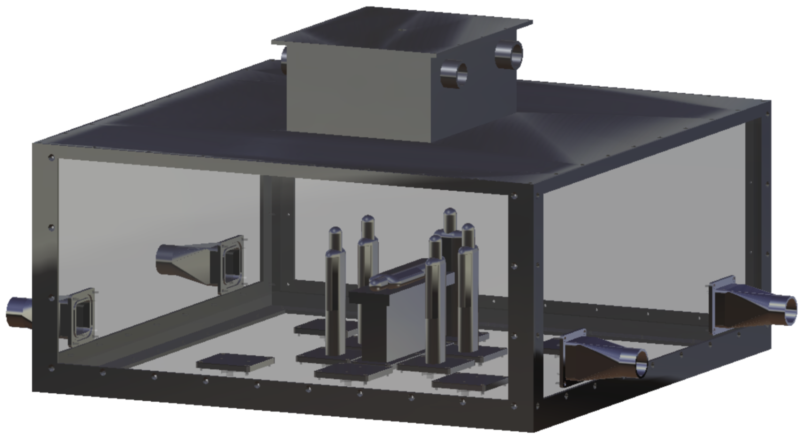

Figure 1: 3D model of the scaled Operatin Room

Keywords: Surgical Site Infections, Laminar Airflow, Operating Room, Fluid Dynamics, Particle Image Velocimetry, Ventilation Systems, Thermal Plumes, Infection Prevention.

Acknowledgement.
This work was supported by the European Union's Horizon Europe research and innovation program under the Marie Skłodowska-Curie Actions (MSCA) Doctoral Networks, project number 101119726. [HumanIC - HORIZON-MSCA-2022-DN-01]

Funded by the European Union

10th International Congress of the Serbian Society of Mechanics
Niš, Serbia, June 18-20, 2025

M.2.2
Original scientific paper

DOI:10.46793/ICSSM25.300B

APPLICATION OF AIR TORQUE POSITION DAMPERS FOR AIRFLOW MEASUREMENT

Siniša M. Bikić[1][0000-0002-1641-8546], Milivoj T. Radojčin[1][0000-0002-2864-7872], Ivan S. Pavkov[1][0000-0002-6472-5209], Hubert J. Debski[2][0000-0002-1916-8896], Rafat M. Al Afif[3][0000-0002-8818-8292]

[1] Faculty of Agriculture,
University of Novi Sad, Trg Dositeja Obradovića 8, 21000 Novi Sad, Republic of Serbia
e-mail: bika@uns.ac.rs , milivoj.radojcin@uns.polj.ac.rs , ivan.pavkov@uns.polj.ac.rs

[2] Faculty of Mechanical Engineering,
Lublin University of Technology, 36 Nadbystrzycka St., 20-618 Lublin, Poland
e-mail: h.debski@pollub.pl

[3]Institute of Chemical and Energy Engineering,
University of Natural Resources and Life Sciences, Vienna, Muthgasse 107/I, 1190 Vienna, Austria
e-mail: rafat.alafif@boku.ac.at

Abstract:

The subject of the paper is a damper, which is referred to as ATP (Air Torque Position) based on its mode of operation. The ATP damper indirectly measures air velocity by assessing the torque applied to the blades and their position. The airflow rate is determined by multiplying the air velocity with the cross-sectional area of the damper. Previous research on the accuracy of measurement and validity of mathematical model of the ATP damper has been analyzed for the entire range of blade angle of attack (0° – 90°). The difference between the measured and the modeled velocity was ±10% of the measured velocity. This way of analysis is more appropriate for the ATP damper as a measuring control device, where, in addition to airflow measurement, the damper also plays a role in regulating the airflow rate. In this work, the accuracy of air velocity and validity of mathematical model of the ATP damper was analyzed for a fixed value of the blade angle of attack. The reason for this is that, in practice, an ATP damper would be used for airflow measurement with a single set value of the blade angle of attack. Within this research the damper with two flat blades has been analyzed, where one blade is a measuring blade, while the other blade is in a fixed position. The following two cases were analyzed: with straight duct sections both upstream and downstream of the damper and with a straight duct section upstream of the damper. For the first case for certain damper blade angles of attacks (20°, 40°, 80° and 90°), the difference between the measured and the modeled velocity was within ±2% of the measured velocity. This data analysis approach shows promise for the application of ATP dampers in airflow measurement in the future.

Key words: ATP damper, air velocity, air flow rate, HVAC

1. Introduction

The ATP damper measures air velocity indirectly by evaluating the torque exerted on the blades and their position (Figure 1). The position of the blade is adjusted by fixing it to the sensor that measures the torque of force exerted by the airflow on the blade.

Based on the measured values of torque (M, Nm) and blade angle of attack (α, °), the airflow velocity (v, m/s) is determined using the existing mathematical model developed by Federspiel [1]:

$$v|v| = G^2(\alpha)\frac{2M}{\rho A_u D_h}, \tag{1}$$

The other terms in Eq.1 are: the correlation function ($G(\alpha)$, -), air density (ρ, kg/m^3), upstream cross-sectional area of the channel (A_u, m^2) and hydraulic diameter (D_h, m).

The correlation function $G(\alpha)$ is fitted by the experimental data and introduced into the damper torque model Eq.2.

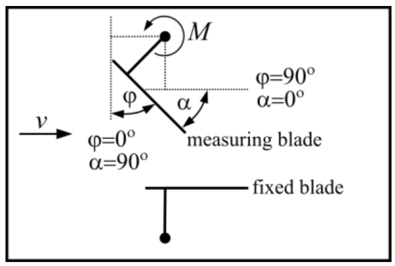

Fig. 1 Schematic diagram of an ATP damper

In previous research, the accuracy of airflow measurements and validity of mathematical model of the ATP damper was analyzed across the entire range of blade angle of attack (0° – 90°). The difference between the measured velocity and the modeled velocity was ±10% of the measured velocity for both the ATP damper with cascade blades [1] and the one with non-cascading blades [2], [3].

It is an airflow meter whose measurement accuracy is affected by local resistances near the meter. Group of authors [4], [5] concluded that connection direction of elbow, the curvature radius of elbow and the length of straight duct will have a great influence on the measurement accuracy of the torque dampers. They confirmed that the combination of perforated plate with porosity below 60% and air damper can effectively eliminate the coupling effect. Researchers [6] found that by connecting two blades, the damper mitigates the influence of nearby components (such as elbows, variable diameters, tees, etc.) on air volume measurement, eliminating the need for additional devices and ensuring measurement accuracy within ±5.5%.

Previous studies have also shown that the following several factors can affect the accuracy of airflow velocity measurements and the validity of the mathematical model when the damper is more open: the presence of local resistance downstream of the damper with cascading blades placed at the entrance of the ductwork [7], the presence of the local resistance upstream of the damper with non-cascading blades placed both within the ductwork and end of the ductwork [8], hysteresis of the damper [9] and the damper's location in the system and blade profiles [10].

The group of authors [11] developed and validated the mathematical model for the damper torque airflow sensor with one blade as follows:

$$q_v = K(\theta)\cdot\sqrt{\frac{2A_1\cdot\beta^2}{\alpha\cdot\rho\cdot(1-\beta^2)}\cdot\frac{M}{B_0}}, \tag{2}$$

The terms in Eq. 2 are: the flow coefficient ($K(\theta)$, -), air density (ρ, kg/m^3), cross-sectional area (A_1, m^2), area ratio of damper blade to pipeline (α, °), area ratio of damper opening annulus to pipeline (β, °), initial damper deviation (B_0, m) and torque (M, Nm).

The flow coefficient $K(\theta)$ is fitted by the experimental data and introduced into the damper torque model Eq.2. As in previous research, the group of authors [11] noted that the measurement of airflow velocity is less accurate when the damper is more open. They concluded that within the typical damper opening range (10°–70°), the quadratic fitting equation of $K(\theta)$ generally satisfies the error tolerance of ±5%. However, the error increases as the opening angle exceeds 70°. The conclusions reached by the authors indicate that the accuracy of measurements should be analyzed for a specific blade angle of attack.

In this work, the accuracy of air velocity and validity of mathematical model (Eq.1) of the ATP damper was analyzed for a certain value of the blade angle of attack. The reason for this is that, in practice, an ATP damper would be used for airflow measurement with a single set value of the blade angle of attack. The previous analysis conducted for entire range of blade angles of attack is more appropriate for the ATP damper as a measuring control device, where, in addition to airflow measurement, the damper also plays a role in regulating the airflow rate. The aim of this analysis is to check if this approach could improve the accuracy of airflow measurement and the validity of the mathematical model of the ATP damper. The authors of the paper believe that this approach could bring the ATP damper closer to practical application for measuring air flow in systems in the future.

2. Material and method

The damper with two flat blades has been analyzed, where one blade is a measuring blade, while the other blade is in a fixed horizontal position (Figure 1). It is about the ATP damper with non-cascading blades, which has minimal energy consumption and the smallest discrepancies between measured and modeled velocities [2].

The schematic representation of the laboratory ATP damper, including its dimensions, is shown in Figure 2. The ATP damper had a square cross-section with dimensions *a* x *a* (250 mm x 250 mm) and a length of *b* = 314 mm. The width and thickness of the blades are *c* = 248 mm and *w* = 0.75 mm, respectively. The length of the blades is *l* = 124 mm. The axis of rotation of the blade O_r was displaced from the axis of the blade O_b in the longitudinal direction of the blade by Δ=43 mm and in the transverse direction of the blade by δ=20 mm. Along the blades, at a distance of *d* = 31 mm from their ends, there were two reinforcements, each *e* = 10 mm wide and *f* = 2 mm thick. There is a gap of width *g* = 1 mm between the blades and the housing of the damper, allowing the blades to be guided.

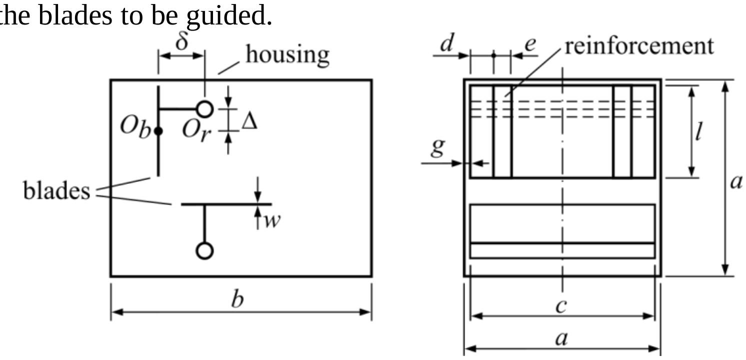

Fig. 2 Schematic representation of the laboratory ATP damper

Two ATP damper installation locations in the HVAC system were considered: within the ductwork itself, with straight duct sections both upstream and downstream of the damper (a), and at the ductwork exit, with a straight duct section upstream of the damper (b). The length of the straight duct section upstream of the damper was 3 m, while the length of the duct section downstream of the damper was 2 m.

The ATP damper was examined at the Faculty of Technical Sciences, the University of Novi Sad, Republic of Serbia in accordance with the recommendations [12] for testing dampers used for airflow regulation in HVAC systems, Figure 3.

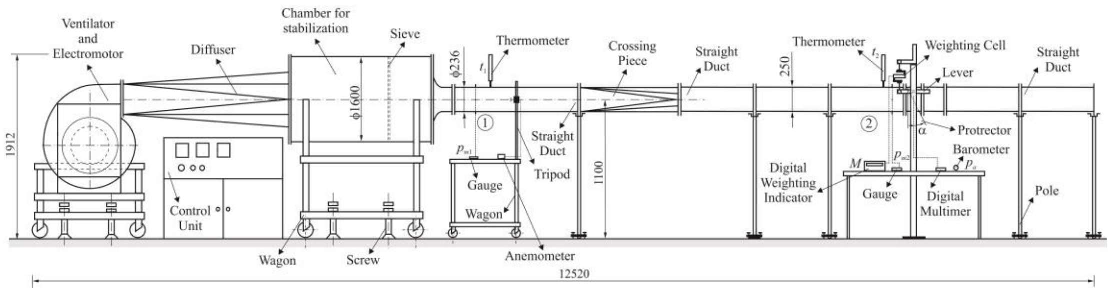

Fig. 3 Schematic diagram of the laboratory facility for testing ATP dampers [2]

The air velocity (v_1, m/s), was measured in the straight duct section with a hot-wire anemometer, on the basis of the one-point method in accordance with the standard recommendations [13]. In addition to the air velocity in the straight duct section, the airstream temperature, (t_1, ^oC), was measured with a glass thermometer, as well as the airstream gauge pressure (p_{m1}, Pa), with a manometer. Directly in front of the ATP damper blade the air stream temperature (t_2, ^oC), was measured with a mercury thermometer and the airstream gauge pressure (p_{m2}, Pa), with a manometer. The atmospheric pressure, (p_a, Pa), was measured with a digital barometer. The air densities at sections 1 and 2 were calculated from the ideal gas state equation. From the mass flow rate equation in the sections (1) and (2), the average air velocity, v_2 [m/s], directly in front of the ATP damper blade was calculated:

$$v_2 = \frac{\rho_1 v_1 A_1}{\rho_2 A_2}, \tag{3}$$

The measurement of the air velocity (v_1, m/s) was performed using a hot-wire anemometer of producer Testo, model 425. According to technical data of producer the measuring range of anemometer is from 0.01 to 30 m/s, resolution 0.01 m/s and measurement uncertainty +/- (0.03 m/s +4% of measuring range) for velocity range from 0.01 to 20 m/s and +/- (0.5 m/s + 5% of measuring range) for velocity range from 20.01 to 30 m/s.

For the purpose of measurement of the static gauge pressures (p_{m1}, Pa) and (p_{m2}, Pa) were used the differential manometers produced by "Testo", model 521. Measuring range of differential manometer is from 0 to 10000 Pa, measurement uncertainty is ±0.1% of the scale, the operation temperature range from 0 to 50 ° C and 1 Pa resolution.

The airstream temperatures (t_1, °C) and (t_2, °C) were measured using thermometers produced by "TLOS". Measuring range of thermometer is from 0 to 50 °C, measurement uncertainty is ±0.05°C of the scale and resolution 0.1 °C. The measurement of atmospheric pressure (p_a, Pa) was performed with the device manufactured by "PCE", model "THB38". Measuring range in measuring atmospheric pressure is from 10000 to 110000 Pa, with the measurement accuracy of +/- 1.5 Pa for the measurement range from 10000 to 99990 Pa and +/- 2 Pa for the measurement range from 100000 to 110000 Pa. The resolution of the device is 0.1 Pa for the measurement range from 10000 to 99990 Pa and 1 Pa for the measurement range from 100000 to 110000 Pa.

Position of the blade could be expressed by angle of attack (α, ^{o}) or angle of damper openness (φ, ^{o}) where $\alpha+\varphi=90^o$ (Figure 1). The position of the blade defined by the angle of attack (α) was used in this research. The blade position defined in this manner aligns with the equations presented in Eq.(1). The blade angle of attack (α) was measured using a rotary linear potentiometer from "Dada Electronics", model "Tyco 10k", which was previously calibrated with a protector. It is an adjustable potentiometer with a shaft diameter of 6 mm, a power rating of 200 mW, and a resistance of 10 kΩ.

The torque (M, Nm) was measured using a custom-made torque meter, which consisted of a lever, load cell, and weighing indicator. A square hollow steel section with a cross-section of 25 x 25 mm was used as the lever, with a lever length of 100 mm. The load cell model PW4MC3 and weighing indicator model WE2110, both from the manufacturer HBM, were used. According to the manufacturer's technical specifications, the load cell model PW4MC3 has a measurement range from 0 to 3000 g, a resolution of 0.5 g, and an accuracy class of C3. The weighing indicator model WE2110 has a measuring range from 0 to 3.5 mV/V and an accuracy class of 6000d.

In the following, the velocity (v_2, m/s) will be referred to as the measured velocity (v_{mer}, m/s). A more detailed description of the laboratory facility and the locations of the measurement equipment used is provided by Bikić et al. [2].

3. Results and Discussion

In the Table 1 were presented the values of fitted correlation function G (α) by the experimental data for the two considered cases: with straight duct sections both upstream and downstream of the damper (a), and at the ductwork exit, with a straight duct section upstream of the damper (b).

α [o]	G_a [-]	G_b [-]
90	1.346661	1.338011
80	1.436084	1.323852
70	1.660437	1.56192
60	2.032030	1.967344
50	2.616781	2.560928
40	3.553852	3.308419
30	6.162295	4.714195
20	6.772173	7.077778
10	10.33271	9.950491
0	18.02794	17.51036

Table 1. The values of correlation functions

Generally speaking, the damper with two flat blades—one being a measuring blade and the other fixed in a horizontal position, like other ATP dampers—shows a difference between the measured and the modeled velocity of ±10% of the measured velocity across the entire range of blade angle of attack (0° – 90°), Table 2 and Table 3. There is one exception for the case with straight duct sections both upstream and downstream of the damper, where, for a blade angle of attack of 30°, the difference between the measured and modeled velocity is ±15% of the measured velocity. This data point also suggests that we should analyze the difference between velocities at certain values of the blade angle of attack.

In the case of a damper with straight duct sections both upstream and downstream, a smaller difference between the measured and modeled velocities is observed. For certain damper blade angles of attacks (20º, 40º, 80º and 90º), the difference between the measured and the modeled velocity was within ±2% of the measured velocity (Table 2). On the other hand, a damper with only an upstream straight section shows a greater difference between the measured and modeled velocities. For certain damper blade angles of attacks (90º, 70º, 50º, 40 º and 30º), the difference between the measured and the modeled velocity was within ±5% of the measured velocity (Table 3). It should be highlighted that for blade angle of attack of 50º the difference between the measured and the modeled velocity was within ±2% of the measured velocity.

α [°]	M [Nmm]	ρ [kg/m^3]	v_{mod} [m/s]	v_{mer} [m/s]	Δv [m/s]	ε_v [%]
90	15,31	1,201	1,48	1,46	-0,02	-1,37
	64,31	1,202	3,04	2,98	-0,06	-2,01
	135,77	1,202	4,41	4,35	-0,06	-1,38
	219,47	1,202	5,61	5,66	0,05	0,88
80	15,41	1,201	1,53	1,50	-0,03	-2,00
	52,39	1,201	2,83	2,78	-0,05	-1,80
	120,18	1,201	4,29	4,23	-0,06	-1,42
	195,17	1,201	5,46	5,48	0,02	0,36
70	13,34	1,196	1,54	1,45	-0,09	-6,21
	50,28	1,196	2,99	2,92	-0,07	-2,40
	104,67	1,196	4,31	4,21	-0,10	-2,38
	188,81	1,197	5,79	5,76	-0,03	-0,52
60	37,97	1,201	2,87	2,8	-0,07	-2,50
	94,4	1,200	4,52	4,45	-0,07	-1,57
	139,55	1,201	5,5	5,51	0,01	0,18
	232,94	1,201	7,1	7,07	-0,03	-0,42
50	30,91	1,201	2,94	2,86	-0,08	-2,80
	64,92	1,201	4,25	4,20	-0,05	-1,19
	110,26	1,200	5,55	5,54	-0,01	-0,18
	178,27	1,200	7,05	7,07	0,02	0,28
40	24,55	1,200	3,05	3,01	-0,04	-1,33
	52,17	1,200	4,45	4,41	-0,04	-0,91
	82,86	1,200	5,6	5,59	-0,01	-0,18
	131,96	1,200	7,07	7,05	-0,02	-0,28
30	32,77	1,201	4,64	4,09	-0,55	-13,45
	65,54	1,200	6,56	5,75	-0,81	-14,09
	84,21	1,200	7,44	6,93	-0,51	-7,36
	135,17	1,200	9,42	8,28	-1,14	-13,77
20	26,65	1,200	4,39	4,45	0,06	1,35
	46,13	1,200	5,77	5,82	0,05	0,86
	65,6	1,200	6,88	6,89	0,01	0,15
	96,36	1,200	8,34	8,26	-0,08	-0,97
10	16,37	1,200	4,25	4,29	0,04	0,93
	32,73	1,200	6,00	5,90	-0,10	-1,69
	47,05	1,200	7,20	7,00	-0,20	-2,86
	69,56	1,200	8,75	8,29	-0,46	-5,55
0	16,47	1,200	5,62	5,94	0,32	5,39
	24,7	1,200	6,89	7,08	0,19	2,68
	36,03	1,200	8,32	8,33	0,01	0,12
	61,76	1,200	10,9	10,78	-0,12	-1,11

Table 2 The results of mathematical model validation with straight duct sections both upstream and downstream of the damper

α [º]	M [Nmm]	ρ [kg/m^3]	v_{mod} [m/s]	v_{mer} [m/s]	Δv [m/s]	ε_v [%]
90	14,29	1,192	1,43	1,45	0,02	1,38
	61,24	1,157	3,01	2,87	-0,14	-4,88
	131,68	1,194	4,34	4,26	-0,08	-1,88
	220,49	1,194	5,62	5,67	0,05	0,88
80	12,04	1,168	1,32	1,40	0,08	5,71
	56,17	1,169	2,85	2,80	-0,05	-1,79
	129,40	1,170	4,33	4,20	-0,13	-3,10
	202,62	1,170	5,42	5,64	0,22	3,90
70	11,10	1,187	1,37	1,41	0,04	2,84
	46,38	1,188	2,79	2,83	0,04	1,41
	104,85	1,19	4,20	4,02	-0,18	-4,48
	173,41	1,188	5,40	5,44	0,04	0,74
60	44,18	1,168	3,08	3,07	-0,01	-0,33
	80,33	1,168	4,16	4,11	-0,05	-1,22
	148,61	1,168	5,66	5,73	0,07	1,22
	225,92	1,169	6,98	6,97	-0,01	-0,14
50	29,10	1,167	2,86	2,80	-0,06	-2,14
	69,21	1,167	4,41	4,42	0,01	0,23
	109,33	1,168	5,54	5,62	0,08	1,42
	174,53	1,168	7,00	7,10	0,10	1,41
40	25,26	1,167	3,03	3,04	0,01	0,33
	57,59	1,167	4,57	4,55	-0,02	-0,44
	89,91	1,168	5,71	5,78	0,07	1,21
	129,31	1,168	6,85	7,07	0,22	3,11
30	35,36	1,167	4,27	4,42	0,15	3,39
	60,62	1,167	5,60	5,76	0,16	2,78
	99,01	1,167	7,15	7,19	0,04	0,56
	142,45	1,167	8,58	8,63	0,05	0,58
20	23,19	1,167	4,24	4,49	0,25	5,57
	36,29	1,166	5,31	5,45	0,14	2,57
	66,54	1,167	7,19	7,25	0,06	0,83
	91,75	1,167	8,44	8,40	-0,04	-0,48
10	16,15	1,166	4,20	4,36	0,16	3,67
	31,29	1,167	5,84	6,07	0,23	3,79
	45,42	1,167	7,04	7,12	0,08	1,12
	66,61	1,167	8,52	8,56	0,04	0,47
0	16,16	1,166	5,57	6,16	0,59	9,58
	23,24	1,166	6,68	6,97	0,29	4,16
	34,35	1,167	8,12	8,27	0,15	1,81
	56,58	1,166	10,43	10,66	0,23	2,16

Table 3 The results of mathematical model validation with straight duct section upstream of the ATP damper

4. Conclusions

Analysis of the difference between measured and modeled airflow velocity of the ATP damper showed that, for certain blade angles of attack, this difference is smaller than across the full range. The analysis considered only the ATP damper with non-cascading blades, where one blade measures and the other remains fixed horizontally. Notably, when the damper includes both upstream and downstream straight sections, the difference between measured and modeled velocities stayed within ±2% at blade angles of 20°, 40°, 80°, and 90°. These results are promising, especially given that, in practice, the damper would measure airflow using a blade fixed to a torque sensor. Therefore, the authors recommend future research focus on flow rate measurement uncertainty at specific blade angles of attack.

References

[1] Federspiel, C., *Using the Torque Characteristics of Dampers to Measure Airflow Part I: Analysis and Testing*, HVAC&R Research, Volume 10, Issue 1, 53-64, 2004.

[2] Bikić, S., Uzelac, D., Bukurov, M., Todorović, B., Tašin, S., *Air torque position damper energy consumption analysis*, Energy and Building, Volume 99, 131–139, 2015.

[3] Bikić, S., Uzelac, D., Bukurov, M., Radojčin, M., Pavkov, I., *Experimental calibration of the mathematical model of air torque position dampers with non-cascading blades*, Thermal Science, Volume 20, Issue 1, 567–578, 2016.

[4] Wen, S. and Liu, J., *CFD design of a novel torque measurement damper without air flow instability effects*, Proceedings of Building Simulation 2023: 18th Conference of IBPSA, Shanghai China, Sept. 4-6, 1990 – 1994, 2023.

[5] Wen, S., Liu, J., Zhang, F., Jing, H., *Numerical and experimental study towards a novel torque damper with minimized air flow instability*, Building and Environment, Volume 217, 2022.

[6] Jing, R., Gao, R., Nie, S., Zhao, X., Yang, C., Li, A., *An adjacent-effects resistant damper integrating control and measurement functions for duct systems*, Building Systems and Components, Volume 17, Issue 2024, 2199–2212, 2024.

[7] Federspiel, C., *Using the Torque Characteristics of Dampers to Measure Airflow, Part II: Model Development and Validation*, HVAC&R Research, Volume 10, Issure 1, 65 – 72, 2004.

[8] Bikić, S., Vukadin, N. Radojčin, M., Pavkov, I., Al Afif, R., *The influence of local resistance on the accuracy of the air velocity measurement with the air torque position damper*, International Journal of Thermofluids, Volume 27, 2025.

[9] Bikić, S., Bukurov, M., Radojčin, M., Pavkov, I., Rackov, M., *Air torque position damper hysteresis*, Flow Measurement and Instrumentation, Volume 71, 2020.

[10] Bikić, S., Todorović, B., Bukurov, M., Radojčin, M., Pavkov, I., *Accuracy analysis of air torque position dampers based on blade profiles and damper locations*, Thermal Science Volume 21, 675-685, 2018.

[11] Yuanpeng, M., Mingsheng, L., Zhixian, M., Zhang, J., *Resistance characteristic analysis based study on a novel damper torque airflow sensor for VAV terminals*, Building and Environment, Volume 175, 2020.

[12]. ANSI/AMCA 500 D, *Laboratory Methods of Testing Dampers for Rating*, ANSI (2007).

[13] ISO 7145, *Determination of flow rate of fluids in closed conduits of circular cross – section. Method of velocity measurement at one point of the cross – section*, International Standard Organization, 1982

Acknowledgments

The study was financed by the Ministry of Science, Technological Development, and Innovation of the Republic of Serbia under contract numbers 451-03-137/2025-03/200117 and 451-03-136/2025-03/200117 and the CEEPUS project grant “Building Knowledge and Experience Exchange in CFD - RS-1012-10-2425” supported by the Central European Exchange Program for University Studies.

M.2.3
Extended abstract

ANALYSIS OF TURBULENT SWIRLING FLOW IN A PIPE DOWNSTREAM OF AN AXIAL FAN IMPELLER: EXPERIMENTAL AND NUMERICAL APPROACHES

Milan Z. Bulajić[1], Novica Z. Janković[1[0000-0003-2645-8602]], Lazar M. Lečić[1], Đorđe S. Čantrak[1[0000-0003-1841-9187]]

[1] Faculty of Mechanical Engineering
University of Belgrade, Kraljice Marije 16, 11000 Belgrade, Serbia
e-mail: mbulajic@mas.bg.ac.rs

Key words: axial fans, CFD, swirling flow, turbulence

1. Introduction

This extended abstract presents a comparison of two different methods for analyzing turbulent swirl flow generated by the axial fan impeller using computational fluid dynamics (CFD). The presence of swirl flow in ventilation systems increases pressure losses and energy consumption and can lead to vibrations, fatigue, and potential mechanical failure. Previous experimental studies have confirmed high levels of swirl flow in such applications.

The investigation was conducted on an industrial W30 fan, model AP400, manufactured by Minel, Serbia. The study followed the ISO 5801 standard, case B, which features a free inlet and a ducted outlet configuration. The flow was analyzed using one-component Laser Doppler Anemometry (LDA), Particle Image Velocimetry (PIV), specially manufactured probes, and Hot-Wire Anemometry. However, this paper focuses solely on the results obtained using 1D LDA.

The simulations are performed using Ansys CFX. Simulation 1 employed an unstructured mesh in the runner domain, while Simulation 2 uses a structured mesh generated with Turbogrid.

The primary objective is to refine the numerical simulation to accurately represent real-world behavior, enabling its use as a reliable template for future research.

2. Methodology

The test rig was installed at the Faculty of Mechanical Engineering, University of Belgrade, and was specifically built for this experiment. A crucial step in the analysis was the 3D scanning of the fan impeller to transfer it into CAD software and subsequently into CFD software such as Ansys Mesh and Turbogrid.

The generated model is designed to replicate real conditions as accurately as possible. At the fan inlet, a large dome is created to ensure that the boundary condition is met, meaning the total pressure at the dome's outer surface equals atmospheric pressure, resulting in zero velocity at that boundary. The outlet duct length is $27.74 \cdot D$, where D is rounded to 400 mm. The outlet duct shape is idealized as a perfect circle, whereas the real test rig contained deviations, misalignments, and creases, which could contribute to discrepancies in the results. Two measuring sections are placed at $z/D = 3.35$ and $z/D = 26.31$ downstream of the fan outlet.

Both simulations consist of three sections: inlet, runner, and outlet. In Simulation 1, the runner section is a full circle with an unstructured mesh refined around the blade surfaces, while Simulation 2 features a blade section (one-seventh of the volume) with a structured mesh generated using Turbogrid. Both simulations were run using k-ω SST turbulence model.

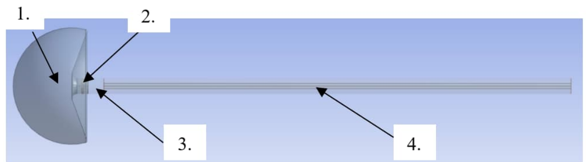

Fig. 1 CAD model used for the simulation. 1 - inlet section, 2 - runner, 3 - non-structured mesh section outlet duct, 4 - structured mesh section outlet duct

3. Results

The results obtained from the CFD simulation are compared with experimental data acquired using a single-component Laser Doppler Anemometry (LDA) system. One of the key advantages of CFD is its ability to provide a detailed analysis of the flow field at any location within the simulation domain. However, to ensure consistency and validation, the comparison is focused on the same measurement planes that were analyzed during the experiments. These planes are located at z/D = 3.35 (Section 1) and z/D = 26.31 (Section 2) downstream of the fan outlet. These sections were selected to capture both the near-field and far-field development of the swirling flow. While the simulation effectively captures the general flow trends, discrepancies in the magnitude of the velocity values are observed when compared to the experimental results. These differences can be attributed to several factors, including assumptions in the numerical model, the idealized representation of the outlet duct, and the absence of certain geometric irregularities present in the experimental setup.

4. Conclusions

This paper presents a numerical comparison of two methods with a previously conducted experimental investigation of the flow characteristics in the ducted outlet of an axial fan without guide vanes. The study aims to assess the accuracy of computational fluid dynamics (CFD) simulations in replicating the complex flow structures observed in the experiment.

The results show a strong correlation in the general flow behavior between the measured and simulated data, particularly in the solid-body circumferential velocity profiles. However, discrepancies in velocity magnitudes are noticeable, especially in the flow rate predictions. These differences are primarily attributed to the idealized representation of the flow field in the numerical model, which omits the geometric imperfections and surface irregularities present in the real experimental setup.

Acknowledgment. Results presented in this paper are the result of the research supported by the Ministry of Science, Technological Development and Innovation of the Republic of Serbia under the Agreement on financing the scientific research work of teaching staff at accredited higher education institutions in 2025, no. 451-03-137/2025-03/200105 and for research staff no. 451-03-136/2025-03/200105.

References

[1] Čantrak Đ., “Analysis of the Vortex Core and Turbulence Structure Behind Fans in a Straight Pipe Using PIV, LDA and HWA Methods”, Ph.D. thesis, Univ. Belgrade, Fac. Mech. Eng., Belgrade, 2012.

[2] Čantrak Đ., Janković N., Ilić D.,“Investigation of the Turbulent Swirl Flow in Pipe Generated by Axial Fans Using PIV and LDA Methods”, Theoretical and Applied Mechanics, Vol. 42, Iss. 3, pp. 211-222, 2015.

[3] Ilić D., Svorcan J., Čantrak Đ., Janković N.,“Experimental and Numerical Research of Swirl Flow in Straight Conical Diffuser”, Processes, Vol .13, 182, 2025.

[4] Benišek M.,“Investigation of the turbulent swirling flows in straight pipes, Ph.D. thesis, Univ. Belgrade, Fac. Mech. Eng., Belgrade, 1979.

10th International Congress of the Serbian Society of Mechanics
Niš, Serbia, June 18-20, 2025

M.2.4

Extended abstract

APPROACHING A MODIFIED SWARM INTELLIGENCE IN HYDRAULIC OPTIMIZATION OF AN INLINE PUMP

Xingcheng Gan[1][0000-0001-6507-8026], Ji Pei[1][0000-0002-6998-1906], Wenjie Wang[1][0000-0003-2562-5026], Jia Chen[1][0009-0002-2296-6992], Shouqi Yuan[1]

[1]National Research Center of Pumps,
Jiangsu University, Xuefu Road 301, Zhenjiang 212013, Jiangsu Province, China.
e-mail: xingcheng.gan@ujs.edu.cn; jpei@ujs.edu.cn; wenjiewang@ujs.edu.cn; jchen@ujs.edu.cn; shouqiy@ujs.edu.cn

Abstract:

Pumps are widely utilized across diverse industrial sectors, significantly contributing to global energy consumption. Given the increasing emphasis on energy conservation and environmental protection, enhancing the energy efficiency of pumps has become crucial for industrial sustainability and reducing global carbon emissions. Centrifugal pumps, particularly inline pumps, are widely utilized due to their compactness and ease of maintenance, though they typically exhibit lower efficiency due to their unique curved inlet structure. Addressing the efficiency of such pumps has become increasingly critical.

This research introduces a modified particle swarm optimization (PSO) algorithm designed specifically to enhance the energy efficiency of an industrial vertical inline pump. The proposed algorithm integrates population classification management, adaptive acceleration strategies, and self-learning mechanisms to overcome common drawbacks of traditional PSO algorithms, including premature convergence and instability. Comparative tests using the basic benchmark function set and the CEC2014 benchmark function set revealed that the proposed PSO algorithm significantly outperforms 10 other well-known PSO variants (e.g. APSO, CLPSO) in terms of search speed, efficiency, and accuracy.

A detailed analysis was conducted on 4,000 design samples generated during the optimization process to thoroughly investigate the relationship between pump design parameters and performance indicators such as head and efficiency. Utilizing Spearman and Pearson correlation analyses, the study identified critical insights into the influence of various design parameters. Notably, it was found that increasing the number of blades and the impeller diameter substantially improved head performance but conversely reduced efficiency. Interestingly, conventional factors such as the blade angles at the leading edge were found to have minimal influence on both efficiency and head, highlighting the importance of mid-blade and rear blade geometry.

Comprehensive computational fluid dynamics (CFD) simulations were performed, along with detailed flow loss visualization, to examine the internal flow characteristics and pinpoint areas of inefficiency within the pump. The analysis revealed significant reductions in internal flow losses in the optimized model, attributed mainly to improved velocity distributions and the elimination of high-velocity regions within the impeller passages.

Experimental validation confirmed the effectiveness of the optimized design, with substantial performance improvements over the original model. Specifically, the optimized pump achieved a notable increase of 10.71% in nominal efficiency, a 5.09% increase in head, and an 8.65% reduction in input power consumption. Additionally, the optimization substantially expanded the

high-efficiency operational range of the pump, further underscoring the practical benefits of the improved design.

In summary, this study's enhanced PSO algorithm exhibits exceptional performance in high-dimensional optimization contexts, addressing inherent limitations of conventional optimization methods. The insights gained from this research not only significantly advance pump optimization methodologies but also provide robust theoretical and practical guidance for future centrifugal pump design and operational efficiency enhancement.

Key words: Pump, Swarm intelligence, Hydraulic optimization, Computational Fluid Dynamics.

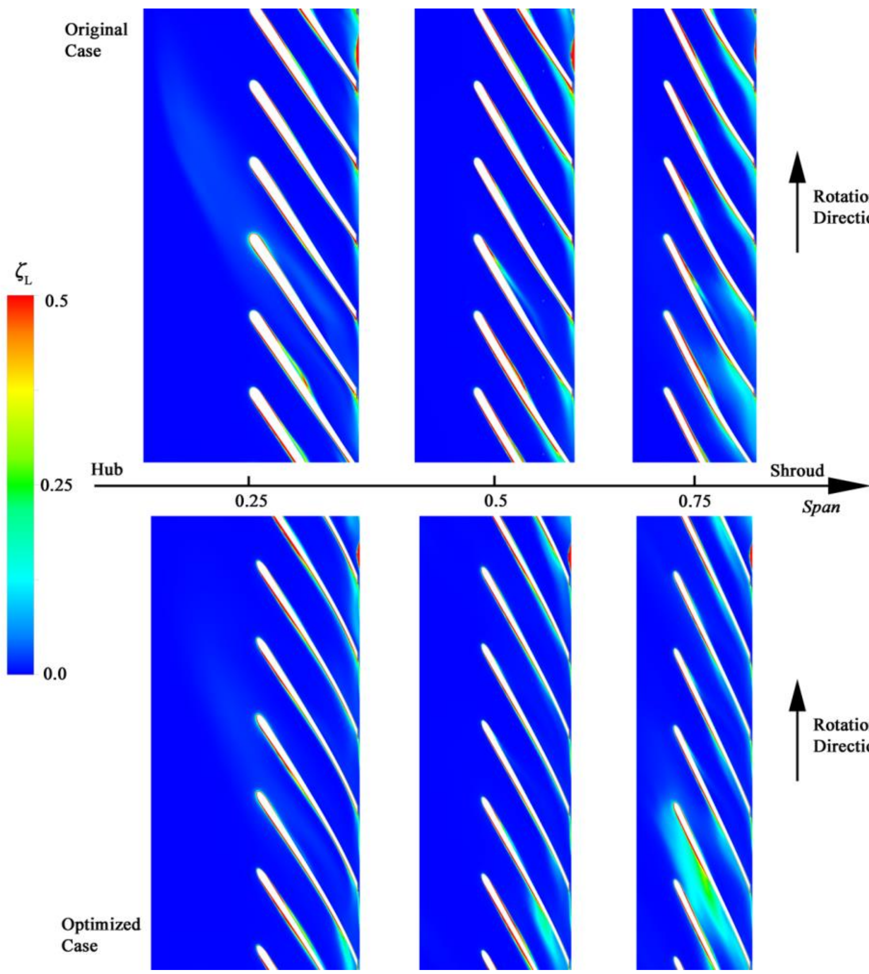

Fig. 1. Flow losses comparison between the optimized and original cases

References

[1] Xu Y., Gan X., Pei J., et al. *Applications of artificial intelligence and computational intelligence in hydraulic optimization of centrifugal pumps: a comprehensive review*. Engineering Applications of Computational Fluid Mechanics, 19(1):2474675, 2025.

[2] Gan X, Pei J, Wang W, et al. *Application of a modified MOPSO algorithm and multi-layer artificial neural network in centrifugal pump optimization*. Engineering Optimization, 55(4): 580-598, 2023.

[3] Gad A G. *Particle swarm optimization algorithm and its applications: a systematic review*. Archives of computational methods in engineering, 29(5): 2531-2561, 2022.

10th International Congress of the Serbian Society of Mechanics
Niš, Serbia, June 18-20, 2025
M.2.5

Extended abstract

A SHORT DISCUSSION ON THE CIRCULATION IN THE TURBULENT SWIRLING FLOW IN THE AXIAL FAN JET

Novica Z. Janković[1[0000-0003-2645-8602]], **Đorđe S. Čantrak**[2[0000-0003-1841-9187]], **Dejan B. Ilić**[3[0000-0003-4562-8881]]

University of Belgrade-Faculty of Mechanical Engineering, Hydraulic Machinery and Energy Systems Department, Kraljice Marije 16, 11120 Belgrade 35, Republic of Serbia
e-mail: [1]njankovic@mas.bg.ac.rs, [2]djcantrak@mas.bg.ac.rs, [3]dilic@mas.bg.ac.rs

Abstract. In this paper is analyzed distribution of the circulation in the turbulent swirling flow in the axial fan jet. Experimental results are obtained by use of the three component LDV system. Development of the circulation profile in the central zone, up to $r = R$ obeys hierarchical distribution downstream, while this is not a case in the outer zones. Positions of the circulation extreme values are also discussed, as well as its gradients.

Key words: turbulence, swirling flow, jet, axial fan, LDV.

1. Introduction

In this extended abstract is presented a short discussion on the distribution of the circulation in the turbulent swirling flow, generated by the axial fan impeller. Performed research of the structure of the turbulent swirling flow in the axial fan jet is presented in details in [1], while some aspects in [2]. The axial fan impeller was built in the test rig following the case A, defined by the ISO 5801 standard [3], which features a free inlet and a free outlet configuration. This case is still very frequent in praxis and, therefore, attracts attention of the scientists and researchers.

2. Methodology

The test rig with specified measuring sections, built at the UB FME, Hydraulic Machinery and Energy Systems Department, is presented in Figure 1. Measuring sections along the axial fan rotating axis are in the range x/D = 0.75D to 5D, with the step 0.5D, except for the first step 0.25D, where the inner casing diameter is D = 0.4 m.

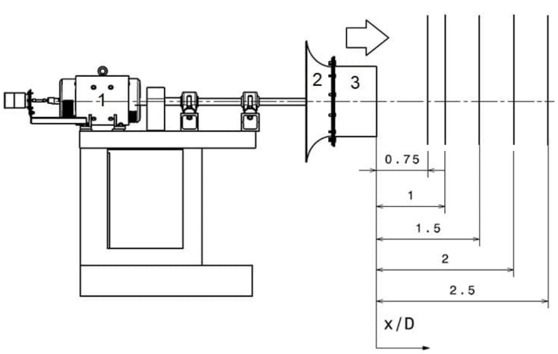

Figure 1:Experimental test rig: 1– DC motor, 2– profiled inlet, 3– fan impeller with casing

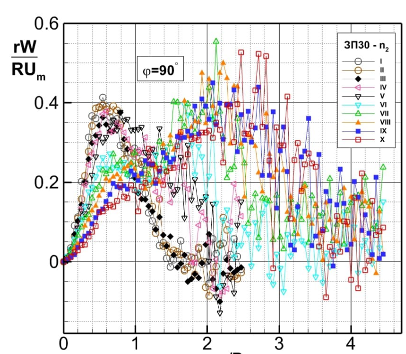

Figure 2: Downstream development of the circulation in the turbulent swirling flow in the axial fan jet

Axial fan impeller with twisted and adjustable blades, positioned in the angle 30° at the outer diameter, is turbulent swirling flow generator. Impeller outer diameter is 0.399 m. Measurements have been performed for the axial fan impeller rotation speed n = 1500 rpm. Flow seeding is provided by an Antari Z3000 fog machine loaded with the Eurolite Smoke Fluid, which was naturally sucked in the test rig by the axial fan impeller. All three velocity components (*U*-axial, *V*-radial and *W*-circumferential) were measured synchronously by use of the three-component LDV (laser Doppler velocimetry) system, manufactured by TSI [[1], [2]]. Uncertainty measurement analysis with this system is thoroughly preformed and presented in [[1], [4]].

3. Experimental results and discussion

Circulation ($\Gamma_W = 2\pi rW$, where r is radius and W averaged circumferential velocity) distribution is of great importance for the study of the vortex characteristic and fluid rotation movement. Figure 2 presents experimentally obtained distribution of the circulation rW, i.e. its non-dimensional form rW/RU_m, where average velocity is U_m = 12.57 m/s, while Reynolds number is Re = 358951. Upper part of the measuring section is denoted with the cylindrical coordinate $\varphi = 90°$. Complex vortex structure is obvious. Circulation in the measuring sections I-IV increases in the central vortex zone up to $r/R \approx 0.5$, where the maxima values are reached. It decreases for the higher values of r/R. Circulation maximum values ($\Gamma_{W,max}$) in other measuring sections are reached in domain $0.5 < r/R < 1$. These maxima have lower values in the downstream measuring sections. This is hierarchically for all measuring sections in the region $0 < r/R < 1$. However, this is not a case in the rest of the measuring section where the circulation variations are heterogeneous and chaotic, what is especially obvious in the domain $2 < r/R < 4$. In this domain circulations in the measuring sections VIII-X have the highest value. It is obvious that the highest decrease rate have the measuring sections I-IV with the highest $\Gamma_{W,max}$, i.e. have the highest negative changes in the radial direction ($\partial_r(Wr) < 0$). Negative values of circulation $\Gamma_{W(I\text{-}IV)} < 0$ occur in the domain $1.5 < r/R < 2.4$, according to the empirical distribution of the circumferential velocity W. It is worth of notice to say that these distributions are interesting for study, because circulation takes part in the production of the correlation $\overline{vw}$ with the following term $-\overline{v^2}\, r^{-1}\partial_r(rW)$.

Acknowledgment. The part of this research was financially supported by the Ministry of Science, Technological Development and Innovation of the Republic of Serbian, for scientific research work of teaching staff at accredited higher education institutions in 2025, no. 451-03-137/2025-03/200105. The work on this paper is finalized during the student demonstrations in Serbia, which started in November 2024., still are in progress and is dedicated to them who stand for the justice in our society.

References

[1] Janković, N.Z., *Experimental and theoretical research of the structure of turbulent swirl flow in axial fan jet*, (in Serbian), Ph.D. thesis, Univ. Belgrade, Fac. Mech. Eng., Belgrade, 2020.
[2] Janković, N. Z., *Investigation of the free turbulent swirl jet behind the axial fan*, Thermal Science, Vol. 21, Suppl. 3, S771-S782, 2017.
[3] ISO 5801:2017 "Fans – Performance Testing Using Standardized Airways". (https://www.iso.org/standard/56517.html)
[4] Ilić, J.T., Janković, N.Z., Ristić, S.S., Čantrak, Đ.S., *Uncertainty analysis of 3D LDA system*, Proc., The 7th International Congress of the Serbian Society of Mechanics, Minisymposium M3: Turbulence, Sremski Karlovci, Serbia, Proceedings, paper No. M3j, pp. 189, 2019.

10th International Congress of the Serbian Society of Mechanics
Niš, Serbia, June 18-20, 2025

M.2.6
Extended abstract

LES FOR MODELLING WIND FLOW IN URBAN BLOCK: ACCURACY, CHALLENGES AND APPLICATIONS

Kristina O. Kostadinović Vranešević[0000-0002-4006-0599]1, **Miloš M. Jočković**[0000-0002-2409-9450]1, and **Anina S. Glumac**[0000-0003-4201-506X]1

[1]University of Belgrade, Faculty of Civil Engineering, e-mail:
kkostadinovic@grf.bg.ac.rs, mjockovic@grf.bg.ac.rs, anina@grf.bg.ac.rs

Abstract. Urban wind flow is highly turbulent due to interactions with complex urban topology. While wind tunnel experiments provide reliable data, they are costly and limited in scope. Large Eddy Simulation (LES) offers a more detailed representation of turbulence, improving accuracy in capturing transient urban wind flows. This study examines LES accuracy, challenges, and applications in modelling wind flow around high-rise buildings, considering an isolated building and a group of five buildings. A validation framework is established through comparisons with available wind tunnel measurements. Results highlight the challenge of modelling conical vortices on flat roofs and demonstrate the role of LES in enhancing wind energy harvesting in urban areas and identifying critical zones for wind-induced peak pressures on building envelope. Despite its advantages, LES accuracy varies with flow complexity, reinforcing the need for experimental validation.

Keywords: ABL, Urban areas, LES, High-rise building, Turbulence, Wind flow patterns.

1. Introduction

Urban wind flow is highly complex and characterised by strong turbulence, flow separation, and recirculation zones shaped by building geometries, street canyons, and surface roughness. Understanding urban wind dynamics is crucial for various applications, including urban wind comfort, pollution dispersion, wind energy potential, and wind loading on structures. Wind effects in urban areas are assessed through wind tunnel experiments and numerical simulations. While wind tunnels are reliable, they are costly and limited in scope. Numerical simulations, particularly Large Eddy Simulation (LES), offer detailed turbulence modelling but require validation with experiments [1]. One of the biggest challenges in LES is accurately predicting peak surface pressures, which are crucial for the wind-induced load on cladding [2].

This study investigates the accuracy, challenges, and applications of LES in modelling urban wind flow around high-rise buildings. Two configurations are analysed: an isolated high-rise building and a group of five. The study establishes a validation framework for numerical simulations, comparing them with available wind tunnel measurements and assessing their accuracy. Characteristic flow structures are examined, highlighting challenges in LES modelling. Finally, the applicability of LES in evaluating wind energy harvesting potential and wind loading is demonstrated.

2. Methodology

Numerical simulations are performed to replicate the available wind tunnel tests, ensuring a valid comparison. The building model, a square-based high-rise at a 1:300 geometric scale, is examined in isolated and group configurations, as shown in Figure 1(a). The computational domain (Figure 1(b)) represents the test section of the atmospheric boundary layer (ABL) wind tunnel at Ruhr University, Bochum, Germany (Figure 1(a)) with all turbulence-inducing elements in a precursor domain. Further details on the LES setup and validation will be provided in the presentation.

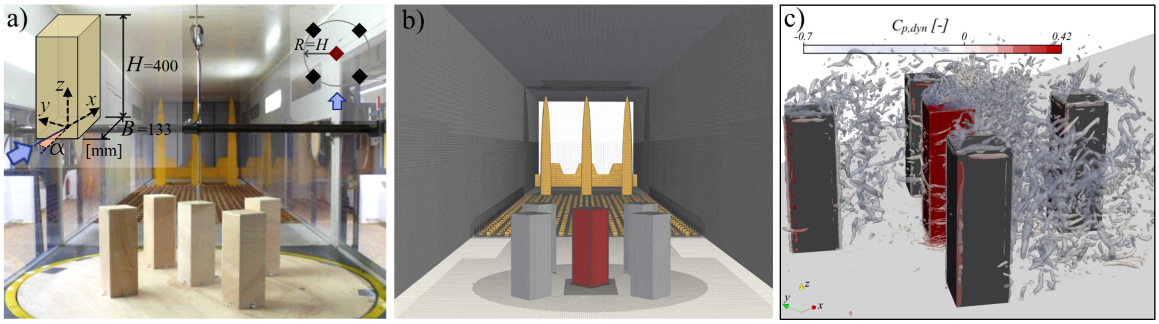

Figure 1: Group configuration at 45° wind angle: (a) mounted in ABL wind tunnel with the geometry of the model at the Ruhr University, Bochum, Germany; (b) computational domain in LES; (c) isocontours of λ_2 invariant at $\lambda_2 = 300000$

3. Results

To illustrate the LES results, Figure 1(c) presents isocontours of the λ_2 invariant for the group configuration at a 45° wind angle. The presentation will offer a detailed analysis of the dominant mean flow structures around the building and the impact of neighbouring buildings by comparing isolated and group configurations at two approaching wind angles, 0° and 45°. Additionally, key wind characteristics relevant to wind energy harvesting will be reviewed. Finally, an evaluation of the peak pressure coefficients on the flat roof will be demonstrated, linking them to flow patterns and providing deeper insight into underlying mechanisms.

4. Concluding remarks

LES has proven to be an effective tool for modelling urban wind flow, but its accuracy depends on the complexity of the analysed configuration. Validation remains crucial, as increasing flow complexity can introduce discrepancies. A key challenge identified is the accurate modelling of conical vortex structures on the flat roofs of high-rise buildings. In wind energy applications, LES enhances the prediction of harvesting potential and optimises turbine type and placement. For wind-induced cladding load, critical zones of high suction are identified on the flat roof.

References

[1] Blocken B., *LES over RANS in building simulation for outdoor and indoor applications: A foregone conclusion?*, Building Simulation, Vol. 11, 821–870, 2018.

[2] Maruta E., Kanda M., Sato J., *Effects on surface roughness for wind pressure on glass and cladding of buildings*, Journal of Wind Engineering and Industrial Aerodynamics, Vol. 74–76, 651–663, 1998.

10th International Congress of the Serbian Society of Mechanics
Niš, Serbia, June 18-20, 2025
M.2.7
Extended abstract

Numerical study of natural convection in a square enclosure with a circular cylinder at different vertical positions

Nikola D. Milosavljevic[1] and **Darko R. Radenkovic**[2] [0000-0002-6522-7260]

[1]University of Belgrade, Faculty of Mechanical Engineering, Serbia, e-mail: d14-2024@studenti.mas.bg.ac.rs

[2]University of Belgrade, Faculty of Mechanical Engineering, Serbia, e-mail: dradenkovic@mas.bg.ac.rs

Abstract. Natural convection in enclosed spaces is a fundamental heat transfer mechanism in thermal engineering and electronics cooling. Numerical simulations have been conducted for the case of natural convection of air within a square enclosure containing a circular cylinder. Convection is driven by the constant temperature difference between the cold walls of the enclosure and the heated cylinder. The simulation results were obtained for a two-dimensional unsteady air flow using the open-source software OpenFOAM. The objective of the simulations was to determine how the vertical position of the cylinder influences heat transfer on the enclosure walls for different Rayleigh number values. The trends in the variation of the local Nusselt number Nu_l along the enclosure walls show good agreement with available numerical results. Initially, the local Nusselt number distribution is symmetric about the horizontal centerline of the enclosure. However, this symmetry is progressively broken as convective heat transfer becomes more dominant. The surface averaged Nusselt numbers on the top and bottom walls are sensitive to the cylinder's position. This influence increases with the Rayleigh number. On the other hand, heat transfer on the side walls shows little dependence on the cylinder's position up to $\mathrm{Ra} = 10^7$.

Keywords: Natural convection, Boussinesq approximation, OpenFOAM.

1. Simulation setup

Considered geometry shown in Figure 1) is defined as in [1]. The enclosure has a square shape with a side length of L. The cylinder changes its position δ along the vertical centerline of the enclosure, ranging from -2.5 to 2.5 in increments of 0.5. The cylinder's radius is $R = L/7$. The walls of the square enclosure are maintained at a constant low temperature T_c, while the cylinder is kept at a constant high temperature T_h.

In this study, radiation effects are considered negligible. The equations describing air flow in the enclosure are solved using the `BouyantBoussinesqPimpleFoam` solver. The turbulent flow regime occurs locally within the boundary layers along the heat exchange surfaces. To calculate turbulence, the k–ε turbulence model is employed. Fluid properties are assumed to be constant, except for density in the buoyancy term, in accordance with the Boussinesq approximation.

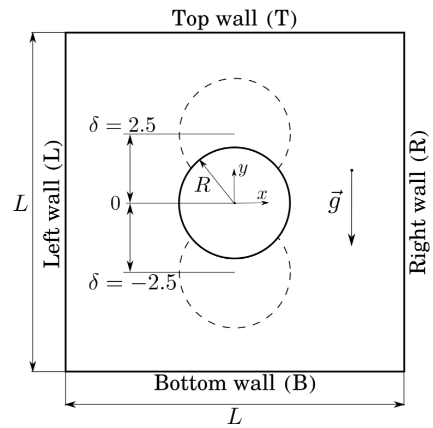

Figure 1: Enclosure geometry.

2. Results and discussion

Position of the cylinder makes the problem fully axisymmetric. Therefore, heat transfer is only analyzed on the walls of the right half of the enclosure. Figure 2 shows the distribution of the local Nusselt number Nu_l as a function of the cylinder's position for $\mathrm{Ra} = 10^4$ and $\mathrm{Ra} = 10^8$. At a Rayleigh number of $\mathrm{Ra} = 10^4$, heat transfer on the enclosure walls is primarily driven by conduction, resulting in a symmetric distribution of Nu_l. As the Rayleigh number increases, convective heat transfer becomes more dominant [2]. The accumulation of cold air in the lower half of the enclosure disrupts the symmetry of the Nu_l values distribution. A comparison with available experimental data and numerical studies is planned in continuation of the study.

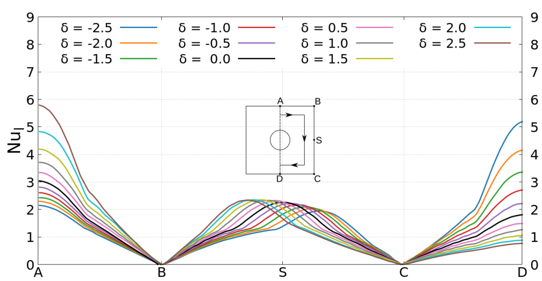

(a) $\mathrm{Ra} = 10^4$

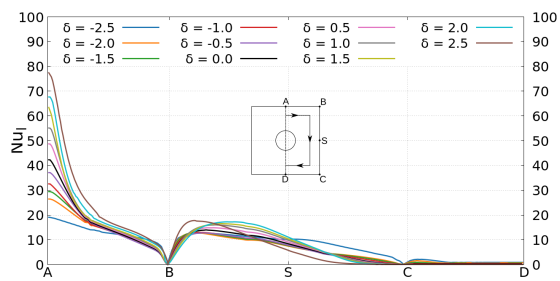

(b) $\mathrm{Ra} = 10^8$

Figure 2: The distribution of the local Nusselt number along the enclosure walls as a function of the cylinder's position and the Rayleigh number.

References

[1] Kim B., Lee D., Ha M., Yoon H., *A numerical study of natural convection in a square enclosure with a circular cylinder at different vertical locations*, International Journal of Heat and Mass Transfer, Vol. 51, 1888-1906, 2008.

[2] Milosavljevic N., *Numerički proračun prirodne konvekcije vazduha u zatvorenom hladnom kućištu u kojem se nalazi zagrejani cilindar*, Mašinski Fakultet, Beograd, 2024.

10th International Congress of the Serbian Society of Mechanics
Niš, Serbia, June 18-20, 2025
M.2.8
Abstract

TESTING OF X-RAY DETECTION IN TURBULENT FLOW FOR SPACE APPLICATIONS USING SILICON DRIFT DETECTOR

Igor Planjanin[1[0009-0003-1136-5304]], **Milan Stojanović**[1[0000-0002-4105-7113]], **Đorđe Čantrak**[2[0000-0003-1841-9187]], **Jelena Svorcan**[2[0000-0002-6722-2711]], **Dušan Marčeta**[3[0000-0003-4706-4602]], **Marko Gavrilović**[1], **Luka Popović**[1[0000-0003-2398-7664]], **Ivan Kokić**[4]

[1] Astronomical Observatory, Research Unit for Space Science and Technologies, Volgina 7, 11000 Belgrade, Serbia
e-mail: iplanjanin@aob.rs

[2] Faculty of Mechanical Engineering, The University of Belgrade, Kraljice Marije 16, 11120 Belgrade 35, Serbia

[3] Faculty of Mathematics, The University of Belgrade, Studentski trg 16, 11158 Belgrade, Serbia

[4] Institute Mihajlo Pupin d.o.o., Volgina 15, 11060 Belgrade, Serbia

Abstract:

Silicon Drift Detectors (SDD) are widely used in space missions for their high energy resolution and compact design, particularly in X-ray and particle spectroscopy. The performance of X-ray detectors in low Earth orbits (LEO) is influenced by environmental conditions. In this context, testing of such detector is required in controlled laboratory, simulating suitable conditions. While these detectors are not directly intended to measure fluid dynamics, environmental conditions encountered in LEO – including rarefied atmospheric gases and localized, quasi-turbulent flows – can cause thermal instability, mechanical disalignment, and influence on data accuracy. This paper presents laboratory testing of X-ray detection, simulating transitional and low-intensity turbulent flow conditions representative of those experienced by satellites in LEO.

Key words: X-ray, detector, turbulence

10th International Congress of the Serbian Society of Mechanics
Niš, Serbia, June 18-20, 2025
M.2.9
Extended abstract

Towards the Characterisation of Flow Perturbation Transmission in Convergent Nozzles affecting Free Water Jet Surfaces

Bernhard Semlitsch[1] [0000-0001-7715-863X]

[1]TU Wien, Institute of Energy Systems and Thermodynamics, Austria, email:
bernhard.semlitsch@tuwien.ac.at

Abstract. Free water jets are elementary for many engineering applications, where a convergent nozzle is commonly used to convert the available potential energy into kinetic energy to obtain high-velocity water jets. The free water jet surface can be severely deformed by flow perturbations, e.g., secondary flows induced by flow separation or bends, and cause unwanted free water jet column breakup. Convergent nozzles accelerate the flow and thereby affect the perturbation properties during conveyance. This transmission characteristic is studied by multiphase large eddy simulations, where the free water jet column interacts with a flat surface. The spectral properties of the flow fluctuations are monitored upstream and downstream of the nozzle, where three different nozzle convergence angles are investigated. The simulations reveal that with increased flow acceleration, i.e. higher nozzle convergence angles, the flow experiences relaminarisation. Furthermore, a change in fluctuation properties is observed after the water jet/flat surface interaction. The numerical simulation results are validated against experimental pressure measurements.
Keywords: Free water jets, Coherent flow structures, Flow perturbations, Large eddy simulation

1. Introduction

The behaviour of vortical flow structures can be described by the vorticity transport equation, which reveals that the vorticity is stretched in the streamwise direction when being accelerated. The other vorticity components remain unaffected, causing turbulence intensity freezing in the core region during flow accelerations [1]. The flow behaves initially ”laminar-like” near the walls during acceleration [2]. Subsequently, transition and fully turbulent flow can be expected if a sufficient propagation length is provided. In case of short convergent cross-sections, initial relaminarisation during acceleration can occur. Thus, the incoming flow perturbations can be manipulated by convergent or divergent cross-flow area sections. This is of particular interest in many engineering applications, such as free water jets, hydro turbine nozzles, or water cannons, where flow distortions would cause unwanted losses or even water column breakup. With the acceleration of breakup in convergent nozzles, incoming flow perturbations can be potentially reduced, and the water jet quality can be improved. Nonetheless, quantitative data guiding the nozzle design are not yet available for this purpose. Therefore, detailed numerical flow simulations of free water jets are performed to understand this phenomenon better.

2. Methodology and setup

Free water jets, including the surrounding ambient air, are simulated by solving the incompressible Navier-Stokes equations, where the volume-of-fluid approach is employed to handle the multiphase environment. A sufficient fine block-structured mesh is utilised, i.e. $y^+ < 1$, to simulate a large proportion of the turbulent flow scales, while the smallest flow scales are modelled implicitly by the numerical dissipation. This approach is also known as implicit large eddy simulation. A recycling-type boundary condition has been selected (with a recycling length of eight times the diameter) to impose the turbulent flow perturbations at the inflow. The employed numerical schemes are of second-order accuracy, where the SuperBee scheme has been used for the convective terms. The time-step was selected such that the Courant number remained below 0.5.

Different nozzle geometries with and without convergence are simulated, where the emerging water jet interacts with a perpendicular plate located two nozzle diameters downstream of the orifice. The nozzle diameter, d_0, is 30 mm. The inflow velocity was chosen to match the experimental conditions by Pollaschek [3], i.e. 20 m/s, to enable the validation of the simulation results, which is shown in Figure 1 (b). Appropriate properties at standard ambient conditions have been selected for water and air.

3. Results

Large eddy simulations of free water jets have been performed to investigate the transmission process of flow perturbations through nozzles, while focusing on the free surface distortion of the water jets. The free surface of the water jet without convergence is exemplarily shown in Figure 1 (a). The effect of initial relaminarisation due to flow acceleration caused by a nozzle convergence has been observed in the cross-correlation analysis between cross-sectional planes. By the time the free water jet interacts with the perpendicular flat surface, the turbulence levels are comparable.

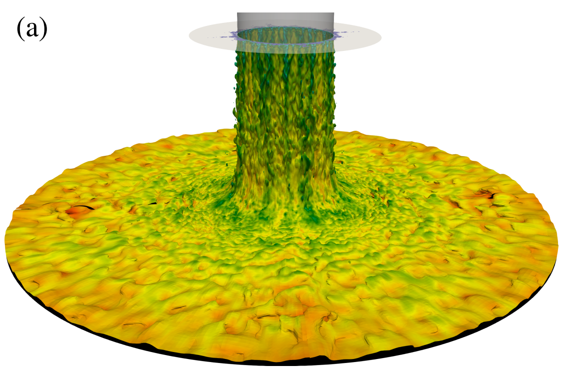

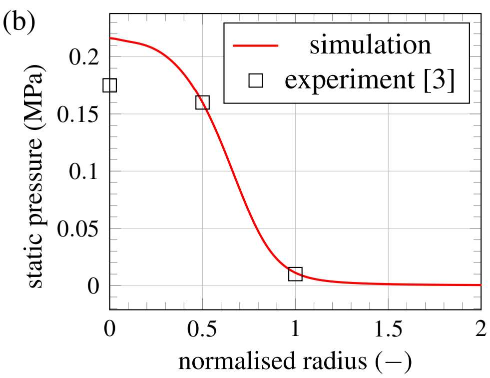

Figure 1: The free surface of a water jet interacting with a perpendicular flat plate is shown by an isosurface coloured by the velocity magnitude. The grey surfaces represent the nozzle geometry and the flat plate.

References

[1] Greenblatt, D., and Moss, E.A., *Rapid temporal acceleration of a turbulent pipe flow*, Journal of Fluid Mechanics, Vol. 514, 65-75, 2004.

[2] Seddighi, M., He, S., Vardy, A.E., and Orlandi, P., *Direct numerical simulation of an accelerating channel flow*, Flow, turbulence and combustion, Vol. 92, 473-502, 2014.

[3] Pollaschek, S., *Numerische Simulation am Freistrahl einer Peltonturbine*, Master thesis - TU Wien, 2013.

10th International Congress of the Serbian Society of Mechanics
Niš, Serbia, June 18-20, 2025

M.2.10
Original scientific paper

DOI:10.46793/ICSSM25.321S

COMPARISON OF NOISE SPECTRA OF THE FLOW PAST A CYLINDER COMPUTED BY DIFFERENT TURBULENCE MODELS

Jelena Svorcan[1][0000-0002-6722-2711], Vidosava Vilotijević[2]

[1] University of Belgrade, Faculty of Mechanical Engineering
Kraljice Marije 16, 11120 Belgrade
e-mail: jsvorcan@mas.bg.ac.rs

[2] University of Montenegro, Faculty of Mechanical Engineering
Džordža Vašingtona bb., 81000 Podgorica
e-mail: vidosavav@ucg.ac.me

Abstract:

Aero-acoustic features are a contemporary and important topic for many mechanical systems, and include various flow phenomena, such as "singing" of wires, cables, metal rods, antennas, etc. as well as wake shedding from different kinds of blades. The aim of the current computational study is to compare and estimate the reliability of available turbulence and acoustic models in ANSYS FLUENT. A spatial, incompressible, transient flow around a cylinder at relatively low Reynolds number Re = 90000 and Mach number M = 0.2 is used as a benchmark and investigated in detail. Both unsteady Reynolds-averaged Navier-Stokes (URANS) and filtered Navier-Stokes (large eddy simulation, LES) equations are solved and resulting flow fields are compared. In both cases, Ffowcs-Williams and Hawkings (FWH) acoustic model is employed. The presented results include oscillating aerodynamic coefficients, instantaneous and averaged flow field visualizations, noise spectra and overall noise levels. Comparisons between the tested turbulence models confirm that the simpler, computationally less expensive URANS approach captures fewer flow features than LES, as well as the resulting noise frequency components, but is applicable for initial studies. On the other hand, both tested turbulence models underestimate the generated noise by roughly 25%. In can be concluded that the agreement with the corresponding, available experimental data seems acceptable for preliminary analyses. Aerodynamic coefficients can be estimated with more reliability than acoustic quantities.

Key words: aero-acoustics, cylinder, flow simulation, CFD, turbulence

1. Introduction

In accordance with the emerging stringent noise regulations, aero-acoustic noise has become a major concern for contemporary mechanical systems, especially when they incorporate wings or blades [1-4]. Since aerodynamically induced noise is often related to shedding wakes, high speeds, flow transition and turbulence, it is being actively investigated [1-10]. With the aim to advance our understanding of the physical phenomena leading to sound generation and propagation in fluids, these studies focus on the connection between aerodynamic and acoustic features, the effects of Reynolds number and the onset of flow separation, wake inspection, etc.

and are dominantly numerical. There are also numerous studies focused on the control of flows past bluff bodies with the main purpose of decreasing the noise levels induced by the inspected flow [11].

In the current research study, a benchmark case corresponding to a fully turbulent vortex street shedding from a cylinder (at Reynolds number Re = 90000) is computationally investigated in detail, so that more complex mechanical systems (such as wind turbine rotors and blades) can be analyzed with more reliability in future studies. More details on the previous experimental and numerical studies, as well as data used for validation, can be found in [12-14]. The intricacy of the inspected flow lies in the fact that the generated sound is directly related to turbulent flow separation and wake propagation, which still presents a genuine challenge to numerical flow simulations, and requires an adequate approach to modeling/partially resolving turbulence.

2. Numerical modelling

The employed numerical modeling approaches are explained in detail in the following subsections.

2.1 Geometry

The cylinder diameter is D = 19 mm. A simple rectangular computational domain is used, extending 5D upstream and 20D downstream of the cylinder. To capture some of the spatial flow features (since planar flow simulations that were conducted did not prove reliable), the rectangular domain is extruded 0.2D in the third, z-direction. In future studies, this length will be additionally investigated (and should most likely be extended further).

The boundaries of the computational domain include an inlet, an outlet, symmetric upper and lower sides (to decrease the size of the computational domain), and lateral surfaces forming a periodic boundary.

2.2 Mesh

The employed computational meshes are generated in accordance with the chosen turbulence models, and are in both cases sufficiently refined around the cylinder walls. The global cell size (throughout the domain, far away from the cylinder) is limited to 2 mm, cell growth rate is 1.2, while the cell size along the cylinder surface is limited to 0.1 mm.

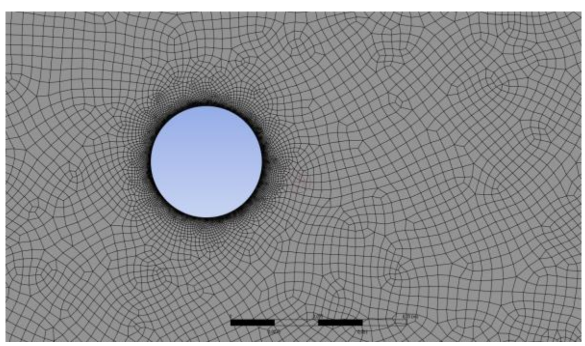

Fig. 1. Detail of the generated LES mesh

For some cases, where flow is resolved by k−ω SST turbulence model, inflation layer is also added (with the first layer thickness y_1 = 0.01 mm, resulting in dimensionless wall distance $y^+ < 3$, and 10 layers of prismatic cells in the wall vicinity). This setup is beneficial because maintaining $y^+ < 3$ ensures that the first cell layer lies within the viscous sublayer, allowing the turbulence model to accurately resolve near-wall shear stresses without relying on wall functions. The added prismatic layers help capture steep velocity and pressure gradients in the boundary layer, which is critical for obtaining reliable aerodynamic force predictions.

Overall, the LES mesh numbers approximately 635000 cells (since in its case, it is recommended to have $y^+ > 30$), while the refined $k{-}\omega$ SST mesh numbers more than 1.1 million cells. A detail of the generated LES mesh is illustrated in Fig. 1.

2.3 Numerical set-up

The investigated unsteady incompressible flows around a cylinder at Reynolds number Re = 90000 and Mach number M = 0.2 (where fully turbulent vortex street can be expected) are resolved by two different turbulence models, $k{-}\omega$ SST and wall-modeled large eddy simulation (WMLES) in ANSYS FLUENT. RANS-based $k{-}\omega$ SST model solves two additional transport equations for turbulence kinetic energy k and its specific dissipation rate ω, and is often employed in aerospace engineering applications. On the other hand, the governing equations in LES approach are obtained by the filtering process, where eddies bigger than the filter size (or grid spacing) are resolved while the resulting subgrid-scale stresses require modeling. This numerical approach is still computationally quite expensive, which is the reason why its algebraic wall-modeled variant WMLES, that can be used on somewhat coarser meshes, is more appealing for industrial applications.

As previously mentioned, the boundary conditions include velocity inlet (with the prescribed velocity V = 69.2 m/s), pressure outlet (with the zero gauge pressure), symmetric (top and bottom) and periodic (lateral) sides. The standard air properties are assumed. The reference values for the estimation of force coefficients are computed from the velocity prescribed at the inlet and cylinder dimensions.

A pressure-based solver was employed, with pressure-velocity coupling by fractional step method that is often combined with the non-iterative time advancement (that is less computationally expensive). Here, the time step is small dt = 5 μs (to capture the wake dynamics), the transient formulation is bounded second order implicit, while the spatial discretizations of the convective terms are as follows: PRESTO! for pressure and bounded central differencing for momentum. Additionally, under-relaxation factor for pressure is reduced to 0.7 to ensure computational stability.

The force coefficients (lift and drag) were continuously monitored during the simulations. Usually, 4000-8000 time steps dt were computed to achieve quasi-convergence.

The Ffowcs-Williams and Hawkings (FWH) acoustic model was activated in the second half of each simulation [10]. For the estimation of mid- to far-field noise, this method based on Lighthill's acoustic analogy is often employed, because it combines the computed near-field flow with the analytically derived integral solutions to wave equations. In this way, the flow solution is decoupled from the acoustics analysis, which greatly simplifies the computations.

Four receivers are defined and monitored, while the noise source is the cylinder wall. Two receivers are located in the vertical y-direction (receivers 1 and 2 were positioned 35D and 128D, respectively, perpendicularly away from the cylinder following the expected flow separation), while the other two receivers are located downstream, in the wake (10D and 20D from the cylinder, respectively, for receivers 3 and 4).

3. Results and discussion

In order to obtain the acoustic imprints, the turbulent flow simulations are first performed and presented here. The quantitative output includes fluctuating aerodynamic coefficients (lift and drag) where it is possible to separate the obtained profiles into mean and fluctuating components (listed in Table 1 and illustrated in Fig. 2), as well as the averaged pressure and skin friction coefficients distributions (illustrated in Fig. 3).

A tabular comparison of the computed and experimental aerodynamic quantities is provided in Tables 1 and 2. The dominant shedding frequency f is represented by the Strouhal number St = fD/V, while lift and drag coefficients are given by their mean and maximal fluctuating values. It can be observed that, in both cases, the numerical shedding slightly differs from the measured, and that flow separation seems a bit delayed in comparison to the observed. Also, while there is an acceptable correspondence between the averaged values of the force coefficients, their fluctuating parts seem over- or under-estimated by computation. However, it should be accentuated that the maximal fluctuating amplitudes are listed, and not their standard deviations.

	St	C_L'	mean(C_D)	C_D'
Experiment	0.018-0.191	0.45-0.60	1.00-1.40	0.18
WMLES	0.248	1.62	1.14	0.34
$k-\omega$ SST	0.248	1.08	0.99	0.07

Table 1. Experimental vs. computed aerodynamic quantities

Time histories of the monitored force coefficients for drag C_D and lift C_L, with respect to dimensionless time $t^* = tV/D$, are depicted in Fig. 2. As can be expected, the profiles obtained by the $k-\omega$ SST turbulence model are simple periodic with much lower amplitudes in comparison to the profiles obtained by WMLES, where the occurrence of irregular vortex break-up seems to be captured.

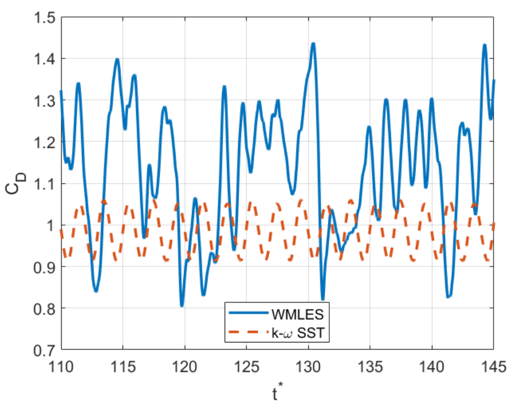

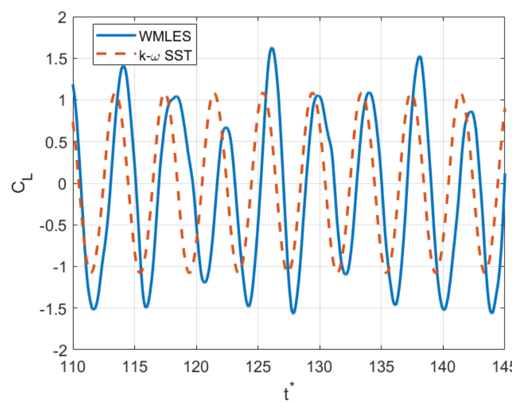

Fig. 2. Computed aerodynamic (lift and drag) coefficients

Finally, the averaged pressure C_p and skin friction C_f distributions are given in Fig. 3. While the main features of the flow (including the shedding frequency and the location of the flow separation) seem similar in both cases, some differences in the flow behavior (both fore and aft of the separation) can be observed.

The obtained qualitative output in the form of different flow field visualizations is depicted in Figs. 4-6. Figure 4 illustrates the obtained instantaneous velocity contours. For both tested turbulence models, the expected alternating vortex shedding is captured. However, in the case of the $k-\omega$ SST turbulence model, the wake gets attenuated/dissipated much sooner (almost at the outlet boundary), and the velocity differences within the computational domain are less accentuated. The same (that the wake is rather dependent on the employed turbulence model) can be concluded for the computed instantaneous pressure contours illustrated in Fig. 5. The computed wakes are additionally presented by vorticity contours and compared in Fig. 6. Again, the vortical structures obtained by WMLES are much better delineated and correspond more to the experimentally observed flow cases.

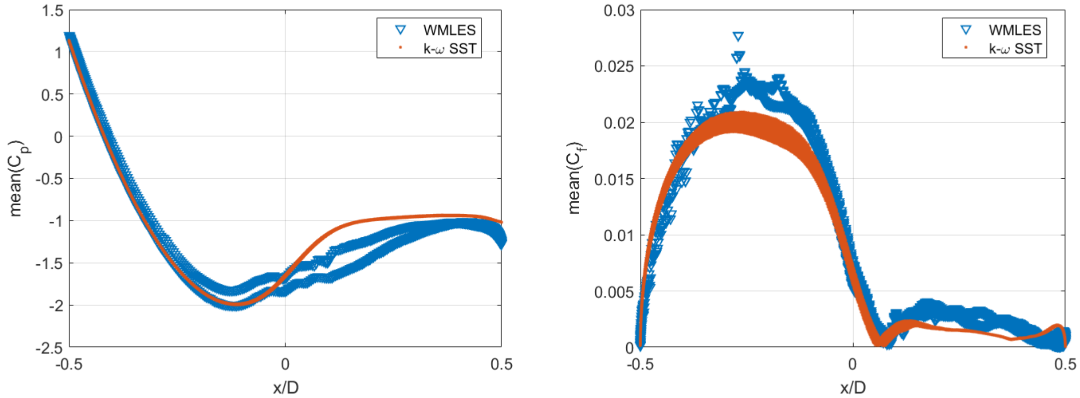

Fig. 3. The computed aerodynamic coefficients, including pressure and skin friction distributions, are presented along the cylinder wall

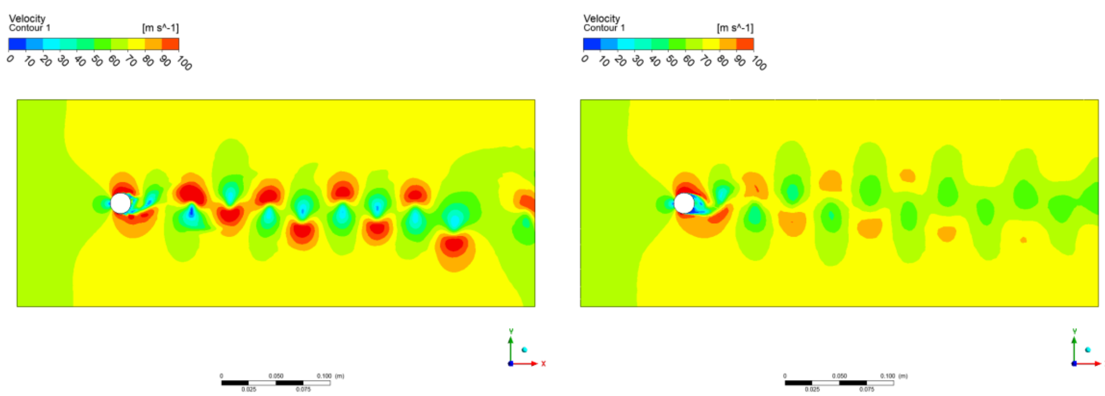

Fig. 4. Computed instantaneous velocity contours: WMLES (left) and $k{-}\omega$ SST (right)

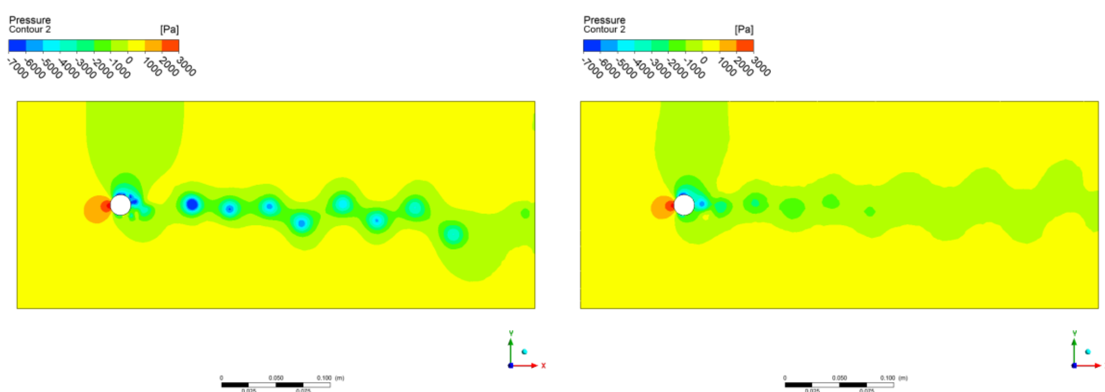

Fig. 5. Computed instantaneous pressure contours: WMLES (left) and $k{-}\omega$ SST (right)

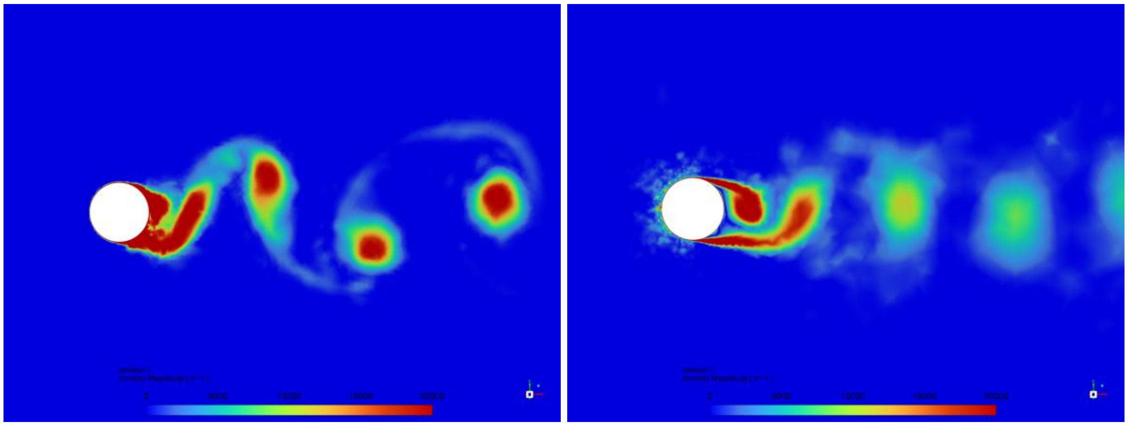

Fig. 6. Computed instantaneous vortical structures: WMLES (left) and k–ω SST (right)

As previously mentioned, in the second half of the simulations, the acoustic model was activated, and four receivers (two located in the perpendicular, y-direction, and two located in the axial, x-direction) were monitored. The noise spectra computed by the two different turbulence models are presented in Fig. 7. It can immediately be observed that WMLES captures more noise frequency components since it captures a greater number of flow features (vortex generation, shedding and break-up). On the other hand, the k–ω SST turbulence model manages to distinguish the main frequencies directly corresponding to the vortex shedding.

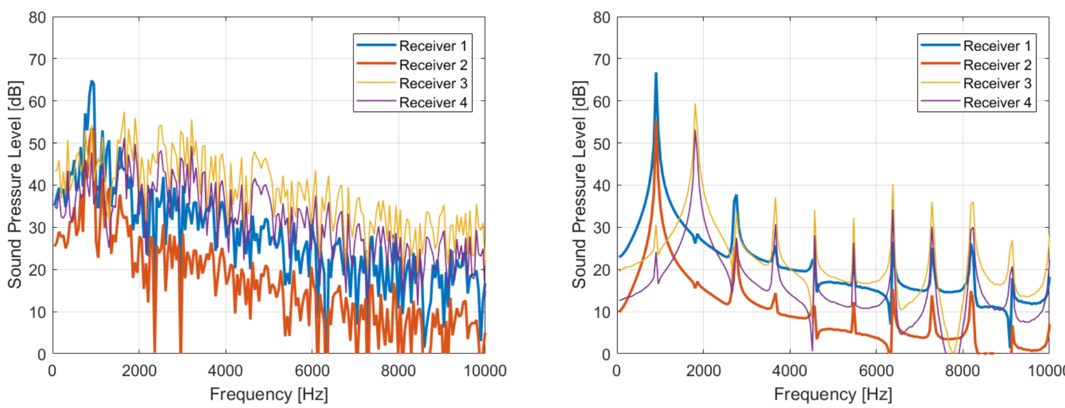

Fig. 7. Computed acoustic spectra: WMLES (left) and k–ω SST (right)

The computed overall sound pressure levels (OASPL), measured in dB, for the four receivers are listed in Table 2, and comparison to experimental data is performed where possible. It can be observed that the relative difference reaches and surpasses 25%, and that the results obtained by the k–ω SST turbulence model are somewhat lower than the ones computed by WMLES, which can again be explained by the “cleaner” noise spectrum obtained in the former case. These values are also dependent on the assumed source correlation length, which can be the focus of future studies.

	Receiver 1	Receiver 2	Receiver 3	Receiver 4
Experiment	-	100.0	-	-
WMLES	86.4	75.1	85.3	78.9
k–ω SST	84.1	72.9	78.3	72.1

Table 2. Experimental vs. computed OASPL in [dB]

4. Conclusions

The paper describes the fluid flow and acoustic computations of the flows around a cylinder performed in ANSYS FLUENT by two different turbulence models. Even though the investigated flow case is well-known and has been often investigated in the past, it is still difficult to simulate and requires further investigative work. Some of the main computational challenges stem from the unavoidable flow separation, vortex forming and shedding, as well as the simplified acoustic model (based on the acoustic analogy) that was employed. The overall noise levels predicted by the presented flow simulations appear to be underestimated compared to the available experimental data by roughly 25%.

In future studies, computational domain should be expanded (in both *y*- and *z*-direction), computational meshes should be additionally refined (particularly in the wake), and different numerical approaches should be tested.

Acknowledgements

This research work was supported by the Ministry of Science, Technological Development and Innovation of the Republic of Serbia through contract No. 451-03-137/2025-03/200105 from February 4th 2025.

References

[1] Liu, Z., Bu, C., Kong, X., Yang, D., *Aeroacoustics Investigation on Nano Coaxial Rotor in Hover*, International Micro Air Vehicle Conference and Flight Competition (IMAV) 2017, IMAV2017-7, 44-50, Toulouse, France, 2017.

[2] Kamliya Jawahar, H., Hanson, L., Akhter, M.Z., Azarpeyvand, M., *Porous ground treatments for propeller noise reduction in ground effect*, Scientific Reports, Vol. 15, 2170, 2025.

[3] Vaezi, E., Madani, S.A.S., Keshmiri, A., *A Parametric study on the effects of winglet cant angle on wing aerodynamics and aeroacoustics*, Scientific Reports, Vol. 15, 1417, 2025.

[4] Wills, A., Moreau, D., de Silva, C., Doolan, C., *Measurement, scaling and optimal dimensions of airfoil leading-edge serrations in isotropic turbulence*, Journal of Sound and Vibration, Vol. 608, 119079, 2025.

[5] Blevins, R.D., *Flow Induced Vibration*, 2nd Ed., Van Nostrand Reinhold Co., New York, 1990.

[6] Ng, Z., Vo, T., Hussam, W., Sheard, G., *Two-dimensional wake dynamics behind cylinders with triangular cross-section under incidence angle variation*, Journal of Fluids and Structures, Vol. 63, 302-324, 2016.

[7] Uruba, V., Procházka, P., *The Reynolds number effect on dynamics of the wake behind a circular cylinder*, AIP Conference Proceedings, Vol. 2189(1), 020023, 2019.

[8] Ezadi Yazdi, M.J., Bak Khoshnevis, A., *Comparing the wake behind circular and elliptical cylinders in a uniform current*, SN Applied Sciences, Vol. 2, 994, 2020.

[9] Rodriguez, I, Lehmkuhl, O., *On the Characteristics of the Super-Critical Wake behind a Circular Cylinder*, Fluids, Vol. 6(11), 396, 2021.

[10] Golliard, T., Mihaescu, M., *Swirling Flow Effects on the Aeroacoustic Signature of an Aerospike Nozzle*, Journal of Turbomachinery, Vol. 147(8), 081009, 2025.

[11] Muddada, S., Hariharan, K., Sanapala, V.S., Patnaik, B.S.V., *Circular cylinder wakes and their control under the influence of oscillatory flows: A numerical study*, Journal of Ocean Engineering and Science, Vol. 6(4), 389-399, 2021.

[12] Revell, J., Prydz, R., Hays, A., *Experimental Study of Aerodynamic Noise vs Drag Relationships for Circular Cylinders*, AIAA Journal, Vol. 16(9), 889-897, 1978.

[13] Nordberg, C., *Fluctuating lift on a circular cylinder: review and new measurements*, Journal of Fluids and Structures, Vol. 17, 57-96, 2003.

[14] Orselli, R., Meneghini, J., Saltara, F., *Two and Three-Dimensional Simulation of Sound Generated by Flow Around a Circular Cylinder*, 15th AIAA/CEAS Aeroacoustics Conference (30th AIAA Aeroacoustics Conference), AIAA 2009-3270, Miami, Florida, 2009.

10th International Congress of the Serbian Society of Mechanics
Niš, Serbia, June 18-20, 2025
M.2.11
Extended abstract

TRANSIENT SIMULATION ON INTERNAL FLOW CHARACTERISTICS AND PRESSURE PULSATION OF VARIABLE SPEED FRANCIS TURBINES DURING ACCELERATION PROCESS

Wenjie Wang[1][0000-0003-2562-5026], **Shan Liu**[1], **Ji Pei**[1][0000-0002-6998-1906]

[1]National Research Center of Pumps,
Jiangsu University, Xuefu Road 301, Zhenjiang 212013, Jiangsu Province, China.
e-mail: wenjiewang@ujs.edu.cn; liushan9912@163.com; jpei@ujs.edu.cn

Abstract:

Francis turbines offer advantages such as compactness, high efficiency, and adaptability to very high head ranges, making them the most common type of hydraulic turbine. Compared to fixed-speed turbines, variable-speed turbines exhibit faster power response, which effectively expands the operational range and enhances overall efficiency. Due to the complexity of the internal structure of the hydraulic turbine, rotor–stator interactions occur between the components, which reduce the efficiency of the hydraulic turbine and affecting the overall stability of the unit's operation. Therefore, studying the internal flow characteristics of the hydraulic turbine during the variable-speed transition process and analyzing the causes of pressure pulsation is of significant importance.

To investigate the internal flow dynamics and pressure pulsation characteristics during the variable-speed operation of the Francis-99 turbine, this paper employs numerical simulations to examine the internal pressure, flow behavior, and energy loss variations over time during the acceleration process. The Hilbert-Huang Transform (HHT) method is utilized to generate the corresponding time-frequency diagram of the pressure pulsation signal, thereby enhancing the accuracy and reliability of feature extraction. The HHT is a powerful tool for analyzing nonlinear and nonsmooth signals. It combines VMD with the Hilbert Transform, which can effectively handle complex signals that are difficult to process using traditional Fourier Transform and Wavelet Transform.

Based on the HHT method, the pressure pulsation signal was decomposed into an intrinsic mode function (IMF) using variational modal decomposition (VMD). VMD is an adaptive, non-recursive decomposition method for signal processing that decomposes a complex signal into several IMFs, each with a distinct center frequency. And Fast Fourier Transform (FFT) was applied to the IMF to identify the components contributing most significantly to the pressure fluctuations.

The final results indicate that as the rotational speed increases, the flow within the flow channel becomes more complex, resulting in higher energy losses. The overall pressure decreases as the rotational speed rises. The primary frequencies of pressure pulsations at the guide vane outlet and runner inlet remained at $30f_n$ and $28f_n$, respectively, with increasing speed. The IMF components that had the greatest influence on the pressure fluctuations were IMF1-IMF2 and IMF1-IMF3, respectively. This suggests that the primary cause of high-amplitude pressure fluctuations in the vaneless space is the rotor-stator interaction between the guide vanes and the runner.

In summary, This study provides a valuable reference for assessing the instability characteristics of hydraulic turbines under variable-speed conditions, and also provides a strong theoretical guideline for future improvements in the operational efficiency of the Francis-99 turbine.

Key words: Variable speed, Francis turbine, Pressure pulsation, Variational modal decomposition, Hilbert transformation.

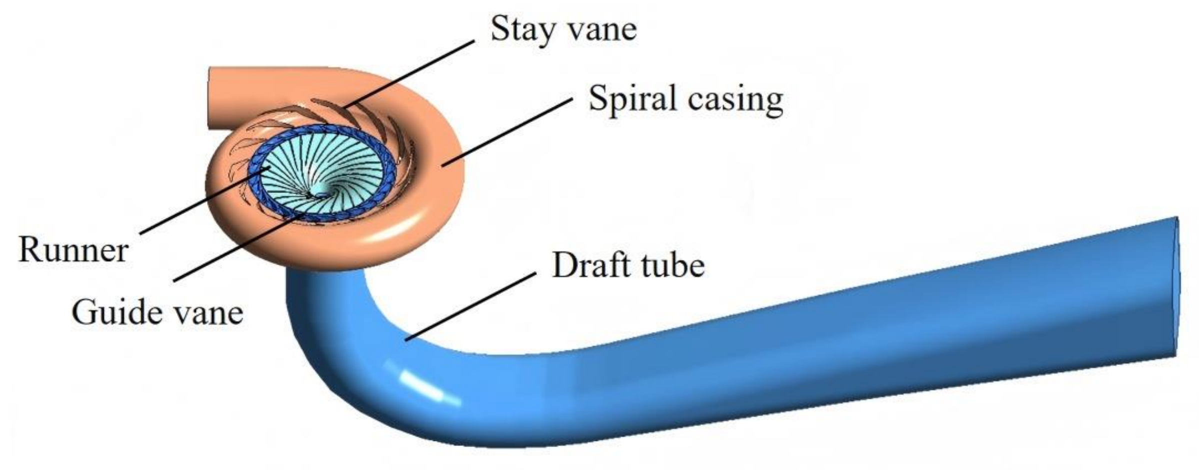

Fig. 1. 3D schematic diagram of the Francis-99 model.

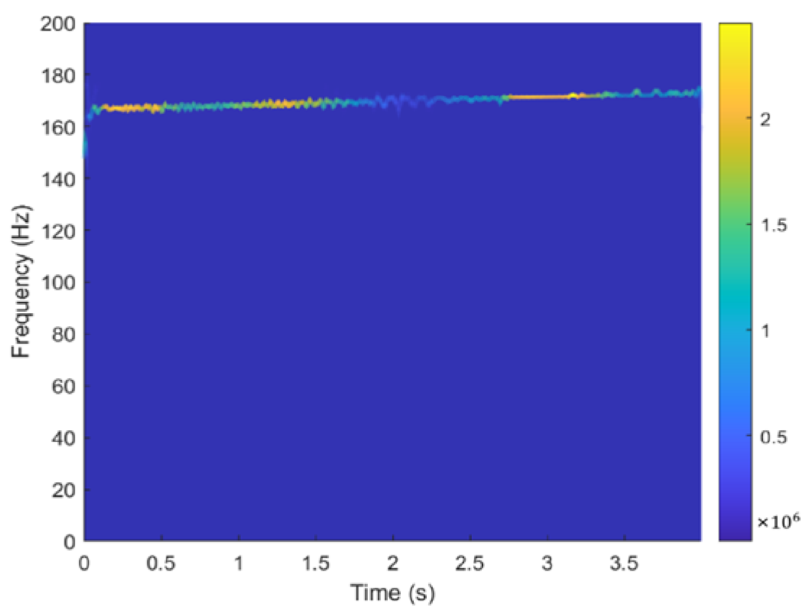

(a) HHT time-frequency domain

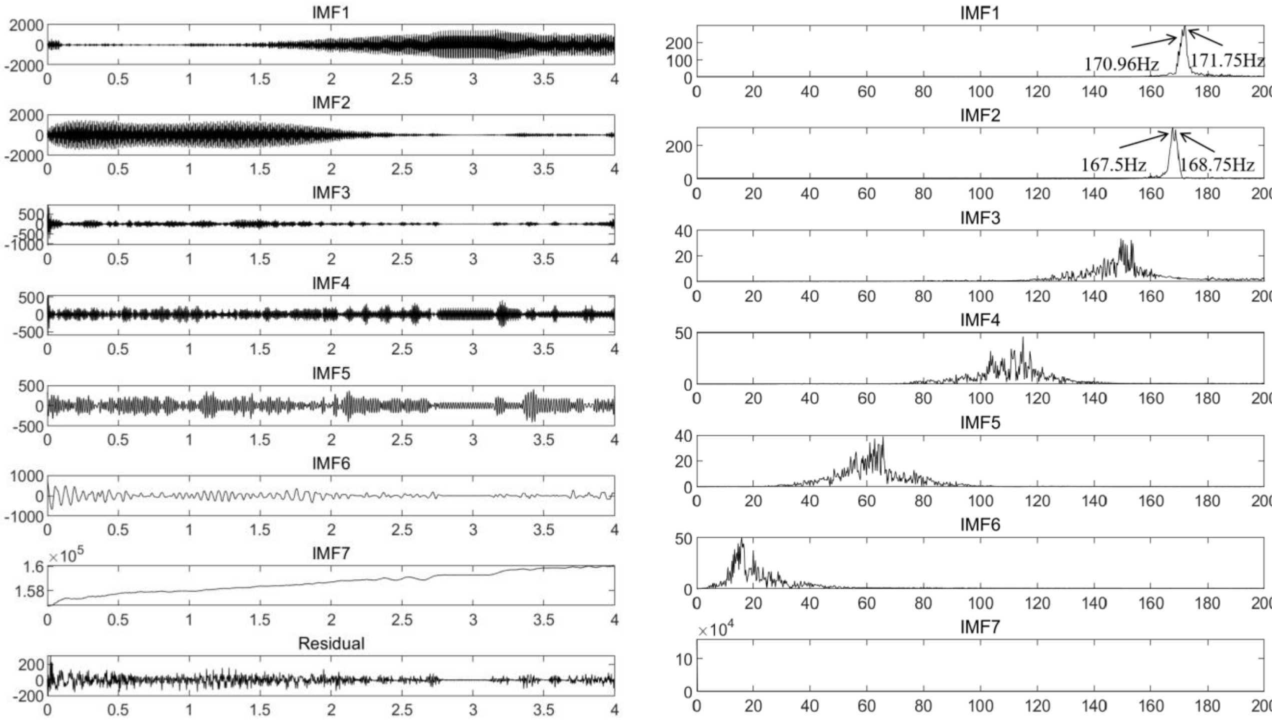

(b) VMD decomposition signal (c) FFT of the IMF

Fig. 2. HHT and VMD decomposition of pressure fluctuations and FFT results at the outlet of guide vane

References

[1] Wang W, Yu Z, Yan Y, et al. *Numerical investigation on vortex characteristics in a low-head Francis turbine operating of adjustable-speed at part load conditions*[J]. Energy, 2024, 302: 131800.

[2] Zheng X, Zhang S, Zhang Y, et al. *Dynamic characteristic analysis of pressure pulsations of a pump turbine in turbine mode utilizing variational mode decomposition combined with Hilbert transform*[J]. Energy, 2023, 280: 128148.

[3] Wang W, Pavesi G, Pei J, et al. *Transient simulation on closure of wicket gates in a high-head Francis-type reversible turbine operating in pump mode*[J]. Renewable Energy, 2020, 145: 1817-1830.

[4] Trivedi C, Agnalt E, Dahlhaug O G. *Experimental study of a Francis turbine under variable-speed and discharge conditions*[J]. Renewable Energy, 2018, 119: 447-458.

Mini-Symposia 3: Biomechanics and Mathematical Biology

Organizers:

Anđelka Hedrih (Mathematical Institute of Serbian Academy of Sciences and Arts, Serbia) and Marat Dosaev (Lomonosov Moscow State University, Moscow, Russia).

M.3.1

Extended abstract

DEFORMATION OF HUMAN CHEST AS AN ELASTIC TRUSS

I. Alpatov[1], M. Dosaev[1][0000-0002-3859-4065], V. Samsonov[1][0000-0002-8930-171X], E. Vorobyeva[2], V. Dubrov[2]

[1] Institute of Mechanics, Lomonosov Moscow State University
Michurinskiy 1, 119192 Moscow, Russia
e-mail: alpatov.ivan@list.ru

[2] Faculty of Fundamental Medicine, Lomonosov Moscow State University
Lomonosovskiy 27, korp. 1, 119991 Moscow, Russia
e-mail: eamnoc@gmail.com

Abstract:

In this study we consider a problem of human chest deformation under load. Our approach is to model human chest as an elastic truss consisting of rigid beams connected by spring elements, that impede the rotation of the beams relative to each other. A custom solver program was developed that allowed to obtain convergent solutions of the chest deformation problem.

Key words: chest deformation, pectus carinatum, mathematical modeling, tree structure

1. Introduction

Modeling of a human chest is a topical problem, especially for use in the treatment of patients with pectus carinatum, which is one of the most common chest deformities. In order to determine personal treatment recommendations, it is necessary to understand how a particular chest will be deformed under a force applied to its keel.

We proposed an approach to modeling a chest using a spatial elastic truss [1]. Geometric model of the chest was obtained by segmenting the ribs and cartilages from a CT scan of a patient with pectus carinatum. Then, based on the segmented data, we built a model consisting of rigid beam-like finite elements that would approximate the original geometry. The connections between beams are elastic elements that hinder relative rotation of the beams around all axes.

The numerical solution to the problem of deformation of such a truss was obtained using the Ansys finite element analysis package. Using this approach, the rib flaring effect was demonstrated, which sometimes occurs in the treatment of pectus carinatum [2]. Unfortunately, in practice it was impossible to stably obtain numerical solution in Ansys as it encountered severe convergence problems. Also, Ansys is a closed source package and it does not allow much control over its numerical methods. That is why we developed new custom solver program that allowed us to obtain convergent solutions for the chest deformation problem.

2. Methodology

The new solver program was written using Python programming language and Pytorch framework. This program is aimed to directly solve the problem of deformation of a general constrained elastic system consisting of rigid rods and joints between them as an optimization problem. Indeed, this static deformation problem can be formulated as the problem of minimizing the potential energy under constraints. Currently our program uses trust region method for solving constrained optimization problem but it is planned to add more methods. Our program also uses Pytorch Autograd engine to automatically calculate gradients and hessians of objective and constraint functions.

The solver program uses a concept of mechanical system with tree structure to easily build a graph of elastic system that allows a concise calculation of potential energy and constraints functions. The program is highly generalized and modular in terms that it can be easily adapted to new kinds of joints, constraints and forces applied to mechanical system.

In our specific case of a human chest model the new method allowed to find mathematical reasons of convergence instability and to use numerical methods tricks to make a solution process much more stable. For our model the constraints are the fixed points of ribs on vertebra, force is applied only to a chest keel in the symmetry plane of the model and rigid beams are connected by elastic joints whose potential energy is calculated from the change of an angle between two beams that form the joint. The geometry of the model was obtained, as in the previous method, from a CT scan of the patient with pectus carinatum. We also studied the dependence of model deformation on joint stiffnesses hyperparameters.

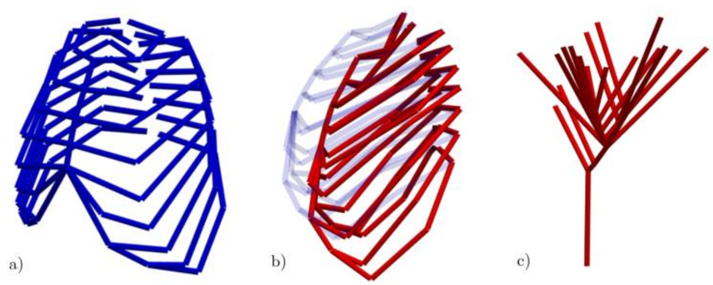

Fig. 1. a) Undeformed and b) deformed chest model, c) tree structure for chest model

3. Results and Conclusion

The solver program was developed that allows to stably obtain convergent solutions for the problems of deformation of elastic trusses. This program was successfully tested on the problem of deformation of human chest under force applied to the chest keel. Human chest was modeled as an elastic truss consisting of stiff beams and elastic joints between them. The proposed solver allowed to investigate the relation between applied force and deformation of the model, particularly, keel point and lower rib cartilages. We also were able to simulate rib flaring effect which is a very common side effect in treatment of patients with pectus carinatum deformity.

References

[1] Alpatov, I., Dosaev, M., Samsonov, V., Vorobyeva, E., & Dubrov, V. *Phenomenological approach to human chest modeling*, Journal of Mechanics in Medicine and Biology. 23(06), 2023. https://doi.org/10.1142/s0219519423400390

[2] Lan Haje, S., Haje D. *Overcorrection during treatment of pectus deformities with DCC orthoses: Experience in 17 cases*, Int Orthop 30, 262–267, 2006.

10th International Congress of the Serbian Society of Mechanics
Niš, Serbia, June 18-20, 2025

M.3.2
Original scientific paper

DOI: 10.46793/ICSSM25.335A

NUMERICAL SIMULATIONS OF BLOOD FLOW IN VESSELS WITH DIFFERENT GEOMETRIES

Nadia M. Antonova[1][0000-0003-1707-0235], Dong Xu[2]

[1] Institute of Mechanics
Bulgarian Academy of Sciences, Akad. G.Bonchev str., Bl.4, 1113 Sofia, Bulgaria
e-mail: antonova@imbm.bas.bg

[2] College of Water Conservancy & Hydropower Engineering
Hohai University, China, No.1 Xikang Road, Nanjing, Jiangsu, China
e-mail: xudong@hhu.edu.cn

Abstract

Modern scientific assumptions about the influence of biomechanical factors on the development of atherosclerosis are based partly on clinical observations that atherosclerotic lesions mainly occur at the mouths of branching vessels, in segments of high curvature or in places with sharply changing geometry, where serious changes in the structure of the blood flow can be observed. Changes in blood flow negatively affect the functioning of the cardiovascular system, leading to deformation of the arteries, which ultimately changes the local rheological properties of the blood.

The study aims to overview different methods for evaluation of hemodynamics in the common carotid artery bifurcation, coronary, abdominal and its iliac branch arteries performing numerical analysis of blood flow based on Navier-Stokes equations. Determined results of velocity distribution, tangential stresses, pulse wave velocity in models of blood vessels with stenoses are analyzed. The effect of non-Newtonian blood rheological properties is discussed.

Key words: numerical simulations, blood flow, common carotid artery (CCA), CCA bifurcation, stenosis, coronary artery, abdominal artery, blood rheological properties, wall shear stress (WSS)

1. Introduction

The application of medical image reconstruction to vessel modeling for use in computational fluid dynamics (CFD) has developed rapidly in recent decades. The typical process for performing numerical blood flow simulation is based on medical imaging, image segmentation, 3D models reconstruction, grid generation, and blood flow analysis by solving the Navier-Stokes equations. With the development of modern imaging technology, MRI, CT, etc., it is now possible to quantify arterial blood flow in subject-specific physiological models and to assess hemodynamics and wall shear stress distribution. With the help of CFD simulations and MRI, the ability to evaluate the complex relationship between hemodynamics and predictions of blood vessel damage may be possible.

The study aims to overview different methods for evaluation of hemodynamics in arteries with different physiological geometries as the carotid and common carotid artery (CCA) bifurcation, coronary and iliac arteries in parallel with numerical analysis of blood flow based on Navier-Stokes equations by different methods.

2. Methods

2.1 Numerical studies of blood flow in the carotid artery bifurcation with stenosis. Influence of blood rheological properties

Several authors have investigated blood flow in the common carotid artery [1-4]. Blood flow in carotid artery bifurcation is studied based on Navier-Stokes equations performing numerical simulations by a finite volume method and considering one wave period [1-3]. Four different cases of the common carotid bifurcation were examined: without stenoses, with one, two and three stenoses. Based on geometry reconstruction a mesh generation is done. The case studies are based on different anatomies presented by the one, two or three stenoses of common carotid bifurcation vessel. Physiological geometry can be imported into a CFD solver. The numerical results of the blood flow in the common carotid bifurcation give detailed picture of the axial velocity and WSS distribution. The flow in the bifurcation is strongly unsteady. For the case of carotid bifurcation without stenoses results for the axial velocity distribution are presented in the character time points T=0 s, 0.1 s, 0.2 s, 0.3 s, 0.4 s, 0.5 s. The results show that the blood flow in carotid bifurcation is unsteady, and the flow disturbances depend on the time and type of the stenoses. The pattern of the velocity and the WSS are obtained and comparison of the peak WSS is done for the four considered cases – without stenoses, with 1, 2 and 3 stenoses. The results show the influence of the stenoses on blood flow in the bifurcation and deposition processes around it. The recirculation zone behind the stenosis is the area of low WSS. This is the most probable area for thrombus formation. The peak WSS is increasing, and the maximum is being achieved earlier with an increase in the number of stenoses. Our observation for the four cases studied by us is that the vorticity magnitude is greatest on the vessel wall. This zone becomes larger formed in the presence of one, two and three stenoses [3].

Mansur et al. [4] performed numerical analysis of the three-dimensional model of pulsatile and non-Newtonian blood flow in a carotid artery with local occlusion using Ansys Fluent. The effect of the shear thinning of blood is simulated using the Carreau-Yasuda model, neglecting the viscoelastic effects. The results obtained show that, compared to Newtonian fluids, non-Newtonian fluids exhibit significant differences in secondary flow patterns and shear flow behavior. Additionally, the axial velocity in the non-planar branch decreases with obstruction. The occlusion of the vessel at 80% and 50% of the internal diameter is analyzed. The results obtained in this study show that, compared to Newtonian fluids, non-Newtonian fluids exhibit significant differences in secondary flow patterns and shear flow behavior. Additionally, the axial velocity in the non-planar branch decreases with obstruction.

Numerical simulations by Perktold et al. (1991) [5] show that incornoration of the shear thinning behavior of blood did not alter the flow characteristics in a stenosed carotid artery significantly. The experimental data of Liepsch et al. [6], however, indicated that the viscoelasticity of the fluid could be of importance for the region of flow reversal.

Symmetrical 30–60% stenosis in a common carotid artery under unsteady flow conditions for Newtonian and six non-Newtonian viscosity models is investigated numerically by A. Razavi et al. [7]. Results show power-law model produces higher deviations, in terms of velocity and wall shear stress, in comparison with other models, while the generalised power-law and modified-Casson models are more prone to the Newtonian state. The differences between models are more significant at low inlet velocities and in the case of the power law and Walburn–Schneck models for even high inlet velocities. Comparing the separation length of the recirculation region at different critical points of the cardiac cycle confirms the necessity of considering blood flow in unsteady mode. Increasing stenosis intensity causes flow patterns to be more disturbed downstream of the stenosis, and WSS appears to develop remarkably at the stenosis throat. The trends of WSS and radial velocity are the same for all blood viscosity models; however, the magnitude of these parameters differs from one model to another.

2.2. Numerical simulation of the spatio-temporal evolution of the flow in the model of abdominal aorta bifurcation with stenosis

The structure of the pulsating flow in the model of the average configuration, including the bifurcation of the abdominal aorta and subsequent bifurcation of the iliac arteries with axisymmetric hemodynamically significant stenosis in the right common iliac artery, is studied by numerical methods by D. Sinitsina et al. [8]. It has been shown that the presence of stenosis in this artery affects the flow structure both downstream and upstream: reverse-flow zones are formed, and transverse flow evolution differs significantly from the structure of the flow in a healthy branch. The stenosis with the spatial curves of the model leads to the formation of a stable single-vortex flow in the external iliac artery for most of the cardiac cycle. In the mentioned artery of the healthy branch various unstable patterns of two-vortex structure form during the cycle. In both internal iliac arteries, there is a transitional flow, from a two-vortex to a single-vortex motion, forming during the cycle. The influence of the presence of stenosis on the structure of the transverse flow in the internal iliac artery is insignificant. The authors conclude that the most likely regions for atherosclerotic lesions of the vascular wall are characterized by the minimum values of time-averaged wall shear stresses and the maximum values of oscillatory shear index, are the stenosis region and the external wall of the common iliac artery.

2.3. Influence of blood rheological properties on the formation of recirculation zones near coronary artery stenosis

The influence of blood rheological properties on the features of recirculation zone formation in hemodynamic flows near coronary artery stenosis is studied by Makhaeva et al. in [9]. The Newtonian model and the Carreau model are used to describe dynamic viscosity. Calculations are performed for an ideal 2D vessel with double and single stenosis, each of which had a degree of overlap of 50 – 80 %, and for a 3D model of a real coronary artery with a stenosis of 50 %, which was reconstructed from X-ray data. On the example of 2D vessel model the formation of recirculation zones after stenosis was theoretically substantiated by methods of mathematical and computer modeling. The formation of stationary vortex regions significantly depended on the blood model used. The relationship between the characteristics of the blood flow recirculation phenomenon and local and general hemodynamic characteristics is known. To demonstrate the relationship between the rheological properties of blood and the characteristics of the phenomenon of blood flow recirculation on more complex vessel geometries, similar computer calculations were performed for a three-dimensional model of a real coronary artery. Comparative analysis of the Newtonian model and the Carreau model showed that the non-Newtonian behavior of blood significantly affects such hemodynamic characteristics of blood flow as viscosity, pressure, shear stress and shear rate. A significant difference in the obtained results is shown in the case of high flow velocities. It was concluded that the Newtonian blood model can be used only in vessels with minimal disturbances in the blood flow pattern [9].

Three viscoelastic constitutive models, defining a more complete rheology of blood, were implemented in ANSYS Fluent, using UDFs, and tested for idealized and patient-specific geometries of right coronary arteries by S. Pinto et al. [10]. The Generalized Oldroyd-B (GOB) model, a quasi-linear model, and two non-linear models, the Multi-mode Giesekus and Simplified Phan-Thien/ Tanner (sPTT) models, were implemented. For right coronary arteries, velocity and wall shear stress were compared, considering a purely shear-thinning model, Carreau model, and the implemented viscoelastic models. An overall reduction of the velocity in regions of higher velocity gradients was observed, considering the non-linear viscoelastic multi-mode models (Giesekus and sPTT). Moreover, the difference in peak wall shear stress values considering these multi-mode viscoelastic models is close to half the magnitude (51%) of Carreau model solutions.

3. Conclusions

An overview of the papers devoted to determination of velocity distribution, tangential stresses, pulse wave velocity in models of blood vessels (carotid, coronary, abdominal) with stenoses and in their branches is done. The influence of blood rheological properties on the formation of recirculation zones near artery stenosis and bifurcation is analysed.

Acknowledgements: The study has been supported by the Bulgarian National Science Fund - Project № КП-06-Н57/14/2021.

References

[1] Antonova N., Dong X., Tosheva P., Velcheva I., *Numerical analysis of 3D blood flow and common carotid artery hemodynamics in the carotid artery bifurcation without stenoses.* J. Series on Biomechanics, vol. 28, 3-4, 50-60, 2013, ISSN:1313-2458.

[2] Antonova N., Xu Dong, Tosheva P., Kaliviotis E., Velcheva I., *Numerical analysis of 3D blood flow and common carotid artery hemodynamics in the carotid artery bifurcation with stenosis*. J. Clinical Hemorheology and Microcirculation, vol. 57, 2, 159-173, 2014, ISSN:1386-0291, DOI:10.3233/CH-141827.

[3] Antonova N., Xu D., Velcheva I., Kaliviotis E., Tosheva P., *Stenosis effects on the fluid mechanics of the common carotid artery bifurcation for unsteady flows.* J. Mechanics in Medicine and Biology, vol.15, 2, 1540008, 2015, DOI:10.1142/S0219519415400084,

[4] Mustafaoğlu M., Kotçioğlu I., Yeşilyurt M.K., *Numerical analysis of the three-dimensional model of pulsatile and non-Newtonian blood flow in a carotid artery with local occlusion.* Mathematical Modelling and Numerical Simulation with Applications, 5(1),97-116, 2025. https://doi.org/10.53391/mmnsa.1522021

[5] Perktold K., Peter R.O., Resch M., Langs G., 1991, *Pulsatile non-newtonian blood flow in three-dimensional carotid bifurcation models: a numerical study of flow phenomena under different bifurcation angles*, J. Biomed. Engineering, vol.13, 6, 507–515, 1991.

[6] Liepsch D., Moravec St., *Pulsatile flow of non-Newtonian fluid in distensible models of human arteries*, Biorheology, vol.21, 571-586, 1984.

[7] Razavi A., Shirani E., Sadeghi M., *Numerical simulation of blood pulsatile flow in a stenosed carotid artery using different rheological models*. Journal of Biomechanics, vol.44(11), 2021-2030, 2011, https://doi.org/10.1016/j.jbiomech.2011.04.023

[8] Sinitsina D. E., Zaitsev D. K., *Numerical simulation of the spatio-temporal evolution of the flow in the model of abdominal aorta bifurcation with stenosis in the one of the common iliac arteries*, J. Phys.: Conf. Ser., 1697, 2020, 012232 DOI 10.1088/1742-6596/1697/1/012232

[9] Makhaeva K.E., *Effect of blood rheological properties on the formation of recirculation zones behind of coronary artery stenosis*., Russian J. Biomechanics, vol. 28, 4, 85–95, 2024. DOI:10.15593/RZhBiomeh/2024.4.07

[10] Pinto S.I.S., Romano E., António C.C., Sousa L.C., Castro C.F., *The impact of non-linear viscoelastic property of blood in right coronary arteries hemodynamics — A numerical implementation*, International J. of Non-Linear Mechanics, vol.123, 2020, Article 103477

10th International Congress of the Serbian Society of Mechanics
Niš, Serbia, June 18-20, 2025
M.3.3
Extended abstract

A CONTIUNOUS–TIME *SIS* CRISS–CROSS MODEL OF CO–INFECTION IN A IN HETEROGENEOUS POPULATION

Marcin Choiński[1] [0000-0001-6157-8963]

[1]Institute of of Information Technology, Warsaw University of Life Sciences – SGGW, Nowoursynowska 159 Street, building 34, 02-776 Warsaw, Poland, email: marcin_choinski@sggw.edu.pl

Abstract. In this paper we introduce and analyze a continuous–time model of co–infection dynamics in a heterogeneous population consisting of two subpopulations that differ in the risk of getting infected by individuals with both diseases. We assume that each parameter reflecting a given process for each subpopulation has different values, what makes the population completely heterogeneous. Such complexity and the population heterogeneity make our paper unique reflecting co–infection dynamics. Moreover, we establish an epidemic spread for each disease not only in a sole subpopulation, but also criss–cross transmission, meaning between different subpopulations. The system has a universal structure, it can be therefore applied to investigate the co–infection for different infectious diseases.

Keywords: Co–infection; *SIS* model; Local stability; Population heterogeneity; Dynamical Systems

1. Formulation of a model and its basic properties

In a population we indicate two subpopulations, a low–risk (*LS*) and a high–risk (*HS*) subpopulation, that relate to the risk of getting infected. *LS* and *HS* have accordingly lower and higher susceptibility to each disease. For every variable and parameter we assign a subscript i equal to 1 and 2 for *LS* and *HS*, respectively. If i has no assigned value, then $i \in \{1,2\}$. By S_1 and S_2 we denote a density of healthy people in *LS* and *HS*, respectively. The variables I_i mean a density of individuals from the given subpopulation that are infected by a pathogen of disease which we call disease *A* (*DA*). Similarly, we define J_i as a density of individuals suffering from disease *B* (*DB*). A density of a group infected by pathogens from both diseases is denoted by K_i.

Migrating and newborn individuals join each subpopulation through S_i class with a recruitment rate C_i. A natural death rate for each subpopulation is equal to μ_i. For *DA* we introduces transmission rates: β_{11}, β_{22}, β_{12}, β_{21} reflecting transmission: among *LS*, among *HS*, from *HS* to *LS* and from *LS* to *HS*, respectively. Indicating four different rates means that *DA* differs in spreading and contracting a pathogen. To get a preliminary insight on co–infection dynamics for the heterogeneous population, for *DB* we assume that individuals differs only in contracting a pathogen. For this reason we take only two transmission coefficients for *DB*: σ_1 for *LS* and σ_2 for *HS*. By γ_i and g_i we denote a recovery rate for *DA* and *DB*, respectively. The disease–mortality rate for *DA* and *DB* is depicted by α_i and a_i.

The proposed model of co–infection reads

$$\dot{S}_1 = C_1 - \beta_{11}S_1I_1 - \beta_{12}S_1I_2 + \gamma_1 I_1 - \mu_1 S_1 - \sigma_1 S_1(J_1 + J_2) + g_1 J_1, \tag{1a}$$

$$\dot{I}_1 = \beta_{11}S_1I_1 + \beta_{12}S_1I_2 - (\gamma_1 + \alpha_1 + \mu_1)I_1 - \sigma_1 I_1(J_1 + J_2) + g_1 K_1, \tag{1b}$$

$$\dot{J}_1 = \sigma_1 S_1(J_1 + J_2) - (g_1 + a_1 + \mu_1)J_1 - \beta_{11}J_1I_1 - \beta_{12}J_1I_2 + \gamma_1 K_1, \tag{1c}$$

$$\dot{K}_1 = \sigma_1 I_1(J_1 + J_2) + \beta_{11}J_1I_1 + \beta_{12}J_1I_2 - (g_1 + a_1 + \gamma_1 + \alpha_1 + \mu_1)K_1, \tag{1d}$$

$$\dot{S}_2 = C_2 - \beta_{22}S_2I_2 - \beta_{21}S_2I_1 + \gamma_2 I_2 - \mu_2 S_2 - \sigma_2 S_2(J_1 + J_2) + g_2 J_2, \tag{1e}$$

$$\dot{I}_2 = \beta_{22}S_2I_2 + \beta_{21}S_2I_1 - (\gamma_2 + \alpha_2 + \mu_2)I_2 - \sigma_2 I_2(J_1 + J_2) + g_2 K_2, \tag{1f}$$

$$\dot{J}_2 = \sigma_2 S_2(J_1 + J_2) - (g_2 + a_2 + \mu_2)J_2 - \beta_{22}J_2I_2 - \beta_{21}J_2I_1 + \gamma_2 K_2, \tag{1g}$$

$$\dot{K}_2 = \sigma_2 I_2(J_1 + J_2) + \beta_{22}J_2I_2 + \beta_{21}J_2I_1 - (g_2 + a_2 + \gamma_2 + \alpha_2 + \mu_2)K_2. \tag{1h}$$

Each parameter is fixed and positive. In particular, every parameter besides C_i is in the range $(0,1)$. Figure 1 is a schematic drawing of the proposed model.

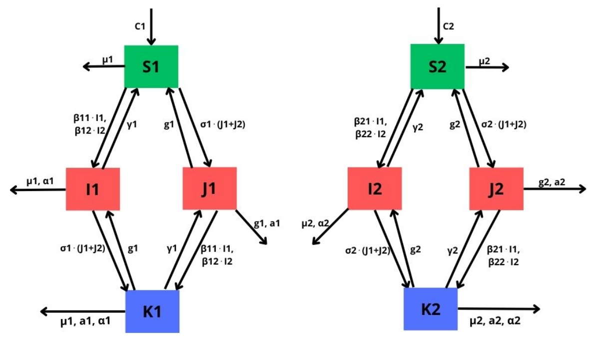

Figure 1: Possible movements between particular classes from system (1).

2. Concluding remarks

We proposed and analyzed the continuous–time model (1) describing co–infection in a heterogeneous population, in which we distinguish two subpopulations. These subpopulations, low–risk *LS* and high–risk *HS*, differ in the risk of getting infected by any of two diseases called disease *A* (*DA*) and disease *B* (*DA*). The values of the parameters for every subpopulation are different, what guarantees complete population heterogeneity. System (1) has four stationary states: disease–free (E_{df}), with sole *DA* or *DB* (E_A and E_B). We also suspect that the endemic state, with two diseases present, exists, but we did not manage to prove it because of complicated computations. State E_{df} exits unconditionally, while provided conditions determine the existence of E_A and E_B. For state E_e we only gave insight into its existence because of the complexity of the computations. For system (1) we computed the basic reproduction number $\mathscr{R}_0$. This number is the maximum of two terms, which forms depend on parameters corresponding to the particular sole infection. Later we investigated the local stability of the stationary state. State E_{df} is locally stable if $\mathscr{R}_0 < 1$, what is expected. Analysis of the local stability for E_A and E_B provided the list of conditions. What is important is that the parameters from both diseases affect the local stability of both states.

References

[1] M. Bodzioch, M. Choiński, U. Foryś, *SIS* criss-cross model of tuberculosis in heterogeneous population, *Discrete and Continuous Dynamical Systems – B*, **24** (2019), 2169–2188, https://doi.org/10.3934/dcdsb.2019089.

10th International Congress of the Serbian Society of Mechanics
Niš, Serbia, June 18-20, 2025
M.3.4
Original scientific paper

DOI:10.46793/ICSSM25.341D

THE PHYSICS OF INTELLIGENCE: CAN THE FERMIONIC MIND HYPOTHESIS PROVIDE A THEORETICAL FRAMEWORK FOR UNDERSTANDING CONSCIOUSNESS?

Eva K. Déli[1], Zoltan Kiss[2]

[1] Faculty of Health Sciences, Institute of Social and Sociological Sciences, Department of Psychology, Debrecen University, Nyíregyháza, Sóstói út 2-4, 4400 Hungary,
eva.kdeli@gmail.com

[2] Institute for Consciousness Studies (ICS), PO Box 30433 Phoenix, Arizona 85046,
zoltan.a.kiss@gmail.com

Abstract:

The rapidly evolving field of artificial intelligence has sparked considerable discussion regarding the potential for artificial consciousness. However, achieving this goal relies on a precise understanding of biological consciousness. At its core, consciousness operates similarly to large language models, functioning as an endothermic information processor and a generator of intellect. Perception arises from a reversible, probabilistic thermodynamic cycle, which imparts probabilistic and quantum characteristics to cognition. At the same time, consciousness possesses intrinsic unity and a fundamental separation, representing fundamental particle features. By adopting the operational principles of elementary particles, the brain gives rise to consciousness, the essential unit of intellect. This novel theory is the fermionic mind hypothesis (FMH), which shows that consciousness is the fundamental unit of intellect, much like fermions form the basis of matter. FMH shows that the physical laws apply to behavior, and emotions represent the four fundamental forces of motivation. Out of these motivation forces, we investigate those we experience in everyday life: gravity and electromagnetism. Emotional electromagnetism shows that the introduction of bias leads to bipolar, discrete behaviors. The reversible perception cycle creates contrasting psychological conditions, the so-called psychological up-and-down spin. Competitors form opposite opinions, dictated by the Pauli exclusion principle. Winners and losers give rise to hierarchical social dynamics akin to atomic organization. The adoption of gravity leads to mental gravity (MG). MG governs competitive thinking and behavior and assists in forming a hierarchic social organization. The fermionic characteristics of consciousness suggest that the brain adapts to its surroundings following physical laws. Our framework explains the operation of consciousness and may facilitate the development of artificial consciousness.

Keywords: consciousness, behavioral and cognitive neuroscience, cognition, neuroscience, behavioral neuroscience, hard problem of consciousness, artificial consciousness

1. Introduction

Understanding consciousness is one of the most pressing scientific questions of our time. While modern neuroscience has advanced through empirical research, leading theories such as Global Workspace Theory [1] and Integrated Information Theory [2] fall short of grounding consciousness in fundamental physical principles. The rapid advancement of artificial intelligence adds urgency to this inquiry, as the parallels between biological and silicon-based cognitive systems may reveal a physical basis for consciousness. This investigation requires an interdisciplinary approach that bridges neuroscience, physics, and mathematics.

Both silicon-based and biological neural systems function as sophisticated information processors, generating intellect through intricate energy dynamics. For instance, energy functions in neural networks measure how well an input aligns with learned patterns. Similarly, biological perception is a thermodynamic process driven by stimuli. Nevertheless, sequential associations form the foundation of experience and cognitive functions, forming a temporal organization. At the heart of this intricate process, the hippocampus converts spatial information into temporal projections, propagating from the past toward the future [3].

Through continuous interaction with the environment, intelligent systems internalize physical principles, giving rise to intuition and insight, which shape thought and behavior. This paper seeks to uncover the shared principles underlying biological and artificial intelligence, ultimately proposing a unified physics framework for cognition. The fermionic mind hypothesis presents a novel theory of consciousness embedded in physical laws [4]. Specifically, the brain constructs an abstract mental space through the intuition and adoption of elementary forces. This study focuses on two fundamental forces central to our everyday experience: electromagnetism and gravity.

2. The temporal nature of consciousness

Our intellectual capacities are deeply rooted in sensory processing. Sensory perception, the complex and continuous assimilation of vast amounts of data, is intricately intertwined with experience-dependent neural activity [5]. This process embodies the potentials and limitations inherent in bodily and environmental interactions. It is the foundation on which consciousness emerges as an embodied experience.

The thalamus modulates sensitivity to incoming sensory stimuli, orchestrating two distinct operational modes. The 'outer' brain swiftly processes high-dimensional sensory input. In contrast, the 'inner' brain refines these signals into temporally distilled information crucial for coordinating behavior [6]. While preserving its inherent depth and meaning, this significant compression of sensory data is akin to a holographic projection that faithfully renders three-dimensional objects in a two-dimensional format. As a result, the constantly evolving stream of thoughts forms the inherent constancy of conscious experience [7].

Without external stimuli, the brain engages in self-reflective associations of the resting state. Stimulus activates the brain's sensory processing, forming a reversible thermodynamic cycle [8]. The regular exothermic cycle dissipates energy. In contrast, an endothermic process requires energy input to accumulate potential. Physical systems produce the arrow of time. This exothermic process reflects the inexorable increase in entropy as prescribed by the second law of thermodynamics (Figure 1). Within an information-theoretic framework, exothermic processes release energy stored from past interactions, cultivating a past-oriented perspective. In contrast, endothermic processes absorb energy in anticipation of future demands.

Shannon's information theory further elucidates how the thermodynamics of perception give rise to emotional, cognitive, and physiological responses. These reversible thermodynamic cycles can orient focus toward the future or the past. A key player in this temporal organization is the brain's extensive memory repository, which can confer remarkable predictive capabilities or a platform for rumination. Energy accumulation characteristic of endothermic states fosters intellect, engendering complexity alongside feelings of contentment, optimism, and hope [9]. In contrast, stress causes past orientation, associated with remorse, regret, and repetitive thinking.

Ultimately, the perception cycle is tied to the past, causing energy dissipation or accumulating energy for future needs. Thus, temporal orientation plays a critical role in shaping intellectual evolution. In this light, individuals with a future-oriented perspective are strategically positioned to harness energy dynamics to enhance their cognitive trajectories and adaptive potential.

3. The psychological spin

The electromagnetic force, one of the four fundamental forces of nature, governs interactions at the elemental level. The electron's spin or intrinsic angular momentum is central to this force, which orients its magnetic field. The Stern–Gerlach experiment demonstrates how an applied magnetic field deflects particles into two distinct trajectories. This bifurcation, admitting only two discrete states labeled as spin-up and spin-down, confirms the quantized nature of spin.

Although emotions are inherently multidimensional and defy simple categorization, recent advances in frequency-based analyses have yielded a binary classification. This frequency-based classification distinguishes positive from negative affect with an impressive accuracy exceeding 96% [10,11]. Within this framework, neutral states occupy a narrow frequency band—typically between 417 and 440 Hz—while deviations toward higher frequencies correspond to stressed states. Lower oscillatory patterns are associated with positive affect [12].

These distinct energy profiles provide a compelling analogy to the quantum mechanical notion of spin, whereby the directional energy flow in neural circuits may be interpreted as a form of "psychological spin" [13] (Figure 1). For instance, a dog's wagging tail can manifest a positive psychological spin, whereas raised hackles indicate a negative state shift. This polarization is connected to emotionally charged experiences. Furthermore, like electric charges, attraction can switch to repulsion instantly, creating love-hate relationships in the social context.

Emotional Electromagnetism (EEM) posits that emotionally charged environments naturally engender biases, leading to discrete separations in opinion [14,15]. Like electrons in an electromagnetic field, individuals in emotionally charged contexts tend to align rigidly, embracing or rejecting stimuli. The Pauli exclusion principle, which applies to fermions, states that no identical fermions can simultaneously occupy the same quantum state. This principle is crucial for organizing electrons in atomic orbitals, contributing to the diverse chemistry of the macroscopic world. The Pauli exclusion principle influences emotional behaviors, suggesting that the evoked cycle of emotional processing occupies an abstract "spin space."

Psychological spin promotes competition and polarization of opinions in social and political spheres, creating division and discord [16]. The simple spin models offer insight into market frictions and herding behavior in economics [17], creating hierarchical social structures and rising inequality. Adaptations of these models, including the Ising model, further elucidate decision-making processes in social and business contexts [18]. In the modern landscape, social media platforms increasingly exploit these dynamics, leveraging our emotional predispositions to influence behavior and steer public discourse. The interplay between energy dynamics, cognitive processing, and emotional valence enriches our understanding of brain function and provides a framework for complex human behavior based on physical phenomena.

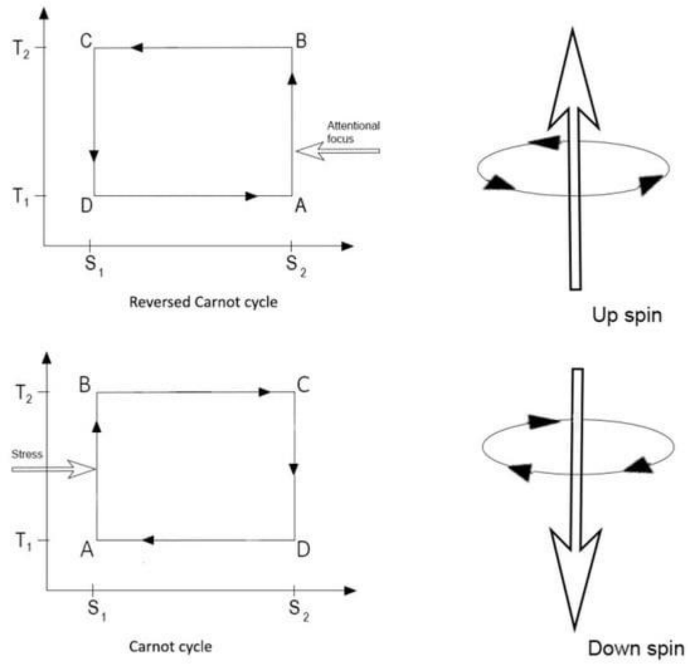

Figure 1. The thermodynamic origin of spin Sensory interaction with the environment triggers the evoked cycle, a thermodynamic cycle representing discrete steps from A through D, which recovers the starting conditions. The endothermic reversed cognitive cycle (top), which requires attentional focus, absorbs energy from the environment, representing up spin. The energy flow supports mental growth and parallels up spin (top right). Stress triggers the exothermic cycle that degrades mental energy (bottom). The energy flow toward the environment parallels down spin (bottom right). (Courtesy of Deli, 2023).

4. Mental Gravity

Einstein's general relativity has reshaped our understanding of gravity as a warping of space-time. It explains how clocks closer to massive bodies tick slower than those further away. This physical time dilation is most extreme near black holes—where time appears to halt. Recent interdisciplinary research has extended the gravity metaphor into the social and behavioral sciences by proposing a concept of "mental gravity" (MG).

In this framework, social or emotional attachments are patterned on the intuition of gravity. As gravity holds matter, people embrace relationships. The pain we feel over the loss of a loved one measures the strength of mental gravity. Neuroscientific studies have reinforced this metaphor. The anterior insular cortex, a key salience network hub associated with interoceptive subjective feelings (reviewed by [19]), social emotions, and empathic pain perception, mediates the internal autonomic inferences and emotional states [20].

Psychology also uncovered that our subjective sense of time is not fixed but fluctuates with our emotional states. Like time dilation measuring gravitational stress, cognitive stress dilates the perception of time [21,22]. Beyond stress, an overestimation of elapsed time also occurs during positive affect [23]. Moreover, recent research suggests that the degree of time dilation is directly proportional to the emotional intensity during an experience [24,25], hinting at an underlying energy relationship [26].

Emotions' connection to energy is also evidenced by the more significant slow down of time perception during the transition to negative states than during the states themselves [27]. Emerging research in affective neuroscience has identified the Default Mode Network (DMN)—a group of interconnected brain regions of the resting state—as a key neural correlate of mental inertia. In states of depression, increased DMN connectivity [28] appears to act like a "mental mass" that slows time perception to a halt [29] in a manner reminiscent of gravitational time dilation. This psychological weight hampers the ability to initiate adaptive behavior.

Time perception regulation involves hormonal pathways, such as striatal dopamine, which is an integral part of the brain's hormonal and energy regulation, underscoring the intimate link between cognitive energy regulation and our perception of time, particularly under stress or information overload conditions.

By conceptualizing physical and mental phenomena within a two-dimensional coordinate system, stress and contentment lie at opposite ends of an information-processing and action-motivation spectrum [30]. Graphing time perception uncovers it as an even function—a graph unchanged under reflection in the y-axis (Figure 3). However, the inverse relationship between the capacity to change and the desire to do so forms an odd function— a graph symmetric to the origin. The subjective experiences of these conditions explain this deviation. In positive emotional states, excess time translates to confidence in self-agency. This confidence is an energy frugality that shows a connection to parasympathetic restorative processes in long-term psychological well-being [31], such as awe at the curve's left minimum (Figure 2). In a stressful context, the feeling of permanence during time pressure, which stress represents, evokes a desperate escape behavior through impatience, impulsivity, and sympathetic arousal [32,33], but without the capacity for meaningful action.

Depression, as a disease of incapacitating "heaviness" and "darkness," existed long before the advent of black hole physics. The similarities between these symptoms and black hole physics suggest that our understanding of physical laws may be innate, rooted in the fermionic organization of consciousness rather than learned (see Table 1).

	Fermion	**Consciousness**
Unity	The unit of matter	The unit of intellect
Thermodynamic outcome	Exothermic cycle → arrow of time	Endothermic cycle → intellect
Constancy	Particle stability	A constant sense of self

Table 1. The characterization of material fermions and the temporal mind

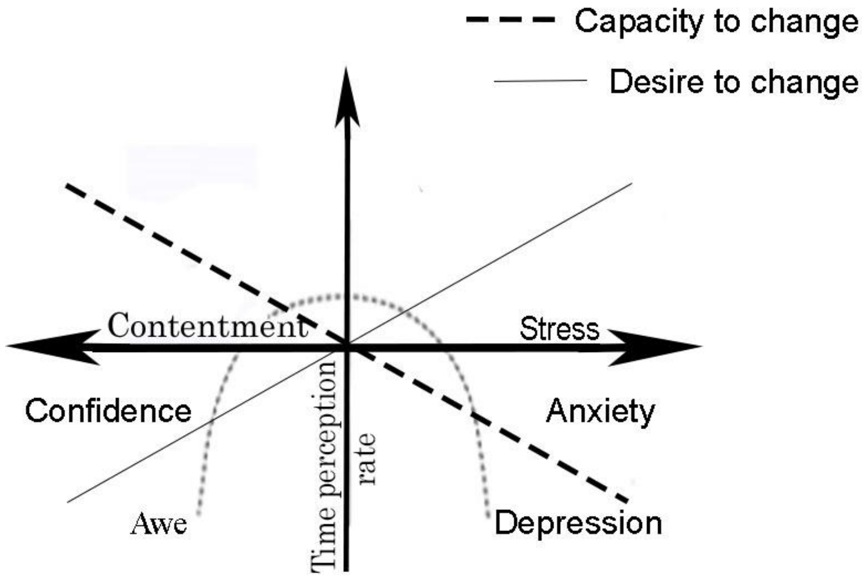

Figure 2. The Psychology of Contentment and Stress The x coordinate represents the transition between stress and contentment, and the y coordinate is the time perception rate. In positive experiences, time perception reduces action motivation, culminating in awe. The pain of stress motivates action but weakens self-confidence. Anxiety can progress to depression when action motivation halts. The capacity to institute change is inversely proportional to the desire to change.

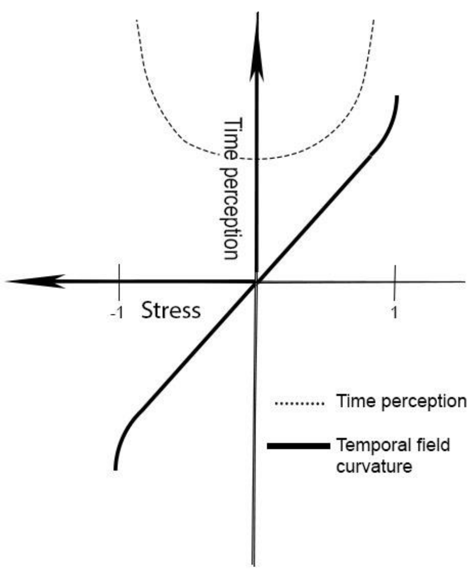

Figure 3. The effect of stress and elation on time perception Both elation (negative temporal curvature, right) and stress (positive temporal curvature, left) expand time perception. However, the contrasting temporal curvatures cause radically different behavioral manifestations. Notice that time perception is shown instead of time perception rate (Figure 2).

5. The Social Consequences of Mental Gravity and Psychological Spin

Recent Kent [28] work revealed that DMN activity and connectivity are the neural correlates of mental mass and a neural mechanism forming mental gravity. Therefore, conscious experience orients neurobiological time, similar to the body's perception of gravitational curvature [34]. Similar to gravity, social behavior may have a geometric foundation; much like space-time curvature dictates particle movement, the collective unconscious shapes individual behavior and social hierarchies.

In this framework, time dilation influenced by relative distance to a gravitational body—has psychological counterparts, where subjective time perception is altered by one's position within the social fabric. Competitive social interactions can thus be seen as generating hierarchies that reflect differential access to time; a scarcity of perceived time is linked to stress, mirroring the effects of gravitational potential [35]. Thus, the financial differences are a symptom of the divergence in access to time, separating the poor from the wealthy segment. As particle interaction shapes the gravitational curvature, competitive interactions shape social structure. Therefore, the existence of a physical body is needed to experience and adopt the fermionic structure: embodiment shapes the manifestation of consciousness.

The dynamics of human behavior and social interaction also resonate with thermodynamic concepts such as temperature and entropy, which offer compelling analogies for behavioral dynamics. In this view, high-arousal states—often associated with exploitative or reactive behaviors—stand in contrast to "cold," adaptive conditions that promote stability and learning.

In another context, analogous to the persistence of motion—or rest—according to Newton's first law, habitual and emotional states exhibit inertia until significantly perturbed by an external stimulus [36]. Like redirecting a moving vehicle, altering one's behavioral trajectory requires a deliberate deceleration—a cognitive slowdown often mediated by learning, acceptance, and gratitude [37]. At the synaptic level, this process is underpinned by reciprocal changes in connectivity, underscoring the neuroplastic nature of learning [5]. Thus, mental gravitational modifications require cognitive effort or social force for extended time. Gravitational changes contrast response to a change in emotional charge; psychological spin—similar to fermionic spin—can flip instantly.

Furthermore, the interplay of electromagnetic forces in neural circuits finds an intriguing parallel in the dynamics of social exchanges. The bidirectional nature of these forces, wherein opposing polarities continuously seek equilibrium, is reminiscent of Newton's third law. Every action is met with an equal and opposite reaction. This symmetry is evident in the reciprocal patterns observed in social interactions, where acts of kindness or aggression precipitate corresponding emotional responses [38]. Consequently, while constructs such as MG and EEM might manifest distinctively, their overlapping influences on behavior complicate efforts to disentangle their contributions (see Table 2).

These interdisciplinary analogies enrich our understanding of neural dynamics and have practical implications, inspiring us to explore new neuroscience and social sciences avenues.

	Mental gravity	**Emotional electromagnetism**
Trigger	Stress	Bias
Symptom	Time shortage	Comparison
Subjective experience	Time perception expands	Competitive drive
Behavioral consequences	Impulsivity	Manipulable
Mental consequences	Intellectual degradation	Short-term focus
Modification	Change takes a long time	Bias can flip instantaneously

Table 2. The comparison of mental gravity and emotional electromagnetism

6. Discussion and Conclusions

Our theoretical framework conceptualizes consciousness as the experiential awareness of one's separateness from the environment. In this context, we introduce the fermionic mind hypothesis (FMH) as a radical, integrative model that unites principles from physical law with mechanisms of predictive memory generation. FMH posits that consciousness emerges from a temporal, complexity-generating system underpinned by fermionic organization, offering a novel lens into cognition.

Grounded in robust findings from psychological and social sciences, FMH transcends traditional reductionist models by incorporating concepts from physics, such as gravity and electromagnetism. By linking emergent neural dynamics with energetic conditions, FMH can merge established paradigms in classical and quantum cognition, potentially heralding a paradigm shift in our understanding of memory formation and cognitive complexity.

Moreover, FMH has significant implications for the study of machine consciousness. It underscores the necessity of embodiment in intelligent systems, suggesting that the physical experience and constraints shape consciousness. This insight carries profound consequences for robotics and artificial intelligence research, indicating that the criteria for conscious experience—and, by extension, moral agency—may extend beyond mere computational capacity to include specific structural and energetic, i.e., emotional prerequisites.

Current research efforts are directed toward validating the predictions of FMH through experimental simulations and advanced neuroimaging studies. Confirming the FMH framework by empirical investigations could result in a paradigm shift with far-reaching implications for medicine, cognitive science, robotics, and our broader understanding of consciousness.

References

1. Baars, Bernard J. *A Cognitive Theory of Consciousness.* Cambridge University Press, 1988.
2. Tononi, G. 'Integrated information theory,' *Scholarpedia*, 10: 4164, 2015.
3. Revach, D., & Salti, M. "Consciousness as the Temporal Propagation of Information." *Front Syst Neurosci.*, 16:759683, March 23, 2022.

4. Deli, E. *Emotional Reasoning; Insight into the Conscious Experience.* CRC Publishing, 2024.
5. Dempsey, W. P., Du, Z., & Nadtochiy, A. 'Regional synapse gain and loss accompany memory formation in larval zebrafish,' *PNAS*, 2022.
6. Zheng, J., & Meister, M. 'The unbearable slowness of being: Why do we live at 10 bits/s?' *Neuron*, 2024.
7. Dabaghian, Y. A. 'Through synapses to spatial memory maps via a topological model,' *Scientific Reports*, 2019.
8. Deli, E., Kisvarday, Z., & Peters, J.F. 'The Thermodynamics of Cognition: A Mathematical Treatment.' *Comput. Struct. Biotechnol. J.*, 19, 784–793, 2021.
9. Deli, E., Kisvarday, Z., & Peters, J.F. 'How the Brain Becomes the Mind: Can Thermodynamics Explain the Emergence and Nature of Emotions.' *Entropy*, 24, 1498, 2022.
10. Esghaei, M., Treue, S., & Vidyasagar, T. 'Dynamic Coupling of Oscillatory Neural Activity and Its Roles in Visual Attention.' *Trends Neurosci.*, 45, 323–335, 2022.
11. Gao, Z., Cui, X., Wan, W., Zheng, W., & Gu, Z. 'Long-range correlation analysis of high-frequency prefrontal electroencephalogram oscillations for dynamic emotion recognition.' *Biomed. Signal Process. Control*, 72, 103291, 2022.
12. Kumar, M., Abhayapala, T. D., & Samarasinghe, P. 'A Preliminary Investigation on Frequency Dependent Cues for Human Emotions.' *Acoustics*, 4(2), 460-468, 2022. https://doi.org/10.3390/acoustics4020028
13. Surov, I.A. 'Quantum Core Affect. Color-Emotion Structure of Semantic Atom.' *Front. Psychol.*, 13, 838029, 2022.
14. Deli, E.K. 'What Is Psychological Spin? A Thermodynamic Framework for Emotions and Social Behavior.' *Psych.*, 2023.
15. Wang, J., & Lapate, R. C. 'Emotional state dynamics impacts temporal memory.' *Cognition and Emotion*, 39(1), 136–155, 2024.
16. Boxell, L., Gentzkow, M., & Shapiro, J.M. 'Cross-Country Trends in Affective Polarization.' *Rev. Econ. Stat.*, 1–60, 2022.
17. Kristoufek, L., & Vosvrda, M. 'Herding, minority game, market clearing, and efficient markets in a simple spin model framework.' *Commun. Nonlinear Sci. Numer. Simul.*, 54, 148–155, 2018.
18. Vazquez, F., Saintier, N., & Pinasco, J.P. 'Role of Voting Intention in Public Opinion Polarization.' *Phys. Rev. E*, 101, 012101, 2020.
19. Craig, A.D. 'How do you feel—now? The anterior insula and human awareness.' *Nat. Rev. Neurosci.*, 10, 59–70, 2009.
20. Barrett, L.F., & Simmons, W.K. 'Interoceptive predictions in the brain.' *Nat. Rev. Neurosci.*, 16, 419, 2015.
21. Remmers, C., & Zander, T. 'Why you don't see the forest for the trees when you are anxious: Anxiety impairs intuitive decision making.' *Clin Psychol Sci*, 6, 48–62, 2018.
22. Robbe, D. 'Lost in time: Relocating the perception of duration outside the brain.' *Neuroscience & Biobehavioral Reviews*, 153: 105312, 2023.
23. Lehockey, K.A., Winters, A.R., Nicoletta, A.J., et al. 'The effects of emotional states and traits on time perception.' *Brain Inf.*, 5, 9, 2018.
24. Biderman, N., Bakkour, A., & Shohamy, D. 'What Are Memories For? The Hippocampus Bridges Past Experience with Future Decisions.' *Trends in Cognitive Sciences*, 24, 542-556, 2020.
25. Ma, A.C., Cameron, A.D., & Wiener, M. 'Memorability shapes perceived time (and vice versa).' *Nat Hum Behav*, 2024. https://doi.org/10.1038/s41562-024-01863-2
26. Toso, A., Fassihi, A., Paz, L., Pulecchi, F., & Diamond, M.E. 'A sensory integration account for time perception.' *PLoS Computational Biology*, 17, 2020.

27. Wang, J., & Lapate, R. C. 'Emotional state dynamics impacts temporal memory.' *Cognition and Emotion*, 39(1), 136-155, 2025.
28. Kent, L. 'Mental Gravity: Depression as Space-time Curvature of the Self, Mind, and Brain.' *Entropy*, 25, 2023.
29. Stanghellini, G., Ballerini, M., Presenza, S., Mancini, M., Northoff, G., & Cutting, J. 'Abnormal time experiences in major depression. An empirical qualitative study.' *Psychopathology*, 2016. DOI:10.1159/000452892.
30. Bannister, S., & Eerola, T. 'Vigilance and social chills with music: Evidence for two types of musical chills.' *Psychology of Aesthetics, Creativity, and the Arts*, 2021.
31. Deli, E., Schoeller, F., Safron, A., Jain, A., Tozzi, A., Adrien, V., & Reggente, N. 'Feeling the Heat: A Thermodynamic Perspective on Emotions, Motivation, and Time Perception.' *Preprints*, 2024112245, 2024.
32. Gladhill, K.A., Mioni, G., & Wiener, M. 'Dissociable effects of emotional stimuli on electrophysiological indices of time and decision-making.' *PLOS ONE*, 17, 2022.
33. Hosseini Houripasand, M., Sabaghypour, S., Farkhondeh Tale Navi, F., & Nazari, M.A. 'Time distortions induced by high-arousing emotional compared to low-arousing neutral faces: an event-related potential study.' *Psychological Research*, 1-12, 2023.
34. Le Bihan, D. 'On time and space in the brain: A relativistic pseudo-diffusion framework.' *Brain Multiphys.*, 1, 100016, 2020.
35. Sato, W., Kochiyama, T., Uono, S., Sawada, R., & Yoshikawa, S. 'Amygdala activity related to perceived social support.' *Scientific Reports*, 10, 2020.
36. Livneh, H. 'Can the Concepts of Energy and Psychological Energy Enrich Our Understanding of Psychosocial Adaptation to Traumatic Experiences, Chronic Illnesses, and Disabilities?' *Front Psychol.*, 13, 768664, March 3, 2022.
37. Huang, Y., Wu, R., Wu, J., Yang, Q., Zheng, S., & Wu, K. 'Psychological resilience, self-acceptance, perceived social support and their associations with mental health of incarcerated offenders in China.' *Asian Journal of Psychiatry*, 102166, 2020.
38. Drigotas, S. M. 'Similarity revisited: A comparison of similarity-attraction versus dissimilarity-repulsion.' *British Journal of Social Psychology*, 1993.

10th International Congress of the Serbian Society of Mechanics
Niš, Serbia, June 18-20, 2025
M.3.5

Extended abstract

MODELLING ZONA PELLUCIDA AS A THERMOSENSITIVE POLYMER UNDER MECHANICAL LOAD

Andjelka N. Hedrih[1][0000-0001-7598-900X], Đorđe Jovanović[1][0000-0003-1222-1292]

[1] Mathematical Institute of the Serbian Academy of Sciences and Arts, Knez Mihailova 36, Belgrade, Serbia
e-mail: handjelka@mi.sanu.ac.rs, giorgakijovanovic@gmail.com

Abstract

Phase transition is a specific property of temperature-sensitive hydrogel which can be triggered by mechanical load. *Zona Pellucida* (ZP) a complex polymer structure that surrounds the oocyte may be consider as a thermosensitive polymer since it exhibits transition in mechanical properties during the period of maturation, fertilization and early embryo development. This transition can be modelled as temperature-sensitive hydrogel under mechanical constrain. Using the mathematical method established for temperature-sensitive hydrogel under mechanical loading we try to predict the critical external stress caused by numerous sperm cells that is necessary to trigger the phase transition. The relaxation parameter was calculated for mouse ZP using the data from the literature. There are possibilities that ZP is behave as a mesomorphic structure and that intermediate states between sol and gel phase exist, but further theoretical analysis are needed to confirm this hypothesis.
Key words: zona pellucida, thermal stress, thermosensitive polymer, phase transition,

1. Introduction

ZP polymer responds to mechanical load (artificial or natural) by changing its mechanical and electrical properties-conductivity and capacitance measured by impedance spectrometry [1]. For different suction pressure the relaxation occurs always at the same frequency [2].

Depending on temperature and mechanical pressure, phase transitions may occur, which alter its capacitance and conductivity. An increase in pressure can disrupt the organization of the ZP, leading to changes in impedance. Number of sperm cells that are necessary for successful fertilization have a role of external mechanical stress and can cause that phase transition that could be a possible mechanism that contribute to sperm penetration. Of a great importance is to predict the critical external stress caused by numerous sperm cells necessary to trigger the phase transition.

2. Methodology

Theoretical modelling approach describe in [3] was used to predict the critical stress necessary to trigger the phase transition. ZP was assumed to be in the form of thin incompressible rectangular layer isolated from oocyte where external load is applied in uniaxial direction. Temperature was set as in physiological conditions at 37°C (310.15K). Nominal stress is express through free energy density function as $s = \frac{dw}{d\lambda_i}$. λ_i is stretch in the principal direction compared to the referential state. Stress–stretch curves are generated from the following equation [3]:

$$\frac{sv}{kT} = \frac{1}{\lambda_S}[Nv(\lambda_3^2 - 1) + (\frac{V}{V_0})\log[1-(\frac{V}{V_0})^{-1}] + 1 + (\chi_0 - \chi_1)(\frac{V}{V_0})^{-1} + 2\chi_1(\frac{V}{V_0})^{-2}], \tag{1}$$

Where v -nominal volume of solvent molecule, N -the number of the polymer chains divided by the volume of the dry polymer, s -nominal stress, $\frac{V}{V_0}$ -is a swelling ratio, λ_3 - stretch direction caused by uniaxial stress, k - Boltzmann constant, T - temperature, χ_0 and χ_1 are the interaction parameters, Nv -parameter representing the crosslink density [3]. Intensity of normal stress is expressed as a function of the number of sperm cells with effective velocity. To determine the critical stress for a phase transition of ZP the number of sperm cells is varied.

The results are discussed with experimental data from [1] where different external suction pressure was applied to obtain ZP impedance. The relaxation parameter τ can be calculated from [1] for the ZP with normal stiffness. Figure 1.

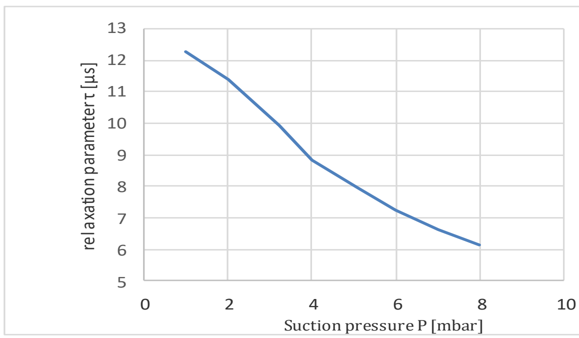

Figure 1. Relation between suction pressure and relaxation parameter obtained from data from [1]

3. Conclusions

In this paper ZP was considered as temperature-sensitive hydrogel under mechanical constrain. The aim is to determine the critical stress necessary to trigger the phase transition in ZP polymer.

The results of the theoretical modelling may be incorporated in IVF protocols in the case of oligospermia to facilitate the phase transition of ZP.

Acknowledgements

The research was supported by the Ministry of Science, Technology and Innovation of Republic of Serbia thought Mathematical Institute SANU.

References

[1] Azarkh D., Cao Y., Floehr J., Schnakenberg U., *Viscoelastic. Properties of zona pellucida of oocytes characterized by transient electrical impedance spectroscopy,* Biosensors, Vol 13, 442, 2023.

[2] Cao Y., Floehr J., Azarkh D., Schnakenberg U., *Microfluidic aspiration-assisted electrical impedance spectroscopy system is a reliable tool for the characterization of oocyte hardening,* Sensors & Actuators: B. Chemical 380, 133316, 2023.

[3] Zheng S., Liu Z., Phase Transition of Temperature-Sensitive Hydrogel Under Mechanical Constraint. Journal of Applied Mechanics, Vol. 85, 021002, 2018.

10th International Congress of the Serbian Society of Mechanics
Niš, Serbia, June 18-20, 2025
M.3.6

Extended abstract

FSI ANALYSIS OF PARAMETRIC STENT GEOMETRY INFLUENCE ON WSS-INDUCED IN-STENT RESTENOSIS

A. Khairulin[1,2][0000-0002-7506-5568], **A. Kuchumov**[1,2][0000-0002-0466-175X]

[1]Department of Computational Mathematics, Mechanics and Biomechanics, Perm National Research Polytechnic University, 614990 Perm, Komsomolskiy prospect 29, Russia, e-mail: targs2@gmail.com

[2] Biofluids Laboratory, Perm National Research Polytechnic University, 614990 Perm, Komsomolskiy prospect 29, Russia, e-mail: kychymov@inbox.ru

Abstract:

Numerical simulations and biomechanical analysis can be generally adopted for in silico clinical trial of cardiovascular devices [1]. Numerical studies of stent FSI simulation were performed recently together with short-term and long-term performance. Some papers consider application of discrete methods like cellular automata or agent-based models considering mechanisms of cell proliferation, migration and apoptosis leading to neointima formation.

Nevertheless, research has demonstrated that biological processes are not the only factors causing alterations in the artery's shape and geometry. Shear stress in the artery wall is also important [2]. In-stent restenosis formation includes low wall shear stress (WSS), accelerated proliferation of smooth muscle cells and larger collagen and elastin synthesis in intimal layer. It was suggested that stent geometry plays a crucial role on development of restenosis induced by wall shear stress (WSS) evolution during the heart cycle. Finding a relation between parametrization of stents and WSS-induced restenosis is a complex task, which is necessary to solve. We propose an approach to find a relation between design and its influence on in-stent restenosis including structural design of stents, numerical simulation of stent behaviour in multi-layered diseased artery and algorithm of WSS-induced restenosis.

To create stent models, a configurator software based on the CAD application Autodesk Inventor (Autodesk Inc., San Francisco, CA, USA) was developed. This tool provides the ability to create sinusoidal and helix stents automatically by parameters input such as diameter, thickness, and mesh configuration. This configurator allows users to enter stent parameters such as length, outer diameter and thickness, twist angle and other parameters. As a result, 24 different geometrical variants of coronary stents were created. Of these, 12 models were produced using a helical line, and the remaining 12 models were based on parametric equations for the formation of sinusoidal coronary stent struts (Fig. 1).

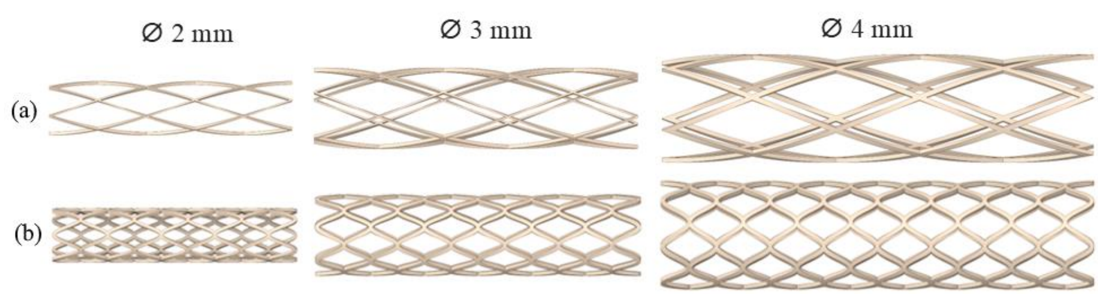

Fig. 1. Helix-shape (a) and sinusoid-shape (b) coronary stents

Two-way FSI problem of blood flow in atherosclerosis-prone artery was considered. Three-layered artery model including intima, media and plaque was assumed. The increase of the coronary artery wall thickness due to wall shear stress variation was modelled. To predict in-stent restenosis, a model including a system of ordinary differential equations was proposed. The coupling algorithm combining blood flow in the stented section of the artery is first simulated to provide the necessary data, such as the velocity field for computing WSS. Then intima thickness growth is estimated using a system of coupled first-order ordinary differential equations that describe the process of LDL accumulation and thickness change over time. A duration equal to 6 months was calculated (the time step was 0.001 months).

It was revealed that an increase in LDL mass was observed with increasing stent diameter. Second, for each stent diameter, an optimal geometry that minimizes LDL mass can be identified. For 3-mm diameter stents, the minimum values of LDL mass ranged from 8×10^{-7} kg to 8.42×10^{-7} kg. For 4 mm diameter stents, the minimum values of LDL mass ranged from 8.49×10^{-7} kg to 9.06×10^{-7} kg. Mean values of LDL mass ranged from 1.49×10^{-6} kg to 1.51×10^{-6} kg.

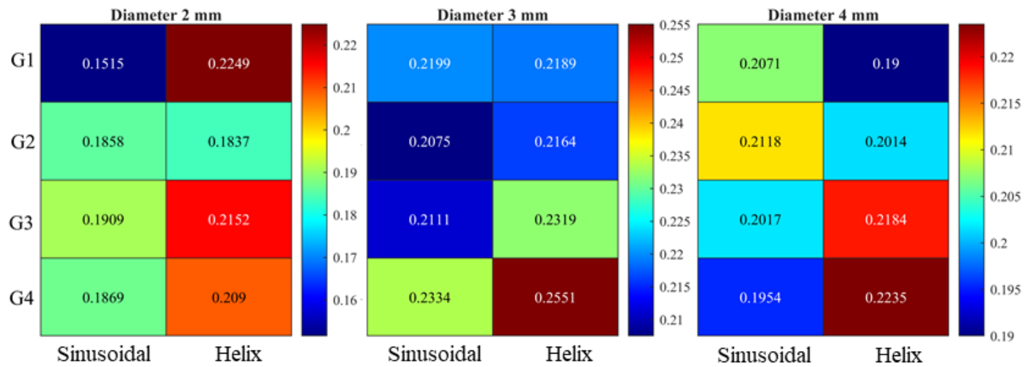

Fig. 2. Maximum and intimal thickening for all stents

The intimal thickening model showed that thickening is observed in areas with low values of wall shear stress, which are less than 3 Pa, which is supported by existing literature data. Helix stents at diameters of 2 and 3 mm show greater thickening compared with sinusoidal stents (Fig. 2). However, sinusoidal stents have a larger thickening area, indicating that helix stents are more effective. Next step will be including manufacturing process into developed model. Our complex approach gives a possibility to obtain the optimal structure and properties for patient-specific stent production in the future.

Acknowledgements

The research was financially supported by the Ministry of Science and Higher Education of the Russian Federation (No. FSNM-2025-0001).

References

[1] K.I. Aycock, T. Battisti, A. Peterson, J. Yao, S. Kreuzer, C. Capelli, S. Pant, P. Pathmanathan, D.M. Hoganson, S.M. Levine, B.A. Craven, Toward trustworthy medical device in silico clinical trials: a hierarchical framework for establishing credibility and strategies for overcoming key challenges, Front Med (Lausanne) 11 (2024). https://doi.org/10.3389/fmed.2024.1433372.

[2] A. Tziotziou, E. Hartman, S.-A. Korteland, A. van der Lugt, A.F.W. van der Steen, J. Daemen, D. Bos, J. Wentzel, A.C. Akyildiz, Mechanical wall stress and wall shear stress are associated with atherosclerosis development in non-calcified coronary segments, Atherosclerosis 387 (2023) 117387. https://doi.org/10.1016/j.atherosclerosis.2023.117387.

10th International Congress of the Serbian Society of Mechanics
Niš, Serbia, June 18-20, 2025
M.3.7
Extended abstract

A TAILED ROBOT ON THREE SUPPORTS

Liubov A. Klimina

Institute of Mechanics
Lomonosov Moscow State University, Michurinskiy prosp. 1, 119192 Moscow, Russia
e-mail: klimina@imec.msu.ru

Abstract:

A bio-inspired tailed robot on three supports is proposed. It moves on a horizontal plane. Supports are located in vertices of an isosceles triangle. The altitude of this triangle is symmetry-axis of the robot. Dry friction in two symmetrical supports is anisotropic. The robot is equipped with a controllable internal flywheel. The shaft of the flywheel is vertical. The robot has a passive tail that is a pendulum with a vertical shaft. There is a spiral spring between the tail and the symmetry-axis of the body. The tail doesn't contact with the supporting plane. Periodical control torque is applied to the flywheel. The control is constructed in such a way to ensure serpentine-style propulsion of the robot towards a prescribed direction. Influence of the tail upon the speed of the center of mass at a steady regime is discussed. It is shown that average speed of the center of mass for the tailed robot can be significantly larger than that for a tailless one.

Key words: tailed robot, anisotropic friction, propulsion, internal mass motion.

1. Introduction

Tails play significant role in locomotion of animals. However, rather few robotic systems are equipped with tail-like links. The main exceptions are snake-robots and fish-robots.

On the other hand, passive elements (e.g. tails) are profitable for robotic systems controlled via internal mass motion. Such links can increase average speed of propulsion or essentially improve some other features (such as maneuverability) [1].

2. Description of the system

Here we discuss a robot that moves on a horizontal plane *OXY* and consists of a rigid body, passive rigid tail and controllable flywheel (Fig. 1). The body has three supports *A*, *B*, *C* located in vertices of an isosceles triangle ($AC = BC$). Center *S* of mass of the body is located at the altitude *CK*. The inner controllable flywheel rotates around *S* axis; *m* is the mass of the body together with the flywheel; *J* and J_f are moments of inertia of the body and the flywheel around *S* axis. The passive tail is the pendulum *SM* rotating around the *S* axis. The mass m_0 of the pendulum is concentrated in the point *M*. There is a spiral spring with the stiffness coefficient *c* between *SK* and *SM*. *x*, *y* are coordinates of the point *S*; φ_1, φ_2 are angles between *SK* and *OX* and *SM* and *OX*, respectively; ω_f is angular speed of the flywheel. $\mathbf{V}_S$ is the speed of the point *S*.

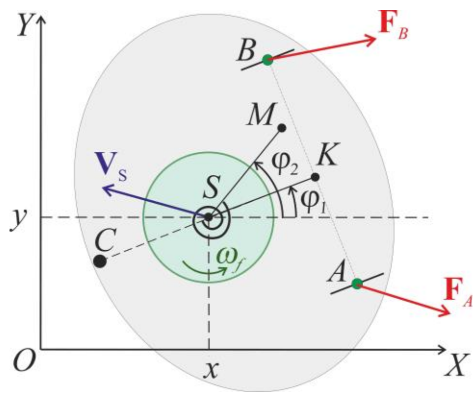

Fig. 1. Scheme of the system.

$\mathbf{F}_A$, $\mathbf{F}_B$ are anisotropic friction forces applied at supports *A*, *B*. The model [2] of anisotropic friction is used. Let $A\xi\eta$ are general axes of friction tensor Θ for the point *A* (the model in the point *B* is the same). $A\xi$ is parallel to *SK*, $A\eta$ is orthogonal to $A\xi$. $\mathbf{V}_A$ is the speed of the point *A*; N_A is the value of normal reaction at the support *A*.

$$\begin{pmatrix} F_\xi \\ F_\eta \end{pmatrix} = -\frac{N_A}{V_A}\Theta \begin{pmatrix} V_{A\xi} \\ V_{A\eta} \end{pmatrix}, \quad \Theta = \begin{pmatrix} \mu_\xi & 0 \\ 0 & \mu_\eta \end{pmatrix}, \quad \mu_\xi < \mu_\eta .$$

Equations of motion are constructed in the Lagrange form. The goal of the control is to organize propulsion of the robot in the direction opposite to ***OX***. Thus, average value of V_{Sx} should be negative at the steady mode of motion, and average values of V_{Sy} and φ_1 should be zero. Due to this goal, the following control torque *U* is applied to the inner flywheel:

$$U = \begin{cases} U_p, & |U_p| \le U_{\max}, \\ U_{\max}\operatorname{sign}(U_p), & |U_p| > U_{\max}, \end{cases} \qquad U_p = -\left(U_{\max}\operatorname{sign}\left(\sin(2\pi w_0 t)\right) - k_0 y - k_1\varphi_1\right).$$

We fix all parameters of the system, except stiffness *c* of the spiral spring: $m + m_0 = 1\text{kg}$, $m_0 = 0.2\text{kg}$, $J = 0.005\text{kgm}^2$, $J_f = 0.001\text{kgm}^2$, $SK = SM = 0.1\text{m}$, $SC = 0.2\text{m}$, $AB = 0.3\text{m}$, $U_{\max} = 0.2\text{Hm}$, $w_0 = 1\text{s}^{-1}, k_0 = -0.1\text{H}, k_1 = 0.1\text{H}$, $\mu_\xi = 0.02$, $\mu_\eta = 0.9$.

2. Main result

Regime of propulsion with negative V_{Sx} exists for $c \in [0, 0.0675] \cup [0.074, \infty)\,\text{kgm}^2\text{s}^{-2}$. The case of infinite *c* corresponds to the tailless robot; for it average speed at the regime equals 0.59m/s. Maximum speed equals 0.72m/s and is achieved for $c = 0.055\,\text{kgm}^2\text{s}^{-2}$. Thus, a tail, even passive, can provide 20% increasing of the average speed of the center of mass of the robot.

References

[1] Pollard B., Tallapragada P., *Passive Appendages Improve the Maneuverability of Fishlike Robots*, IEEE/ASME Transactions on Mechatronics, Vol. 24(4), 1586–1596, 2019.

[2] Zmitrowicz A., *Mathematical Descriptions of Anisotropic Friction*, International Journal of Solids and Structures, Vol. 25(8), 837–862, 1989.

10th International Congress of the Serbian Society of Mechanics
Niš, Serbia, June 18-20, 2025
M.3.8
Extended abstract

A NUMERICAL STUDY OF THE BELOUSOV-ZHABOTINSKY REACTION NETWORK

S. Maćešić[1], A. Ivanović-Šašić[2][0000-0002-1600-5549], Ž. Čupić[2][0000-0002-4939-6718]

[1] University of Belgrade, Faculty of Physical Chemistry, Studentski trg 12-16, Belgrade, Serbia.
e-mail: stevan.macesic@ffh.bg.ac.rs

[2] University of Belgrade, Institute of Chemistry, Technology and Metallurgy, National Institute of the Republic of Serbia, Njegoševa 12, 11000 Belgrade, Serbia.
e-mail: ana.ivanovic.sasic@ihtm.bg.ac.rs , zcupic@ihtm.bg.ac.rs

Abstract

This paper presents a numerical investigation of the Belousov Zhabotinsky reaction network under both spatially uniform and non-uniform conditions, with the aim of gaining deeper insights into complex reaction systems and pattern formation in the studied system. Numerical simulations were performed in both cases spatially uniform and non-uniform to explore the behavior of the BZ reaction. For the spatially uniform system, the system of ordinary differential equations representing the system dynamics was solved using the MATLAB function ode15s. Reaction-diffusion equations governing the spatially non-uniform system were solved using advanced numerical methods which in case of spatially non-uniform system incorporate finite element analysis to handle partial differential equations (PDEs) efficiently. In spatially uniform case numerical analysis has shown oscillatory dynamics that is in agreement with experimental findings. In case of spatially non-uniform system two phenomena were found: diffusion induced traveling waves that propagate from the center of the domain and Turing patterns.

Key words: Belousov-Zhabotinsky, oscillatory reactions, numerical simulations, finite element analysis

1. Introduction

The Belousov-Zhabotinsky (BZ) [1] reaction is a classic example of a non-linear chemical oscillator with significant implications for the study of complex systems and nonlinear dynamics. This reaction offers insights into phenomena such as chaos, pattern formation, and self-organization, making it a crucial subject for exploring the principles of chaos theory and complex systems. An important aspect of the BZ system is modelling, which can greatly improve the understanding of this system and contribute to its practical applications. This paper will present a numerical study of the characteristics of the BZ reaction model, providing a comprehensive introduction to the topic.

2. Model

The BZ oscillatory reaction network in this study involves 12 reaction steps, four of which are reversible, and 16 chemical species, including Br^-, HOBr, H^+, Br_2, H_2O, $HBrO_2$, Br_2O, BrO_3^-, BrO_2, Ce_3^+, Ce_4^+, $CH_2(COOH)_2$, $CHBr(COOH)_2$, P_1, P_2, and $Br_{2(g)}$. $CH_2(COOH)_2$ and BrO_3^- are the reactants, and $CHBr(COOH)_2$, $Br_{2(g)}$, P_1, and P_2 are the products. Simulations were done under constant pH with H^+ and H_2O concentrations fixed. To improve efficiency, the concentrations of $CH_2(COOH)_2$ and BrO_3^- were treated as constants, leading to a model with eight variables: a, *b*, *c*, *d*, *e*, *f*, *g*, *h*, corresponding to concentration of species Br^-, HOBr, Br_2, $HBrO_2$, Br_2O, BrO_2, Ce_3^+, and Ce_4^+ respectively.

$$\frac{\mathrm{d}\boldsymbol{a}}{\mathrm{d}\boldsymbol{t}} = \mathrm{D}_1\nabla^2\boldsymbol{a} - \boldsymbol{k_1ab} + \boldsymbol{k_{-1}c} - \boldsymbol{k_2\,d} - \boldsymbol{k_4a} + \boldsymbol{k_8c} + \boldsymbol{k_{10}h} \tag{1}$$

$$\frac{\mathrm{d}\boldsymbol{b}}{\mathrm{d}\boldsymbol{t}} = \mathrm{D}_2\nabla^2\boldsymbol{b} - \boldsymbol{k_1ab} + \boldsymbol{k_{-1}c} + \boldsymbol{2k_3e} - \boldsymbol{2k_{-3}b^2} + \boldsymbol{k_4a} + \boldsymbol{k_5d^2} + \boldsymbol{k_{11}e} \tag{2}$$

$$\frac{\boldsymbol{dc}}{\boldsymbol{dt}} = \mathrm{D}_3\nabla^2\boldsymbol{c} + \boldsymbol{k_1ab} - \boldsymbol{k_{-1}c} - \boldsymbol{k_8c} - \boldsymbol{k_{12}c} \tag{3}$$

$$\frac{\mathrm{d}\boldsymbol{d}}{\mathrm{d}\boldsymbol{t}} = \mathrm{D}_4\nabla^2\boldsymbol{d} - \boldsymbol{k_2ad} + \boldsymbol{k_4a} - \boldsymbol{2k_5d^2} - \boldsymbol{k_6d} + \boldsymbol{k_6f^2} + \boldsymbol{k_7f\,g} - \boldsymbol{k_{-7}dh} \tag{4}$$

$$\frac{\mathrm{d}\boldsymbol{e}}{\mathrm{d}\boldsymbol{t}} = \mathrm{D}_5\nabla^2\boldsymbol{e} + \boldsymbol{k_2a\,d} - \boldsymbol{k_3e} + \boldsymbol{2k_{-3}d^2} - \boldsymbol{k_{11}e} \tag{5}$$

$$\frac{\mathrm{d}\boldsymbol{f}}{\mathrm{d}\boldsymbol{t}} = \mathrm{D}_6\nabla^2\boldsymbol{f} + \boldsymbol{2k_6d} - \boldsymbol{2k_6f^2} - \boldsymbol{k_7f\,g} + \boldsymbol{k_{-7}dh} \tag{6}$$

$$\frac{\mathrm{d}\boldsymbol{g}}{\mathrm{d}\boldsymbol{t}} = \mathrm{D}_7\nabla^2\boldsymbol{g} - \boldsymbol{k_7f\,g} + \boldsymbol{k_{-7}dh} + \boldsymbol{k_9h} + \boldsymbol{k_{10}h} \tag{7}$$

$$\frac{\mathrm{d}\boldsymbol{h}}{\mathrm{d}\boldsymbol{t}} = \mathrm{D}_8\nabla^2\boldsymbol{h} + \boldsymbol{k_7f\,g} - \boldsymbol{k_{-7}dh} - \boldsymbol{k_9h} - \boldsymbol{k_{10}h} \tag{8}$$

3. Methods and results

The equations (1) – (8) for the BZ reaction network under both spatially uniform (well stirred reactor) and non-uniform conditions were solved using numerical methods with the FEniCS package [2], which employs the finite element method to efficiently handle the partial differential equations in the non-uniform case. An implicit Euler scheme was used for time discretization. A circular computational domain was employed to simulate a thin solution layer, with homogeneous Neumann boundary conditions applied at the boundaries. In the case of spatially non-uniform case, our numerical analysis revealed two distinct phenomena based on the stability of the spatially uniform system. In unstable systems, diffusion induces traveling waves that emerge from the center of the domain and propagate outward. As time progresses, the wave origin shifts, and the waves move towards the domain center. In stable systems, diffusion leads to the formation of Turing patterns, with regions of high and low [Br^-] concentrations emerging from the center and expanding outward, stabilizing at the domain's boundaries.

4. Conclusion

The results of this study reveal two distinct phenomena based on the system's stability: the emergence of traveling waves in unstable conditions and the formation of Turing patterns in stable conditions. These findings provide valuable insights into the complex dynamics of non-linear chemical systems and highlight the role of diffusion in pattern formation. The ability to model and simulate these behaviors enhances our understanding of the BZ reaction and its potential applications in areas like chemical computing and smart materials.

References

[1] Belousov, B., *Periodicheskaya reaktsiya i ego mekhanizm*, Sbornik Referatov po Radiatsionnoi Meditsine za 145–149, 1958.
[2] Langtangen, H. P., Anders L.. *Solving PDEs in python: the FEniCS tutorial I*. Springer Nature, 2017.

10th International Congress of the Serbian Society of Mechanics
Niš, Serbia, June 18-20, 2025

M.3.9

Extended abstract

BIOMECHATRONIC SYSTEM FOR MONITORING EATING BEHAVIOR

Magomed Magomedov[1], Rasul Magomedov[2]

[1]Research Institute of Biomechatronics
9 Entuziastov Street, Mahachkala, Russia
e-mail: *mxsauno@mail.ru*

[2] Faculty of Computational Mathematics and Cybernetics, Lomonosov MSU,
Leninskie gory 1, b.52, Moscow, Russia
e-mail: *rasulmag1609@gmail.com*

Abstract

Monitoring eating behavior is becoming increasingly important today in the fight to reduce morbidity and mortality from their leading cause - NCDs. Although insufficient chewing increases the risk of NCDs, 64 to 80% of people do not attach importance to this. As a person cannot continuously keep track of his chewing movements, we have developed a gadget, which allows to monitor the thoroughness of chewing food. Using artificial intelligence, we have learned to recognize signals related only to ingestion from the many recorded schedules of eating of different consistencies, head movements and jaw movements when speaking.

Key words: eating behavior, morbidity, NCD, quantity of chews, food volume, euglycemia, biomechatronic food intake monitoring system, artificial intelligence, chew signals.

1. Introduction

In studies on the relationship between chewing and NCD the status of chewing is associated with NCD both directly and through obesity and metabolic syndrome. The aim of the work is to develop a device that helps to monitor the thorough chewing of food.

Recently it was found that:

- adults with preserved chewing capacity have an increased likelihood of ideal behavioral CVH [1];
- an increase in the risk of CVD by 3.5 times with age is associated with a decrease in the ability to chew with age [7];
- increasing quantity of chews 2 times reduces food volume by 14.8%;
- longer oral exposure promote satiety and maintain euglycemia;[2]
- the size of the bite and the timing of sensory exposure might lead to greater satiety for the same number of calories; [3,4].

Nevertheless, from 65 to 80% of people of different ages do not pay attention to the number of chewing. [5]

2. Biomechatronic food intake monitoring system

As a person cannot continually keep track of his chewing motions we have developed a gadget - biomechatronic food intake monitoring system (BFIMS).(Fig.1) [6]

Another important property of the proposed BFIMS is the ability to determine the amount of food taken. Using artificial intelligence, we have learned to recognize signals related only to ingestion from the many recorded schedules of eating of different consistencies, head movements and jaw movements when speaking. Thus, unlike traditional methods of determining the potential volume of food, the gadget allows us to determine the volume of food actually taken more precisely.

We obtained more than 1000 graphs of episodes of chewing food of different textures, swallowing, head movements and talking. Processing these signals using neural network allows us today to determine the amount of food taken with an accuracy of 86% through swallowing. Our work on collecting a test sample for the neural network is still ongoing.

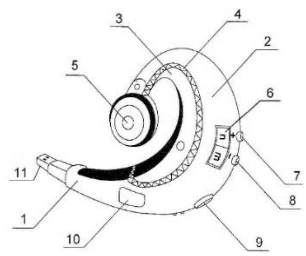

Fig. 1. The biomechatronic food intake monitoring system: 1 - earphone with the framework, 2 -upper section of the, framework, 3 - lower section of the framework, 4 - elastic ring, 5 – speaker, 6 - liquid crystal display, 7, 8 - buttons for setting the threshold value of the number of chews in a chewing cycle, 9 – switch, 10 - battery compartment, 11 - USB port.

References

[1] Rangé, H., Perier, M.-C., Boillot, A., Offredo, L., Lisan, Q., Guibout, C., Thomas, F., Danchin, N., Boutouyrie, P., Jouven, X., et al. *Chewing capacity and ideal cardiovascular health in adulthood: A cross-sectional analysis of a population-based cohort study*, Clin. Nutr., 39, 1440–1446, 2019.
[2] Zhu Y, Hollis JH., J Acad. *Increasing the number of chews before swallowing reduces meal size in normal-weight, overweight, and obese adults*, NutrDiet, 114(6), 926-931, 2014.
[3] Forde CG, van Kuijk N, Thaler T, de Graaf C, Martin N. *Oral processing characteristics of solid savoury meal components, and relationship with food composition, sensory attributes and expected satiation*, Appetite. 60(1), 208-219 2013.
[4] Forde CG, Leong C, Chia-Ming E, McCrickerd K. *Fast or slow-foods? Describing natural variations in oral processing characteristics across a wide range of Asian foods*, Food Funct., 8(2), 595-606, 2017.
[5] Magomedova, A., G., Singh, Ram, B., Horuichi, Rie, *Regional Differences in Chronobiological Behavioral Factors among School Children in the Russian Federation*, World Heart Journal, Nova Science Publishers, Inc. (United States), vol. 13, № 1, 269-272, 2021.
[6] Magomedov, M., Kh., (RU) Patent. *A chewing motion tracking device (options) and an earpiece*. Russia, 2012. 000224_000128_2011111125_20120927_A_EN
[7] Aoyama, N. Fujii, T.; Kida, S.; Nozawa, I.; Taniguchi, K.; Fujiwara, M.; Iwane, T.; Tamaki, K.; Minabe, M. *Association of Periodontal Status, Number of Teeth, and Obesity: A Cross-Sectional Study in Japan*, J. Clin. Med. 10, 208, 2021.

Mini-Symposia 4: Nonlinear Dynamics

Organizers:

Julijana Simonović (Faculty of Mechanical Engineering, University of Niš, Serbia) and
Nikola Nešić (Faculty of Technical Sciences, Kosovska Mitrovica)

M.4.1

Extended abstract

MOTION ANALYSIS OF A SINGLE-MASS VIBRO IMPACT SYSTEM

Ljubiša Garić[1][0000-0002-4914-8968], Nikola Nešić[2][0000-0001-6237-4735], Julijana Lekić[3][0000-0003-1896-6797], Saša Jovanović[4][0009-0006-9728-0695], Dejan Stošović[5][0000-0002-0476-1566]

[1,2,3,4,5]Faculty of Technical Sciences, University of Priština in Kosovska Mitrovica, Knjaza Miloša 7, 38220 Kosovska Mitrovica, Serbia

[1]e-mail: ljubisa.garic@pr.ac.rs
[2]e-mail: nikola.nesic@pr.ac.rs
[3]e-mail: julijana.lekic@pr.ac.rs
[4]e-mail: sasa.m.jovanovic@pr.ac.rs
[5]e-mail: dejan.stosovic@pr.ac.rs

Abstract:

Vibro-impact systems form the basis of many industrial machines. This paper presents an analysis of the horizontal rectilinear motion of a single-mass oscillator, examining three cases. In the first case, an oscillator without damping and without impact is studied. In the second case, an oscillator without damping but with an impact against a stopper is analyzed. In the third case, a vibro-impact oscillator with damping, an excitation force, and an impact against a stopper is investigated. Typically, periodic vibro-impact systems with equal time intervals between two consecutive impacts are used. Under these conditions, impacts occur during the system's forced motion, generating various effects that can be either detrimental or beneficial. Harmful effects need to be minimized, while beneficial effects should be enhanced to increase the process's productivity. This paper's analysis of the vibro-impact system aims to determine the range of existence for periodic vibro-impact regimes.

Keywords: free vibration, forced vibration, vibro-impact oscillator, damping

1. Introduction

Vibro impact problems are studied by many authors [1]-[3]. This paper's analysis of the vibro-impact system aims to determine the range of existence for periodic vibro-impact regimes.

2. Mathematical models

In the first case, the mathematical model of an oscillator without impact, shown in Figure (1a), is examined. The system consists of a mass and a spring. The motion occurs under the influence of the spring force, with no damping force present, making it a system in which free undamped oscillations take place.

In the second case, the mathematical model of an oscillator with impact, shown in Figure (1b), is examined. The system consists of a mass, a spring, and a stopper. The motion occurs under the influence of the spring force, with no damping forces present, making it a system in which free undamped oscillations take place.

In the third case, the mathematical model of an oscillator with impact, shown in Figure (1c), is examined. This system consists of a mass, a spring, a damper, and a stopper, representing real-world conditions. The motion occurs under the influence of an external excitation force, making it an oscillatory system with periodic motion, where forced damped oscillations take place.

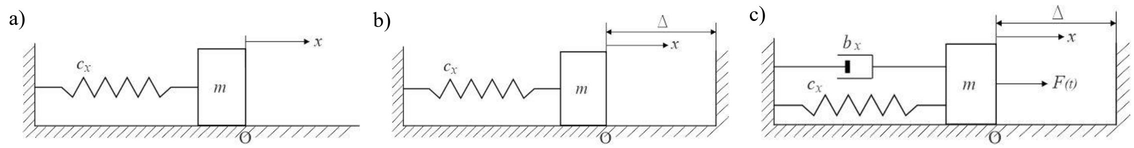

Fig. 1. Mathematical models of an oscillator: a) without damping and without impact, b) without damping and with impact, c) with damping and impact.

3. Results

The results for the first two cases are shown in Figure 2, with the graphs generated in Mathcad 14. Free undamped oscillations in these two systems are possible in cases where there is no damping and when the collision of the mass with the stationary stopper is perfectly elastic, meaning that the coefficient of restitution upon impact is **R = 1**. In this case, the velocity of the mass before impact is equal to the velocity after impact, representing assumed ideal conditions.

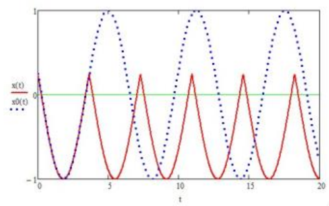

Fig. 2. Oscillator undamped free motion without impact (dashed line) and with impact (solid line)

In the analysis of the vibro-impact processes of the oscillator in Figure (1c), the main result obtained from the system analysis is the determination (definition) of the conditions (ranges) for the existence of periodic vibro-impact regimes. Figure 3 shows the areas of existence for vibro-impact regimes I, II, and III. The graphs were constructed using the mathematical software Wolfram Mathematica 7, when $R = 0.7$, and l=1,2,3. The figure shows that as the multiplicity l increases, the areas of existence for the vibro-impact regimes also increase. The diagrams in Figures 3a, 3b, and 3c allow the determination of the frequency interval for the realization of the vibro-impact process when the value of the distance Δ is known.

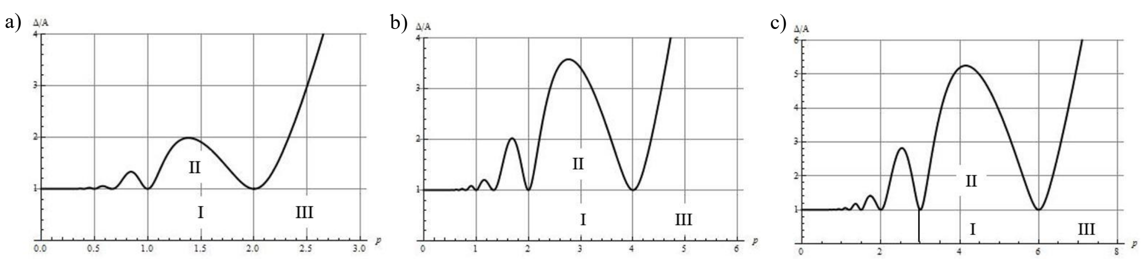

Fig. 3. The areas of existence of vibro-impact regimes when: a) l=1, b) l=2, c) l=3.

4. Conclusions

The results obtained in the analysis of the vibro impact system allow for stabilization of the system's motion. The results obtained from these models can provide some ideas and directions for analyzing vibro-impact systems to increase their efficiency.

References

[1] Babicki V. I., *Theory of Vibro-Impact Systems and Applications*, Springer-Verlag, Berlin, 1998.

[2] Jakovlevic M. I., *Elementi teorii optimalnogo upravlenija periodičeskimi režimami vibroudarnih sistem: Sistemi, linejnie v promežutkah meždu soudareniami*, Moskva 2010

[3] Beards C. E., *Structural Vibration: Analysis and Damping*, University of London, 1996

10th International Congress of the Serbian Society of Mechanics
Niš, Serbia, June 18-20, 2025
M.4.2

Extended abstract

ASYMPTOTIC METHODS OF NONLINEAR MECHANICS THROUGH A SERIES OF SCIENTIFIC PROJECTS, MAGISTER'S AND DOCTORAL DISSERTATIONS: NONLINEAR PHENOMENA, TRIGGER OF COUPLED SINGULARIES AND FREQUENCIES AS BIFURCATION PARAMETERS

Katica R. (Stevanović) Hedrih[1, 2][0000-0002-2930-5946]

[1] Mathematical Institute of Serbian Academy of Sciences and Arts, Belgrade, Serbia
e-mail: katicah@mi.sanu.ac.rs,khedrih@sbb.rs
[2] Faculty of Mechanical Engineering, The University of Niš, , Serbia
e-mail: katicahedrih@gmail.com

Abstract: The first part of the announcement presents a series of first scientific projects, master's theses done at the Faculty of Mechanical Engineering in Niš, using the asymptotic methods of nonlinear mechanics Krylov-Bogolubov-Mitropolski, as well as doctoral theses. This formed the Serbian School of Nonlinear Oscillations, which is continued by contemporary young researchers. The second part of the announcement presents nonlinear phenomena of nonlinear oscillations obtained using the asymptotic methods of nonlinear mechanics. It points out the phenomena of bifurcation and explains how the frequencies of coercive forces can be given the properties of bifurcation parameters.

Key words: Serbian school of nonlinear oscillations, nonlinear phenomena, trigger of coupled singularities, bifurcation parameters.

1. Introduction

The first part of the Report will discuss the founders of the Serbian School of Nonlinear Oscillations. These are the first head of the Department of Mechanics at the Faculty of Mechanical Engineering in Niš, Professor Dr. Danilo P. Rašković, and his successful student Katica (Stevanović) Hedrich. The second part of the communication presents nonlinear phenomena of nonlinear oscillations obtained by applying asymptotic nonlinearities through research on successfully implemented projects over the past, more than half a century. The second part of the communication is formed as a dictionary of terms of the phenomena of nonlinear dynamics and methods for their study.

For more than two decades, the head of the Department of Mechanics at the Faculty of Mechanical Engineering in Niš. The Serbian School of Nonlinear Oscillations was formed through nine project cycles of five years each, and the last project lasting ten years, whose leader was Professor Hedrich. Through research, in each project team, two to three magister's theses, or doctorates, have been defended. The last heads of this Department of Mechanics, in the direct line of mentorship, are, in turn, Professor Dr. Dragan Jovanović and Professor Dr. Julijana Simonović. The last doctoral student in this direct line, who defended his doctorate, is Nikola Nešić, under the mentorship of Dr. Julijana Simonović.

The second part of the communication presents nonlinear phenomena of nonlinear oscillations obtained by applying asymptotic nonlinearities through research on successfully implemented projects over the past, more than half a century. It points out resonant jumps, singularities, coupled singularity triggers, bifurcation phenomena and explains how the frequencies of coercive forces can be given the properties of bifurcation parameters and explain the phenomena of resonant jumps and energy transfer between nonlinear modes of a nonlinear oscillatory system with multiple degrees of freedom of motion.

2. Main topics

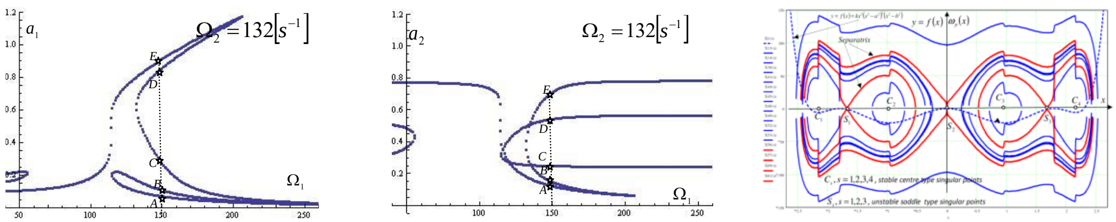

a b c

Figure 1. a) and b) Frequency characteristic curves for the amplitude of the first time harmonic $a_1 = f_1(\Omega_1)$, for the amplitude of the second time harmonic $a_2 = f_2(\Omega_1)$, for the phase of the first time harmonic $\varphi_1 = f_3(\Omega_1)$ and for the phase of the second time harmonic $\varphi_2 = f_4(\Omega_1)$ of eigen time function modes in one amplitude mode on discrete value of excited frequency Ω_2 =132 [s^{-1}] , with noted proper five stationary values on star points A, B, C, D and E.; c) A phase portrait of the dynamics of a generalized rolling pendulum, which rolls, without slipping, along a curvilinear path defined by a polinomial of the eighth degree in the form $y = f(x) = kx^2(x^2 - a^2)^2(x^2 - b^2)$, where a, b and k, are known constants ($k=1$; $a=1,8$; $b=2,3$; $c=1$; $(g/\kappa)\approx 10$; $r=1$; $\Omega=1$) , in a rotate vertical plane around the vertical axis at a constant angular velocity Ω, and in Earth's field of gravity, in phase coordinates x, $\omega_P(x)$.

3. Conclusions

Communication is formed as a dictionary of terms of the phenomena of nonlinear dynamics and methods for their study. A preface of terms, definitions and graphics is given that are useful for every researcher. The figures show the amplitude and phase-frequency characteristics of nonlinear dynamics, as well as phase portraits of rolling bodies.

References

[1] Hedrih (Stevanovi?) R. K., (2018), Non-linear phenomena in vibro-impact dynamics: Central collision and energy jumps between two rolling bodies, Dedicated to memory of Professor and important scientist Ali Nayfeh (December 21, 1933-March 27, 2017). Nonlinear Dynamics, February 2018, Volume 91, Issue 3, pp 1885-1907. DOI :10.1007/s11071-017-3988-x. ttps://link.springer.com/article/10.1007/s11071-017-3988-x

[2] Hedrih (Stevanović) R. K., (2017), Central collision of two rolling balls: theory and examples, Advances in Theoretical and Applied Mechanics, Vol. 10, 2017, no. 1, 33-79. https://doi.org/10.12988/atam.2017.765.

[3] Hedrih (Stevanović) R. K.,(2017), Generalized rolling pendulum along curvilinear trace: Phase portrait, singular points and total mechanical energy surface, Computer Algebra Systems in Teaching and Research, Edited by Alexander Prokopenya and Agnieszka Gil-Swiderska, Publisher Siedlce University of Natural Sciences and Humanities (Siedlce, Poland), 2017, Vol. VI, pp. 204216. ISSN 2300-7397. http://www.castr.uph.edu.pl.

[4] Hedrih (Stevanović) R. K., and Simonović, J.D., *Multi-frequency analysis of the double circular plate system non-linear dynamics*, NONLINEAR DYNAMICS, **67**(3) (2012), 2299–2315.

[5] Simonovic J.D.,, *Dynamics and Stability of Dynamics Hybrid Systems*, doctoral dissertation, University of Nis Mechanical Faculty, (2012), 337.

10th International Congress of the Serbian Society of Mechanics
Niš, Serbia, June 18-20, 2025

M.4.3

Original scientific paper

DOI:10.46793/ICSSM25.366L

A NOVEL FINITE TIME STABILITY ANALYSIS OF A CLASS NONLINEAR FRACTIONAL ORDER MULTI-STATE TIME DELAY SYSTEMS: A NEW GRONWALL - BELLMAN INEQUALITY APPROACH

Mihailo P. Lazarević[1][0000-0002-3326-6636], Stjepko Pišl[1], Darko Radojević[2],

[1] Faculty of Mechanical Engineering, The University of Belgrade, Kraljice Marije 16,

11120 Belgrade 35,Serbia, e-mail: mlazarevic@mas.bg.ac.rs, stjepko.pisl@gmail.com

[2]Dunav Insurance Company, Ustanicka 128, 11050 Belgrade, Serbia e-mail: drmasf@yahoo.com

Abstract :

In this contribution, the finite-time stability analysis (FTS) for a class of nonlinear two=term fractional-order multi-state time delay systems (FOTDS) is studied. Based on a new Gronwall-Bellman inequality, a new FTS stability criterion for such systems are established in term of the Mittag-Leffler function. Finally, we provide numerical example to illustrate the applicability of the proposed stability conditions.

Key words: finite-time stability, fractional order, nonlinear, multi-state, time delay

1. Introduction

Time delay often appears in many real-world engineering systems and it may lead to bifurcation, chaos and even instability, [1]. Stability and control design of time-delay systems are widely studied due to the effect of delay phenomena on system dynamics, which often leads to poor performance or even instability. While the concept of Lyapunov stability, recognized as infinite time behavior, has been well investigated and developed, here, we consider system stability in the non-Lyapunov sense- *finite-time stability* (FTS) because the system restrains its trajectory to a predefined time-varying domain over a finite time interval for a bounded initial condition, [2]. As an important role in the study of the transient behavior of control systems, FTS may help achieve better anti-interference and robustness over a time interval as well as improve the control precision, [3]. Also, it is observed that the stability of time delay systems may be destroyed by its uncertainties and nonlinear perturbations, so it is necessary to study the FTS analysis of time delay systems with uncertain parameters and nonlinear perturbation, [4].

Additionally, fractional-order dynamical systems have garnered significant attention from researchers and engineers in recent years [5], particularly concerning various types of stability. Fractional-order time-delay systems (FOTDS) refer to dynamical systems that include both fractional-order derivatives and time delays. Consequently, the stability analysis of FOTDS has emerged as a challenging issue [6-7]. Here, we are interested in FTS where FTS analysis of FOTDS of retarded type is initially investigated and presented in [7-9] using generalized

Gronwall inequality (GGI).Namely, Gronwall-type inequalities, also known as Gronwall–Bellman inequalities, are essential tools for analysis of the behavior of solution of differential equations with integer/fractional order and serve to check the boundedness property of the considered system. Recently, authors [10] introduced and applied a new Gronwall-Bellman inequality for a particular class of fractional order system.

In this article, inspired by the above discussions,at first time, we will analyze the FTS problem of a given class of nonlinear two-term fractional order multi-state time delay systems where novel delay independent condition for the FTS of the considered system has been presented.

2. Preliminaries and problem statement

2.1 Preliminaries

This section is devoted to presenting some basic notations and essential definitions and concepts of Riemann-Liouville fractional integral, Caputo fractional derivative. Throughout this paper, the norm $\|(\cdot)\|$ denotes any vector norm, i.e. $\|(\cdot)\|_1$, $\|(\cdot)\|_2$, or $\|(\cdot)\|_\infty$, or the corresponding matrix norm induced by the equivalent vector norm, i.e. 1–, 2–, or ∞ – norm, respectively.

Definition 2.1*:* [11] The left Caputo fractional derivative of order α, ($n-1\le\alpha<n\in\mathbb{Z}^+$) of the function $h(t)$ is:

$$ {}^C D^{\alpha}_{t_0,t} h(t) = \frac{1}{\Gamma(n-\alpha)} \int_{t_0}^{t} (t-\tau)^{n-\alpha-1} h^{(n)}(\tau)\, d\tau, \tag{2.1}$$

where $h^{(n)}(\tau)=d^n h(\tau)/d\tau^n$, and $\Gamma(\cdot)$ is the Gamma function, $\Gamma(\xi)=\int_0^\infty s^{\xi-1}e^{-s}ds$.

Definition 2.2 [12] The Mittag-Leffler function with one parameter is given as:

$$E_\alpha(h)=\sum_{k=0}^{\infty} h^k/\Gamma(k\alpha+1),\ \left(\alpha=1,\quad E_1(h)=e^h\right),\quad \alpha>0,\, h\in C \tag{2.2}$$

Lemma 2.1 [12] ${}_0I_t^{\alpha}\left({}^cD_0^{\alpha}h(t)\right)=h(t)-\sum_{k=0}^{n-1}\frac{t^k}{k!}h^{(k)}(0),\quad n-1<\alpha<n, t>0$ (2.3)

Lemma 2.2 Let $\alpha>\beta>0, n-1<\beta<n$ and $h(t)\in AC^n[a,b]$. Then

$$ {}_0I_t^{\alpha}\left({}^cD_0^{\beta}h(t)\right)= {}_0I_t^{\alpha-\beta}h(t)-\sum_{k=0}^{n-1}\frac{t^{k+\alpha-\beta}}{\Gamma(\alpha-\beta+k+1)}h^{(k)}(0). \tag{2.4}$$

Remark 1. Assume that $1<\beta<\alpha<2$, then we get:

$$ {}_0I_t^{\alpha}\left({}^cD_0^{\beta}h(t)\right)= {}_0I_t^{\alpha-\beta}h(t)-\frac{h(0)\cdot t^{\alpha-\beta}}{\Gamma(\alpha-\beta+1)}-\frac{h^{(1)}(0)\cdot t^{\alpha-\beta+1}}{\Gamma(\alpha-\beta+2)},\quad t\ge 0 \tag{2.5}$$

Lemma 2.3 (*Theorem 2.1,* [10]) Let $0<\alpha<1$ and consider the time interval $I=[0,T)$, where $T\le\infty$. Suppose *a(t)* is a nonnegative function, which is locally integrable on *I* and *b(t)* and *g(t)* are nonnegative, nondecreasing continuous functions defined on I, with both bounded by a positive constant, M. If $z(t)$ is nonnegative, and locally integrable on I and satisfies

$$z(t) \le a(t) + b(t)\int_0^t z(s)ds + g(t)\int_0^t (t-s)^{\alpha-1} z(s)ds, \tag{2.6}$$

Then

$$z(t) \le a(t) + \sum_{n=1}^{\infty}\sum_{i=0}^{n}\binom{n}{i} b^{n-i}(t) g^{i}(t) \frac{[\Gamma(\alpha)]^{i}}{\Gamma(i\alpha+n-i)}\int_0^t (t-s)^{\{i\alpha-(i+1-n)\}} a(s)ds. \tag{2.7}$$

Corollary 2.3. [10]) Suppose the conditions in Lemma 2.5 (*Theorem 2.1*) are satisfied and *a(t)* is nondecreasing on $0 \le t < T$. Then

$$z(t) \le a(t) E_{\alpha}\left(g(t)\Gamma(\alpha)t^{\alpha}\right)\exp\left(\frac{1}{\alpha}b(t)t\right) \tag{2.8}$$

2.2 Problem statement

We will consider the nonlinear fractional-order two-term $0 < \beta < 1 < \alpha < 2, \beta = \alpha - 1$ multi-state delay system given by the following equation:

$${}^{c}\mathrm{D}_t^{\alpha}\boldsymbol{x}(t) = A_0\boldsymbol{x}(t) + \sum_{i=1}^{n} A_i\boldsymbol{x}(t-\tau_i) + A_{\beta}{}^{c}\mathrm{D}_t^{\beta}\boldsymbol{x}(t) + B_0\boldsymbol{u}(t) + \mathrm{g}\left(t, x(t), x(t-\tau_g)\right) \tag{2.9}$$

with the associated continuous function of the initial state as well as the initial value of the first derivative of $\dot{x}(t)$:

$$\boldsymbol{x}(t) = \boldsymbol{\psi}_x(t), t \in [-\tau, 0], \quad \dot{x}(0) = x_0', \tag{2.10}$$

where τ_g, τ_i, $\mathrm{i} = 1,2,...,n$, are the time state delays, $\tau_m = \max(\tau_1, \tau_2, ..., \tau_n)$, $\tau_g, \tau_i > 0$ and without losing generality it is assumed that $\tau_m = \tau_g = \tau$; $x(t) \in R^n$ is the state vector and $u(t) \in \mathbb{R}^m$ is the control input; A_0, A_β, A_i, $i = 1,2,...,n$, and B_0 are constant matrices with appropriate dimensions; $\psi_x(t) \in C([-\tau, 0], R^n)$ is the initial function of $x(t)$ with the norm $\|\psi_x\|_C = \sup_{-\tau \le s \le 0}\|\psi_x(s)\|$. Here, the following assumption for the nonlinear term $g(.)$ is introduced. The nonlinear term $\mathrm{g}(t, x(t), x(t-\tau_g))$ satisfies the condition, i.e. there is a continuous function $M(t)$ on $[0, +\infty]$ such that $\left\|\mathrm{g}\left(t, x(t), x(t-\tau_g)\right)\right\| \le M(t)\left(\|x(t)\| + \|x(t-\tau_g)\|\right)$. Behavior of system (2.9) with given initial function (2.10) is observed over time interval $J = [t_0, t_0 + T] \subset R$, where T may be either a real positive number or symbol ∞. The norm $\|x(t)\|_\infty$ will be used here as well: $\sup_{t\in[0,T]}\|A_i\| = a_i$, $i = 0,1,2,...,n,\beta$, $\sup_{t\in[0,T]}(M(t)) = m$ and $\sup_{t\in[0,T]}(B_0) = b_0$, $\sup_{t\in[0,T]}(A_\beta) = a_\beta$.

Definition 2.3 [7,13]: The nonlinear fractional-order two-term $0 < \beta < 1 < \alpha < 2, \beta = \alpha - 1$ delay system with state time delays given by nonhomogeneous state equation (2.9) satisfying initial conditions (2.10) is *finite-time stable* w.r.t. $\{\delta, \varepsilon, t_0, \chi_u, J, \|(\cdot)\|\}$, $0 < \delta < \varepsilon$, if and only if:

$$\rho < \delta, \quad \|\boldsymbol{u}(t)\| < \chi_u\} \quad \Rightarrow \quad \|\boldsymbol{x}(t)\| < \varepsilon, \quad \forall t \in J. \tag{2.11}$$

where $\rho = \max\left\{\|\psi\|_C, \|x_0'\|\right\}$ and χ_u is positive constant.

Definition 2.4 [7,13]: The nonlinear fractional-order two-term $0<\beta<1<\alpha<2,\ \beta=\alpha-1$ delay system with sate delays given by homogeneous state equation (2.9) $u(t)\equiv 0$, satisfying initial conditions (2.10) is *finite-time stable* w.r.t. $\left\{\delta,\varepsilon,t_0,J,\|(\cdot)\|\right\},\ 0<\delta<\varepsilon,$ if and only if:

$$\rho<\delta \quad \Rightarrow \quad \|\boldsymbol{x}(t)\|<\varepsilon, \quad \forall t\in J. \tag{2.12}$$

where $\rho = \max\left\{\|\psi\|_C, \|x_0'\|\right\}$.

3. Main Results

3.1 FTS analysis of nonlinear fractional order multi-state time delay system

Theorem 3.1: The nonlinear two-term fractional order multi-state time delay system (2.9) satisfying initial conditions (2.10) is *finite-time stable* w.r.t. $\left\{\delta,\varepsilon,t_0,\chi_u,\chi_0,J,\|(\cdot)\|\right\},\ \delta<\varepsilon,$ if the following condition holds:

$$\left[\left(1+\left(1+a_\beta\right)|t|\right)\right]E_\alpha\left(a_\Sigma t^\alpha\right)exp\left(\frac{1}{\alpha}a_\beta t\right)+\frac{b_o\chi_u^*|t|^\alpha}{\Gamma(\alpha+1)}\le\varepsilon/\delta \tag{3.1}$$

where $\chi_u^* = \chi_u/\delta$ and $a_\Sigma = \left(a_0+2m+\sum_{i=1}^n a_i\right)$.

Proof: The fractional order satisfies $0<\beta<1<\alpha<2,\ \beta=\alpha-1$ and if an integral of fractional order ${}_0I_t^\alpha,\ t_0=0$ is applied on both sides, one has

$${}_0I_t^\alpha\left({}^c\mathrm{D}_t^\alpha\boldsymbol{x}(t)-A_\beta{}^c\mathrm{D}_t^\beta\boldsymbol{x}(t)\right)={}_0I_t^\alpha\left(A_0\boldsymbol{x}(t)+\sum_{i=1}^n A_i\boldsymbol{x}(t-\tau_i)+B_0\boldsymbol{u}(t)+\mathrm{g}\left(t,x(t),x\left(t-\tau_g\right)\right)\right) \tag{3.2}$$

Following properties of the fractional derivatives $0<\beta<1<\alpha<2,\ \beta=\alpha-1$ and taking into account *Lemmas* 2.1,2.2 solution can be obtained in the form of the equivalent Volterra integral equation:

$$\begin{aligned}x(t)&=\psi_x(0)+t\dot{x}(0)-\psi_x(0)\frac{A_\beta\cdot t^{\alpha-\beta}}{\Gamma(\alpha-\beta+1)}+\frac{1}{\Gamma(\alpha-\beta)}\int_0^t(t-s)^{\alpha-\beta-1}A_\beta x(s)ds+\\&+\frac{1}{\Gamma(\alpha)}\int_0^t(t-s)^{\alpha-1}\left(A_0\boldsymbol{x}(s)+\sum_{i=1}^n A_i\boldsymbol{x}(s-\tau_i)+B_0\boldsymbol{u}(s)+\mathrm{g}\left(\mathrm{s},x(s),x\left(s-\tau_g\right)\right)\right)ds.\end{aligned} \tag{3.3}$$

or taking into account $\beta=\alpha-1$,

$$\begin{aligned}x(t)&=\psi_x(0)+t\dot{x}(0)-\psi_x(0)\frac{A_\beta\cdot t}{\Gamma(2)}+\frac{1}{\Gamma(1)}\int_0^t A_\beta x(s)ds+\\&+\frac{1}{\Gamma(\alpha)}\int_0^t(t-s)^{\alpha-1}\left(A_0\boldsymbol{x}(s)+\sum_{i=1}^n A_i\boldsymbol{x}(s-\tau_i)+B_0\boldsymbol{u}(s)+\mathrm{g}\left(\mathrm{s},x(s),x\left(s-\tau_g\right)\right)\right)ds.\end{aligned} \tag{3.4}$$

By employing the norm $\left\|(\cdot)\right\|$ on both sides of the previous expression, one gets

$$\|x(t)\| \le \|\psi_x(0)\| + |t|\|\dot{x}(0)\| + \|A_\beta\|\|\psi_x(0)\|\frac{|t|}{\Gamma(2)} + \int_0^t \|A_\beta\|\|x(s)\|ds + \tag{3.5}$$

$$+\frac{1}{\Gamma(\alpha)}\int_0^t \left|(t-s)\right|^{\alpha-1}\left\|\left(A_0(s)\boldsymbol{x}(s) + \sum_{i=1}^n A_i(s)\boldsymbol{x}(s-\tau_i) + B_0\boldsymbol{u}(s) + g\left(\mathrm{s}, x(s), x\left(s-\tau_g\right)\right)\right)\right\|ds.$$

Consequently, we have

$$\begin{aligned}\|x(t)\| &\le \|\psi_x\|_C\left[1+\frac{a_\beta|t|}{\Gamma(2)}\right] + \|x_0'\||t| + a_\beta\int_0^t\|x(s)\|ds + \\ &+\frac{1}{\Gamma(\alpha)}\int_0^t\left|(t-s)\right|^{\alpha-1}\left\|\left(A_0(s)\boldsymbol{x}(s) + \sum_{i=1}^n A_i(s)\boldsymbol{x}(s-\tau_i) + B_0\boldsymbol{u}(s)\right) + g\left(\mathrm{s}, x(s), x\left(s-\tau_g\right)\right)\right\|ds.\end{aligned} \tag{3.6}$$

Previous expression (3.6) based on assumption on *g(.)* can be rewritten as

$$\begin{aligned}\|x(t)\| &\le \|\psi_x\|_C\left[1+\frac{a_\beta|t|}{\Gamma(2)}\right] + \|x_0'\||t| + a_\beta\int_0^t\|x(s)\|ds + \\ &+\frac{1}{\Gamma(\alpha)}\int_0^t\left|(t-s)\right|^{\alpha-1}\left[a_0\|x(s)\| + \sum_{i=1}^n a_i\|x(s-\tau_i)\| + b_0\|u(s)\| + m\left(\|x(s)\| + \|x(s-\tau)\|\right)\right]ds,\end{aligned} \tag{3.7}$$

or taking into account $a_{0m} = a_0 + m$ (3.5) and introducing nondecreasing function $\omega(t) = \|\psi_x\|_C\left[1+\frac{a_\beta|t|}{\Gamma(2)}\right] + \|x_0'\||t|$, it yields

$$\begin{aligned}\|x(t)\| &\le \omega(t) + a_\beta\int_0^t\|x(s)\|ds + \\ &+\frac{1}{\Gamma(\alpha)}\int_0^t\left|(t-s)\right|^{\alpha-1}\left[a_{0m}\|\boldsymbol{x}(s)\| + \sum_{i=1}^n a_i\|x(s-\tau_i)\| + m\cdot\|x(s-\tau)\|\right]ds + \frac{b_0\chi_u|t|^\alpha}{\Gamma(\alpha+1)}.\end{aligned} \tag{3.8}$$

Also, the next nondecreasing function is introduced $y(t) = \sup_{\theta\in[-\tau,t]}\|x(\theta)\|, \forall t\in[0,T]$, where for $\forall t^\bullet \in [0,t]$, the following conditions satisfy $\left\|x\left(t^*\right)\right\| \le \sup_{t^*\in[t-\tau,t]}\left\{\left\|\boldsymbol{x}\left(t^*\right)\right\|\right\} \le y\left(t^*\right),\ \left\|x\left(t^*-\tau_i\right)\right\| \le y\left(t^*\right)$.

Applying the previous inequalities, the expression (3.8) takes the following form:

$$\|x(t)\| \le \omega(t) + a_\beta\int_0^t y(s)ds + \frac{a_\Sigma}{\Gamma(\alpha)}\int_0^t\left|(t-s)\right|^{\alpha-1}y(s)ds + \frac{b_0\chi_u|t|^\alpha}{\Gamma(\alpha+1)}, \tag{3.9}$$

where $a_\Sigma = \left(\sum_{i=1}^n a_i + (m + a_{0m})\right)$. Taking into account $\forall\theta\in[0,t]$ and $\theta - s \to s^* \to s$ one obtains

$$\|\boldsymbol{x}(t)\| \le \omega(t) + a_\beta\int_0^\theta y\left(\theta - s^*\right)ds^* + \frac{a_\Sigma}{\Gamma(\alpha)}\int_0^\theta\left|s^*\right|^{\alpha-1}y\left(\theta-s^*\right)ds^* + \frac{b_0\chi_u|t|^\alpha}{\Gamma(\alpha+1)}, \tag{3.10}$$

or

$$\|\boldsymbol{x}(t)\| \le \omega(t) + a_\beta \int_0^t y(s)\,ds + \frac{a_\Sigma}{\Gamma(\alpha)} \int_0^t |t-s|^{\alpha-1} y(s) ds + \frac{b_0 \chi_u |t|^\alpha}{\Gamma(\alpha+1)}. \tag{3.11}$$

Moreover, based on the property of the function $y(t)$, we conclude that:

$$\begin{aligned} y(t) &= \sup_{\theta\in[-\tau,t]} \|x(\theta)\| \le \max\left\{ \sup_{\theta\in[-\tau,0]} \|x(\theta)\|,\ \sup_{\theta\in[0,t]} \|x(\theta)\|, \right\} \le \\ &\le \max\left\{ \|\psi_x\|_C, \omega(t) + a_\beta \int_0^t y(s)\,ds + \frac{a_\Sigma}{\Gamma(\alpha)} \int_0^t |t-s|^{\alpha-1} y(s) ds + \frac{b_0 \chi_u |t|^\alpha}{\Gamma(\alpha+1)}, \right\} \\ &= \omega(t) + a_\beta \int_0^t y(s)\,ds + \frac{a_\Sigma}{\Gamma(\alpha)} \int_0^t |t-s|^{\alpha-1} y(s) ds + \frac{b_0 \chi_u |t|^\alpha}{\Gamma(\alpha+1)}. \end{aligned} \tag{3.12}$$

Now, if we take $\rho = \max\left\{\|\psi\|_C, \|x_0'\|\right\}$ we can obtain

$$\begin{aligned} x(t) \le y(t) &\le \rho\left[\left[1 + \frac{a_\beta |t|}{\Gamma(2)}\right] + |t|\right] + a_\beta \int_0^t y(s)\,ds + \frac{a_\Sigma}{\Gamma(\alpha)} \int_0^t |t-s|^{\alpha-1} y(s) ds + \frac{b_0 \chi_u |t|^\alpha}{\Gamma(\alpha+1)} \\ &\le \varpi(t) + a_\beta \int_0^t y(s)\,ds + \frac{a_\Sigma}{\Gamma(\alpha)} \int_0^t |t-s|^{\alpha-1} y(s) ds + \frac{b_0 \chi_u |t|^\alpha}{\Gamma(\alpha+1)}. \end{aligned} \tag{3.13}$$

Observing that $\varpi(t)$ is a nondecreasing function on $J_0 = [0,T]$ and applying *Corollary 2.3* we get

$$x(t) \le \rho\left[\left(1 + \frac{a_\beta |t|}{\Gamma(2)}\right) + |t|\right] E_\alpha\left(a_\Sigma t^\alpha\right) \exp\left(\frac{1}{\alpha} a_\beta t\right) + \frac{b_0 \chi_u |t|^\alpha}{\Gamma(\alpha+1)}\ . \tag{3.14}$$

Finally, using the basic condition of Theorem 3.1, and $\rho < \delta,$ we can obtain the required FTS condition: $\|\boldsymbol{x}(t)\| < \varepsilon, \quad \forall t \in J.$

Corollary 3.3 The nonlinear fractional order time-delay system (2.9), $A_\beta \equiv 0$ is *finite-time stable* w.r.t. $\left\{\delta, \varepsilon, t_0, \chi_u, J, \|(\cdot)\|\right\},\ 0 < \delta < \varepsilon,$ if it satisfies the following condition:

$$\left[1 + |t|\right] E_\alpha\left(a_\Sigma t^\alpha\right) + \frac{b_0 \chi_u^* |t|^\alpha}{\Gamma(\alpha+1)} \le \varepsilon / \delta\,. \tag{3.15}$$

Corollary 3.4 The homogeneous system nonlinear fractional order time-delay system (2.9), $A_\beta \equiv 0,\ u(t) \equiv 0$ is *finite-time stable* w.r.t. $\left\{\delta, \varepsilon, t_0, J, \|(\cdot)\|\right\},\ 0 < \delta < \varepsilon,$ if it satisfies the following condition:

$$\left[1 + |t|\right] E_\alpha\left(a_\Sigma t^\alpha\right) \le \varepsilon / \delta\,. \tag{3.16}$$

4. Numerical example

Let us consider the following nonlinear fractional-order multi-state system $0 < \beta < 1 < \alpha < 2,\ \beta = \alpha - 1$ with constant time delays, where are $\tau_1 = \tau_2 = \tau$:

$$\begin{aligned} &{}^{c}\mathrm{D}_t^{\alpha}\boldsymbol{x}(t)-A_{\beta}{}^{c}\mathrm{D}_t^{\beta}\boldsymbol{x}(t)=A_0\boldsymbol{x}(t)+A_1x(t-\tau_1)+A_2x(t-\tau_2)+B_0u(t)+\mathrm{g}(t,x(t),x(t-\tau)) \\ &x(t)=\psi_x(t),\ \ x'(t)=0,\ -\tau\le t\le 0 \end{aligned} \tag{4.1}$$

and

$$A_0=\begin{bmatrix}-0.8 & 0\\ 0 & -0.5\end{bmatrix},\ A_1=\begin{bmatrix}0.1 & 0\\ 0 & 0.3\end{bmatrix}\ \ A_2=\begin{bmatrix}0.1 & 0\\ 0 & 0.1\end{bmatrix}, A_{\beta}=\begin{bmatrix}0.3 & -0.2\\ 0.4 & 0.1\end{bmatrix},\ \mathrm{B}_0=\begin{bmatrix}0\\ 1\end{bmatrix} \tag{4.2}$$

with the associated continuous function of initial state: $\psi_x(t)=[0.0,\ 0.02]^T,t\in[-\tau,0]$ and $g(t,x(t),x(t-\tau))=(-x_1(t)x_2(t-\tau)\ \ -x_2(t)x_1(t-\tau))^T$, $\tau=0.1$, $\alpha=1.2,\ \beta=0.2$. For control $u(t)=\sin t$, it follows that $\chi_u=1$. It is easily checked that assumption is satisfied for $M=1$. Also, one can get $\|A_0\|=0.8$, $\|A_1\|=0.3$, $\|A_2\|=0.1,\|A_{\beta}\|=0.5$, $\|B_0\|=1.,\delta=0.021$ and $\varepsilon=1$. Based on FTS criterion (3.1), in Theorem 3.1, one can calculate that the estimated time of FTS of the system (4.2) is $T_e\approx 0.745\,s$.

5. Conclusion remarks

In this contribution, the FTS of (non)homogeneous nonlinear fractional order $0<\beta<1<\alpha<2,\ \beta=\alpha-1$ with multi-state state delays is studied. By use of a new Gronwall-Bellman inequality, new FTS criteria are obtained where sufficient conditions are derived for the FTS of considered FOTDS. Finally, the simulation example shows the validation of the proposed novel stability criterion of FTS.

Acknowledgement

This work is supported by the Ministry of Education, Science and Technological Development of the Republic of Serbia under the Grant No. 451-03-137/2025-03/200105 from 04. 02. 2025.

References

[1] Zavarei M., Jamshidi M., *Time-Delay Systems: Analysis, Optimization and Applications*, North-Holland, Amsterdam, 1987.

[2] Gu, K., Kharitonov, V.L., Chen, J.*: Stability of Time-Delay Systems.* Birkhauser, Boston, MA 2003.

[3] Lee, J.; Haddad, W.M. *On finite-time stability and stabilization of nonlinear hybrid dynamical systems.* AIMS Math. 6, 5535–5562,2021.

[4] Liu P.L., *A delay decomposition approach to robust stability analysis of uncertain systems with time-varying delay*, ISA Trans. 51 (6),694-701, 2012.

[5] Monje, C. A., Chen, Y., Vinagre, B. M., Xue, D. and Feliu-Batlle, V., *Fractional-Order Systems and Controls: Fundamentals and Applications,* Springer, ISBN 9781849963350, 2010. https://link.springer.com/book/10.1007/978-1-84996-335-0.

[6] Lazarević M. P., *Finite Time Stability Analysis of PDα Fractional Control of Robotic Time-Delay Systems,* Mechanics Research Communications, Vol. 33, No. 2, 269–279, 2006.

[7] Lazarević M., A.Spasić, *Finite-Time Stability Analysis of Fractional Order Time Delay Systems: Gronwall`s Approach,* Mathematical and Computer Modelling, 49, pp.475-481,2009.

[8] Lazarević P.M., D. Radojević, S. Pišl, and G. Maione, *Robust finite-time stability of uncertain neutral nonhomogeneous fractional-order systems with time-varying delays*, Theoretical and applied mechanics (TAM), Vol.47 issue 2, 241–255. 2020.

[9] Lazarević P.M., D. Radojević, G. Maione, S. Pišl, *Finite-time stability of neutral fractional-order time varying delay systems with nonlinear parameter uncertainties and perturbations*, 8th International Congress of Serbian Society of Mechanics Kragujevac, ISBN 978-86-909973-8-1 Serbia, June 28-30, 2021, pp.652-661.

[10] Wu, Q. *A new type of the Gronwall-Bellman inequality and its application to fractional stochastic differential equations.* Cogent Math. 2017; 4(1):1279781 doi: 10.1080/23311835.2017.1279781

[11] Kilbas A., Srivastava H., Trujillo J., *Theory and Applications of Fractional Differential Equations*, Elsevier, Amsterdam, 2006.

[12] Kochubei A., Y. Luchko, Eds, *Handbook of Fractional Calculus with Applications, Volume 1: Basic Theory*, Walter de Gruyter GmbH, Berlin/Boston,2019.

[13] Liang C.,W.Wei, J.Wang, *Stability of delay differential equations via delayed matrix sine and cosine of polynomial degrees,* Adv. Difference Equ., (1):1–17, https://doi.org/10.1186/s13662-017-1188-0,2017.

10th International Congress of the Serbian Society of Mechanics
Niš, Serbia, June 18-20, 2025
M.4.4

Extended abstract

Elliptical, Circular orbits and applications

Miodrag Mateljević[1] [0000-0002-9226-0023]

[1]Faculty of Mathematics, University of Belgrade, Studentski Trg 16, Belgrade, Republic of Serbia,

email: miodrag@matf.bg.ac.rs

Abstract. In this paper, among other things, we consider the application of Newton's law of gravity to Kepler's laws, how the earth really moves in the Earth-Moon system and visualization of the Earth-Moon system and tides (the rise and fall of water bodies on Earth). In particular, we consider centripetal force as real force and centrifugal "force" as pseudo-force.
Keywords: Centrifugal "force", Two bodies, Earth-Moon system, Tides .

1. Introduction - instructions

Let s consider circular otion f an bject along he circumference f a circle f radius B. Suppose hat t s niform, with a constant rate f rotation and constant angential peed, constant angular elocity . Then he acceleration $\mathbf{A} = i\omega i\omega Re^{i\omega t} = -\omega^2 Re^{i\omega t}$, $B = {}^2R$ and $B = m\omega^2 R = mv^2/R$.

Let s consider circular otion f an bject along he circumference f a circle f radius B. Suppose hat t s niform, with a constant rate f rotation and constant angential peed, constant angular elocity . The path f otion can be written as $\mathbf{r} = Be^{i\omega t}$

Hence velocity $\mathbf{v} = i\omega Re^{i\omega t}$, $v = \omega R$ and acceleration $\mathbf{a} = i\omega i\omega Re^{i\omega t} = -\omega^2 Re^{i\omega t}$, $a = \omega^2 R$.

Since $\omega = v/R$ we have $a = v^2/R$ and $F = mv^2/R$.

Centrifugal force is a fictitious force in Newtonian mechanics (also called an *inertial* or *pseudo* force) that appears to act on all objects when viewed in a rotating frame of reference. It appears to be directed radially away from the axis of rotation of the frame. The magnitude of the centrifugal force F on an object of mass m at the distance r from the axis of a rotating frame of reference with angular velocity ω is: $F = m\omega^2 r$.

This fictitious force is often applied to rotating devices, such as centrifuges, centrifugal pumps, centrifugal governors, and centrifugal clutches, and in centrifugal railways, planetary orbits and banked curves, when they are analyzed in a non-inertial reference frame such as a rotating coordinate system.

1.1 Bucket rotating

We show that the surface of water in a bucket rotating with constant angular velocity will have parabolic shape.

The centrifugal force is $F_{cf} = m\omega^2 r$ and the gravitational force is $F_{grav} = -mg$. The water surface is orthogonal to the direction of the resultant force

$$F = F_{cf} + F_{grav}.$$

Thus the slope of the water surface is

$$tg\theta = dz(r)/dr = \frac{|F_{cf}|}{|F_{grav}|} = \frac{m\omega^2 r}{mg}.$$

From this we get by integration $z - z_0 = \frac{\omega^2 r^2}{2g}$.

We can also use $F\cos\theta = gdm$ and $F\sin\theta = dmr\omega^2$.

Thus we get indeed a parabolic surface in the rotating water in the bucket.

1.2 Projectile moving in horizontal direction

Let the projectile be launched with an initial velocity v in horizontal direction from a point O which is on distance d from the earth and let OC intersect surface of the earth at O', where C is center of the earth. Let vector OO' points in positive direction of y-axis.

For the projectile motion we have $x = vt$ and $y = gt^2/2$. Therefore trajectory is given by $y = f(x) = g\frac{x^2}{2v^2}$. Hence $f' = gx/v^2$, $f'' = g/v^2$ and the curvature of trajectory is

$$\kappa = \frac{gv^4}{(v^4 + g^2x^2)^{3/2}}. \tag{1}$$

In particular, $\kappa(0) = g/v^2$ and $\kappa(0) \leq 1/r$ if and only, if $rg \leq v^2 = r^2\omega^2$.

Let K circle with center M on OO' of radius R which contains point O such that $2R < d$.

Demonstrating Why Water Stays in a Bucket Revolving in a vertical circle K.

Water stays in a bucket revolving in a vertical circle K if $gr \leq v^2 = r^2\omega^2$.

Duel Newton - Mach.

1.3 Earth-Moon system

In addition we consider the application of Newton's law of gravity to Kepler's laws and solution of two body problems, to describe how the earth really moves in the Earth-Moon system and visualization of the Earth-Moon system and tides (the rise and fall of water bodies on Earth). For a Textbook of General Astronomy see [2] and for an introduction to tides [1].

2. Concluding remarks

Although most of the discussion refers to classical physical theories, we believe that it is novel that within the framework of certain models we try to precisely apply mathematical theory and clarify the derivations. In particular vwe use theory related to conservative system with one degree of freedom.

References

[1] T. Gerkema, An introduction to tides, https://core.ac.uk/download/pdf/80950747.pdf

[2] Young, C. A. (1889). A Textbook of General Astronomy (PDF). p. 288. Archived (PDF) from the original on 2019-10-05. Retrieved 2018-08-13.

10th International Congress of the Serbian Society of Mechanics
Niš, Serbia, June 18-20, 2025

M.4.5
Extended abstract

NONLINEAR VIBRATION OF A PLATFORM SYSTEM WITH NON-IDEAL MOTOR

Nikola Nešić[1] [0000-0001-6237-4735], **Julijana Simonović**[2] [0000-0002-2330-6948], **Jeferson Lima**[3] [0000-0001-5526-2014], **José Manoel Balthazar**[4] [0000-0002-6082-4832], and **Angelo Marcelo Tusset**[5] [0000-0003-3144-0407]

[1]University of Priština in Kosovska Mitrovica, Faculty of Technical Sciences, Serbia, email: nikola.nesic@pr.ac.rs
[2]University of Niš, Faculty of Mechanical Engineering, e-mail: julijana.simonovic@masfak.ni.ac.rs
[3,5]Federal University of Technology - Paraná/Brazil (UTFPR) Brazil, e-mail: jefersonjl82@gmail.com, a.m.tusset@gmail.com
[4]Universidade Tecnológica Federal do Paraná- Campus Ponta Grossa, Ponta Grossa, PR, Brasil, Faculdade de Engenharia de Bauru - FEB/UNESP, Bauru, São Paulo, e-mail: jmbaltha@gmail.com

Abstract. This paper analyzes a nonlinear system influenced by non-ideal excitation through a dual perspective: its nonlinearity and the presence of non-ideal excitation. The investigation is carried out using numerical methods, specifically the Incremental Harmonic Balance (IHB) method and the Runge-Kutta method. The study examines the nonlinear dynamic behavior of a structure supporting an unbalanced rotating machine with a limited power supply while emphasising the interaction between the motor and the structure—an aspect often overlooked in conventional design approaches. The research explores the Sommerfeld effect and nonlinear phenomena such as amplitude jumps, multi-mode interactions, and the stability of solutions. Findings demonstrate that increasing the magnitude of external excitation significantly impacts the system's dynamics, leading to greater instability at lower frequencies before the resonant peak. Furthermore, variations in the parameters of the rotational system result in multiple amplitude peaks and regions of instability. These findings underscore the necessity of incorporating motor-structure interaction into engineering design, recognizing that real motors act as non-ideal energy sources. The outcomes contribute to advancements in design and control strategies, paving the way for innovative vibration suppression techniques and enhancing the stability and performance of engineering systems.

Keywords: Non-ideal excitation, Incremental harmonic balance method (IHB), Nonlinear Systems, Sommerfeld effect.

1. Introduction

Sources of non-ideal vibrations can be different [1, 2].This paper investigates the vibration of the platform structure subjected to excitation of non-ideal motor. Equation of motion describing considered system is given by:

$$\ddot{x}+2\zeta\dot{x}+\omega_0^2 x+\gamma x^3 = f_0\cos\left(\Omega t - D_0\cos\left(d_0\Omega t\right)\right), \tag{1}$$

where parameters D_0 and d_0 are defined by the active interaction between the vibrating system and the excitation source, ζ is the damping coefficient, ω_0 is the linear stiffness coefficient and γ

nonlinear parameter. Equation (1) is solved using Runge-Kutta (Figure 1(a)) and IHB (Figure 1(b)) methods [3].

2. Results

3d surfaces (Figure 1(a)) are numerically calculated using the Runge-Kutta Dormand–Prince method with C++ and CUDA to parallelism. The approximative solutions obtained with the IHB method (Figure 1(b)) contain four harmonics. Stability of solutions is investigated with Floquet theory [4].

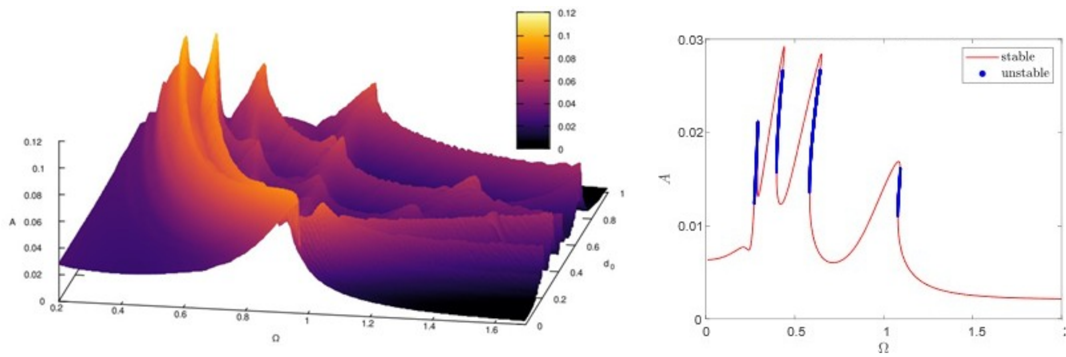

(a) Influence of d_0 (b) Floquet stability for $d_0 = 1$

Figure 1: Amplitude frequency response ($\gamma = 1300, D_0 = 3.2, f_0 = 0.01, \zeta = 0.05, \omega_0 = 0.9487$)

3. Conclusion

Mentioned methods allow one to get additional frequency responce curves that include variation of another relevant parameters not presented here, and stability of the solution. That way systems with non-ideal excitation can be analyzed, and in case of synthesis optimal parameters can be selected.

Acknowledgement. The part of this research was financially supported by the Ministry of Science, Technological Development and Innovation of the Republic of Serbia (Contract No. 451-03-136/2025-03/200109 and 451-03-18/2025-03/200155).

References

[1] Balthazar, J.M. et al., *An overview on non-ideal vibrations*, Meccanica, Vol. 38, 613-621, 2003.

[2] Balthazar, J.M. et al., *An overview on the appearance of the Sommerfeld effect and saturation phenomenon in non-ideal vibrating systems (NIS) in macro and MEMS scales*, Nonlinear Dynamics, Vol. 93, 19-40, 2018.

[3] Nešić N. et al., *Vibration suppression of a platform by a fractional type electromagnetic damper and inerter-based nonlinear energy sink*, Applied Mathematical Modelling, Vol. 137, 115651, 2025.

[4] Nešić N. et al., *Vibration and stability of a nonlinear nonlocal strain-gradient fg beam on a visco-Pasternak foundation*, Facta Universitatis, Series: Mechanical Engineering, 2023.

10th International Congress of the Serbian Society of Mechanics
Niš, Serbia, June 18-20, 2025
M.4.6
Extended abstract

MODEL IDENTIFICATION OF A LOCALLY NONLINEAR STRUCTURE

Tamara Nestorović[1][0000-0003-0316-2171], Aneeb Ul-Hasnain[1], Atta Oveisi[1][0000-0002-6507-9448]

[1] Mechanics of Adaptive Systems
Ruhr-Universitt Bochum, Universittsstr. 150, D-44801 Bochum, Germany
e-mail: tamara.nestorovic@rub.de

Abstract:

Linear approximations can be employed to effectively model various systems providing a simplified and interpretable representation of their behavior within a specific input range. Nevertheless, linear models possess inherent limitations as their validity is restricted to specific input conditions. As a result, there has been an increasing tendency towards nonlinear modeling in numerous application domains, as the consideration of such models frequently yields superior outcomes.

In this work the nonlinear modeling is proposed for dynamic structure with a local geometric nonlinearity. The structure under consideration is a clamped-clamped flexible beam consisting of two parts with different thicknesses, where the thickness of one of the parts is considerably smaller in comparison with the other part. The lengths of the two parts are also different, so from the geometric point of view the physical model is not symmetric. Under assumption of the existence of a linear underlying model, the nonlinear model is developed by augmentation of the underlying state-space linear model by nonlinear polynomial terms. The identification task is therefore twofold: *i*) extraction of the underlying linear state-space model by best linear approximation using the subspace state-space model identification from the input-output measurement data and *ii*) estimation of the nonlinear polynomial coefficients and order for the best nonlinear approximation. For the structure under consideration the excitation inputs are multi-sine force signals exerted by the vibration exciter – shaker, whereas the output represents corresponding signals from the accelerometers placed along the beam and its derivatives. The underlying linear model was identified by optimizing the amplitude frequency response in the frequency range of interest. For optimization of the nonlinear polynomial coefficients the Levenberg-Marquardt algorithm was implemented. Comparison of the model outputs from the best linear approximation model and the nonlinear model shows better performance of the nonlinear model and justifies thus the necessity of consideration of nonlinearities and their modeling.

Key words: nonlinear polynomial model, state-space, identification

1. Nonlinear structure modelling background

For the structure under investigation shown in Figure 1, the clamped-clamped beam consisting of two parts connected by screws, the model identification task consists of the estimation of a best linear approximation (BLA) state-space model and its subsequent augmentation by the nonlinear polynomial terms in order to capture the nonlinear dynamics of the structure.

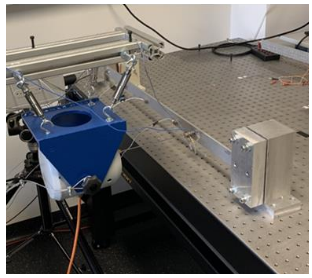

Fig. 1. Experimental setup with the locally nonlinear clamped-clamped beam and transducers for the data acquisition

The overall model of the structure is represented by a polynomial nonlinear state-space model in discrete time in the following the form:

$$\mathbf{x}(\mathrm{k}+1)=\mathbf{A}\mathbf{x}(\mathrm{k})+\mathbf{B}\mathbf{u}(\mathrm{k})+\mathbf{E}\zeta(\mathbf{x}(\mathrm{k}),\mathbf{u}(\mathrm{k})),\ \mathbf{y}(\mathrm{k})=\mathbf{C}\mathbf{x}(\mathrm{k}) \tag{1}$$

with the state vector **x**, input **u**, output **y** and the state, input and output matrices **A**, **B**, **C** respectively. The coefficients of the polynomial term $\mathbf{E}\zeta$ are identified based on the measured input-output data from the experiment.

2. Results

Applying described procedure, the nonlinear model based on the BLA and estimation of the polynomial nonlinear model part has been identified. The advantage of the nonlinear model over the linear one has been demonstrated exemplarily by comparison of the model outputs from the BLA and the nonlinear model as shown by Table 1 and Fig. 2.

Std.	Nonlinear degree	RMS value for the linear model	RMS value for the nonlinear model
0.65	2	2.9444	0.2350
0.65	2-3	2.9444	1.3544

Table 1. Comparison of the RMS error values for an exemplary random excitation signal with a standard deviation of 0.65 and different degrees of the nonlinear polynomial model extension

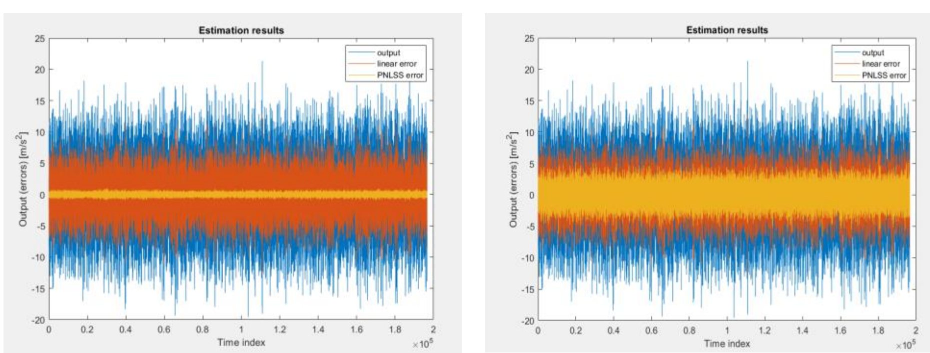

Fig. 2. Illustration of the superiority of the nonlinear vs. linear model by comparison of the model output errors with respect to the experimentally measured system response to a random excitation

M.4.7
Extended abstract

NONLINEAR PUSHOVER ANALYSIS: ASSESSMENT OF A MOMENT-RESISTING STEEL FRAME

Katarina Slavković[1] [0009-0009-9231-2856], **Andrija Zorić**[2] [0000-0002-3107-9204], **Marina Trajković Milenković**[3] [0000-0001-6874-758X], and **Predrag Petronijević**[4] [0000-0003-4601-5825]

[1]National Institute of the Republic of Serbia, Mathematical Institute of the Serbian Academy of Sciences and Arts, Serbia, e-mail: katarina.slavkovic@mi.sanu.ac.rs

[2]University Af Aiš, Aaculty Af Aivil Anginering and Architecture, Aerbia, e-mail: andrija.zoric@gaf.ni.ac.rs

[3]University Af Aiš, Aaculty Af Aivil Anginering and Architecture, Aerbia, e-mail: marina.trajkovic@gaf.ni.ac.rs

[4]University Af Aiš, Aaculty Af Aivil Anginering and Architecture, Aerbia, e-mail: predrag.petronijevic@gaf.ni.ac.rs

Abstract. The paper analyzes the response of a characteristic moment-resisting steel frame structure using the pushover method and investigates the effect of varying column cross-sectional dimensions on its seismic performance. The calculation is based on constructing the force-displacement rela-tionship and determining the target displacement, which represents the maximum displacement at the top of the structure during an earthquake. The analysis involves simulating the behavior of a nonlinear mathematical model subjected to monotonically increasing horizontal forces and gravi-tational loads until the target displacement is reached. The system response at target displacement is compared with regulatory values to assess safety. Multiple frame models were analyzed to de-termine the maximum acceleration level at which the structure still meets regulatory requirements. The results indicate that a structure designed for a lower acceleration level can withstand stronger seismic forces, with some damage, and an adequate design approach can significantly influence the behavior of steel frame structures under earthquake action.

Keywords: Nonlinear analyses, nonlinear deformations, pushover analysis, plastic hinges, moment-resistant steel frame, ground accelerations.

1. Introduction

In seismically active regions, ensuring the seismic resilience of buildings is a key challenge for en-gineers. One simpler nonlinear method for evaluating structural response to seismic action is static pushover analysis, which identifies critical locations where significant nonlinear deformations are expected and provides insight into overall structural behavior. The pushover analysis in Eurocode 8, based on the N2 method [1, 2], requires analyzing uniform and modal lateral force distributions to account for load redistribution during plastic deformations. Given the methodology for calculating the target displacement, which is essentially the mean value of possible displacements with poten-tial result scattering, the regulations require that the capacity curve, which is the main output of the pushover analysis, must cover displacement values from zero to 150% of the target displacement. A three-bay moment-resisting steel frame structure, with a span of 6 meters and a story height of 3 meters, comprising five stories, was a nalyzed. The analysis was conducted using a Type 1 elastic spectrum, with an initial acceleration value of 0.1g, increasing in 0.1g increments until the structure no longer met regulatory requirements. It was determined that the structure did not meet the horizontal acceleration requirement of 0.4g. Subsequently, modifications were analyzed to improve the seismic performance of the structure.

A total of 8 models were analyzed, and the key results are presented in Figure (1). Each marked point represents the force and displacement at plastic hinge formation. The vertical dashed lines indicate the target displacements per regulations, where the first line in the corresponding color represents the target displacement value, and the second one represents 150% of the target displacement. The initial model was tested to find the acceleration at which the structure fails to meet requirements. Corrections were made, and the final model meets the 0.4g acceleration limit.

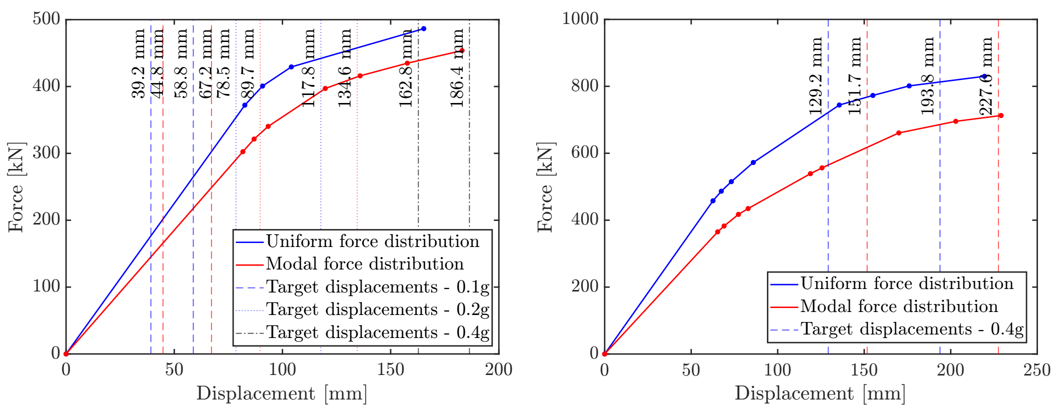

(a) (b)

Figure 1: Pushover curves result: (a) Initial model, (b) Final model

2. Conclusion

In this study, the behavior of a steel frame structure under seismic loads was examined using nonlinear static analysis. By analyzing the formation of plastic hinges, the structure's resistance to different levels of ground acceleration and the impact of dimensional adjustments to structural elements on its seismic response were assessed. The results show that a structure designed for a maximum horizontal ground acceleration of 0.1g can withstand up to 0.2g, although with a certain degree of damage. A careful selection of column cross-sections increases the maximum shear force the structure can withstand. Larger profiles on lower floors enable a more favorable stiffness distribution and improve seismic response. However, excessive increases in cross-section sizes can raise material costs and reduce energy dissipation efficiency during earthquakes.

References

[1] SRPS EN 1998-1:2015, *Eurocode 8: Design of Structures for Earthquake Resistance – Part 1: General Rules, Seismic Actions and Rules for Buildings*, Institute for Standardization of Serbia, Belgrade, 2015.

[2] Fajfar P., *A Nonlinear Analysis Method for Performance-Based Seismic Design*, Earthquake Spectra, Vol. 16, 573–592, 2000.

10th International Congress of the Serbian Society of Mechanics
Niš, Serbia, June 18-20, 2025
M.4.8

Extended abstract

THE INFLUENCE OF THE RADIUS OF CURVATURE ON THE FORCED OSCILLATIONS OF AN ELASTICALLY COUPLED SYSTEM OF TWO DOUBLY CURVED SHALLOW NANO-SHELLS

Marija Stamenković Atanasov[1][0000-0002-1676-9469], Julijana Simonović[1][0000-0002-2330-6948], Ivan Pavlović[1][0000-0003-0062-4342]

[1] Department of Theoretical and Applied Mechanics, Faculty of Mechanical Engineering, University of Niš, A. Medvedeva 14, 18000 Niš, Serbia;
e-mail: marija.stamenkovic.atanasov@masfak.ni.ac.rs, julijana.simonovic@masfak.ni.ac.rs, ivan.pavlovic@masfak.ni.ac.rs;

Abstract:

Coupled nano-shell systems play a crucial role in various medical and nanotechnological applications due to their unique mechanical properties and shape versatility. These systems have the property of surface curvature that can adapt to different locations. The radius of curvature in such systems plays a key role in the amplitudes of oscillations, with all other parameters of the coupled system and periodic excitation being the same. This study examines the forced vibration behaviour of an orthotropic nano-system (Fig. 1), modelled as two elastically connected, doubly curved shallow nano-shells. The nano-shells are simply supported and connected by an elastic layer, which is approximated by the Winkler model of discretely distributed springs of linear stiffness k, acting on the surface of the nano-shells.

We notify the displacements of nano-shells $u_i(x,y,t)$ in direction x, $v_i(x,y,t)$ in direction y, and transversal displacement of nano-shell in direction z is $w_i(x,y,t)$, $i=1,2$, (where 1 denotes the nano-shell 1 and 2 the nano-shell 2)

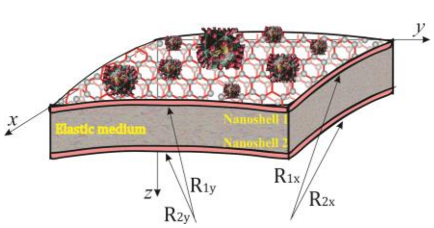

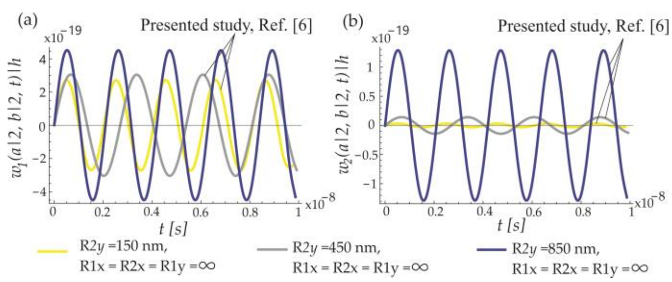

Fig. 1. The double graphene nano-system is composed of two nano-shells and coupled by Winkler-type elastic layer

Fig. 2. Effect of the radii of curvatures on the transverse displacement of nano-system (a) Nano-shell 1; (b) Nano-shell 2

Utilizing the Eringen constitutive elastic relation [1-3] and Novozhilov linear shallow shell theory [4], we derive a system of six coupled nonhomogeneous partial differential equations (PDEs) describing the forced transverse vibrations of the system. The forced vibration analysis is conducted using modal analysis [5].

The coupled nonhomogeneous ordinary differential equations ODEs for the time modes of the transverse vibrations, which describe the forced vibrations of the damped nano-system can be presented in the concise matrix form

$$\mathbf{M}\{\ddot{\mathrm{S}}\}+(\alpha\mathbf{K}+\beta\mathbf{M})\{\dot{\mathrm{S}}\}+\mathbf{K}\{\mathrm{S}\}=\{\mathrm{F}\}, \tag{1}$$

where {S} contains time functions for all displacements u_i, v_i and w_i ($i=1,2$), **M** and **K** are mass and stiffness matrices which contains mass, extensional and bending stiffness, respectively.

Damping is implemented using the assumption of Rayleigh-type proportional damping, defined by the coefficients α and β, i.e. Specifically, the damping matrix is a linear combination of the mass matrix β**M** and the stiffness matrix α**K**, Kelly [5].

We analyse the effects of the one-sided and double-sided curved nano-shells on the transverse displacement for the first three modes in detail. Also, when the parameters of curvatures of nano-shell 1 tends to infinity, the system is reduces to nano-system of an elastically connected nano-plate and a doubly curved shallow nano-shell [6], Fig. 2.

Also, we analyse the effects of several parameters, namely, the nonlocal parameter, coupling strength (stiffness *k),* external excitation, damping proportional coefficients, and the radius of curvature of the nano shells of nano-system in detail. The study reveals how the amplitude of the excited upper nano-element behaves with increasing nonlocal parameter and decreasing radii of curvature of the lower nano-shell, Fig. 2. Additionally, the damping proportional coefficients and external excitation significantly influence the transverse displacements of both nano-elements. Specifically, an increase in damping proportional coefficients reduces the transverse displacements, while an increase in external excitation to the upper nano-element increases them.

This study provides numerical data relating the vibration characteristics of the nano-system to its geometric and material properties. The proposed mathematical model of the nano-systems can be applied in the development of new nano-sensors, which respond to transverse vibrations based on the geometry of the nano-shell elements.

Key words: coupled nano-shells, doubly curved shell, forced vibrations, linear stiffness coupling, nonlocal parameter.

Acknowledgments:

This research was financially supported by the Ministry of Science, Technological Development and Innovation of the Republic of Serbia (Contract No. 451-03-136/2025-03/200109).

References

[1] Eringen, A. C., Edelen, D. G. B. *On nonlocal elasticity*, International Journal of Engineering Science, Vol. 10, 233-248, 1972.
[2] Eringen, A. C. *On differential equations of nonlocal elasticity and solutions of screw dislocation and surface waves*, Journal of Applied Physics, Vol. 54, 4703-4710, 1983.
[3] Eringen, A. C. *Nonlocal continuum field theories,* Springer Science & Business, 2002.
[4] Amabili, M. *Nonlinear vibrations and stability of shells and plates*, New York: Cambridge University Press, 2008.
[5] Kelly, S. G. *Mechanical vibrations: theory and applications*, Cengage learning, 2012.
[6] Atanasov, M. S., Pavlović, I. R., Simonović, J., Borzan, C., Păcurar, A., & Păcurar, R. *Forced Dynamics of Elastically Connected Nano-Plates and Nano-Shells in Winkler-Type Elastic Medium.* Applied Sciences, 15(5), 2765, https://doi.org/10.3390/app15052765, 2025.

10th International Congress of the Serbian Society of Mechanics
Niš, Serbia, June 18-20, 2025

M.4.9

Original Scientific Paper

DOI:10.46793/ICSSM25.384T

CONVERGENCE OF ANALYTICAL-NUMERICAL ALGORITHM FOR INVERSE KINEMATICS OF NIRYO ONE ROBOT

Vuk Todorovic[1], **Nikola Nesic**[2] [0000-0001-6237-4735], and **Srdjan Jovic**[3] [0000-0003-1387-6207]

[1,2,3]University of Pristina in Kosovska Mitrovica, Faculty of Technical Sciences, Serbia
[1]email: vuk.todorovic01@gmail.com
[2]email: nikola.nesic@pr.ac.rs
[3]email: srdjan.jovic@pr.ac.rs

Abstract. In this paper, we analyzed the convergence of an analytical-numerical algorithm (presented in detail in a previous paper by the authors [1]) used to solve the inverse kinematics of a Niryo One robot. The testing procedure involves selecting certain parameters related to the analytical-numerical algorithm and the test itself. Afterward, a set of evenly spaced points in a reduced joint space of the robot was selected so that we could determine the forward kinematics of those known points. As a result, we had a set of possible robot configurations against which we tested whether the analytical-numerical algorithm converges. The convergence was then determined as the ratio of times the analytical-numerical algorithm converged to the total number of trials in the given test procedure. Among the selected parameters is an offset used to reduce the actuation range of each joint during the test, which may cause a significant nonlinear change in the results, hence why we performed the test multiple times while varying this parameter and presented the results in the form of a graph.

Keywords: Inverse Kinematics, Analytical-Numerical Algorithm, Algorithm Convergence, Niryo One.

1. Introduction

The inverse kinematics (IK) problem of an open chain manipulator is a fundamental problem in robot mechanics. It consists of determining the joint angles needed to achieve a specific target configuration of a robot. The inverse of this problem, determining the configuration that can be achieved with a particular set of joint angles, is known as the forward kinematics (FK) problem, which has well-established and reliable methods to solve it. Of particular interest are 6R manipulators, that is, manipulators comprised of six revolute joints. The number of solutions to the IK commonly has more than one real solution for a particular configuration. Primrose [2] proved that an upper bound to the number of real solutions for manipulators with seven revolute joints is 16, which was used by Lee et al. [3] to determine that 6R has the same number of real solutions. Note that this does not consider that some joints on a 6R robot may have a limited range of actuation, which is often the practice case.

The theoretical formulation commonly used for the analysis of robot mechanics is known as screw theory, based on the Mozzi-Chasles theorem [4]. This formulation views all rigid-body motions comprised of a rotation around and a translation along a screw axis. Based on this, there exist two common approaches to solving the IK: *analytical closed form solutions* and *numerical approximate solutions*. Of interest to us are the Paden-Kahan (PK) Subproblems [5, 6, 7]–used for determining an analytical solution to a specific subset of robots based on their geometry and the Newton-Raphson (NR) method [8]–used for nonlinear root-finding; the numerical method used for finding approximate solutions.

In this paper, we will analyze the convergence of an analytical-numerical algorithm (ANA) used to solve the IK of a Niryo One robot manufactured by Niryo Robotics, which was proposed in [1]. The algorithm can find up to eight real solutions, but the effectiveness of the algorithm was not tested in the said paper; instead, only a demonstrative experiment was performed on a real Niryo One robot. Here, our goal is to numerically determine the probability of the proposed algorithm converging to a real solution, such that it is within the robot's range of actuation. Using custom-written Python code [9] and based on the parameters chosen and the sample size, in the best case, the probability was equal to 92.53 %. An interesting nonlinear change in probability was observed when determining the IK near the end of the robot's actuation range, with the most significant cause likely being the nonlinear nature of the NR method. In addition, the testing procedure is general and might prove useful in testing other IK algorithms.

In the next chapter, we briefly summarize the aforementioned algorithm for the IK solution to the Niryo One robot. After that, we will analyze the test performed and its parameters. We end the paper with the results and their discussion.

2. Niryo One Characteristics

Here, we will present only the relevant specifications for the Niryo One robot; the rest are available in [1].

The repeatability of Niryo One is reported to be ± 0.5 mm in [10], although there is no confirmation on the official Niryo Robotics site [11] or in the robot's mechanical specifications [12]

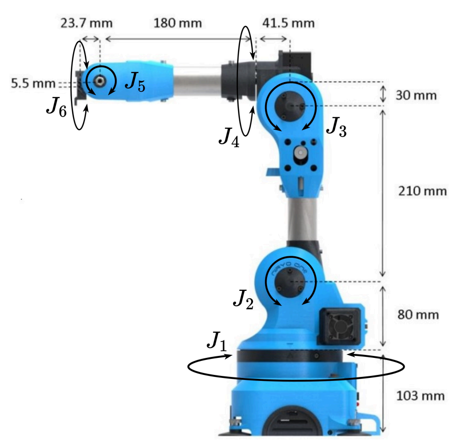

Figure 1: Link lengths, joint location and positive direction of the Niryo One robot, where J_i represents the i-th joint [1]

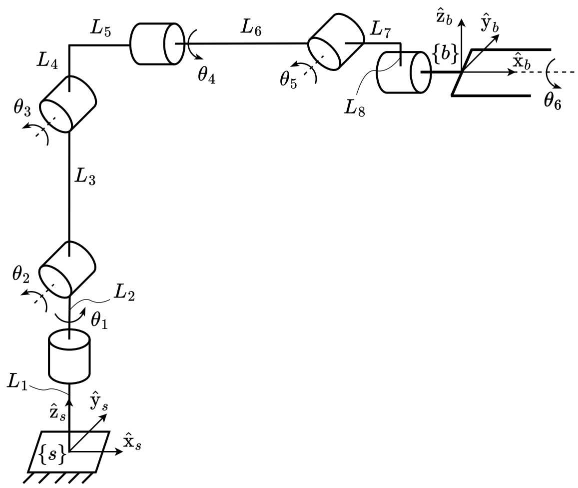

Figure 2: Kinematic model of the Niryo One robot [1]

Joint	Lower limit (rad)	Upper limit (rad)
1	−3.054 326 190 99	3.054 326 190 99
2	−1.910 088 333 38	0.640 012 236 706
3	−1.394 343 539 42	1.570 098 195 09
4	−3.050 137 400 79	3.054 326 190 99
5	−1.745 329 251 99	1.920 036 710 12
6	−2.530 029 283 69	2.530 029 283 69

Table 1: Niryo One's range of actuation rounded to 12 significant digits. The values are obtained from the robot's Raspberry Pi due to their values being at odds with the robot's mechanical specification [12]. The joint numbering corresponds to Figure 1

3. Analytical-Numerical Algorithm for Solving the Inverse Kinematics of the Niryo One Manipulator

The ANA used in [1] to solve the robot's IK consists of two parts:

1. A closed-form analytical solution obtained by approximating one link to zero $L_8 \approx 0$ (see Figure 2) and using the PK subproblems.

2. The final solution as a numerical approximation using the NR method initialized by the analytical solution in the previous step.

A block diagram of the ANA is shown in Figure 3; for details on the PK subproblems and the NR method, see [5, 6] and [8], respectively. The solutions obtained from the algorithm can be represented by a graph, as in Figure 4.

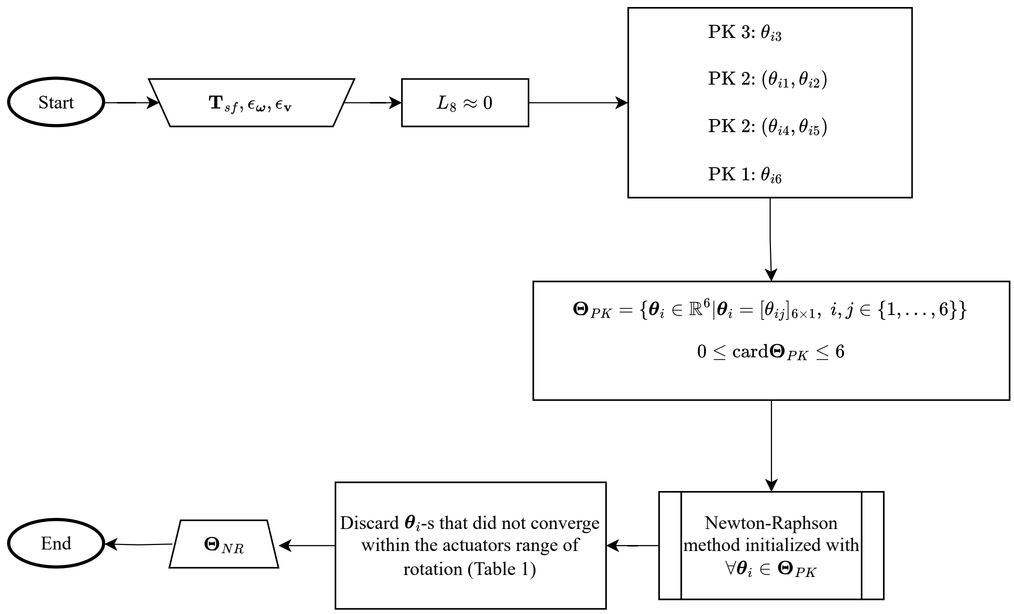

Figure 3: ANA for Niryo One [1], where $\mathbf{T}_{sf}$–desired configuration, ϵ_v–allowed positional error tolerance, ϵ_ω–allowed angular error tolerance, $\mathbf{\Theta}_{PK}$–set of solutions to the analytical part of the algorithm, $\mathbf{\Theta}_{NR}$–set of solutions to the numerical part of the algorithm after discarding solutions that are outside the actuation range specified in Table 1; final solution set

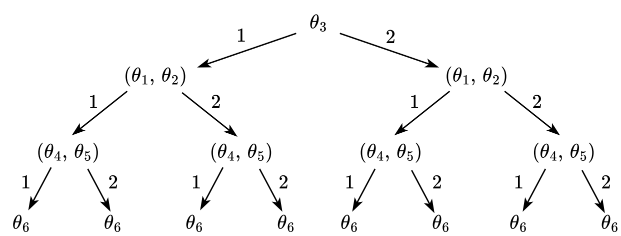

Figure 4: Graf used to represent the analytical solutions with the nodes representing the angle coordinates and branches representing different solution sets [1]

4. Testing and Results

Described in a general sense, we have calculated the IK for many different configurations based on the FK of the robot and then determined the probability of convergence based on the number of times that the ANA converged in those trials.

We start by describing the steps in testing the ANA, after which we will present the results:

Step 1. **Parameter selection:** $\theta_{\text{offset}} > 0$–actuation limit offset, $k \geq 2$–arithmetic progression length, $r \geq 1$–maximum number of iterations of the NR method part of the ANA, $\epsilon_v \geq 0$–allowed positional tolerance for the NR method part of ANA, and $\epsilon_\omega \geq 0$–allowed angular tolerance for the NR method part of ANA.

Step 2. **Reduced actuation range segregation:** Use the intervals for the i-th joint actuation range $[\varphi_{i1},\ \varphi_{i2}]$ (see Table 1) reduced by the actuation limit offset $[\varphi_{i1} + \theta_{\text{offset}},\ \varphi_{i2} - \theta_{\text{offset}}]$ for constructing an arithmetic progression corresponding to each joint with the number of terms being equal to k in each progression:

$$\Phi_i = \{\phi_{i1},\ \ldots,\ \phi_{ik}\}, \tag{1}$$

where

$$\phi_{i1} = \varphi_{i1} + \theta_{\text{offset}}, \quad \phi_{ik} = \varphi_{i2} - \theta_{\text{offset}}, \quad \phi_{ij+1} - \phi_{ij} = \text{const.}, \quad j = 1,\ \ldots,\ k-1.$$

Step 3. **Joint subspace construction:** Build the joint subspace from the arithmetic progression sets from the previous step:

$$\Phi = \Phi_1 \times \cdots \times \Phi_6, \tag{2}$$

where $\times$ denotes the Cartesian product.

Step 4. **Configuration subspace construction:** Determine the configuration space points according to the joint subspace from the previous step:

$$C = \{\mathbf{T}_i \in SE(3) \mid \mathbf{T}_i = FK(\boldsymbol{\phi}_i), \quad \forall \boldsymbol{\phi}_i \in \Phi\}, \tag{3}$$

where $SE(3)$–special Euclidean group, $FK(\boldsymbol{\phi}_i)$–FK equation defined by the product of exponentials formula from screw theory (see [8] and [5] for more details).

Step 5. **Solving the IK:** Calculate the inverse kinematics using the ANA with the parameters r, ϵ_v and ϵ_ω from step 1 and all the elements of the configuration subspace C.

Step 6. **Probability calculation:** Determine the probability of the ANA from converging as the ratio of the number of times the ANA converged in the previous step and the number of configuration points against which we are testing,

$$p = \frac{c}{\operatorname{card}\Phi} \cdot 100\,\% = \left(1 - \frac{d}{\operatorname{card}\Phi}\right) \cdot 100\,\% \tag{4}$$

where p–probability of convergence, $\operatorname{card}\Phi$–cardinality of the set Φ, c–number of times the ANA converges, d–number of times the ANA diverges.

The first step in the test has a significant influence on the results. The offset parameter θ_{offset} is introduced due to unavoidable floating-point arithmetic errors; the algorithm is prone to diverging when the desired configuration causes the robot's actuators to move near the end of their range. It is so important that we simulated several different offset values. The arithmetic progression length k should be as high as possible (its main limitation being memory requirements and execution speed of the hardware) due to it directly influencing the cardinality of the joint subspace Φ,

$$\operatorname{card}\Phi = k^6. \tag{5}$$

Table 2 presents the parameters chosen for our test. Based on this, our sample size equals 117 649. Also of note is that the positional tolerance ϵ_v was chosen based on the robot's repeatability (see Section 2).

The test was performed using the Python programming language, version `3.12.5`. In it, we used the well-established NumPy library [13], version `2.1.1`, and Mehanika robota library [9], version `2025.3.24`. We also used NumPy's double-precision floating points, i.e. `numpy.float64` numbers for all the variables relevant to the computation. The programming code used for the test is shown in Code 1 in the Appendix, while the test results can be seen in Figure 5.

Parameter	Unit	Value
θ_{offset}	rad	$\{0.0005, 0.0255, 0.0505, 0.0755, 0.1005, 0.1255, 0.1505, 0.1755, 0.2005\}$
k	None	7
r	None	20
ϵ_v	m	0.0005
ϵ_ω	rad	0.001

Table 2: Parameters chosen for the test

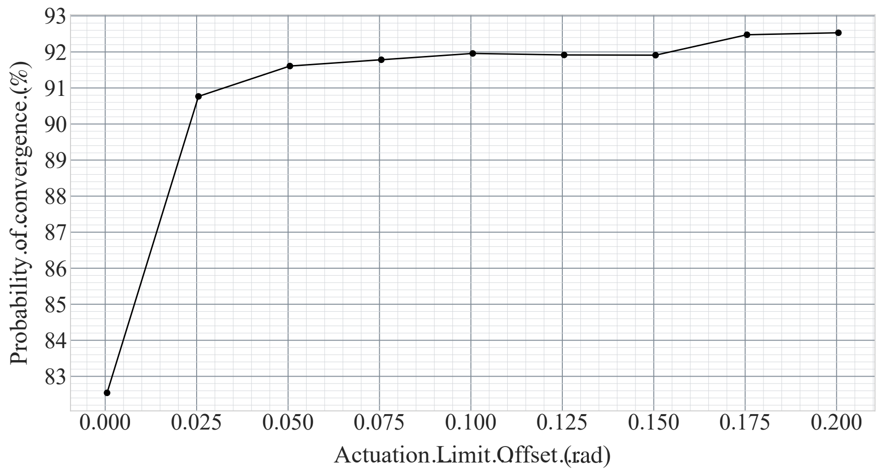

Figure 5: Test results

5. Discussion

Observing Figure 5, we see a notable change in the probability of convergence when applying the ANA to configurations that require the joints to move near the end of their actuation range. In particular, the data are very nonlinear. First, changing drastically, and then it somewhat stabilizes after a few iterations of the actuation limit offset. We conjecture that this is induced by errors during floating-point arithmetic and the nonlinear nature of the equations being solved in the second part of the ANA. More precise results may be possible by expanding to a larger data type (float128, i.e., quadruple-precision format, for instance) or by increasing the number of sample points, i.e., the arithmetic progression length in the first step of the test. Perhaps switching from Python to a lower-level programming language would result in a performance boost in the test.

Nonetheless, the procedure used for the test can help test other algorithms because of its general structure, especially if the first step (parameter selection) is adjusted. The first two parameters can only vary in value, but the rest can be changed as needed by a particular test. Perhaps the only noteworthy change in the test steps might be the way the reduced actuation range segregation is performed. The current method is to split the actuation range relative to the size of the range itself. Perhaps a more suitable approach in some cases might be to have a fixed step while segregating the actuation ranges of each joint and introduce a “step parameter” in the first step.

6. Conclusion

The data show that a probability of convergence of 92.53 % is the best that can be expected from the ANA. For practical purposes that require continuous operation for all possible configurations, this is insufficient. Although it might still be helpful in the educational and academic aspects, the nonlinearity of the probability of convergence for configuration near the end of the joints actuation range might entail more research directions for the IK numerical algorithms.

Also of note is the procedure used for the test to test the ANA. Its a general aspect coupled with some adjustments can be used to test other IK algorithms.

Acknowledgement. This research has been supported by the Serbian Ministry of Science, Technological Development and Innovations research grant No. 451-03-18/2025-03/200155.

Appendix

```
import numpy as np
import mehanika_robota.roboti.niryo_one as n_one

theta_offset = [
    0.0005,
    0.0255,
    0.0505,
    0.0755,
    0.1005,
    0.1255,
    0.1505,
    0.1755,
    0.2005
]

k             = 7
epsilon_v     = 0.5e-3
epsilon_omega = 1e-3

for j in range(len(theta_offset)):
    Phi = np.stack(
        np.meshgrid(*[
            np.linspace(
                n_one.NiryoOne.TETA_OPSEG[str(i + 1) + '_min']
                + theta_offset[j],
                n_one.NiryoOne.TETA_OPSEG[str(i + 1) + '_max']
                - theta_offset[j],
                k,
                dtype=np.float64
            ) for i in range(6)
        ]),
        axis=-1
    ).reshape(-1, 6)

    d = 0
    for i in range(len(Phi)):
```

```python
        try:
            n_one.inv_kin(
                n_one.dir_kin(Phi[i]),
                epsilon_omega,
                epsilon_v
            )
        except n_one.InvKinError:
            d += 1

    np.set_printoptions(precision=16, suppress=True)

    print(
        f'convergence probability = {(len(Phi) - d)/len(Phi)*100:.10f}%\n'
        f'theta_offset: {theta_offset[j]}\n'
    )
```

Code 1: Python code used for the test

References

[1] Todorovic V., Blagojevic M., & Nesic N., *Application of Screw Theory and its Implementation in Python for Controlling a Niryo One Manipulator*, Accepted for publication in Scientific Technical Review 74(2), Military Technical Institute, Serbia, 2025.

[2] Primrose E. J. F., *On the input-output equation of the general 7R-mechanism*, Mechanism and Machine Theory 21(6), 509-510, 1986.

[3] Lee H.Y., & Liang C.G, *A New Vector Theory for the Analysis of Spatial Mechanisms*, Mechanism and Machine Theory 23(3), 209-217, 1988.

[4] Ceccarelli M., *Screw Axis Defined by Giulio Mozzi in 1763 and Early Studies on Helicoidal Motion*, Mechanism and Machine Theory 35(6), 761-770, 2000.

[5] Murray R., Li Z., & Sastry S., *A Mathematical Introduction to Robotic Manipulation*, CRC Press, USA, 1994.

[6] Paden B., *Kinematics and Control of Robot Manipulators*, PhD thesis, Department of Electri-cal Engineering and Computer Sciences, University of California, USA, 1986.

[7] Kahan W., *Lectures on Computational Aspects of Geometry*, Unpublished, 1983.

[8] Lynch K., & Park F., *Modern Robotics: Mechanics, Planning, and Control*, Cambridge Uni-versity Press, UK, 2017.

[9] Todorovic V., url: https://github.com/VuckoT/mehanika_robota, 2024.

[10] Kickstarter Niryo One project, url: https://www.kickstarter.com/projects/niryo/niryo-one-an-open-source-6-axis-robotic-arm-just-f, accessed 10.3.2025.

[11] Niryo Robotics website, url: https://niryo.com, accessed 10.3.2025.

[12] Niryo Robotics, *Niryo One Mechanical Specifications*, 2018.

[13] Oliphant T., url: https://numpy.org, 2005.

List of Reviewers

1. **Cajic Milan,** Research Associate, Department of Mechanics, Mathematical Institute of Serbian Academy of Sciences and Arts, Belgrade, Serbia
2. **Cantrak Djordje,** Full Professor, Department of Hydraulic Machinery and Energy Systems, Faculty of Mechanical Engineering, University of Belgrade
3. **Coric Stanko,** Associate Professor, Department of Engineering Mechanics and Theory of Structures, Faculty of Civil Engineering, University of Belgrade
4. **Cukanovic Dragan,** Associate Professor, Department of Applied Mechanics, Faculty of Technical Sciences, Kosovska Mitrovica
5. **Dosaev Marat,** Full Professor, Institute of Mechanics, Lomonosov Moscow State University, Moscow, Russian Federation
6. **Hedrih Andjelka,** Research Associate, Department of Mechanics, Mathematical Institute of Serbian Academy of Sciences and Arts, Belgrade, Serbia
7. **Ilic Dejan,** Associate Professor, Department of Hydraulic Machinery and Energy Systems, Faculty of Mechanical Engineering, University of Belgrade
8. **Karlicic Danilo,** Research Associate, Department of Mechanics, Mathematical Institute of Serbian Academy of Sciences and Arts, Belgrade, Serbia
9. **Lazarevic Mihailo,** Full Professor, Department of Mechanics, Faculty of Mechanical Engineering, University of Belgrade, Serbia
10. **Manoach Emil,** Full Professor, Institute of Mechanics, Bulgarian Academy of Science, Sophia, Bulgaria
11. **Paunovic Stepa,** Research Associate, Department of Mechanics, Mathematical Institute of Serbian Academy of Sciences and Arts, Belgrade, Serbia
12. **Pavlovic Ivan,** Associate Professor, Department of Mechanics, Faculty of Mechanical Engineering, University of Nis, Serbia
13. **Simonovic Julijana,** Associate Professor, Department of Mechanics, Faculty of Mechanical Engineering, University of Nis, Serbia
14. **Stamenkovic Atanasov Marija,** Teaching Assistant with PhD, Department of Mechanics, Faculty of Mechanical Engineering, University of Nis, Serbia
15. **Stojanovic Sreten,** Full Professor, School of Electrical Engineering, University of Belgrade
16. **Stojanovic Vladimir,** Associate Professor, Department of Mechanics, Faculty of Mechanical Engineering, University of Nis, Serbia
17. **Svorcan Jelena,** Full Professor, Department of Aerospace Engineering, Faculty of Mechanical Engineering, University of Belgrade.

ISBN 978-86-905512-1-7